ORNL-3591
UC-4 – Chemistry
TID-4500 (28th ed.)

REACTOR CHEMISTRY DIVISION
ANNUAL PROGRESS REPORT
FOR PERIOD ENDING JANUARY 31, 1964

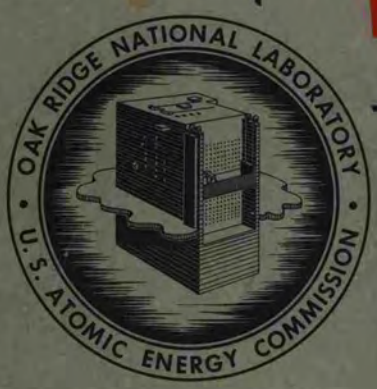

OAK RIDGE NATIONAL LABORATORY
operated by
UNION CARBIDE CORPORATION
for the
U.S. ATOMIC ENERGY COMMISSION

Printed in USA. Price: $3.50 Available from the
Office of Technical Services
U. S. Department of Commerce
Washington 25, D. C.

ORNL-3591
UC-4 – Chemistry
TID-4500 (28th ed.)

Contract No. W-7405-eng-26

REACTOR CHEMISTRY DIVISION ANNUAL PROGRESS REPORT

For Period Ending January 31, 1964

Director

W. R. Grimes

Associate Directors

E. G. Bohlmann
H. F. McDuffie
G. M. Watson

Senior Scientific Advisors

F. F. Blankenship
C. H. Secoy

MAY 1964

OAK RIDGE NATIONAL LABORATORY
Oak Ridge, Tennessee
operated by
UNION CARBIDE CORPORATION
for the
U. S. ATOMIC ENERGY COMMISSION

Summary

PART I. MOLTEN-SALT REACTORS

1. High-Temperature Phase Equilibrium Studies

Investigations of high-temperature phase equilibria were continued for systems having potential use in molten-salt-reactor technology. Much of the phase diagram for the MSRE solvent system, $LiF-BeF_2-ZrF_4$, was described in detail. Investigation of the complex equilibria in the system $LiF-NaF-ZrF_4$ was completed upon determination of crystallization behavior of the ternary compound $LiF \cdot NaF \cdot 4ZrF_4$. The hypothesis that some ten of the sodium fluoride–rare-earth trifluoride systems would approximate the model system $NaF-YF_3$ in crystallization behavior was tested and corroborated. An investigation of the system $KCl-UCl_3$ was initiated as part of an effort to evaluate molten chlorides as fast reactor fuels. Optical and x-ray crystallographic data were obtained for a number of compounds, primarily complex fluorides. A determination of the crystal structure of $6LiF \cdot BeF_2 \cdot ZrF_4$ established the existence of separate BeF_4^{2-} and ZrF_8^{4-} ions in this solid phase. The new compound $XeF_2 \cdot XeF_4$ was isolated and was shown by x-ray diffraction studies to contain discrete XeF_2 and XeF_4 molecules in the crystal. Refinement of the crystal structure of Cr_2F_5 was completed, and the ligand-field distortions caused by its ions were characterized.

2. Radiation Chemistry of the MSR System

Postirradiation examination of the several capsules from three in-pile tests of MSRE fuel-graphite-metal compatibility continues to furnish evidence of evolution of F_2 and CF_4, graphite damage, and other potentially unfavorable phenomena. All cases of unusual behavior, however, seem to be consequences of F_2 generation at low temperatures under conditions which will not normally obtain in MSRE.

Radiolytic formation of F_2 at temperatures below 100°C was observed over a 5-month interval in two capsules that were fitted for sampling of the evolved gases. Fluorine release proceeded at a maximum rate near room temperature ($G = 0.01$ to 0.02 molecule of F_2 per 100 ev absorbed) and decreased to zero rate at −70°C and +80°C. At the low temperature, slow diffusion in the crystals presumably limited the evolution rate, while at high temperatures the back reaction of radiolytic products appeared to be controlling. Deliberate addition of F_2 produced results which confirmed this picture and which demonstrated that F_2 reacts more rapidly with salt which has previously lost most of its F_2 by radiolysis. These observations conclusively eliminated the specter of fluorine generation at reactor operating temperatures. In reactor components such as freeze valves or freeze flanges, and in tanks for storage of irradiated salt, however, the temperature must be kept high enough (200°C seems sufficient) to prevent salt radiolysis.

Chemical analyses of graphite cores from the large capsules of one assembly revealed the presence of appreciable (0.1 to 0.5% by weight) quantities of uranium, as well as molybdenum, lithium, and container metals. Autoradiography, before and after neutron activation, and x radiography of transverse sections of the cores showed that the uranium was present in a 2-mil-thick layer on the surface of the specimens. Neutron activation analyses gave slightly lower results for uranium than obtained by chemical analyses. The deposition of uranium was probably a consequence of fuel radiolysis during reactor shutdowns in the course of the in-pile exposure. To test this conjecture, the design of the current in-pile experiment (47-6) provides for heaters on

each capsule to prevent radiolysis during shutdown.

Salient features of the fluorine generation and recombination processes have been verified with simulated MSRE fuels, and with some of the component fluorides, on exposure to pure gamma, beta, and x radiation.

An INOR-8 capsule containing MSRE salt and graphite was exposed to gamma radiation from a Co^{60} source for ~7400 hr at temperatures ranging from 38 to 150°C. The salt received a calculated 0.45×10^{20} ev hr^{-1} g^{-1}. After an induction period of about 600 hr, fluorine gas was generated at rates (G values) varying between 0.03 to 0.07 molecule of fluorine per 100 ev absorbed at temperatures up to 110°C. At 150°C any fluorine gas which had been generated was recombined. At 130°C recombination rates roughly equaled generation rates. No evidence of any appreciable reaction of the F_2 gas with the graphite to generate CF_4 was obtained.

Experiments to investigate fluorine evolution from studies of behavior of solid MSRE fuel mixtures under fast electron bombardment have yielded values of G_{F_2} as a function of dose up to a total dose of about 1.6×10^{18} Mev per g of salt. At doses below about 8×10^{17} Mev/g, maximums in the fluorine production rates were observed or indicated in each experiment. In one of the experiments exposed to a greater dose, a second increase in fluorine evolution rate was observed after a total dose of about 9 to 10×10^{17} Mev/g. It is observed that reduction of the dose rate by a factor of about 2 causes an increase in the initial rates of fluorine evolution per unit dose (G_{F_2}). The maximum G_{F_2} observed was 0.02. Similar experiments with solid LiF showed that fluorine was not evolved as a result of bombardment with fast electrons but was taken up in small amounts.

Soft x-ray irradiation of a solid mixture similar to the MSRE fuel gave evidence of radiolytic decomposition with yields of volatile fluorine compounds equivalent to G_{F_2} (moles F_2 per 100 ev absorbed) values ranging from 0.0006 to 0.04. In some cases elemental fluorine was identified, but, generally, the products were carbon tetrafluoride and carbonyl fluoride. Prefluorination of the salt removed carbon-containing impurities and encouraged liberation of elemental fluorine. Fine particles liberated volatile fluorine-containing products at about ten times the rate from coarse particles. The compound $6LiF \cdot BeF_2 \cdot ZrF_4$, one of the complex compounds which crystallize from the MSRE fuel, decomposed with an equivalent G_{F_2} of about 0.02. Prefluorinated thorium fluoride liberated elemental fluorine at rates of about 0.005 molecule per 100 ev. Neither lithium nor zirconium fluorides gave any evidence of radiolysis.

3. Chemical Studies in Molten Salts

Observations with sessile drops for the purpose of studying wetting behavior implied that molten fluorides penetrate graphite by capillarity only when the surface tension of the liquid is less than some critical value, which may be as high as 180 dynes/cm. Conversely, melts with high surface tensions, like those for use in the Molten-Salt Reactor Experiment, wetted neither graphite nor metal. The role of oxide at the liquid-solid interface in causing decreasing contact angles was demonstrated.

Moisture removal from specimens of MSRE graphite has been tested under conditions simulating those expected prior to MSRE startup. Very little water was released from the graphite; exposure to moist environments did not cause any water adsorption, and even prior immersion of the specimen in liquid water was ultimately followed by the release of only a very small amount of chemisorbed water. The results of the tests indicate that water contamination from the MSRE graphite will not be serious.

Continuing studies of UO_2 and ZrO_2 behavior in equilibrium with melts simulating mixtures of MSRE fuel salt and flush salt have provided additional evidence that no appreciable formation of $(U\text{-}Zr)O_2$ solid solution occurs in the range 500–700°C. The equilibrium ratio of $[Zr^{4+}]/[U^{4+}]$ in the melt, above which UO_2 was found to dissolve and ZrO_2 was found to precipitate as the only stable oxide phase, was measured in this temperature range as a function of Zr^{4+} concentration in the melt. While there was an increasing temperature dependence at low U^{4+} and Zr^{4+} concentrations, this critical ratio was below the $[Zr^{4+}]/[U^{4+}]$ ratios expected in fuel salt, and in its mixtures with flush salt; that is, a sufficient margin of protection against UO_2 precipitation appears to be afforded by the previously specified ZrF_4 concentration in the MSRE fuel salt.

The equilibrium behavior of the reaction of HF and H_2O with molten $2LiF \cdot BeF_2$ containing oxides has been examined as a means to study further the chemistry of such melts. The equilibration of a stream of H_2 containing small concentrations of HF and H_2O with $2LiF \cdot BeF_2$ solutions was found to be rapid and conveniently measurable. Using melts saturated with BeO, the resulting P^2_{HF}/P_{H_2O} quotient, in combination with literature data for the same reaction involving pure BeF_2, gave γ_{BeF_2} values of 0.16–0.4 in the range 500–700°C. Results for melts saturated with ZrO_2, combined with thermochemical data, gave γ_{ZrF_4} values of ~ 0.02. Similar results and calculation gave γ_{UF_4} values of the same order of magnitude. These are crude estimates of γ_{ZrF_4} and γ_{UF_4}, however, owing to uncertainties in the thermochemical data. Equilibrium data in the literature for the hydrofluorination of UO_2 to UF_4, in combination with the present results, suggest that these γ values are actually near unity. The present observed P^2_{HF}/P_{H_2O} quotients (in atmospheres) in equilibrium with ZrO_2-saturated melts, combined with a previous estimate of the solubility product of ZrO_2, yield the expression

$$[O^{2-}] = 5 \times 10^{-4} \, (P_{H_2O}/P^2_{HF}) \text{ moles/kg} ,$$

relating observed equilibrium P_{H_2O}/P^2_{HF} quotients to the oxide ion concentration of dilute $2LiF \cdot BeF_2$ melts at 600°C.

Measurements of the total uranium concentration and the reducing power in molten $LiF\text{-}BeF_2\text{-}ZrF_4$ systems saturated with UF_3 under reducing conditions have been interpreted to give maximum values for UF_3 solubility in MSRE fuel mixtures at temperatures from 550 to 700°C. The values are somewhat below those expected by analogy with reported results for the solubility of PuF_3 and CeF_3 in fluoride melts.

Measurements of the viscosities of molten fluoride mixtures were made with the use of a rotating-spindle viscometer over the range 475–830°C. Compositions representing the MSRE fuel and coolant mixtures were measured at temperatures between 475 and 600°C and found to have viscosities between 9 and 25 centipoises. The effect of additions of LiF (up to 6.7 mole %) on the viscosity of $LiF\text{-}BeF_2$ mixtures was determined in the range 525–840°C and found to be quite large; decreases in viscosity of up to two orders of magnitude were noted at 700°C. Extension of the measurements to higher concentrations of LiF and to solute cations of higher valence is in progress.

Electroanalytical methods for molten $LiF\text{-}BeF_2$ solutions are being examined as an approach to the analysis of MSRE fuel salt for corrosion-product metal ions, oxide ion, U(IV), and Zr(IV). Stationary electrodes of pyrolytic graphite and platinum have been used, with hot-pressed boron nitride for electrical insulation. Stationary-electrode polarography gave the expected current peaks, proportional to concentration, in the reduction of Fe(II), although the precision was not good ($\sim$13%). Anodic-stripping voltammetry was found to give good precision for both Fe(II) and Ni(II), 3.5 and 1%, respectively.

Chloride salt systems which were studied promise to facilitate the prompt separation of protactinium from irradiated thorium, by a volatilization technique, with the possibility of producing U^{233} of high isotopic purity.

Phase equilibria in the $AlCl_3\text{-}ThCl_4$, $AlCl_3\text{-}ZrCl_4$, and $ThCl_4\text{-}ZrCl_4$ systems have been studied. The solubility of $ThCl_4$ in $AlCl_3$ was indicated to be substantially below 10 mole %. A simple eutectic was indicated in the $AlCl_3\text{-}ZrCl_4$ system. Although the literature implies a two-liquid-phase region at intermediate compositions, this was not found. Appreciable supercooling was observed, however. A brief examination of the $ThCl_4\text{-}ZrCl_4$ system indicated little mutual solubility. It had been speculated that the inclusion of $ZrCl_4$ might enhance the solubility of $ThCl_4$ in $AlCl_3$.

4. Fluoride Salt Production

Raw materials have been purchased and improvements to the fluoride processing facility have been made preparatory to the production of the coolant, flush, and fuel mixtures for operation of the MSRE. As a continuing effort for process development, studies of impurity removal rates and of various process control methods have been made. The use of stronger reducing agents for the removal of structural-metal cations from fluoride mixtures is being investigated, and both beryllium metal and zirconium metal appear promising for this application.

The densification of Li^7F by a combination of heating and HF treatment was confirmed in intermediate-scale apparatus, and preparations were made to apply this treatment to the entire supply of Li^7F raw materials.

The reduction of sulfate to sulfide with beryllium metal may permit the controlled removal of sulfur by $HF\text{-}H_2$ sparging without formation of nickel sulfide, provided the $H_2S\text{-}H_2$ ratio is held below a critical value, known as a function of temperature.

PART II. AQUEOUS REACTORS

5. Chemistry of Pressurized-Water Reactor Systems

In a continuing study of the chemical behavior of the water in the pressurized-water loop of the Oak Ridge Research Reactor, use of a side-stream sampling system which permits the analysis of much larger volumes of water than previously possible has confirmed previous estimates of the low level of water-borne corrosion products and activity. In addition, determination of specific activities, based on the measurable amounts of the parent nuclides removed from these large volumes of water, is now possible. The initial results showed that a burst of active solids at loop startup contained iron of long activation time and was presumably released from in-flux walls. Also present was chromium of short activation time, which presumably was released from out-of-flux walls. Subsequent samples showed decreased specific activities of iron, suggesting that the principal source was out-of-flux deposits. A 260°C test of magnetite (Fe_3O_4) as an adsorbent of soluble iron in loop water showed that all the iron was adsorbed by the Fe_3O_4. The amount of iron involved was very large (equivalent to 1 atom per A^2), which suggests that the adsorbed iron penetrated the Fe_3O_4 lattice. In the same test no appreciable cobalt got by the Fe_3O_4, although only 20% was actually found on the Fe_3O_4. In laboratory tests, a measurement of the solubility of magnetite indicated a value of $4\text{–}9 \times 10^{-8}$ *M* in water which had a room temperature pH of 4.6–4.8.

6. Chemical Support for High-Flux Reactors

The three-year-old program on corrosion of aluminum fuel cladding and the effect of adherent corrosion products on heat transfer in the Advanced Test Reactor and in the High Flux Isotope Reactor was completed. Aluminum alloy 6061 promises adequate corrosion resistance as cladding material for the relatively short-lived fuel elements in both reactors, provided the pH of the cooling water is maintained at 5.0 with nitric acid. Even with this precaution the low thermal conductivity of the adherent corrosion product (Al_2O_3) will cause fuel plate temperatures so high as to make careful design of the fuel elements essential.

Evaluation of materials for use in more permanent regions of the High Flux Isotope Reactor has continued. Coupling of stainless steel to 6061 aluminum causes pitting of the aluminum in the contact or crevice area; pitting is more severe with martensitic than with austenitic stainless steels. As a result of these tests, the aluminum sections will be thickened to allow for the anticipated corrosion. Type 6061 aluminum exposed freely to water with a pH of 5.0 at 100°C shows negligible corrosion, even at flow rates as high as 80 fps. Although QMV beryllium corrodes at about 2 mils/yr and shows a tendency to pit, the beryllium reflector should last its design lifetime. Type 420 stainless steel is subject to cracking and appears unusable in the reactor.

Estimates have been made of the radiolytic decomposition of water and the changes in hydrogen ion concentration which might occur in the primary coolant of the High Flux Isotope Reactor under several possible operating conditions. The expected steady-state concentrations of H_2, H_2O_2, and O_2 are in the neighborhood of 10^{-4} to 10^{-3} *M*, depending on the concentration of excess oxidant and on temperature and power density. It is possible that HO_2 may provide the desired hydrogen ion concentration of 10^{-5} *M*. It is likely that conditions can be maintained in the HFIR under which little or no change in HNO_3 concentration will occur. Additional experiments in the ETR would provide a firmer basis for estimating HNO_3 stability in the HFIR, and the feasibility of making such tests is being explored.

7. Mechanisms of Corrosion of Zirconium Alloys

Studies of zirconium and Zircaloy-2 in high-temperature solutions have used a revised autoclave system in which simultaneous measurements of the dc capacitance and polarization of the electrode can be made. The results of these measurements demonstrated that the products of the corrosion enter quantitatively into formation of the protective film according to the logarithmic relationship, and that the dielectric properties of the oxide are approximately constant during the period investigated.

It was also found that the capacitance was unaffected by the addition of Cu^{2+} as $CuSO_4$ to $[Cu^{2+}] = 6.5 \times 10^{-2}$ *M*. The open-circuit potential increased anodically by 300 mv, demonstrating that Cu^{2+} is an oxidizing agent whose rate of reduction is comparable to that for O_2.

Results previously obtained at long exposure times have been confirmed. The results are consistent with the anion-vacancy mechanism for zirconium corrosion.

The mechanism of radiation corrosion of Zircaloy-2 is being studied by comparing the weight gain and film impedance behavior of irradiated specimens with unirradiated controls during postirradiation exposure to steam-oxygen mixtures at 300°C. Film-free, as-pickled, and prefilmed specimens have been irradiated. Experimental results obtained so far provide evidence that changes produced within the alloy during irradiation lead to acceleration of corrosion. No significant effects of the irradiation on the protective properties of the oxide film have been detected.

8. Physical Chemistry of High-Temperature Aqueous Systems

Electrical conductances of K_2SO_4 and $KHSO_4$ solutions (in H_2O) were measured at temperatures from 0 to 800°C and at pressures from 1 to 4000 bars. By means of the Fuoss-Onsager conductance equation,

$$\Lambda = \Lambda_0 - Sc^{1/2} + Ec \log c + Jc,$$

values of Λ_0 for K_2SO_4 were obtained. At each of several high temperatures the Walden product (viscosity times equivalent conductance) for K_2SO_4 solutions was found to be nearly constant at densities varying from 1.0 to 0.5 g/cm^3. From the measurements on both $KHSO_4$ and K_2SO_4 solutions, the dissociation constant of the bisulfate ion was calculated at 100, 200, and 300°C, at several densities. Above 300°C the constant became too small (less than 10^{-5}) to be evaluated.

By means of a new optical cell, the effects of pressure on liquid-liquid immiscibility for UO_2SO_4-H_2O solutions from 0.28 to 4.53 *m* were extended to 1700 bars at temperatures up to 400°C. All curves of temperature vs pressure were linear to the highest pressure, each having a slope, $\Delta t/\Delta p$, of approximately +0.075°C/bar.

Temperatures between 300 and 410°C for the appearances of critical phenomena (where liquid ≡ vapor) and liquid-liquid immiscibility were determined in the condensed system UO_3-Li_2O-SO_3-D_2O at concentrations of SO_3 from 0.05 to 1.0 *m*. Based on these and previous data, isotherms were drawn to describe boundary limits of liquid-liquid immiscibility, critical phenomena, and appearance of solids in this system.

A double oxide of UO_3 and NiO was synthesized at 300°C in the systems UO_3-NiO-SO_3-H_2O and UO_3-NiO-N_2O_5-H_2O. The new compound, $NiO{\cdot}3UO_3$, was observed to be thermally stable to somewhat above 900°C.

Computer methods for the reduction of data from potentiometric measurements of cation hydrolysis to hydroxyl numbers as a function of pH have been developed. These methods greatly simplify an otherwise tedious and laborious task. These computations permit consistency tests of the data, which may lead to correction of small errors in the concentrations and which verify the manner in which liquid-junction potentials are treated.

The study of Th^{4+} hydrolysis has been extended down to 0°C to aid in the identification of the hydrolysis mechanism. Comparison of the previously reported results at 95°C with a number of possible mechanisms indicates one scheme of three hydrolysis products and three schemes of four hydrolysis products which are consistent with the data. Similar tests of the data at 25 and 0°C, in progress, may indicate which is correct.

A study of the hydrolysis of Fe^{2+} at temperatures up to 200°C has begun. The preliminary results at 95, 150, and 200°C indicate, as has been observed at 25°C, that the principal species formed is $FeOH^+$ and that hydrolytic precipitation greatly limits the range of hydroxyl numbers which can be studied. The tendency of this ion to hydrolyze increases rapidly with temperature; the formation

quotients of $FeOH^+$ are now estimated to be $10^{-7.5}$, $10^{-6.3}$, and $10^{-5.9}$ at 95, 150, and 200°C, respectively.

Isopiestic ratios with reference to NaCl solutions were determined at 152°C for the chlorides of lithium, potassium, cesium, and barium and the sulfates of sodium and magnesium at concentrations above 0.75 *M*. Osmotic coefficients were calculated with the aid of recently published high-temperature vapor pressure data for NaCl. Osmotic coefficients at 152° go through a maximum with increasing concentration, in contrast to the normal monotonic increase at 25°. Lithium chloride behaves as other alkali halides, rather than displaying the anomalous behavior observed at 25°C.

9. Interaction of Water with Particulate Solids

A series of experiments on heats of immersion of thorium dioxide in water at 25°C have disclosed no measurable effect by organic vapor contaminants in the vacuum outgassing system and no measurable effect of prewetting the sample (before outgassing) with either water or concentrated ammonium hydroxide. Mild mechanical agitation of agglomerated thoria reduced the material to a very fine powder, but produced only minor changes in surface area or in total heat of immersion. However, the "slow" portion of the heat of immersion observed with the original material was eliminated.

The determination of an adsorption isotherm for water on thoria yielded a typical type II isotherm showing multilayer adsorption involving both chemical and physical adsorption. Heats of immersion depend markedly on the amount of presorbed water. The heat at completion of a monolayer was only 27% of that for samples with no presorbed water.

A sensitive microbalance has been incorporated into a gravimetric adsorption apparatus for precise study of adsorption and desorption phenomena, as well as for the preparation of samples for calorimetric study. The balance has been found to be subject to a thermomolecular flow error in a rather specific pressure range. Detailed study of this phenomenon has indicated that the error introduced may be minimized, but not eliminated, by careful attention to several experimental details.

Determination of the electrical resistance of water and dilute KCl solutions in a ceramic thoria capillary has disclosed systematic and reproducible effects of the flow of liquid through the capillary.

Vibratory compaction of oxide fuel congeries is an attractive technique for fabricating thorium-based fuel rods. The reported failure of similar fuel compacts through inleakage of water during reactor shutdown and subsequent bursting of the fuel rod on reactor startup led to a study of the permeability of Kilorod fuel and the relationship of this permeability to waterlogging failure. Data from scouting experiments indicate that a combination of electroosmotic forces and transport of fines within typical fuel compacts studied to date would present a problem under reactor operating conditions. The measured permeabilities fall in an intermediate range, which would allow waterlogging through a cladding defect at zero or low power, but allow such slow egress of water upon a sudden rise in fuel element temperature that catastrophic element failure could occur from internal pressure. Continuing studies will attempt to derive the quantitative relation of permeability, surface area, and void fraction to waterlogging susceptibility and failure and to develop techniques to minimize such failure.

PART III. GAS-COOLED REACTORS

10. Diffusion Processes

Thermal transpiration data on argon with Pyrex glass capillaries under several different temperatures can be described by expressions derived on the basis of the "dusty gas" model, a model which considers gas migration in porous media as a transport through localized, uniform agglomerations of giant pseudo-gas molecules. Recently published data at extremely low pressures showed considerable deviations from theory, but have since been explained in terms of the dusty gas model by postulating an accommodation effect.

A prototype gaseous diffusion apparatus has been constructed to investigate intermolecular interactions. Experiments with the gas pair He-Ar over the range 0–120°C, conducted for purposes of calibration, are nearing completion. The results obtained thus far indicate that values of the diffusion coefficient, over the temperature range cited, can be determined with a precision of at least ±3%.

The classical trace-layer technique was employed to determine diffusion coefficients for uranium, protactinium, and thorium in a pyrolytic carbon and porous graphite at temperatures ranging from 1400 to 2300°C. It was found that the diffusion behaviors of the actinides studied were similar. The ratio of diffusion coefficients in a direction parallel to the basal planes of the pyrolytic carbon to those in the perpendicular direction was 380; the associated activation energy, applicable to both directions, was 60.8 kcal/mole. Values of the coefficients ranged from 10^{-7} to 10^{-12} cm^2/sec. Results for a porous graphite fell in between the two sets of values obtained for pyrolytic carbon, with approximately the same activation energy.

Studies of self-diffusion of beryllium in beryllium oxide were continued. Experiments with unirradiated, high-density (97% of theoretical) polycrystalline BeO over the range 1100 to 1800°C were concluded. Self-diffusion coefficients in the unirradiated specimens may be summarized by the equation

$$D = 2.49 \times 10^{-3} \exp(-62.5 \times 10^3/RT)\ cm^2/sec.$$

A diffusion model based on vacancy migration was proposed. The model predicts identical activation energies for diffusion in both *a* and c directions in single crystals and predicts an activation energy of the correct order of magnitude. The model also predicts that the frequency factor in the direction perpendicular to the c axis is about 50% higher than that in the direction parallel to the c axis.

In-pile measurements of self-diffusion at 700°C during irradiation suggest an enhancement of 3 orders of magnitude in the diffusion coefficient for a flux of approximately 10^{13} *nv* (>1 Mev). Measurements on specimens which had been previously irradiated to 5.7×10^{19} *nvt* (>1 Mev) indicated a significant decrease in activation energy and an increase in diffusion rates. Corresponding measurements on specimens irradiated to only 2×10^{19} *nvt* did not show significant changes from the results obtained with the unirradiated specimens. Measurements on unirradiated specimens of lower densities (77.2, 82.5, and 90.2% of theoretical) indicated that diffusion is greatly enhanced with lower densities.

11. Reactivity of Graphite and of Fueled Graphite Spheres with Oxidizing Gases

A 1-in.-diam sphere of Speer Mod-2 graphite was reacted with He-CO_2 and He-H_2O mixtures. The apparent order of the reaction at 975°C was found to be ~0.7 for both CO_2 at 300 to 1650 vpm (parts per million by volume) and H_2O from 100 to 760 vpm. The data suggest that the apparent order of both reactions increases at lower concentrations. Activation energies measured at 110 and 460 vpm of H_2O were found to decrease from ~58 to ~40 kcal/mole as the temperature was increased from 825 to 1025°C. Hydrogen additions retarded the H_2O-graphite reaction.

Various lots of fueled graphite spheres were exposed to a partial pressure of steam of ~730 mm Hg at 800 to 1000°C. The rate of reaction of the fuel body with steam, the rate of production of hydrogen, and the CO/CO_2 ratio in the effluent gases were determined. Similar studies were made using unfueled spheres of Speer Mod-2 and ATJ graphites for comparison with fueled graphite. Reaction rates ranging from 1 to 5 mg g^{-1} hr^{-1} were found at 900°C for the various fueled spheres, excluding a value of ~0.2 found for the one impregnated lot. Activation energies of ~60 kcal/mole were found from 800 to 1000°C for both the unfueled and the fueled graphite spheres. The reaction rate increased with increasing burnoff over the entire range of burnoff experienced. The CO/CO_2 ratio in the effluent gases varied widely.

12. Irradiation Behavior of High-Temperature Fuel Materials

The study of release of fission gas from pyrolytic-carbon-coated carbide fuel particles during irradiation has continued. Duplex and triplex types of coatings on uranium and uranium-thorium carbide particles have been irradiated at temperatures up to 2500°F and heavy-metal burnups up to 20 at. %. The fission-gas release rates were determined by measuring the krypton and xenon isotopes over a range of temperatures and burnups. The fuel was also subjected to a series of thermal cycles, some of which were in the phase transformation range. The condition of the fuel after irradiation was determined by metallographic examination. Postirradiation anneal tests up to

3250°F were performed on the same particles for which fission-gas release rates had been measured during irradiation.

Pyrolytic-carbon-coated UC_2 and $(U,Th)C_2$ particles dispersed in graphite were examined after irradiations at 1500°F. The elements, as $1\frac{1}{2}$-in. spheres, were made with both fueled and unfueled shells. Some were in the form of fuel cylinders sealed in graphite spheres. In general, the spheres remained dimensionally stable and contained no macrocracks. Weight changes were small, and compressive and impact strength was unchanged. Fission product release was low.

Most of the 36 EGCR prototype capsules which have been irradiated and examined have performed satisfactorily. However, eight of these capsules failed in various ways. Detailed examination showed that each of these failures had been associated with, and in most cases was a direct result of, conditions outside those of the EGCR design. Three types of capsule failure, causing a loss of fission gas, were found: severe cladding fractures were a result of stresses caused by expansion of the UO_2 coupled with nitride embrittlement of the cladding; minor cladding fractures occurred at depressions in the cladding, which were caused by a lack of internal support for the cladding; in one case, a pressure transducer fractured. Adverse effects, similar to but less severe than those in the failed capsules, were observed in several of the capsules which performed satisfactorily.

13. Fission-Gas Release from Single-Crystal UO_2

The study of fission-gas release from UO_2 single crystals during irradiation has indicated that burnup and fission rate have a large influence on the gas release rate. Increased fission rate has been observed to retard the escape of fission gas, and the release rate decreases with burnup. The latter effect is possibly caused by irradiation smoothing of the specimen surface. A model has been proposed to explain the high-temperature gas release, based on the concept that a trapping mechanism (rather than diffusion) is the rate-controlling process for escape of fission gas from UO_2.

14. Effect of Radiation on Ceramic Materials

Four types of sintered BeO compacts (two grain sizes and two densities) were irradiated at 100, 650, and 1100°C. Gross damage (fracturing and powdering) and volume expansion decreased with increasing temperature and increased with increasing fast-neutron dose. At 650 and 1100°C, BeO of low density and fine grain size clearly withstood irradiation better than the other three types. The primary manifestation of damage is grain-boundary separation, but considerable transgranular fracture was seen in photomicrographs of large-grained BeO. Irradiated single crystals of BeO show volume increases which decrease with increasing temperature, but which are considerably less than volume increases in compacts similarly irradiated. Optical studies and density measurements of single crystals irradiated at 650 and 1100°C indicate that agglomerates of defects, aligned in planes perpendicular to the c axis, produce a substantial anisotropic crystal expansion beyond that due to the anisotropic lattice expansion. This combined anisotropic expansion, generally believed to produce grain-boundary separation at low temperatures ($\sim$100°C), may also be the dominant mechanism above 650°C.

The temperature and energy of recrystallization of irradiated steatite, forsterite, and lava A are being determined by thermal analysis. A twin-crucible apparatus, which was built, has several-fold greater sensitivity in the temperature range below 600° than the single-crucible apparatus used previously. The recrystallization of irradiated steatite was examined by x-ray and petrographic methods. The annealing of the radiation change in several other ceramic materials is being studied by thermal conductivity measurements.

Equations were derived for calculating elastic constants from the flexural and torsional resonant frequencies of a supported cantilever plate.

15. Special Studies for Gas-Cooled Reactor Program

The neutron flux spectra of the ORR B-9 core position and P-06 poolside irradiation facility were measured. Bare cobalt was used as the thermal flux monitor; cobalt clad in a 40-mil thickness of cadmium was used as the resonance flux monitor; Np^{237} and nickel, each clad in a 40-mil

thickness of cadmium, were used as threshold detectors for the fast flux. The neutron flux above 0.18 Mev was calculated from the nickel and neptunium measurements on the assumptions that all the slowing down is due to hydrogen and that the reactor is infinite and homogeneous.

Twenty-five metals were tested for thermoelectric stability under PBRE conditions. Metals exhibiting 2% or less error in their output against platinum at 420°C after exposure for 141 days at 982°C were Chromel-P, Special Chromel-P, Ni-18Mo, Geminol-N, and Special Alumel.

The radiation stability of CF_4 in prefluorinated nickel cells has been investigated. Radiolytic products are F_2, C_2F_6, and COF_2 with ratios of the latter two dependent on trace oxygen content. A literature survey revealed that SO_2 has a high thermal stability, reacts extensively with graphite at high temperatures, and has not been investigated experimentally for radiolytic damage.

16. Equilibrium Studies in the System ThO_2-UO_2-UO_3

The equilibrium between orthorhombic U_3O_{8-y} and the cubic solid-solution ThO_2-UO_{2+x} has been determined at the oxygen pressure of 1 atm of air over the range from 700 to 1600°C. In addition, portions of the isobaric surface, $P_{O_2} = 0.2$ atm, within the one-phase, cubic solid-solution region have been determined. The boundary composition of the cubic phase at 700°C is very close to $X_{ThO_2} = 0.4$, $X_{UO_3} = 0.267$, $X_{UO_2} = 0.333$, and changes very little with temperature to above 1200°C. At higher temperatures the UO_3 mole fraction (excess oxygen content) increases smoothly as X_{ThO_2} decreases. A maximum oxygen content close to $X_{UO_3} = 0.4$ is reached at about 1525°C, the U_3O_{8-y}-to-UO_{2+x} transition temperature. The mole fraction of ThO_2 reaches zero at this temperature. Compositions of the U_3O_{8-y} phase are in good agreement with the literature.

PART IV. NUCLEAR SAFETY

17. Fission Products Released by Nonnuclear Heating of Fuel Materials

An investigation of the effect of burnup on the release of fission products from aluminum-uranium alloy fuel material in laboratory-scale apparatus showed that the release of iodine and rare gases was much higher from specimens irradiated to 3.2% burnup than from trace-level-irradiated material. Little change in release with increasing irradiation in the range 3.2 to 23.6% burnup was noted, except for cesium, which was released to a greater extent at the highest burnup level.

Present emphasis in research designed to assess the hazards of loss-of-coolant reactor accidents is on the behavior of released fission products, but information on amounts of fission products released from overheated fuels is still being obtained. A recently completed hot-cell facility permitted both types of studies, in addition to tests of a proposed reactor confinement filter system. The distribution of fission products from irradiated aluminum-uranium alloy and clad UO_2 fuel specimens melted in controlled atmospheres was observed, and diffusion tubes were employed to study the effect of filters and other materials on the distribution of activity associated with small particles or in the vapor form.

Iodine released from molten aluminum-uranium alloy fuel was found to deposit much faster on a dry stainless steel surface than on the same material saturated with steam, while the reverse behavior was exhibited by cesium. These observations indicate that cesium iodide was not an important component of the aerosol formed under test conditions. The small amount of condensate recovered in the moist-air experiment contained only about 6% of the released iodine and cesium.

When trace-level-irradiated, stainless-steel-clad UO_2 fuel was melted, a relatively large fraction of the released iodine (35%) and of the tellurium (49%) was found to remain airborne in the dry-air atmosphere of the aerosol tank after an aging period of approximately 1.5 hr. A surprisingly large fraction of the released iodine (19%) was caught on the roughing filter, possibly because of the very low iodine concentrations in the aerosol, and the iodine which passed through the filters was poorly retained on bronze screens and in charcoal traps, indicating that a part of the iodine was not in the molecular form.

Particle-size studies were performed by collecting particles on a specially prepared grid of an electrostatic precipitator, on filters, and on the walls of diffusion tubes. Particles remaining in the aerosol after the aging period in the aluminum-uranium alloy melting experiments ranged in size

from about 0.015 to 3 μ. About 95% of the iodine reaching the filters, representing 17% of the iodine originally in the fuel, was found to be in the molecular form, according to its deposition rate in the diffusion tube; the other 5%, representing 1.0% of the fuel inventory, was associated with particles about 26 A in diameter. No evidence of the presence of cesium iodide in the aerosol was found in the diffusion tube data.

Particles produced on melting stainless-steel-clad UO_2 ranged from about 0.01 to 2 μ in diameter; some of the larger particles that were shaped like wafers were identified as FeO. Diffusion tube data indicated a more complicated particle spectrum in the aged aerosol reaching the filters than was observed in the aluminum-uranium alloy experiments. Iodine was associated with particles of 12 (molecular), 24, and 108 A in diameter, carrying approximately 80, 15, and 5%, respectively, of the airborne iodine.

Unclad miniature UO_2 fuel pins, arranged in a seven-pin cluster with the center pin irradiated at the tracer level, were melted in purified helium by use of tungsten resistance rods in order to simulate nuclear heating (center of the fuel hotter than the outside) and reactor core melting conditions with the outside fuel rods cooler than those in the center. Two experiments of this type showed that the release of fission products from these arrangements was approximately one-half that found in previously reported tests, where single unclad UO_2 fuel pins were melted. The third assembly which used the seven-pin cluster arrangement was constructed so that the helium sweep gas traversed a path providing longer and closer contact with the shields and base plate before leaving the furnace. The amount of volatile fission products transported to the filter in this experiment was less by a factor of 10 than in the other two cluster experiments, where a direct gas path was available.

18. Fission Products Released During In-Pile Destruction of Reactor Fuels

In-pile experiments are being continued in the Oak Ridge Research Reactor (ORR) to study the characteristics and behavior of fission products released by melting or vaporizing miniature stainless-steel-clad UO_2 fuel elements in a helium atmosphere or by burning pyrolytic-carbon-coated UC_2–graphite fuel elements in air.

Studies have been made of the effects of gas velocity on fission product release and behavior, of the fine-particle and vapor forms of released fission products, of the particulate material collected by filters, of the distribution of released fission products, and of the fractionation of fission products.

In the experiments in which pyrolytic-carbon-coated uranium carbide–graphite fuel was burned in air in the ORR, a large fraction of less volatile fission products was retained in the unburned fuel. The release of Sr, Zr, Ba, Ce, and U from the high-temperature zone of the furnace was very low, but large fractions of I, Te, and Cs were released. Forty percent of the ruthenium was released from the furnace in one experiment and 5.7% in the other. The side of the fuel specimen with the least amount of uranium carbide burned preferentially, indicating that the graphite matrix oxidized more rapidly than the pyrolytic-carbon-coated fuel particles. This belief was also supported by discovery of undamaged fuel particles that fell away from the burning fuel specimen.

In experiments performed to study the effect of helium flow rate on fission product release, the flow was increased sixfold over that employed in previous experiments, with other conditions remaining unchanged. The increased helium flow rate lowered the maximum temperature of the fuel. At a given temperature, release of fission products generally from the fuel itself and release of the more volatile isotopes, I, Te, and Cs, from the high-temperature zone of the furnace did not appear to be affected by an increased flow rate, but release of the less volatile isotopes from the furnace increased fourfold with the sixfold increase in flow rate. The diffusion tube deposit indicated that fission products occurred in the vapor form in the experiment with the highest flow rate, rather than as particles with an average diameter of about 25 A, which were observed in the other experiments.

The distribution of released fission products and uranium deposited from a gas flowing laminarly through a diffusion tube was analyzed to yield information about vapors, gas-borne particles in the range of 10 to 100 A in diameter, and the amounts of released material associated with these forms. In most of the experiments the data indicate that particles having an average diameter of

about 25 A were released. Considerable amounts of released I^{131}, Te^{132}, and Cs^{137} are always carried by these fine particles. Smaller amounts of released Sr^{89} and Ba^{140} always, of uranium frequently, and of Ru^{106} infrequently are carried by these particles in the UO_2 melting experiments, but these substances did not appear to be carried by particles of this size in the uranium carbide–graphite burning experiments. In the case of the UO_2 melting experiments, Zr^{95} and Ce^{144} are very seldom carried by particles of this size, but they are usually carried by these particles in the uranium carbide–graphite burning experiments. Besides being carried by these small particles, the various fission products and uranium are probably also carried by larger particles which pass through the diffusion tube and are retained on the filters.

In the experiment with the highest gas flow rate, considerable amounts of released I^{131}, Sr^{89}, and Ba^{140} and smaller amounts of Te^{132} and Cs^{137} were carried as vapors. However, only small amounts of Zr^{95}, Ce^{144}, Ru^{106}, and uranium are carried as vapors. The appearance of vapor forms of these materials at higher gas velocities could be caused by their more rapid transport from the release site and their greater dilution, both of which would reduce the tendency for particle formation.

The sweep gas from the in-pile fuel melting and burning experiments is passed through a series of filters to obtain information about the particulate material which is formed. Most of the filters, especially those initially encountered by the gas stream, have been too radioactive for electron microscopy, but data on a few filters have been obtained. Particles ranging in size from 0.015 to over 1 μ occurred downstream from the initial filter in the UO_2 melting experiments. Median particle diameters ranged from 0.01 to 5 μ in the corresponding filters in the uranium carbide–graphite burning experiments. In the UO_2 experiments agglomerates of like-sized particles and particles of various densities were observed. In some cases particles were spheres and in others they appear to be platelets.

The distribution of the released fission products and uranium between the various parts of the in-pile fuel destruction assemblies is determined by radiochemical and chemical analysis. In a typical experiment, 60 to 90% of the more volatile fission products, I, Te, and Cs, escaped from the high-temperature zone of the furnace and were distributed more or less evenly between the cold stainless steel enclosure of the furnace, the diffusion tube, and the roughing filter. A Gelman HV-70 filter collected about 3% of the inventory of iodine and cesium. Approximately 3% of the iodine, 4% of the cesium, and less than 0.5% of the tellurium were found downstream of the HV-70 filter. Four percent of the ruthenium escaped from the hot zone, and half of that was stopped by the HV-70 filter. Most of the remainder was found on the membrane filter or its support. The other fission products (Sr, Ba, Zr, and Ce) and uranium were released from the hot zone in amounts of 1% or less. Not more than 0.25% of the inventory of these materials was found downstream of the HV-70 filter. The filters exhibited a rather low percentage of effectiveness against the materials which arrived at their faces, but the materials which penetrated were very small fractions of the total inventory.

In fission product release experiments, fission products appear in varying proportions in various locations, and sample compositions are in general different from those predicted for normal fission yields. This fractionation occurs because differences in the physical and chemical characteristics of individual fission products result in differences in their behavior in release, transport, or deposition processes. Fractionation of fission products is expected to occur similarly in reactor accidents.

A study was made in which the fractionation predicted by several different models was compared with experimental results. The vapor transpiration model, in which fractionation is brought about by evaporation of the fission products from the fuel and by their removal by a carrier-gas stream, gives the most satisfactory agreement with the data from the in-pile fission product release experiments. The theory predicts a straight line when certain ratios of fission products are plotted against each other on log-log coordinates. The theory, with information from the literature on vapor pressures of fission product materials and experimental data on the amounts vaporized, was used to predict successfully the proportions of fission products in various experimental samples. This appears to validate the assumptions of the model and to identify the mechanism of fractionation. The heats of vaporization and thus the chemical forms of the fission products during

vaporization are also identified in the same operation. In most of the experiments with stainless-steel-clad UO_2, the Sr, Ba, and Zr were vaporized in the metallic form; however, in one they were in the oxide form.

19. Release of Fission Products During Melting of Fuels Under Transient Reactor Conditions

Two experiments performed in the TREAT reactor simulated accidents that could occur during the startup of a new reactor, where the only fission products available for release are those due to fissions that occur during a very short period just prior to fuel failure. Reactor periods of 108 and 87 msec, with integrated reactor power of 320 and 328 Mwsec, respectively, were used in these experiments. In the first experiment, the stainless steel cladding melted and the UO_2 temperature rose above 2600°C, but the sample did not melt. The outside diameter of the pellets increased 2%. Approximately 65% of the UO_2 specimen melted in the second experiment, the outer diameter of the unmelted portion of the specimen increased 18%, and 10% of the UO_2 flowed out of the unmelted pellet shell. Meaningful samples of the released aerosols were collected, and particle-size distributions were obtained. Fission product release under the conditions of these experiments was shown to be related to the physical characteristics of precursor species present while the fuel was at or near its maximum temperature. Furthermore, it was determined that the release from the high-temperature zone was less than 2% for isotopes that did not have volatile precursors.

20. Behavior of Radioiodine

An investigation was made of the origin, identity, and behavior of iodine compounds which appear when air and iodine vapor are mixed. Information is needed on these points in order to design radioiodine removal systems. Rates of deposition of iodine compounds were measured by use of successive diffusion tubes having surfaces of silver, rubber, and activated carbon. Elemental iodine deposited on the silver with its characteristic diffusion coefficient of about 0.08 cm^2/sec; a compound or group of compounds deposited on the rubber to give an indicated diffusion coefficient of about 0.05 cm^2/sec, suggestive of a molecular weight of the order of 300 or higher; other iodine materials deposited on the activated carbon to yield a diffusion coefficient of 0.10 cm^2/sec, implying a molecular weight somewhat lower than that of I_2. This behavior was typical of iodine from two greatly differing sources. As the iodine concentration in air decreased, the proportion of iodine present in forms other than molecular iodine increased.

The sorption characteristics of fission products are of significance in predicting their deposition behavior in flowing gas systems. The adsorption of iodine on commonly used stainless steels has been explored with metal temperatures ranging from 24 to 700°C and with iodine vapor concentrations varying from 0.0004 to 2200 mg/m^3. Iodine vapor was found to react chemically with stainless steel surfaces to form metal iodides. The capacity of the surface varied with the condition of the adsorbing surface. Passivity towards iodine adsorption was frequently observed after a small amount of material was sorbed. The kinetics of the chemisorption process also varied, apparently with changing surface conditions, even during the course of a single experiment. The iodine sources used were analyzed for forms other than I_2. Methyl iodide was found, but it constituted less than 0.1% of the total iodine. Fractional sublimation of the iodine sources in vacuum ensured that only I_2 was used in the adsorption experiments.

Charcoal traps remove molecular iodine from gases with a high degree of efficiency, but they are susceptible to destruction when exposed to oxidizing gases at high temperatures, conditions which could conceivably exist in a reactor accident. Preliminary experiments to explore alternate trapping materials indicated that a bed of platinized alumina (a hydroforming catalyst) would serve only to delay the passage of iodine when the bed is exposed to flowing air at temperatures above 400°C. Trapping of radioiodine by high-temperature exchange with nonradioactive iodine in a bed of potassium iodide appears to be feasible up to temperatures at which significant oxidation of the inorganic iodine occurs (600°C or higher).

21. Fission Product Retention in Reactor Confinement Systems

A combination of filters and charcoal traps, proposed for use in the confinement system of the

Oak Ridge Research Reactor, was tested in the Hot-Cell Confinement Mockup Facility and in the laboratory using irradiated uranium-aluminum alloy specimens as the source of fission product aerosols. A minimum efficiency of 99.97% for retention of radioiodine and an efficiency greater than 99.99% for retention of particulate matter were found with aerosols produced in normal air and in a steam-air mixture.

A method of characterizing radioactive aerosols by use of a series of uniform fibrous filters has been developed. The distribution of radioactive particles in the fibers is interpreted in terms of the three main mechanisms of filtration, which are diffusion, interception, and inertial impaction. A description of experiments using a radioactive test aerosol containing Zn^{65} particles 20 to 300 A in diameter, and conducted at linear velocities of 0.4 to 88 fpm, and an analysis of the data in the diffusion region were reported previously.

The data obtained at flow rates of 10 to 88 fpm (interceptional and impaction regions) have been analyzed in terms of theories of fiber filtration. These experiments were conducted with filter mats having a volume fraction of fibers well above the region treated theoretically. Extrapolation of theoretically predicted curves yielded fiber efficiencies not in agreement with those obtained experimentally, making it difficult to estimate particle sizes accurately in the higher flow range. Experiments in which the volume fraction of fibers was lowered to less than 0.1 have been completed, and analysis of the data is in progress. It is believed that these data can be treated according to a theory of filtration to characterize particle sizes more accurately in this flow region.

Certain intrinsic processes which tend to limit or attenuate the escape of fission products have not been fully utilized in predicting the consequences of a nuclear-reactor accident. Theoretical analyses of two such processes were performed to determine whether the attenuation effects are of sufficient magnitude to warrant further investigation or to warrant possible consideration in containment system design.

A study was made of the process of diffusional deposition of particles in containment vessel leaks. Particles containing significant amounts of hazardous fission products will be produced during a nuclear reactor accident. Viscous flow equations were combined with equations for the penetration of particles through diffusion channels to give expressions relating decontamination factor with leak dimension; two leak geometries were considered: cylindrical and thin rectangular. The decontamination factor was found to be a strong function of both leak dimension and particle size, increasing as either decreases. Calculated decontamination factors of 50 and higher were obtained for particles 2 μ and less in diameter if leaks corresponding to 10^{-6} cm^3/sec, as measured under accident conditions, are eliminated.

A theoretical study was made of particle agglomeration and its effect on the penetration of filter systems in dual containment systems by fission products carried by particulate matter. A simplified model was analyzed in which the particulate matter was assumed to be pure iodine, and all particles with diameters less than 0.3 μ were assumed to penetrate the filters. It was shown that agglomeration would occur rapidly enough that the particles, even though initially much smaller, would reach a 0.3-μ size in a short time ($<$20 min for typical water reactor systems). This time is directly proportional to the containment volume and inversely proportional to the power level. Assuming that the filter efficiency of the secondary-containment sweep-gas filtration system is zero for particles less than 0.3 μ in diameter, the fraction of the core activity released to the atmosphere during that time was calculated for some conditions of interest. For one reactor system treated, less than 10^{-5} of the iodine available would be released. It was shown that conditions existing during a reactor accident could not be as pessimistic as those of this model.

Studies of the behavior of iodine in activated charcoal systems are continuing in support of the NS "Savannah" program. Additional tests indicated that variation in composition of the iodine vapor source was the most probable cause of several cases of abnormal iodine penetration of charcoal beds observed earlier in small-scale laboratory tests. Mass spectrometric analysis indicated the presence of trace quantities of HI, ICl, CH_3I, and two unidentified masses, in addition to molecular iodine. Diffusion channel analysis indicated diffusion coefficients in air of 0.10 cm^2/sec, representative of low-molecular-weight compounds such as HI or CH_3I, and 0.08 cm^2/sec, probably representative of I_2.

The effectiveness of activated charcoal for removing the volatile compounds of iodine was studied. Moisture in a room-temperature system

lowers the effectiveness of charcoal for iodine compounds, but this effect diminishes at temperatures around 100°C. Whetlerite charcoal produces efficiencies of >99.9% for removal of iodine compounds in the presence of moisture at 100°C.

In-place testing of the activated charcoal units in the reactor compartment ventilation system of the ship is continuing. A total of 16 normal iodine tests (I^{127}) and 8 radioactive tests (I^{131}) on the new charcoal units installed in March–April 1963 indicate that satisfactory performance of these units can be expected.

PART V. OTHER ORNL PROGRAMS

22. Corrosion Studies for Chemical Reprocessing Plants

Evaluation of materials for use in the Transuranium Processing Facility has continued. Addition of 1 *M* HNO_3 reduces the corrosiveness of 3 *M* HCl to Hastelloy C at 43°C by an order of magnitude, but the addition of 0.1 *M* HNO_3 is not beneficial. Hastelloy C does not corrode in solutions of mono-2-ethylhexylphenylphosphonic acid in diethylbenzene or Alamine 336 chloride in diethylbenzene. Zircaloy-2 can withstand mixed solutions of nitric and hydrochloric acids at 43°C with low corrosion rates and with no evidence of hydride formation. Zircaloy-2 shows similar behavior in boiling 6 *M* HNO_3 solutions containing up to 0.5 *M* HCl, but in boiling 6 *M* HCl solutions containing up to 0.5 *M* HNO_3 corrosion at rates up to 20 mils/yr picks up significant amounts of hydrogen. Zircaloy-4 is not better than Zircaloy-2 in most process solutions and is much worse in boiling 6 *M* HCl. Tantalum platings on Hastelloy and stainless steel showed negligible corrosion in hot hydrochloric acid solutions, but an adherent bond between plate and base metal was not maintained in one case.

23. Chemical Support for Saline Water Program

Determinations were made of the solubilities of metastable $CaSO_4 \cdot 2H_2O$ at 40 and 60°C, of metastable $CaSO_4 \cdot \frac{1}{2}H_2O$ at 125°C, and of $CaSO_4$ (anhydrite) at 125, 150, 175, and 200°C in NaCl-H_2O solutions varying from 0 to 4 *m* in NaCl. These data agreed with Debye-Hückel theory at all temperatures and over a wide range of concentration when a function of the ionic strength (I), $I^{1/2}/(1 + 1.5\, I^{1/2})$, was used. Thermodynamic values for the reaction $CaSO_4 \cdot XH_2O(\text{solid}) \rightleftharpoons Ca^{2+} + SO_4^{2-} + XH_2O$, in H_2O solution, were calculated.

The work on aluminum corrosion in saline water has emphasized studies in 1 *M* NaCl at 150°C. In general, aluminum in this environment has shown the expected similarity to its behavior in high-purity water. Thus, solution pH and the replacement or relative-area effect have been shown to be major variables. Of 11 commercially available alloys tested, the low content magnesium and/or manganese are most promising.

24. Solvents for Fluoride Volatility Process

The search for high-capacity solvents for use in the Fluoride Volatility Process for recovering uranium from aluminum-based reactor fuels was continued. Partially completed investigations of the ternary systems LiF-KF-AlF_3 and KF-ZrF_4-AlF_3 suggest that the latter system has great potential for processing uranium-aluminum alloys. Use of a three-step process makes possible dissolution of approximately 26 mole % AlF_3 at temperatures below 600°C.

25. SNAP-8 Chemistry Studies: The Chemistry of Hydrogen-NaK Systems

The fate of the hydrogen entering the circulating NaK of the SNAP-8 reactor primary coolant circuit from the zirconium-uranium hydride fuel elements depends on the rates of hydrogen diffusion through the primary system walls and on factors governing hydrogen solubility in NaK. Data on such phenomena are important to the operation of the system. The diffusion of hydrogen through metal walls in upstream contact with NaK might differ from diffusion of the gas in the absence of NaK. Measurements of the effect of dissolution of hydrogen in NaK on subsequent diffusion rates have been initiated. Reasonable permeability values for Hastelloy N (INOR-8) were obtained at temperatures up to 550°C. No particular effect of NaK was evident at these temperatures.

An apparatus for the determination of the solubility of hydrogen in NaK at low pressures has been designed and fabricated.

26. Effects of Radiation and Heat on Organic Materials

A dosimeter that consists of a dilute solution of $C_{10}H_{22}$ and $C_2H_2Cl_4$ in C_8F_{16} with water slightly in excess of saturation has been calibrated for measuring the gamma field in a nuclear reactor.

Cross links are induced in polystyrene at a rate of 1 link per 3280 ev of gamma radiation absorbed from a Co^{60} source or per 1420 ev received from mixed radiation from the ORNL Graphite Reactor. Fast neutrons produce considerably larger yields of H_2, CH_4, and C_6H_6 from polystyrene than do gamma rays; the yield of free radicals that are stable at room temperature is independent of the type of radiation absorbed.

Liquid-phase pyrolyses of chromatographically pure biphenyl were performed at 422, 438, and 446°C for times up to 50 hr with the biphenyl decomposition limited to less than 1.5%. The first-order decomposition process is described by the specific rate constant, $1.2 \times 10^{-12} \exp(-62{,}000/RT)$ hr^{-1}. The initial products consisted essentially entirely of hydrogen, benzene, terphenyls, and quaterphenyls in amounts which were consistent with simple stoichiometry. The effects of increased surface area, of changes in the type of surface, of added oxygen and water, and of added deuterium were determined, and some information about the mechanism of the pyrolysis reaction was obtained.

27. Preparation of Pure Materials

The techniques for preparing single crystals of lithium fluoride by a modified Stockbarger method were developed until the total cationic impurity level was reduced to less than 1 ppm, and the procedure was standardized in order to prepare a series of crystals having differing ratios of Li^6 to Li^7. Results of measurements of the low-temperature thermal conductivity of crystals prepared by this technique (measurements at another laboratory) were reported to permit significant inferences relating isotopic composition to phonon scattering.

Zone refining was tested as a means of purifying lithium fluoride from cationic impurities such as manganese, calcium, magnesium, and sodium. Single-pass vertical-tube experiments gave results which indicated that the separation coefficient for manganese was significantly larger than those for the other ions. A preliminary investigation of the phase diagram of the system $LiF\text{-}MnF_2$ did not reveal a basis for an explanation of the behavior of manganese. An automatic, two-zone, apparatus for obtaining more accurate determinations of separation coefficients was constructed.

Vacuum volatilization proved to be useful for the purification of LiF, KF, AlF_3, and ZrF_4. Products with low oxide content were obtained; in the case of KF, because KOH is volatile, a pretreatment of the melt with a fluoride salt which formed an insoluble, nonvolatile, oxide prevented the contamination of the product with KOH.

Studies were concluded of the production of pure $Be(OH)_2$ via solvent extraction of beryllium acetylacetonate, BeX_2, and ultimate precipitation of the hydroxide from aqueous solution by means of ammonia. Quantitative expressions were developed for the variation of the important extraction system parameters with solution composition at 25°C; the kinetics of the process were studied, and the reaction

$$BeX^+ + H^+ \rightarrow Be^{2+} + HX$$

was shown to be the rate-controlling step in the hydrolysis of BeX_2; a quantitative treatment was developed for the decontamination of beryllium from other metallic impurities which form stable species with complexing agents such as EDTA; the efficacy of the process was demonstrated by the purification of beryllium which had been deliberately contaminated with 1000 ppm each of soluble salts of Na^+, Mg^{2+}, B(III), Cu^{2+}, Al^{3+}, Fe^{3+}, and Cr^{3+}. Four batches of product, each equivalent to 500 g of BeO, were produced, in 85% yield, by precipitation upon treatment of a nitrate solution at 75°C with ammonia gas; the total content of all metallic impurities present in measurable amounts was less than 5 ppm.

28. Chemical Support for the Controlled Thermonuclear Program

Improvements in vacuum technology were achieved as a result of several research efforts. Use of a time-of-flight mass spectrometer permitted the analysis of organic fragments from various commercially available vacuum pump oils and changes in the specifications for oils to be used in the

forepumps and roughing pumps in large thermonuclear test systems. Very high compression ratios for hydrogen were measured by the use of two diffusion pumps in series; it appears possible to reach lower ultimate pressures by the series technique. Adsorption and desorption of contaminant gases from metal surfaces at liquid nitrogen temperatures and under conditions of low fractional surface coverage have been studied, and the heats of desorption have been measured in an ultrahigh-vacuum facility having a test volume of almost 300 liters; knowledge of these heats permits more effective removal of the contaminant gases via a temperature cycling process. Acceptance tests for high-vacuum valves were developed, and a metallurgical basis for the selection of bakeable flange-gasket combinations was discovered.

Studies of the behavior of high-vacuum ionization gages led to diagnostic procedures for determining whether a particular gage is operating reliably. Suspicion was focused on thoriated iridium filaments as the source of previously unexplained amounts of CO_2 as a residual gas in ultrahigh vacuum systems; reaction of the filament with organic contaminant gases is believed to give rise to the CO_2.

Synthetic samples of β-eucryptite ($LiAlSiO_4$) were obtained and were studied as sources of lithium ions at high temperature.

Contents

PART II. AQUEOUS REACTORS

PART IV. NUCLEAR SAFETY

PART V. OTHER ORNL PROGRAMS

Part I
Molten-Salt Reactors

1. High-Temperature Phase Equilibrium Studies

PHASE EQUILIBRIA AMONG THE FLUORIDES

R. E. Thoma H. Insley[1] C. F. Weaver[3]
J. H. Burns T. N. McVay[2] G. M. Hebert

Experimental studies of many fluoride systems which have potential use in molten-salt-reactor technology have been continued. The data from which phase diagrams have been derived were obtained from thermal-gradient-quenching experiments, thermal analyses of melts (using both heating and cooling cycles), and visual observations of phase changes produced by heating and cooling.[4] In samples from all experiments, the solid phases were identified by use of the polarizing light microscope and the x-ray diffractometer. The crystal structures of new compounds isolated in the course of these studies have been determined with single-crystal x-ray diffraction techniques.

Fuel System for the Molten-Salt Reactor Experiment

The ORNL Molten-Salt Reactor Program has from its inception in 1956 been aimed at demonstration of a thermal reactor, capable of development into a breeder, which would serve as an economical stationary power producer. Good neutron economy has, therefore, been one of its important goals, and low capture cross section for thermal neutrons has been among the requirements of components of the fuel system. The LiF-BeF_2 system (with separated Li^7) was chosen as the fuel (and blanket) solvent as soon as it was demonstrated that suitably melting UF_4- and ThF_4-containing mixtures could be provided. The NaF-BeF_2 system, whose solvent properties are similarly useful, has also been studied. Its neutron economy is appreciably poorer, but it might compete as a one-region converter fuel if the (unknown) costs of fuel reprocessing proved so high that throwaway of a cheap fuel solvent was required.

Complete phase diagrams, determined either at ORNL or at Mound Laboratory, are now available for all of the limiting binary and ternary systems involved in the LiF-BeF_2-ThF_4-UF_4 and NaF-BeF_2-ThF_4-UF_4 systems.[5-16]

The fuel system for the MSRE has recently been simplified by omission of ThF_4 from the initial loading; it has proved necessary, however, to include a sufficient amount of ZrF_4 to ensure that any oxide precipitate that might occur would be ZrO_2 rather than UO_2. The fuel composition for

[1]Consultant, National Bureau of Standards (retired).

[2]Consultant, University of Alabama (retired).

[3]At present on leave at University of California, Berkeley.

[4]H. A. Friedman, G. M. Hebert, and R. E. Thoma, *Thermal Analysis and Gradient Quenching Apparatus and Techniques for the Investigation of Fused Salt Phase Equilibria*, ORNL-3373 (Dec. 18, 1962).

[5]C. J. Barton *et al.*, *J. Am. Ceram. Soc.* **41**, 63 (1958).

[6]R. E. Thoma *et al.*, *J. Phys. Chem.* **63**, 1266 (1959).

[7]D. M. Roy, R. Roy, and E. F. Osborn, *J. Am. Ceram. Soc.* **36**, 185 (1953).

[8]D. M. Roy, R. Roy, and E. F. Osborn, *J. Am. Ceram. Soc.* **37**, 300 (1954).

[9]L. V. Jones *et al.*, *J. Am. Ceram. Soc.* **45**, 79 (1962).

[10]R. E. Thoma *et al.*, *J. Phys. Chem.* **64**, 865 (1960).

[11]C. F. Weaver *et al.*, *J. Am. Ceram. Soc.* **44**, 1461 (1961).

[12]C. F. Weaver *et al.*, *J. Am. Ceram. Soc.* **43**, 213 (1960).

[13]R. E. Thoma *et al.*, *J. Am. Ceram. Soc.* **46**, 37 (1963).

[14]J. F. Eichelberger *et al.*, *J. Am. Ceram. Soc.* **46**, 279 (1963).

[15]R. E. Thoma *et al.*, to be published in *Nuclear Science and Engineering*.

[16]C. F. Weaver *et al.*, *Phase Equilibria in Molten Salt Breeder Reactor Fuels. I — The System LiF-BeF_2-UF_4-ThF_4*, ORNL-2896 (Dec. 27, 1960).

first operation in the MSRE will be about (in mole %) 65 LiF, 29 BeF_2, 5 ZrF_4, and 1 UF_4. A study has been made of the crystallization reactions which occur as LiF-BeF_2-ZrF_4-UF_4 mixtures of this and similar compositions are cooled slowly. The solid phase $2LiF \cdot BeF_2$ begins to crystallize at temperatures near 435°C; $7LiF \cdot 6UF_4$ also begins to crystallize below 416°C. Complete equilibrium seldom prevails throughout the crystallization process; the usual cooling paths involve a glassing of the BeF_2-rich liquids that are low melting and thus are the last to freeze. Crystals of pure BeF_2 are generally not found, but the last liquid to solidify forms glasses which incorporate variable amounts of the phases listed above.

Determination of the phase diagram (Fig. 1.1) for the system LiF-BeF_2-ZrF_4 is nearing completion. Invariant equilibrium points, insofar as they are known, are listed in Table 1.1. Equilibria in the subsystem BeF_2-$2LiF \cdot ZrF_4$-ZrF_4 have proved to be the most difficult to determine quantitatively, since (1) it is very difficult to remove minor amounts of contaminant oxides from viscous BeF_2 mixtures and (2) crystalline BeF_2 is often nucleated very slowly from mixtures in which it is the principal component.

A strange phenomenon has been observed in mixtures of BeF_2-ZrF_4 and in LiF-BeF_2-ZrF_4 mixtures containing <15 mole % LiF at temperatures as much as 200°C above the liquidus. Globules

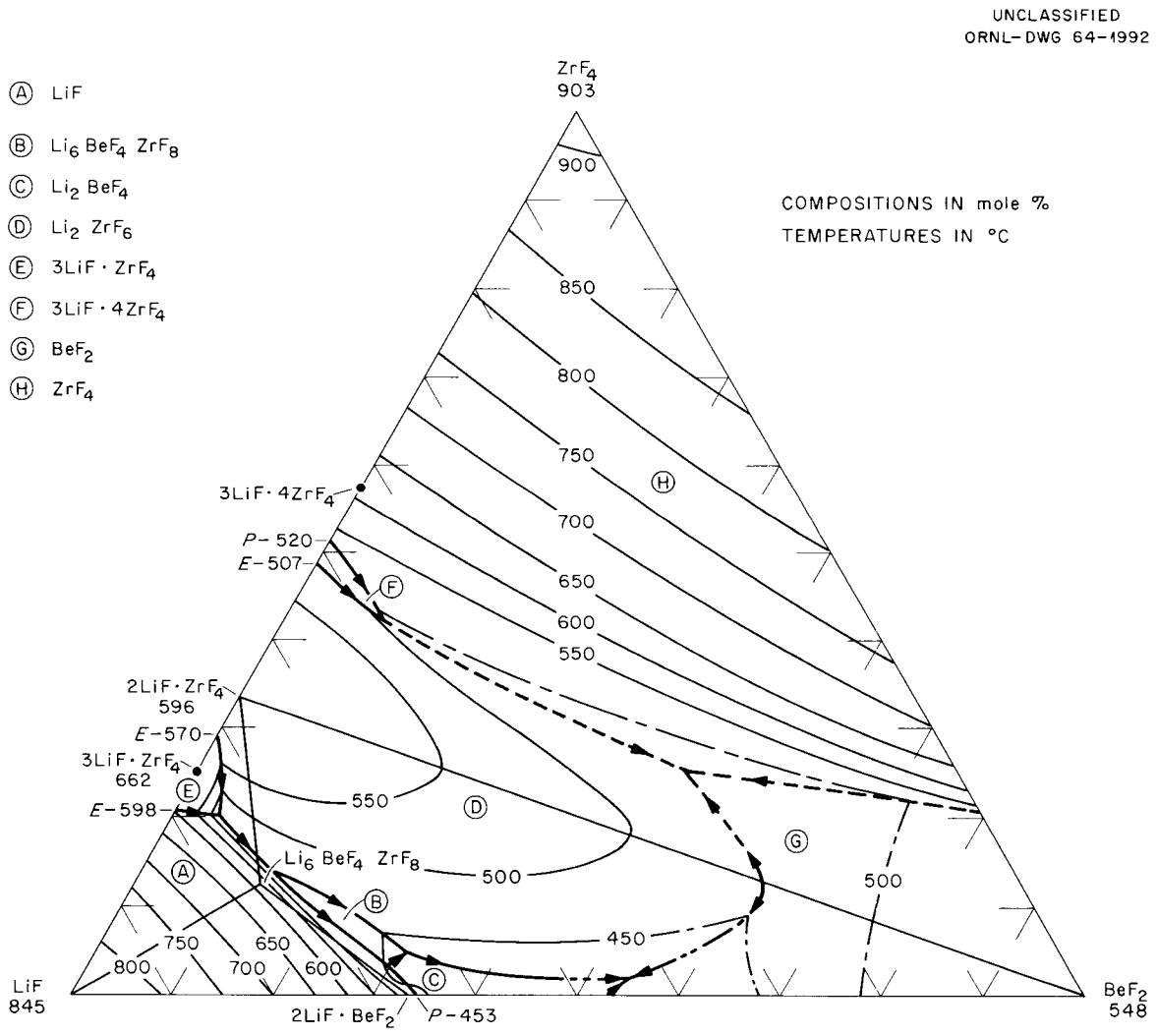

Fig. 1.1. The System LiF-BeF_2-ZrF_4.

Table 1.1. Invariant Equilibria in the System $LiF-BeF_2-ZrF_4$

Composition (mole %)			Temperature (°C)	Type of Equilibrium	Solids Present at Invariant Temperature
LiF	BeF_2	ZrF_4			
75	5	20	~480	Peritectic	β-$3LiF \cdot ZrF_4$, LiF, $2LiF \cdot ZrF_4$
73	13	14	470	Peritectic	LiF, $2LiF \cdot ZrF_4$, $Li_6BeF_4ZrF_8$
67	29.5	3.5	445	Peritectic	LiF, $2LiF \cdot BeF_2$, $Li_6BeF_4ZrF_8$
64.5	30.5	5	428	Peritectic	$2LiF \cdot BeF_2$, $2LiF \cdot ZrF_4$, $Li_6BeF_4ZrF_8$
48	10	42	530	Peritectic	$2LiF \cdot ZrF_4$, $3LiF \cdot 4ZrF_4$, ZrF_4
44	54	2	~360	Eutectic	$2LiF \cdot BeF_2$, BeF_2, $2LiF \cdot ZrF_4$
27	48	25	~460	Eutectic	$2LiF \cdot ZrF_4$, BeF_2, ZrF_4

coalesce on the bottom of vessels containing these mixtures; as the temperature is increased, the globules gradually enlarge and rise to the surface of the liquid as gas bubbles, presumably as a vapor rich in ZrF_4. The assumption that the globules are vapor pockets at all times is unsatisfactory, because the quenched melts appear to contain two kinds of glassy particles (Fig. 1.2), as though two immiscible liquids were preserved by the rapid freezing process.

The System $LiF-NaF-ZrF_4$

Recent determinations of the modes in which the ternary compound $LiF \cdot NaF \cdot 4ZrF_4$ crystallizes from molten mixtures of the components have brought the long investigation of the system $LiF-NaF-ZrF_4$ to a close. The liquidus surface and the solid state equilibria along several of the sections involving two solids are believed to be quantitatively defined. Composition-temperature equilibria have been established from the liquidus to about 400° for the subsystems $LiF-3NaF \cdot ZrF_4$, $3LiF \cdot ZrF_4-3NaF \cdot ZrF_4$, $2LiF \cdot ZrF_4-7NaF \cdot 6ZrF_4$, and $3LiF \cdot 4ZrF_4-3NaF \cdot 4ZrF_4$. Invariant equilibrium reactions occur at the compositions and temperatures given in Table 1.2. Only qualitative information about solid state equilibria elsewhere in the system can be given, since ineffectiveness of our optical and x-ray identification methods in detecting minor quantities of a phase exsolved from a major quantity of a similar one precludes quantitative observations. A typical solid state boundary which has not been described in detail is that involving $3NaF \cdot ZrF_4$ as a host. More than half the sodium sites in this phase can be occupied by lithium ions along the section $3NaF \cdot ZrF_4-3LiF \cdot ZrF_4$. In addition, partial solubility takes place between $3NaF \cdot ZrF_4$ and $5NaF \cdot 2ZrF_4$. The compound $3NaF \cdot ZrF_4$, therefore, becomes the composition apex of a solid solution volume, the equilibrium boundary of which is not amenable to accurate determination using conventional identification methods.

The unique capacity of the system $LiF-NaF-ZrF_4$ for containing large amounts of ZrF_4 in solution at temperatures below 550°C is well known and has been used extensively in reprocessing zirconium-matrix fuel elements.[17–19] The completed phase diagram of the system (Fig. 1.3) shows that the equilibrium solubility is even higher than had been inferred on the basis of all previous experiments.

Complex Compounds of Sodium Fluoride with Rare-Earth Trifluorides

Phase behavior in the $NaF-YF_3$ system has recently been described in detail.[20] Two stable

[17] S. Lawroski (ed.), "Fused-Salt Processing," *Reactor Fuel Processing* 2(3) 18–19 (1959).

[18] *Chem. Technol. Div. Ann. Progr. Rept. June 30, 1962*, ORNL-3314, p. 39.

[19] *Chem. Technol. Div. Ann. Progr. Rept. May 31, 1963*, ORNL-3452, p. 26.

[20] R. E. Thoma, G. M. Hebert, H. Insley, and C. F. Weaver, *Inorg. Chem.* 2, 1005 (1963).

UNCLASSIFIED
PHOTO 61296

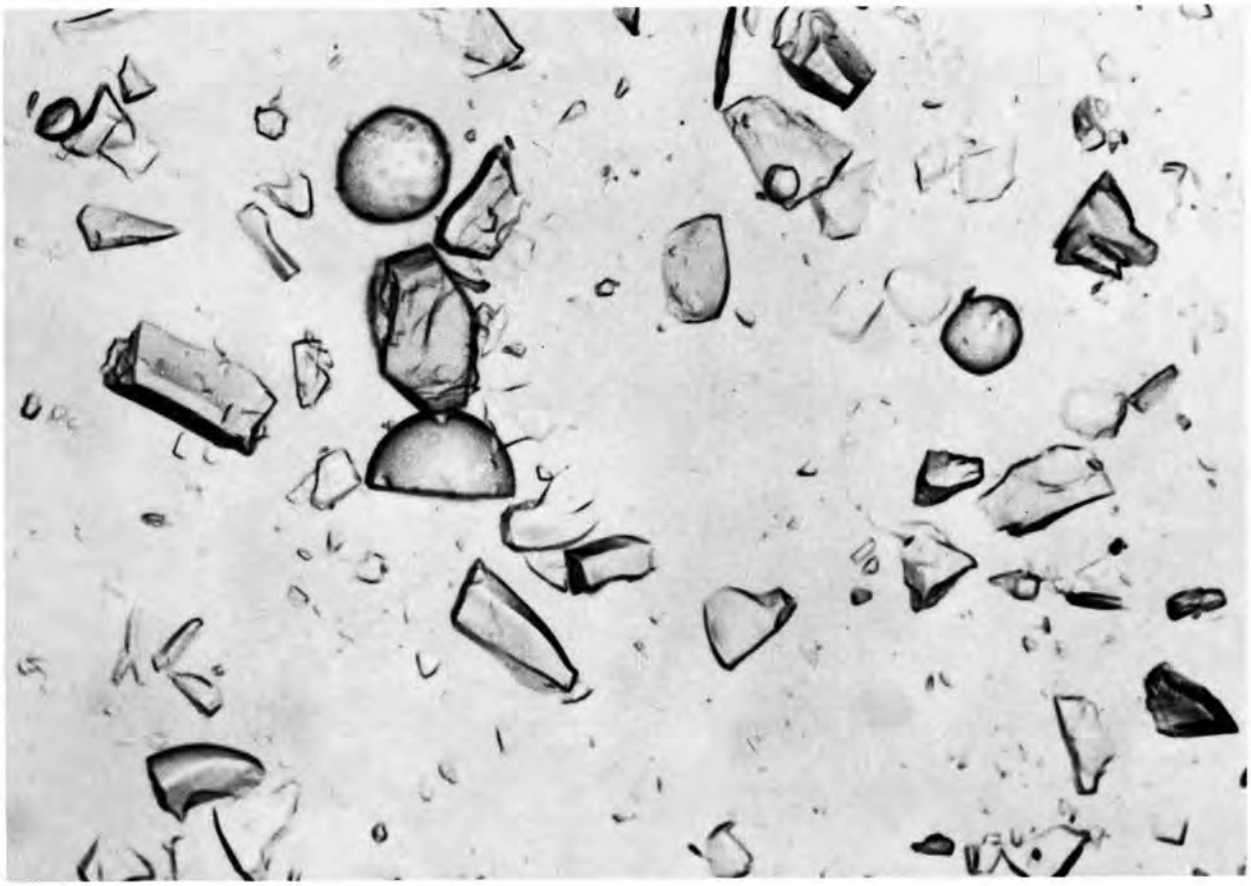

Fig. 1.2. Droplets Formed at 820°C, Broken Away from Occluding Conjugate Liquid in a Quenched Sample of ZrF_4-BeF_2-LiF (60-30-10 mole %). 100×.

Table 1.2. Invariant Equilibria in the System LiF-NaF-ZrF_4

Composition (mole %)			Temperature (°C)	Type of Equilibrium	Solids Present at Invariant Temperature
LiF	NaF	ZrF_4			
37	52	11	598	Eutectic	NaF, LiF, $3NaF \cdot ZrF_4$
55	22	23	572	Eutectic	α-$3LiF \cdot ZrF_4$, $3NaF \cdot ZrF_4$ss, LiF
42	29	29	460	Peritectic	β-$3LiF \cdot ZrF_4$, $3NaF \cdot ZrF_4$ss, $2LiF \cdot ZrF_4$
30	37	33	437	Peritectic	$3NaF \cdot ZrF_4$, α-$5NaF \cdot 2ZrF_4$ss, $2LiF \cdot ZrF_4$
27	38	35	430	Peritectic	$2NaF \cdot ZrF_4$, α-$5NaF \cdot 2ZrF_4$ss, $2LiF \cdot ZrF_4$
26	37	37	425	Eutectic	$2NaF \cdot ZrF_4$, $7NaF \cdot 6ZrF_4$, $2LiF \cdot ZrF_4$
30.5	24	45.5	449	Eutectic	$7NaF \cdot 6ZrF_4$, $3NaF \cdot 4ZrF_4$ss, $2LiF \cdot ZrF_4$
4	41	55	514	Peritectic	$3NaF \cdot 4ZrF_4$ss, $LiF \cdot NaF \cdot 4ZrF_4$, ZrF_4
41.5	8.5	50	466	Peritectic	$3LiF \cdot 4ZrF_4$ss, ZrF_4, $LiF \cdot NaF \cdot 4ZrF_4$

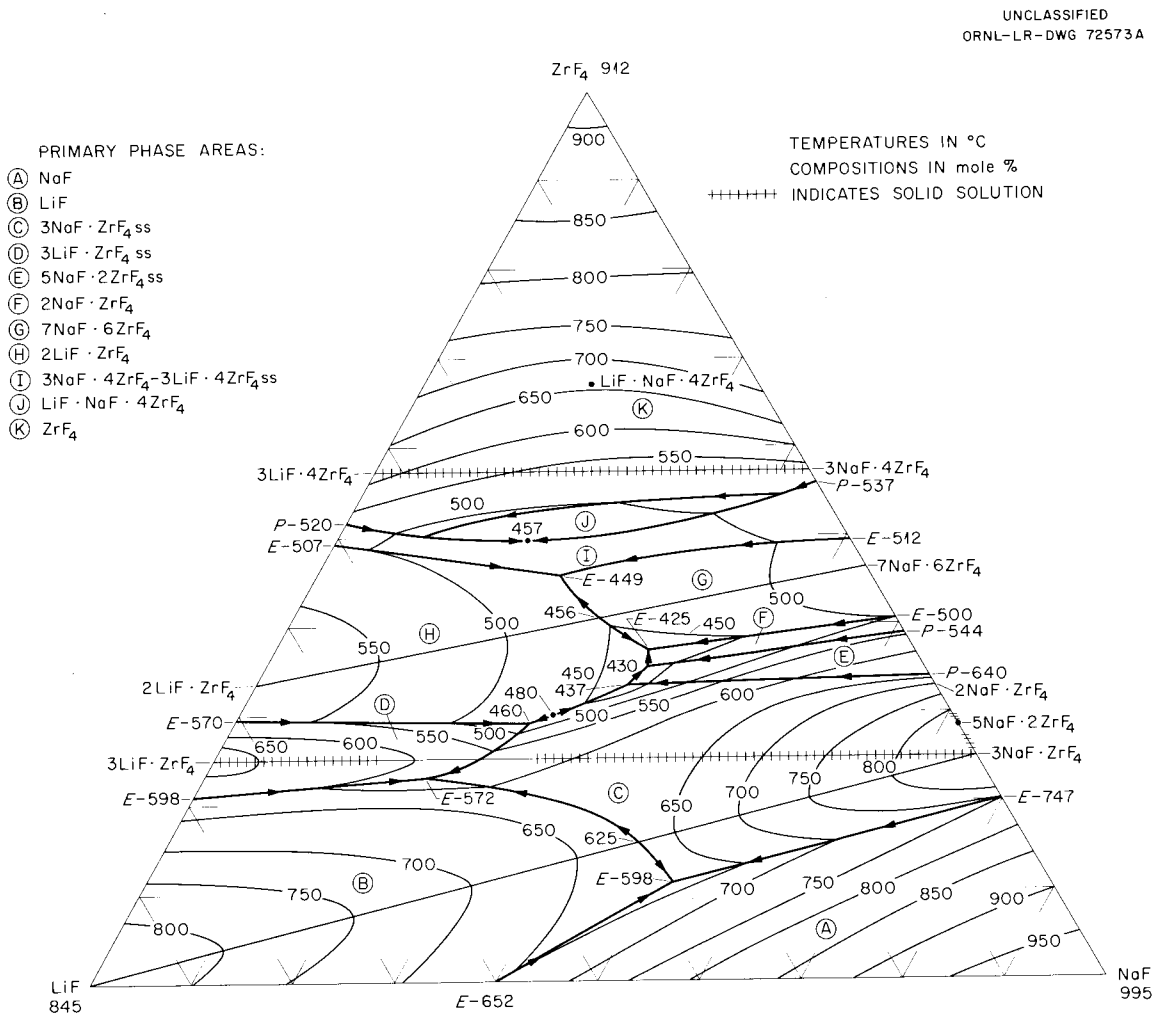

Fig. 1.3. The System LiF-NaF-ZrF_4.

complex compounds $NaF \cdot YF_3$ and $5NaF \cdot 9YF_3$ occur in this system; each of these exists in two polymorphic forms. The higher-temperature form in each case is fluorite cubic, and these cubic phases form a continuous solid solution. Pure crystals of $NaF \cdot YF_3$ invert below 691°C to a hexagonal form, while cubic $5NaF \cdot 9YF_3$ inverts below 710°C to an ordered (perhaps tetragonal) form of this material.

The ratio of cation radii Na^+/M^{3+} lies between 1.02 and 1.21 where M^{3+} is elements 62 through 71 (samarium through lutecium), while the ratio is 1.11 where M^{3+} is Y^{3+}. The trifluorides of elements 62 through 71 are isomorphous with orthorhombic[21] YF_3. It was speculated,[20] accordingly, that behavior of these rare earths with NaF would be similar to that observed for YF_3. This prediction has been shown to be generally true by a nearly completed experimental study of the several systems.

The binary systems of NaF with the entire lanthanide series fall into two classes. The trifluorides of the lighter rare earths, lanthanum, cerium, and praseodymium, form with NaF a single intermediate crystal phase, the hexagonal $NaF \cdot MF_3$ compound, which melts incongruently to MF_3 and liquid. The heavier group, SmF_3 to

[21] A. Zalkin and D. H. Templeton, *J. Am. Chem. Soc.* **75**, 2453 (1953).

LuF_3, shows with NaF the cubic and hexagonal phases of $NaF \cdot MF_3$ and the cubic $5NaF \cdot 9MF_3$ phase in behavior very similar to that of YF_3. Curiously, similar behavior is also shown by NdF_3 (atomic number 60, radius ratio Na^+/Nd^{3+} = 0.99) even though no orthorhomic form of NdF_3 has been observed. The trifluoride of promethium (atomic number 61), which has not been studied, should also behave as does YF_3.

Unit-cell dimensions and refractive indices (see Table 1.3) obtained to date for the complex compounds vary monotonically with the radius of the M^{3+} ion. The optical properties and lattice constants for the cubic and hexagonal crystal phases $NaSmF_4$ to $NaLuF_4$ varied from about 5.60 to 5.40 A, while the hexagonal lattice constants of $NaLaF_4$ to $NaLuF_4$ ranged from a = 6.17 to a = 5.80 A, and c = 3.80 to c = 3.40 A, respectively. The minor variance in crystallographic properties and phase behavior through this series of NaF-based systems suggests that corresponding similarity in such properties may be expected through the other corresponding alkali fluoride–rare-earth trifluoride binary systems.

It appears that alkali and lanthanide cations substitute (to degrees which vary with the disparity in size) randomly for each other in these three crystalline structures. When the disparity

Table 1.3. Lattice Constants and Refractive Indices for $NaF-MF_3$ Compounds

M	Na^+/M^{3+} Radius Ratio	Lattice Constants					Refractive Indices			
		Hexagonal 1:1			Cubic 1:1	Cubic 5:9	Hexagonal 1:1		Cubic 1:1	Cubic 5:9
		a_0	c_0	$\rho^{(a)}$			N_ω	N_ϵ		
La	0.93	6.182	3.793	4.72	*b*	*b*	1.486	1.500	*b*	*b*
Ce	0.95	6.130	3.737	4.90	*b*	*b*	1.493	1.514	*b*	*b*
Pr	0.96	c	c	c	*b*	*b*	1.494	1.516	*b*	*b*
Nd	0.99	6.095	3.729	5.05	5.655	5.67	c	c	c	1.518
Pm	1.00	c	c	c	c	c	c	c	c	c
Sm	1.02	6.065	3.640	5.36	c	5.617	1.492	1.516	c	1.510
Eu	1.04	c	c	c	c	c	c	c	c	c
Gd	1.05	6.012	3.614	5.64	c	5.597	1.482	1.507	c	1.496
Tb	1.09	c	c	c	c	c	c	c	c	c
Dy	1.11	5.980	3.563	5.90	c	5.550	1.487	1.509	c	1.497
Y	1.11	5.95	3.52	4.34	5.447	5.530	1.464	1.486	1.430	1.470
Ho	1.12	c	c	c	c	c	c	c	c	c
Er	1.15	5.960	3.496	6.17	c	5.514	1.482	1.504	c	1.492
Tm	1.16	c	c	c	c	c	c	c	c	c
Yb	1.18	c	c	c	5.420	5.480	c	c	c	1.490
Lu	1.21	c	c	c	5.428	c	c	c	1.432	1.484
U	1.29	6.167	3.77	5.92	c	c	1.552	1.564	*b*	*b*
Pu	1.32	6.117	3.746	6.13	c	c	1.523	1.552	*b*	*b*

[a] Calculated density.

[b] No compound observed.

[c] Data not available.

in radius is great, the structure(s) with partial ordering of the ions tend to be favored.

Initially, it appeared that the hexagonal structure adopted by the low-temperature modification of $NaYF_4$ was isostructural[22] with β_2-Na_2ThF_6, described by Zachariasen[23] as hexagonal, space group $P32$, with one formula weight per cell. This conclusion suggested that the hexagonal phases expected throughout the sodium fluoride–lanthanide trifluoride systems (as well as those in the sodium fluoride–actinide trifluoride systems) were describable by the same space group. Among the compounds which Zachariasen considered isomorphous with β_2-Na_2ThF_6 were $NaLaF_4$ and $NaCeF_4$.[23] He proposed that the unit cell of the lanthanide complex compounds contains $\frac{3}{2}$ formula weights with the sites for fluoride ions unchanged but that the Na^+ and La^{3+} ions occupy sites corresponding to the Na^+ sites in β_2-Na_2ThF_6 in a statistical manner. We have prepared and examined single-crystal specimens of these three compounds as well as several other hexagonal phases of formula $NaMF_4$, where M = yttrium or a lanthanide element. The unit-cell dimensions are included in Table 1.3, and the space groups are presented in Table 1.4. These data show that these similar compounds are not all isostructural. A complete structure determination on $NaNdF_4$ is in progress, and the remaining rare-earth compounds of this series will be examined for isomorphism.

An interesting feature of the x-ray photographs of all these compounds (except β_2-Na_2ThF_6) is the presence of diffuse streaks which result from the disorder described by Zachariasen but not previously observed directly. Rows of sharp spots on the films are interleaved halfway by diffuse streaks perpendicular to the c axis. Such streaks are characteristic of stacking disorder in crystals; in the present case, this results from random occupancy of cation sites by Na^+ and the M^{3+} ions. The details of this disorder will be investigated further once the $NaNdF_4$ structure is known.

Table 1.4. Space-Group Symmetries of $NaMF_4$ Compounds

Space Group $P6_3$ or $P6_3/m$	Space Group $P6$, $P\bar{6}$, or $P6/m$
$NaYF_4$	$NaLaF_4$
$NaSmF_4$	$NaCeF_4$
	$NaNdF_4$
	$NaErF_4$
	β_2-Na_2ThF_6 [a]

[a]Not distinguishable from $P32$ because the thorium atom dominates the scattering.

CHLORIDES AS FAST REACTOR FUELS

H. A. Friedman R. E. Thoma

Fluoride mixtures, while suitable as fuels for molten-salt thermal reactors, moderate much too efficiently for use as fuels in fast reactors. If the physical properties of isotopically separated molten chloride mixtures meet the usual design requirements for salt reactors (i.e., possess high heat-transfer coefficients, low viscosity, and low vapor pressure at operating temperatures, and are chemically compatible with construction metals), then chloride core fluids may be developed for a molten-salt fast breeder reactor.[24] Such a reactor, which has received some preliminary attention in eastern Europe,[25] would almost certainly require core fluids containing 30 to 55 at. % heavy metals, ranging from 5 : 1 mixtures of plutonium : uranium to one containing wholly plutonium as the heavy metal. Liquidus temperatures should probably not exceed 500 to 550°C, because of temperature limits on metal equipment.

Uranium tetrachloride should be quite soluble in any of several chloride solvents at temperatures markedly below 500°C. Nevertheless, this solute is considerably less stable with respect to reduction to the trichloride than is UF_4 with respect to UF_3, and, consequently, UCl_4 should be a strong

[22]J. H. Burns and D. J. Duchamp, *Reactor Chem. Div. Ann. Progr. Rept. Jan. 31, 1962*, ORNL-3262, p. 15.

[23]W. H. Zachariasen, *Acta Cryst.* 1, 265 (1948).

[24]L. G. Alexander, "Molten-Salt Fast Reactors" in *Proceedings of Conference on Breeding, Economics, and Safety in Large Fast Power Reactors*, ANL-6792 (in press).

[25]M. Taube, "Fused Plutonium and Uranium Chlorides as Nuclear Fuel for Fast Breeder Reactors," pp. 353–63 in *Proceedings of a Symposium on Power Reactor Experiments, Vienna, Oct. 23–27, 1961*, vol. I, IAEA, Vienna, 1962.

oxidant and an aggressive corrosion agent.[26] Uranium trichloride, in contrast, promises from the available thermodynamic data to be much less aggressive. Newton,[27] for example, has calculated that UCl_3 should be stable in contact with metals as active as iron. While the case is likely to be somewhat less favorable in practice, it seems likely that UCl_3 (and $PuCl_3$) must be the major fissionable metal compounds in such fuels. Unfortunately their phase behavior is likely to prove less suitable than that of the tetrachlorides.

Relatively little is known of phase behavior in chloride systems from which suitable fuels may be chosen. Some information concerning binary systems of UCl_3 and $PuCl_3$ has been reported by Barton *et al.*[28] of ORNL and by Leary[29] and his associates at the Los Alamos Scientific Laboratory. From these relatively simple binary systems the behavior of relatively simple ternary systems was estimated. It seems likely that sufficient solubility of the chlorides can be obtained at

[26]George Scatchard *et al.*, *Chemical Problems of Non-Aqueous Fluid-Fuel Reactors*, MIT-5001 (Oct. 15, 1952).

[27]R. F. Newton, personal communication.

[28]C. J. Barton, pp. 131–37 in *Phase Diagrams of Nuclear Reactor Materials*, ORNL-2548 (ed. by R. E. Thoma) (Nov. 6, 1959); C. J. Barton, unpublished data (KCl-UCl_3).

[29]J. A. Leary, *Temperature-Composition Diagrams of Pseudo-Binary Systems Containing Plutonium(III) Halides*, LA-2661 (Apr. 9, 1962).

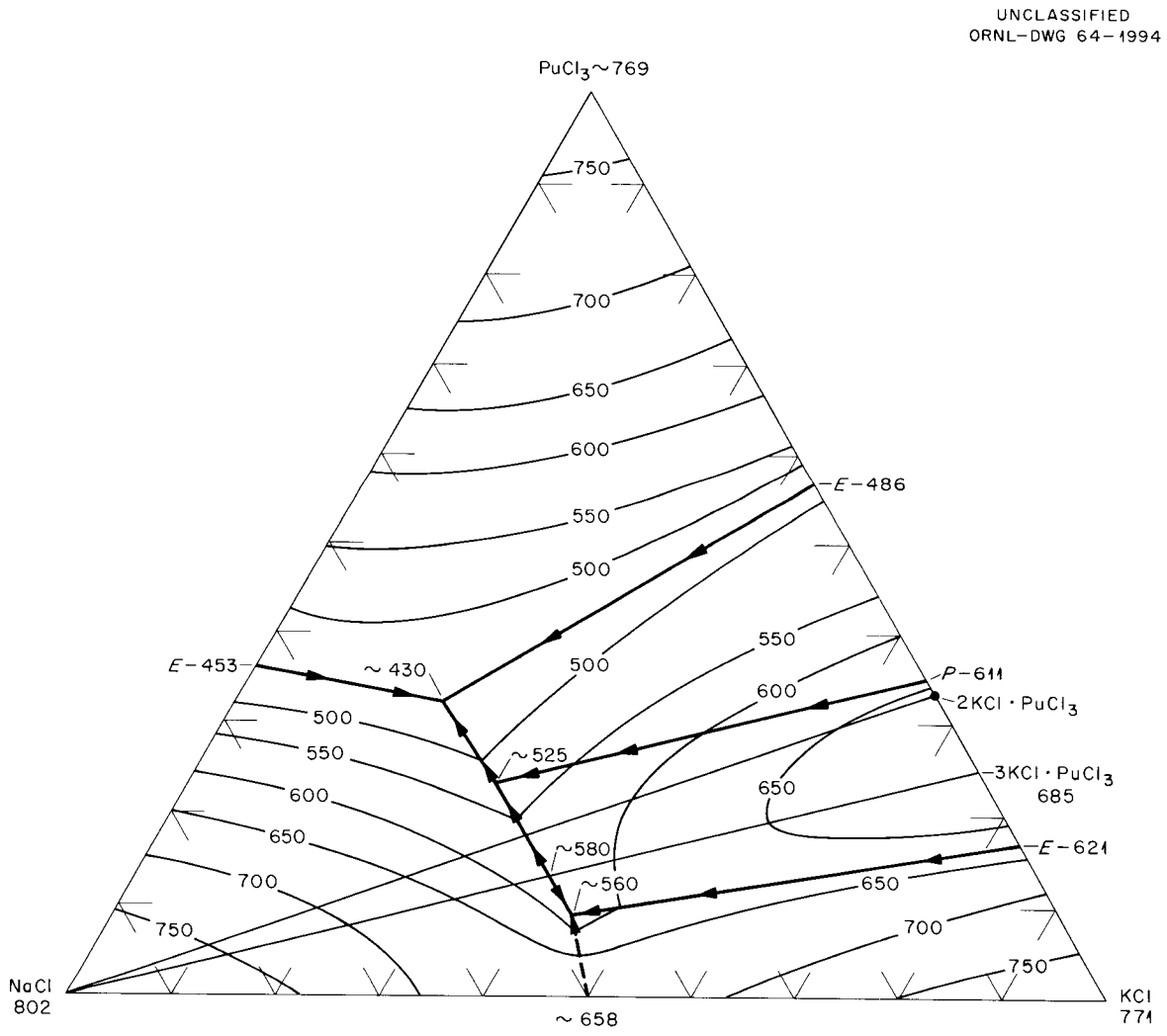

Fig. 1.4. Predicted Phase Behavior for the System NaCl-KCl-$PuCl_3$.

550°C in solvents such as NaCl-KCl or NaCl-$MgCl_2$. A diagram predicted for NaCl-KCl-$PuCl_3$ from the known limiting binary systems is shown as Fig. 1.4, as an example of the expected behavior.

A study of phase equilibria in systems with UCl_3 as a component has been started. Initial attention has been focused on the KCl-UCl_3 binary. Most of the effort to date has been expended on methods of preparation of pure, oxide-free UCl_3-KCl mixtures. After a survey of methods for preparing uranium chlorides, hydrochlorination of uranium metal was tested. Considerable difficulty was encountered, both in keeping the system free from water, and in obtaining consistent analytical results. An attempt to produce UCl_3 in the presence of molten KCl did not yield the expected molten mixture of UCl_3-KCl; analytical results indicated that nearly 90% of the uranium is in the tetravalent state. Reduction of UCl_4 in molten KCl by hydrogen appeared to give a 65 to 90% reduction of the uranium. Experiments are continuing in efforts to compare the stability of UCl_3 toward oxidation or disproportionation in molten alkali chlorides with the corresponding tendencies in the pure state.

CRYSTAL STRUCTURE DETERMINATIONS

Crystal Structure of $6LiF \cdot BeF_2 \cdot ZrF_4$

D. R. Sears J. H. Burns

Crystals of the stoichiometric compound $6LiF \cdot BeF_2 \cdot ZrF_4$ appear as a primary phase in solidified MSRE fuel solvent.[30] The structure of this ternary compound may be useful in the explanation of radiation damage and postirradiation behavior of MSRE fuel and in understanding the solubility relationships in fluoride-fuel systems. For these reasons, and because the stereochemistry of metal ions displaying eightfold coordination is currently of interest,[31] a complete crystal-structure analysis of $6LiF \cdot BeF_2 \cdot ZrF_4$ was undertaken.

This substance is tetragonal, having a centrosymmetric unit cell of dimensions $a_0 = 6.57$ A, $c_0 = 18.62$ A; the space group is $I4_1/amd - D_{4h}^{19}$. There are four formula weights per unit cell.

[30] *MSRP Semiann. Progr. Rept. Aug. 31, 1962*, ORNL-3369, p. 121.

[31] J. L. Hoard and J. V. Silverton, *Inorg. Chem.* **2**, 235 (1963); R. J. H. Clark *et al.*, *Nature* **199**, 559 (1963).

Table 1.5. Site Symmetry and Least-Squares Adjusted Parameters of $6LiF \cdot BeF_2 \cdot ZrF_4$

	Site Symmetry	$x^{(a)} \pm \sigma_x$	$y \pm \sigma_y$	$z \pm \sigma_z$	$B \pm \sigma_B$ (A^2)
(4) Zr^{4+}	$\bar{4}2m$	$\frac{1}{2}$	$\frac{1}{4}$	$\frac{1}{8}$	0.3 ± 0.05
(4) Be^{2+}	$\bar{4}2m$	0	$\frac{3}{4}$	$\frac{1}{8}$	5.1 ± 1.5
(16) F^-(I)	m	0	0.5347 ± 0.0018	0.4208 ± 0.0004	1.4 ± 0.2
(16) F^-(II)	m	0	0.0248 ± 0.0016	0.2904 ± 0.0003	1.0 ± 0.1
(16) F^-(III)	m	0	−0.0563 ± 0.0017	0.0754 ± 0.0004	1.4 ± 0.2
(16) Li^+(I)	2	0.2249 ± 0.0056	0	0	2.5 ± 0.5
(8) Li^+(II)	mm	0	$\frac{1}{4}$	0.1062 ± 0.0020	1.9 ± 0.7

[a] Symmetry center taken as origin.

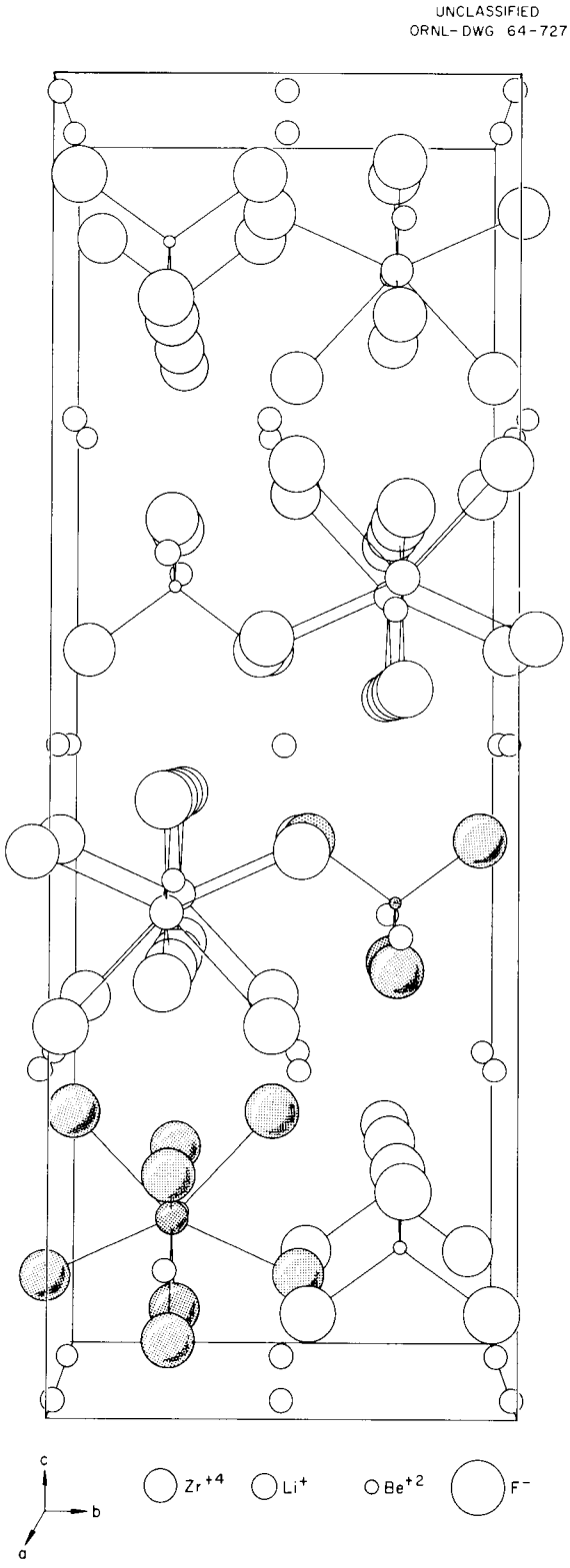

Fig. 1.5. Perspective Drawing of the Structure of $Li_6BeF_4ZrF_8$.

Partial three-dimensional photographic x-ray intensity data were collected. The structure was solved by the heavy-atom technique with the aid of Patterson, electron density, and difference syntheses projected down the [010] direction; the atomic parameters were refined by least-squares adjustment.

Coordinates and thermal parameters of the ions are shown in Table 1.5, and the contents of one unit cell are illustrated in Fig. 1.5. In this figure, ions in the immediate environment of one zirconium ion and of one beryllium ion are shaded in order to accentuate significant features of the coordination of these metal ions.

Both the Be^{2+} and Zr^{4+} ions have discrete coordination polyhedra. The beryllium ion is surrounded by four equidistant fluoride ions at 1.57 A, forming a nearly regular tetrahedron. In this respect the beryllium coordination is similar to that in Li_2BeF_4,[32] another primary phase in the $LiF\text{-}BeF_2\text{-}ZrF_4$ system. About the zirconium ion there are four fluoride ions at 2.07 A and four at 2.16 A, arranged as two interpenetrating tetrahedra with a common center; these eight fluoride ions form an irregular dodecahedron. This type of eightfold coordination is common for early transition-metal ions,[31] including that of the zirconium ion in K_2ZrF_6.[33] The other eight-coordination polyhedron frequently observed is the square antiprism exhibited by ZrF_4 itself.[34]

Lithium ions in $6LiF \cdot BeF_2 \cdot ZrF_4$ satisfy electroneutrality and serve to connect the polyhedral ions described above but do not appear to have additional important stereochemical significance. Thus the formula should be written $Li_6BeF_4ZrF_8$.

The structure is not closely packed; the possible significance of the free spaces is under continuing study.

The Crystal Structure of the Molecular Addition Compound $XeF_2 \cdot XeF_4$

J. H. Burns R. D. Ellison[35]
H. A. Levy[35]

When a mixture of XeF_2 and XeF_4 was sealed into a glass tube, the molecular addition com-

[32] W. H. Zachariasen, *Norsk. Geol. Tidsskr.* **9**, 65 (1926).

[33] H. Bode and G. Teufer, *Acta Cryst.* **9**, 929 (1956).

[34] R. D. Burbank and F. N. Bensey, Jr., *The Crystal Structure of Zirconium Tetrafluoride*, K-1280 (Oct. 31, 1956).

[35] Chemistry Division.

pound $XeF_2 \cdot XeF_4$ was produced. The vapor pressure of each of these compounds is a few millimeters at room temperature; hence crystals were readily grown in the tube by cooling a small spot on its wall. One such crystal, attached to the tube wall, is shown in Fig. 1.6. The characteristic pyramidal habit makes it easily distinguishable from the laths of XeF_4 and the rhombohedra of XeF_2.

A complete three dimensional crystal-structure analysis of $XeF_2 \cdot XeF_4$ was carried out; this has been discussed in detail elsewhere.[36] The structure was solved by a combination of heavy-atom and direct methods and was refined by the method of least squares. The existence in the crystal of discrete XeF_2 and XeF_4 molecules with linear and square-planar configurations, respectively, was established, and a description of their thermal motions was obtained. A perspective drawing of the structure, giving interatomic distances, is shown in Fig. 1.7. The short intermolecular distances in the addition compound are similar to those in the crystals of the two compounds and suggest that there is electrostatic attraction between molecules.

UNCLASSIFIED
PHOTO 64620

Fig. 1.6. Photomicrograph of a Single Crystal of $XeF_2 \cdot XeF_4$. 25×.

UNCLASSIFIED
ORNL-DWG 63-7716

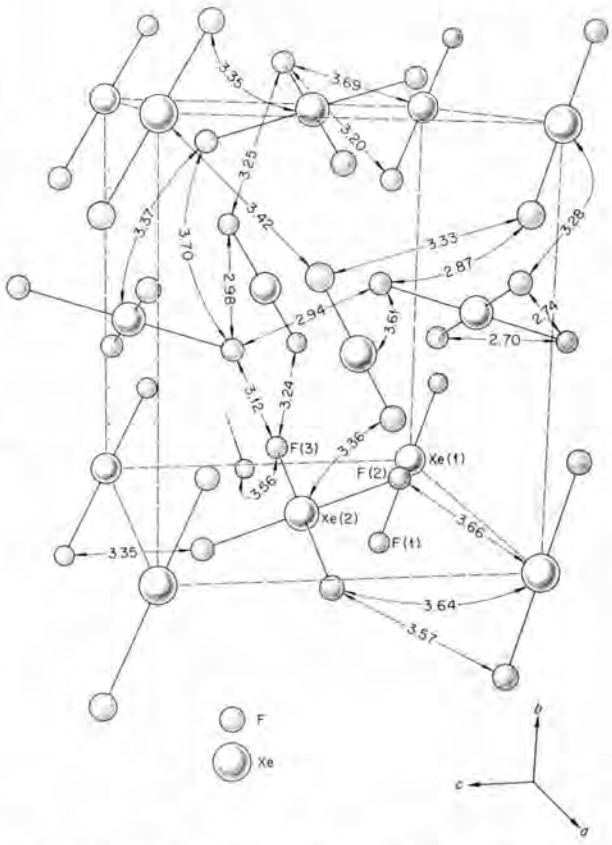

Fig. 1.7. Perspective Drawing of the Structure of $XeF_2 \cdot XeF_4$, Showing Interatomic Distances.

The Crystal Structure of Cr_2F_5 (ref. 37)

J. H. Burns H. Steinfink[38]

The main features of the Cr_2F_5 structure have presented previously;[39] a refinement has now been

[36] *J. Phys. Chem.* **67**, 1569 (1963); *Chem. Div. Ann. Progr. Rept. June 20, 1963*, ORNL-3488, pp. 112–13; *Acta Crystallographica* (in press).

[37] J. H. Burns and H. Steinfink, to be published in *Acta Crystallographica*.

[38] Consultant, University of Texas.

[39] H. Steinfink and J. H. Burns, *Reactor Chem. Div. Ann. Progr. Rept. Jan. 31, 1963*, ORNL-3417, p. 15.

Table 1.6. Crystallographic Data for Some Pure Crystalline Phases

Compound	Optical Properties	X-Ray Data
SmF_3	Uniaxial (−), $N_\omega = 1.595$, $N_\epsilon = 1.586$	Hexagonal, $a_0 = 6.952$, $c_0 = 7.122$, space group $P6_3/mcm$[a]
GdF_3	Biaxial (−), $N_\alpha = 1.574$, $N_\gamma = 1.600$	Orthorhombic, $a_0 = 6.570$, $b_0 = 6.984$, $c_0 = 4.393$, space group $Pnma$[b]
DyF_3	Biaxial (−), $N_\alpha = 1.568$, $N_\gamma = 1.600$	Orthorhombic, $a_0 = 6.460$, $b_0 = 6.906$, $c_0 = 4.376$, space group $Pnma$[b]
ErF_3	Biaxial (+), $N_\alpha = 1.560$, $N_\gamma = 1.998$	Orthorhombic, $a_0 = 6.354$, $b_0 = 6.846$, $c_0 = 4.380$, space group $Pnma$[b]
LuF_3	Biaxial (+), $N_\alpha = 1.550$, $N_\gamma = 1.588$	Orthorhombic, $a_0 = 6.151$, $b_0 = 6.758$, $c_0 = 4.467$, space group $Pnma$[b]
$RbF \cdot SrF_2$	Biaxial, $N_\alpha = 1.396$, $N_\gamma = 1.400$, $2V$ large, microcline twinning	3.55, 2.176, 1.855
$CsF \cdot BaF_2$	Cubic, $N = 1.476$	4.48, 3.18, 2.68
$3KF \cdot AlF_3$	Mean refractive index = 1.368, birefringence $\simeq$ 0.002, polysynthetic twinning common	Cubic, $a_0 = 8.49$[c]
$KF \cdot AlF_3$	Uniaxial (−), $N_\omega = 1.380$, $N_\epsilon = 1.371$	Tetragonal, $a_0 = 3.550$, $c_0 = 6.139$[d]
$NaF \cdot MF_3$	See Table 1.3, this chapter	
$5NaF \cdot 9MF_3$	See Table 1.3, this chapter	
$4NaF \cdot ThF_4$	Isotropic, $N = 1.400$	Cubic, $a_0 = 11.04$, $\rho = 4.70$, $Z = 8$
α-$NaThF_5$	Biaxial (−), mean refractive index = 1.503, $2V$ small, polysynthetic twinning common	Monoclinic, $a_0 = 17.55$, $b_0 = 10.32$, $c_0 = 13.13$, $\beta = 90^\circ 16'$
$(Na,K)U_2F_9$[e]	Biaxial (−), $N_\alpha = 1.514$, $N_\gamma = 1.584$	Orthorhombic, $a_0 = 8.60$, $b_0 = 7.02$, $c_0 = 11.18$, space group $Pna2_1$ or $Pnam$
KH_2PO_5[f]		Orthorhombic, $a_0 = 4.67$, $b_0 = 5.49$, $c_0 = 8.43$, space group $P222_1$, $\rho = 2.34$, $Z = 2$
$NiO \cdot 3UO_3$	$N_\alpha = 2.20$, $N_\gamma = 2.36$, exhibits parallel extinction	4.04, 3.27, 2.019[g]
$2LiF \cdot NaF \cdot 2ThF_4$	Uniaxial (+), $N_\omega = 1.517$, $N_\epsilon = 1.520$	

[a] *National Bureau of Standards Monograph* 25, Sect. 1, 1961.

[b] A. Zalkin and D. H. Templeton, *J. Am. Chem. Soc.* **75**, 2453 (1953).

[c] ASTM X-Ray Diffraction Data Card No. 3-0615.

[d] C. Brosset, *Z. Anorg. Allgem. Chem.* **239**, 301 (1938).

[e] Solid solution with Na/K ratio of about 2.5.

[f] Submitted for publication in *Inorganic Chemistry* by G. Mamantov *et al.*

[g] W. L. Marshall and J. S. Gill, to be published in the *Journal of Inorganic and Nuclear Chemistry.*

completed with the use of the iterative least-squares method and anisotropic temperature factors. The discrepancy factor,

$$R = \frac{\Sigma \, ||F_{obs}| - |F_{calc}||}{\Sigma \, |F_{obs}|} ,$$

reached a value of 0.032 based on 285 observed structure amplitudes; this indicates good agreement between model and data.

In Fig. 1.8 the structure of Cr_2F_5 is represented by octahedra which are joined together by shared edges and corners. The corners of each octahedron are occupied by fluoride ions, and the center of each by a chromium ion. There are two types of octahedra, as detailed in the upper left of the figure. The one containing the Cr(III) ion is regular within experimental error; the average of its six Cr-F bond lengths is 1.89 A. The octahedron with the Cr(II) ion at its center has two bonds of 1.96 A, two of 2.01 A, and two considerably elongated to 2.57 A. The elongation is explained by ligand-field theory as being caused by repulsion of the ligands by the additional electron in the $3d_{z^2}$ orbital which extends toward them.

The thermal motion of the ions is qualitatively as expected from their arrangement in the structure. The Cr(III) ion moves isotropically but the Cr(II) ion has a larger component of thermal displacement along the direction of the long Cr-F bond. The fluoride ions move with greater amplitudes in directions perpendicular to their bonds to chromium ions than along them.

Electron interchange between chromium ions should not occur readily, because a change of valence would require a change in fluoride-ion environment, but a certain amount of substitutional solid solution is possible and the compound has been found to have the composition range $CrF_{2.4}$ to $CrF_{2.45}$.[40]

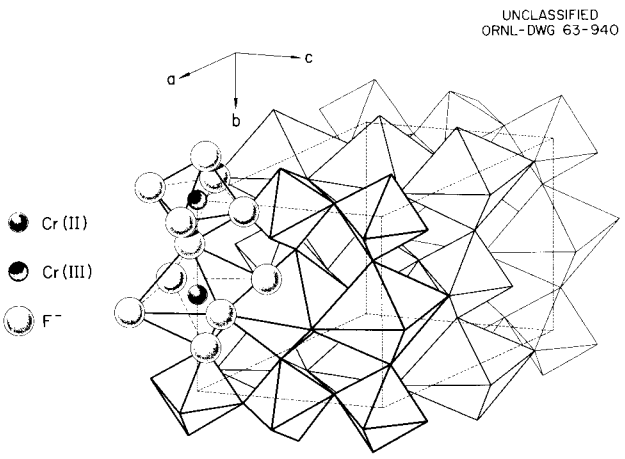

Fig. 1.8. The Structure of Cr_2F_5.

Crystallographic Data for Some Pure Materials

R. E. Thoma
H. Insley[41]
J. H. Burns
T. N. McVay[42]

Crystallographic data were obtained for a number of pure phases, some of which were isolated recently in phase studies (see Table 1.6). Other new data were obtained for crystal phases whose identity is well established. Only the three principal peaks in the x-ray diffraction patterns are listed for crystal phases whose symmetry has not yet been established.

---

[40] B. J. Sturm, *Inorg. Chem.* **1**, 665 (1963).

[41] Consultant, National Bureau of Standards (retired).

[42] Consultant, University of Alabama (retired).

2. Radiation Chemistry of the MSR System

IN-PILE TESTS OF MSR MATERIALS

F. F. Blankenship S. S. Kirslis
J. E. Savolainen

The chemical and physical compatibility of the fuel, graphite, and container metal (INOR-8)[1] for the Molten-Salt Reactor systems in the absence of irradiation remains on a sound footing. A continuing program of in-pile testing[2] has pursued the question of compatibility of these materials under irradiation. With possible exceptions that are discussed below, no changes of consequence at operating conditions have been found. This favorable behavior stems from the fact that the MSR materials are mutually stable, virtually, under equilibrium conditions; off-equilibrium species resulting from radiolysis are working against a restorative free-energy drive, and the kinetics for restoration are favored by higher temperatures and, in some cases at least, by the radiation itself.

There are, nevertheless, small but finite and equal concentrations of both F^0 atoms and electrons, or of their chemical equivalents, in the fuel as a result of fissioning. When other factors are constant, concentrations of these species increase with (probably as the square root of) power density; they may provide mechanisms for transport or other alterations in the fuel-container system for which possible evidence is still being sought.

Until recently, postirradiation examinations were carried out on sealed assemblies in which fission products had been allowed to decay for weeks or months after fissioning had ceased. Such examinations disclosed that radiolysis from fission product decay had been releasing F_2 from the fluoride crystals in the frozen fuel and that the effects of this F_2 were dominant among the chemical changes observed upon examination. Evolution of F_2 and the consequent chemical effects occurred even during the reactor shutdowns that intervened during the exposure period. Thus, while it was reassuring that most of the specimens had survived both the operating conditions and the postirradiation fluorination in good physical condition, it was difficult to glean unequivocal evidence of what really occurred under operating conditions. This difficulty is to be alleviated in future in-pile exposures by using heaters on the irradiated capsules to maintain temperature during reactor shutdowns; as shown in subsequent sections, temperatures above 150°C suppress the F_2 generation and its undesired effects.[3]

A summary of findings from recent in-pile experiments follows; amplification of most of the information can be found in MSRE project reports.[4,5] The in-pile engineering was carried out by the Irradiation Engineering Group of the Reactor Division. The Hot-Cell Operations Group in the Operations Division handled the postirradiation work.

Experiment ORNL-MTR-47-4

Xenon Recovery from Graphite. – Four of the irradiated capsules from experiment ORNL-MTR-47-4 contained, as has been described earlier,[6] ½-in.-diam cylindrical graphite cores which were surrounded by 25 g of fuel (containing 1 g of uranium) whose composition was LiF-BeF_2-ZrF_4-ThF_4-UF_4 (70-23.3-5-1-0.7 mole %). The frozen

[1] INOR-8 is a nickel alloy with about 17% molybdenum, 7% chromium, and 5% iron on an atomic percent basis.

[2] F. F. Blankenship *et al.*, *Reactor Chem. Div. Ann. Progr. Rept. Jan. 31, 1963*, ORNL-3417, p. 17.

[3] See section on "Radiolysis by Gamma Radiation," this report.

[4] *MSRP Semiann. Progr. Rept. July 31, 1963*, ORNL-3529, p. 80.

[5] *MSRP Semiann. Progr. Rept. Jan. 31, 1964* (in preparation).

[6] F. F. Blankenship *et al.*, *Reactor Chem. Div. Ann. Progr. Rept. Jan. 31, 1963*, ORNL-3417, p. 18.

fuel in these capsules had generated F_2 gas sufficient to produce pressures of several tens of atmospheres during the postirradiation decay period. Xenon, expected as a fission product, was absent from the cover gas collected from these capsules at the time the F_2 was found. This was attributed to the formation of relatively nonvolatile xenon fluorides. After remaining in storage for five months, two of the graphite cores were heated under vacuum, and the released gas was collected and analyzed. Some 7.5% of the initially expected theoretical yield of xenon from fission was recovered from each core. This xenon must have persisted in the graphite as an oxide, since, under the conditions of storage, xenon fluorides should have disappeared by both hydrolysis and volatilization.

Nonvolatile Constituents in Graphite. – Large pieces (0.8 g or more), for which the ratio of mass to surface area originally exposed to the salt was similar to that for the entire core, were analyzed chemically to produce the data shown in Table 2.1. These data show that, of all constituents of the fuel, uranium, lithium, and molybdenum were selectively concentrated in the graphite. The mechanism by which deposition in the graphite occurred is not known, but subsequent examinations, including metallography, agreed with the chemical analyses that it was not by penetration as fuel. Tests by chemical leaching[7] and by metallographic examination[8] show that there is no deposition of uranium in or on the metal (INOR-8) capsule walls.

Circular cross sections of the graphite cores were activated in the ORNL Graphite Reactor at a flux of 5×10^{11} neutrons cm^{-2} sec^{-1} for 8 hr. Contact autoradiography before and after the activation showed that the uranium was in the outer rim, and gamma spectrometry provided a measure of the amount present. The results by activation analyses are compared with the chemical analyses in Table 2.2. The chemical analyses suggest a correlation of deposited uranium with power level (or perhaps with the consequent rate of F_2 generation after irradiation). Analysis by neutron activation, which should probably be preferred because of the simplicity and directness of the technique, does not support such a correlation. Both analyses, however, show the deposition to be substantial; if the graphite contains 1 mg of

[7] *MSRP Semiann. Progr. Rept. Jan. 31, 1963*, ORNL-3419, p. 90.

[8] *MSRP Semiann. Progr. Rept. Jan. 31, 1963*, ORNL-3419, p. 85.

Table 2.1. Chemical Analyses on Samples from ORNL-MTR-47-4 Graphite-Fuel Compatibility Test

	Weight Percent									
	U	Li	Zr	Be	Th	Ni	Cr	Fe	Mn	Mo
Original fuel	3.89	11.6	10.1	4.8	5.8	0.0025	0.0024	0.0096		
Irradiated fuel										
Capsule 12	3.36 4.08					<0.018	<0.004	<0.004	<0.001	<0.013
Capsule 45	3.96 3.81					0.016	<0.007	<0.007	<0.007	<0.025
Graphite										
Capsule 12	0.136	0.04	<0.017	0.0008	N.D.[a]	0.013	0.014	N.D.	0.019	0.062
Capsule 24	0.214	0.052	0.0054	0.003		0.015	<0.012	<0.015	<0.005	0.089
Capsule 36	0.13	0.06	0.004	0.0003		<0.03	0.01	<0.006		0.04
Capsule 45	0.523	0.062	<0.016	0.002	N.D.	0.01	0.04	N.D.	0.01	0.062
Capsule 3A[b]	0.00088	<0.001		0.00003		0.012	0.004	0.067	<0.014	<0.035

[a] N.D., not detected.

[b] Unirradiated control capsule.

Table 2.2. Uranium in ORNL-MTR-47-4 Graphite

Capsule	Power Density[a] (w/cm^3)	Sample[b]	Chemical Analysis (mg of U per g)	Activation Analysis (mg of U per g)
12	67	D	1.3	
24	83	D	2.1	
		B		0.6
		C		1.5
45	117	D	5.2	
		B		1.5
		C		1.4
36	85	D	1.3	
		A		0.7
		B		1.2

[a]Nominal power density in fuel surrounding graphite.

[b]Relative locations along core, top to bottom, are designated A, B, C, and D.

U per g, it has taken up about 0.5% of all uranium in the capsule.

Contact autoradiography showed a high concentration of radioactivity from fission products (presumably mostly from daughters of gaseous products) to a depth of about 0.2 mm in the periphery of the graphite cross sections. Neutron activation did not appreciably affect this radioactivity; this indicated that the uranium was in the same region as the fission products. A closer resolution of the uranium distribution (see Fig. 2.1) was obtained from x radiography by a technique (recently developed in the Metals and Ceramics Division) in which the interference from fission product activity is negligible. The main deposit of uranium penetrated the graphite to a depth of less than 0.05 mm, though there were also fringed proliferations that extended perhaps three times as deep. Facilities for attempted identification by x-ray diffraction are nearing completion, but nothing is yet known of the chemical form of the uranium in the graphite.

It seems clear that uranium is deposited in the outer layers of the graphite but not on or in the metal wall, and that uranium, lithium, molybdenum, and other metallic constituents of INOR-8 are deposited in the graphite in preference to Be, Zr, and Th. Mechanisms, such as oxidation to UF_6 or reduction to UF_3 and to U and formation of UC_2, for which the situations resulting from F_2 release might provide appropriate conditions can be imagined. None of the mechanisms, however, predict in detail the observed behavior, and they all appear less applicable at high (reactor operating) temperatures, where no off-equilibrium behavior has been demonstrated. It remains to be seen whether these deposition phenomena are a problem in MSRE or are an artifact of our present experimental procedures.

Metallographic Examination of the Graphite. – The autoradiography and x radiography of the graphite cores mentioned above were performed on specimens that had been mounted and polished for metallographic observation. Under the metallographic microscope, there were no signs of radiation damage, chemical alteration, penetration of salt, nor even of the ~1% by weight concentration of uranium that apparently existed in a 2-mil layer at the surface of the graphite. These results were the same for the four graphite cores in the assembly, with the exception that a shiny film, quite apparent to the eye, that had appeared on one of the specimens was also clearly depicted on the surface of the graphite in the metallographs of that particular core, This 0.1-mil-thick film, absent prior to heating to 1000°C in vacuum during a gas recovery mentioned above (see "Xenon Recovery from Graphite"), was identifiable only as probably metallic from its metallographic appearance. However, the container for the 1000°C

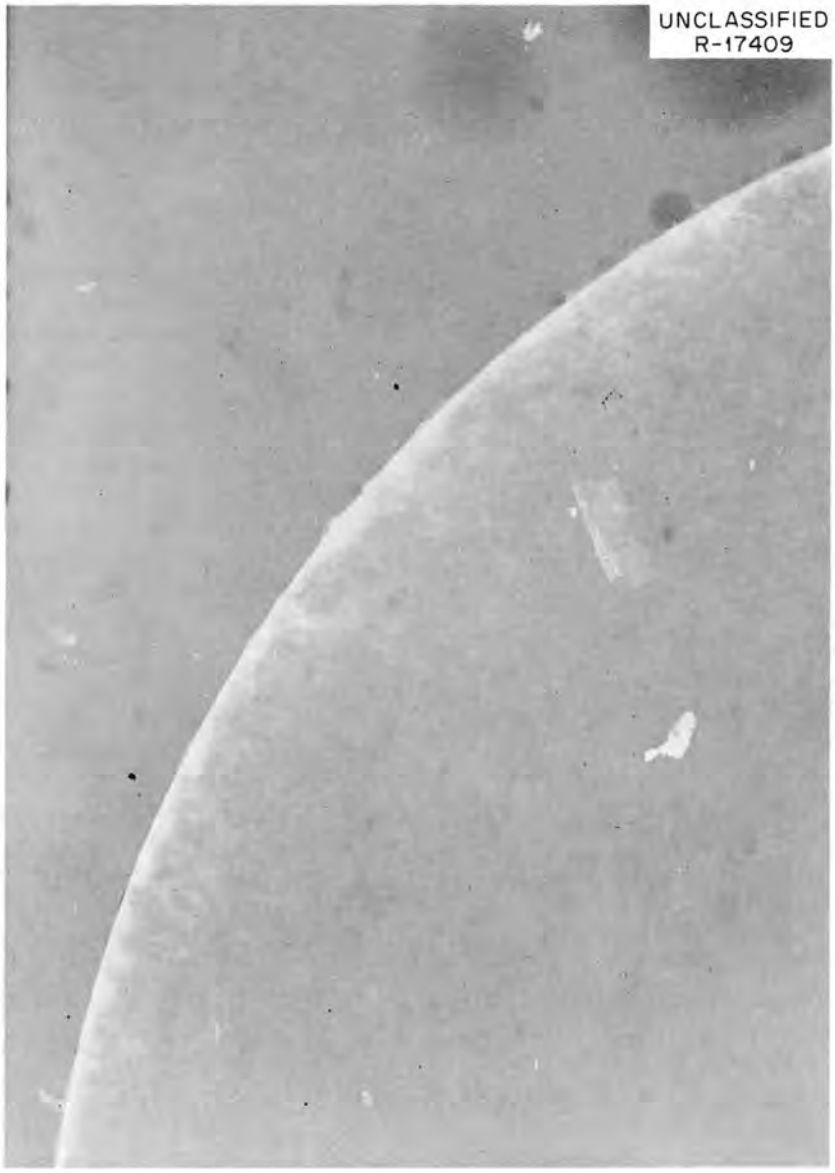

Fig. 2.1. Enlargement of X Ray of Graphite Core ($\frac{1}{2}$-in. Diameter), Showing Deposit in the Surface.

bakeout was stainless steel, and in accord with recent results[9] on the volatility of components from stainless steel, the film may well have been volatilized manganese and chromium.

The 47-4 assembly also contained two smaller capsules of INOR-8 that contained cylindrical graphite crucibles ($\frac{1}{2}$ in. in diameter) filled, to within about 0.25 in. of the top, with fuel. Graphite exposed below the liquid level in these capsules appeared quite unaltered in metallographs. These two capsules, because of differences in fuel composition and flux, differed by a factor of 6 in power density. The higher-powered capsule produced fluorine in a quantity sufficient to give about 30 atm of F_2 during the five-month postirradiation period; the graphite above the liquid level in this capsule had a spongy, severely corroded

[9]D. Bourgette, "Vaporization of Iron, Nickel and Cobalt Base Alloys Between 760°C and 980°C and 5×10^{-7} to 1×10^{-9} Torr," pp. 497–502 in *Transactions of the 10th National Vacuum Symposium (October 1963)*, Macmillan, New York (to be published).

appearance. The other capsule produced no F_2 and no damage to its graphite. Graphite from the small capsules could not be satisfactorily sampled for most other types of analyses. However, attempts to compare the two liners by x radiography to establish the presence or absence of uranium deposition are in progress.

Apparent Burnup of Uranium in the Graphite. – Comparison of burnup of uranium in the graphite with that in the liquid fuel is of obvious importance in establishing when the uranium entered the graphite. Comparison of uranium content of the graphite with that of Ce^{141} (judged to be least likely of the readily analyzable fission products to have arrived in the graphite by other means) suggests that burnup of uranium in the graphite is as much as 35% that in the liquid fuel. This result is no aid in distinguishing between uranium deposition under normal (high-temperature) in-pile operation and that which may have occurred during or immediately following freeze-thaw cycles that occurred in the in-pile runs. The evidence does, however, confirm the view that the uranium deposition did not occur entirely, and perhaps not importantly, during the postirradiation period.

Optical Characteristics of Fuel from Microscopy. – The general appearance, under a petrographic microscope, of the irradiated fuel was that of recognized, optically identifiable phases normally present in the fuel, plus phases not identified because of their opacity or fineness, which would be expected in rapidly cooled, unirradiated melts. The best crystallization appeared to be associated with the most highly irradiated fuel; crystallite sizes varied markedly, and, in some capsules, sizes suitable for identification were difficult to find.

The compound $2LiF \cdot BeF_2$ was brownish purple, whereas without irradiation it is not colored; the more intensely colored material had a range of refractive indices, both higher and lower than the characteristic values, but some coloration was noticeable in crystals that had apparently not been damaged sufficiently to cause changes in refractive indices. The compound $2LiF \cdot ZrF_4$ had decreased refractive indices, but any color centers had either bleached or were outside the visible spectrum. No UF_3 was detected, even in samples that had lost much F_2, but the usual UF_4 compounds were present.

In view of the altered indices of refraction, and absence of UF_3, the chemical reduction associated with the F_2 evolved from the crystals seemed to have been shared widely among the predominant phases and not confined to the more easily reduced uranium-containing phase. On melting, reaction should occur, and the UF_4 should become selectively reduced at the expense of the other reduced species.

Experiment ORNL-MTR-47-5

Results from the Gas Samples Collected During Irradiation. – As described earlier,[10] two of the capsules (0.66 and 0.34 mole % UF_4 in the fuel respectively) in the assembly for ORNL-MTR-47-5 were equipped as shown in Fig. 2.2 to allow gas sampling during irradiation. Otherwise, the capsules were similar to those used in the earlier irradiation.

Some 61 gas samples were swept from the capsules into 250-ml collection cylinders and analyzed

[10] F. F. Blankenship *et al.*, *Reactor Chem. Div. Ann. Progr. Rept. Jan. 31, 1963*, ORNL-3417, p. 24.

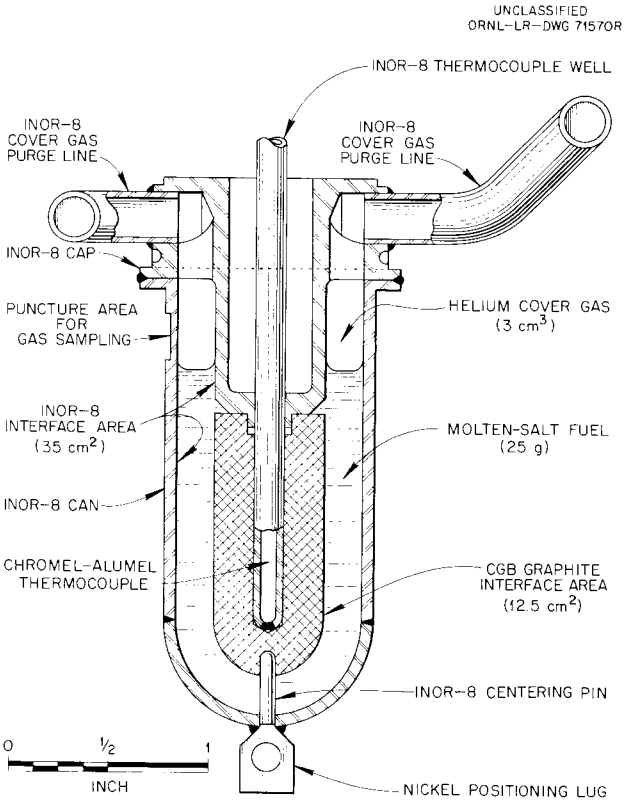

Fig. 2.2. Purged-Type Graphite-Fuel Capsule.

at ORNL by mass spectrometry. Gas from fissioning molten fuel, accounting for 33 of the samples, was collected after chosen accumulation periods and operating conditions in an attempt to follow the CF_4 production, if any, at operating temperatures. Traces of CF_4 were found in less than half the samples; thus CF_4 was probably present but at concentrations too low to measure with accuracy. An attempted correlation of CF_4 content with long-lived xenon in the gas, which involved uncertain approximations and weighting, suggested that while the CF_4 generation was low, it might correspond to about 6% of the rate of production of xenon. Capsule parameters had been so chosen that a similar rate would be expected in the MSRE if for a given power density the rate of production of CF_4 varied directly with the area of graphite-fuel interface.

These results imply a considerable margin of safety for operation of the MSRE, but the scatter in the data was such that the experiment is being repeated with more sensitive detection techniques. The concern is not with the loss of graphite as CF_4, but with the loss of fluoride ions from the fuel and the consequent reduction of UF_4 to UF_3 and possibly to U^0. The results already at hand show that such a process does not account for the uranium deposition discussed earlier in this chapter and that changes resulting from loss of CF_4 will probably not be of crucial significance even for long-term operation of the MSRE.

It was during the reactor shutdowns, which periodically interrupted the collection of gas at operating conditions, that the true nature of the evolution of F_2 came to light. At shutdowns the capsules were promptly cooled to about 40°C, and after variable induction periods, an accumulation of gas in the capsules was noted by pressure measurements. The accumulating gas was found to be F_2 and to be released from the frozen fuel at G_{F_2} values (molecules of F_2 per 100 ev of absorbed energy) from about 0.005 to 0.031, although on occasion the induction period persisted throughout the shutdown. No correlation between capsule power density just before shutdown and either G_{F_2} values or duration of induction periods was observed; more often than not, though, both capsules gave similar G_{F_2} values for a particular shutdown. There were seven shutdowns of sufficient duration for the effects to be noted.

Short periods of low-power operation (4 hr) were arranged during MTR startups in order to observe the behavior at varied levels of fissioning in the solid fuel which covered the range from 2 to 10 w/cm^3 and temperatures from 85 to 325°C. Except for some suspicious indications at the lower temperatures, no accumulation of gas was detectable; this indicated, as was later confirmed, that the susceptibility of the solid fuel to radiolytic decomposition diminishes greatly or disappears at relatively low annealing temperatures (e.g., 200°C). An accelerated rate of recombination with increasing temperatures was found in subsequent post-irradiation studies, and this is undoubtedly related to the pronounced and favorable temperature effect. At any rate, the operating ranges in which frozen salt in freeze valves and freeze flanges can be maintained without evolving F_2 appear to be ample for practical purposes.

Evolution of F_2 During Postirradiation Decay. – On January 23, 1963, after 2000 hr of irradiation at an average thermal flux of 2×10^{13} neutrons $cm^{-2}\ sec^{-1}$, the assembly was withdrawn from the reactor; 11 days later the gas evolution from the two capsules was being monitored in an ORNL hot cell. The F_2 evolved into an evacuated gas space in which the rate of accumulation was followed by pressure measurements precise to 0.01 psia or 0.1 std cm^3 of F_2. The gas was occasionally collected and analyzed; this restored the vacuum and provided a measure of the leak rate, which was generally quite small. The loss of F_2 for the first 95 days of the cooling period is shown in Fig. 2.3, where the loss has been expressed in terms of the percent of the fluoride ions removed from the fuel.

The effect of temperature was found to be quite pronounced, as shown in Fig. 2.4, which is a differential form of the data in Fig. 2.3. An initial G_{F_2} value of 0.04, based on the design capsule power densities of 65 and 35 w/cm^3, was previously reported.[11] During the reactor cycle before final shutdown, the capsule power densities were approximately twice the design values, according to revised estimates based on measured average fluxes and the insertion position history of the experiment. Correspondingly, the calculated yield curve in Fig. 2.4, which approximates the initial ambient-temperature fluorine generation curve for the higher-power capsule, represents a G_{F_2} value

[11] *MSRP Semiann. Progr. Rept. July 31, 1963*, ORNL-3529, p. 89.

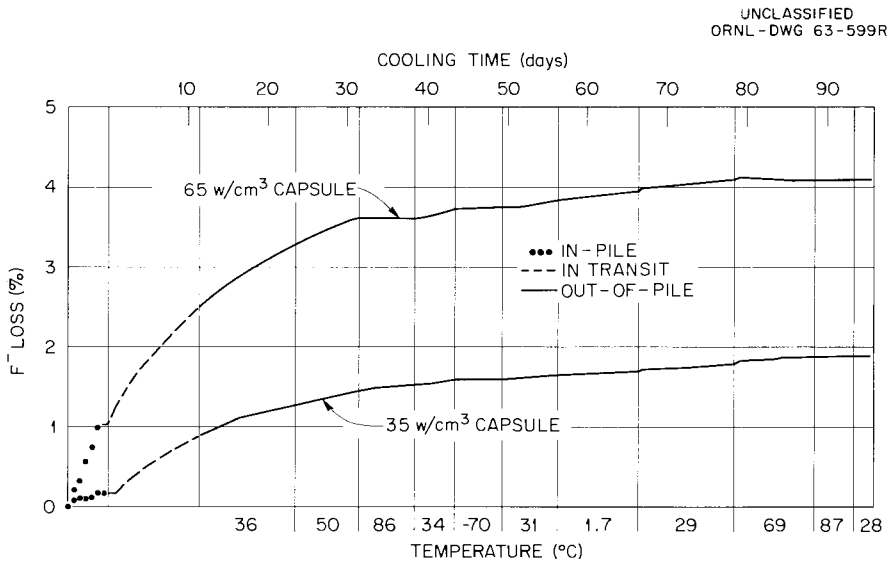

Fig. 2.3. Loss of Radiolytic Fluorine from MTR-47-5 Capsules.

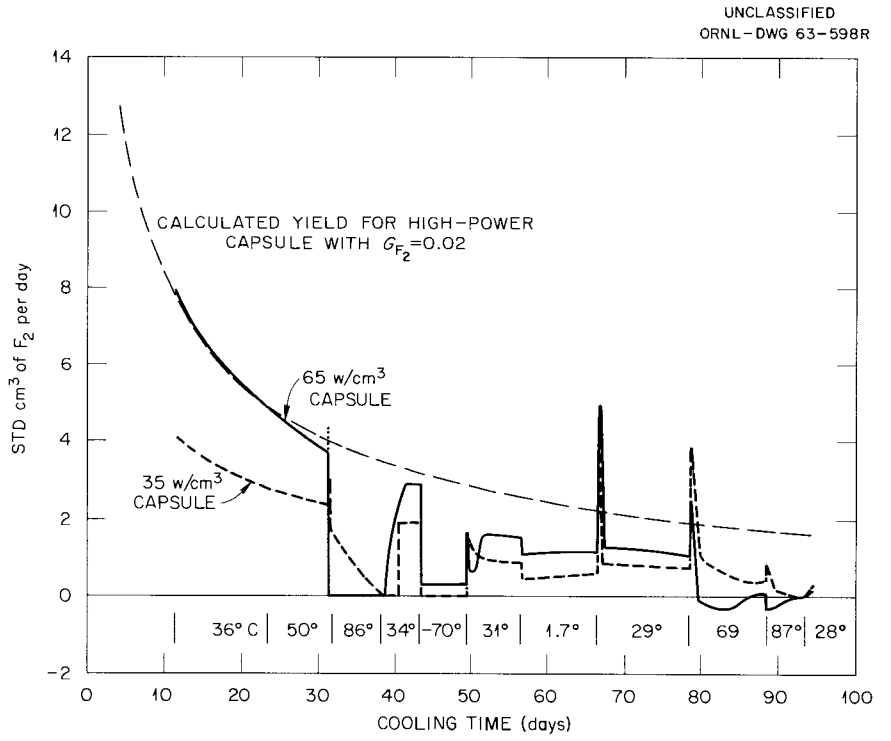

Fig. 2.4. Postirradiation Fluorine Release in MTR-47-5 Capsules.

of 0.02. A further revision of this G_{F_2} value may be necessary when better estimates of capsule power densities are available from uranium isotopic analyses of the irradiated fuels. The jagged rate curve is a consequence of equilibration periods at various temperatures. Either cold (–70°C) or warm (80°C) temperatures sufficed to suppress the evolution. Intermediate behavior found between these extremes implied that a maximum, which shifted somewhat with time, occurred near 35°C or higher. Bursts of F_2 occurred immediately after a temperature rise, and several days were sometimes required for a steady state after a drop in temperature.

Beginning on day 113, the effect of various partial pressures of added F_2 gas was explored. Above 50°C there was a pronounced pressure effect in the expected direction, that is, decreasing loss at increasing pressure, but since the actual rates seemed to depend markedly on the history of the fuel (probably on the state of chemical reduction in the surface layers), it was not possible to determine a quantitative expression for the effect of pressure. Qualitatively the reaction order with respect to F_2 pressure appears to have been initially near unity and to have decreased to 0.5 or lower. Below 50°C, evolution continued even at 1 atm of F_2. The results are depicted in integral form for the higher-powered capsule in Fig. 2.5. Consumption of F_2 was clearly evident at increasing rates as the temperature was increased. As the fuel consumed more fluorine, higher temperatures were required to give further consumption at measurable rates.

These data suggest that rate of evolution of F_2 is controlled at low temperatures by rates of diffusion of radiolytic species within the solid, and at higher temperatures by a back reaction whose rate is strongly temperature dependent.

Analyses of Gas from Sealed Capsules. – For the first five months following the in-pile irradiation, the assembly could not be dismantled without disturbing the investigation of F_2 evolution described above. The four other sealed capsules in the assembly were punctured, and the cover gas was analyzed as soon as the rate of F_2 evolution in the swept capsules diminished to the point that it was difficult to measure changes.

Two of the sealed capsules were designed to provide extremes in the ratio of graphite to metal areas to which the fuel was exposed. Capsule 1 (see Fig. 2.6) had a graphite liner and a graphite core with a total salt-graphite interface area of 27 cm^2; the liquid extended above the liner and flooded 7 cm^2 of INOR-8 wall. Capsule 2 (see Fig. 2.7) had only a small disk of graphite (1 cm^2 of graphite-fuel interface) and provided 46 cm^2 of metal-fuel interface. The other two capsules (see Fig. 2.8) were of smaller diameter; they each contained a

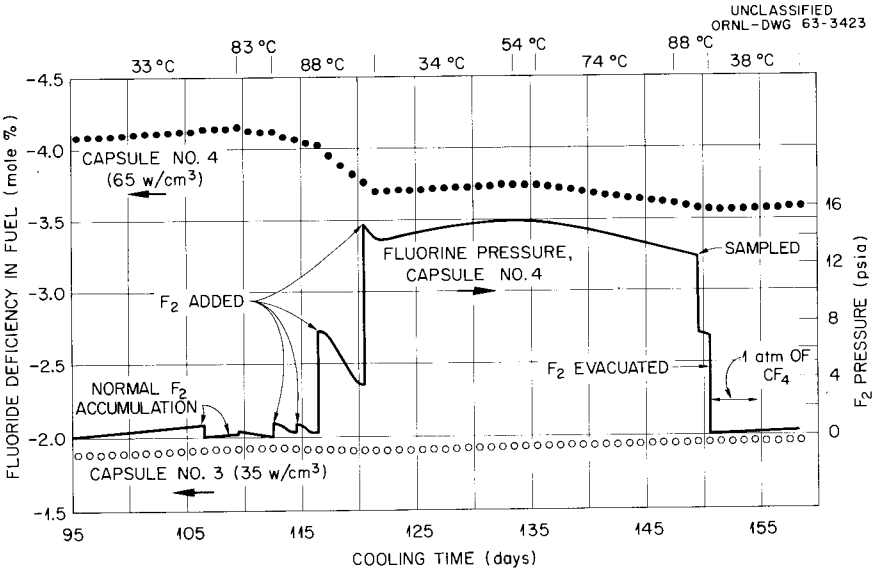

Fig. 2.5. Effect of F_2 Pressure and Temperature on Recomposition of Radiatively Reduced Fuel.

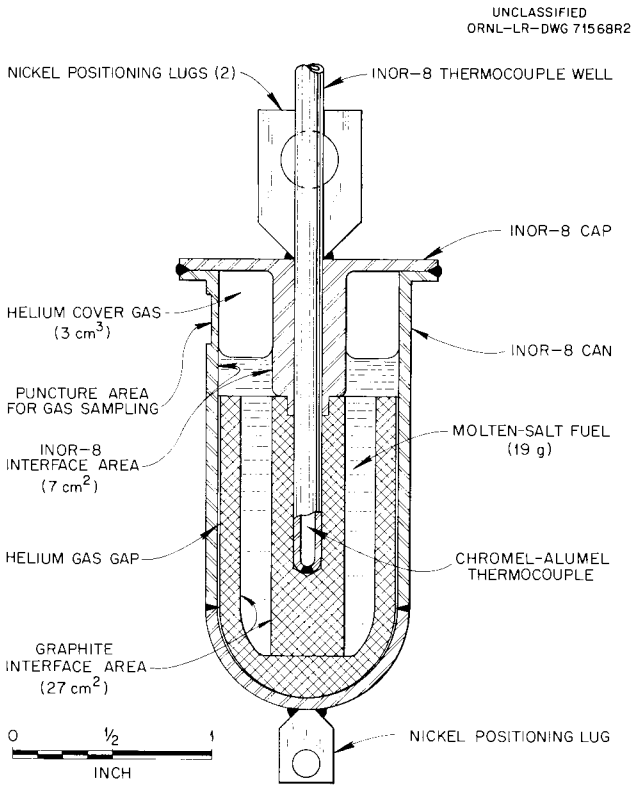

Fig. 2.6. Capsule Design with Large Area of Graphite-Fuel Interface.

mounted graphite (AGOT) bar (3 g) that had been prepermeated with fuel; no other fuel was added; therefore these capsules, initially at least, exposed no metallic surface to the salt.

Analyses of the gas drawn from these four capsules are shown in Table 2.3 along with some details of the in-pile exposures. It is clear that the three capsule geometries yielded very different quantities of F_2 and CF_4; capsule 2 yielded about 39 cm^3 of F_2 and 70 cm^3 of CF_4, capsule 1 yielded about 2.5 cm^3 of F_2 and 0.6 cm^3 of CF_4, and the small capsules yielded none of either gas. The notion that salt-metal interface area affects radiolytic generation of F_2 from solid salt appears absurd. The possibility that graphite surfaces somehow catalyze back reactions or otherwise slow the generation process seems almost equally unlikely. It seems more plausible to ascribe the pronounced difference in behavior to large differences in cooling rates of the fuel and to consequent differences in crystallite size and degree of stress introduced into the crystallites. The small capsules, with the gas envelope around the fuel, cooled most slowly and, perhaps, produced least readily damaged fuel. Capsule 2 clearly should have cooled most rapidly.

Conditions of Capsule Contents on Disassembly. – Few detailed examinations of specimens from the six capsules have been made. Extensive exploration of these specimens with a newly available hot-cell x-ray diffractometer is anticipated, and, to preserve suitable samples for this machine, most of the capsule contents have been held relatively intact after opening. The large capsules were opened by cutting off the top and sawing longitudinally through the metal to expose the contents. These capsules showed no visible evidence of corrosion or other alterations that could be attributed to unfavorable compatibility behavior at operating temperatures. Several of the capsules did, however, show changes of one type or another that required explanation. The main changes, as they have been recognized by visual observation, are enumerated below.

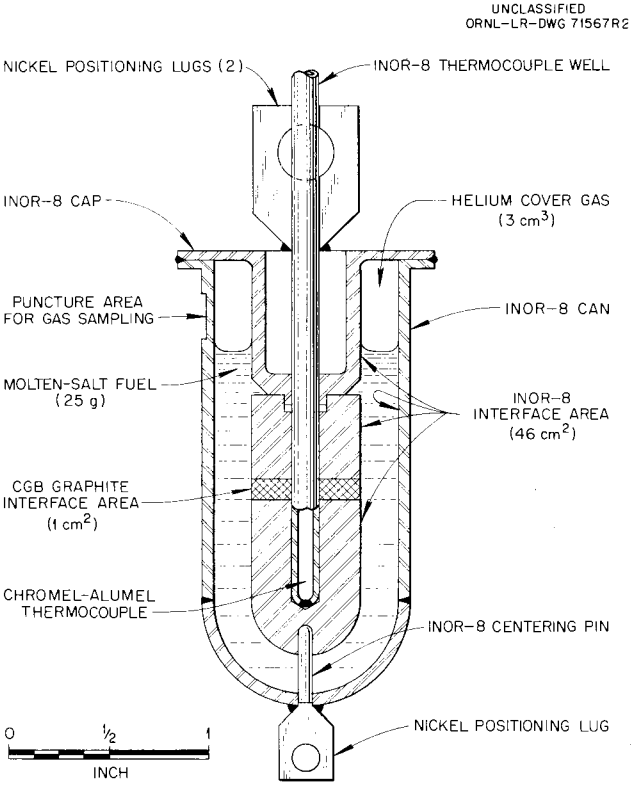

Fig. 2.7 Capsule Design with Small Area of Graphite-Fuel Interface.

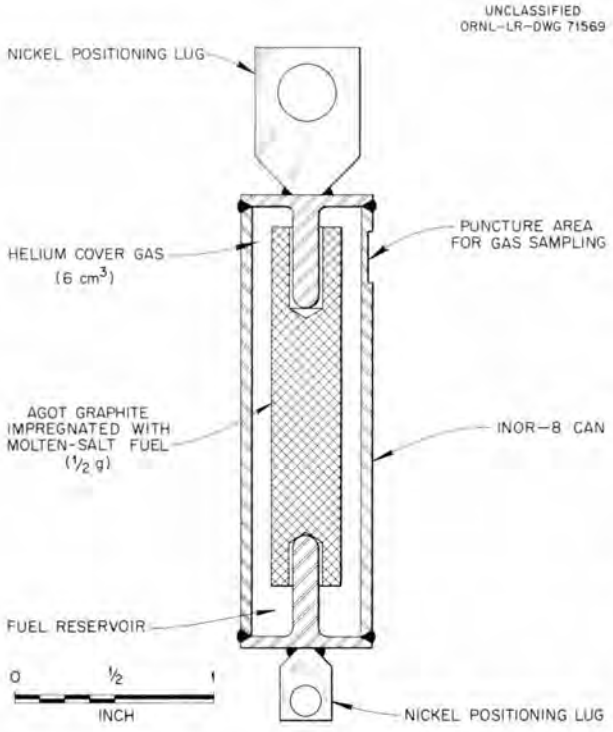

Fig. 2.8. Capsule Design for Graphite Impregnated with Fuel.

The swept capsules lost considerable quantities of F_2 during reactor shutdowns; reheating after such F_2 losses might lead to deposition of readily reducible materials. In these capsules, unusual films were noted (see Fig. 2.9), particularly at the graphite-fuel interface. The identification of the films and comparison with expected deposition by reduction have not yet been attempted. The lower-powered of these capsules showed an unusual number of bubbles at the fuel-wall interface. A few bubbles have been noticed before; they evidently originate in the molten fuel, but no adverse chemical effects associated with them have yet been established.

In capsule 2, in which 38 mg of carbon was converted to CF_4, the 0.5-g disk of carbon appeared to be eroded and friable. The permeated graphite rods in the small capsules had lost weight, presumably by volatilization of the fuel.

Many of the irradiated capsules exhibit black deposits or discoloration on the metal exposed to the gas space; deposits of carbon from radiolytic decomposition of CF_4 might have a similar appearance, but such identification has not been established. The black deposit in capsule 1 appeared to be unusually heavy; and it may prove helpful in

Fig. 2.9. Separated Halves of Capsule 4, with Graphite in Place, Showing Films Associated with Chemically Reduced Fuel.

Table 2.3. ORNL-MTR-47-5 Gas Analyses and Exposure Conditions

	Capsule Type			
	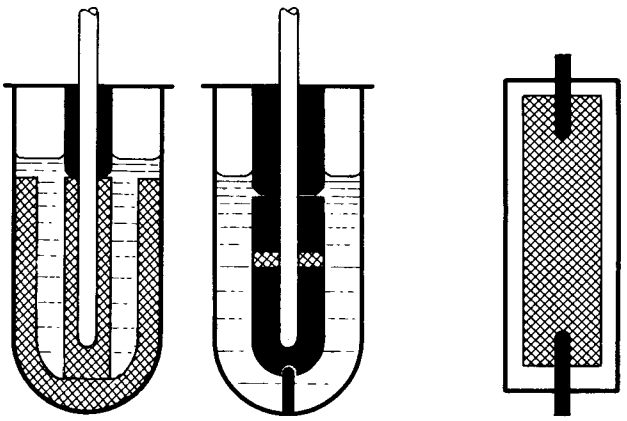			
Capsule Designation	1	2	Rear	Front
Weight of graphite, g	14.362	0.536	3.6655	3.6353
Weight of fuel, g	18.928	25.240	0.6465	0.5037
U in fuel, mole %	0.659	0.659	0.339	0.659
Weight of 93.26% U^{235}, g	0.770	1.027	0.01345	0.0205
Neutron flux,[a] neutrons cm^{-2} sec^{-1}	1.94×10^{13}	2.24×10^{13}	1.91×10^{13}	3.87×10^{13}
Fission power density,[b] w/cm^3	65.0	75.0	32.5[c]	130.0[c]
Burnup, %[d]	7.7	8.8	7.6	14.7
Volume of cover gas, ml (STP)	5.67	115	2.63	2.76
F_2,[e] %	43	34	0	0
CF_4, %	10	61	0	0
He + A, %	41	2.0	99.6	98.2
Kr,[f] %	2.7 (73%)	0.11 (40%)	0.055 (40%)	0.20 (51%)
Xe,[f] %	<0.01 (<0.05%)	0.024 (1.7%)	0.32 (46%)	1.57 (81%)
Air + CO_2, %	3.5	2.7	0	0

[a]Calculated from Co^{60} analysis of capsule metal.

[b]Calculated from the tabulated neutron fluxes and the known fuel densities at 1300°F.

[c]Calculated for fuel itself; overall power densities in the impregnated graphite are 15% of these.

[d]Calculated from the tabulated neutron fluxes.

[e]Corrected to include SiF_4, OF_2, COF_2, etc.

[f]Numbers in parentheses are percentages observed of yields calculated from burnups.

identifying the source of some of the black material. Other black deposits on the metal in the same capsule are believed to be blackened splotches of distilled salt; they were found in the interstice between the graphite liner and the INOR-8 container.

Preliminary Examination of the Fuel. – Small samples of fuel were chipped or filed from the ingots for survey by gamma spectrometry and chemical microscopy. The samples were generally selected from the outer surface in an effort to include unusual films and deposits. Such a selection was not the best for providing well-crystallized fuel phases for recognition under the microscope, and accordingly the results were less informative than in some of the previous examinations.

Petrographically, Li_2BeF_4 was again found, but the color was described as brown or olive drab. A phase thought to be Li_2ZrF_6 appeared to be pink-yellow. The more strongly reduced fuel contained uncharacterizable phases that were red, blue, and green-olive in color. Frequently encountered opaque material probably came from the films. No uranium compounds were definitely recognized, and a well-crystallized birefringent phase with a high index, which was found in capsule 2, was not identified. Such results emphasized the need for examination by x-ray diffraction.

A detailed study by gamma spectrometry of weighed samples is awaiting the use of shielded instruments in the High-Radiation-Level Examination Laboratory. Preliminary checks showed that the cerium-praseodymium activity accompanied that of zirconium-niobium and was only slightly less. In the samples from nonreduced fuel the ruthenium activity was about one-tenth that of zirconium-niobium; these activities were nearly equal in samples from reduced fuel, which indicated that ruthenium might be a significant component in some of the films.

Conclusions and Current Experiments. – Obviously, one of the main difficulties in drawing conclusions from the experiments described above is the confusion ensuing from freeze-thaw cycles that are concomitant with F_2 release. When this is alleviated, as by the use of heaters in current and future experiments, unequivocal indications of favorable behavior should be forthcoming.

The irradiation assembly (47-6) currently in preparation will use a variety of uranium concentrations (0.5 to 4.0 mole %), power densities (12 to 60 w/cm^3), operating temperatures (500 to 800°C), and capsule geometries to study fuel stability and corrosive behavior. Points of particular interest are the uranium deposition, if any, and a more precise measurement of CF_4 production. Since INOR-8 seems relatively immune to corrosive influence, molybdenum coupons will be included in some of the capsules as possible indicators of corrosion.

FLUORINE EVOLUTION FROM SOLID FLUORIDES UNDER IRRADIATION

The production of fluorine gas was first observed in molten-salt capsule experiments after irradiation in the MTR.[12] It was concluded that the fluorine was generated by self-irradiation from fission product decay at temperatures well below the melting point of the salt (450°C). Based on data from these MTR capsule experiments, it was suggested that a relatively low yield (G value) of less than 0.025 fluorine molecule per 100 ev absorbed in the solid salt would suffice to explain the fluorine produced in any of the capsules and, further, that "recombination" processes appeared to be sufficiently rapid, even at temperatures somewhat below 350°C, to prevent any loss of F_2 from the salt.

To verify this surprising behavior of the MSRE fuel salt and to obtain information regarding the nature of the processes involved without the complications of in-pile exposure and fission product production, simulated MSRE fluoride fuel mixtures, as well as samples of the constituent fluorides, have been irradiated with Co^{60} gamma rays, electrons from a Van de Graaff generator, and x rays. Each of these irradiations has been shown to produce F_2 in measurable quantity from MSRE fuel material.

Gamma Irradiation of a Simulated MSRE Fuel Salt in the Solid Phase

H. C. Savage E. L. Compere
J. M. Baker

To investigate further the radiation behavior of solid fluoride salt of composition proposed as the fuel salt in the MSRE, a capsule experiment was

[12]F. F. Blankenship *et al.*, *Reactor Chem. Div. Ann. Progr. Rept. Jan. 31, 1963*, ORNL-3417, pp. 17–30.

designed to measure possible generation and "recombination" of fluorine gas in solid fluoride salt while exposed to gamma irradiation. Test conditions and results obtained from this experiment are described.

Experimental Equipment. – The experimental equipment was an adaptation of that used in previous gamma irradiation studies[13] to the requirements of containing a fluoride salt which might have to be melted (at temperatures above 500°C) and which might generate appreciable quantities of fluorine, carbon tetrafluoride, or other gases. It consisted of an all-welded INOR-8 autoclave 0.780 in. in inside diameter × 3.185 in. long with a volume of 25 cm^3. A heating jacket around the autoclave body was used for temperature control. Multipass cooling channels, through which air was circulated, maintained the temperature of the outside wall of the assembly below 75°C, as required for operation in the Co^{60} irradiation cavity. The temperatures of the fluoride salt autoclave and container walls were continuously monitored by seven thermocouples. Figure 2.10 is a photograph of the components of the autoclave assembly.

Two $\frac{1}{8}$-in. nickel tubes provided a means of continuously monitoring the autoclave pressure and also for removing samples from the gas phase above the salt into four 50-cm^3 INOR-8 sample tanks which were interconnected to the gas phase of the autoclave.

Gamma Irradiation Test. – Thirty-five grams of powdered fluoride salt of a composition and purity simulating a possible MSRE fuel was placed in the autoclave prior to final welding of the closure cap. The salt was then melted by means of a heating jacket which surrounded the autoclave, and the 0.25-in.-diam graphite spheres (eight each of AGOT, R-0025, and pyrolytic graphite) which were attached to the end closure were placed in the molten salt. The salt was then allowed to freeze and the final closure weld made. All these operations were carried out in a dry box under a helium-gas atmosphere.

The solid salt covered the 24 graphite spheres and left a free space of 7.3 ml in the autoclave at room temperature. There was an additional volume of 23.3 ml in the connecting lines, gages, valves, etc., external to the autoclave. All interior surfaces of the autoclave and associated equipment were prefluorinated at 95°C prior to the salt addition.

The autoclave assembly was placed in the northeast corner of the east cavity of the Chemical Technology Division Co^{60} facility on February 18, 1963, and remained there until December 23, 1963 (7391 hr). In this position the salt at its center line received 0.45×10^{20} ev hr^{-1} g^{-1}. This calculated dose rate was verified by another calculation based on the observed temperature-rise rate of the outer stainless steel container due to the gamma heating effect immediately after insertion of the source.

The test was begun with 16 psia of pure helium in the gas space over the solid salt. The gas pressure was monitored for any subsequent change in pressure indicating the generation of F_2 gas and any subsequent recombination. Figure 2.11 indicates the chronological changes in pressure that were observed at various temperatures, with and without irradiation. For the initial 600 hr at 55°C, there was no significant change in pressure (<0.3 psi). The pressure then started to rise at a rate of ~2.7 psi per 1000 hr for a period of 744 hr. The temperature was then lowered to 38°C, and the rate increased to 5.4 psi per 1000 hr for the next 380 hr. After the temperature was raised to 66°C, a relatively high rate of pressure increase (23 psi per 1000 hr) was observed for 51 hr, followed by 96 hr at 6.3 psi per 1000 hr. At this time, after 1871 hr of irradiation, a gas sample was removed from the autoclave; the total absorbed dose is estimated to be 0.85×10^{23} ev/g.

Mass spectrographic analysis of the sample (Table 2.4) and flushes, which purged essentially all the gas from the autoclave, showed that it contained 14.4 std cm^3 of F_2 and small amounts of CF_4, COF_2, SiF_4, CO_2, and oxygen (after correcting for helium and for a small amount of air introduced while transferring the sample). Calculations confirmed that the observed pressure rise corresponded to the generation of these gases. These data, of autoclave pressure rise, dose rate, and gas yield, were combined to give the relation

$$G_{F_2}\left(\frac{\text{molecules of } F_2}{100 \text{ ev absorbed}}\right) = 0.0073 \times \left(\frac{\Delta \text{ psi}}{1000 \text{ hr}}\right).$$

A total pressure rise between hours 600 and 1871 of 6.1 psi occurred, corresponding to an average G_{F_2} of 0.035.

[13] L. F. Woo, T. H. Mauney, and E. L. Compere, *Reactor Chem. Ann. Progr. Rept. Jan. 31, 1963*, ORNL-3417, pp. 107–109.

Purging during the sampling operation resulted in a final atmosphere of pure helium over the fluoride salt. Testing was resumed at ambient (66°C) temperature. Gas buildup continued, and the autoclave temperature was taken to 110°C. A pressure decrease resulted for 412 hr, at an average rate of −4.2 psi per 1000 hr. At subsequent temperatures of 62, 85, 95°C, and finally again at 110°C, steady pressure rises were observed. At hour 3619 the system was sampled a second time, yielding 11.6 std cm^3 of F_2 and small quantities of the other gases cited above.

Resumption of irradiation at 100°C again resulted in the buildup of several psi of pressure. The temperature was increased to 150°C, resulting in a steady pressure decline (−22 psi per 1000 hr) until the original helium pressure was reached. The third sample (hour 4412) was withdrawn and the autoclave purged. The sample was found to be essentially pure helium (~100 ppm of F_2, no CF_4, etc.). Subsequent operation at 110°C resulted in a period of 552 hr with essentially no pressure change followed by a period of steady rise for 576 hr (4.2 psi per 1000 hr).

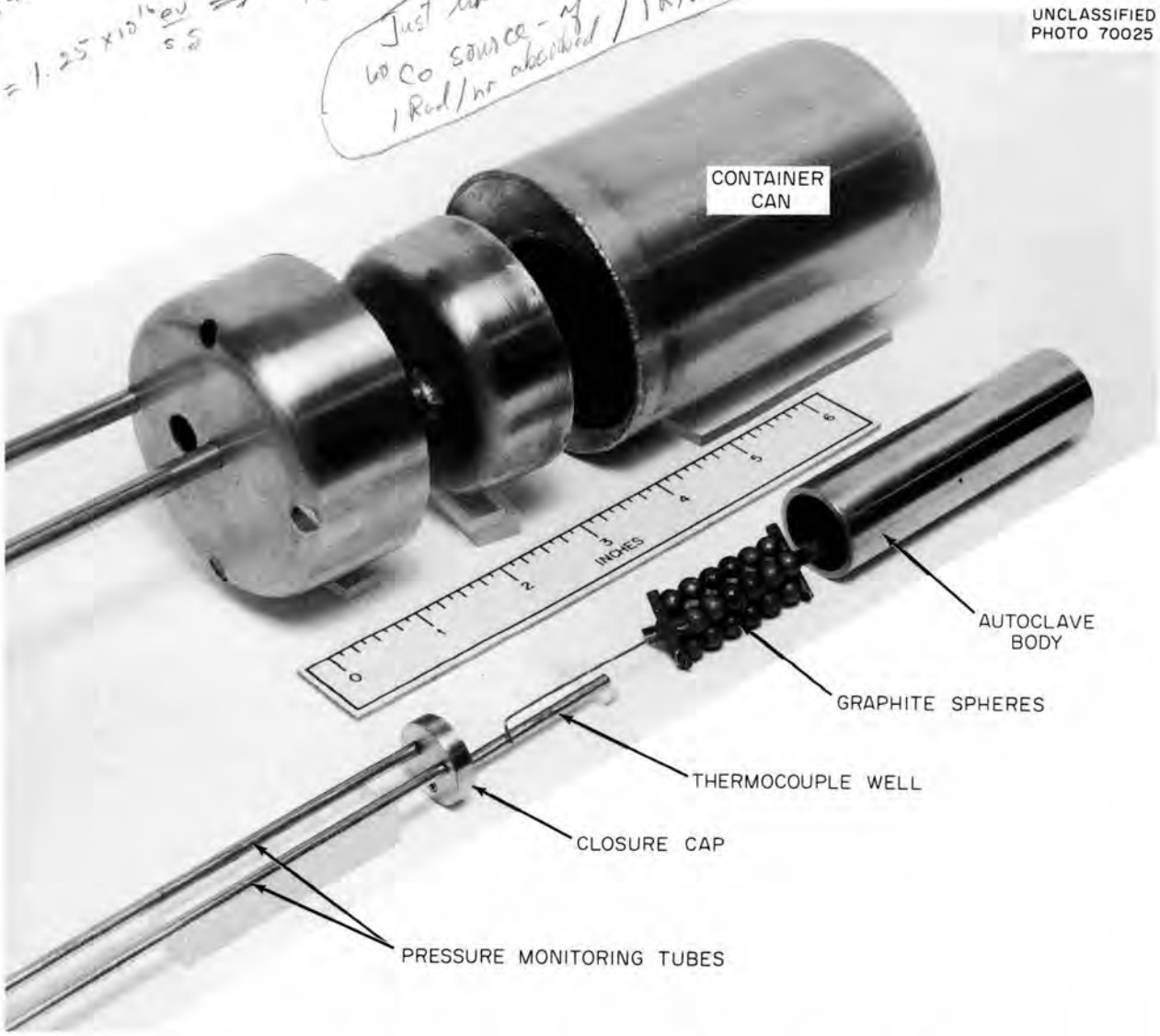

Fig. 2.10. Photograph of Component Parts of Autoclave for Gamma Radiation of Fluoride Salt.

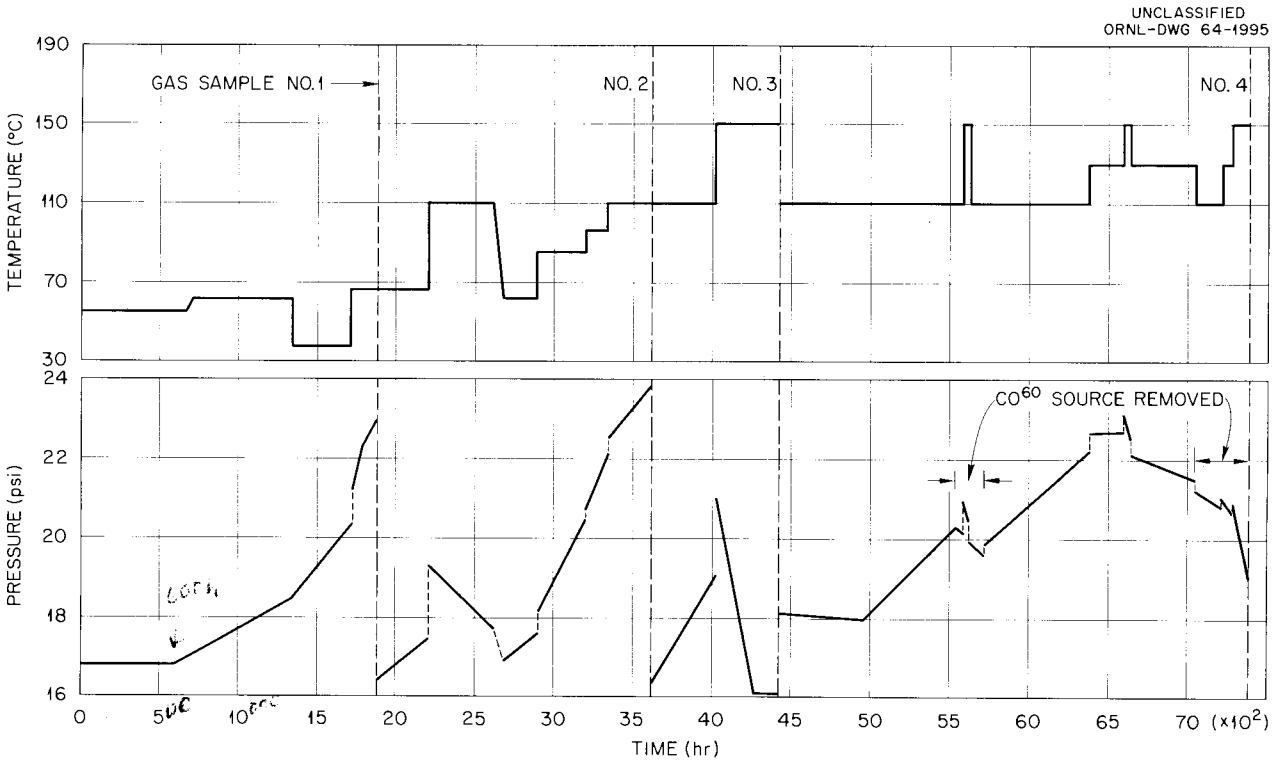

Fig. 2.11. Pressure and Temperature vs Time in a Fluoride Salt Autoclave Under Gamma Irradiation.

Table 2.4. Gas Volume[a] Removed from Gamma-Irradiated Fluoride Salt Autoclave

(Based on mass spectrographic analysis of samples and flushes)

Sample No.	Volume (std cm^3)					
	F_2	CF_4	COF_2	SiF_4	CO_2	Excess O_2[b]
1	14.4	0.26	0.03	0.02	0.39	1.4+
2	11.6	0.39	0.04	0.01	0.10	0.7
3	Trace	0	0	0	0	
Manifold	Trace	0	0	0	0	
4	4.0	0.24	0	0	0.03	0.4
Total	30.0	0.89	0.07	0.03	0.52	2.5+

[a]Helium and air components excluded.

[b]O_2 as determined, less the oxygen in atmospheric ratio to N_2 as determined.

The temperature was maintained at 110° C and the source removed. The pressure fell (−1.5 psi per 1000 hr) during 47 hr. The temperature was increased to 150°C for 29 hr, during which time the pressure decreased at a rate of −19 psi per 1000 hr. Subsequent operation at 110°C for 90 hr resulted in a pressure decrease of −3.9 psi per 1000 hr.

The source was reinserted with an autoclave temperature of 110°C, and a steady pressure rise ensued. At hour 6381 the temperature was increased to 130°C. The pressure change was negligible during 215 hr, so the temperature was again increased to 150°C for 48 hr; the pressure decreased at a rate of −15 psi per 1000 hr. Operation at 130°C until hour 7052 resulted in a pressure decrease of −2.2 psi per 1000 hr.

Observations with the source removed were then conducted at several temperatures prior to taking the final (4th) sample. At 110°C the pressure decreased at a rate of −2.3 psi per 1000 hr, at 130°C at a rate of −6.0 psi per 1000 hr, and at 150°C at a rate of −21 psi per 1000 hr.

Discussion. – It is evident from these observations that essentially pure F_2 gas is produced by the gamma irradiation of solid simulated MSRE fuel salt in the presence of graphite. In the absence of irradiation or at suitable temperatures, even in the presence of irradiation, the gas will disappear at a measurable rate, presumably recombining with the salt.

The generation of F_2 appears to require a substantial induction period, originally and after complete (sample 3, 150°C) recombination. Similar induction periods and some production of F_2 have been reported in the case of neutron-irradiated LiF, as summarized by Billington and Crawford.[14]

In our experiment the threshold appeared at a specific dose of 2.7×10^{22} ev absorbed per g. This is somewhat more than an order of magnitude less energy than appeared to be the threshold for various effects in the neutron irradiation experiments cited[14] above.

The generation of F_2 appeared to reach a steady-state rate of about 6+ psi per 1000 hr, corresponding to a G_{F_2} of ~0.05 molecule of F_2 per 100 ev absorbed (0.03 to 0.07). Such values of G_{F_2} are consistent with the previous in-pile capsule experiments.[12] The rate appeared, at temperatures below 110°C, to increase somewhat with temperature, but data are inadequate for a firm conclusion.

The gas recombined completely at 150°C and appeared roughly to balance production and recombination at 130°C. Increases in temperature from 110 to 130°C and from 130 to 150°C in the absence of irradiation appeared to increase the recombination rate about threefold. No influence of pressure on this recombination was convincingly demonstrated, though rates were perhaps lower at the lower partial pressures of F_2. Until the autoclave is opened and the contents examined, no conclusions can be drawn as to the possibly important effects of the physical condition (cracks, crystal size, etc.) and geometry of the salt cake on the rates of F_2 generation and recombination.

No reaction of F_2 with graphite was evident. The traces of CO_2, CF_4, and COF_2 could come from traces of organics, or from CO_2 picked up in handling the sample. There was sufficient oxygen in the original salt to account for the observed excess oxygen.

Fluorine Evolution from Solid Fluoride Salts Under Irradiations by Van de Graaff Electrons

J. E. Baker G. H. Jenks

Investigation of fluorine evolution from solid, MSRE-type, fused salt under fast electron bombardment has been attempted to establish whether irradiation of the solid salt results in evolution of fluorine in amounts required to explain the amounts found in capsules after in-pile tests[15] and to evaluate G_{F_2} as a function of several variables, including irradiation dose and dose rate, crystal size in the salt, and salt composition.

Experimental. – Equipment employed in these experiments included the Chemistry Division Van de Graaff, an irradiation cell,[16] and auxiliary equipment with which provisions were made for (1) evacuation of the cell and connecting lines,

[14] D. S. Billington and J. H. Crawford, Jr., *Radiation Damage in Solids*, Princeton University Press, Princeton, N.J., 1961. See esp. chap. 8, "Radiation Damage in Ionic Crystals"; Sect. 8.4c, "Structural Effects Caused by Thermal Neutron Irradiation of LiF."

[15] *MSRP Semiann. Progr. Rept. July 31, 1963*, ORNL-3529, p. 89.

[16] C. F. Weaver and R. E. Thoma, Apr. 30, 1963, unpublished internal communication.

(2) fluorination of the system, (3) addition of purified helium, (4) addition of fluorine-helium control samples, and (5) sweeping gas from the cell through potassium iodide solution. The cell was removed from the auxiliary equipment for filling with salt and for irradiations.

In general terms, determinations of the fluorine evolution caused by fast electrons were carried out by exposing a salt sample to the radiations for the desired period of time and then determining the gain in the amount of fluorine within the cell due to the irradiation. The cell was filled to atmospheric pressure with a mixture of known amounts of helium and fluorine (4 to 6% fluorine) prior to irradiation. These fluorine additions were made to minimize fluorine loss to the cell and to favor the formation of a steady state with respect to the amount of fluorine sorbed by the salt. Precautions were taken to minimize fluorine loss to the cell walls and to impurities by pretreating with fluorine. Control experiments were made to determine fluorine loss or gain under irradiation without salt in the cell. Control experiments without radiation to determine fluorine loss to the cell and/or salt were made at suitable intervals.

Fluorine analyses were made by spectrophotometric measurement of the amount of iodine formed by passage of a gas sample through potassium iodide solution. A few check analyses of the composition of cell gases by the mass spectrographic method were also obtained.

Radiation doses totaling up to 1.6×10^{18} Mev/g were employed in the experiments with the MSRE salt and up to 2.5×10^{18} Mev/g with a sample of pure LiF. These doses were accumulated in series of exposures, mostly 1 to 2 hr in length. No changes in the cell system were made during the series of exposures other than sweeping gas from the cell for analyses and introducing fresh charges of a helium-fluorine mixture. The cell was evacuated between gas charges. Evacuation periods of 20 or 2 sec were employed in different experiments. Other experimental conditions are summarized in Table 2.5.

Two samples of salt which had been exposed to a total dose of about 7.5×10^{17} Mev/g in two different experiments were examined for crystallite size by petrographic microscopy.

Results of Experiments with MSRE Fuel. – Observed changes (after correction as described

Table 2.5. Summary of Experimental Conditions Employed in Van de Graaff Experiments

Conditions	MSRE Salt[a]	LiF[b]
Sample		
Size, mils	33 to 47[c]	33 to 47[c]
Bulk density in cell, g/cm^3	1.0	1.3
Weight in path of electrons, g/cm^2	0.37	0.47
Total weight exposed, g	0.29[d]	0.37[d]
Total weight in cell, g	0.7	0.9
Crystallite size, unirradiated material, μ	<1	
Intensity of electrons impinging on salt, μa	0.61 to 2.04	1.09 to 2.04
Estimated average rate of energy deposition in salt at 1 μa, Mev hr^{-1} g^{-1}	6.3×10^{16}[e]	7.6×10^{16}[e]
Estimated temperature in salt at 1 μa, average and maximum, °C	25 to 30	25 to 30

[a]Analysis of fuel stock material made for L. F. Woo showed LiF, BeF_2, ZrF_4, UF_4, and ThF_4 (69-23-5.2-1.1-1.7 mole %).

[b]Crystalline Li^7F obtained from C. F. Weaver.

[c]Particles of crushed solid.

[d]Assuming no mixing of material during experiments.

[e]Calculated from measured values for the current and energies of electrons passing into cell and from published information on the rate of energy absorption from electron beams as a function of absorber depth. Backscattering was neglected. It is estimated that this may have introduced a ±10% error.

below) in the amount of fluorine within the cell following the radiation exposures for the several experiments with MSRE salt are shown in Fig. 2.12. Each point represents the results of one determination within a series. The exposure current and duration (2 hr unless otherwise shown) for each determination are listed in the legend. The location of a point on the abscissa corresponds to the sum of the doses accumulated prior to the given exposure and one-half of that during the exposure.

Out-of-radiation controls for experiment 9 were made prior to irradiation and after each exposure within the series. The length of exposure for each of these controls was near that obtained in the preceding radiation exposure. The losses or apparent losses found in these varied from 33 to 143 μg but were mostly in the range 50 to 80 μg, and the scatter of the results appeared random. The average value was 69.8 $\pm$ 4.4 μg probable error. The fewer control results for experiments 4 and 5*a* indicated that the scatter in these results was also random. Average values were 51 and 18 μg for 4 and 5*a* respectively. Control experiments in which the cell without salt was irradiated at 1.09 and 2.04 μa showed that fluorine was released at a low rate through the exposures. The observed rate increased approximately linearly with increasing dose to a maximum of about 7 μg per 1.09 μa-hr at a dose of 36 μa-hr. (It is likely that the fluorine was released from a Teflon gasket.)

Corrections deduced from the results of the control experiments were applied to the results shown in Fig. 2.12 to obtain more nearly correct values for fluorine evolution rates caused by irradiation. Total amounts of F_2 evolved are plotted in Fig. 2.13 as a function of dose. The G_{F_2} corresponding to a rate of 200 μg per 1.09 μa-hr is 0.016. That for any other point may be found from this relation. The maximum G_{F_2} observed was 0.02.

The petrographic examination of the irradiated salt showed that the crystallite size was >10 μ, compared with <1 μ in the unirradiated material taken from the same cell.[16]

Results of Experiments with LiF. – No fluorine evolution was detected in two experiments in which the total doses were 1.37×10^{18} and 2.57×10^{18} Mev/g and the dose rates were 8.6×10^{16} and 1.6×10^{17} Mev hr^{-1} g^{-1}. However, an uptake of

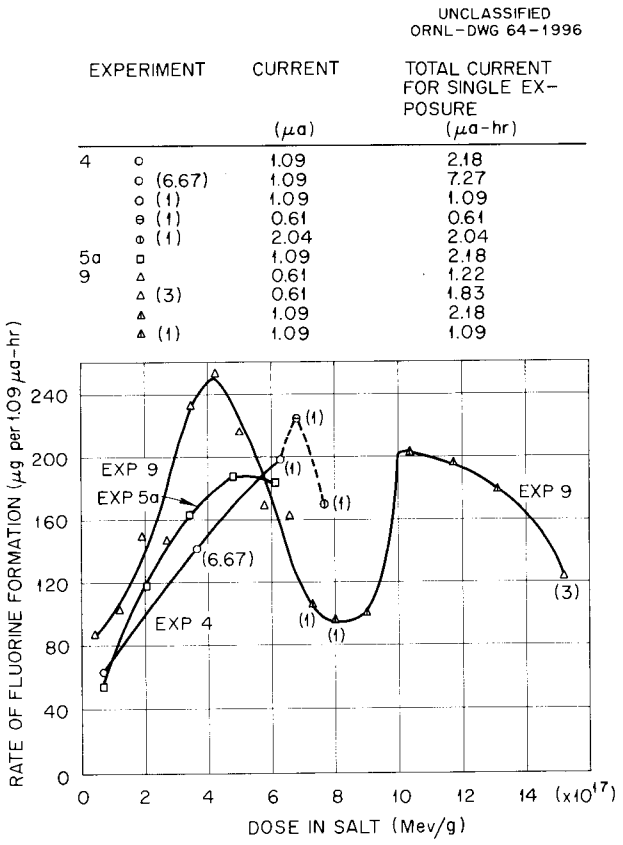

Fig. 2.12. Corrected Rate of Fluorine Formation per 1.09 μa-hr Electron Irradiation (MSRE Salt).

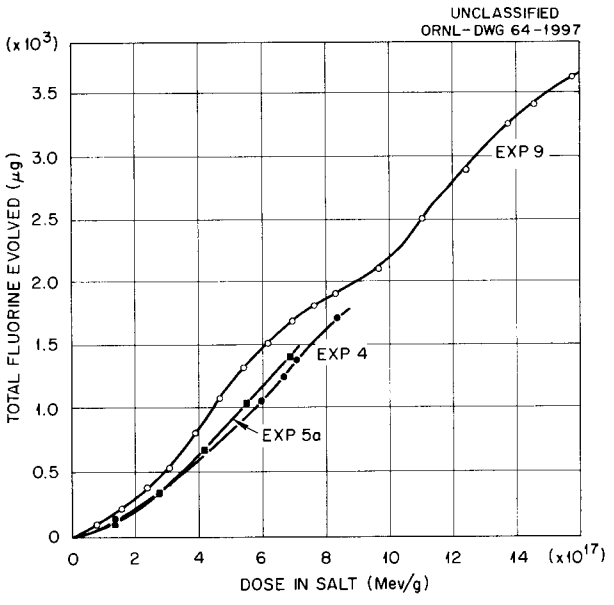

Fig. 2.13. Total Fluorine Evolved During Electron Irradiations (MSRE Salt).

fluorine by the LiF was induced by the irradiations. In the higher dose rate experiment, the rates of uptake were mostly in the range 4 to 6 μg per 1.09 μa-hr (4 to 6 μg per 8.3×10^{16} Mev/g), and there was no significant dependence upon dose. In the other experiment the uptake rates increased irregularly with dose from near zero at the start to about 10 to 20 μg per 1.09 μa-hr near the end of the experiment.

Discussion. – The experimental investigation is incomplete, and final interpretations of the data obtained so far have not been made. However, some general comments on the data and tentative interpretation of some features can be made.

The results of these experiments have demonstrated that fluorine is evolved in substantial amounts from solid MSRE fuel under electron irradiation, and, in this respect, this irradiation system is similar to the in-pile capsule systems and to other out-of-pile irradiation systems described in this chapter. The maximum G_{F_2} values observed in this work are less than those reported by the other investigators by factors of 2 to 3.

The fuel salt data obtained at doses below about 8×10^{17} Mev/g are considered first. A maximum in the evolution rate obviously occurred in experiment 9. Unfortunately, experiments 4 and 5 were terminated before the presence or absence of maximums were clearly established. However, there are indications of maximums in these data, and the suggestion, made previously,[17] that steady states were achieved in these experiments is withdrawn.

Comparison of the results of experiments 9, 4, and 5*a* shows that one effect of reducing the dose rate by a factor of about 2 was to increase the initial rates of fluorine evolution per unit dose (G_{F_2}). A similar effect of changing dose rate is indicated by the results of the two final determinations in experiment 4. It seems likely that the difference between initial yields found in this work and those reported by others resulted in large part from the difference in the dose rates employed.

The occurrence of a maximum in the evolution rate curve of experiment 9 suggests that back reaction of fluorine with defects (produced by the loss of fluorine) in the MSRE fuel is an important factor in limiting the amount of fluorine evolved. The concentration of defects must increase as fluorine is evolved, so that a leveling off of the amounts of evolved fluorine would be expected if back reaction is important. In addition, or alternatively, the increase in crystallite size during irradiation may also be important in reducing the rate of fluorine production and/or diffusion to the surface.

The increase in fluorine evolution rates after a dose of 10^{18} Mev/g shows that some marked change occurred in the salt in this dose range. The nature of the change is unknown. It can be postulated that a coalescence of defects occurred after which they were less available for recombination with fluorine. It is also possible that a breakup of crystals occurred and that this resulted in an increase in the rate of fluorine production and/or diffusion.

Experiments are continuing to elucidate the factors involved in the evolution of fluorine from fuel salt.

Fluorine Evolution from Inorganic Fluorides Under Irradiation with Soft X Rays

W. T. Rainey, Jr. D. N. Hess
T. H. Mauney

Because of the great difficulty and expense of performing experiments with salts containing mixed fission products, and because of the difficulty of interpreting the results of such experiments (which involve the presence of low concentrations of many chemical species), it seemed appropriate to study the phenomenon in the laboratory with the use of purified solids and "pure" radiations. The use of soft x rays as a radiation source has been shown effective for introducing large amounts of ionizing energy with relatively small, safe, and inexpensive equipment.[18] Study of radiolysis of solid metallic fluorides under x radiation during the past year has been primarily of a screening nature in order to determine the variables which are important.

Preliminary experiments and two irradiations of MSRE fuel salt were performed with a G-E Maxitron 250 therapy x-ray unit made available by the Biology Division. All subsequent irradiations were

[17] *MSRP Semiann. Progr. Rept. July 31, 1963*, ORNL-3529, p. 98.

[18] R. C. Palmer, M. D. Peterson, and D. C. Bardwell, *J. Chem. Phys.* **28**, 167 (1958).

performed with Muller 300 MG radiographic x-ray units from the Chemical Technology Division and the Inspection Engineering Department. All machines were operated at maximum rated current with an anode voltage of 250 kv. Dosimetry indicated that the Maxitron delivered energy to fuel salt at about four times the rate of the Muller machines.

The apparatus and techniques were designed to allow the largest possible absorption of energy in the sample, while ensuring the satisfactory containment and collection of the reactive gases. A typical irradiation cell is shown in Fig. 2.14. Thin (0.005-in.) nickel diaphragms form the ends of a cylindrical nickel container, to which are attached a Monel coupling and a Monel valve,

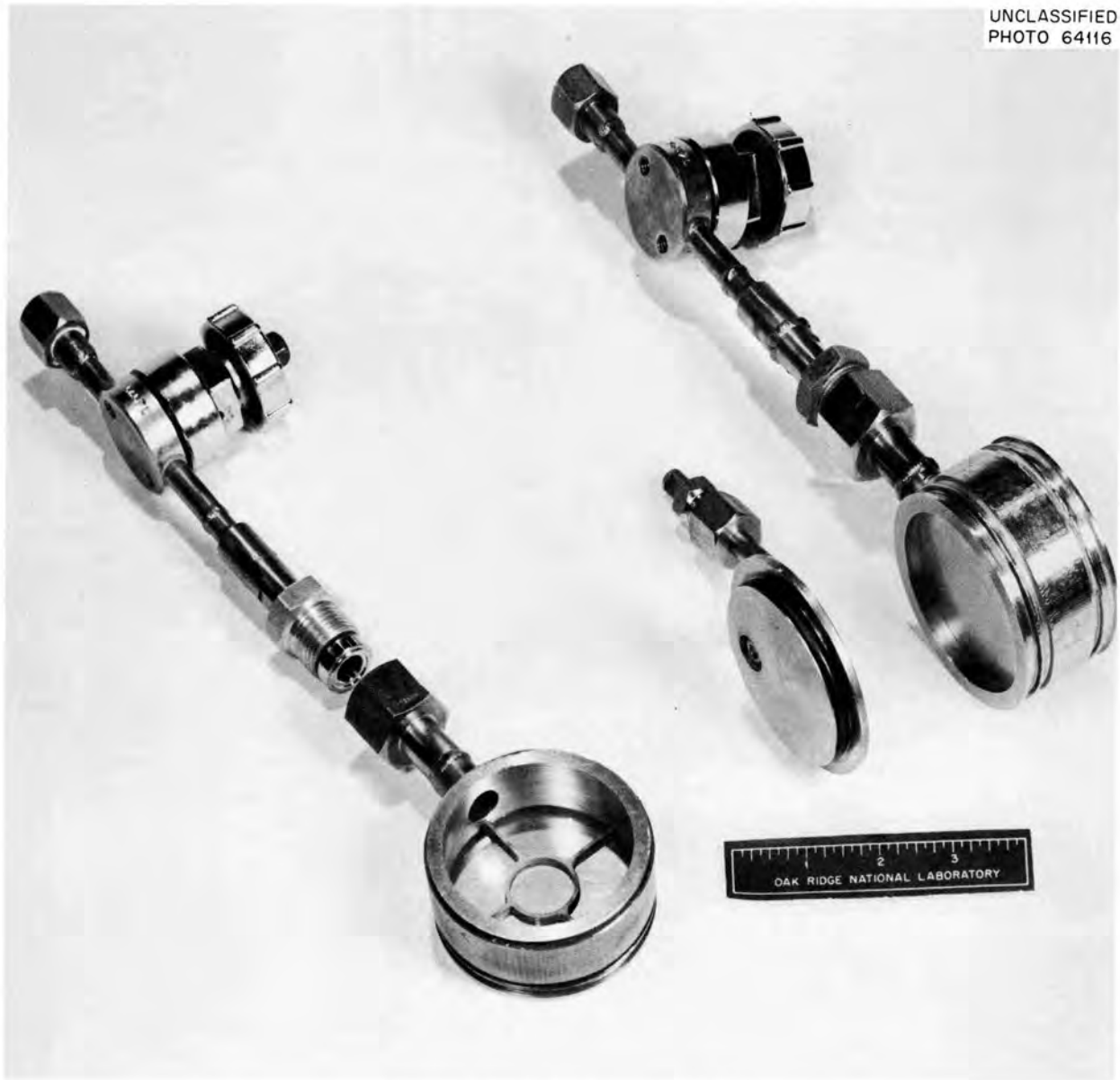

Fig. 2.14. X-Ray Irradiation Vessel.

arranged to permit loading, evacuation, pretreatment, and gas analysis. Before use, the irradiation cells were treated with fluorine at 150°C until a concentration of 500 ppm of fluorine in helium could be contained overnight at room temperature without consumption. Normally, a treatment of 10 to 14 days with fluorine was required to prefluorinate the cells. The fluoride salts (50 to 100 g/test) were loaded into the prefluorinated cells in a helium-filled dry box.

Energy input to the salt was measured by difference with the use of the Fricke dosimeter (ferrous sulfate–sodium chloride–sulfuric acid solution).[19] The difference in energy transmission through the empty cell and the cell filled with salt was assumed to be the dose to the salt. The conversion of ferrous ion to ferric ion was determined by spectrophotometry and was used in calculation of the absorbed dose, assuming $G(Fe^{3+}) = 15.6$ (ferric ions formed per 100 ev absorbed). Reproducibility of measurements generally was better than 10%. The rate of energy input (0.02 w or lower) was not sufficient to cause any problem of local overheating, and, to date, all irradiations in this program have been performed at ambient temperature, 30 to 35°C. The total energy absorption was not sufficient to cause appreciable changes in salt composition.

Gas samples were analyzed by mass spectrometric methods with instruments prefluorinated and calibrated for fluorine and fluorine compounds. In most experiments the products of radiolysis were found to be CF_4 and COF_2. In calculating the $G(F_2)$ value, all volatile fluorine compounds were assumed to have been formed from equivalent amounts of F_2 liberated from the salt. Table 2.6 summarizes the results of irradiations performed to date.

The MSRE fuel salt used in all irradiations was composed of lithium, beryllium, zirconium, thorium, and uranium fluorides (70-23-5-1-1 mole %). Irradiation of the powdered salt in the as-received condition resulted in formation of volatile carbon-fluorine compounds only. After fluorination of the fuel salt at 150°C until traces of UF_6 appeared in the cover gas, elemental fluorine, as well as volatile fluorine compounds, was found with an average

[19] J. Weiss, *Nucleonics* 10(7), 28 (1952).

Table 2.6. Summary of X-Ray Irradiation Experiments

Salt	Treatment	Dose Rate (Mev g^{-1} hr^{-1})	Total Dose (Mev/g)	Products			$G(F_2)$
				F_2	CF_4	COF_2	
		$\times 10^{12}$	$\times 10^{14}$				
Fuel salt	None	28	2.6		X	X	0.006–0.008
	Fluorinated at 150°C	6.9	14	X	X	X	0.002–0.004
	Particles <0.002 in.	6.8	14				
	Particles <0.002 in., fluorinated at 85°C	7.9	75	X	X	X	0.005–0.040
	Particles 0.023–0.033 in., fluorinated at 85°C	7.9	73		X	X	0.0006–0.004
ThF_4	Fluorinated at 160°C	18	45	X	X	X	0.003–0.008
LiF	None	1.8	6.0				
ZrF_4	None	7.0	19				
	Fluorinated at 160°C	7.0	4.5				
$6LiF \cdot BeF_2 \cdot ZrF_4$	Fluorinated at 160°C	3.4 (?)	12(?)		X	X	0.020–0.030(?)

equivalent G of 0.003. There has never been evidence, from the results of successive irradiations following fluorination, that adsorbed fluorine was liberated from surfaces by the radiation treatment.

The test salt was found to contain a wide range of particle sizes. A fine fraction (<0.002 in. in diameter) of the fuel salt was irradiated to a dose of 1.4×10^{15} Mev/g without evidence of decomposition. The salt was fluorinated at about 85°C and reirradiated. Volatile fluorine compounds were liberated with a G value of 0.02. A coarse fraction (0.023 to 0.033 in. in diameter) of the same salt, after a similar fluorination, liberated products with a G value of 0.002.

As further indicated in Table 2.6, other irradiations have been concerned primarily with the simpler component fluorides of the fuel salt. Thorium fluoride, which had been prefluorinated to exhaustion at 160°C, liberated fluorine, as well as other volatile products, with a G value of about 0.005. Under similar conditions, zirconium fluoride showed no evidence of radiolysis. Lithium fluoride, difficult to irradiate to a high total dose because of its low mass absorption coefficient, did not generate any volatile fluorine products. After fluorination at 160°C, $6LiF \cdot BeF_2 \cdot ZrF_4$, related to the MSRE fuel solvent, liberated CH_4 and COF_2 with G values of about 0.02. Studies of the crystal structure of this salt (see the section, "Crystal Structure of $6LiF \cdot BeF_2 \cdot ZrF_4$," chap. 1, this report) have disclosed the presence of relatively large contiguous voids in the lattice. The significance of such structures with respect to the escape of radiolytic products is being investigated.

Results to date indicate that x-ray irradiation is a useful source of energy for the study of radiolysis of metal fluorides and that the composition of the salt is an important parameter. It may be concluded, at least qualitatively, that the rate of fluorine liberation is a function of particle size or surface area and that the presence of impurities easily fluorinated inhibits the liberation of fluorine.

An increase in effective dose rate of more than tenfold has recently been arranged by the acquisition of a beryllium-window x-ray tube and the construction of irradiation cells in which thin diaphragms of beryllium metal are used. The increased dose rate should permit a more effective override of adventitious impurities present in the test materials. The results to date have also pointed up the importance of obtaining materials in the purest possible state; the program now includes attention to established techniques for improving the purity of the test salts.

3. Chemical Studies in Molten Salts

INTERFACIAL BEHAVIOR OF MOLTEN FLUORIDES WITH GRAPHITE AND METALS[1]

P. J. Kreyger[2] S. S. Kirslis
F. F. Blankenship

The wetting behavior of molten salts on graphite and metals is relatively unexplored.[3] The fluoride melts for the Molten-Salt Reactor Experiment, even with additional fluorides from corrosion and fissioning, do not wet graphite in the absence of extraneous impurities, but many other kinds of salts do, and there was need for delineation of the controlling factors. Among the impurities that are presumed to have a pronounced effect, oxide is outstanding in inducing wetting, generally by altering the melt-solid interface. A familiar example is the spreading of salt melts on an oxide layer on metal.

In the MSRE the oxide layer will presumably be removed from the metal walls, and nonwetting of the fuel is predicted on the basis of interfacial behavior manifested by sessile-drop experiments on metals.

One of the most sensitive indicators of wetting behavior is the contact angle. In the sense used here, wetting is defined in terms of the contact angle as measured inside the drop, and 90° marks the transition from wetting (<90°) to nonwetting (>90°). This definition was adopted because of its applicability to the effect of pressure on the penetration of graphite by molten salts, in contrast with definitions which emphasize whether or not a liquid film spreads completely.

To study wetting behavior, a vacuum-tight apparatus for observing sessile drops on horizontal plaques was assembled and equipped to operate with a static or flowing atmosphere of various gases. The shape of the drop was recorded photographically. Mass analyses of gas samples and an electrolytic analyzer for water content were used to determine the composition of gases to which the drop was exposed. Slight vibration of the sessile drop, mechanically induced from the hood ventilation system, provided a favorable condition for reaching the equilibrium contact angle and resolved much of the confusion associated with differences in advancing and receding contact angles.

Wetting Behavior on Graphite

In Table 3.1, the contact angles between the molten salts and graphite in pure helium are given, together with the surface tensions of the salts. In Fig. 3.1, the cosine of the contact angle between molten fluorides and graphite is plotted against the surface tension at 700°C. The experimental points can be represented by a straight line. A point representing subcooled NaF at 700°C (ref. 4) fits well on the line. Although more data are desired, the results obtained now indicate that the change from nonwetting to wetting on graphite occurs with a molten-salt surface tension of about 180 dynes/cm.

The simple view that a decrease in surface tension tends toward wetting can be misleading. For example, in the preparation of cermets,[5] a

[1] P. J. Kreyger and S. S. Kirslis, *Sessile Drops of Molten Halides on Graphite and Metals*, paper presented at the American Chemical Society Winter Meeting, Denver, Colo., Jan. 19–24, 1964.

[2] Euratom exchange scientist assigned to the Reactor Chemistry Division of ORNL.

[3] *MSRP Semiann. Progr. Rept. July 31, 1963*, ORNL-3529, p. 125.

[4] B. S. Ellefson and N. W. Taylor, *J. Am. Ceram. Soc.* **21**, 205 (1938).

[5] L. M. Parikh and M. Hemenik, *J. Am. Ceram. Soc.* **40**, 316 (1957).

Table 3.1. Contact Angle Between Molten Halides and Graphites

Salt	Temperature (°C)	Contact Angle (deg)	Surface Tension (dynes/cm)
$2LiF \cdot BeF_2$	500 to 800	147 ± 12[a]	~230[b]
Fuel salt[c]	500 to 800	140 ± 8	~230[b]
LiF-NaF[d]	700 to 800	120 ± 4	~220[e]
Flinak[f]	500 to 720	90 ± 4	~184[e]
CsF	700	41 ± 2	107
KCl	810	68 ± 2	97

[a]Accuracy is estimated from the spread in results.

[b]Calculated from sessile drops — previous measurements yielded about 200 dynes/cm.

[c]$LiF\text{-}BeF_2\text{-}ZrF_4\text{-}ThF_4\text{-}UF_4$ (70-23-5-1-1 mole %).

[d]60-40 mole %.

[e]G. W. Mellors and S. Senderoff, *Research Summary URS-70*, Parma Research Laboratory, Union Carbide Corporation.

[f]LiF-NaF-KF (46-12-42 mole %).

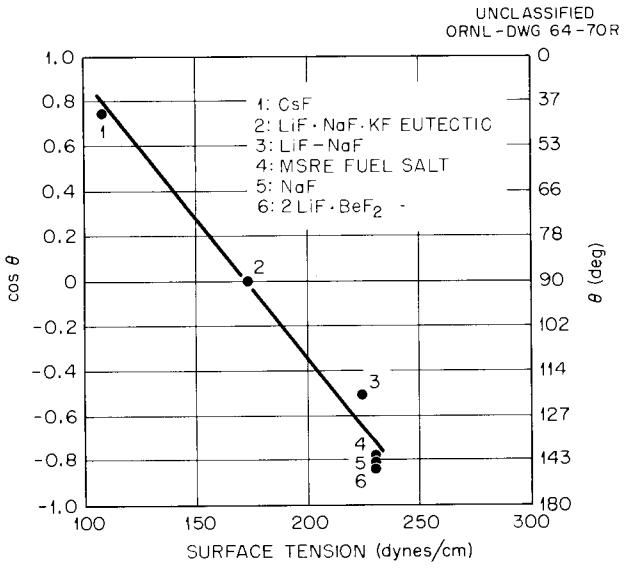

Fig. 3.1. Contact Angle Between Molten Fluorides and Graphite vs Surface Tension at 700°C.

decrease in surface tension of the liquid may accentuate either the wetting or nonwetting, depending on the sign of the numerator in the expression

$$\cos\theta = (\gamma_{s,g} - \gamma_{s,l})/\gamma_{l,g} ,$$

where γ is the interfacial tension and s, l, and g stand for solid, liquid, and gas respectively. Evidently, the changes in $\gamma_{s,l}$ with $\gamma_{l,g}$ are too small to change the sign of the numerator.

With other materials, such as organic liquids and plastics, a decreasing surface tension of a family of liquids is associated with a regular change from nonwetting to greater and greater wetting of a given solid. Such cases, apparently characteristic of low-surface-energy solids that allow significant changes in $(\gamma_{s,g} - \gamma_{s,l})$, have been treated.[6]

That salts on metals and graphite should follow the latter behavior even though $\gamma_{s,g}$ is quite large was an enlightening result of the sessile-drop experiments with molten salts. The obvious implication is that $\gamma_{s,l}$ is also quite large, at least for molten fluorides having a high surface tension.

In a pure static helium atmosphere the contact angle between either $2LiF \cdot BeF_2$ or MSRE fuel and graphite was about 145° at temperatures between 450 and 700°C, and the drop remained unchanged for indefinitely long periods.

Up to 400 ppm of O_2 in water-free helium did not change the contact angle; however, traces of H_2O

[6]L. I. Osipow, *Surface Chemistry*, pp. 237–48, Reinhold, New York, 1962.

changed the contact angle drastically. For instance, in flowing helium containing 10 ppm of H_2O, the contact angle of the MSRE fuel changed from 150 to 20° within 1 hr while a visible layer of scum-oxides was formed. Essentially the same occurred with $2LiF \cdot BeF_2$, although the wetting proceeded less rapidly (Fig. 3.2). In some cases the visible layer on the surface of the drop became a shell that was finally ringed by a wetting liquid. The presence of oxides in the salt was not a sufficient condition for wetting; it was the formation of an oxide layer that was responsible for the wetting of graphite. This can be substantiated by the fact that substitution of dry helium for moist helium stopped the advance of the wetting. The drop shape remained unchanged under dry helium, and wetting started again when the circulation of moist helium was recommenced.

The sensitivity of the contact angle toward water vapor present in the helium was much less for LiF-NaF and for the LiF-NaF-KF eutectic mixtures. Up to 200 ppm of H_2O did not change the contact angle, while extended exposure of the droplet to 1000 ppm of H_2O did decrease the contact angle slightly (10°). These salts are much less reactive toward water because of the absence

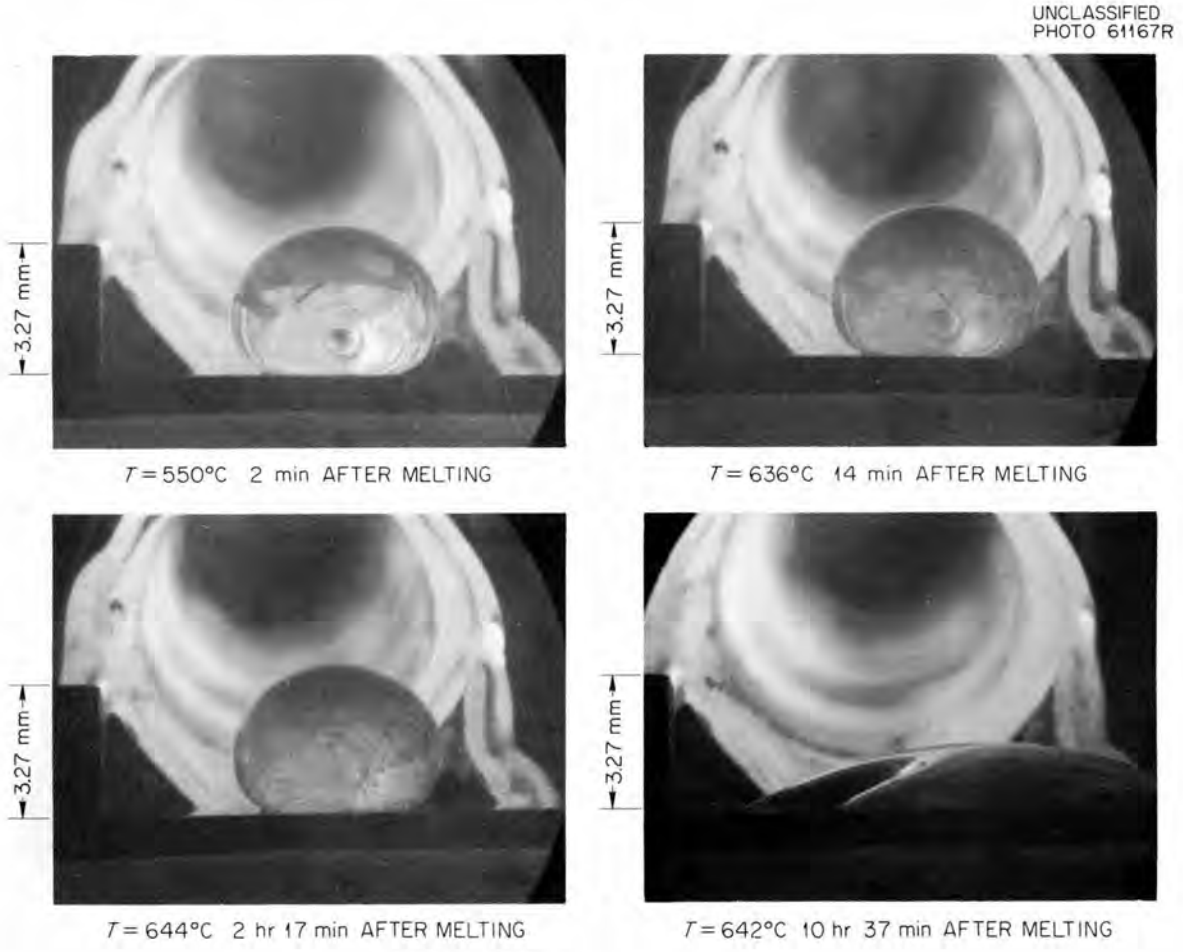

Fig. 3.2. Effect of Moisture in Helium on Wetting of Graphite by MSRE Coolant for Different Elapsed Times After Melting.

of BeF_2, and only a slow hydrolysis occurred; also the resulting oxide was more soluble.

The aforementioned values of the contact angle and its change in the presence of water vapor were the same for the three types of graphite investigated (AGOT, CGB, and pyrolytic) and were also independent of the orientation of the graphite sample. However, chemisorbed oxygen on the graphite appeared to be of relatively slight significance in all the experiments, provided that degassing of graphite was carried out at 650°C or above.

Induced Wetting on Graphite

The experimental material available indicates the following role of water vapor in inducing spreading on graphites. Water vapor present in the gas diffuses to the curved liquid-gas interface and reacts there with salt to produce oxide – for instance, BeO in the case of $2LiF \cdot BeF_2$ salt. The oxides formed at the liquid-solid-gas contact build up an oxide ring that becomes wetted by the liquid. New oxide is then formed on the fresh liquid at the contact line between solid and liquid. In other words, the liquid "crawls" on its own oxide. This mechanism clearly requires that the salts wet their oxides. Wetting of oxides by salts was confirmed by experiments, but the hypothesized oxide layer between salt and graphite has not been clearly observed metallographically.

Wetting Behavior on Metals

In Table 3.2 the contact angles between several salts and oxide-free metal surfaces are listed, together with the surface tension of the salt. The contact angle was decreased greatly by oxide layers on the metal surface. If sufficient oxide was present on the metals, the contact angle was 0° and complete spreading ensued. However, when the oxide layer was removed before formation of the sessile drop (by hydrogen treatment at high temperatures for nickel and copper and by heating to approximately 800°C for gold and platinum), the value of θ was >0. In contrast to the behavior on graphite, spreading of the melts on metals occurred when helium containing 10% oxygen was passed over the nonwetting drops. Removal of the oxide layer in situ resulted in the recoalescence of the liquid. Figure 3.3 illustrates this by depicting the spreading and recoalescence of $2LiF \cdot BeF_2$ on gold.

The observed nonwetting contact angles between the fluoride salts and metals have some practical consequences. In a nonwetting system, gas bubbles adhere to the wall and can easily form a gas film between the wall and liquid. Such a situation influences both heat transfer and flow properties. Surface-tension measurements of some fluorides by the bubble pressure technique should be quite sensitive to whether or not an oxide-free metal bubble tip is used. If the liquid does not wet, the outside diameter rather than the inside diameter

Table 3.2. Contact Angle Between Molten Halides and Metals

Metal	Salt	Temperature (°C)	Contact Angle (deg)	Surface Tension (dynes/cm)
Gold	Li_2BeF_4	525 to 625	138 ± 2	~230
Platinum	Li_2BeF_4	640 to 740	127 ± 3	~230
Nickel	Li_2BeF_4	480 to 600	115 ± 2	~230
Copper	Li_2BeF_4	460 to 540	95 ± 2	~230
Nickel	Fuel salt	670	~133	~230
Platinum	LiF-NaF	770	~100	217
Platinum	Flinak	640	~75	180
Copper	Flinak	680	~40	175
Nickel	NaCl-KCl	670	~35	

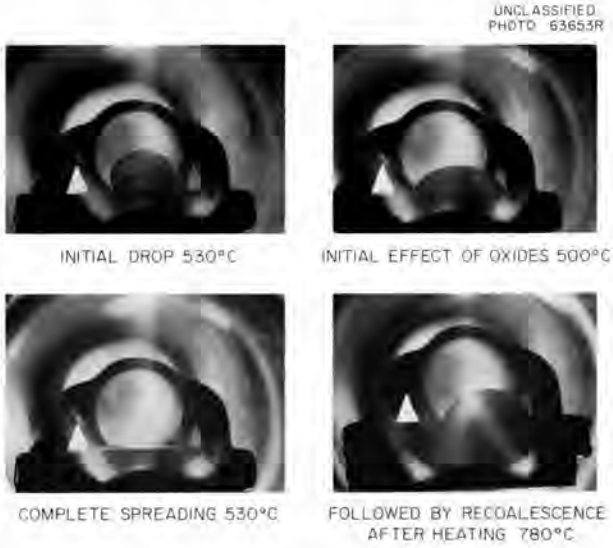

Fig. 3.3. Spreading of $2LiF \cdot BeF_2$ on Gold in Presence of Oxygen Followed by Recoalescence After Heating to Remove Oxygen.

of the tip determines the maximum bubble pressure. The existing data on the surface tensions of high-surface-tension salts seem to be approximately correct and to have been obtained by use of inside diameters; this leads to the unproved and rather implausible implication that the work was carried out with oxide-coated, or otherwise altered, bubble tips.

REMOVAL OF MOISTURE FROM MSR GRAPHITE

W. K. R. Finnell F. A. Doss J. H. Shaffer

Any water vapor which is present in the MSRE core system will react with the molten fluoride fuel mixture to produce HF and ZrO_2; therefore it is desirable, if not essential, that the ingress of water to the MSRE fuel system be minimized. The moderator graphite is one obvious source of such water, and the MSRE startup program includes plans for removal of water by heating the completed but empty reactor core to 650°C while helium gas is circulated through the reactor core. An additional long-term cleaning of the reactor core by circulating a uranium-free salt mixture will be conducted before the actual fuel salt is added to the system. A brief study has been made to determine the quantity of water which can be removed from the MSRE graphite, and other graphites, by purging with helium.

This study has been made on short (6- to 12-in.) pieces of graphite having the same cross section as the MSRE moderator elements. Each piece was enclosed in a close-fitting Inconel can (Fig. 3.4) which was mounted in a furnace and connected to a system for recirculation of helium gas over the specimen and through magnesium perchlorate and a Dry Ice cold trap in a drying train. The water-vapor content of the helium emerging from the graphite was measured continuously with a MEECO moisture analyzer as the temperature of the graphite was raised at controlled, constant rates (5 to 65°C/hr) to 700°C.

Earlier tests[7] with AGOT and TS281 graphites (both much more permeable than the MSRE moderator) showed that physically adsorbed water and what appeared to be chemisorbed water could be removed by purging with helium. Water vapor was shown to readsorb readily from moist helium on such graphite blocks during 2-hr exposure periods. Similar observations have also been made on other grades of permeable graphite. The behavior of a typical material (CS-312 graphite) is shown in Fig. 3.5.

The chemical specification for MSRE moderator graphite limits permissible oxide contamination to 30 cm^3 of CO (STP) per 100 cm^3 of graphite when evolved gases are held in contact with the graphite specimen while heating to 1800°C. This test does not include water which would be removed by evacuation at room temperature. If this quantity of CO is initially present in the assembled reactor moderator as water vapor, then approximately 465 g of H_2O would be available for reaction with the fuel salt mixture. This amount of H_2O would be equivalent to about 100 ppm of oxide ion in the fuel salt mixture.

Before the actual MSRE graphite became available, a section of a development test bar was supplied as representative of MSRE graphite. As indicated in Fig. 3.6, essentially no water was removed from this bar by the purging treatment. Moreover, when the graphite was exposed to moist helium, very little water was physically adsorbed and essentially none was chemisorbed by this graphite. Exposure of the graphite to moist helium for periods up to 12 hr failed to produce evidence

[7] J. H. Shaffer and H. F. McDuffie, *Trans. Am. Nucl. Soc.* 6(2), 355 (1963).

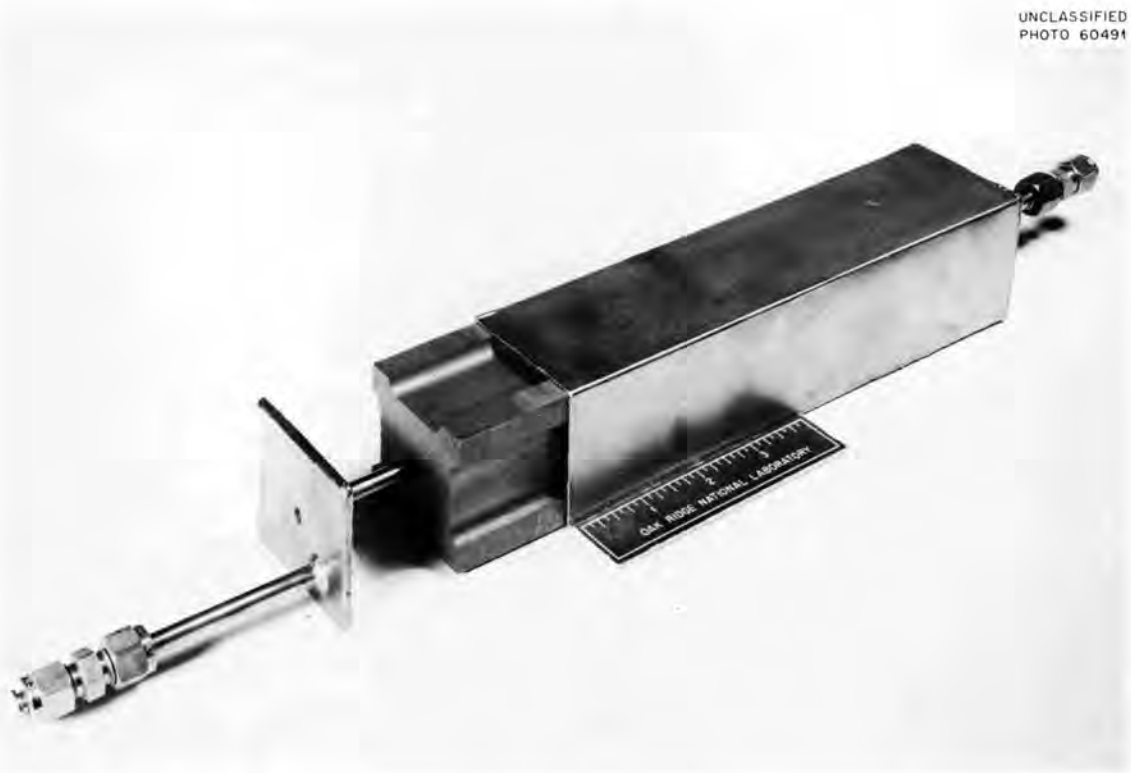

Fig. 3.4. Graphite Test Assembly for Moisture Removal Studies by Helium Purging at Elevated Temperatures.

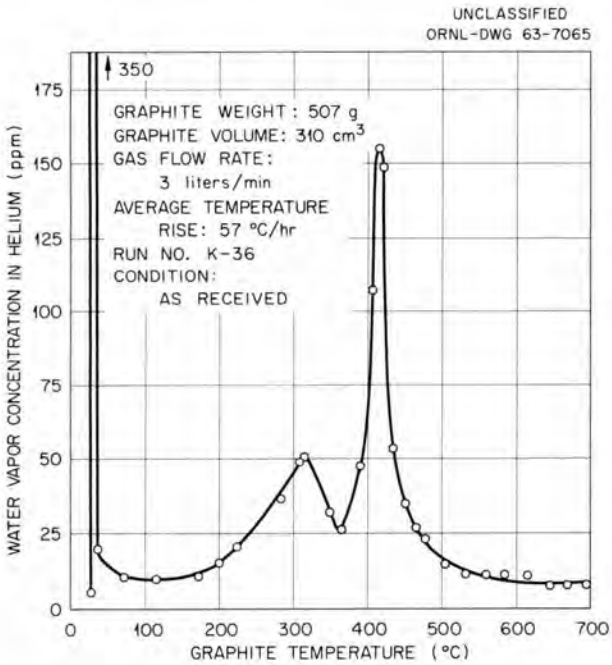

Fig. 3.5. Removal of Moisture from CS-312 Graphite by Helium Purging While Heating to 700°C.

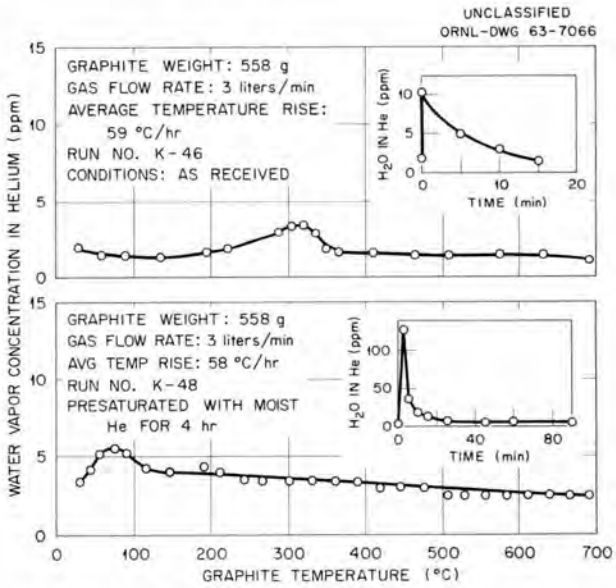

Fig. 3.6. Removal of Moisture from MSRE Graphite by Helium Purging While Heating to 700°C. Insets: Removal by purging at room temperature.

for chemisorbed moisture. (The insets in Fig. 3.6 illustrate removal of water on purging at room temperature.) To provide a test under extreme conditions, the graphite block was immersed in water for 1 hr, was allowed to drain at room temperature, and was then heated to 100°C while purging with helium. Upon subsequent heating to 700°C while purging with helium, some evidence of chemisorbed-water removal was noted (Fig. 3.7). However, a subsequent exposure of the graphite block to moist helium for 4 hr again failed to show any chemisorption of water vapor.

More recently, actual MSRE moderator elements (rejected for mechanical defects) have been made available and are being tested. For one such element (bar No. 1228, shown in Fig. 3.8), essentially no physically adsorbed water was removed by the helium purging technique at room temperature. The chemisorbed water that was removed by helium purging while heating to 700°C corresponded to only 1.32 cm^3 of water vapor per 100 cm^3 of graphite. It is of interest that results obtained by outgassing three graphite samples from the same moderator element in accordance with the graphite specifications were 11.9, 1.5, and 1.3 cm^3 of CO (STP) per 100 cm^3 of graphite.[8] The agreement between the two concordant outgassing results and the amount of chemisorbed water removed indicates that the MSRE graphite will contain less than 2 cm^3 of CO per 100 cm^3 of graphite and that it will release this oxygen in the form of water vapor during the planned pretreatment. The total amount is, of course, less than 10% of the amount permitted by the specifications.

On the basis of these data, the unclad-graphite moderator for the MSRE should not release dangerous quantities of water vapor into the reactor core system. While quantities of adsorbed moisture found in "as received" graphites have been small, the helium purge treatment that is planned during reactor startup operations should provide an effective means for its removal. Furthermore, there should be little or no contamination to the graphite moderator by moist air during possible maintenance operations on the reactor core. Additional studies of moisture removal from rejected MSRE moderator elements will be made to provide a broader base for these conclusions.

[8] J. P. Blakely, Reactor Chemistry Division, to W. H. Cook, Metals and Ceramics Division, intra-laboratory communication, Feb. 4, 1964.

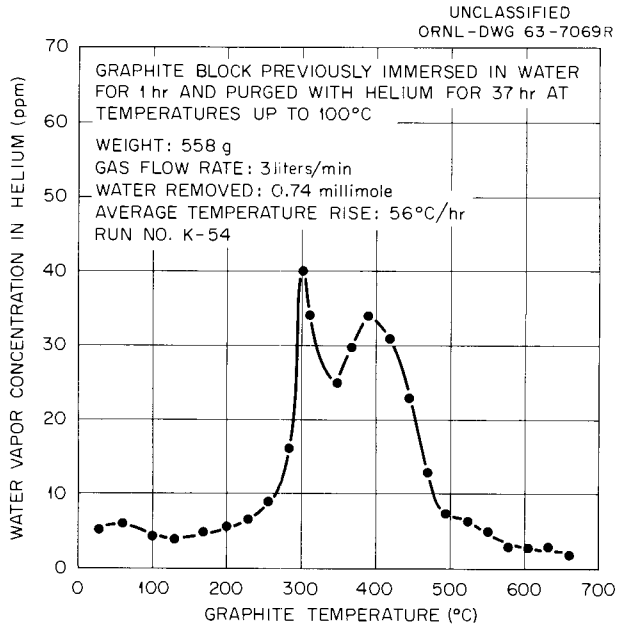

Fig. 3.7. Removal of Moisture from MSRE Graphite by Helium Purging While Heating to 700°C.

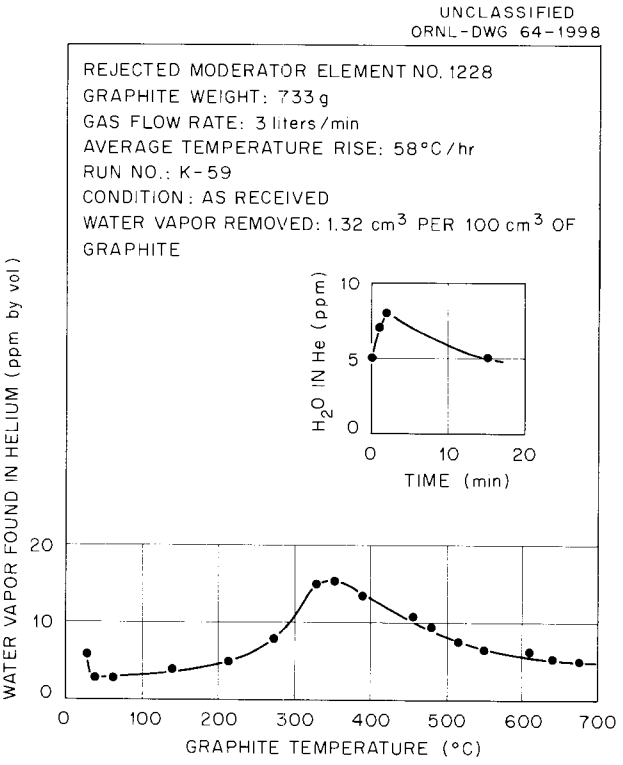

Fig. 3.8. Removal of Moisture from MSRE Graphite (Grade CGB) by Helium Purging While Heating to 700°C. Inset: Removal by purging at room temperature.

OXIDE BEHAVIOR IN $2LiF \cdot BeF_2$ (ref. 9)

J. E. Eorgan C. F. Baes, Jr.
H. H. Stone B. F. Hitch

Previously reported results[10] on the solubility behavior of UO_2 and ZrO_2 in $2LiF \cdot BeF_2$ suggested that the separate pure oxides are the stable phases at 600°C rather than $(U\text{-}Zr)O_2$ solid solutions, and that they dissolve in accordance with the simple solubility product behavior,

$$Q_{UO_2} = [U^{4+}]\,[O^{2-}]^2 \sim 1 \times 10^{-5}\ \text{mole}^3\ \text{kg}^{-3},$$

$$Q_{ZrO_2} = [Zr^{4+}]\,[O^{2-}]^2 \sim 3 \times 10^{-5}\ \text{mole}^3\ \text{kg}^{-3}.$$

These studies have continued,[11] the equilibrium reaction

$$U^{4+}\,(\text{soln}) + ZrO_2\,(c) \rightleftharpoons UO_2\,(c) + Zr^{4+}\,(\text{soln}),$$

$$Q = [Zr^{4+}]/[U^{4+}], \quad (1)$$

being investigated as a function of temperature and as a function of the U^{4+} and Zr^{4+} concentrations. The results of these measurements are summarized in Fig. 3.9. The equilibrium quotient for this reaction specifies the $[Zr^{4+}]/[U^{4+}]$ ratio when both UO_2 and ZrO_2 are present as solid phases at equilibrium. Since the actual ratio in the MSRE fuel is >5, with $[Zr^{4+}] \sim 1.3$ moles/kg, while the present results indicate the equilibrium ratio is ~1.5, it is anticipated that only ZrO_2 would precipitate as a result of oxide contamination of the fuel. The equilibrium ratio $[Zr^{4+}]/[U^{4+}]$ appears to decrease with increasing temperature. As the concentrations of Zr^{4+} and U^{4+} decrease, corresponding in reactor operation to flush salt contaminated with decreasing amounts of fuel salt, the equilibrium ratio increases, as does its dependence on temperature. The points in Fig. 3.9 at the lowest Zr^{4+} concentrations correspond to the solubilities of UO_2 and ZrO_2 in flush salt saturated with BeO. These values (in moles/kg) are presently estimated to be:

	500°C	600°C	700°C
$[Zr^{4+}]$	0.0079	0.0098	0.0119
$[U^{4+}]$	0.0016	0.0026	0.0044
Ratio	5.0	3.8	2.7

Previously reported results in these dilute solutions[11] were scattered, partly because of analytical difficulties and, more importantly, because of the slowness of approach to saturation in such solutions. Indeed, throughout the range of the data in Fig. 3.9, it now appears that some of the previously reported ratios were in error because equilibrium had not been attained, and the results shown in Fig. 3.9 are considered the most accurate that are presently available. Measurements are being continued, and the rates of approach to oxide saturation are being studied carefully.

No evidence has been found for oxide solid phases, other than BeO, UO_2, and ZrO_2, in these experiments. The variation of the equilibrium ratio with Zr^{4+} concentration is attributed to activity coefficient variations. The further effect of the $[Li^+]/[Be^{2+}]$ ratio on the equilibrium $[Zr^{4+}]/[U^{4+}]$ ratio is presently being determined.

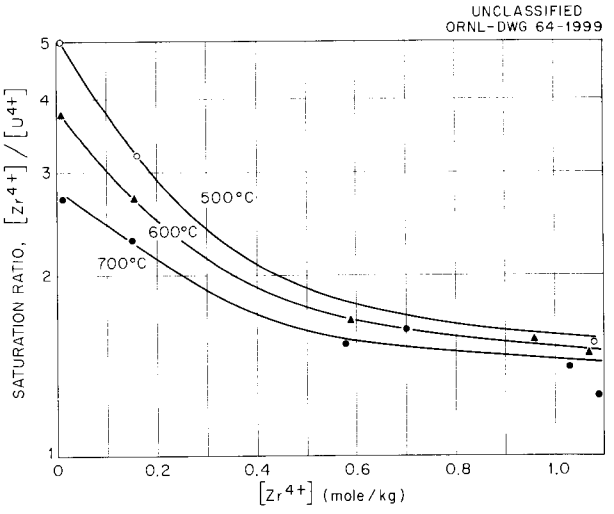

Fig. 3.9. Ratio $[Zr^{4+}]/[U^{4+}]$ at UO_2 and ZrO_2 Saturation of $2LiF \cdot BeF_2$ as a Function of $[Zr^{4+}]$.

[9] C. F. Baes, Jr., J. H. Shaffer, and H. F. McDuffie, *Trans. Am. Nucl. Soc.* 6(2), 393 (1963).

[10] *Reactor Chem. Div. Ann. Progr. Rept. Jan. 31, 1963*, ORNL-3417, p. 38.

[11] *MSRP Semiann. Progr. Rept. July 31, 1963*, ORNL-3529, p. 111.

The absence of $(U\text{-}Zr)O_2$ solid-solution formation was verified by two additional experiments.

First, 0.3 mole of UO_2 per kg of melt was found to dissolve rapidly and completely in $2LiF \cdot BeF_2$ containing initially 1.3 moles of Zr^{4+} per kg. The resulting mixture of melt and precipitated ZrO_2 was equilibrated for five weeks at 600°C, with ZrO_2 additions occasionally being made, up to a total of 1.3 moles per kg of melt. No loss of U^{4+} from the melt to the solid phase was detected during this period, thus indicating no $(U\text{-}Zr)O_2$ solid-solution formation. Subsequently, sufficient UF_4 was added to precipitate UO_2, and the system was equilibrated further. In Fig. 3.10 are photomicrographs of the starting materials and the well-crystallized oxide mixture which resulted from this experiment. X-ray diffraction examination of this mixture indicated only cubic $UO_{2.00}$ and monoclinic ZrO_2 to be present.

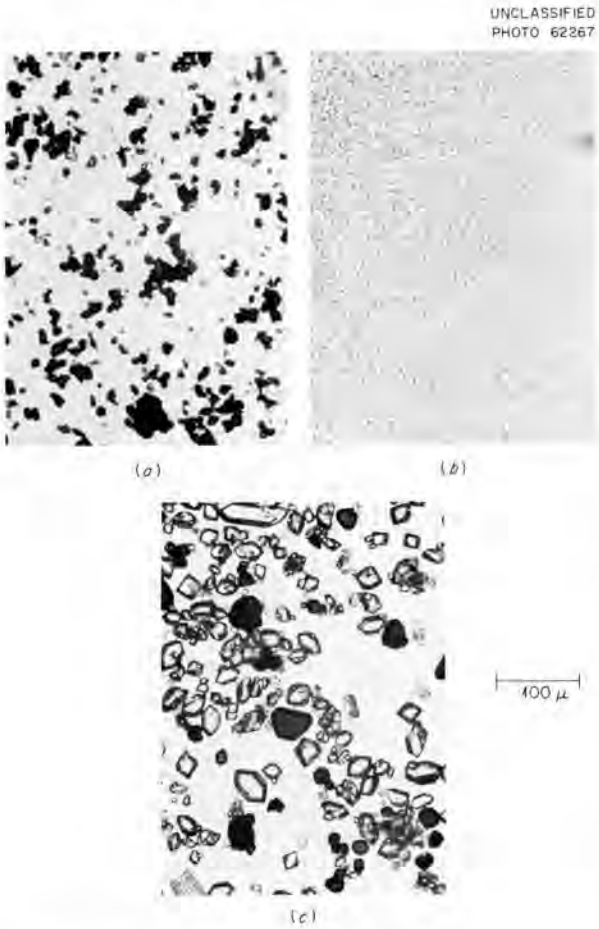

Fig. 3.10. Photomicrographs of (*a*) $UO_{2.12}$ Starting Material, (*b*) ZrO_2 Starting Material, and (*c*) Mixture of Well-Crystallized UO_2 and ZrO_2 Resulting from Equilibration with $2LiF \cdot BeF_2$-UF_4-ZrF_4 at 500–700°C.

Secondly, $(U\text{-}Zr)O_2$ solid solutions were prepared by firing mixtures of UO_2 and ZrO_2 at 1800°C. These solid solutions were equilibrated with $2LiF \cdot BeF_2$ for a few days at 600°C and decomposed into the separate pure oxides.

These results, which indicate that $(U\text{-}Zr)O_2$ solid solutions should not form under reactor conditions, are in disagreement with published phase diagrams for the UO_2-ZrO_2 systems,[12] which predict that in the temperature range considered here, two immiscible solid solutions, one rich in UO_2 and the other rich in ZrO_2, should be the stable solid phases. This inconsistency is thought to be due to the difficulty of attaining equilibrium in the conventional phase studies of such refractory oxide solids. The phase diagram will be investigated further at temperatures above 700°C, with $2LiF \cdot BeF_2$ being used as a medium for equilibration, in order to determine the lower temperature limits of solid-solution formation.

HF-H_2O EQUILIBRIUM WITH MOLTEN $2LiF \cdot BeF_2$

A. L. Mathews[13] M. K. Kemp[14]
C. F. Baes, Jr.

The equilibrium

$$H_2O(g) + 2F^-(\text{soln}) \rightleftharpoons O^{2-}(\text{soln}) + 2HF(g) \qquad (2)$$

is of considerable importance in the chemistry of molten fluoride salt systems. By this reaction, water present initially, or later introduced from the gas phase, produces oxides in the melts. (The reverse of this reaction is employed to remove oxides by the H_2-HF purification procedure.) It is of considerable interest to know the position of this equilibrium as a function of temperature, melt composition, and, particularly, oxide concentration. In addition, since metal oxides have a limited solubility in $2LiF \cdot BeF_2$, wherein the

[12] I. Cohen and B. E. Schaner, *J. Nucl. Mater.* 9, 18–52 (1963).

[13] ORINS Oak Ridge Graduate Research Fellow from the University of Mississippi.

[14] ORNL temporary summer student employee, 1963.

solubility of BeO has been estimated to be ~0.07 mole per kg,[15] study of the reaction represented by Eq. (2) in melts saturated with a metal oxide should provide data on the thermodynamic activity of the corresponding metal fluoride; that is, for the reaction

$$H_2O(g) + (2/X)MF_x\,(soln) \rightleftharpoons (2/X)MO_{x/2}(c) + 2HF(g) \quad (3)$$

the equilibrium constant

$$K_M = \frac{P_{HF}^2}{P_{H_2O}\, a_{MF_x}^{2/X}} \quad (4)$$

(wherein HF and H_2O are assumed to be ideal gases in the temperature range 500 to 700°C) contains only the measurable quotient P_{HF}^2/P_{H_2O} and the activity of the fluoride, MF_x, formed from the oxide $MO_{x/2}$. Thus a study of such equilibria could provide needed thermodynamic information as well as a practical understanding of the behavior and removal of oxides as contaminants in molten fluoride systems.

The experimental procedure is the following: A stream of H_2 gas is presaturated with HF and H_2O by passing it through aqueous HF solution in a thermostated container, and the resulting dilute mixture of HF and H_2O in H_2 is then bubbled through the molten-salt solution under study. The compositions of both the influent and effluent gas streams are obtained by alkalimetric titration (for HF) and by Karl Fischer analysis (for H_2O). By varying the input gas composition, it was found that equilibrium is rapidly attained with these dilute gas mixtures (P_{HF} and $P_{H_2O} \leq 0.03$ atm). Good material balance between the influent and effluent gas was obtained, and no appreciable increase in HF solubility has thus far been induced by the presence of oxides in the melts.

Results have been obtained for LiF-BeF_2 melts saturated with BeO (Fig. 3.11) and for melts saturated with ZrO_2 (Fig. 3.12), as a function of temperature and with a limited variation in melt composition. In Fig. 3.11 the P_{HF}^2/P_{H_2O} quotients obtained in studies with pure liquid BeF_2 are also shown. This curve is from the recent

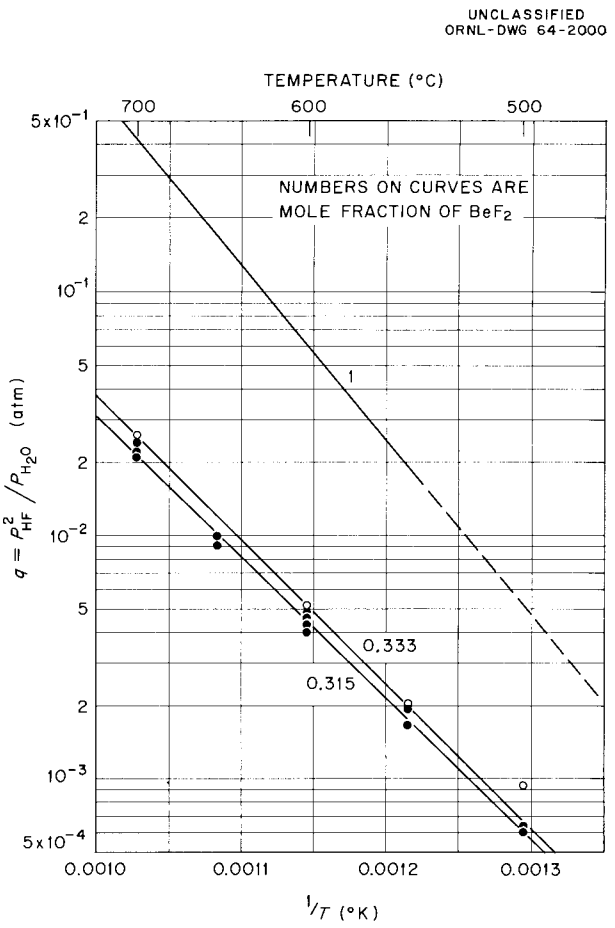

Fig. 3.11. Variation of Equilibrium P_{HF}^2/P_{H_2O} Quotients with Temperature in LiF-BeF_2 Melts Saturated with BeO. Numbers on curves are mole fraction of BeF_2. The curve for pure BeF_2 is based on refs. 16 and 17.

data of Greenbaum *et al.* on the vapor pressure of BeF_2 (ref. 16) and on the equilibrium[17]

$$BeO(c) + 2HF(g) \rightleftharpoons BeF_2(g) + H_2O(g)\,. \quad (5)$$

A similar curve for P_{HF}^2/P_{H_2O} quotients in equilibrium with ZrO_2 and pure ZrF_4, shown in Fig.

[15] *MSRP Semiann. Progr. Rept. Jan. 31, 1963*, ORNL-3419, p. 110.

[16] M. A. Greenbaum *et al.*, *J. Phys. Chem.* 67, 36 (1963).

[17] M. A. Greenbaum, M. L. Arin, and M. Farber, *J. Phys. Chem.* 67, 1191 (1963).

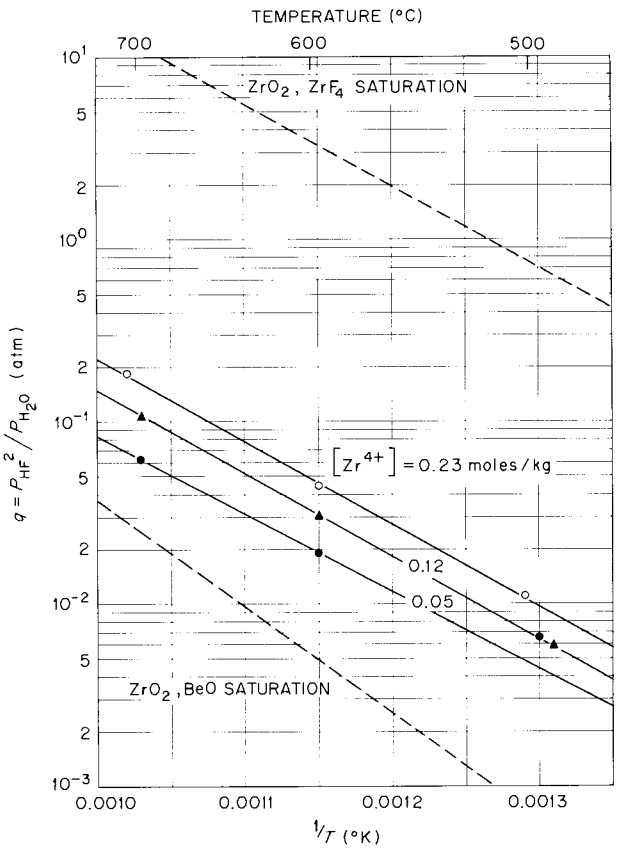

Fig. 3.12. Variation of Equilibrium P_{HF}^2/P_{H_2O} Quotients with Temperature for $2LiF \cdot BeF_2$ Melts Saturated with ZrO_2. Numbers on curves are ZrF_4 concentration in moles/kg. The upper dashed curve represents P_{HF}^2/P_{H_2O} values (based on thermochemical data, refs. 18 and 19) in equilibrium with ZrO_2 and ZrF_4 solids. The lower dashed curve represents BeO saturation of the melt (from Fig. 3.11).

3.12, is based on free-energy data in the literature.[18,19] Such quotients, which correspond to equilibria with the oxide and pure fluoride, may be taken as the equilibrium constant, K_M, for reactions represented by Eq. (3) above (i.e., with $a_{MF_x} = 1$). Designating such quotients as q_M^0 ($\equiv K_M$) and the quotients observed for MF_x dissolved in melts as q,

$$a_{MF_x} = (q/q_M^0)^{x/2} . \quad (6)$$

Thus, for the present data

$$a_{BeF_2} = q/q_{Be}^0 , \quad (7)$$

$$a_{ZrF_4} = (q/q_{Zr}^0)^2 . \quad (8)$$

From these relationships the activity coefficients listed in Tables 3.3 and 3.4 have been calculated. The equilibrium constant for melts saturated with ZrO_2,

$$K_{Zr} = \frac{P_{HF}^2/P_{H_2O}}{a_{ZrF_4}^{1/2}} , \quad (9)$$

requires that q vary directly as the square root of the ZrF_4 activity, or that q vary directly as the square root of the Zr^{4+} concentration in the dilute solutions employed here. This is seen to be approximated by the data in Fig. 3.13, wherein $q/[Zr^{4+}]^{1/2}$ is plotted vs temperature.

Table 3.3. Activity Coefficient of BeF_2 in LiF-BeF_2

Mole Fraction BeF_2	γ_{BeF_2} [a]		
	500°C	600°C	700°C
0.315	0.38	0.24	0.16
0.333	0.39	0.26	0.19

[a] $\gamma_{BeF_2} = a_{BeF_2}/$(mole fraction BeF_2) with pure BeF_2 (*l*) as the standard state.

While the data collected on solutions saturated with UO_2 thus far are limited, the relative solubilities of UO_2 and ZrO_2 have been measured. Combination of the ratio $[Zr^{4+}]/[U^{4+}]$, for melts saturated with both UO_2 and ZrO_2, with the data in Fig. 3.12, yields calculated results which correspond to melts saturated with UO_2. Values of

[18] Alvin Glassner, *The Thermochemical Properties of the Oxides, Fluorides and Chlorides to 2500°K*, ANL-5750 (1957).

[19] J. F. Elliott and M. Gleiser, *Thermochemistry for Steelmaking*, vol. 1, Addison-Wesley, Reading, Mass., 1960.

Table 3.4. Estimates of ZrF_4 and UF_4 Activity Coefficients in Li_2BeF_4

Component	Concentration (moles/kg)	γ_{MF_4}[a] 500°C	600°C	700°C	Source of q_M^0
ZrF_4	0.05 to 0.2	(0.022)	(0.021)	(0.023)	Thermochemical data (refs. 18, 19)
UF_4	0.02 to 0.07	(0.0082)	(0.0076)	(0.0064)	Thermochemical data (refs. 18, 19)
		1.06	0.69	0.58	Kuhlman (ref. 20)

[a] $\gamma_{MF_4} = a_{MF_4}/$(mole fraction MF_4), with pure MF_4 (c) as the standard state.

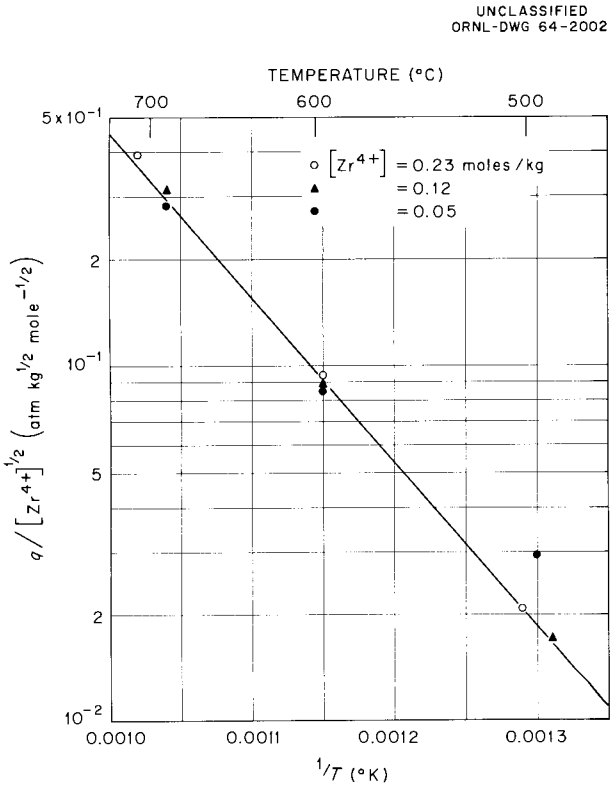

Fig. 3.13. Variation of $(P_{HF}^2/P_{H_2O})/[Zr^{4+}]^{1/2}$ with Temperature in $2LiF \cdot BeF_2$.

q_U^0, calculated from available thermodynamic data,[18,19] in turn yield the values for γ_{UF_4} listed in Table 3.4.

While the values of γ_{UF_4} and γ_{ZrF_4} so calculated are of the same order of magnitude, they are subject to a large uncertainty because of possible errors in the thermochemical data used in their estimation; for example, a 4-kcal error in the free energy of the reaction

$$UO_2(c) + 4HF(g) \rightleftharpoons UF_4(c) + 2H_2O(g) \quad (10)$$

changes the resulting γ_{MX_4} value about tenfold. Experimental equilibrium constants for the above reaction have been reported by a number of investigators,[20–22] and should provide more reliable q_U^0 values. The results of Kuhlman[20] have been used to calculate the second set of γ_{UF_4} values shown in Table 3.4. Note that the values are a hundredfold higher than those based on the thermochemical data. It is noteworthy that Feder has suggested[23] that ΔH_f for HF should be more negative by about 1 kcal. If this change is made, γ_{ZrF_4} and the first set of γ_{UF_4} values are increased by about a factor of 10 and are in better agreement with the second set of γ_{UF_4} values. These latter values in general would be preferred in any case, except that the results of the various investigations of the above reaction (Eq. 10) are in poor agreement with one another. The results

[20] C. W. Kuhlman, *Equilibrium Ratio of Hydrogen Fluoride and Water in the Fluorination of Uranium Dioxide at High Temperatures*, Mallinckrodt Chemical Works, MCW-118 (July 1948).

[21] G. G. Briggs, *Chemical Equilibria and Reaction Rates for Hydrofluorination of UO_2 from "Ammonium Diuranate" and from UO_3*, NLCO-720 (1958).

[22] C. J. Rodden, *Summary Report on Long Range Program for the Period May 1, 1953 to July 31, 1953*, New Brunswick Laboratory, NYO-2043 (1953).

[23] "Thermodynamics of Nuclear Materials," *Proceedings of the Symposium on Thermodynamics of Nuclear Materials*, IAEA, p. 162, Vienna, May 21–25, 1962.

of Kuhlman, chosen for the present estimate of γ_{UF_4}, give the lowest γ_{UF_4} values; the others give γ values which are as much as four times larger. Using $2LiF \cdot BeF_2$ melts saturated with both UO_2 and UF_4, a direct measurement of q_U^0 is planned in order to obtain more reliable determinations of γ_{UF_4}. A similar measurement of q_{Zr}^0 will also be attempted in the case of $2LiF \cdot BeF_2$ melts saturated with ZrO_2 and ZrF_4.

Considering the equilibrium in Eq. 2, the equilibrium constant may be written

$$K_0 = \frac{P_{HF}^2 [O^{2-}] \gamma_{O^{2-}}}{P_{H_2O} [F^-]^2 \gamma_{F^-}^2} . \quad (11)$$

Since, in the present measurements, the melts were dilute and of the approximately constant composition $2LiF \cdot BeF_2$, $[F^-]$ may be taken as constant, and also γ_{F^-} and $\gamma_{O^{2-}}$. Thus the quotient

$$\frac{P_{HF}^2 [O^{2-}]}{P_{H_2O}} = Q_0 \quad (12)$$

may be taken as constant – that is, equal to $K_0 [F^-]^2 \gamma_{F^-}^2 / \gamma_{O^{2-}}$. Accordingly, the various q values found at any one temperature may be taken as inversely proportional to $[O^{2-}]$. The only estimate which can be made for Q_0 at the moment is based on a previous estimate of the solubility product of ZrO_2 in $2LiF \cdot BeF_2$ at 600°C,[15]

$$Q_{ZrO_2} = [Zr^{4+}] [O^{2-}]^2 = 3.2 \times 10^{-5} \text{ mole}^3 \text{ kg}^{-3}, \quad (13)$$

and the present data for ZrO_2-saturated melts (Fig. 3.13):

$$Q_0 = (q/[Zr^{4+}]^{1/2}) Q_{ZrO_2}^{1/2} = 0.096 \times 2.2 \times 10^{-5} = 5.4 \times 10^{-4} \text{ (atm mole kg}^{-1}\text{)} (600°C). \quad (14)$$

A direct determination of Q_0 is planned in future experiments in which P_{HF}^2 / P_{H_2O} will be measured as a function of the concentration of oxide added to the melt. When the product Q_0 is known as a function of temperature and composition, the present technique should provide a ready means of measuring oxide solubility products more accurately as well as a means of making oxide analyses more sensitive than any yet available.

SOLUBILITY OF URANIUM TRIFLUORIDE IN MSRE FUEL SALT MIXTURE

Wiley Jennings F. A. Doss J. H. Shaffer

It is expected that low concentrations of UF_3 will exist in the MSRE fuel salt as a consequence of the chemical equilibrium established during corrosion of the INOR-8 surface. The chromium metal present as a constituent of the alloy will react with the UF_4 in the salt to produce UF_3 until the activity of the chromium in the surface of the metal is lowered to an equilibrium value:[24]

$$Cr + 2UF_4 \rightleftharpoons 2UF_3 + CrF_2$$

Values for this equilibrium have been presented as functions of temperature and composition for molten $NaF\text{-}ZrF_4$ mixtures (used in the ARE fuel), and for NaF-KF-LiF mixtures, and it was reported that when BeF_2 replaced ZrF_4 as a constituent of the melt the nature of the corrosion reactions appeared essentially unchanged.[25] Because the concentration of UF_4 which is to be used in the MSRE fuel is much lower than that used in the ARE, the expected concentration of UF_3 will be correspondingly lower.

Another possible source of a low concentration of UF_3 is the depletion of the fluorine concentration of the melt which would accompany the formation and escape of small quantities of CF_4 as a result of radiolytic fluorine generation at high temperatures. Removal of fluorine would leave a reduced melt containing trivalent uranium. The production of radiolytic fluorine and CF_4 is known to occur during postirradiation operations with frozen MSRE fuel salt in the presence of graphite.[26] Nevertheless, CF_4 production from molten fissioning MSRE fuel salt mixtures has been shown to be either absent or just at the borderline of

[24] J. A. Lane, H. G. MacPherson, and F. Maslan (eds.), *Fluid Fuel Reactors*, p. 599, Addison-Wesley, Reading, Mass., 1958.

[25] W. R. Grimes and D. R. Cuneo, pp. 457–58 in *Reactor Handbook*, vol. I, 2d ed., Interscience, New York, 1960.

[26] W. R. Grimes, *Radiation Chemistry of MSR System*, ORNL-TM-500 (Mar. 13, 1963).

present methods of detection; as discussed in Chap. 2, experiments are in progress to test this point more carefully.

Because of the expected occurrence of UF_3, even at a low concentration level, studies of its chemical behavior have been initiated, and the results of solubility measurements are presented.

Trivalent uranium was prepared in situ by the addition of zirconium metal turnings to fluoride mixtures containing UF_4. An approximate 50% excess of zirconium over the amount required for stoichiometric reduction of all UF_4 to UF_3 was used. The presence of UF_3 as a primary phase in cooled samples of these melts was established by petrographic observations and x-ray diffraction data.

Values for the solubility of UF_3 in the fluoride mixtures were obtained by chemical analyses of filtered salt samples withdrawn from the melt at selected temperatures. Analyses for trivalent uranium were made by an indirect hydrogen evolution method that did not necessarily distinguish trivalent uranium from other reducing agents; however, no others should have been present. Analyses for total dissolved uranium in the salt samples were made by a well-established analytical method. For these highly reduced melts, values of total uranium represent maximum values for trivalent-uranium concentrations.

The results of UF_3 solubility determinations in the mixture LiF-BeF_2-ZrF_4-ThF_4-UF_4 (70-23-5-1-1 mole %) over the temperature range of 550 to 700°C have been reported.[27] This fluoride mixture composition was previously proposed as the MSRE fuel and was used in the in-pile test program.[28,29] The UF_3 solubilities ranged from about 0.1 to 0.7 mole % at 550 and 700°C respectively. The heat of solution, calculated from a semilogarithmic plot of solubility vs the reciprocal of the absolute temperature, was 21.6 kcal/mole.

Values for the solubility of UF_3 in the currently proposed MSRE fuel mixture, LiF-BeF_2-ZrF_4-UF_4 (65.0-29.17-5.0-0.83 mole %) have now been obtained (Fig. 3.14). The reported values of the U^{3+} concentrations at the higher temperatures

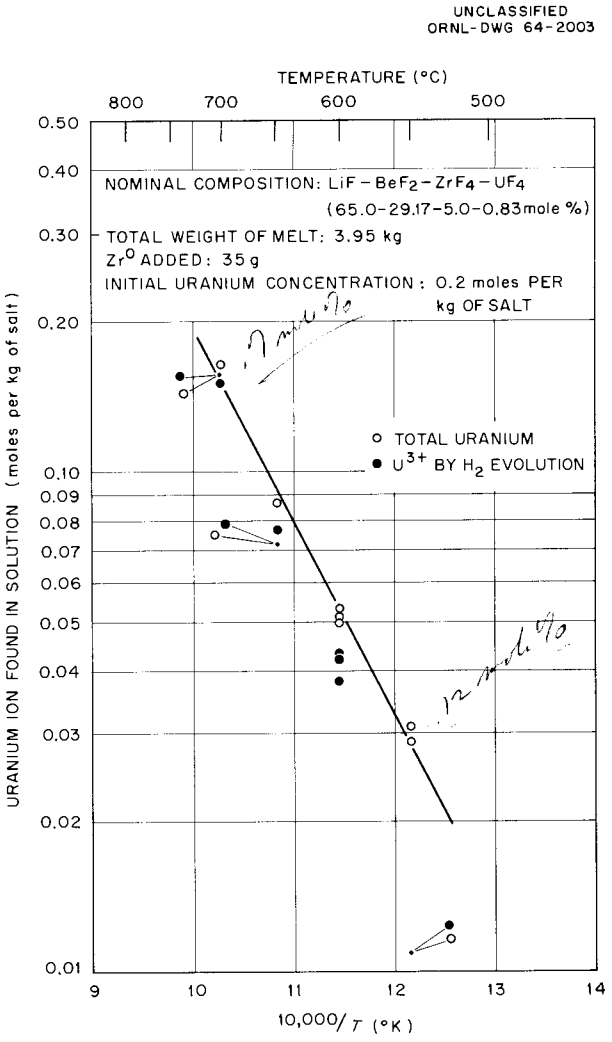

Fig. 3.14. Solubility of UF_3 in the MSRE Fuel Salt Mixture.

very nearly correspond to values of the total uranium concentrations; the cause of the poorer agreement at the lower temperatures is not understood. The presence of graphite in the reduced MSRE fuel mixture was found to have no effect on the UF_3 solubility. For this test a cleaned graphite cylinder was submerged in the "reduced" fuel mixture; filtered salt samples were again withdrawn for chemical analyses. Values for the concentrations of total dissolved uranium were in good agreement with those obtained prior to the graphite insertion. The values for U^{3+} again appeared to deviate from those for the total uranium concentrations at the lower temperatures.

---

[27] *MSRP Semiann. Progr. Rept. July 31, 1963,* ORNL-3529, p. 134.

[28] *MSRP Semiann. Progr. Rept. July 31, 1963,* ORNL-3529, p. 80.

[29] F. F. Blankenship *et al., Reactor Chem. Div. Ann. Progr. Rept. Jan. 31, 1963,* ORNL-3417, p. 17.

Although the values for the total uranium concentrations in the MSRE fuel mixture have been assumed to represent maximum values for UF_3 solubility, they are, nevertheless, considerably lower than those predicted by analogy with rare-earth and plutonium solubilities in $LiF\text{-}BeF_2$ mixtures. Whereas the apparent solubility of UF_3 in the MSRE fuel mixture at 600°C is 0.22 mole %, the solubility of PuF_3 in $LiF\text{-}BeF_2$ (63-37 mole %) at 600°C was reported as 0.43 mole %.[30] The solubility of CeF_3 in the same solvent was reported as 0.55 mole %.[31] The effect of the solvent composition on PuF_3 solubility was shown to be large in $LiF\text{-}BeF_2$ and $NaF\text{-}BeF_2$ melts.[30] Studies in progress should reveal the effects of solvent composition on the solubility of UF_3.

VISCOSITIES OF MOLTEN SALTS

W. T. Ward Stanley Cantor

The measurement of viscosities of molten inorganic fluorides and mixtures of fluorides has been continued to provide support for the development of the molten-salt reactor concept and to increase the understanding of the behavior of such materials. The use of the oscillating cup viscometer[32] has been suspended temporarily while a series of survey measurements is being made with a commercial rotating-spindle viscometer.[33]

The viscosities of an MSRE-type fuel mixture, $LiF\text{-}BeF_2\text{-}ZrF_4\text{-}UF_4$ (66.5-28.7-4.0-0.8 mole %), and coolant, $LiF\text{-}BeF_2$ (66-34 mole %), were measured over the range of 475 to 625°C.[34] The data for these salt mixtures are given in Fig. 3.15 and appear to be represented adequately by linear log η vs $(1/T)$ relations. The equations for the correlating lines in Fig. 3.15 are $\eta = 0.0916 \exp(4098/T)$ for the fuel mixture and $\eta = 0.116 \exp(3755/T)$ for the coolant, in which η is the viscosity in centipoises and T is the temperature in °K.

Tentative data are also given in Fig. 3.15 for the viscosities of BeF_2 and $LiF\text{-}BeF_2$ mixtures of 2.24, 4.39, and 6.71 mole % LiF. Experimental difficulties associated with these measurements resulted in rather large variability, and the data presented are smoothed averages. Because of large changes in viscosity with temperature, it was not practical to measure the viscosities of all mixtures over the same temperature range. The maximum temperature was about 840°C in all cases; the minimum temperatures are indicated by the ends of the lines in Fig. 3.15.

Viscosities of mixtures of LiF and BeF_2 with larger percentages of LiF are being measured, and the relation between viscosity and concentration will be determined over a wide range of concentrations. In addition, the effects of solute

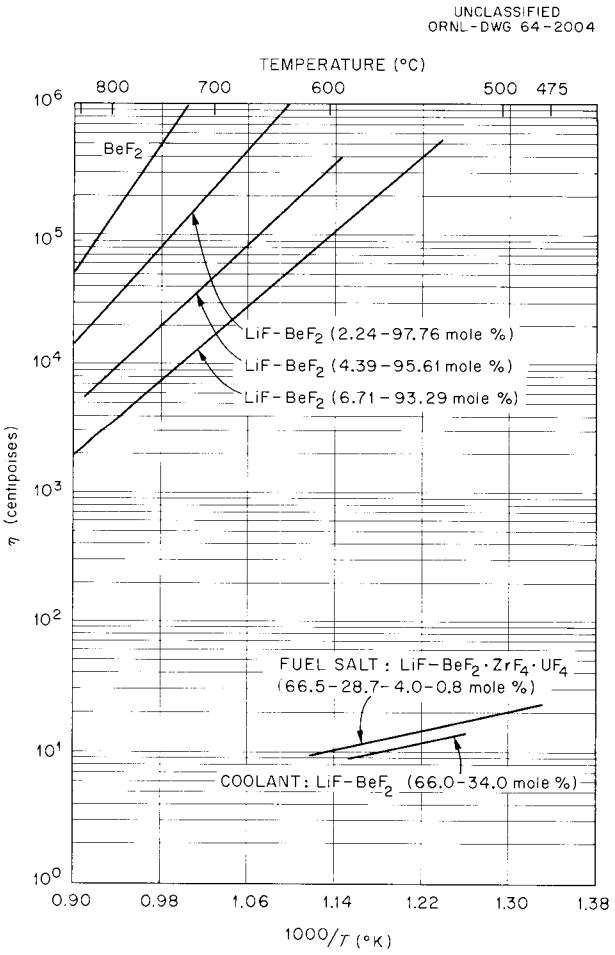

Fig. 3.15. Viscosity-Temperature Relation for $LiF\text{-}BeF_2$ Mixtures and for an MSRE-Type Fuel Mixture.

[30] C. J. Barton, *J. Phys. Chem.* **64**, 306 (1960).

[31] W. R. Grimes *et al.*, *Chem. Eng. Progr. Symp. Ser. Pt. VII*, **55**(27), 65–70 (1959).

[32] P. B. Bien and S. Cantor, *Reactor Chem. Div. Ann. Progr. Rept. Jan. 31, 1963*, ORNL-3417, p. 48.

[33] Brookfield model LVT viscometer.

[34] *MSRP Semiann. Progr. Rept. July 31, 1963*, ORNL-3529, p. 129.

cation valence will be studied by measurement of the viscosities of solutions of MgF_2, YF_3, and UF_4 in BeF_2.

ELECTROCHEMICAL STUDIES IN MOLTEN FLUORIDES

Gleb Mamantov[35]

Essentially no electroanalytical work has previously been reported for molten fluorides, although considerable research has been performed in recent years with systems of chlorides and nitrates. A practical interest at Oak Ridge National Laboratory in molten fluorides, stemming from the Molten-Salt Reactor Experiment and the fluoride volatility process for recovery of uranium from spent reactor fuel elements, has prompted the initiation of a program of electrochemical studies in molten fluorides. Progress in the first phase of this program, electroanalytical in nature, is reported at this time.

The fuel of the MSRE may be considered as consisting of a solvent of LiF-BeF_2 (65.0-29.2 mole %) containing ZrF_4 and UF_4 as solutes (5.0 and 0.8 mole % respectively). The coolant salt for the MSRE will consist of the molten mixture of LiF-BeF_2 (66-34 mole %). Electroanalytical determination of iron, nickel, chromium, copper, oxide ion, and the different oxidation states of uranium would be very desirable if the procedure could be applied directly to the molten fuel. Accordingly, LiF-BeF_2 (66-34 mole %) has been chosen as a solvent base for electroanalytical studies of interest to the MSRE.[36]

The molten salt is contained in a cylindrical graphite vessel inside a nickel container. A photograph of this container, showing connections for the electrodes and for the introduction of cover gases, is presented in Fig. 3.16. A pyrolytic-graphite electrode, first used by Laitinen and Rhodes,[37] serves as an indicator electrode. Hot-pressed boron nitride has been used successfully for insulating the electrode material and defining the electrode area. The potential of the indicator electrode is measured against that of a platinum quasi-reference electrode (in the absence of a satisfactory reference electrode); another platinum electrode, located in a separate graphite compartment, is used as a counter electrode. A fourth platinum electrode was used as the cathode in the purification of the melt by pre-electrolysis. Details of the experimental arrangement have been reported.[38-40]

Stationary-electrode polarography and chronopotentiometry have been used for the study of electrode reactions, as well as for analytical purposes.[41] These methods have now been applied successfully to studies in molten LiF-BeF_2. Figure 3.17 shows a polarogram for the reduction of Fe(II). The theoretically predicted peak-shaped polarogram was obtained only at fast scan rates (1 v/min or greater); at conventional polarographic scan rates, convection interfered. The peak current was found to be proportional to concentration. The reproducibility to date has not been good (average deviation is approximately 13%). A chronopotentiogram for the same electrode process is shown in Fig. 3.18.

Anodic-stripping voltammetry, particularly suitable for the determination of trace quantities of metals,[42] was found to give good reproducibility when applied to iron in molten LiF-BeF_2. Figure 3.19 shows five consecutive anodic-stripping polarograms of iron (plating time, 90 sec; initial potential, −1.10 v; area, 9.3×10^{-2} cm^2; temperature, 508°C; and molality, 6×10^{-3}). The relative average deviation in i_p was 3.5%; thus the reproducibility was much better than that obtained by cathodic voltammetry. Equally good

---

[35]Consultant, Chemistry Department, University of Tennessee.

[36]A complementary study in the Analytical Chemistry Division of ORNL is being made with the use of the eutectic mixture LiF-NaF-KF (46.5-11.5-42 mole %) by D. L. Manning in cooperation with the author.

[37]H. A. Laitinen and D. R. Rhodes, *J. Electrochem. Soc.* 109, 413 (1962).

[38]G. Mamantov and D. L. Manning, *Voltammetry and Chronopotentiometry of Iron in Molten Fluorides*, paper presented at the American Chemical Society, Southeastern Regional Meeting, Charlotte, N.C., Nov. 14–16, 1963.

[39]G. Mamantov and D. L. Manning, "Electrochemical Studies in Molten Fluorides," submitted to *Nuclear Science and Engineering*.

[40]D. L. Manning and G. Mamantov, "Rapid Scan Voltammetry and Chronopotentiometric Studies of Iron in Molten Fluorides; Fabrication and Use of a Pyrolytic Graphite Indicator Electrode," to be published in *Journal of Electroanalytical Chemistry*.

[41]P. Delahay, *New Instrumental Methods in Electrochemistry*, Interscience, New York, 1954.

[42]J. G. Nikelly and W. D. Cooke, *Anal. Chem.* 29, 933 (1957).

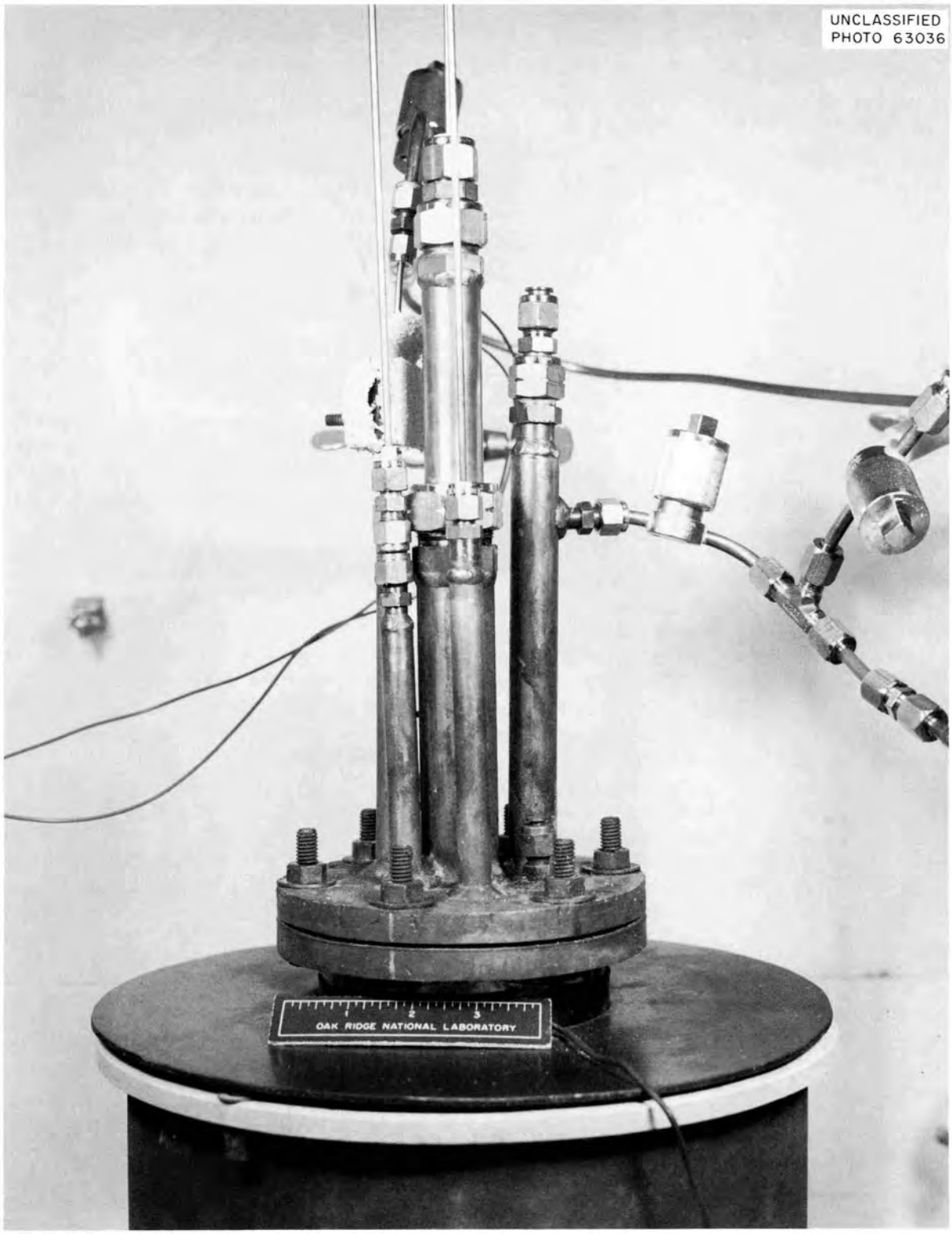

Fig. 3.16. Experimental Arrangement for Electrochemical Studies in Molten $LiF\text{-}BeF_2$.

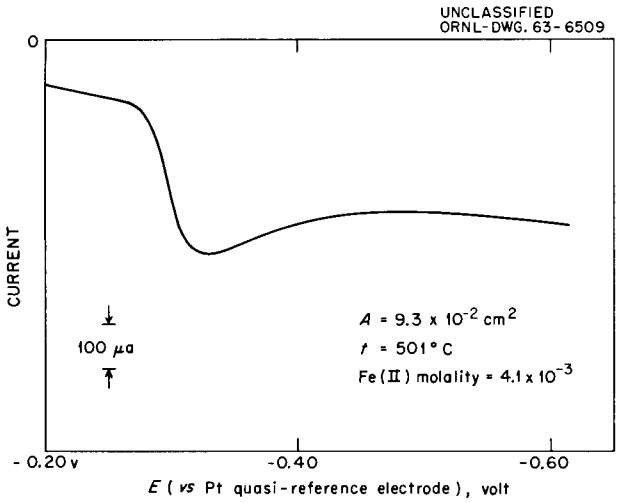

Fig. 3.17. Polarographic Reduction of Fe(II) in Molten LiF-BeF_2.

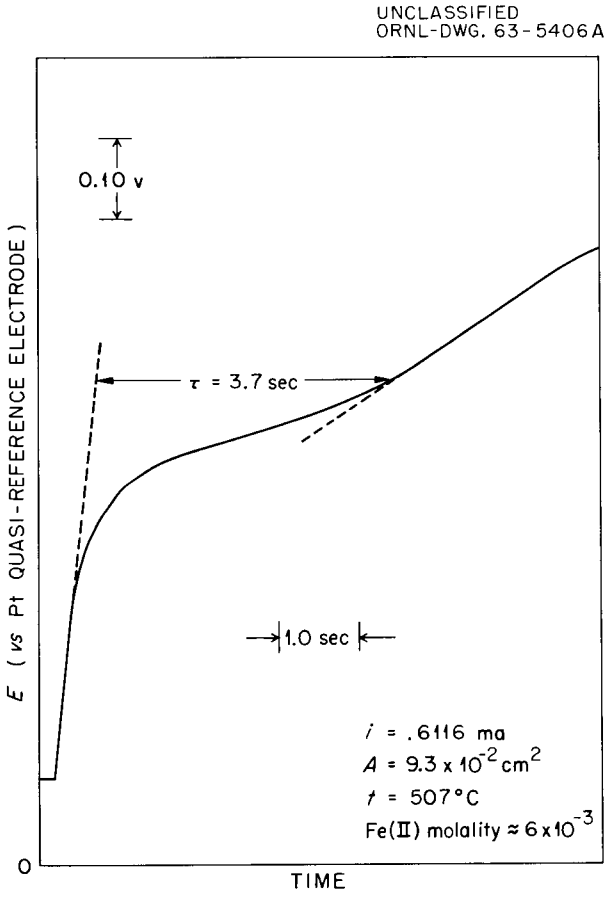

Fig. 3.18. Chronopotentiagram for the Reduction of Fe(II) in Molten LiF-BeF_2.

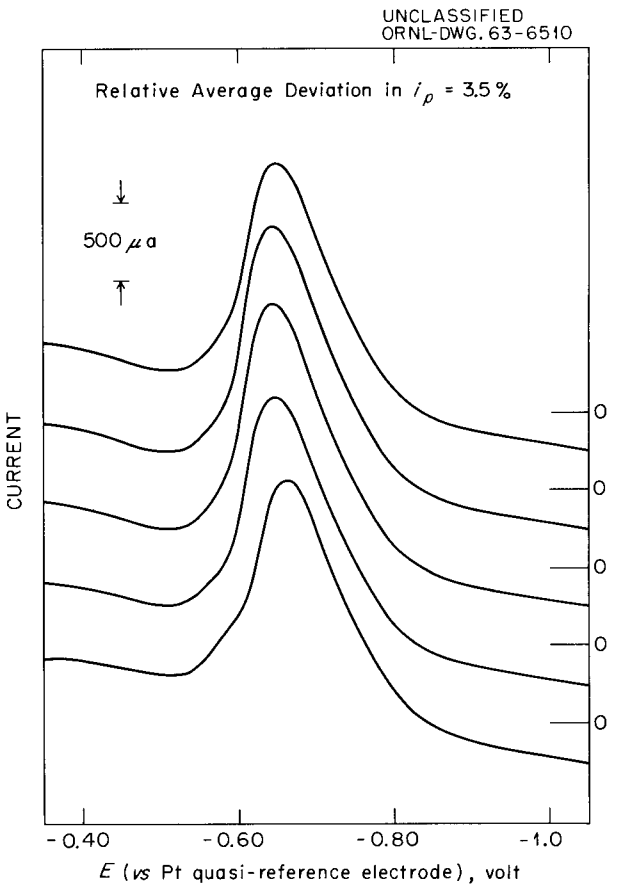

Fig. 3.19. Anodic Stripping of Iron from a Pyrolytic Graphite Electrode in Molten LiF-BeF_2.

results were obtained when anodic-stripping voltammetry was applied to nickel (1% relative average deviation for five runs).

The current-voltage curves recorded at the pyrolytic-graphite electrode, especially at faster scan rates, were better defined than those recorded at platinum indicator electrodes. No difficulty was encountered in maintaining a reproducible electrode surface. After each scan the metal was removed from the electrode by anodic oxidation at zero volts vs the platinum quasi-reference electrode.

Further electrochemical studies, including the reduction of Zr(IV) and oxidation and reduction of U(IV), are in progress. Development of an Ni/NiF_2 reference electrode enclosed in a boron nitride riser is also being investigated.

SALT SEPARATION CHEMISTRY OF PROTACTINIUM FROM IRRADIATED THORIUM

A. J. Shor E. L. Compere

The prompt separation of protactinium from reactor-irradiated thorium would minimize neutron losses and would result ultimately in the formation of U^{233} of high isotopic purity. Separation processes could be facilitated by handling the thorium and/or the protactinium as a mobile material. Low-melting salt compositions should be attractive for this purpose. Volatilization techniques have been suggested for the separation.

An interesting separation has been reported[43] in which $AlCl_3$ was heated with irradiated, finely divided thoria in a sealed tube, after which aluminum and protactinium chlorides were volatilized in the temperature range of 75 to 150°C and condensed in a cool region, leaving behind thorium and uranium chlorides. The elaboration of any such processes requires a detailed study of the phase and separation chemistry of the chloride salt systems. Knowledge of the vapor pressures, phase relationships, chemical complexes possibly existing in various phases, and the general thermodynamic characterization of the protactinium salts are desirable.

A preliminary study of the phase relationships of the thorium chloride–aluminum chloride system has been made. In addition, a study of the ability of $ZrCl_4$ to increase the mutual solubility of the components of this system has been attempted by investigating the aluminum chloride–zirconium chloride and thorium chloride–zirconium chloride binary systems.

Materials and Experimental Equipment

Since work on the phase behavior of these salt systems has suffered from the lack of availability of components of adequate purity, considerable attention was devoted to the preparation of suitable starting materials. Aluminum chloride was synthesized[44] from the elements by use of high-purity analytical-reference aluminum metal, and thorium chloride was resublimed from material originally prepared by Dean and Chandler.[45] Commercially obtained zirconium chloride, specified as "reactor grade," was resublimed prior to use. Materials were characterized by chemical, thermal, spectrochemical, and x-ray analyses.

Table 3.5 summarizes the results of chemical analyses. The empirical formulas shown are

[43] J. G. Malm and S. Fried, "Separation of Protactinium from Contaminants," U.S. Patent 2,893,825, July 7, 1959; USAEC; Application Apr. 11, 1951.

[44] Work performed by D. E. Lavalle and R. B. Quincy, Jr., Inorganic Preparation Group, ORNL Analytical Chemistry Division.

[45] O. C. Dean and J. M. Chandler, *Nucl. Sci. Eng.* **2**, 57–72 (1957).

Table 3.5. Analysis of Chloride Salts

	$ThCl_4$	$AlCl_3$	$ZrCl_4$
Melting point, °C			
Observed	760 to 765	192	436
Literature	770	192.4	437
Chemical analyses, wt %			
Cation			
Observed	61.74	20.31	39.16
Theoretical	62.07	20.23	39.14
Chloride			
Observed	36.4	79.60	58.3
Theoretical	37.93	79.77	60.86
H_2O			
Observed	0.50	0.27	0.07
Empirical formula	$ThCl_{3.86}(H_2O)_{0.10}$	$AlCl_{2.98}(H_2O)_{0.02}$	$ZrCl_{3.83}(H_2O)_{0.01}$

slightly below stoichiometric values for chloride. Based on the sharpness and accuracy of melting-point determination of the pure substances, the purity of the salts was deemed adequate for the phase studies.

The hygroscopic character and volatility of the salts required the use of a satisfactory dry box. All exposed operations have been conducted in a special argon atmosphere having a water content of 10 to 20 ppm. The chloride mixtures were confined in fused quartz capillaries or welded nickel or Inconel capsules fitted with thermocouple wells. These containers were designed to withstand the substantial pressures associated with $AlCl_3$ and the corrosive attack of the chloride salts.

Thermal studies were made by heating and cooling the specimens at a predetermined rate of 1 to 2°C/min and observing the time-temperature relationship. In most cases the temperature of a reference capsule identical geometrically to the specimen and similarly filled, but with inert Al_2O_3, was compared with the specimen capsule temperature by using the so-called differential thermal analysis (DTA) technique. The availability of a semiautomatic DTA apparatus[46] permitted parallel runs and more efficient data production.

In order to detect and identify subtle phase changes and to confirm evidence of supercooling observed, direct visual studies with quartz capillaries heated in transparent alkali nitrate salt baths were attempted.[47] Uniformity of temperature, ease of visual observation, and control of experimental conditions proved excellent with this latter technique.

Experimental Observations

$AlCl_3$-$ThCl_4$ Systems. – Observations were made at 10 mole % $ThCl_4$ and at 90 mole % $ThCl_4$ with metal capsules in the temperature range of 100 to 800°C. After several thermal cycles, leaks developed at the upper temperature range in each case. Inspection of the capsule showed no visible internal corrosive attack but did indicate defective welding techniques to be the cause of the ruptures. Observations prior to the leaks are taken as valid. Temperature halts at 190 to 200°C corresponding to the $AlCl_3$ triple point (reported as 192.6°C at 171.5 cm Hg) were observed at both compositions. A rather broad transition was noted between 740 and 770°C (the melting point of $ThCl_4$ is variously reported between 750 to 770°C). Considerable supercooling was observed for both transition temperatures.

Direct observations of heating and cooling cycles (up to 350°C) were made by sealing various compositions in 1-mm-ID 3-mm-OD quartz capillary tubes. A range of concentrations including 1, 0.9, 0.75, 0.5, 0.25, 0.10, and 0 mole fraction of $ThCl_4$ in $AlCl_3$ were observed. In the region of low $ThCl_4$ concentration it was visually observed that a phase change occurred at about the triple point of pure $AlCl_3$. No interaction of the liquid $AlCl_3$ with the $ThCl_4$ was evident during repeated thermal cycling of the mixtures over a period of several days. At high $ThCl_4$ concentrations similar observations were made but were less conclusive, in part because of the masking effect of the presence of relatively large amounts of $ThCl_4$. Russian work, reported by Korshunov,[48] indicates that mutual solubility of $AlCl_3$ and $ThCl_4$ is low. Our work indicates that the solubility of $ThCl_4$ in $AlCl_3$ will be much below 10 mole %. Techniques other than thermal analysis will be used to determine this solubility.

$AlCl_3$-$ZrCl_4$ System. – A number of compositions in this system have been studied by differential thermal analysis. Transition temperatures, as estimated from differential temperature vs absolute temperature data, are listed in Table 3.6. The upper and lower temperature halts during heatup are presumed to be liquidus and eutectic temperatures. Corresponding observations during cooldown indicate substantial supercooling of the $AlCl_3$-rich compositions.

A combination of visual observations of several salt mixtures of 5 and 14 mole % $ZrCl_4$ in $AlCl_3$ using 1-mm-ID quartz capillary tubes and thermal analysis clearly shows a transition from liquid to solid on cooling at about 120 to 130°C. By thermal analysis, melting starts at about 160°C, which corresponds to the presumed eutectic melting temperature.

[46] Apparatus loaned by R. E. Thoma of ORNL Reactor Chemistry Division.

[47] C. J. Barton, G. M. Hebert, and W. L. Marshall, *J. Inorg. Nucl. Chem.* 21, 141–51 (1961).

[48] B. G. Korshunov *et al.*, *Izv. Vysshikh Uchebn. Zavedenii Tsvetn. Met.* 6, 114–18 (1960); (also *Chem. Abstr.* 55, 18519g).

Morosov and Tsegledi have reported[49] a eutectic at 17 mole % $ZrCl_4$ for the $AlCl_3$-$ZrCl_4$ system at 116°C, another transition at about 127°C, and indicate the presence of two liquid phases at intermediate compositions above 127°C. None of these have been observed in this study. The transition at 127°C observed by the Russian workers may be related to our observation of supercooling at the $AlCl_3$-rich end of the composition range.

From our observations indicated above, we find no present necessity of inferring any phenomena other than a eutectic in the 5 to 14 mole % $ZrCl_4$ region, at ~160°C. An effort will be made to locate this more precisely.

$ThCl_4$-$ZrCl_4$. – Observations of temperature halts for compositions of 0.0, 0.25, 0.5, 0.75, and 1.0 mole fraction of $ZrCl_4$ in $ThCl_4$ up to a temperature of 550°C show only a single differential temperature peak. This peak corresponded closely to the melting point of the pure $ZrCl_4$. Although study of the properties of ternary mixtures of these salts would be required to completely investigate the possibilities of $ZrCl_4$ for acting as a "bridging solvent," the evidence developed so far for the $ThCl_4$-$ZrCl_4$ system indicates little mutual solubility. Further measurements are planned in the ternary system.

[49] I. S. Morosov and L. Tsegledi, *Zh. Neorgan. Khim.* **6**, 2766–75 (1961); see also, N. K. Druzhinina, *Tr. Vses. Alyumin-Magnievyi Inst.* **50**, 143–46 (1963); (also *Chem. Abstr.* **59**, 9382h).

Table 3.6. Summary of $AlCl_3$-$ZrCl_4$ Thermal Analysis Data

$ZrCl_4$ Concentration in $AlCl_3$[a]-$ZrCl_4$ Mixture (mole %)	Temperature Halts (°C)			
	Heatup		Cooldown[b]	
	Liquidus	Eutectic	Liquidus	Eutectic
0	192		170	
	192		172	
5		176		136
		166		139
	195[c]	166		132
	185[c]	157		126
14	194	161		125
	192	161		123
	189	158		128
33	c	182	314[d]	144
50	c	167	366	143
	372	161	366	140
	372	162	367	145
67	402	162	397	146
	399	161	397	142
	398	162	394	143
100	436[e]		438[e]	

[a] As $AlCl_3$ monomer.

[b] Supercooling clearly indicated in several cases in this column.

[c] Very vague liquidus.

[d] Capsule leaked.

[e] Run using thermal curves, non-DTA, from precision potentiometer with well-defined sharp temperature halt.

4. Fluoride Salt Production

J. H. Shaffer F. A. Doss
W. K. R. Finnel Wiley Jennings W. P. Teichert

The primary function of the production facility of the Reactor Chemistry Division is the preparation of fluoride fuel, flush, and coolant salts for the MSRE. An important secondary function is the production of fluoride salt mixtures for use in other molten-salt research programs within the division, in engineering tests connected with MSR development programs, and in chemical reprocessing studies requiring the use of fused salts. Intermediate-scale tests of processes which might be used in the large fluoride production facility are made during the course of many of the nonroutine production runs. As an additional function, technical service operations are provided for engineering development programs.

Fluoride mixtures are prepared from high-quality fluoride salts in two batch processing units, each having a capacity of about 2 ft^3. Since fluoride production for the MSRE will require large quantities of each mixture, a premelting furnace was installed to provide molten raw-material charges for each of the two processing units. Fluoride mixtures are sparged with anhydrous HF and hydrogen to reduce impurities to very low concentrations.[1-3] The purified melts are transferred in the molten condition through sintered-nickel filters into clean nickel containers and allowed to freeze for storage until needed.

[1]G. J. Nessle and W. R. Grimes, *Chem. Eng. Progr. Symp. Ser.* **56**(28), 51 (1960).

[2]G. J. Nessle *et al.*, *Reactor Chem. Div. Ann. Progr. Rept. Jan. 31, 1960*, ORNL-2931, p. 64.

[3]J. H. Shaffer, F. A. Doss, and J. E. Eorgan, *Reactor Chem. Div. Ann. Progr. Rept. Jan. 31, 1962*, ORNL-3262, p. 27.

FLUORIDE PRODUCTION OPERATIONS

Fluoride Salt Production During 1963

Approximately 470 kg of fluoride mixtures containing $LiF-BeF_2-ZrF_4-UF_4$ was prepared, by operation of the large production facility, for chemical research programs and experimental engineering tests related to the molten-salt research program. An additional 435 kg of the mixture $NaF-LiF-ZrF_4$ (37.5-37.5-25.0 mole %) was prepared in this facility for use by the Chemical Technology Division in pilot-plant studies of reactor fuel reprocessing schemes. A total of 120 kg of various fluoride mixtures was prepared in smaller batches for use by other ORNL groups and for subcontract work on corrosion at Battelle Memorial Institute.

Anticipated Production During 1964

The first production mixture in 1964 is to consist of 15,300 lb of Li^7F-BeF_2 (66-34 mole %) to be used as coolant and flush salt mixtures in prenuclear test operation of the reactor system. These mixtures will be chemically identical but will differ in Li^6 concentration; raw-material batches having the highest Li^6 concentrations will be used to make the coolant salt mixture. Approximately 5800 lb of coolant mixture will be prepared to fill a required volume of about 42 ft^3. The required volume of flush salt is about 73 ft^3, for which the remaining 9500 lb of binary salt mixture will be prepared. These production estimates include a calculated 10% excess to allow for the usual contingencies.

The reactor fuel salt mixture will be made from an $LiF-BeF_2-ZrF_4$ solvent mixture to which UF_4 will be added as the eutectic mixture $LiF-UF_4$ (73-27 mole %). The overall composition of the fuel salt mixture will be $LiF-BeF_2-ZrF_4-UF_4$ (65.0-29.1-5.0-0.9 mole %); fissionable U^{235} will comprise about a third of the total uranium content. Some 11,260 lb of the fuel mixture will be prepared for the first reactor loading of 73 ft^3.

Status of Raw-Material Procurement

All raw materials required for the first complete reactor loading, and additional Li^7F for the planned replacement of the flush salt and fuel mixture, are on hand at the production facility with the exception of enriched UF_4, which is readily available. The actual quantities are as follows:

Li^7F	22,000 lb
BeF_2	12,000 lb
ZrF_4 (Hf-free)	2,300 lb

PROCESS DEVELOPMENT

Removal of Structural-Metal Impurities

The INOR-8 alloy used as the structural-metal container in the MSRE contains 6 to 8% chromium as a constituent. It is expected[4] that the chromium activity in the surface layer of metal in contact with MSRE fuel will be depleted until the following equilibrium is established:

$$Cr + 2UF_4 \rightleftharpoons 2UF_3 + CrF_2 .$$

If molten fluoride mixtures introduced into the MSRE contain nonequilibrium concentrations of structural-metal fluorides more easily reduced than UF_4 (e.g., NiF_2 or FeF_3), corrosion of the INOR-8 container could occur. When chromium metal was added to a mixture of $LiF-BeF_2$ (66-34 mole %) at 600°C which contained dissolved cations of nickel and iron, these metals were displaced from solution by a corresponding amount of chromium ion.

Because structural-metal fluorides are present as impurities in the fluoride raw materials, an important phase of the production process has consisted in reducing them to the metallic state and separating them from the purified molten salt by decantation and filtration. Hydrogen gas has been used as a reducing agent, and studies of the thermodynamics of the reduction process have been reported.[5] During the past year the effect of hydrogen flow rate on the reduction process has been studied, and the use of stronger reducing agents including zirconium and beryllium metal has been brought under investigation.

Reduction of FeF_2 by Hydrogen

In small-scale experiments, a small quantity of FeF_2 was added to approximately 2 kg of $LiF-BeF_2$ (66-34 mole %), along with radioactive Fe^{59} so that the removal of iron from solution could be determined by chemical and radiochemical analyses of salt samples. Prior to each experiment the added iron was redissolved in the salt mixture by hydrofluorination. The results shown in Fig. 4.1 indicate the importance of hydrogen flow rate in providing better liquid-gas contact and of the temperature of the melt in which diffusion in the liquid film is probably the controlling process.

Since the gas-liquid contact conditions of these experiments could not be scaled to larger equipment, additional studies were made in the large production equipment. The melt temperature for these experiments was maintained at 700°C. Reduction rates were measured during the processing of a 110-kg batch of $LiF-NaF-ZrF_4$ (27.5-27.5-45.0 mole %) which initially contained 2000 to 3000 ppm by weight of iron. The results indicated that hydrogen sparging rates of about 10 liters/min would accelerate the reduction rate by about 300% over that obtained with the hydrogen flow rate of 3 liters/min customarily used. Confirmation of this effect was obtained during the processing of a 70-kg batch of $LiF-BeF_2$ (66-34 mole %) which initially contained 200 to 300 ppm by weight of iron. The experimental parameters were the same as in the preceding large-scale experiment. The

[4] J. A. Lane, H. G. MacPherson, and F. Maslan (eds.), *Fluid Fuel Reactors*, p. 599, Addison-Wesley, Reading, Mass., 1958.

[5] C. M. Blood, *Solubility and Stability of Structural Metal Difluorides in Molten Fluoride Mixtures*, ORNL-TM-760 (Sept. 21, 1961); C. M. Blood *et al.*, "Activities of Some Transition Metal Fluorides in Molten Fluoride Mixtures," Seventh International Conference on Coordination Chemistry, Stockholm, June 24–28, 1962.

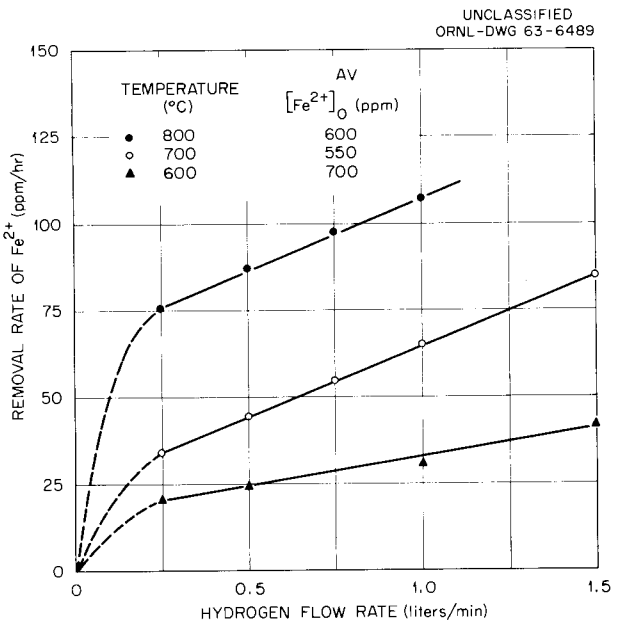

Fig. 4.1. Reduction of Fe^{2+} in LiF-BeF_2 (66-34 Mole %) at 600 to 800°C by Hydrogen Sparging.

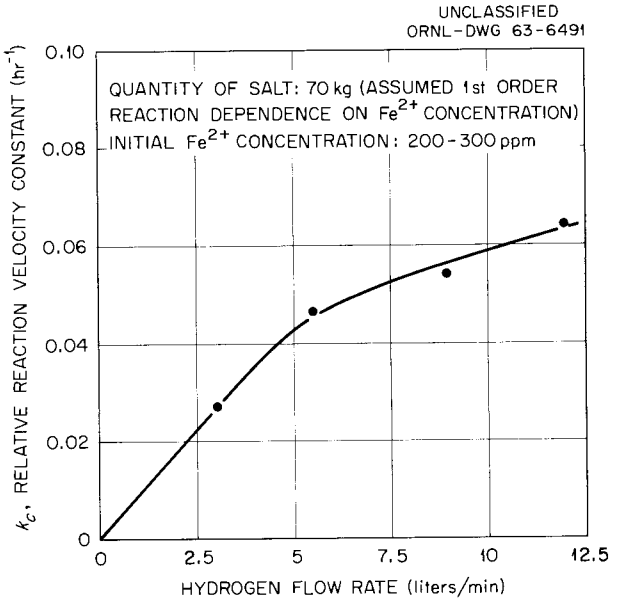

Fig. 4.2. Effect of Hydrogen Sparge Rates on the Relative Rate of Reduction of Fe^{2+} from Solution in LiF-BeF_2 (66-34 Mole %) at 700°C in the Fluoride Production Facility.

results, shown in Fig. 4.2, again demonstrated the advantage of using higher hydrogen sparging rates for removing structural-metal impurities from molten fluorides.

Reduction of Structural Metals by Beryllium and Zirconium

The use of metallic reducing agents such as beryllium and zirconium metal for removing more noble structural-metal impurities from molten salts should be more effective than the current technique of hydrogen sparging. Exactly known amounts of the metals, in finely divided form if desired, can be introduced either along with the dry components of the mixture, after the raw materials have been melted, or after HF treatment has been used to remove essentially all the water and oxide initially present. For salt mixtures containing only lithium and beryllium, plus impurities, it seems probable that beryllium would be the agent of choice for reductions, since no new component would be introduced into the melt. Any of these metals would reduce quadrivalent uranium; it is not contemplated that they would be used after the uranium had been added to the purified solvent base.

In one experiment, beryllium metal turnings were added in weighed increments to a molten mixture of LiF-BeF_2 (66-34 mole %) at 600°C. The melt initially contained about 12 millimoles of Fe per kg of melt and about 4 millimoles of Cr per kg of melt as fluorides. Filtered samples of the molten mixture were withdrawn about 4 hr after each Be^0 addition. During each reaction period the fluoride mixture was sparged with helium. The results obtained from this experiment, shown in Fig. 4.3, illustrate the reduction of iron to a relatively low concentration. In another experiment the addition of zirconium metal to a mixture of LiF-BeF_2 (66-34 mole %) at 600°C was found to remove relatively large quantities of chromium ion from solution. The results are illustrated in Fig. 4.4.

The comparative reducing powers of beryllium and zirconium were studied in one experiment. For this test, 575 g of ZrF_4 was added to 2.55 kg of LiF-BeF_2 (66-34 mole %), and the mixture was sparged with helium at 600°C for 6 hr. About 31 g of beryllium metal chips was added, and the helium sparging continued for 24 hr. Chemical analyses of filtered salt samples taken before and after the beryllium metal addition showed a loss of dissolved zirconium from 10.1 wt % to 6.2 wt %.

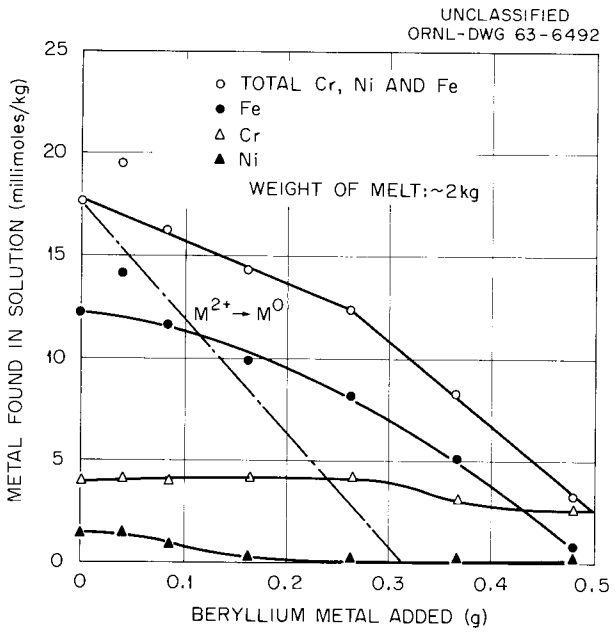

Fig. 4.3. Reduction of Structural-Metal Fluorides from Solution in LiF-BeF_2 (66-34 Mole %) at 600°C by Beryllium Metal.

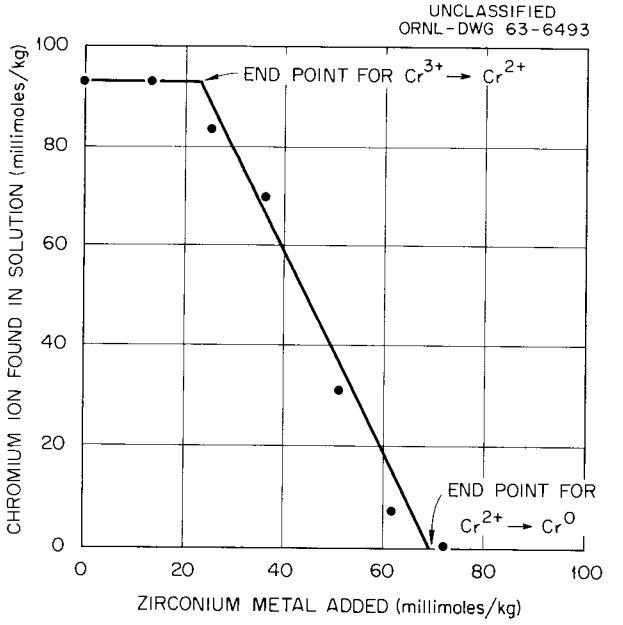

Fig. 4.4. Removal of Chromium from Solution in LiF-BeF_2 (66-34 Mole %) at 600°C by Additions of Zirconium Metal.

There was no evidence of reduced metal species in the salt samples as determined by a hydrogen-evolution analytical method. Although these results demonstrate that massive additions of beryllium metal to a melt containing ZrF_4 would cause substantial composition changes, they do not prevent consideration of the use of very small quantities of beryllium to remove structural-metal cations from such fluoride mixtures.

The encouraging results obtained thus far suggest that additional development of metal reduction should prove of value in the purification of molten salt mixtures. Metal reduction may be used as a substitute for, a supplement to, or a final treatment after hydrogen reduction.

LiF Densification

As previously reported,[6] the Li^7F, as received, was found to have a low bulk density. Subsequent examination showed that it also contained substantial amounts of unconverted LiOH and/or water. Densification by heating to 650°C had appeared promising in laboratory tests. Intermediate-scale tests were made with the use of a cylindrical nickel vessel, mounted horizontally in a tube furnace and equipped with a rotating vane agitator for the contents. The apparatus simulated existing production-scale equipment (discussed below), in which it seemed possible to treat the 22,000 lb of LiF. For the intermediate-scale tests, approximately 1 kg of LiF was loaded into the vessel, the agitator was started, and the temperature was slowly raised while a sweep gas was being passed through the system to remove evolved water. Anhydrous HF was mixed with the helium sweep gas while the charge was being heated to about 200°C to convert LiOH, either initially present or formed by pyrohydrolysis, to LiF; otherwise, heating to 650°C in a helium stream would permit the LiOH to be fused with the LiF to give an intractable mass.

The production-scale equipment is a horizontal Monel reaction vessel (17 in. in diameter by 8 ft long) equipped with a full-length agitator and a heating jacket. The apparatus had been used in the conversion of solid $ZrCl_4$ to ZrF_4 by treatment

[6] *Reactor Chem. Div. Ann. Progr. Rept. Jan. 31, 1963*, ORNL-3417, pp. 53–57.

with anhydrous HF at elevated temperatures. Its capacity is about 75 to 100 kg of Li^7F.

Removal of Sulfates from 2LiF-BeF_2 (ref. 7)

Sulfur is present as sulfate in the BeF_2 raw material to be used in preparing MSRE fuel salt and flush salt, the concentration in various batches averaging ~300 ppm. While preliminary studies have shown that sulfate is effectively removed from molten fluorides by the usual HF-H_2 purification procedure,[8] bench-scale experiments during the past year[9] have indicated that a principal sulfur removal mechanism in this procedure, in addition to the evolution of H_2S, is corrosion of the nickel and copper container materials. This was similarly true when helium or hydrogen sparging was used as a sulfur removal treatment.

The available thermodynamic data indicate that, indeed, direct reaction of SO_4^{2-}, its thermal decomposition products SO_3 and SO_2, or H_2S with nickel or copper to form the metal sulfides and oxides is to be expected at the temperatures of salt purification (600 to 800°C). In the case of nickel, penetrating corrosive attack can result above 645°C, from the formation of an Ni-NiS eutectic (Ni–35 at. % S, mp 645°C).

These considerations suggested that corrosive attack of the container during sulfur removal could be greatly decreased if the sulfate was first reduced to the sulfide by an active metal such as beryllium:

$$SO_4^{2-}(soln) + 4Be^0(cryst) \rightleftharpoons 4BeO(cryst) + S^{2-}(soln) , \quad (1)$$

followed by sulfide removal with HF:

$$2HF(g) + S^{2-}(soln) \rightleftharpoons H_2S(g) + 2F^-(soln) . \quad (2)$$

The reaction of H_2S with nickel should be prevented if a sufficient excess of hydrogen is present. The minimum ratios of H_2S to H_2 required for the formation of nickel and copper sulfides are shown as a function of temperature in Fig. 4.5.

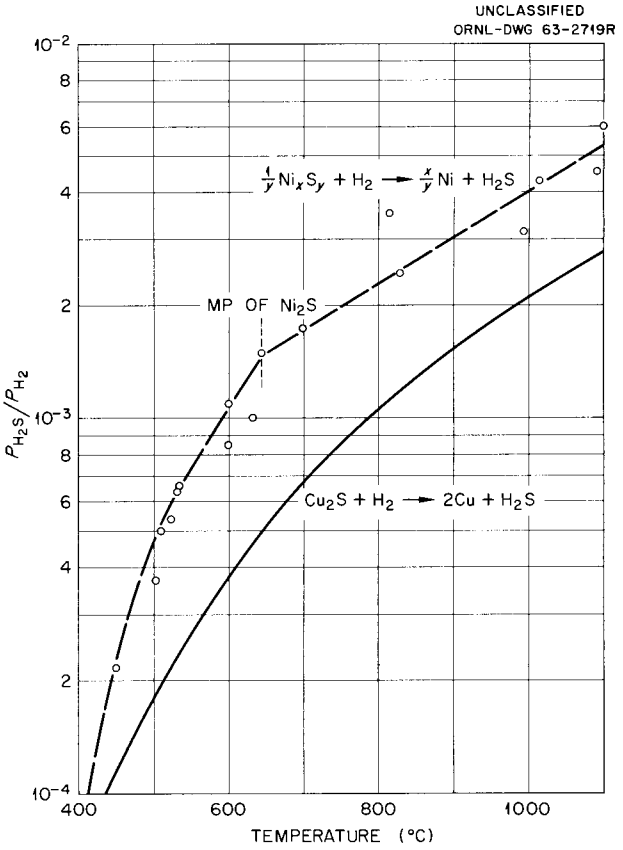

Fig. 4.5. Ratio of H_2S to H_2 Pressures Required to Produce Sulfides of Nickel and Copper. The data points are from T. Rosenquist [*J. Iron Steel Inst. (London)* 176, 37 (1954)]; the lower solid curve is calculated from free-energy data [J. F. Elliott and M. Gleiser, *Thermochemistry for Steelmaking*, vol. 1, Addison-Wesley, Reading, Mass., 1960].

In a test of this procedure, 500 ppm of sulfate was added to 250 g of 2LiF·BeF_2 containing an excess of beryllium metal. The reduction to sulfide was found to be nearly complete after 1 hr at 600°C. Subsequently, 93% of the total sulfur added was removed as H_2S by HF-H_2 sparging in the temperature range 600 to 800°C. Most of the residual sulfur is believed to have been lost to the upper walls of the vessel during a brief period at the beginning of the HF-H_2 treatment when the H_2S-H_2 ratio was above the minimum ratio required to produce nickel sulfide.

This procedure should be effective in removing sulfur during fluoride salt purification without appreciable corrosion of the equipment used. The

---

[7] Contributed by J. E. Eorgan, C. F. Baes, Jr., B. F. Hitch, and M. K. Kemp.

[8] *MSRP Semiann. Progr. Rept. Feb. 28, 1961*, ORNL-3122, p. 120.

[9] *MSRP Semiann. Progr. Rept. July 31, 1963*, ORNL-3529, p. 117.

kinetics of the process and the position of equilibrium (2) have not yet been fully investigated, though H_2S-H_2 ratios within a factor of 2 of the critical value for nickel sulfide formation have been observed. The rate at which sulfur can be removed by this procedure should be controlled by the HF sparging rate. The maximum removal rate possible without nickel corrosion is readily calculated from the hydrogen flow rate and the critical ratio. In units of mg of sulfur per liter of H_2 (STP), this maximum rate is estimated as 1.6, 2.4, and 3.1 at 600, 700, and 800°C respectively. Thus, to remove 100 ppm of sulfur from a kilogram of $2LiF \cdot BeF_2$ would require at least 100/2.4 = 42 liters of H_2 at 700°C. If more rapid removal rates are desired, these may be permissible at a temperature below that of the nickel–nickel sulfide eutectic (645°C), where the nickel corrosion effects may be tolerable. After the sulfur is removed from the melt, the nickel sulfide formed could then be reduced by hydrogen sparging. These procedures are being further investigated.

SERVICE OPERATIONS

MSRP Support

During operation of the MSRE, supplemental additions of U^{235} will be made to the fuel mixture through a port in the fuel-pump housing. This fuel enrichment will be accomplished by dissolving a known quantity of the eutectic mixture LiF-UF_4 (73-27 mole %) that is highly enriched in U^{235} into the molten fuel mixture. The preparation of this salt mixture and its transfer into the enrichment capsules will be the responsibility of the fluoride production group. Five such capsules were filled with the eutectic mixture containing depleted uranium for development studies on a mockup facility at the engineering test loop.

Filling operations are normally performed for experimental engineering tests of the MSRP. Approximately 200 kg of simulated MSRE fuel salt mixture was loaded into the prototype fuel-pump test loop. Another 170 kg of simulated barren fuel salt mixture (without UF_4) was loaded into the engineering test loop.

Liquid-Metals Handling

Activities with liquid-metals handling have normally been associated with programs other than MSRP. However, five dash pots were filled with NaK for use in the flexible mount for the MSRE primary fuel pump. In-pile test capsules for the gas-cooled reactor program were also filled with NaK on two occasions. Potassium metal fills were made twice each on a liquid-level indicator experiment and a boiling-potassium engineering test assembly. Thirteen capsules were also filled with potassium for corrosion tests.

Part II
Aqueous Reactors

5. Chemistry of Pressurized-Water Reactor Systems

F. H. Sweeton
C. F. Baes, Jr.
R. W. Ray
T. H. Handley[1]

The purpose of this program continues[2] to be increasing the basic understanding of pressurized-water reactor (PWR) chemistry as an approach to more economical PWR operation. Part of this effort has been a study of the chemistry of the pressurized-water loop of the ORR, and the rest has been devoted to related laboratory studies.

LOOP CHEMISTRY

The pressurized-water loop of the ORR was constructed and operated for the Maritime Reactor Program. The last test fuel elements for this program were removed in the fall of 1962, when one of the test specimens leaked fission products. The first test fuel element in the Army program was inserted ten months later. During the intervening time the loop was operated without test specimens except for the insertion, for about three months, of a hydraulic mockup of the Army type of test fuel element to be inserted later. The temperature was held at about 40°C during most of this time. With the insertion of the Army test specimens the temperature was raised to 149°C and later to 179°C.

Prior to the insertion of the Army experiments, analyses of the soluble and suspended corrosion products in the loop water were made periodically with 1-liter samples of water withdrawn from the loop. These results have been reported.[3]

With the insertion of the Army experiments, we adopted a new sampling technique using a continuous sampler. By means of a filter and ion exchangers, this sampler concentrated the suspended solids and ionic constituents from a side stream of cooled loop water. Flow rates up to 300 liters/day were possible; enough solids and ionic material could be collected in a few days to allow, for the first time, spectrochemical analysis of water-borne material in addition to the radiochemical analysis previously obtained. The results from the continuous sampler are given in Table 5.1. The pore size of the sampler filter, the operating temperature of the loop, and the concentrations of the major constituents of the corrosion products are indicated. The calculated activation times listed in the last five columns are the irradiation times required to give the observed specific activities in the approximate maximum thermal and fast neutron fluxes seen in the loop. These calculated activation times provide a clue to the irradiation history of the various water-borne activities.

From the analyses, which show a great variation in concentration and activation times of the insoluble and soluble components of the corrosion products, the following observations may be made:

1. The high initial concentration of insoluble iron is consistent with previously observed high activity levels at startup. The long activation time of this iron combined with the short duration of its high concentration indicates that this material was probably scale loosened mechanically when the fuel test assemblies were inserted into the loop just prior to this first test.

2. The significant decrease in calculated activation times of the insoluble iron in later samples indicates that subsequent to the initial burst, the

[1] Analytical Chemistry Division.

[2] C. F. Baes, Jr., and T. H. Handley, *Reactor Chem. Div. Ann. Progr. Rept. Jan. 31, 1963*, ORNL-3417, pp. 61–63.

[3] *Army Reactors Program Ann. Progr. Rept. Oct. 31, 1963*, an ORNL report in press.

iron activity was coming in large part from out-of-flux regions.

3. Nickel was transported largely in the soluble form, and chromium largely in the insoluble form. Iron was not consistent in this respect.

4. The activation time of Mn^{54} in the *insoluble* crud qualitatively agrees with that of the iron activities, indicating that the Mn^{54} has probably remained to a fair degree with its parent, the Fe^{54} nuclide in normal iron; however, in the case of the *soluble* Mn^{54}, its long apparent activation time indicates that it was dissolving in the loop water faster than its parent, Fe^{54}, or else was not being removed as effectively.

5. The high initial concentration of insoluble chromium is similar to that of iron, but its short activation time precludes that much of it came from the in-flux region of the loop.

When further such sampling data have been collected and compared with loop operating conditions, it should be possible to draw more definite conclusions about the behavior of water-borne activity and, in particular, about the activity transport mechanisms involved.

Analyses of the fission products in loop water have normally shown low concentrations and have appeared to vary with the presence of small amounts of U^{235} on test specimens inserted in the loop.[3]

Table 5.1. Characterization of Soluble and Insoluble Corrosion Products in Water of ORR Pressurized-Water Loop

Sampling Time		Filter Pore Diameter (μ)	Loop Temperature (°C)	Concentration (moles/liter)			Calculated Activation Time[a] (days)				
Start	End			Fe	Ni	Cr	Fe^{55} (2.94y)	Fe^{59} (45.1d)	Co^{58} (72.0d)	Mn^{54} (300d)	Cr^{51} (27.8d)
Insoluble Components											
				$\times 10^{-9}$	$\times 10^{-9}$	$\times 10^{-9}$					
8–30–63	8–31–63	0.45	149	444	41	551	110	42	13	107	0.23
8–31–63	9–03–63	0.45	149	16	1.2	5.6	49	13	10	22	0.33
9–03–63	9–13–63	0.45	149	6.4	0.4	0.7	29	4.9	3.4	19	0.60
9–19–63	10–11–63	0.45	149	20	0.8	2.0	8.4	3.1	4.4	8.7	0.32
11–01–63	11–13–63	0.10	149–179[b]	206	3.7	19	13	2.3	4.6	1.0	0.16
Soluble Cations											
				$\times 10^{-9}$	$\times 10^{-9}$	$\times 10^{-9}$					
8–30–63	8–31–63	0.45	149	60	507	0	<8	<0.5	0.04	30	
8–31–63	9–03–63	0.45	149	70	44	0	6.4	1.2	0.75	94	
9–03–63	9–13–63	0.45	149	119	16	0.3	4.2	0.72	2.8	35	<0.3
9–19–63	10–11–63	0.45	149	646	277	0.7	0.22	0.06	0.17	4.6	<0.03
11–01–63	11–13–63	0.10	149–179[b]	11	6.6	0.4	56	11	5.6	576	<0.2

[a]For this calculation it has been assumed that the thermal and fast fluxes were 5.0 and 4.0×10^{13} neutrons cm^{-2} sec^{-1}, respectively, that the irradiation was continuous until sampling time, and that the radioactive nuclide remained with its parent. The last assumption should be valid for Fe^{55}, Fe^{59}, and Cr^{51}, whose parents are nuclides of the same elements, but may well be in error for Co^{58} and Mn^{54}, whose parents are Ni^{58} and Fe^{54}. The activation time for Co^{60} was not calculated, because the concentration of cobalt in the samples was too low to be detected by the analysis.

[b]Temperature 149°C until 11–07–63, 179°C thereafter.

HIGH-TEMPERATURE ADSORBENTS

One part of the present program is the study of potential high-temperature adsorbents for controlling movement of radioactivity through a pressurized-water reactor system. The first adsorbent studied was magnetite, Fe_3O_4, because it has the potential advantage that adsorbed iron activity may be able to diffuse into the crystal lattice, giving a very large effective adsorption capacity. Earlier tests had demonstrated qualitatively that Fe_3O_4 can be an effective adsorbent.[2]

Most of the magnetite studies have been carried out with a synthetic material, Mapico Black, which is much purer than normal natural material. The Mapico Black, as received, was made up of submicron particles. It was sintered at temperatures of 1000, 1200, and 1400°C, giving products with specific surface areas of 2.4, 0.06, and 0.03 m^2/g.

An in-pile test of this Fe_3O_4 as an adsorbent was made following preliminary in-pile and out-of-pile tests, reported elsewhere.[3] A small flow of cooled and filtered loop water was passed through a stainless steel and nickel system in which it was heated to 260°C, filtered through a nickel frit with 2-μ pores, passed over a column of the 1400°C-fired Fe_3O_4, cooled, refiltered, and finally passed through organic ion exchangers. The flow rate of the water was equivalent to 1.8 Fe_3O_4 column volumes per minute. A larger flow of the same cooled, filtered water was simultaneously passed through an organic cation exchanger, making possible spectrochemical and radiochemical analyses of the water. At the end of the test essentially all the Fe^{59} activity that entered the adsorbent system was found on the Fe_3O_4. This corresponded to an adsorption of iron so large that the average surface area available per adsorbed atom was only about 1 A^2, indicating that the adsorbed iron had probably penetrated into the Fe_3O_4 lattice. During the test the surface area of the Fe_3O_4 decreased about 25%. In the same test less than 1% of the cobalt activities got by the Fe_3O_4, although only 20% was actually found on the adsorbent. On the other hand a large part of the manganese activity went through the adsorbent system and was found on the following cation exchanger.

SOLUBILITY OF Fe_3O_4

In a laboratory test of the solubility of Fe_3O_4 an HCl solution saturated with H_2 was pumped through a bed of radioactive Fe_3O_4 in a nickel column held at 260°C. The pH and the iron concentration of the outlet solution were determined after the solution was cooled. The results indicate that the saturation Fe^{2+} concentration at 260°C in in an HCl solution having a room temperature pH of 4.6 to 4.8 is 0.04 to 0.09 μM.[3] The apparatus is being modified to increase its sensitivity so as to allow measurements at lower solubilities. The solubility studies will be continued with variations of the pH and the temperature.

6. Chemical Support for High-Flux Reactors

CORROSION STUDIES FOR ATR AND HFIR

J. C. Griess H. C. Savage
J. L. English J. F. Winesette
L. L. Fairchild

Effect of Heat Flux on the Corrosion of Aluminum by Water

Two very high-performance reactors, the Advanced Test Reactor (ATR) and the High-Flux Isotope Reactor (HFIR), are presently being built. Both will use thin plate-type fuel elements, and in both, for many reasons, it will be advantageous to clad the plates with aluminum. Heat will be removed by a very dilute acid solution flowing at 40 to 45 fps through narrow channels. High power densities can result in hot-spot heat fluxes as high as 2×10^6 Btu hr^{-1} ft^{-2}. Although the temperature of the bulk cooling water will be less than 200°F, the high heat fluxes across the cladding will produce hot-spot surface temperatures approaching 400°F; at this temperature corrosion of aluminum cladding could be a problem.

During the past three years, an experimental program was conducted to evaluate the feasibility of using aluminum-clad fuel elements in the two reactors and to determine the effect of corrosion products adhering to the corroding surfaces on heat transfer. During the past year, the experimental program was completed, and the results have been reported.[1] An abstract of this report is given in the following paragraphs.

The corrosion of 1100, 6061, and X8001 aluminum alloys – and the resultant formation of an adherent corrosion product on the corroding surface – was investigated under conditions (except radiation) comparable to those that will exist on the surface of fuel-element cladding during operation of the ATR and HFIR. Since early experiments indicated that corrosion penetration of the aluminum cladding is unlikely during the short reactor cycles (provided the water chemistry is properly controlled), most of the studies in this investigation were concerned with the effect of variables on the rate of formation of corrosion product films. These films have low thermal conductivity, and can be a major factor in producing high fuel-element temperatures which could lead to fuel-plate mechanical instabilities.

All three alloys corroded to the same extent under the same test conditions until the corrosion product (boehmite) that formed on the surface became thick enough to spall spontaneously from the surface, usually about 2 mils thick. Spallation from the surface of the 1100 and 6061 alloys was always accompanied by localized attack of the underlying metal, whereas only uniform attack was observed with the X8001 alloy under all conditions.

All three alloys developed corrosion product coatings at the same rate when tested under the same conditions. The thermal conductivity of the corrosion product was determined to be 1.3 Btu hr^{-1} ft^{-1} $(°F)^{-1}$. The pH of the water was an important variable in determining the corrosion rate and the rate of corrosion product buildup on aluminum. Under the same conditions, the corrosion and oxide formation rates were 2.7 times greater when the pH of the water was 5.7 to 7.0 than when the pH was 5.0 (with nitric acid); pH was not a significant variable within the former range. Changes in pH during a test resulted in abrupt changes in the rate of oxide formation and presumably also in rate of corrosion. The data indicated that up to the point of film spallation about 70% of the aluminum that was oxidized remained on

[1] J. C. Griess, H. C. Savage, and J. L. English, *The Effect of Heat Flux on the Corrosion of Aluminum by Water. Part IV. Tests Relative to the Advanced Test Reactor and Correlation with Previous Results*, ORNL-3541 (to be published).

the surface as boehmite regardless of test conditions; the rest was lost to the water.

The rate of oxide formation on the specimens decreased with exposure time and increased as the surface temperature increased. The controlling temperature was that at the aluminum oxide–water interface (surface temperature). Considering only the data acquired with the water at a pH of 5.0 and at heat fluxes between 1 and 2×10^6 Btu hr^{-1} ft^{-2}, the thickness of oxide built up on the corroding surface was described reasonably well by the empirical equation

$$X = 443\theta^{0.778} \exp\left[\frac{-4600}{K}\right],$$

where X is corrosion product thickness in mils, θ is time in hours, and K is surface temperature in degrees Kelvin. With pH values between 5.7 and 7.0 the same relationship applied except that the first coefficient in the above equation was 1200 instead of 443. Within the range of 1 to 2×10^6 Btu hr^{-1} ft^{-2}, heat flux was unimportant except in the manner in which it influenced surface temperatures. Below 1×10^6 Btu hr^{-1} ft^{-2}, heat flux per se was a significant variable; considerably lower oxide thicknesses were observed than calculated by the above correlation.

The results of the experimental program indicate that the 6061 aluminum alloy, which has mechanical strength superior to either 1100 or X8001, will have adequate corrosion resistance for use as cladding for both the ATR and HFIR fuel plates, provided the pH of the water is maintained at 5.0 with nitric acid. However, the increase in fuel-plate temperatures resulting from the buildup of the corrosion product layer must be evaluated carefully to determine its effect on the mechanical and irradiation behavior of individual fuel plates and on the overall fuel-element stability.

Corrosion Tests for the High Flux Isotope Reactor

Corrosion studies were continued during the past year with a wide variety of materials to be used in the "permanent" portions of the High Flux Isotope Reactor. A number of the tests were continuations of experiments which were described previously,[2] whereas others represent new tests.

Both laboratory and loop tests were conducted in pH 5.0 water at 100°C and below. The laboratory tests used water in equilibrium with air; water in the loop tests contained between 4 and 5 ppm of dissolved oxygen. Water velocities in the loop tests varied from 0.5 fpm to 81 fps and all specimens were electrically insulated from the loop system. Specimens coupled to each other were usually prepared by bolting together two or more flat specimens with a bolt of the same alloy as one in the couple.

Corrosion of Aluminum. – Table 6.1 presents the more pertinent data on the behavior of 1100 and

[2] J. C. Griess *et al.*, *Reactor Chem. Div. Ann. Progr. Rept. Jan. 31, 1963*, ORNL-3417, pp. 66–68.

Table 6.1. Corrosion of Aluminum Contacted by Dissimilar Metals in pH 5.0 Water at 100°C

Material	Exposure Time (hr)	Maximum Pit Depth on Al (mils)
6061-T4 Al (control)	12,473	0
6061-T4 Al to 6061-T4 Al	10,970	8
6061-T4 Al to QMV Be	12,473	6
6061-T4 Al to type 304 SS	12,473	15
6061-T4 Al to type 17-4 PH SS	12,473	8
6061-T4 Al to types 304 and 17-4 SS	12,473	25
6061-T4 Al to types 304 and 420 SS	12,473	10
6061-T6 Al to type 410 SS	12,000	44
1100 Al to carbon-filled Teflon	2,000	13

6061 aluminum in contact with dissimilar materials. The data were obtained at 100°C and flow rates ranging from 0 to approximately 3 fpm. Uncoupled 6061-T4 aluminum was not prone to pitting attack, but crevice and/or galvanic attack took place in all other instances. The latter forms of attack resulted in pitting on contact surfaces only. The most serious pitting occurred on 6061-T4 aluminum contacted by hardened type 410 stainless steel, where the maximum observed pit depth was 44 mils after an exposure period of 12,000 hr. Corrosion rates for all aluminum specimens as well as for other members of the dissimilar metal couples were less than 1 mil/yr.

In other studies, couples prepared from specimens of 6061-T4 aluminum, specimens of pure nickel, and several types of copper-containing aluminum alloy rivets showed, after exposures not exceeding 1600 hr at 100°C, severe corrosion of the rivets and nearly complete consumption of the rivet heads. Specimens of 6061-T4 aluminum welded with 4043 aluminum filler metal exhibited excellent corrosion resistance after 4000 hr at 100°C; specimens showed slight weight gains after exposure, and no pitting was observed on either the weld or the parent metal. A specimen of 1100 aluminum with approximately 50% of the total surface area anodized was exposed for 2000 hr at room temperature in deionized water; no pitting was found on the anodized surface, but a few pits to 4.0 mils in depth were observed at the junction between the anodized and the non-anodized surfaces.

Specimens of "electrolized" 6061-T6 aluminum, on which a thin layer (97% Cr, balance Fe and Si) had been deposited through a proprietary process by the Electrolizing Corporation, Chicago, Ill., performed poorly in pH 5.0 water at 100°C. During an exposure period of 2520 hr, severe flaking and blistering of the electrolized layer occurred at areas contacted by 1100 aluminum and by type 304 stainless steel. Pits up to 10.8 mils in depth were found in the 6061-T6 aluminum at sites from which the electrolized layer had flaked.

Specimens of 6061-T6 aluminum have been exposed for 5616 hr at 100°C in pH 5.0 water at flow rates from 22 to 81 fps. Slight weight gains occurred on specimens exposed at flow rates below 51 fps. Weight losses corresponding to <0.1 mil/yr were shown by specimens exposed to flow rates in the 51 to 72 fps range, and flow rates of 72 to 81 fps produced losses equivalent to corrosion at 0.1 mil/yr. Specimens of X8001-F aluminum were exposed at 100°C for 4614 hr in two velocity ranges, 22 to 33 fps and 33 to 51 fps. In the lower velocity range, as-scrubbed weight-change data showed a slight gain; in the higher velocity range, corrosion rates based upon as-scrubbed weight losses were less than 0.1 mil/yr. In no case was pitting attack observed on the specimens.

As a result of these tests, aluminum sections in HFIR are to contact only austenitic stainless steel, and the aluminum sections are to be thickened to allow for the anticipated corrosion which will result.

Corrosion of Beryllium. – Duplicate specimens of hot-pressed QMV reactor-grade beryllium were exposed for 12,473 hr at 100°C in pH 5.0 water at a velocity of approximately 2 to 3 fpm. Both specimens were subject to a moderately heavy pitting attack, with pits ranging up to 3.5 mils in depth. The average as-scrubbed corrosion rate was 0.5 mil/yr. When coupled with 6061-T4 aluminum, a slightly higher pitting frequency was observed on the beryllium contact surface than on surfaces removed from the contact zone. After 12,473 hr at 100°C, the maximum pit depth was 5.9 mils; pits were somewhat deeper on the contact surface than on other surfaces. The defilmed corrosion rate was 0.4 mil/yr. QMV beryllium in contact with type 304 stainless steel for 12,473 hr at 100°C was also subject to a higher pitting frequency on contact surfaces than on the exposed surfaces. The maximum depth of pitting on contact surfaces was 8.2 mils. Duplicate specimens exhibited defilmed corrosion rates of 0.5 and 0.6 mil/yr. The contact surfaces between two beryllium specimens showed a greater frequency of pitting than the exposed surfaces but no increase in intensity. After 10,970 hr the maximum pit depth observed was 3.8 mils. The average defilmed corrosion rate for the coupled specimens was 0.3 mil/yr.

Quadruplicate specimens of QMV beryllium were exposed for 10,443 hr at 100°C and flow rates of 12.5 and 23 fps. The average corrosion rate at each velocity was 1.9 mils/yr. All specimens were subject to pitting attack ranging up to 6.0 mils in depth.

In another test, duplicate specimens of QMV beryllium were exposed at 100°C to each of four velocity ranges. Average corrosion rates are summarized below:

Velocity (fps)	Corrosion (mils/yr)
22 to 33	2.0 ± 0.1 (5589 hr)
33 to 51	1.9 ± 0.2 (5589 hr)
51 to 72	2.0 ± 0.2 (10,203 hr)
72 to 81	1.9 ± 0.1 (10,203 hr)

Pitting attack was present on all specimens with maximum depths ranging to 4.7 mils. All tests suggest that, in spite of the pitting and generalized corrosion, the beryllium reflector in HFIR should last its design lifetime.

Corrosion of Type 420 Stainless Steel. – A hardened type 420 stainless steel specimen was made a member of a couple with 6061-T4 aluminum and type 304 stainless steel and exposed in pH 5.0 water for 12,473 hr at 100°C. The 420 stainless steel was hardened to 43 Rockwell C. During the last 1000 hr of exposure, two cracks (see Fig. 6.1) formed in the body of the type 420 specimen. The type 420 stainless steel specimen also exhibited some rather serious pitting attack. The pits were generally much larger in diameter than in depth and were quite grainy. The maximum depth of pitting was 4.3 mils. The defilmed corrosion rate on the specimen was 0.2 mil/yr.

UNCLASSIFIED
PHOTO Y-54417

Fig. 6.1. Cracks in Hardened Type 420 Stainless Steel After 12,473 hr at 100°C in pH 5.0 Water. Etched in glyceria regia. 9X.

EFFECTS OF REACTOR OPERATION ON HFIR COOLANT

G. H. Jenks

The primary cooling system of the High Flux Isotope Reactor (HFIR) will use a dilute solution of HNO_3 (10^{-5} *M*) circulating under high pressure. It is expected that no gas phase of appreciable volume will exist in the reactor although dissolved gases will be present. The temperature of the core exit water will be about 75°C. The average power density in the core water, generated by absorption of energy from fast neutrons and gamma rays, will be about 100 w/cm^3. The nitric acid is added to the coolant in order to inhibit the corrosion of the aluminum fuel-element cladding.[3] The inhibition is believed to result from the hydrogen ion concentration, and hydrogen ions from other sources would presumably be equally effective.

It has been recognized that the HFIR radiations will effect some decomposition of the water and that the HNO_3 may also be decomposed to some extent.[4] Large amounts of decomposition of either compound could adversely affect the safety and/or performance of the reactor. Accordingly, a study was undertaken to obtain estimates of the extent of the radiolytic decomposition of water and HNO_3 and the changes in hydrogen ion concentration which might result.

Preliminary considerations revealed the following regarding the decomposition of the water:

1. Steady-state concentrations of molecular products in the neighborhood of 10^{-3} to 10^{-4} *M* would be expected. The expected concentrations would be influenced by several factors including (*a*) the concentration of excess oxidant (O_2 or H_2O_2) in solution, (*b*) temperature, and (*c*) radiation intensity.

2. The radiolytic product HO_2 might be present at concentrations in the neighborhood of 10^{-5} *M*.

---

[3] J. C. Griess *et al.*, *Reactor Chem. Div. Ann. Progr. Rept. Jan. 31, 1963*, ORNL-3417, pp. 64–66.

[4] A. O. Allen, *The Radiation Chemistry of Water and Aqueous Solutions*, Van Nostrand, Princeton, N. J., 1961.

This compound is known to have a low constant[5] for dissociation into $H^+ + O_2^-$ at 25°C (pK = 4.4). It thus appeared possible that this compound would significantly affect the hydrogen ion concentration in the core.

3. Reactions between molecular and radical decomposition products have been proposed by others[4] to explain the occurrence of the low steady-state concentrations and other features of the radiation chemistry of water. Rate constants for the reactions at or near 25°C have also been reported.[6] Assuming, then, that the activation energies for the reactions can be estimated reasonably accurately, and that the rates of formation of radiolytic products ($G_{product}$) are known or can be estimated for HFIR conditions, it is possible to calculate steady-state concentrations of the products.

Preliminary considerations of the effects of reactor radiations on the HNO_3 revealed the following:

4. The nitrate ion is known to react with the hydrated electron at a high rate. The initial reaction product is presumed to be NO_2 but nitrite and a reduction product of nitrite are formed in further reactions. Back reactions to higher oxidation states, including NO_3^-, also occur, and the steady-state concentrations of the several ionic and neutral species are then expected to depend upon the relative rates of the forward and reverse reactions. However, the radiation chemistry of oxides and oxygen acids of nitrogen is not completely understood,[3] and rate constants are unknown for some reactions which are probably important in the radiolysis of nitrate solutions.

5. Nitrate is apparently stable in reactor coolant waters under some conditions which have been tested.[7,8] In particular,[7] it was apparently stable in the ETR coolant outside the core at all reactor powers and nitrate concentrations investigated – up to 80 Mw (about 23 w/cm^3 average power density in core water) and about 1.2×10^{-5} *M* NO_3^-, respectively. The possibility that significant concentrations of reduction products of NO_3^- might exist in a steady state during irradiation has not been considered in reported work.

6. The presence of excess oxidant in the solution probably favors the stability of the nitrate.

On the basis of these preliminary findings it was concluded that calculations of the steady-state concentrations of the radiolytic products of water under HFIR conditions were desirable to aid in establishing reactor operating conditions which will tend to minimize water decomposition and/or suitably control the hydrogen ion concentration. The general approach employed in making the calculations was that described above in paragraph 3. Estimates of the activation energies and rates of product formation were made from consideration of available data including those for the steady-state concentrations of H_2, O_2, and H_2O_2 in the ORR and ETR. It was concluded (*a*) that the $G_{product}$ values in the ORR (about 15 w/cm^3) were probably near those reported for lower-intensity radiations, (*b*) that the $G_{H_2O_2}$ values in the ETR (50 w/cm^3) were probably greater and G_{OH} lower than those in the ORR, and (c) reasonable estimates for the activation energies could be made. Particular values of $G_{H_2O_2}$ and G_{OH} for the ETR were chosen to bring the calculated and the reported experimental values into agreement. These *G* values were assumed to prevail under HFIR conditions also.

The calculations involved the solutions of six simultaneous equations with six unknowns. The solutions were arrived at by computer calculation using a code written by H. Zeldes and adapted by him for use with these equations.

As expected, most of the results show a marked dependence of steady-state concentration upon the concentration of excess oxidant. Increasing temperature is effective in reducing the concentrations in most cases. Changes in power density produce relatively small effects on the steady-state concentrations. The values calculated at several temperatures for an excess oxygen concentration of 5×10^{-4} *M* and 100 w/cm^3 are illustrated in Figs. 6.2 and 6.3.

The results again point to the possibility that HO_2 may provide the required hydrogen ion concentration. However, because of various uncertainties in the estimates and because of a lack of information on the chemistry of HO_2 at the higher temperatures prevailing near fuel-element

---

[5]Gideon Czapski and B. H. J. Bielski, *J. Phys. Chem.* **67**, 2180 (1963).

[6]L. M. Dorfman, *Science* **141**, 493 (1963).

[7]F. C. Haas, *Maintenance of ETR Coolant*, IDO-16463 (Aug. 15, 1958).

[8]A. R. Anderson and W. R. Marsh, *The Results of Radiation Chemical Measurements During the Early Operational Period of DIDO*, AERE C/R 2855 (November 1959).

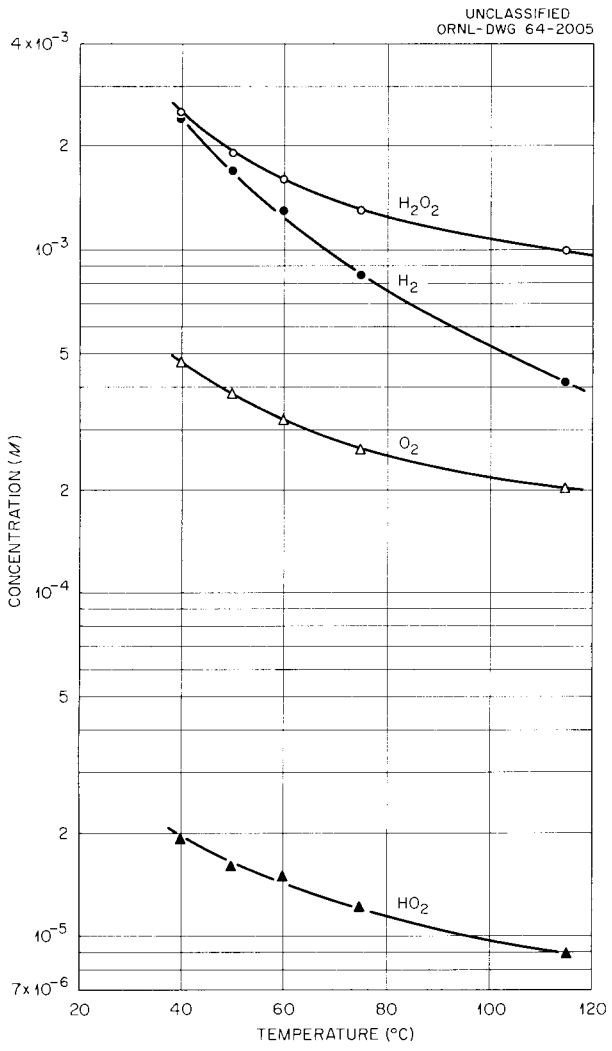

Fig. 6.2. Calculated Concentrations of H_2, O_2, H_2O_2, and HO_2 in HFIR Core at 100 w/cm^3 and an Excess Oxygen Concentration of 5×10^{-4} M.

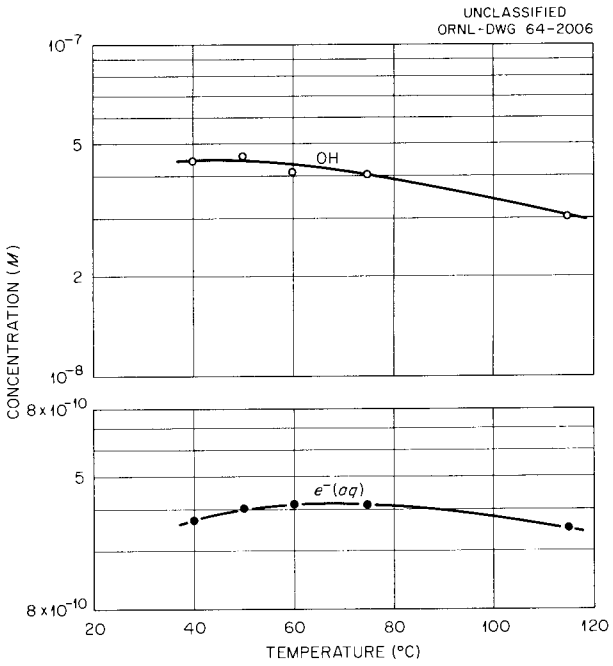

Fig. 6.3. Calculated Concentrations of e^-_{aq} and OH in HFIR Core at 100 w/cm^3 and an Excess Oxygen Concentration of 5×10^{-4} M.

surfaces (up to about 200°C), it is not possible to say that HO_2 will inhibit the aluminum corrosion. However, a test of this possibility in the HFIR would be worth while.

An assessment of the stability of HNO_3 in HFIR was based on comparison between estimated steady-state concentrations of the oxidizing and reducing species formed in radiolysis of water in the ETR and HFIR, and on available information regarding the radiation chemistry of nitrate-nitrite solutions. It was estimated that the concentrations of these species which can be maintained in HFIR, by adjustment of the concentration of excess oxidant, will differ by only small amounts from those which prevailed in the ETR tests in which NO_3^- was apparently stable outside the core.[7] Consequently, it is believed likely that the overall behavior of NO_3^- in HFIR will be similar to that observed in the ETR tests. Additional tests of NO_3^- stability in the ETR coolant with the reactor power at 175 Mw (the present power level) would provide a firmer basis for estimating NO_3^- behavior in HFIR. The feasibility of making such tests is being explored.

The possibility that a significant concentration of reduction products of NO_3^- would form during passage of coolant through the core was also considered. It can be estimated that conditions can be maintained in HFIR, again by adjustment of excess oxidant concentration, under which no more than 25% of the NO_3^- will undergo a reduction reaction during passage through a fuel channel. The net amount reduced would be less than this by some unknown amount because of back oxidation reactions. It can also be estimated

that the concentration of NO_3^- near a fuel-element surface will be near that prevailing in the bulk of the solution within a channel.

In summary, it is likely that conditions can be maintained in HFIR under which little or no net change in HNO_3 concentration will occur. Additional experiments in the ETR would provide a firmer basis for estimating HNO_3 stability in HFIR, and the feasibility of making such tests is being explored.

7. Mechanisms of Corrosion of Zirconium Alloys

G. H. Jenks

ELECTROCHEMISTRY OF ZIRCALOY-2 CORROSION IN HIGH-TEMPERATURE AQUEOUS SOLUTIONS

A. L. Bacarella A. L. Sutton

In previously reported work[1-4] equipment and techniques were developed to study electrochemistry in high-temperature aqueous environments and were used in studies of corrosion of zirconium and Zircaloy-2 in oxygenated 0.05 *m* H_2SO_4 solutions at 200 to 300°C. Additional experiments with this system have been made to determine the corrosion at longer exposure periods.

A revised autoclave system has been developed and used for simultaneous measurement of the differential capacity and the corrosion rate as a function of time at exposure temperature. Solutions can be added to the autoclave during an experiment, and the effect of these additions on the electrochemical parameters can be determined.

Film-Growth Kinetics

In previous reports[1-4] the results of rate-time measurements were interpreted according to the logarithmic rate law. The rates were analyzed as a function of time, and the kinetic constants in the logarithmic expressions were correlated with temperature. The logarithmic rate law is

$$dX/dt = Ae^{-BX} , \quad (1)$$

where X is the total amount of oxygen reacted at time t, dX/dt is the corrosion rate, and A and B are constants for a given set of experimental conditions. Integration of Eq. (1) provides a relation between X and time,

$$X = \frac{1}{B} \ln (ABt + a) , \quad (2)$$

where $a = 1$ if the logarithmic law is followed from $t = 0$, and if no film is originally present at $t = 0$. Substitution of Eq. (2) in Eq. (1) and inverting yields:

$$1/(dX/dt) = Bt + a/A , \quad (3)$$

which is the basis of the rate-time correlations previously reported and from which the constant B has been evaluated and correlated with temperature.

Previously, rate-time data were obtained, and film thickness as a function of time could be calculated by integrating the rate-time results. However, such calculations assume that all the corrosion product goes into the protective film. More recent studies reported here have measured the differential capacity, C_T (which is a measure of oxide film thickness X), and (simultaneously) the linear polarization resistances, which are a measure of the corrosion rate, $R = dX/dt$. The film thickness can be calculated from the capacitance and rate data, and the results of these calculations can then be used to determine whether all the products of the observed corrosion actually contribute to formation of the protective film.

[1] A. L. Bacarella, *J. Electrochem. Soc.* **108**, 331 (1961).

[2] A. L. Bacarella, *HRP Progr. Rept. Oct. 31, 1959*, ORNL-2879, p. 149.

[3] A. L. Bacarella, *HRP Quart. Progr. Rept. July 31, 1960*, ORNL-3004, p. 75.

[4] A. L. Bacarella, *Reactor Chem. Div. Ann. Progr. Rept. Jan. 31, 1963*, ORNL-3417, pp. 72–76.

Capacities were determined by measuring the initial slope of the voltage-time curve resulting from the application of galvanostatic pulses. Since the capacity is inversely proportional to X, a plot of $1/C_T$ vs log t should be linear according to Eq. (2) for t large so that $ABt >> a$. In Fig. 7.1 a plot of $1/C_T$ vs log t is presented for crystal-bar zirconium in oxygenated 0.05 m H_2SO_4 at 256°C. Except for the first two measurements at 18 and 30 min, for which steady-state temperature was not attained, a satisfactory linear relation was obtained; the deviations near zero time were in the direction expected from Eq. (2).

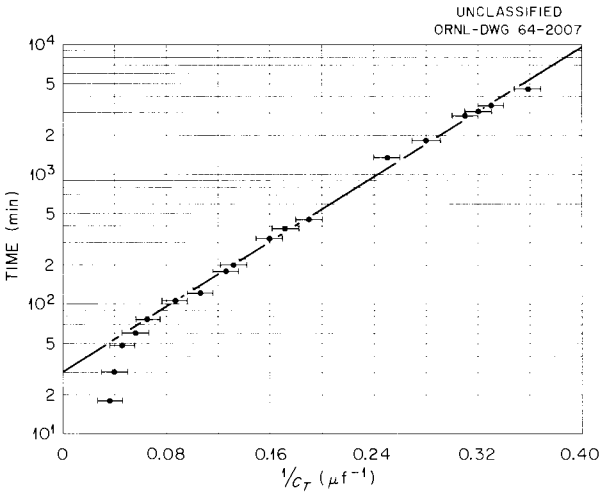

Fig. 7.1. Reciprocal Capacitance vs Log Time for Zirconium in Oxygenated 0.05 m H_2SO_4 at 256°C.

The results of the rate measurements which were made simultaneously with the differential capacity measurements are presented in Fig. 7.2. The value of B = 0.16 cm^2 per μg of O_2 calculated from the slope of the plot of $1/R$ vs t is in excellent agreement with the previous value,[4] B = 0.17 cm^2 per μg of O_2 for Zircaloy-2 at 258°C in the same environment.

A value of the film thickness can be calculated from the rate and capacitance data using Eqs. (1) and (4),

$$X_J = X_i C_i / C_J , \qquad (4)$$

which is valid if the dielectric constant of the oxide does not change with changing thickness of the film.

It can be shown from Eqs. (1) and (4) that

$$\frac{R_i}{R_J} = e^{-BX_i}\left(1 - \frac{C_i}{C_J}\right), \qquad (5)$$

where R_i, R_J, C_i, and C_J are the rates (Fig. 7.3) and capacities at times i and J respectively.

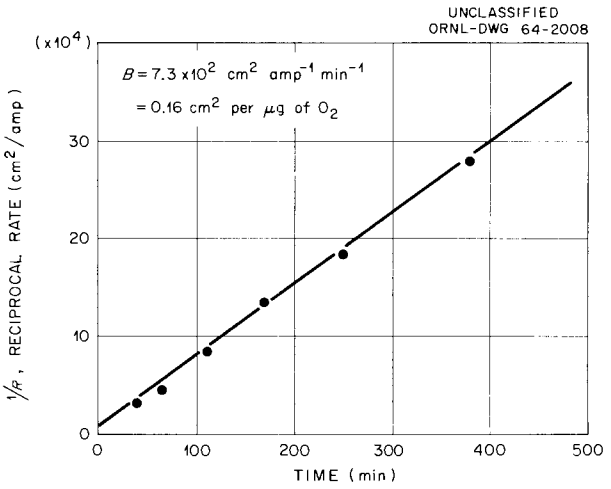

Fig. 7.2. Hyperbolic Plot of Rate-Time Data [$1/R = (1/A) + Bt$] for Zirconium in Oxygenated 0.05 m H_2SO_4 at 256°C.

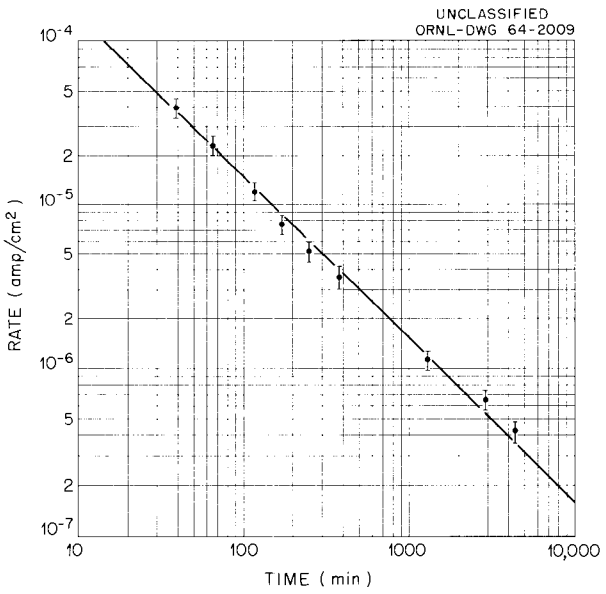

Fig. 7.3. Polarization Measurements of Rate as a Function of Time for Zirconium in Oxygenated 0.05 m H_2SO_4 at 256°C.

From data at 400 and 1300 min, the film thickness, X, at 400 min calculated from Eq. (5) is 21 μg of O_2 per cm^2. If the rate data shown in Fig. 7.2 are plotted linearly as rate vs time, the film thickness at 400 min can be calculated by integrating the area under the curve. The film thickness at 400 min calculated by this method was 24 μg of O_2 per cm^2. The thickness was also calculated using Eq. (2) and the values of A and B obtained from the $1/R$ vs t plot in Fig. 7.2. The resulting value of X at 400 min was 20 μg of O_2 per cm^2. These values of the film thickness are in very satisfactory agreement; they demonstrate that all the products of corrosion go into the film in accordance with Eq. (2) and that the dielectric properties of the oxide are approximately constant.

The dielectric constant at 256°C determined from the data is 68. However, the dielectric constant is a function of temperature; it was observed that $C_{25°C} = C_{256°C}/1.9$ and consequently $\epsilon_{25°C} = 68/1.9 = 36$. This value is reasonable when compared with the value of 27 reported by Charlesby[5] for anodic films on zirconium.

The effects of $CuSO_4$ additions on the open-circuit potential and capacitances were also investigated in this system. The copper was added to the system after 4500 min of prior exposure. The capacitances were independent of Cu^{2+} additions up to the highest concentration tested (6.5×10^{-2} M), but the open-circuit potential increased in the anodic direction approximately 300 mv over the range of Cu^{2+} additions. These results demonstrate that the capacitances were affected by the film thickness only, and did not include the pseudo-capacities relating to faradaic processes such as reduction of Cu^{2+} and O_2 at the oxide/solution interface. The increase in the anodic direction of the open-circuit potential E_0 (vs the standard calomel electrode) from −0.310 v at $Cu^{2+} = 0$ to ±0.000 v at $Cu^{2+} = 6.5 \times 10^{-2}$ demonstrated that Cu^{2+} was an oxidizing agent and that it was reduced at rates comparable to the rates of reduction of O_2. Since steady-state potentials were observed after each Cu^{2+} addition, it was concluded that the oxide/solution interface was unchanged by the Cu^{2+} additions and that the reduction was probably $Cu^{2+} + e \rightarrow Cu^{+}$.

[5]J. T. Polling and A. Charlesby, *Proc. Phys. Soc. (London)* **67B**, 20 (1954).

Kinetics at Long Exposure Periods

Conclusions concerning the corrosion of Zircaloy-2 at long exposure times at 290°C were not made in previous reports because of the appearance of some localized attack on a portion of the Zircaloy-2 electrode.[4] More recent measurements on electrodes whose entire surfaces were chemically polished ($HF\text{-}HNO_3\text{-}H_2O$) have eliminated the localized attack and have duplicated the previously published results. A steady-state corrosion rate [$(7 \pm 2) \times 10^{-7}$ amp/cm^2], which was independent of potential, was observed after several days exposure at 295°C. In one experiment, at −0.200 v vs Pt/O_2 (90°C), which was approximately 750 mv anodic to the open-circuit potential, the anodic rate approached a steady state, 7.2×10^{-7} amp/cm^2, at 10,000 min and remained at this rate for the duration of the experiment, an additional 18,000 min. These results suggest that the corrosion reaction involves the continuous formation and dissolution of a film on the surface of the metal.

Other measurements on this system have shown that (1) both the anodic and cathodic partial process rates decrease with increasing film thickness and (2) the activation energies for these partial process reactions are independent of film thickness. The activation energy for the anodic reaction is 30 ± 2 kcal/mole, and for the cathodic reaction, 7 ± 2 kcal/mole. It was also observed that the corrosion reaction is essentially under anodic control after a short exposure period.

These observations are consistent with a proposed oxygen ion migration through anion vacancies in the oxide as the anodic reaction in zirconium corrosion. The activation energy for the diffusion of oxygen in anion-deficient zirconium dioxide was reported as 28.1 and 33.4 kcal/mole (refs. 6 and 7). Such a mechanism for the anodic reaction would also be expected to be highly polarizable, and the corrosion reaction would essentially be under anodic control. Also the rate of the anodic reaction would be a function of film thickness since the concentration gradient

[6]W. O. Kingery *et al.*, *J. Am. Ceram. Soc.* **42**, 393 (1959).

[7]D. L. Douglass, *Corrosion Mechanism of Columbium, Zirconium, and Their Alloys — I. Diffusion of Oxygen in Columbium Pentoxide and Zirconium Dioxide*, paper presented at the Conference on the Corrosion of Reactor Materials, Salzburg, June 1962.

for anion vacancies decreases as the film thickness increases. The anion vacancies are formed at the metal/oxide interface and react with oxygen at the oxide/solution interface. The decrease in the cathodic rate with increase in film thickness is also consistent with this model if it is assumed that the cathodic rate is a function of the concentration of anion vacancies at the oxide/solution interface,

$$\tfrac{1}{2}O_2 + \square^{2+} + 2e \longrightarrow \boxed{O^{2-}},$$

where $\square^{2+}$ is the anion vacancy and $\boxed{O^{2-}}$ is an oxygen ion in the ZrO_2 lattice. The rate of the cathodic reaction may also be affected by the trapping of electrons at oxygen vacancies, but the cathodic process is not rate controlling. Other models for corrosion which have not been considered may also prove consistent with the electrochemical observations.

OXIDE GROWTH AND CAPACITANCE ON PREIRRADIATED ZIRCALOY-2

R. J. Davis

The mechanism of radiation corrosion of Zircaloy-2 is being studied by comparing the behavior of irradiated specimens with unirradiated controls. Measurements of weight gain and ac film impedance are made periodically during postirradiation exposure to 300°C steam plus oxygen. The first objective is to determine whether the primary radiation damage which accelerates corrosion occurs in the metal or in the oxide film. Earlier progress has been described.[8]

Equipment and Procedures

Tubular specimens, $1\frac{3}{4}$ in. long, $\frac{3}{16}$ in. OD, $\frac{1}{8}$ in. ID, have been employed with three variations of irradiation capsule. In the type I capsule, the specimen was encased in a helium-filled aluminum enclosure and was in contact with aluminum. In the type II design, the specimen was in contact with a Zircaloy-2 block and end-cap disks of zirconium foil. The capsule was helium filled and the gas was free to circulate within the outer aluminum enclosure. In the type III arrangement the specimen was contained in a helium-filled, leak-tight Zircaloy-2 autoclave. A tabulation of the preirradiation and irradiation treatments of each numbered specimen is given in Table 7.1.

[8] R. J. Davis and G. H. Jenks, *Reactor Chem. Div. Ann. Progr. Rept. Jan. 31, 1963*, ORNL-3417, pp. 70–72.

Table 7.1. Preirradiation and Irradiation Treatment of Specimens

Specimen No.	Control[a] Specimen No.	Preirradiation Treatment	Capsule Type	Fast Neutron (>1 Mev) Flux (neutrons cm^{-2} sec^{-1})	Irradiation Temperature (°C)	Irradiation Time (days)
	2	Prefilmed[b]				
7	6	Prefilmed[b]	I	1×10^{13}	100	10
8	9	As pickled	I	1×10^{13}	100	10
10	11	As pickled	II	7×10^{12}	300	$5\frac{3}{4}$
12	13	Prefilmed[b]	II	7×10^{12}	300	$5\frac{3}{4}$
15	14	Bare[c]	III	1×10^{13}	100	10
17	16	Prefilmed[b]	III	1×10^{13}	100	10

[a] Controls held at irradiation temperature in helium while specimens were irradiated.

[b] Prefilmed: exposed four days at 300°C in steam-oxygen mixture.

[c] Bare: heated 16 hr at 500°C in helium, inside Zircaloy-2 autoclave. Irradiated in autoclave.

After irradiation the specimens and controls were exposed to steam-oxygen mixtures at 300°C. Periodically the specimens were weighed and the film impedances were measured. In most cases, impedances were measured in 0.1 *M* NH_4NO_3 and in 1.0 *M* NH_4NO_3 and at 20, 100, 10^3, 10^4, and 10^5 cps.

Impedances were measured on one unirradiated specimen (No. 2) with and without a radioactive pin (8 mr/hr at 6 in.) inside the specimen. The impedances measured in and out of a gamma-ray field (on specimen No. 2) were the same within the precision of measurement.

Results

The specimens irradiated as pickled (Nos. 8 and 10) gained weight during irradiation (3.5 and 6.2 $\mu g/cm^2$ respectively) and lost weight during the first few hours of postirradiation exposure. After several days exposure the irradiated specimens corroded at rates higher (by a factor of 2) than the controls.

Two of the three specimens irradiated with preformed film (Nos. 7 and 12) gained weight (3.2 and 4.1 $\mu g/cm^2$ respectively) during irradiation, and no irradiation effect on postirradiation corrosion could be affirmed. The third specimen (No. 17) did not gain weight during irradiation. This specimen corroded more slowly than the control during the first five days of postirradiation exposure and faster than the control during the next 30 days (Fig. 7.4).

The specimen irradiated film-free (No. 15) gained a little weight (2.2 $\mu g/cm^2$) during the irradiation procedure. However, the control (No. 14) also gained 1.2 $\mu g/cm^2$. These weight gains correspond to about 75 to 140 A of oxide or about the thickness expected to form on film-free metal when exposed to room atmosphere. It is indicated, therefore, that these weight gains occurred after the irradiation when the film-free surfaces were exposed to room atmosphere. The postirradiation corrosion rate of this irradiated specimen was about twice that of the control (Fig. 7.5).

Most of the film impedance data were similar to the findings of others.[9,10] A few of the data are shown to illustrate the irradiation effects (Figs. 7.6 and 7.7). The data are reported as the two parameters, the reciprocal of the equivalent series capacitance, $1/C_s$, and the loss tangent, tan δ. The significance of these parameters is discussed briefly below.

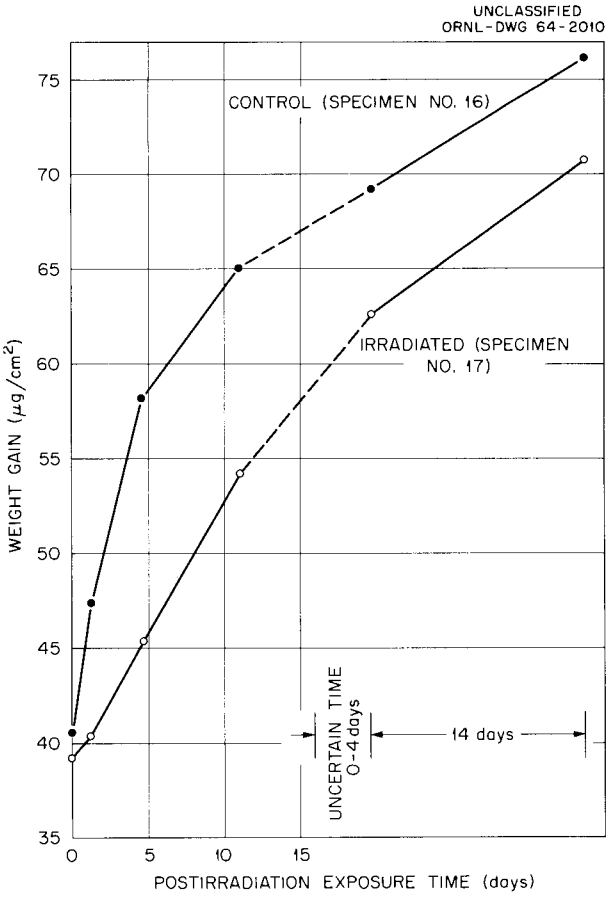

Fig. 7.4. Postirradiation Corrosion of Specimen Irradiated with Preformed Film.

Reciprocal capacitance vs weight gain at small weight gain is shown in Fig. 7.6 for specimen No. 15 (irradiated bare at 100°C) and its control. Data for a standard pickled specimen (not heated in helium prior to exposure) are also shown. The difference of about 5 $\mu g/cm^2$, along the weight-gain axis, between the standard pickled specimen and control No. 14 corresponds to a film thickness of about 300 A. A displacement of similar magnitude between specimen No. 15 and control No. 14 also occurred. The change in slope of Nos. 15 and 14 occurred after 2 hr of exposure.

[9] A. B. Reidinger, "The Corrosion Behavior of Zircaloy," M.S. thesis, Union College, Schenectady, N.Y., May 1958.

[10] L. Young, *Trans. Faraday Soc.* **55**, 842 (1959).

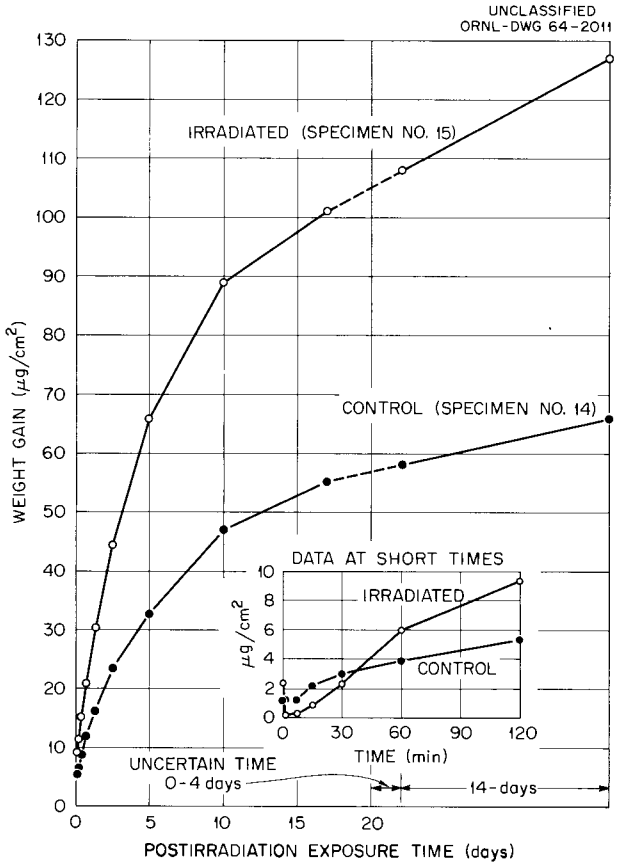

Fig. 7.5. Postirradiation Corrosion of Specimen Irradiated Film-Free.

The loss tangent, tan δ, values for those specimens which were irradiated at 300°C (No. 10, as pickled, and No. 12, with preformed film) were high relative to those for controls immediately after irradiation, dropped by a factor of 5 to 10 during 7 min of postirradiation exposure, and thereafter were similar to those for controls (Fig. 7.7). The loss tangent data for the specimen irradiated bare (No. 15) and its control are also shown in Fig. 7.7. Values of tan δ for both the irradiated and control specimens were very high for several hours then dropped to the range found for the other specimens.

Discussion

Film impedance data have not been quantitatively and completely explained on any theoretical basis.[11,12] It is predicted from theoretical considerations of properties of an ideal dielectric (pure capacitance), and it is known empirically,[9] that the reciprocal of the equivalent series capacitance, $1/C_s$, of corrosion films on Zircaloy-2 is proportional to the thickness of the film. It is known that among a series of zirconium alloys, the ratio of $1/C_s$ to weight gain, W, is highest for the most corrosion-resistant alloy and progressively lower for poorer alloys.[13] The best films are therefore characterized by the steepest slope on plots of $1/C_s$ vs W (such as Fig. 7.6). It is consistent with simple theory (and found empirically)[10] that higher values of tan δ are found with leaky films, that is, with films which allow some current flow. Leaky films are expected to be less corrosion resistant.

[11] L. Young, *Anodic Oxide Films*, pp. 155 ff., Academic Press, New York, 1961.

[12] R. G. Breckenridge, *Imperfections in Nearly Perfect Crystals* (ed. by Shockley, Hollomon, Maurer, and Seitz), pp. 219 ff., Wiley, New York, 1952.

[13] J. N. Wanklyn and D. R. Silvester, *J. Electrochem. Soc.* **105**, 647 (1958).

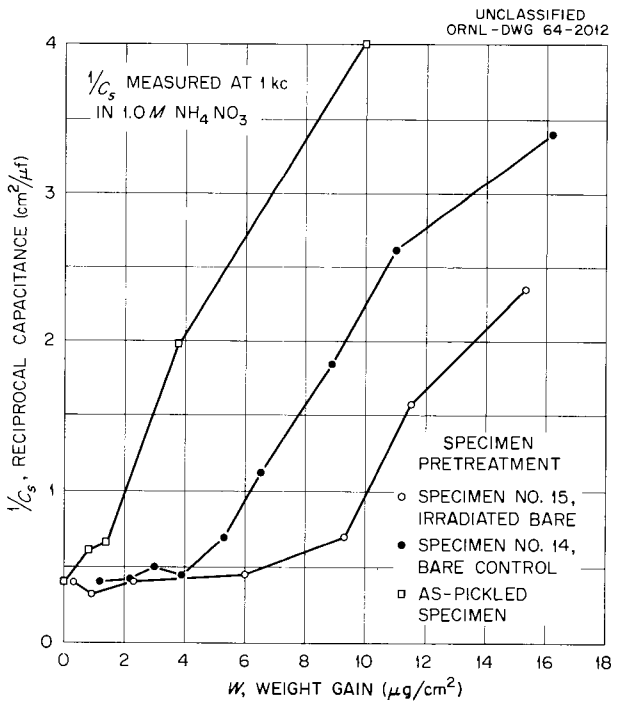

Fig. 7.6. Film Capacitance vs Weight Gain at Small Weight Gains.

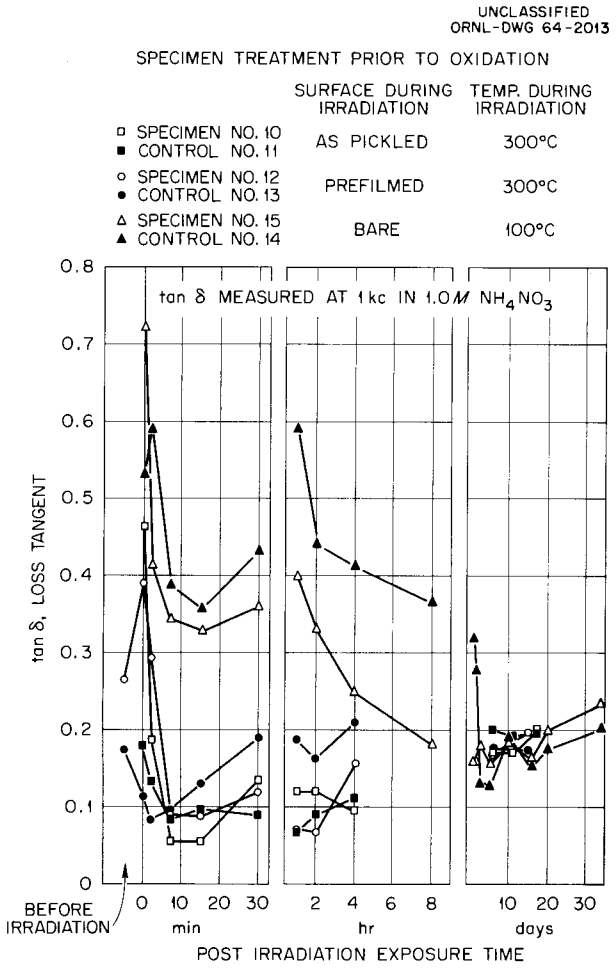

Fig. 7.7. Loss Tangent Behavior During Postirradiation Corrosion.

The sharp changes in the slopes of the $1/C_s$ vs W plots on Fig. 7.6 indicate that during the first 2 hr of exposure of the bare specimen, a film of inferior corrosion-resistant quality formed, and normal film formed thereafter. The irradiation effect was to increase the amount of inferior film. The decrease in tan δ after several hours postirradiation exposure of the bare specimens (Fig. 7.7) is added evidence that a change from inferior to normal corrosion film occurred.

The high tan δ values observed immediately after 300°C irradiation of as-pickled and prefilmed specimens (Fig. 7.7) show that the combination of irradiation, 300°C temperature, and helium environment caused the films to develop the leaky character described above. Neither irradiation at 100°C nor 300°C exposure without irradiation resulted in leaky films. The leaky character quickly disappeared on postirradiation exposure to oxidizing environment.

In summary, three irradiation effects have been observed:

1. Irradiation damage to metal enhanced postirradiation corrosion. With a specimen irradiated film-free, the rate was double that of a control during five weeks of exposure. With specimens irradiated as pickled and one irradiated with preformed film the rates exceeded those of controls only after several days exposure. Except for some additional low-impedance film on initially bare specimens during the first few hours postirradiation exposure, the film grown on radiation-damaged metal has as good impedance quality as that on controls.

2. Irradiation of corrosion film at 100°C in helium temporarily retarded postirradiation corrosion. One prefilmed specimen corroded only 20% as much as a control during the first day of postirradiation exposure. No difference in film impedance was associated with the retarded corrosion.

3. Irradiation of corrosion film at 300°C in helium reduced the film impedance. The impedance recovered during a few minutes exposure in the oxidizing environment.

The overall results are regarded as evidence that the observed enhancement of corrosion resulted, primarily, from an increase in chemical reactivity of the metal produced by radiation damage within the metal. Changes within the oxide or in material immediately adjacent to the oxide-metal interface were, apparently, produced during irradiation of prefilmed or pickled specimens, but these were not correlated with an enhancement of corrosion. Also, reasonable explanations of these changes can be visualized which are consistent with the conclusion that the primary enhancement of corrosion results from metal damage.

Experimental work to confirm the experimental findings is in progress.

8. Physical Chemistry of High-Temperature Aqueous Systems

ELECTRICAL CONDUCTANCES OF AQUEOUS SOLUTIONS AT TEMPERATURES FROM 0 TO 800°C AND PRESSURES UP TO 4000 BARS

Potassium Sulfate Solutions[1]

A. S. Quist H. R. Jolley[2]
W. L. Marshall

The electrical conductances of 0.0005032, 0.002199, and 0.004986 *m* K_2SO_4 solutions (in H_2O) have been measured at temperatures from 25 to 800°C and at pressures from 1 to 4000 bars.[1,3]

A three-dimensional representation of the effect of density and temperature on the equivalent conductance of 0.0005032 *m* K_2SO_4 is presented in Fig. 8.1. The maximum value of the equivalent conductance of this solution was found to be 1070 $cm^2\ ohm^{-1}\ equiv^{-1}$ at a density of 0.52 g/cm^3 at 499°C.

The equivalent conductances of potassium sulfate at infinite dilution, Λ_0, were obtained by a variation of the method of Owen.[4] The Fuoss-Onsager conductance equation[5] contains three unknown quantities, Λ_0, E, and J:

$$\Lambda = \Lambda_0 - Sc^{1/2} + Ec \log c + Jc .$$

This equation was solved simultaneously, using three different concentrations of K_2SO_4, to produce values of Λ_0 given in Table 8.1.

Using Franck's values for the viscosity of water at elevated temperatures and pressures,[6] and values of Λ_0 from Table 8.1, the Walden product, $\Lambda_0\eta_0$, was calculated for each Λ_0. The results of

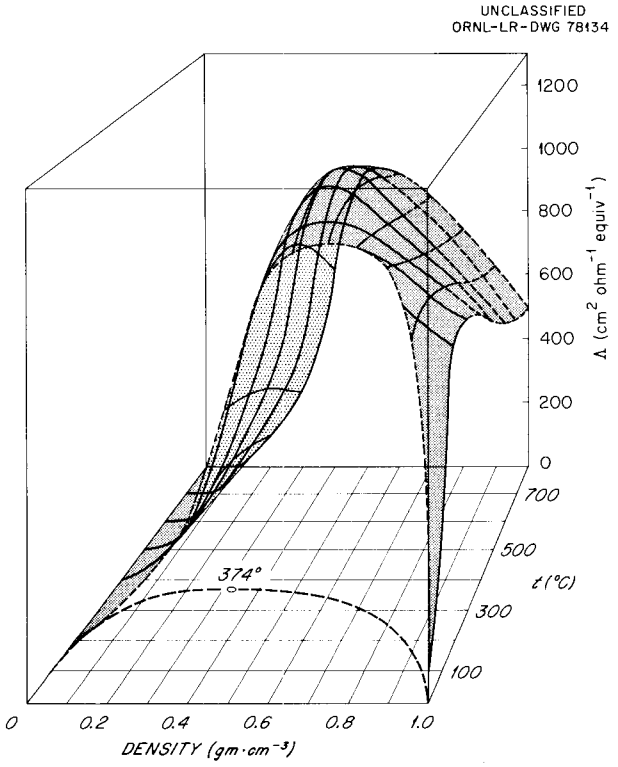

Fig. 8.1. Equivalent Conductances of 0.0005032 *m* K_2SO_4 Solutions as a Function of Density and Temperature.

[1]Summary of published paper: A. S. Quist *et al.*, *J. Phys. Chem.* **67**, 2453 (1963).

[2]Summer participant, 1961–63, Loyola University, New Orleans.

[3]A. S. Quist *et al.*, *Reactor Chem. Div. Ann. Progr. Rept. Jan. 31, 1963*, ORNL-3417, pp. 77–82.

[4]B. B. Owen, *J. Am. Chem. Soc.* **61**, 1393 (1939).

[5]R. M. Fuoss and L. Onsager, *J. Phys. Chem.* **36**, 2689 (1932); **61**, 668 (1957).

[6]E. U. Franck, *Z. Physik. Chem. (Frankfurt)* **8**, 107 (1956).

Table 8.1. Values of Λ_0 for K_2SO_4 in H_2O Solution

Temperature (°C)	Density (g/cm^3)							
	0.3	0.4	0.5	0.6	0.7	0.8	0.9	1.0
100								426
200							844	741
300						1021	921	821
400	779	1254	1303	1247	1099	968	879	
500	711	1252	1367	1190	1028	912		
600	608	1199	1348	1150	979	871		
700	447	1042	1278	1105	946			
800	354	822	1184	1027				

these calculations are shown in Fig. 8.2, where $\Lambda_0\eta_0$ is plotted against density at several temperatures. The rapid decrease of the Walden product below 0.5 g/cm^3 probably indicates that measurements were not carried out at low enough concentrations to obtain reliable values of Λ_0 from the Owen method.

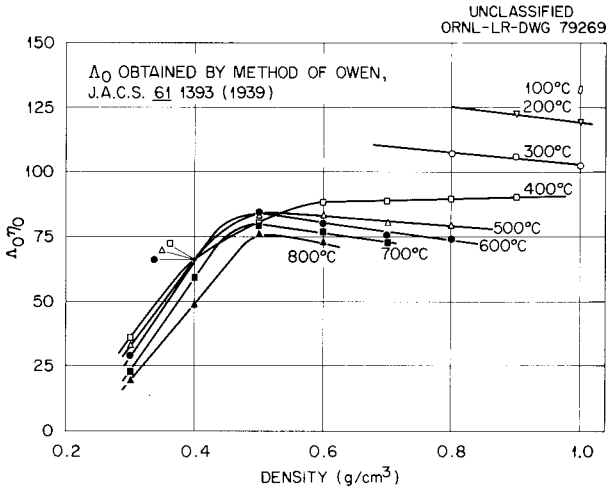

Fig. 8.2. The Walden Product, $\Lambda_0\eta_0$, vs Density for Aqueous K_2SO_4 Solutions.

Potassium Bisulfate Solutions

A. S. Quist W. L. Marshall

In another study the electrical conductances of dilute $KHSO_4$ solutions were measured at temperatures from 0 to 715°C and at pressures from 1 to 4000 bars. From these measurements the dissociation constant of the bisulfate ion was calculated at temperatures of 100, 200, and 300°C, at several densities. Above 300°C the dissociation constant became too small (less than 10^{-5}) to be evaluated by the present method.

Experimental Procedures. – The conductance cell and most of the experimental methods have been described previously.[1,3,7] The concentrations of potassium bisulfate solution were 0.00007365, 0.0002256, 0.0004316, 0.0008174, 0.002401, and 0.005049 *m*. However, in the case of the 0.00007365 *m* solution at the higher temperatures, the correction for the background conductance of the solvent amounted to about one-half the measured conductance, and so the large uncertainty associated with the corrected conductance values prevented their use in further calculations.

Calculation of Equivalent Conductances. – Extensive use was made of an IBM 7090 computer for the evaluation of the experimental data. A computer program was written which made the necessary corrections for the resistance of the electrical leads, corrected these values for the effect of frequency on the resistance, calculated specific conductances, subtracted the specific conductance of pure water (interpolated from a table of experimentally determined values), and

[7] E. U. Franck, J. E. Savolainen, and W. L. Marshall, *Rev. Sci. Instr.* **33**, 115 (1962).

then calculated equivalent conductances. From the overall results, values of equivalent conductances at integral temperatures and densities were obtained.

Results and Discussion. – The types of curves obtained when the specific conductances of $KHSO_4$ are plotted vs temperature, at constant pressure, are shown in Fig. 8.3 for 0.005049 *m* $KHSO_4$ at

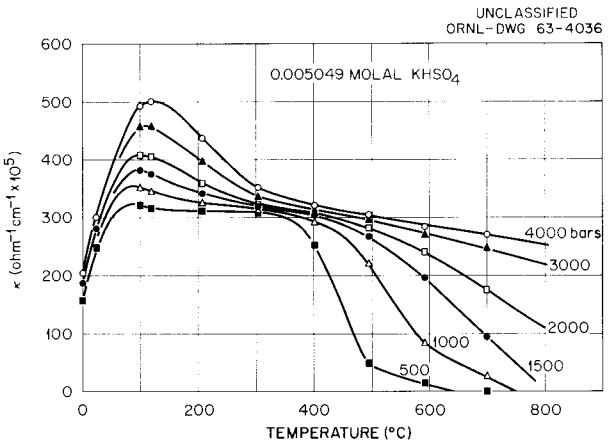

Fig. 8.3. Specific Conductances of 0.005049 *m* $KHSO_4$ Solutions as a Function of Temperature at Several Pressures.

several pressures. Increasing the pressure has very little effect on the specific conductances of K_2SO_4 solutions for temperatures below approximately 250°C.[1,3] However, as shown in Fig. 8.3, increasing the pressure increases considerably the specific conductance of $KHSO_4$ solutions at both low and high temperatures. At the high temperatures the increase in the specific conductance on increasing the pressure is due primarily to the correspondingly large increase in density. In the case of $KHSO_4$ at the low temperatures, the increase in conductance is due to the increasing ionization of HSO_4^- with increasing pressure.

The degree of ionization of the HSO_4^- ion decreases with increasing temperature. This is apparent by considering the shape of the curves in Fig. 8.3. At a constant pressure, increasing the temperature from 0 to about 100°C results in a large increase in the specific conductance. This is due to the correspondingly large decrease in the viscosity of H_2O, with a resulting increase in the mobility of the ions. Although the viscosity of H_2O decreases with increasing temperature above 100°C, the decreasing values of the specific conductance of $KHSO_4$ indicate that association of ions is taking place. Since this effect was not observed with K_2SO_4 solutions, it indicates that H^+ and SO_4^{2-} are associating to form HSO_4^-.

The effect of density on the molar conductance of 0.002401 *m* $KHSO_4$ solutions at several temperatures is shown in Fig. 8.4. At densities

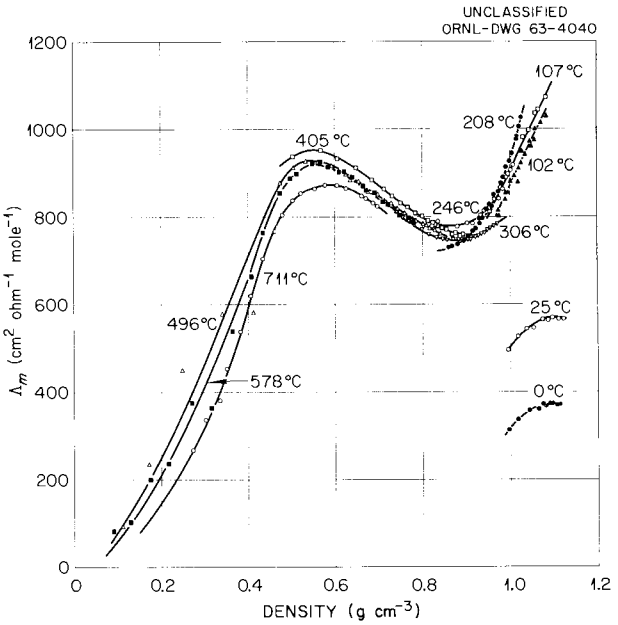

Fig. 8.4. Molar Conductances of 0.002401 *m* $KHSO_4$ Solutions as a Function of the Density of the Solution at Several Temperatures.

below approximately 0.8 g/cm^3 the graphs are similar to those observed with K_2SO_4. Above 0.8 g/cm^3 the increase in ionization of the HSO_4^- ion with increasing pressure and decreasing temperature is apparent.

A direct comparison of the specific conductances of solutions of K_2SO_4 and $KHSO_4$ of nearly equal concentrations is shown in Fig. 8.5. At a pressure of 4000 bars and at temperatures above about 300°C, the specific conductance of a $KHSO_4$ solution is nearly the same as that of a K_2SO_4 solution which is one-half the concentration of the $KHSO_4$ solution. This indicates that even at 4000 bars, the HSO_4^- does not dissociate significantly above about 300°C.

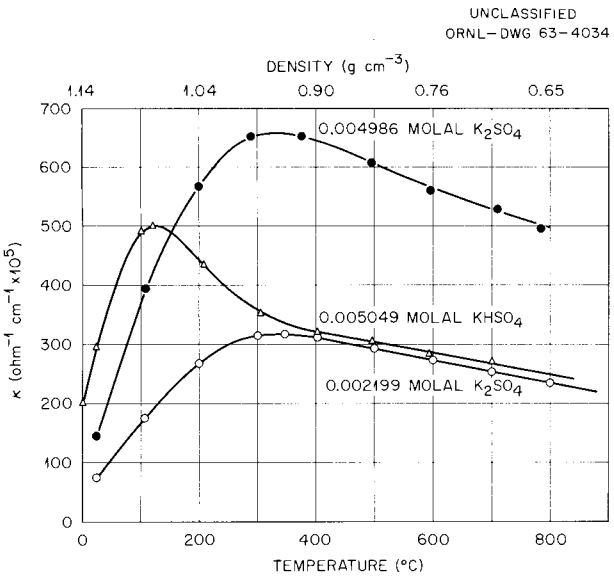

Fig. 8.5. Comparison of the Specific Conductances of $KHSO_4$ and K_2SO_4 Solutions as a Function of Temperature. Pressure = 4000 bars.

Values for the dissociation constant of the bisulfate ion were calculated from the data, using the Davies method.[8] For the present case the equations used are as follows:

$$K_2 = \frac{[H^+][SO_4^{2-}]}{[HSO_4^-]} \frac{f_{H^+} f_{SO_4^{2-}}}{f_{HSO_4^-}},$$

$$K_2 = \frac{\theta^2 C_0}{1-\theta} f_{SO_4^{2-}},$$

$$\theta = \frac{\Lambda(\text{exp}) - 0.5\Lambda(K[HSO_4])}{\Lambda(K[H][SO_4]) - 0.5\Lambda(K[HSO_4])},$$

$$\Lambda_i = \Lambda_i^0 - S_i I^{1/2}.$$

In these equations, $f_{SO_4^{2-}}$ refers to the Debye-Hückel activity coefficient; θ is the fraction of bisulfate ion dissociated; C_0 is the stoichiometric $KHSO_4$ concentration; $\Lambda(K[HSO_4])$ is the equivalent conductance of $KHSO_4$, assuming that it dissociates only into K^+ and HSO_4^- ions; and $\Lambda(K[H][SO_4])$ is the equivalent conductance of $KHSO_4$, assuming it dissociates completely into K^+, H^+, and SO_4^{2-} ions.

Values of the equivalent conductances at infinite dilution, Λ_i^0, were obtained at 100, 200, and 300°C, at saturation pressures from an evaluation of the data presently available in the literature,[1,9-11] and from the present data. Values of the limiting equivalent conductances at higher densities were calculated from the values obtained at saturation pressure by assuming that $\Lambda_0\eta_0$ was a constant at constant temperature (i.e., assuming the validity of Walden's rule).

For the case in which $KHSO_4$ is assumed to dissociate into only K^+ and HSO_4^- ions, the limiting Onsager slope is calculated in the usual manner. When $KHSO_4$ is considered to dissociate into K^+, H^+, and SO_4^{2-}, the calculation is not so simple because three different ions are present. In this case the method of Onsager and Kim[12] was used. The results of these calculations are shown in Table 8.2. The values reported by Lietzke *et al.*[13] are based on measurements of the solubility of Ag_2SO_4 in H_2SO_4 solutions along the liquid-vapor equilibrium region. From the change in the equilibrium constant with pressure, the volume change for the ionization of HSO_4^- may be calculated. The value obtained is approximately -30 cm^3/mole at 100 and 200°C. At 300°C the calculated volume change is greater, but the uncertainty in the result due to experimental error is too large to give much significance to this value.

EFFECT OF PRESSURE ON LIQUID-LIQUID IMMISCIBILITY IN THE SYSTEM UO_2SO_4-H_2O, 75–1600 BARS, 290–410°C (ref. 14)

W. L. Marshall J. S. Gill

By use of a new optical cell (Fig. 8.6) co-developed with E. S. Cantrell of the Plant and

[8] E. C. Righelleto and C. W. Davies, *Trans. Faraday Soc.* **26**, 592 (1930).

[9] A. A. Noyes *et al.*, "The Electrical Conductivity of Aqueous Solutions," *Carnegie Inst. Wash. Publ. No.* 63, Washington, D.C., 1907.

[10] J. E. Smith and E. B. Dismukes, *J. Phys. Chem.* **67**, 1160 (1963).

[11] S. W. Benson *et al.*, *J. Chem. Phys.* **22**, 209, 212 (1954); *J. Am. Chem. Soc.* **85**, 1044, 1047 (1963).

[12] L. Onsager and S. K. Kim, *J. Phys. Chem.* **61**, 215 (1957).

[13] M. H. Lietzke, R. W. Stoughton, and T. F. Young, *J. Phys. Chem.* **65**, 2247 (1961).

[14] A detailed paper by W. L. Marshall and J. S. Gill on the effect of pressure to 330 bars, with comments on the recent results to 1600 bars, is given elsewhere [*J. Inorg. Nucl. Chem.* **25**, 1033 (1963)]. Additional details of the extension of these studies to the higher range of pressure are presented in this report.

Table 8.2. Second Dissociation Constant of H_2SO_4

Temperature (°C)	$-\text{Log } K_2$				
	At Saturation Pressure		At Density (g/cm^{-3}) of –		
	Literature[a]	This Work	0.8	0.9	1.0
100	3.01	3.25			2.81
200	4.49	4.66		4.32	3.60
300			(7.4)	5.3	4.4

[a]See ref. 13.

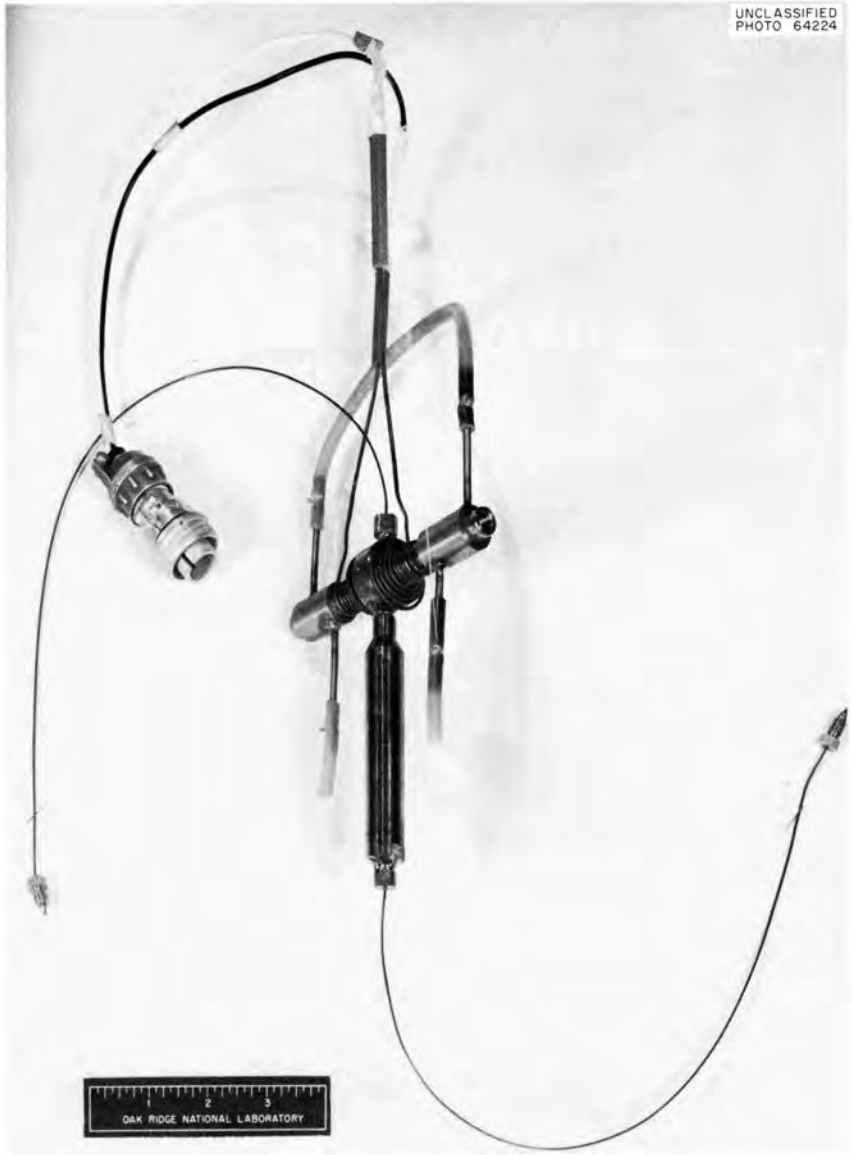

Fig. 8.6. High-Temperature, High-Pressure Optical Cell.

Equipment Division, an earlier study of the effect of hydrostatic pressures to 330 bars on two-liquid-phase formation by UO_2SO_4-H_2O solutions has been extended to 1600 bars. Details of most of the experimental procedures are presented elsewhere.[14] The additional experimental data are shown in Fig. 8.7, where the temperature of second-liquid-phase formation vs the hydrostatic pressure

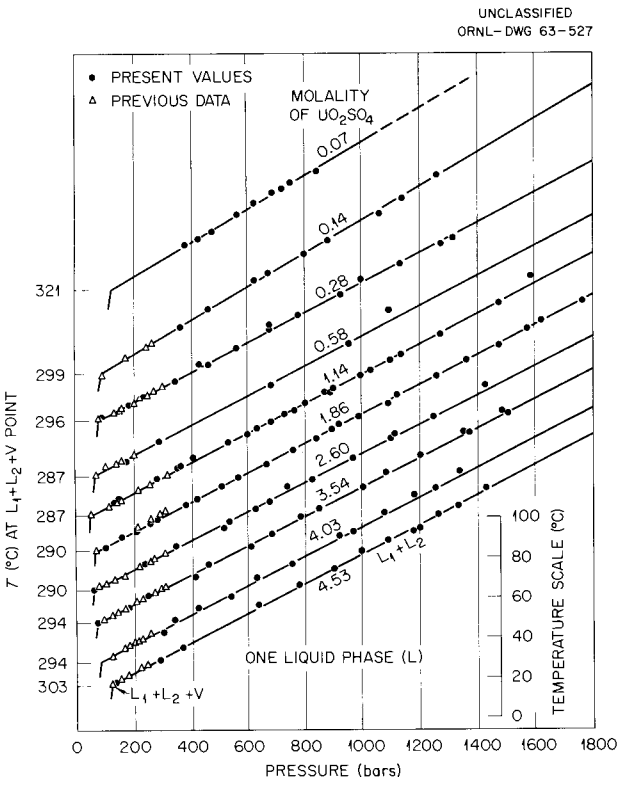

Fig. 8.7. Effect of Hydrostatic Pressure on the Temperature of Liquid-Liquid Immiscibility of UO_2SO_4-H_2O Solutions.

is plotted. The previous data, limited to 330 bars, are shown also. Thus it is observed that the curves of temperature vs pressure are linear at least to the highest pressures studied. In Fig. 8.8 the data on Fig. 8.7 (except data for 0.07 and 0.14 *m* UO_2SO_4) have been normalized to the same origin of ΔT(°C) and ΔP(bars), that is, where these two values equal zero at the three-phase (two liquid phases plus vapor) point. The average, revised value of the slope, $\Delta T/\Delta P$, is +0.075°C/bar for UO_2SO_4 solutions from 0.28 to 4.53 *m*. From Franck's estimates of the dielectric constants (D) of water,[6] the value $\partial t/\partial p$ at constant DT at the $L + V$ point of H_2O is estimated to be +0.075°/bar at 290° and +0.079°/bar at 300°C. Thus liquid-liquid immiscibility appears to correlate well with a function of theoretical significance, the product of the dielectric constant of the solvent times the absolute temperature.

INVESTIGATIONS ON THE SYSTEM UO_3-Li_2O-SO_3-D_2O: LIQUID-LIQUID IMMISCIBILITY AND CRITICAL PHENOMENA, 300–410°C (ref. 15)

E. V. Jones W. L. Marshall

In preceding studies[16–18] at temperatures between 300 and 430°C, boundaries of liquid-liquid immiscibility, critical phenomena, and solid-liquid equilibria were presented for systems containing SO_3 and H_2O, which contained, in addition, the components UO_3, CuO, and NiO, individually and combined. Combinations of the individual systems showed solubility characteristics of the metallic oxide components that were present in the highest concentration.

Since other preliminary studies had shown that (1) the addition of Li_2SO_4 to a UO_2SO_4-D_2O solution raised the temperature of two-liquid-phase formation,[19] (2) the addition of Li_2SO_4 to solutions of UO_2SO_4 inhibited corrosion, by UO_2SO_4, of container materials used in aqueous homogeneous reactors,[20] and (3) Li_2O in high concentration was phase stable in supercritical solutions of D_2SO_4 and D_2O,[21] it was of interest to make a systematic

[15]Summary of paper by W. L. Marshall and J. S. Gill: to be published in *J. Inorg. Nucl. Chem.* (1963).

[16]W. L. Marshall, J. S. Gill, and Ruth Slusher, *J. Inorg. Nucl. Chem.* **24**, 889 (1962).

[17]W. L. Marshall *et al.*, *J. Inorg. Nucl. Chem.* **24**, 995 (1962).

[18]W. L. Marshall and E. V. Jones, *J. Inorg. Nucl. Chem.* **25**, 1021 (1963).

[19]H. F. McDuffie, chap. 3, pp. 85–129 in *Fluid Fuel Reactors*, ed. by J. A. Lane, H. G. MacPherson, and F. Maslan (Investigations by R. S. Greeley, S. R. Buxton, and J. C. Griess), Addison-Wesley, Reading, Mass., 1958.

[20]J. C. Griess and E. G. Bohlmann, U.S. Patent 2,950,167 (to U.S. Atomic Energy Commission, Aug. 23, 1960); *Chem. Abstr.* **55**, 344c (1961).

[21]W. L. Marshall, Ruth Slusher, and F. J. Smith, *J. Inorg. Nucl. Chem.* **25**, 559 (1963).

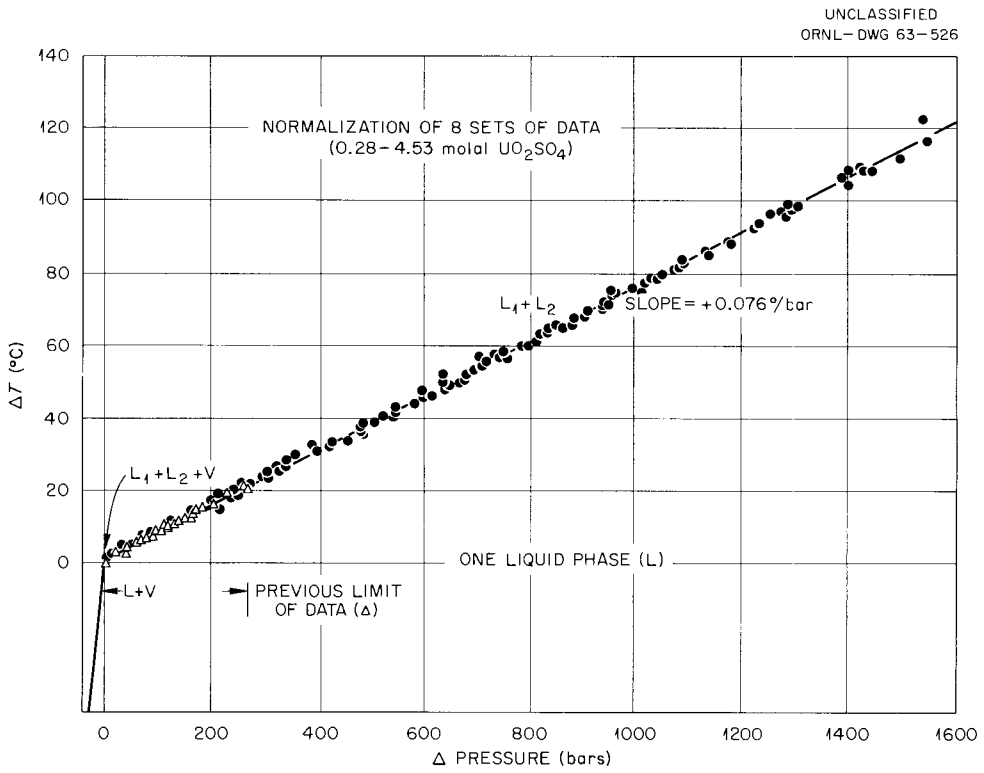

Fig. 8.8. Effect of Hydrostatic Pressure on Liquid-Liquid Immiscibility of UO_2SO_4-H_2O Solutions. At $\Delta T = 0$, $\Delta P = 0$, T and P vary between 290 and 300°C and between 70 and 90 bars respectively.

study of certain areas of the system UO_3-Li_2O-SO_3-D_2O above 300°C. The results will be correlated with information derived from studies of the separate three-component systems UO_3-SO_3-D_2O and Li_2SO_4-D_2SO_4-D_2O. The reagents used, the preparation of solutions, and all experimental procedures have been described previously.[17,21]

The experimentally observed temperatures of phase changes are given in Table 8.3, together with references to the type of change which occurred. There are three sets of data in Table 8.3, one each for constant molal ratios UO_3:Li_2O of 3:1 (set *A*), 1:1 (set *B*), and 1:3 (set *C*). In each set, another ratio, $R = (m_{UO_3} + m_{Li_2O}):(m_{SO_3})$, is varied in a series of experiments at constant molality of SO_3. The temperatures of appearances of liquid-liquid immiscibility, critical phenomena, or solid phases are recorded. The experimental temperatures are shown graphically in Figs. 8.9 and 8.10.

The data in Table 8.3, together with the previous results for the two separate systems UO_3-SO_3-D_2O and Li_2SO_4-D_2SO_4-H_2O, were used to draw isotherms showing the phase boundaries at four concentrations of SO_3: 0.05, 0.1, 0.5, and 1.0 *m*. These isotherms, shown in Fig. 8.11, are believed to describe reasonably well the regions of liquid-liquid immiscibility and occurrence of critical phenomena as functions of composition.

From Fig. 8.11 it is seen that the boundary of liquid-liquid immiscibility at the high concentrations of SO_3, even where the molal ratio UO_3:Li_2O = 1:3, extends to solution phases containing stoichiometrically neutral salts (R = 1.0), but at low concentrations of SO_3 and at high R this second liquid phase is not observed. By allowing for the increase in SO_3 concentration, the temperature of liquid-liquid immiscibility is observed to rise considerably upon addition of Li_2SO_4 to a UO_2SO_4

Table 8.3. Temperatures (°C) of Appearance of Liquid-Liquid Immiscibilities and Critical Phenomena in the System UO_3-Li_2O-SO_3-D_2O

R	SO_3 Molality					
	1.000	0.600	0.300	0.200	0.100	0.050
			Set *A*			
1.000	314.0 L	311.9 L	308.5 L	<312.0 S	<312.0 S	<290 S
0.800	326.8 L	317.9 L	316.1 L	318.4 L	323.0 L	<305 S
0.600	361.0 L	344.9 L	341.2 L	340.3 L	343.3 L	<320 S
0.500	377.4 L	363.8 L	355.2 L	350.7 L	352.9 L	~338 S
0.400	400 C	382.1 L	372.8 L	360.6 L	362.0 L	~347 S
0.300	406 C	390 C	384 C	380 C	373 L	~361 S
0.200	405 C	391 C	383 C	380 C	378 C	376 C
0.100	406 C	394 C	384 C	380 C	378 C	374 C
0.000	407 C	397 C	383 C	379 C	376 C	374 C
			Set *B*			
1.000	334.7 L	<327 S	<311 S	<298 S	<284 S	<267 S
0.800	354.1 L	342.8 L	339.6 L	<305 S	<294 S	<274 S
0.600	380.8 L	360.3 L	353.3 L	353 L + S	363.0 L	<290 S
0.500	400 L	386.5 L	368.3 L	366 L + S	364.5 L	<310 S
0.400	408 C	392 C	384 C	380 L + S	374.6 L	372 L + S
0.300	410 C	390 C	384 C	381 C	376 C	375 C
0.200	407 C	392 C	385 C	380 C	376 C	375 C
0.100	408 C	392 C	383 C	382 C	376 C	375 C

R	SO_3 Molality						
	1.000	0.800	0.600	0.300	0.200	0.100	0.050
				Set *C*			
1.000	349.0 L	352.5 L	<340 S (348) L	<335 S	~298 S	<310 S	<303 S
0.800	368.5 L	365.8 L	365.6 L	361.0	356.5 L	<312 S	<325 S
0.700	382.2 L	372.0 L	370.9 L	367.5 L	361.0 L	<316 S	<355 S
0.650	388.4 L						
0.600	405 C	393.0 L (395) C	380.4 L	370.8 L	368.2 L	366.5 L	365.2 L
0.500	403 C	397 C	393 C	380 C	379 C	375 C	374 C
0.400	409 C	399 C	390 C	381 C	379 C	375 C	373 C
0.300	409 C	397 C	388 C	382 C	379 C	375 C	374 C
0.200	410 C	401 C	390 C	382 C	378 C	376 C	373 C
0.100	409 C		392 C	381 C	377 C	375 C	373 C

Key: Molal ratio UO_3:Li_2O = 3:1 in set *A*, 1:1 in set *B*, and 1:3 in set *C*

$R = (m_{UO_3} + m_{Li_2O})/(m_{SO_3})$

L = appearance of second liquid phase

C = occurrence of critical phenomenon (where L ≡ V)

S = appearance of a solid phase

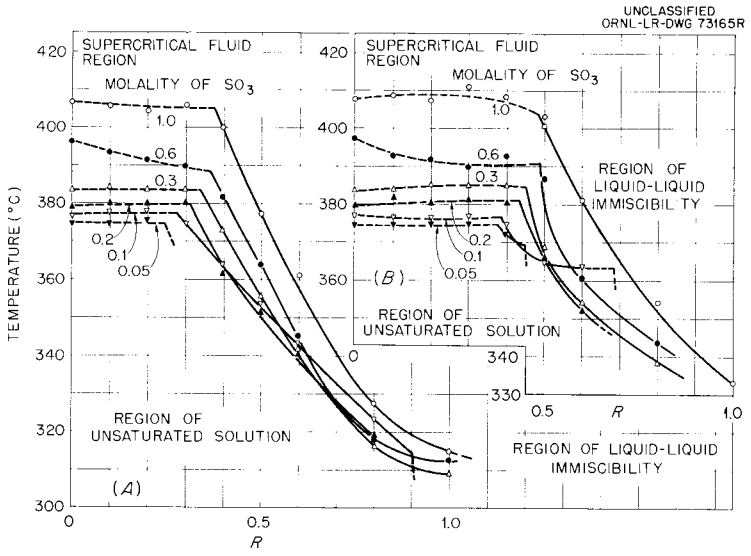

Fig. 8.9. Liquid-Liquid Immiscibility and Critical Phenomena in the System UO_3-Li_2O-SO_3-D_2O, 300–410°C. The ratio $R = (m_{UO_3} + m_{Li_2O})/m_{SO_3}$; molal ratio UO_3:Li_2O = 3:1 in set *A* and 1:1 in set *B*.

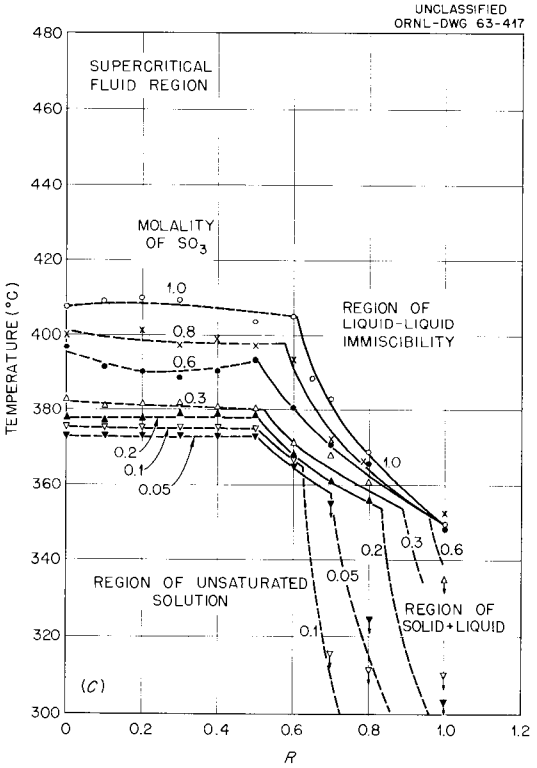

Fig. 8.10. Liquid-Liquid Immiscibility, Critical Phenomena, and Precipitation of Solid in the System UO_3-Li_2O-SO_3-D_2O, 300–410°C. The ratio $R = (m_{UO_3} + m_{Li_2O})/m_{SO_3}$; set *C*, where molal ratio UO_3:Li_2O = 1:3.

solution, thus confirming some preliminary observations.[19]

THE COMPOUND $NiO \cdot 3UO_3$ (ref. 22)

W. L. Marshall J. S. Gill

In an investigation of the five-component system UO_3-CuO-NiO-SO_3-H_2O at 300°C,[23] a double oxide of UO_3 and NiO was reported to exist as a saturating solid phase in the presence of particular compositions of liquid phase. The objectives of this present study were to confirm the identity of this oxide and to present a few of its characteristics.

In general, the experimental procedures and reagents used were the same as described previously for the preparation and evaluation of $CuO \cdot 3UO_3$.[24] The concentrations of H_2SO_4 and HNO_3 in the solution phases in all runs were between 0.01 and 0.1 *m*. The autoclave containing a solution and a solid mixture was rocked in a constant-temperature furnace for times varying

[22]Summary of paper by W. L. Marshall and J. S. Gill: to be published in *J. Inorg. Nucl. Chem.* (1964).

[23]W. L. Marshall and J. S. Gill, *J. Inorg. Nucl. Chem.* **22**, 115 (1961).

[24]J. S. Gill and W. L. Marshall, *J. Inorg. Nucl. Chem.* **20**, 85 (1961).

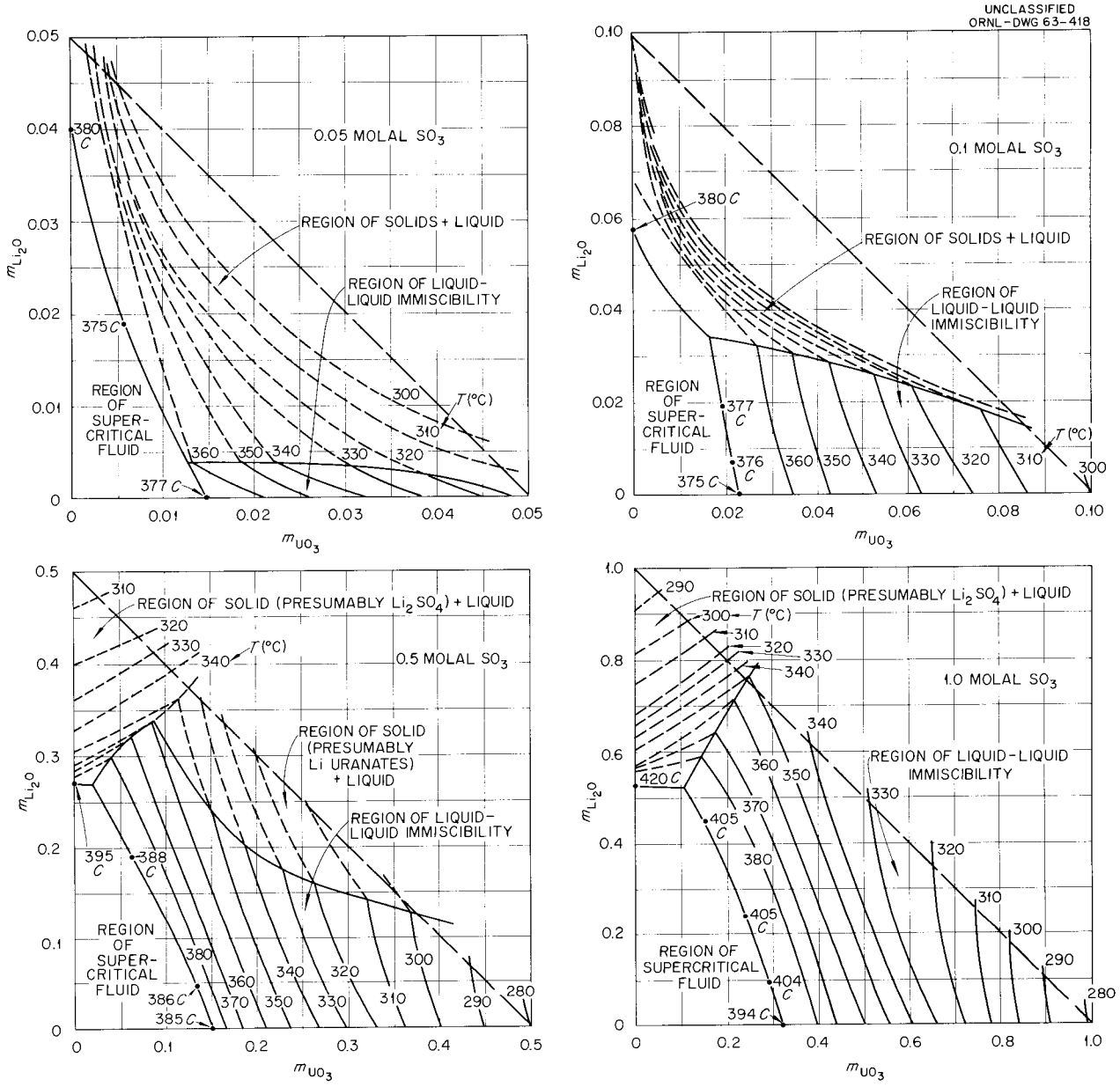

Fig. 8.11. Isotherms Showing Boundary Regions of Liquid-Liquid Immiscibility, Critical Phenomena, and Formation of Solid Phases in the Condensed System UO_3-Li_2O-SO_3-D_2O; 280–420°C; 0.05, 0.1, 0.5, and 1.0 *m* SO_3; *C* = Critical Phenomena.

from one to six days before cooling of the assembly and removing its contents for chemical analysis.

In Table 8.4 are listed (for $NiO \cdot 3UO_3$) the principal x-ray diffraction *d* values and their relative intensities obtained with a recording diffractometer. An evaluation of the $NiO \cdot 3UO_3$ showed that the compound was thermally stable up to a temperature of about 950°C. A gradual cumulative loss of ~0.5 wt % (probably H_2O) was recorded for both samples through gradual heating from 110 to 950°C over a period of 12 days. There was no significant change in the x-ray diffraction patterns of the solids after heating at 949°C, although a very small amount of U_3O_8 was indicated by the patterns. Between 950 and 980°, a further rather abrupt loss of ~1.7% occurred, corresponding to decomposition of UO_3 in the compound to U_3O_8. Formation of the structures of U_3O_8 and NiO and disappearance of $NiO \cdot 3UO_3$ were confirmed by x-ray diffraction. For five days of further heating from 1000 to 1200°C, the loss of weight became gradual again, amounting to ~0.8% further loss.

Table 8.4. Powder Pattern X-Ray Diffraction *d* Values for $NiO \cdot 3UO_3$ (Cu K_α Radiation, $\lambda = 1.54$ A)

Relative Peak Height	Value of *d*
6	5.09
6	4.69
100	4.04
5	3.67
20	3.27
1	2.95
1	2.627
8	2.554
7	2.530
1	2.479
2	2.194
2	2.102
1	2.076
19	2.019
1	1.963
4	1.886
1	1.833
6	1.723
8	1.710
4	1.633
2	1.51
1	1.36
1	1.31

CATION HYDROLYSIS AT ELEVATED TEMPERATURES

C. F. Baes, Jr. C. E. Roberts
N. J. Meyer[25] R. J. McNamee[26]
J. Balanchandra[27]

Studies of the hydrolysis of metal cations at elevated temperatures have been in progress for several years as an approach to the fuller understanding of the chemical behavior of aqueous systems at elevated temperatures. A study of UO_2^{2+} hydrolysis (25–94°C)[28] has been completed; studies of Th^{4+} hydrolysis (0–94°C)[29,30] and Fe^{2+} hydrolysis (to 200°C) are in progress. This report summarizes the status of these studies and describes the methods developed to process the experimental data.

Method of Data Reduction

The conversion of the data for each point in a potentiometric titration to a value of the hydroxyl number $\bar{n}$, the average number of OH^- ions per hydrolyzing metal ion M^{z+} in solution, and the corresponding acid concentration is simple in principle but involved and laborious in practice. The basic steps used (see Table 8.5) are (1) to

[25]Professor of Chemistry, Bowling Green State University, Bowling Green, Ohio.

[26]Operations Analysis Division, ORGDP.

[27]Alien guest from Atomic Energy Establishment, Trombay, Bombay, India, 1962–1963.

[28]C. F. Baes, Jr., and N. J. Meyer, *Inorg. Chem.* 1, 780–89 (1962).

[29]*Reactor Chem. Div. Ann. Progr. Rept. Jan. 31, 1963*, ORNL-3417, p. 96.

[30]*Reactor Chem. Div. Ann. Progr. Rept. Jan. 31, 1962*, ORNL-3202, p. 67.

Table 8.5. Reduction of Hydrolysis Data

Quantities Specified for Each Titration[a]	
$m_{i,0}$, V_0, d_0, g_0	Values for initial cell solution
$m_{i,t}$, d_t, g_t	Values for titrant solution
$m_{i,r}$	Values for solution chosen as reference point of titration
D_i	Liquid-junction parameters for each ion
Quantities Specified for Each Point in Titration	
V_t	Total volume of titrant solution added
ΔE	Difference between observed emf and the emf at reference point of titration
Computations for Each Point in Titration	
1. m_i	Molality of each ion, from $m_i = m_{i,0} + W(m_{i,t} - m_{i,0})$, where W is the dilution factor $V_t d_t g_t / (V_0 d_0 g_0 + V_t d_t g_t)$
2. h	Acid concentration, by iterative solution of the equation $\Delta E = \frac{RT}{F} \ln (m_{H,r}/h) + D_H(m_{H,r} - h) + \Sigma D_i(m_{i,r} - m_i)$ (Nernst Term); (LJP[b] term for H^+); (LJP term for other ions)
3. $\bar{n}$	Hydroxyl number, from $\bar{n} = (h - m_H)/m_M$

[a] m_i = molality of each ion, d = density, g = grams of water per gram of solution.
[b] Liquid-junction potential.

compute, from the volumes and compositions of the initial cell solution and titrant solution, the acidity (m_H) expected in the absence of hydrolysis, (2) to compute from the measured emf the actual acidity (h), and (3) to compute from these two quantities and the concentration of the hydrolyzing cation the hydroxyl number ($\bar{n}$).

To obtain $\bar{n}$ and h values, it is desirable to compute, in addition, the concentrations of all ionic species in the solution, since they affect the liquid-junction potential which can, in turn, appreciably affect the measured emf's. The inclusion of liquid-junction terms in the equation relating the cell emf to the acidity requires an iterative solution for the acidity h. Finally, the completed computation often shows that systematic errors are present which significantly affect $\bar{n}$ in the important initial stages of hydrolysis. In these stages the differences $h - m_H$ on which $\bar{n}$ depends are small but are quite sensitive functions of the assigned values of the initial acidity $m_{H,0}$, the reference acidity $m_{H,r}$, and a liquid-junction parameter D_H. This necessitates corrections of these quantities and a recalculation of the data.

In the present hydrolysis studies, data reduction has been performed, to an increasing extent, with the aid of the 7090 computer. The computed results of a titration are inspected by plotting $h - m_H$ (the difference between the measured acidity and that expected for no hydrolysis) vs W (the dilution factor), which is approximately proportional to the amount of titrant added and is a linear function of the formal acidity (see Table 8.5). Ideally, from the point of highest acidity in the titration (at either the beginning or the end), the data points on such a plot should lie on a line of zero slope and zero intercept which is terminated by an upward break at the point in the titration where hydrolysis first becomes detectable (Fig. 8.12). If, however, an error has been made

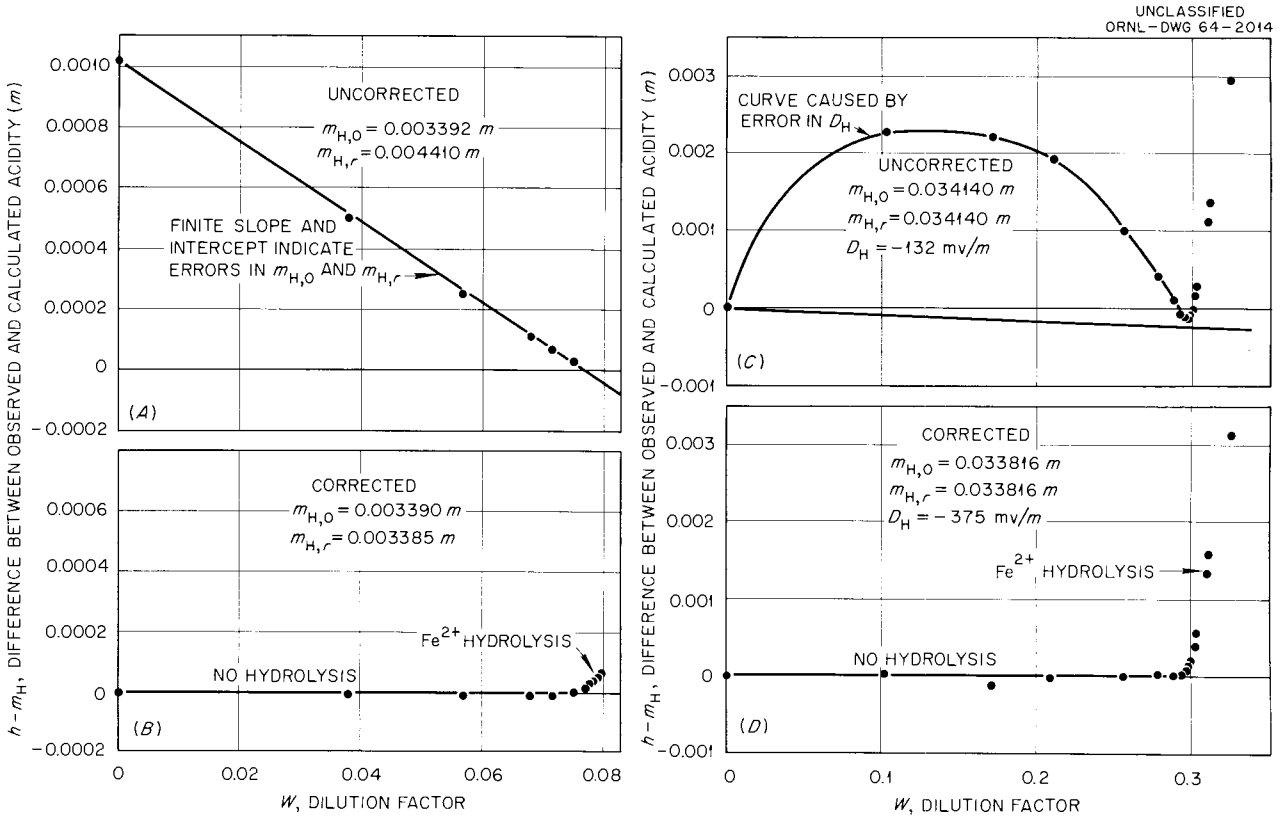

Fig. 8.12. Deviation of the Calculated Acidity from the Formal Acidity in Titrations of $FeCl_2$–HCl–0.1 m (Na)Cl Solutions at 95°C. The dilution factor, W, is proportional to the amount of added base. (*A*) and (*B*) illustrate the effect and correction of a large error in $m_{H,r}$; (*C*) and (*D*) illustrate the effect and correction of a large error in D_H.

in $m_{H,0}$ and/or $m_{H,r}$, the data in this region define a straight line of finite slope and intercept indicating significant (and erroneous) values of $\bar{n}$. The slope S and intercept I of this line can be used to correct $m_{H,0}$ and $m_{H,r}$ as follows:

$$\text{corrected } m_{H,0} = (m_{H,0} + I)(m_{H,t})/(m_{H,t} + S + I)\,, \quad (1)$$

$$\text{corrected } m_{H,r} = m_{H,r}\,(m_{H,t})/(m_{H,t} + S + I)\,. \quad (2)$$

(It is usually assumed that there is no error in $m_{H,t}$, since it is the most accurately known quantity.) Further, it can be shown that if an error has been made in D_H (which determines the value of the largest liquid-junction potential term), the otherwise linear curve will be approximately parabolic. The correction in D_H required to reduce this curve to a straight line is given by the approximation

$$\text{corrected } D_H^c \sim D_H - \frac{4RT}{F}\,\frac{\Delta(h - m_H)}{m_{H,r}^2}\,, \quad (3)$$

where $\Delta(h - m_H)$ is the deviation of the parabola from the expected straight line at the point where $m_H = \frac{1}{2}m_{H,r}$. The use of these correction procedures is illustrated in Fig. 8.12; they have been very useful as a means of eliminating small errors in $m_{H,0}$, $m_{H,r}$, and D_H, and, at the same time, of verifying the validity of computation 2, Table 8.5.

The form in which the liquid-junction potential is represented (Table 8.5, computation 2) can be derived from the Henderson equation[28] when it is applied to titrations in which the ionic strength is held constant, and the concentrations that vary are low compared with the inert-electrolyte concentration. The coefficients D_i can be estimated

from the conductance and charge of the ion i, or they can be measured experimentally. Strictly speaking, terms used should be of the form

$$D_i([i]_r - [i]),$$

where $[i]_r$ and $[i]$ are the actual concentrations of ion i at the reference point and at the point of the titration being computed. Such usage would require a foreknowledge of the hydrolysis reactions being investigated. Fortunately, the influence of the changing concentrations of the hydrolyzing ion and its hydrolysis products on the liquid-junction potential is usually negligible; recalculation of the data with inclusion of all the liquid-junction terms indicated by the assumed hydrolysis schemes showed such effects to be negligible in these studies of UO_2^{2+} (ref. 28) and Th^{4+} hydrolysis.

Th^{4+} Hydrolysis from 0 to 95°C

The measurements of Th^{4+} hydrolysis in 1 *M* $NaClO_4$ at 95° have been reported previously,[29] but interpretation of the results, as well as the results of others[31,32] in this system at 25°C, has been delayed until hydrolysis measurements at 0°C could be completed. Extension of the temperature range of Th^{4+} hydrolysis data was thought to be desirable, since it would provide additional data from which the obviously complicated hydrolysis scheme involved might better be determined.

In measurements at 0°C, noticeably slow reaction rates were encountered for the first time under conditions where precipitation was not expected ($\bar{n} < 2$). This led to difficulties with the glass electrodes used; the slow emf drift with time associated with the glass electrode resulted in appreciable errors not encountered with fast reactions. Accordingly, the quinhydrone electrode was chosen to complete the measurements. With this electrode, the attainment of a constant acidity after each addition of titrant (often requiring many minutes) was easily observed owing to the stability of this electrode. Figure 8.13 indicates the results obtained.

The results of Hietanen[32] at 25°C in this system were interpreted by her in terms of a "core + links"

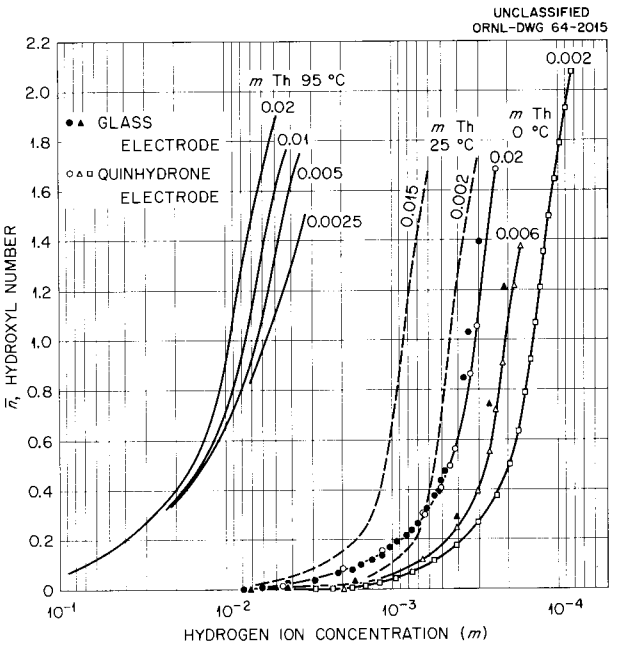

Fig. 8.13. Hydrolysis of Th^{4+} in 1 *m* $(Na)ClO_4$, 0–95°C.

sequence in which successive $Th(OH)_3^+$ groups are added to Th^{4+} to yield $(Th)_x(OH)_y$, where $x{:}y$ = 2:3, 3:6, 4:9 ... $(n + 1){:}3n$. The similar study of Kraus and Holmberg,[31] which included a more detailed examination of the early stages of hydrolysis, led them to conclude that $Th(OH)_2^{2+}$ and $Th_2(OH)_2^{6+}$ definitely were formed, and that $ThOH^{3+}$ and $Th_2(OH)_3^{5+}$ might be formed; this suggests the series

$$x{:}y = (1{:}1),\ 1{:}2,\ 2{:}2,\ (2{:}3)\ .$$

Subsequently, Lefebvre,[33] in an attempt to reconcile these differing conclusions, proposed the scheme

$$x{:}y = 1{:}2,\ 2{:}2,\ 5{:}12,\ 6{:}X,$$

where X = 18–21. For $\bar{n}$ values less than 2, only the first three species were thought to be important.

The present results at 95°C were compared with a number of possible schemes involving these and other species by use of the "General Least Squares" program of Busing and Levy[34] with the

[31] K. A. Kraus and R. W. Holmberg, *J. Phys. Chem.* **58**, 325 (1959).

[32] S. Hietanen, *Acta Chem. Scand.* **8**, 1626 (1954).

[33] Jean Lefebvre, *J. Chim. Phys.* **55**, 227 (1958).

[34] Chemistry Division; cf. R. M. Rush, J. S. Johnson, and K. A. Kraus, *Hydrolysis of U(VI): Acidity Measurements in Chloride Solutions and Absorption Spectra in Chloride and Perchlorate Solutions*, ORNL-3278 (Feb. 7, 1963).

"Calculation of Hydroxyl Number" subroutine of Rush.[34] The results of these tests are summarized in Fig. 8.14, where the fit of various schemes of three or four hydrolysis products to the data are compared. As noted previously,[29] it seems clear from the data at 95°C that mononuclear products are formed in the initial hydrolysis. Both 1:1 and 1:2 species were assumed to be present in every case.

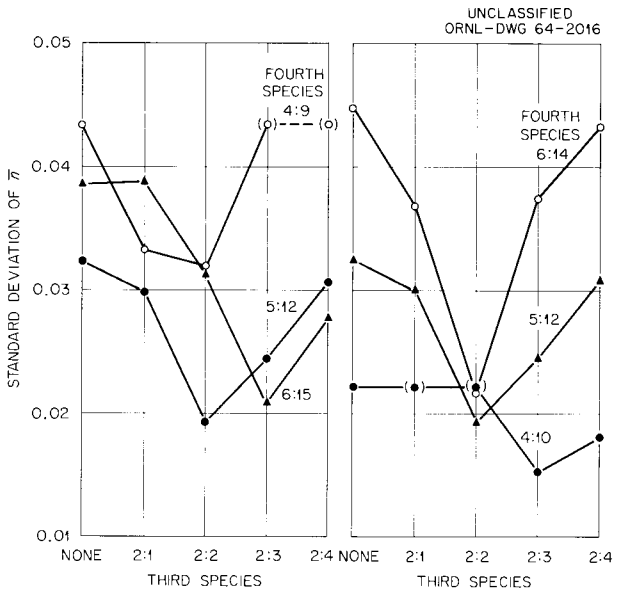

Fig. 8.14. Comparison of Various Th^{4+} Hydrolysis Schemes with Observed Results at 95°C. The values of x and y for the species $Th_x(OH)_y$ are shown (x:y) for the third and fourth species, the first and second species being Th(OH) and $Th(OH)_2$ (x:y = 1:1 and 1:2) in every case.

The assumption of 4:10 as the only additional product seems to give the lowest standard deviation (σ) of calculated from observed $\bar{n}$ values for a scheme of three:

$$1{:}1,\ 1{:}2,\ 4{:}10;\ \sigma = 0.0222\ .$$

Three schemes of four species were found which gave standard deviations <0.02:

$$1{:}1,\ 1{:}2,\ 2{:}2,\ 5{:}12;\ \sigma = 0.019\ ;$$

$$1{:}1,\ 1{:}2,\ 2{:}3,\ 4{:}10;\ \sigma = 0.015\ ;$$

$$1{:}1,\ 1{:}2,\ 2{:}4,\ 4{:}10;\ \sigma = 0.018\ .$$

Since the standard deviations of these fits approach the scatter of the data, it is not reasonable to choose the one giving the lowest standard deviation as the necessarily correct scheme.

While similar tests of the data at 25 and 0°C are not yet complete, the scheme

$$1{:}1,\ 1{:}2,\ 2{:}2,\ 5{:}12$$

has been fitted to the data at these temperatures. Because the contribution of the 1:1 species is small, and because only data below $\bar{n} = 2$ were employed in the tests, this scheme is essentially that of Lefebvre. The resulting standard deviation for the data of Kraus and Holmberg at 25°C was 0.024, which confirms the consistency of Lefebvre's proposed scheme. However, the standard deviation found at 0°C (0.08) was considerably larger, and it is not yet clear whether this is caused by poorer accuracy in the data resulting from the slow reaction involved or whether another scheme yet to be tested will prove more suitable. It is hoped that, when the analysis of the data at lower temperatures is completed, one scheme of four species will emerge as being consistent with all the data from 0 to 95°C.

Fe^{2+} Hydrolysis from 95 to 200°C

The principal ionic species of iron, thought to be present in high-temperature pressurized water systems operated under reducing conditions, are Fe^{2+} and its hydrolysis products.[35] It is, therefore, of considerable interest to investigate the hydrolytic behavior of this ion at temperatures approaching those employed in such systems (e.g., 260°C). Such an investigation is presently in progress.

The cell being used, which is contained in a titanium bomb, employs two hydrogen electrodes of the type described previously:[30]

$$\mathrm{Pt,\ H_2} \left| \begin{array}{l} \mathrm{NaCl},\ (0.1 - a - 2b)\ m \\ \mathrm{HCl},\ a\ m \\ \mathrm{FeCl_2},\ b\ m \end{array} \right\| \begin{array}{l} \mathrm{NaCl},\ (0.1 - c)\ m \\ \mathrm{HCl},\ c\ m \end{array} \Bigg| \mathrm{H_2,\ Pt}$$

This concentration cell has the advantage that the resulting emf is independent of the hydrogen pressure, since both half cells are exposed to a common atmosphere. In addition, the hydrogen

[35] *Reactor Chem. Div. Ann. Progr. Rept. Jan. 31, 1963*, ORNL-3417, pp. 61–63.

was expected to reduce any traces of Fe(III) present in the stock solutions used. It was observed, however, that such reduction was rapid only when sufficient acid was present initially (>0.01 *m*) to prevent extensive hydrolysis of the Fe(III). Since the hydrolysis of Fe^{2+} did not become detectable until nearly all the free acid initially present was neutralized by added NaOH, it was possible, using the methods described previously [Fig. 8.12 and Eqs. (1), (2), and (3)], to determine accurately the initial acidity – which was the reference acidity – for each titration.

Preliminary results at 95, 150, and 200°C are presented in Fig. 8.15, along with a curve representing the results of Hedström[36] in 1 *M* $NaClO_4$ at 25°C. Hedström found that hydrolytic precipitation occurred at $\bar{n} < 0.01$. In the present measurements, precipitation occurred at $\bar{n} < 0.1$. The range of $\bar{n}$ values which can be measured is thus greatly restricted. It presumably can be increased by decreasing the Fe^{2+} concentration used, but at the cost of increased interference from traces of acidic or basic impurities which may be present in the solutions used. For example, even at the relatively high concentration of 0.01 *m* Fe^{2+}, a 10^{-5} *m* concentration of an acidic or a basic impurity can introduce an error of 0.001 in the hydroxyl number.

[36]B. O. A. Hedström, *Arkiv Kemi* **5**, 457 (1952).

The results obtained thus far are consistent with the simple hydrolysis reaction found by Hedström:

$$Fe^{2+} + H_2O \rightleftharpoons FeOH^+ + H^+ , \qquad (4)$$

in that $\bar{n}$ varies inversely as the hydrogen ion concentration (Fig. 8.15). Hedström estimated the equilibrium quotient for this reaction as $10^{-9.5}$ at 25°C. The equilibrium quotients at 95, 150, and 200°C are presently estimated to be, respectively, $10^{-7.5}$, $10^{-6.3}$, and $10^{-5.9}$.

ISOPIESTIC VAPOR-PRESSURE MEASUREMENTS OF AQUEOUS SALT SOLUTIONS AT ELEVATED TEMPERATURES

B. A. Soldano P. B. Bien
C. H. Secoy

An investigation of the osmotic behavior of representative salt types at elevated temperatures[37–40] has been extended to ~152°C. The

[37]B. A. Soldano and C. S. Patterson, *J. Chem. Soc.* **1962**, p. 937.

[38]B. A. Soldano *et al.*, pp. 224–35 in *The Structure of Electrolytic Solutions*, Wiley, New York, 1958.

[39]C. S. Patterson, L. O. Gilpatrick, and B. A. Soldano, *J. Chem. Soc.* **1960**, p. 2730.

[40]B. A. Soldano and M. Meek, *J. Chem. Soc.* **1963**, p. 4424.

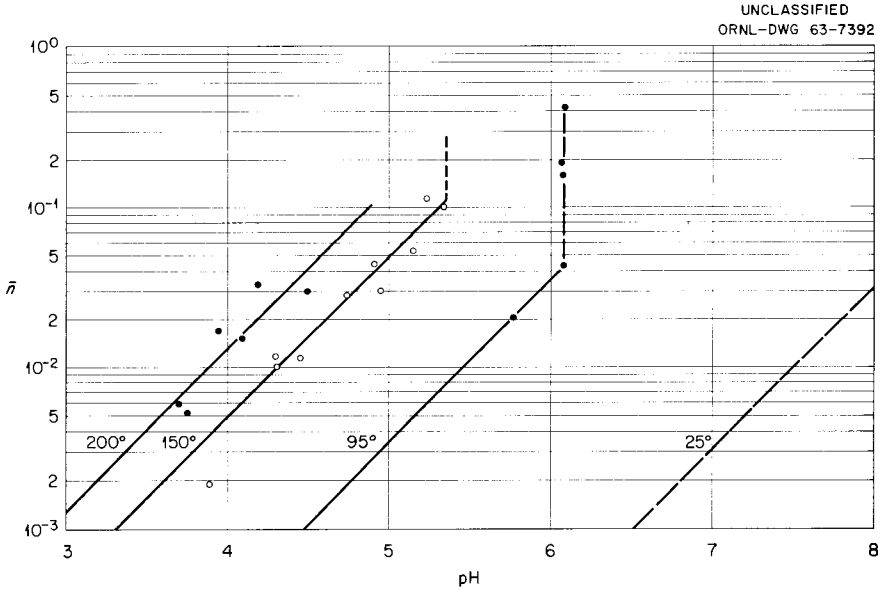

Fig. 8.15. Hydrolysis of 0.01 *m* Fe^{2+} in 0.1 *m* (Na)Cl, 25–200°C. The dashed line is from the results of Hedström [B. O. A. Hedström, *Arkiv Kemi* **5**, 457 (1952)]. The vertical breaks indicate hydrolytic precipitation.

concentration range examined varied from ~0.75 *m* to the limit defined by the salt's solubility. The results are compared with those at 25°C.

The experimental results are presented (Table 8.6) both as isopiestic ratios relative to sodium chloride and as osmotic coefficients, the latter referenced to the primary standard vapor pressure measurements of NaCl as obtained by Gardner, Jones, and deNordwall.[41]

The isopiestic ratio at fixed water activity is defined as $R = \gamma m_{std}/\gamma m$, where γ is the idealized number of ions formed per mole of salt in the assumed standard state (i.e., $\gamma = 3$ for $BaCl_2$), and *m* is the molality of the solute. The experimental ratios for the 1-1 electrolytes at 152°C are reported at rounded molalities as obtained from an *R* vs *m* plot. All osmotic coefficients were calculated by means of the relationship $R\phi_{NaCl} = \phi_i$. The primary standard data for NaCl required in our calculations at 152°C were those of deNordwall *et al.*[41] The ϕ-*m* curve for NaCl at 151.4°C was drawn from a least-squares fit.

Figure 8.16 permits a comparison of osmotic coefficients obtained at 25°C with those at high temperature. It is apparent that a first-order change has occurred in the behavior of the alkali halides (as well as in the case of multivalent salts), since the curves at 25 and at 151.4°C are decidedly and fundamentally different. For example, in place of the sharp rise in the osmotic coefficients of the alkali halides with increasing salt concentration, observed at 25°C, a pronounced curvature downward is now common to the coefficients at 151.4°C. So dominant is the effect that gives rise to downward curvature that LiCl is apparently willing to forego its usual precedence in the alkali halide family and behave like KCl. The curvature itself is inherent in the NaCl results, as deNordwall *et al.* have already pointed out,[41]

[41]E. R. Gardner, P. J. Jones, and H. J. deNordwall, *Trans. Faraday Soc.* **59**, 1994 (1963).

Table 8.6. Isopiestic Ratios at 151.4°C with NaCl as Standard

M	ϕ_{NaCl}[a]	*R*					
		LiCl	KCl	CsCl	$BaCl_2$	Na_2SO_4	$MgSO_4$
0.75	0.8830[b]	1.0303	0.9594	0.9150	0.9294	0.7539	
0.85	0.8894	1.0288	0.9573	0.9130	0.9282	0.7446	
0.95	0.8957	1.0273	0.9543	0.9111	0.9271	0.7353	
1.00	0.8987	1.0266	0.9540	0.9101	0.9268	0.7307	
1.25	0.9134	1.0229	0.9487	0.9052	0.9236	0.7075	
1.50	0.9270	1.0192	0.9423	0.9004	0.9208	0.6843	
1.75	0.9398	1.0155	0.9379	0.8955	0.9179	0.6611	0.498
2.00	0.9516	1.0118	0.9325	0.8906	0.9150	0.6379	0.493
2.50	0.9722	1.0044	0.9217	0.8808		0.5915	0.483
3.00	0.9889	0.9970	0.9110	0.8711		0.5451	0.474
3.50	1.0016[b]	0.9896	0.9002	0.8614			0.464
4.00	1.0106[b]	0.9822	0.8894	0.8516			0.454
4.50	1.0156[b]	0.9748	0.8786	0.8418			0.444
5.00	1.0167[b]	0.9674	0.8678	0.8321			0.434
5.50	1.0138[b]	0.9600	0.8571	0.8224			0.425
6.00	1.0072[b]	0.9526	0.8463	0.8126			0.415

[a]From ref. 41.

[b]Extrapolated values.

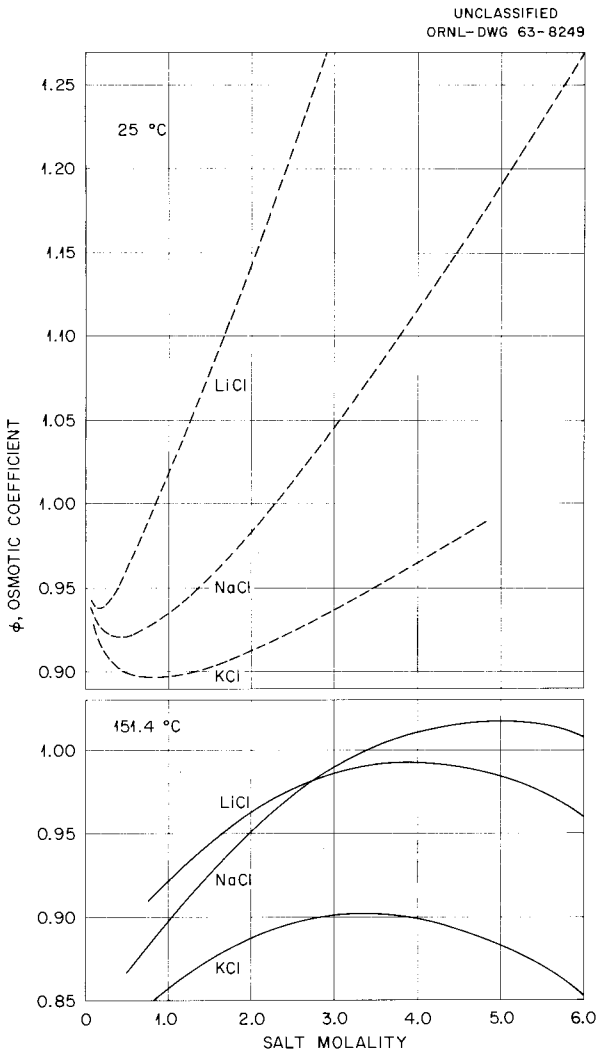

Fig. 8.16. Comparative Osmotic Coefficients as a Function of Molality at 25 and 151.4°C.

but the unusual behavior of the LiCl solutions suggests that this curvature must be the result of an effect dominating the behavior of all concentrated solutions at elevated temperatures.

With the benefit of hindsight, this concentrated solution effect, now clearly observed at elevated temperatures, should not have been totally unexpected. The ϕ-m plot for NaCl at 100°C, obtained from Smith's vapor pressure data,[42] shows an inflection (changing from concave upward to concave downward) at a concentration between 3 and 4 m. The calculated ratios ($R = \phi_{KBr}/\phi_{NaCl}$) at 90 and 100°C, when plotted as a function of the molality, give curves which appear to shift in a clockwise direction about the origin with increasing temperature. This "clockwise shift" is common to many of the salts that we have studied. It is particularly pronounced in LiCl-NaCl systems. The data of deNordwall *et al.*[41] at higher temperatures confirm the inflection observed in Smith's[42] data at 100°C; the curves become increasingly concave downward as temperature rises. Considering the increasing downward concavity of the ϕ_{NaCl}-m curves, and the increasingly negative slope of the R-m curves with rising temperature, one should expect the ϕ_{salt}-m curves to show maximums at temperatures and concentrations characteristic of the particular salt.

At 152°C, the "structural" anomalies normally associated with the properties of hydrogen-bonded solvents (strongly exemplified by the LiCl system at 25°C in particular) and the sharp rise in the osmotic coefficients with increasing molality appear to be absent from water. Below this temperature, aqueous salt solutions tend, with increasing intensity, to be predominantly characterized by structural factors culminating in the familiar pattern observed at 25°C (Fig. 8.16).

Current theories of aqueous solution behavior seem to provide no satisfactory interpretation of these data. The concave curvature could be obtained mathematically by a distance-of-closest-approach term[43] in the Debye-Hückel equation, but this distance has, heretofore, been empirically employed to rationalize differences in behavior of concentrated solutions of specific salts. These data show the curvature to be of the same magnitude for such divergent salts as LiCl and NaCl. This apparently conflicting situation, involving two diverse demands on the distance, would seem to require a dualistic role of the "distance of closest approach" in electrolyte solutions.

---

[42] R. A. Robinson and R. H. Stokes, *Electrolyte Solutions*, Butterworths, London, 1955.

[43] E. Glueckauf, personal communication.

9. Interaction of Water with Particulate Solids

SURFACE CHEMISTRY OF THORIA

C. H. Secoy

Heat of Immersion of ThO_2 in Water

H. F. Holmes E. L. Fuller, Jr.

The apparatus and techniques previously described[1] have been used in a continuing series of calorimetric measurements of heats of immersion of thorium dioxide in water at 25°C. Primary attention has been directed in this study toward measurements on specimens with known quantities of preadsorbed water. The effects of chemical and mechanical pretreatment of the surface and the possibility of contamination of the material during the preliminary outgassing have been examined briefly.

Effects of Outgassing Conditions and of Chemical Pretreatment. – All samples of ThO_2 studied in the calorimeter had been outgassed by pumping to pressures of $\sim 1 \times 10^{-5}$ mm Hg at temperatures up to and including 500°C for 24 hr prior to seal-off in the sample capsule. It has recently been shown that the surface of TiO_2 can be reduced by organic vapors present in the vacuum system used to outgas it at 450°C.[2] Insertion of a liquid-nitrogen-cooled trap between the TiO_2 and any source (including stopcock grease) of organic vapors diminished the effect, and addition of oxygen at the outgassing temperature served to reoxidize the surface. As a consequence of this study, which has led to a recent criticism of heats of immersion determined with solids previously activated at high temperatures,[3] the possibility of such reduction of ThO_2 has been examined.

The existence of carbonate groups on the surface of ThO_2 after exposure to laboratory air has recently been shown by infrared spectra of ThO_2 surfaces;[4] the same study indicated that the surface carbonate could be removed by treatment with strong alkali. Since all ThO_2 specimens in this study are exposed (before outgassing) to laboratory air, removal of the surface carbonate might be necessary. Graphon,[5] a commercial carbon black, shows heats of immersion which depend on whether the specimen has previously been treated with water. Tests have been made, accordingly, to establish whether these implied effects can be important.

Table 9.1 shows heats of immersion for three separate batches of ThO_2 obtained after different pretreatments. All were sealed in capsules after outgassing for 24 hr at $\sim 1 \times 10^{-5}$ mm Hg. Some of the specimens were given the "standard" outgassing, some were soaked in water or ammonium hydroxide solution prior to outgassing, and some were protected by a liquid-nitrogen-cooled trap during outgassing.

The data shown in Table 9.1 reveal that no combination of these treatments had a real effect on the heat of immersion of ThO_2. We conclude that pretreatment with water or NH_4OH may be used, if necessary, and that special protection of the surface during outgassing at 500°C is time consuming and unnecessary.

Effect of Mechanical Pretreatment. – Some of the thorium dioxide preparations contained much agglomerated material. In an effort to ensure homogeneous sampling, various modes of mechanical agitation were employed to break up the agglomerates. About 100-g samples of ORNL DT 102W

[1] C. H. Secoy and H. F. Holmes, *Reactor Chem. Div. Ann. Progr. Rept. Jan. 31, 1963*, ORNL-3417, pp. 124–29.

[2] C. M. Hollabaugh and J. J. Chessick, *J. Phys. Chem.* **65**, 109 (1961).

[3] J. J. Chessick, *J. Phys. Chem.* **66**, 762 (1962).

[4] L. G. Tensmeyer and M. E. Wadsworth, *Quantitative Determination of Adsorbed Sulfates on Thoria by Means of Infrared Spectroscopy*, Technical Report No. III, University of Utah, 1959.

[5] G. J. Young, *et al.*, *J. Phys. Chem.* **58**, 313 (1954).

Table 9.1. Heat of Immersion of ThO_2 in H_2O at 25°C

Protection and Pretreatment			Heat of Immersion (ergs/cm^2)		
Soaked	N_2 Trap	O_2 Added	650°C[a]	800°C[a]	1200°C[a]
No	No	No	1117 ± 18	1091 ± 24	556 ± 8
No	Yes	No	1146	1060	557
No	Yes	Yes	1126	1051	551
In H_2O	No	No	1145, 1117	1095	
In NH_4OH	No	No	1074, 1120	1070	

[a]Original firing temperature.

ThO_2 (prepared by calcining thorium oxalate at 650°C) were placed in 1-liter bottles and subjected to the following treatment. Sample *A* was rotated end-over-end for 6 hr at 57 rpm in a Pyrex bottle; samples *B* and *C* likewise rotated for 12 and 24 hr, respectively, in polyethylene bottles; and sample *D* was placed on a commercial paint shaker for 2 hr in a polyethylene bottle. In each case the agglomerates, ranging up to 5 mm, were reduced to a very fine powder. The original material is designated as sample *O* in this discussion.

Portions of the resulting materials were outgassed at 500°C and 10^{-5} mm Hg for 24 hr prior to immersion in the calorimeter. The slow heat evolution for the original material, and similarly prepared samples, was not present in the case of the mechanically pretreated samples. The total immersion heat for each sample as an average of at least three determinations is tabulated in Table 9.2 along with the corresponding specific surface areas as determined by the Analytical Chemistry Division. The heats of immersion are in good agreement for all agitated samples. The average value (1185 ergs/cm^2) corresponds quite closely to the 1117 ergs/cm^2 for the DT 37-100 thorium dioxide[1] even though the latter had a BET specific surface area of only 14.7 m^2/g. The low value for the original material indicates either that the rate of penetration of water into the internal surfaces of the agglomerates is too slow to be detected in the calorimeter or that this portion of the surface is completely unavailable to water.

Effects of Preabsorbed Water. – Heats of immersion of specimens with known quantities of preadsorbed water should give a quantitative measure of variation of adsorption energy with surface coverage and should provide clues as to the origin of the slowly released heat of immersion observed with samples of high specific area outgassed at high temperatures.[1] In addition, heats of immersion of samples previously equilibrated with water vapor at pressures near saturation should give measurements of surface area by the absolute method of Harkins and Jura.[6]

Table 9.2. Heat of Immersion of Mechanically Agitated ThO_2

Sample	q (joules/g)	S (m^2/g)	h_i (ergs/cm^2)
O	29.20	36.3	804
A	39.50	33.1	1193
B	44.26	37.7	1174
C	42.81	35.7	1191
D	41.26	35.1	1175
		Average *A*–*D*	1185 ± 11

Measurements described in this section were made on samples of thorium dioxide (ORNL lot No. DT 37-100, surface area 14.7 m^2/g by BET nitrogen adsorption) which had been prepared from the oxalate by calcination at 650°C. All samples were outgassed for 24 hr at 500°C and then, without exposure to the laboratory atmosphere, were equilibrated at 25.0°C with known pressures of water

[6]W. D. Harkins and G. Jura, *J. Am. Chem. Soc.* **66**, 1362 (1944).

vapor (from degassed saturated salt solutions)[7] for 72 hr (one duplicate was equilibrated for only 24 hr). Sample weights before and after equilibration gave the amount of water adsorbed.

Figure 9.1 shows the adsorption data as a plot of water adsorbed per gram of ThO_2 as a function of relative pressure of water vapor; the curve is a typical type II isotherm showing multilayer adsorption. A BET plot of the first three points of Fig. 9.1 yields, if 10.6 A^2 is the area of an adsorbed water molecule, about 28 m^2/g for the surface area of the specimen. This twofold discrepancy between surface areas by N_2 and by H_2O adsorption is probably because part of the H_2O is chemisorbed while the BET theory is valid only for physical adsorption. [Data in the subsequent section show that not all the adsorbed water is removed by prolonged outgassing at 500°C, even though a constant sample weight is achieved in much less than 24 hr. Wadsworth[8] has shown that infrared spectroscopy fails to detect hydroxyl groups on ThO_2 surfaces only after heating of specimens to 1300°C.] It seems clear that water must be expected to chemisorb on ThO_2 which has been outgassed to 500°C.

Figure 9.2 shows the heats of immersion (per unit area by N_2 adsorption) of these samples as functions of preadsorbed water. The energetic importance of the first water molecules adsorbed is apparent since the heat of immersion at completion of the monolayer (vertical line labeled w_M) has decreased to 28% of the value (1117 $ergs/cm^2$) for "dry" ThO_2. If the film-covered solid actually had a surface area of 14.7 m^2/g it would be thermodynamically impossible for the heat of immersion to fall below the surface energy (118.5 $ergs/cm^2$, labeled h_L in Fig. 9.2) of water at 25°C. It seems obvious that the film-covered solid presents less surface to the immersion liquid, as might be expected of a porous solid whose pores fill at pressures much below the saturation pressure of water vapor. This is one reason why Harkins and Jura restricted their absolute surface area determinations to nonporous crystalline solids.

The heats of immersion of the three samples with less than 118.5 $ergs/cm^2$ were released rapidly; all other samples yielded an appreciable fraction

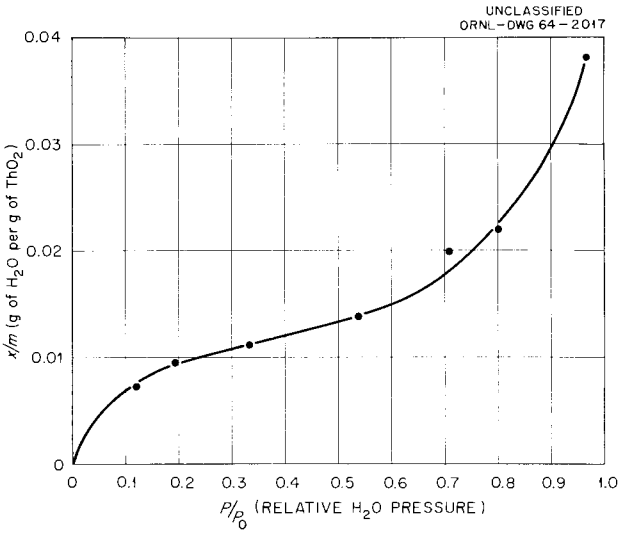

Fig. 9.1. Adsorption of H_2O on ThO_2 at 25°C.

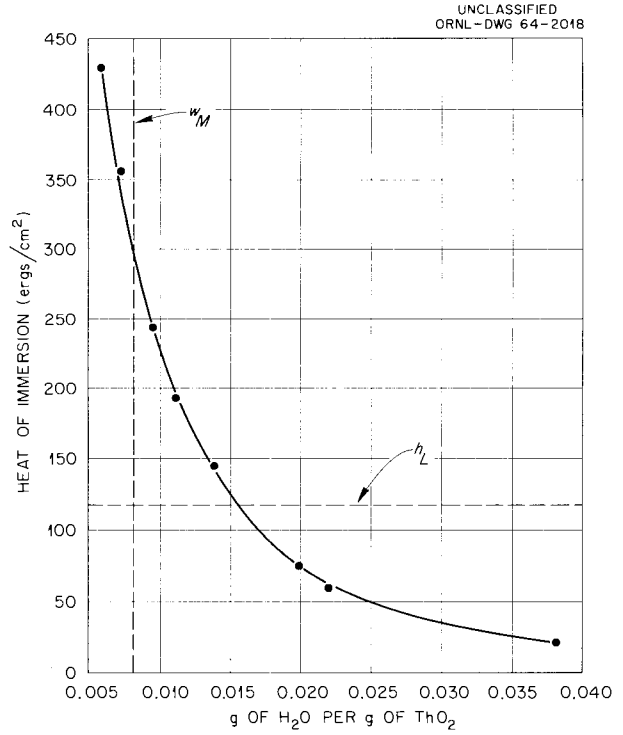

Fig. 9.2. Heat of Immersion of ThO_2 with Preadsorbed H_2O.

[7] A. Wexler and S. Hasegaura, *J. Res. Natl. Bur. Std.* **53**, 19 (1954).

[8] M. E. Wadsworth *et al.*, *The Surface Chemistry of Thoria*, Progress Report, University of Utah, 1959.

of the immersion heat slowly. The fractions of slowly liberated heat were smaller than those from "dry" ThO_2 and decreased with increasing amounts of preadsorbed water. It is generally conceded that chemisorption may be slow while physical adsorption is rapid, but chemisorption (which should be complete during preadsorption at relatively low relative pressures) cannot be responsible for a phenomenon which is observable at relative H_2O pressures as high as 0.538. Most, if not all, of the heat liberated slowly must be due to slow diffusion of water into the pore structure of the ThO_2. This is compatible with the assumption that decrease in effective surface area with increasing quantity of preadsorbed water causes the heats to fall below 118.5 ergs/cm^2.

With the adsorption data one can readily convert the calorimetric data to energy per mole adsorbed. Figure 9.3 is a differential plot of the data as a function of surface coverage. The horizontal lines represent average heats of adsorption over the indicated range. The sharp decrease in energy of adsorption as surface coverage increases in the monolayer region is self-evident. The steepness of the curve and the scarcity of data in the monolayer region introduce a considerable amount of uncertainty in the shape of the curve below a monolayer. An additional factor in the uncertainty is the fact that the surface coverage is based on the sample weight in vacuum at 500°C where the sample still has an unknown amount of chemisorbed water. It should be noted that the quantities in Fig. 9.3 are net heats of adsorption; they differ by the heat of condensation of water (10.5 kcal/mole) from isosteric heats of adsorption calculated from adsorption isotherms at different temperatures.

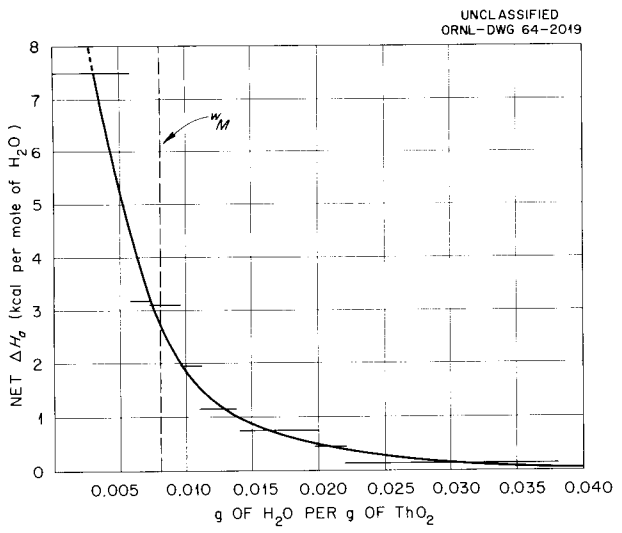

Fig. 9.3. Differential Heat of Adsorption of H_2O on ThO_2 at 25°C.

Water Adsorption by Gravimetric Methods

E. L. Fuller, Jr. H. F. Holmes

Heats of immersion and precisely known adsorption isotherms for the same materials permit calculation of thermodynamic functions of adsorbed molecules as a function of the amount adsorbed and yield valuable information about the state of the adsorbed molecules. Adsorption isotherms at different temperatures provide isosteric heats of adsorption and provide a valuable check on the calorimetric measurements. More quantitative information concerning the state of the surface after outgassing is also needed to provide additional information concerning the extent of chemisorption. The apparatus should be constructed so as to give weight losses during outgassing and the extent of irreversible water adsorption. An apparatus for gravimetric measurement of water adsorption has been constructed to fill these varied needs.

Balance and Associated Apparatus. – A Cahn electromagnetic microbalance (model R.G.) of 1 g capacity and 10^{-7} sensitivity was installed for the gravimetric adsorption studies. A high-input-impedance 1-mv potentiometric recorder kept a continuous record of sample mass on a 10-in. chart. The ring sample pan suspensions on the balance beam were removed and replaced by rigid, hard-waxed hangdown wires (0.001-in. tungsten). With this modified suspension the standard deviation for consecutive weighings of a 500-mg weight was 0.56 μg as compared to 63 μg for the suspensions supplied by the manufacturer. Preliminary investigations indicated a steady, long-term drift of –0.08 μg/hr inherent in the instrument, and independent of the mass on the pans.

The environmental control system is shown schematically in Fig. 9.4. This system permits determination of isotherms from 77.5°K up to the vicinity of room temperature and pretreatments up to 500°C. "Prepurified" nitrogen gas or helium

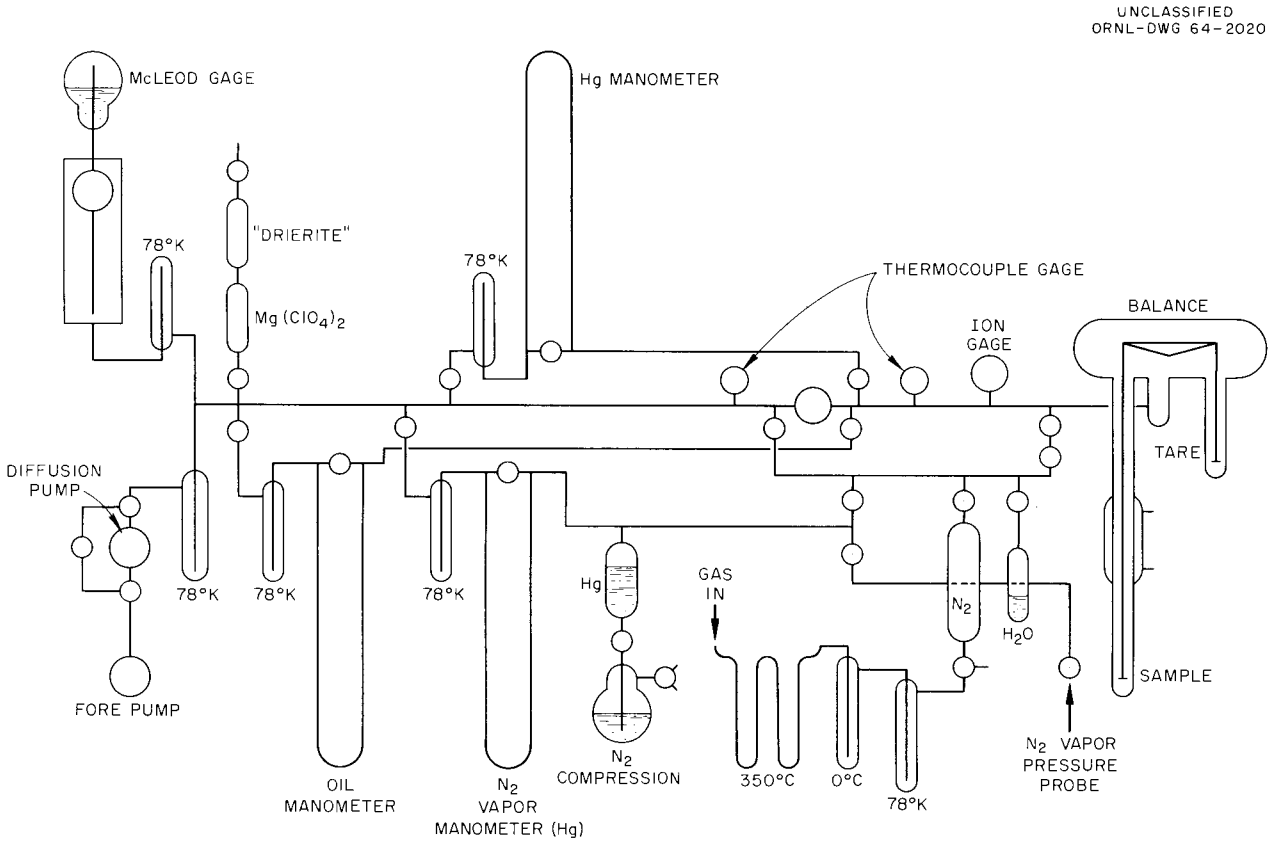

Fig. 9.4. Gravimetric Adsorption System (Schematic).

gas is passed through a purification train consisting of (1) 24 in. of 10-mm Pyrex tubing filled with copper turnings (previously reduced with hydrogen gas) at 350°C, (2) a trap packed with 3-mm Pyrex beads at 0°C, and (3) a similarly packed trap at 78°K (liquid nitrogen). Nitrogen, thus treated, is used to fill the vapor pressure manometric system and for BET surface area determinations. Barium chloride dihydrate is decomposed, after degassing, to supply pure water. An ample supply of this water is condensed in the H_2O reservoir and aliquot portions are extracted as vapor on demand.

The combination of the mechanical fore pump and the oil diffusion pump will evacuate the system to 10^{-6} mm Hg. Pressures in the balance chamber are measured on an ionization gage (10^{-7} to 10^{-3} mm Hg), an oil manometer (up to 45 mm Hg), and a mercury manometer. Two thermocouples measure pressures in the intermediate range (10^{-3} to 1 mm Hg).

Environmental temperatures were maintained around the sample from 20 to 30°C with a mercury-regulated water bath; at 77.5°K with a constant-level liquid-nitrogen bath (stirring effected by bubbling nitrogen gas through the liquid); and at temperatures up to 500°C with a resistance furnace.

The Effect of Thermomolecular Flow. – Before its incorporation into the vacuum system, the balance had been found to give very satisfactory performance in the weighing of samples at room temperature and at atmospheric pressure. After installation in the system it was found that the buoyancy corrections could be accurately calculated from the temperature, pressure, sample and tare volumes, and the known properties of the gas over the entire range of pressures and temperatures being used (0 to 760 mm Hg and 77°K to 500°C). However, it soon became apparent that another effect occurring in the pressure range of approximately 10^{-3} to 10 mm Hg was far more important than any conceivable buoyancy correction; this

effect was ultimately attributed to thermomolecular[9] flow of gases in the balance system.

It has long been known that, in adsorption studies at low pressures with the manometer and sample at different temperatures, a correction must be applied to determine the true pressure in equilibrium with the sample. This has been referred to as thermal transpiration or the thermomolecular pressure effect, and empirical methods based on experimental measurements are available[10] to make the necessary pressure corrections. In the steady state there is no net flow of gas molecules across the temperature gradient. However, the molecules flowing from the hot zone to the cold zone have more kinetic energy, and therefore greater momentum, than the molecules flowing in the opposite direction. It is this momentum difference that causes a real force to be exerted on the sample and/or the suspension wire; this force may, under certain conditions, be equivalent to several milligrams in weight change.

The thermomolecular flow effect was first observed in simulated nitrogen adsorption measurements at 77°K. When a platinum weight and aluminum pan were used in the pressure range 10^{-3} to 2 mm Hg an apparent weight gain was observed; the maximum effect (about 100 μg) occurred at 0.2 mm Hg. Similar behavior with a smaller maximum effect (10 μg) was shown with the empty Pyrex sample pans. Above pressures of 2 mm Hg at 77°K the effect is insignificant (or absent) and calculated buoyancy corrections correctly describe the weight change of a constant mass at varying pressure.

The effect is observable at room temperature where maximum effects are about -20 and -50 μg at 0.01 to 0.02 mm Hg of water vapor and helium respectively. The reproducibility of the effect appears to be ± 2 μg for water vapor; the effect is independent of temperature in the 17 to 32°C range, is independent of the material (glass or platinum) used, and is independent of several other minor parameters tested. The driving force responsible, with the entire system at "constant" temperature, is not clear; it is surmised that the pilot lamp for the null-sensing photocell introduces a temperature gradient along the tare suspension wire and produces the small and reproducible effect.

The effects observed at room temperature and at 77°K are insignificant when compared to those with the sample tube at elevated temperatures. Blank experiments were done with the sample tube at 300 and 500°C using helium and nitrogen with the platinum-weight–aluminum-sample-pan assembly and with the empty Pyrex sample pans. Thermomolecular flow effects as large as 1000 μg were observed. The maximum effect was found to occur at a pressure of approximately 0.2 mm Hg, and only buoyancy effects occurred at pressures larger than 10 mm Hg. Thermomolecular flow effects were largest for the combination of helium and the Pyrex sample pans. Most important, it was found that either a positive or a negative effect could be obtained depending on the location of the temperature gradient. By careful adjustment of the position of the furnace it was possible to reduce the effect to less than 100 μg.

The general temperature and pressure dependence of the thermomolecular flow effect observed in these experiments was the same as that obtained by other workers.[9] However, it should be emphasized that the exact temperature and pressure dependence of the thermomolecular flow effect is specific only for the experimental arrangement under which it was obtained. As an example of this one can estimate from the experimental data at 300°C that, in order to obtain good reproducibility between experiments, the position of the temperature gradient must be reproduced to about 0.01 mm.

These findings emphasized the extreme care which must be exercised in the interpretation of mass measurements made at reduced pressure in a system in which thermal gradients are present. The present system is adequate for accurate adsorption measurements near room temperature, where the estimated uncertainty is only 2 μg. In addition, accurate BET surface area measurements with nitrogen at 77°K can be made because the pressures required are all above the region in which thermomolecular flow occurs. However, the thermomolecular flow effect is a serious obstacle to be overcome before using the present system for adsorption measurements at elevated temperatures. Theoretical attempts to quantitatively evaluate the effect have been entirely inadequate. This is partly due to the difficulty of such treatments, for the maximum effect occurs in the transition region

[9]Most of the pertinent material on the effect of thermomolecular flow can be found in vol. 1 (1960) and vol. 3 (1962) of *Vacuum Microbalance Techniques*, Plenum Press, New York.

[10]S. C. Liang, *J. Appl. Phys.* **22**, 148 (1951).

between a Knudsen gas and an ordinary Boyle gas. Various experimental arrangements minimize the effect, but it has not been eliminated in the present study or by other workers. It appears that the most feasible solution to the problem is to minimize the effect by careful arrangement of the experimental apparatus and then obtain by experiment a correction curve for the optimum geometry.

Results with ThO_2. – A sample of DT 37-100 thorium dioxide (305.742 mg) was placed on the balance and evacuated to constant weight at 25°C. The temperature was then increased to 500°C in steps and the accompanying weight loss was determined. The results are shown in Fig. 9.5 as percentage weight loss. All measurements were made while pumping at pressures from 1 to 2×10^{-5} mm Hg. Sixteen to twenty hours were required for the sample to equilibrate at each temperature. A dark-gray color never previously observed on this specific material prevailed on the upper 2 or 3 mm of the sample, noted when the furnace was removed. The "standard" 24-hr outgassing interval was exceeded in this case (about 82 hr at 500°C).

A conventional nitrogen BET surface area determination[11] was then made on this sample at 77.5°K. The data are given in standard form in Fig. 9.6. The specific surface area, 13.8 m^2/g, is less than the 14.7 m^2/g determined after outgassing for 1 hr by the Analytical Chemistry Division; this discrepancy is probably associated with the coloration.

Further studies are under way to investigate the correlation between the weight losses on heating, the coloration, surface area, and related thermodynamic properties. An extensive gravimetric study of the adsorption of water vapor will be carried out at various temperatures to evaluate the isosteric heats of adsorption and other thermodynamic properties of the surface interaction. Calorimetric measurements will be extended to samples containing lesser amounts of preadsorbed water to complete the present study. Additional investigations are under way to determine pore sizes, particle sizes, and crystallite sizes in the mechanically pretreated samples to enable more complete evaluation of the surface energetics involved in water immersion. It is hoped that a program can be initiated to determine the cause and possible effect of the discoloration of thorium dioxide at high temperature.

[11] D. M. Young and A. D. Crowell, *Physical Adsorption of Gases*, chap. 5, Butterworths, Washington, D.C., 1962.

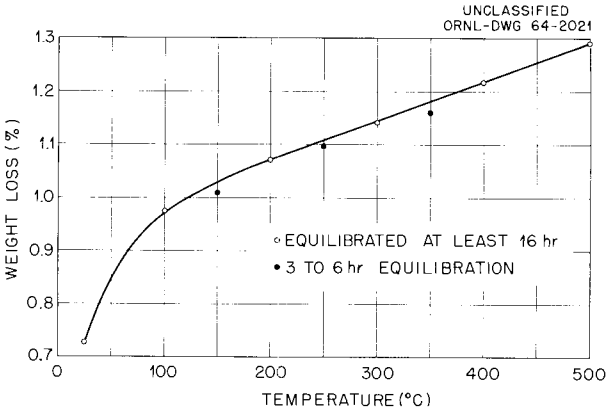

Fig. 9.5. Weight Loss on Heating ThO_2 in Vacuum.

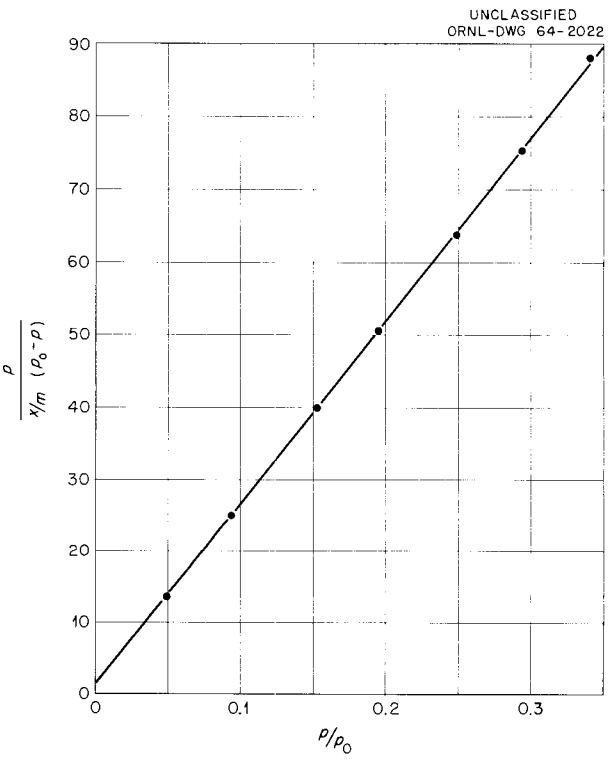

Fig. 9.6. BET Plot for N_2 on DT 37-100 ThO_2.

Electrical Properties of the Thorium Oxide–Water Interface

C. S. Shoup, Jr.

To gain a better understanding of the electrical properties of the thorium oxide–water interface, a

study was made of the conductance of aqueous solutions flowing through ceramic ThO_2 capillaries of known geometry. The specific conductivity of the bulk solution (λ_b) was monitored throughout each experiment and compared to the resistance (R) through the capillary as measured with a Jones bridge. An apparent cell constant (k') for the capillary was determined from the relation $k'/R = \lambda_b$.

Values of k' were found to increase with increasing λ_b, indicating the presence of a significant amount of surface conductance. At sufficiently high electrolyte concentrations, however, k' was observed to be independent of λ_b.

By treating the system as two parallel paths of resistance, the conductance can be expressed as the sum of the surface and bulk conductances:

$$\frac{1}{R} = \frac{\lambda_b}{k'} = \frac{\lambda_b}{k_b} + \frac{\lambda_s}{k_s} ,$$

where k_b is the cell constant for the conductance path through the bulk solution and k_s is a cell constant associated with the specific surface conductivity, λ_s. Thus

$$\frac{k'}{k_b} = \frac{\lambda_b/k_b}{(\lambda_b/k_b) + (\lambda_s/k_s)}$$

and is merely the ratio of the conductance of the bulk solution to the total conductance through the system.

In these experiments, k_b was assumed to have the value measured for k' with solutions of high specific conductivity, λ_b, and was identical to the cell constant determined from the geometry of the capillaries (95 to 144 cm^{-1}). Values of k_b previously determined by conductance measurements with porous plugs of ThO_2 powder ranged from about 5 to 11 cm^{-1}.

In general, the ratio k'/k_b at a given λ_b was found to be the same for all the porous plugs and was independent of the nature of the electrolyte. When an aqueous solution was permitted to flow through a previously dried ThO_2 capillary, however, the resistance through the capillary decreased with time. The resistance found by extrapolating to the start of flow resulted in a value of k' such that the ratio k'/k_b was identical to that observed for the porous plugs at the same specific bulk conductivity. In all cases, k'/k_b was observed to approach unity in a logarithmic manner, and the surface conductance was equal to the conductance through the bulk solution ($k'/k_b = 1/2$) when $\lambda_b \cong 1.7 \times 10^{-6}$ ohm^{-1} cm^{-1}.

A series of measurements were made on a capillary under flowing conditions after the resistance had reached a stable value and the specific conductivity of the bulk solution had become the same on both sides of the capillary. The resulting values of k'/k_b were lower than those obtained by extrapolation to the start of flow, but still approached unity with concentrated solutions.

When a solution which had been flowing through the system was permitted to remain stagnant in the capillary, the conductance was observed to increase substantially. Within a few minutes after flow was resumed, however, the conductance dropped to a reproducibly stable value for each value of λ_b. Repeated washing of the capillary failed to eliminate this phenomenon. Since the history of these capillaries is not fully known, additional ceramic ThO_2 capillaries (with impurities limited to a few ppm) have been obtained for subsequent investigations.

PERMEABILITY OF VIBRATORILY COMPACTED FUELS

M. J. Kelly J. C. Griess

The vibratory compaction of loose oxide fuels into suitably dense systems within fuel rods and the adaptability of the process to remote operation make the technique attractive for fabricating thorium-based fuels. The reported in-reactor failure of a few fuel compacts[12] showed that the mechanism of this type of failure must be adequately understood in order to minimize or eliminate such failures. Presumably these failures were caused by the entrance of water through a cladding defect during zero or low-power operation, followed by expansion of the water upon increasing reactor power, resulting in distortion or gross failure of the fuel element. This phenomenon is known as waterlogging.

The permeability of these fuels is of interest because of its relation to waterlogging. High permeability and low void volume in the compact

[12] J. Belle (ed.), *Uranium Dioxide, Properties and Nuclear Applications*, p. 638, Naval Reactors, Division of Reactor Development, USAEC, 1961.

facilitate the release of water from a waterlogged fuel element during reactor startup. Conversely, if the fuel were impermeable with no accessible void volume, waterlogging could not occur.

Present studies are concerned with the quantitative relation of surface area, theoretical density, and permeability of the fuel to waterlogging susceptibility of Kilorod-type fuel elements.

The measurement of permeability is an easily applied technique consisting of measurement of flow through a porous permeable sample under controlled conditions. The resulting data are reported in the form of a permeability coefficient

$$k = (\text{flow rate}) \frac{(\text{viscosity})}{(\text{area})\,(\text{pressure/length})}$$

for incompressible fluids. Suitable corrections allow for the compressibility of gases as working fluids, but in high-density compacts data points at several pressures must be taken to eliminate slip flow effects.

In the absence of any surface interaction between the fluid and compact, the same calculated coefficient will be obtained if the data are taken in the viscous flow region whether the working fluid is liquid or gas.

To obtain the data reported, experimental permeabilities were obtained for tubular samples of compacted sol-gel oxides by measuring the flow rate of gases (argon and air) and liquids (water, methanol, and benzene) under known pressure gradients at various temperatures. The pressure gradient for liquid flow was provided by regulated air pressure applied to a calibrated pipet containing the liquid which was connected directly to the sample. Flow rate was calculated from the displacement-time plot. Gas flow measurements were taken with the gas pressure as the driving force, and the flow rate calculated from the time required to replace a known liquid volume with the exhausted gas at room pressure. This value was then corrected to the mean pressure within the sample and plotted as shown in Fig. 9.7.

Two sets of samples were prepared by the Metals and Ceramics Division for the experiments reported here. Six samples were sol-gel oxide compacted into $\frac{7}{16}$-in.-OD stainless steel tubes from two sieve fractions with a packed length of ~15 cm. Table 9.3 contains the initial results from these samples.

Five other samples were prepared in 0.43-in.-ID stainless steel tubes which contained a porous sintered filter at one end. These samples had a packed length of ~14 cm and were prepared from various size fractions of sol-gel oxide. Table 9.4 summarizes available data from these samples.

The large differences between liquid and gas permeabilities recorded in Table 9.3 were unexpected; however, later data indicate that probably two mechanisms are responsible.

The fact that the system is heterogenous with mixed size fractions allows many interstitial volumes where packing is not as dense as the bulk density indicates. The fine particles from these volumes are transported by the flowing liquid to nearby crevices where they pack to a higher density and restrict the flow. The result is a smaller value for apparent permeability. This effect is not observed with gas flow since the low-density gas will not provide transport to the fine fractions.

The second mechanism results from the surface properties of the oxide. The highly charged surface and small flow passages cause a streaming potential which appears as a back-pressure phenomenon. This appears as a lower apparent permeability to liquid flow. The low dielectric of gases keeps this effect minimal with gas flow.

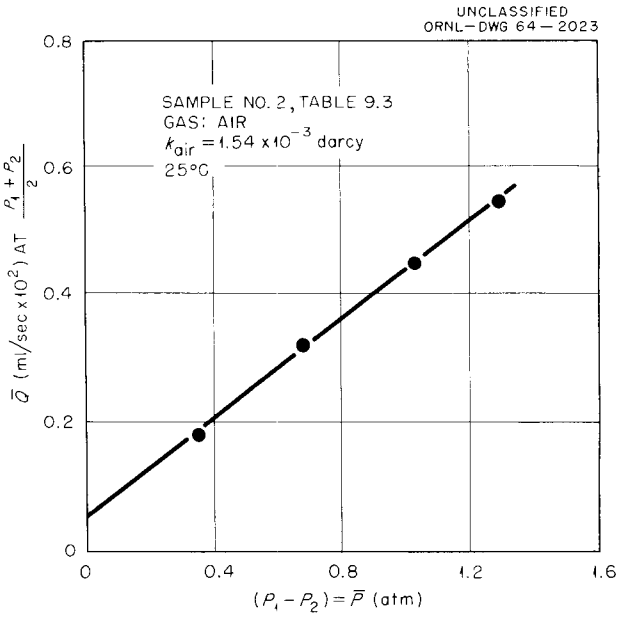

Fig. 9.7. Typical Gas Permeability Data.

Evidence supporting the second mechanism is shown in Table 9.5 and Fig. 9.8. These data were collected in a continuous set; that is, after initial saturation of the compact it remained full of liquid. Water was the initial fluid, followed by methanol and benzene. It was felt that this technique would minimize further transport of the fines after initial saturation. In general these data demonstrate the probability of a surface effect, since the apparent permeability increases with decreasing dielectric strength at constant temperature. The decrease in apparent permeability with temperature may be due to the increased combined specific conductance of the liquid and the surface of the porous medium.

Table 9.3. Observed Permeabilities for Samples of the Same Mixture at Varying Packed Densities

Sample Code[a]	Packed Density[b]	Initial Permeability[c]		Later Values, Water[d]
		Water	Air	
		$\times 10^{-3}$	$\times 10^{-3}$	$\times 10^{-3}$
1	88.3	0.24	1.99	
2	88.0	0.30	1.54	0.62_2
3	88.4	0.46	4.38	0.37_2
4	84.6	0.45	15.8	0.95_2, 1.6_3
5	85.3	0.59	11.7	3.83_2
6[e]	84.6	0.70		

[a] All samples from sol-gel oxide (65%, 6/16 mesh; 35%, −200 mesh).
[b] Percent of theoretical.
[c] Values in darcys (multiply by $\sim 10^{-8}$ for cgs units).
[d] Subscript indicates order.
[e] BET surface area = 0.26 m^2/g; similar measurements not available on other samples.

Table 9.4. Gas Permeabilities for Various Size Fractions and Packed Densities

Sample Code	Packed Density[a]	Gas Permeability (darcys)	Surface Area (BET) (m^2/g)	Size Fraction
A	89.6	2.84×10^{-4}[b]	0.37	45%, 6/16 mesh; 25%, 16/50 mesh; 15%, 50/140 mesh; 15%, −140 mesh
B	90.6	3.82×10^{-4}[b]	0.42	45%, 6/16 mesh; 25%, 16/50 mesh; 15%, 50/140 mesh; 15%, −140 mesh
C	∼87	4.43×10^{-3}[b]	0.28	65%, 6/16 mesh; 35%, −200 mesh
D	82.9	6.5×10^{-2}[c]	*d*	No fines below 325 mesh
E	86.5	5.16×10^{-3}[c]	*d*	No fines below 325 mesh

[a] Percent of theoretical.
[b] Argon.
[c] Air.
[d] Not yet available.

Table 9.5. Effect of Dielectric Strength and Temperature on Observed Permeability[a]

Fluid	Permeability Observed (darcys)	Dielectric (nominal)	Temperature (°C)
	$\times 10^{-4}$		
Water	6	80	25
Methanol	9	33	24
Benzene	10	3	25
Air	15	1	25
Water	4.5		73
Benzene	7		74

[a]All data from sample No. 2, Table 9.3.

This is suggested by an equation developed by Scheidegger[13] for a simple capillaric model. This evidence is not unequivocal but seems too specific to be entirely fortuitous.

Evidence for the first mechanism is more specific. Gas permeability values are the same for a sample when taken before liquid saturation and after subsequent drying of the sample whether by vacuum drying at 100°C or merely by air drying by passing room-temperature air through the sample. The indicated surface area of the material using the technique of Carman[14] is much lower than the surface area determined by BET (N_2). This may be assumed due to bridging of the larger particles, which makes the fines noncontributors to the gas permeability. The final evidence for fines transport is the inability to reproduce a liquid permeability value on a sample that has been adequately dried, although the reproducibility is fairly good as long as the sample remains wet.

The evidence for fines transport plus the fact that all samples examined thus far are in the intermediate range of permeability for water indicate that waterlogging upon failure of the cladding would present a problem under reactor conditions. Continuing studies will attempt to derive the quantitative relation between permeability, surface area, and void fraction to waterlogging susceptibility and failure and to develop techniques to minimize such failure.

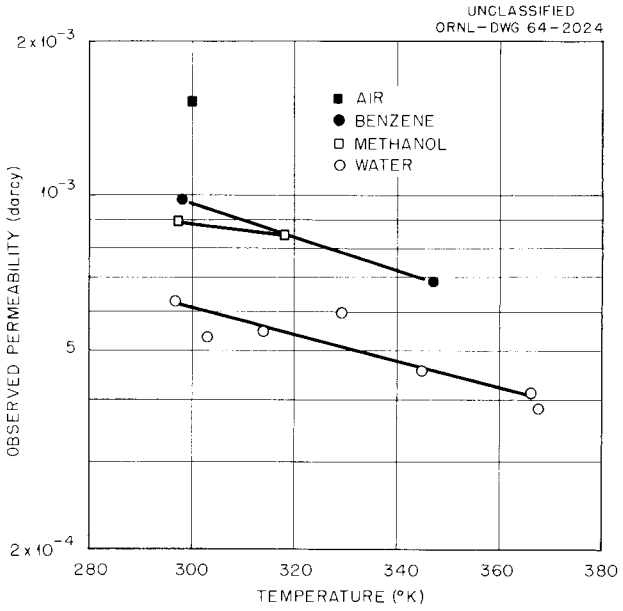

Fig. 9.8. The Effect of Fluid and Temperature on Observed Permeability.

[13]A. E. Scheidegger, *The Physics of Flow Through Porous Media*, p. 191, MacMillan, New York, 1960.

[14]F. C. Carman, *Flow of Gases Through Porous Media*, p. 88, Butterworths, London, 1956.

Part III

Gas-Cooled Reactors

10. Diffusion Processes

TRANSPORT PROPERTIES OF GASES

A. P. Malinauskas E. A. Mason[1]

Studies of the migration of gases through porous media, primarily directed toward understanding the factors which govern fission-gas transport through unclad, gas-cooled nuclear reactors, resulted in the formulation of the "dusty-gas" model in which the medium is described as an agglomeration of giant, immobile, pseudo-gas molecules (dust) that are uniformly distributed within the physical boundaries of the septum.[2] Application of this model to gas transport under a concentration gradient demonstrated its utility, not only under the extreme conditions wherein either the molecular encounters in the gas phase or the corresponding collisions with the solid surfaces are negligible, but also in the mathematically difficult transition region, that is, at pressures at which both types of encounters contribute significantly to the transport characteristics.[2] In its present form, however, the dusty-gas model does not provide for viscous effects, and an extension to include transport under pressure gradients necessitated inclusion of an adjustable parameter (if the pressure drop were taken as an independent variable) in order that the theoretical expressions correctly describe the experimental results.[3,4]

Mathematical complexity restricted a consideration of the effect of thermal gradients to those cases where only a pure gas is involved, that is, to the phenomenon known as thermal transpiration (also called the thermomolecular pressure effect). It is in the description of this effect that the value of the dusty-gas model can perhaps be best appreciated, for the treatment has uncovered a relation, previously unsuspected, between the thermal transpiration effect and the translational component of the thermal conductivity of the gas,[5,6] as well as an explanation of the observed apparent unattainability of the "low-pressure limit."[7]

Thermal Transpiration

Thermal transpiration is the phenomenon in which a net flow of gas molecules is caused by a temperature gradient which is significant over the length of a mean free path.[8] Unlike heat transfer, however, the direction of flow is *from the colder to the warmer region.*

In a closed system, the thermally induced flow causes the gradual formation of a pressure gradient which continues to develop until the counterflow of the gas due to the pressure difference just equals that due to the temperature gradient. It is under this steady-state condition that the thermal transpiration phenomenon is generally studied.

The principal components of the apparatus commonly used to investigate the effect are illustrated in Fig. 10.1. Two volumes, V_1 and V_2, which contain a pure gas at identical pressure, are interconnected by a capillary, c, of small internal cross

[1]Consultant, University of Maryland, Institute for Molecular Physics.

[2]R. B. Evans III, G. M. Watson, and E. A. Mason, *J. Chem. Phys.* **35**, 2076 (1961).

[3]R. B. Evans III, G. M. Watson, and E. A. Mason, *J. Chem. Phys.* **36**, 1894 (1962).

[4]R. B. Evans III, G. M. Watson, and J. Truitt, *J. Appl. Phys.* **34**, 2020 (1963).

[5]E. A. Mason, R. B. Evans III, and G. M. Watson, *J. Chem. Phys.* **38**, 1808 (1963).

[6]E. A. Mason, *J. Chem. Phys.* **39**, 522 (1963).

[7]E. A. Mason and A. P. Malinauskas, *The Effect of Accommodation on Thermal Transpiration*, ORNL-TM-754 (Jan. 6, 1964).

[8]L. B. Loeb, *The Kinetic Theory of Gases*, 3d ed., pp. 353–64, Dover Publications, New York, 1961.

section. A temperature drop, $\Delta T = T_2 - T_1$, is imposed across the gas in such a manner that the transition from T_1 to T_2 lies along the capillary, as shown by the dotted lines which define the temperature regions in the figure. The migration of the gas molecules is monitored by determining the pressures in p_1 and p_2, in V_1 and V_2, respectively, as a function of time, until the steady-state condition is attained. Secondary transpiration effects are minimized, in the event that the pressure-sensing devices are at temperatures other than T_1 and T_2, by connecting the pressure indicators to the respective volumes with tubes having a much larger internal diameter than that of the capillary.

Data obtained in this laboratory for argon with 0.100-mm-ID Pyrex glass capillaries are presented in Fig. 10.2, where the steady-state value of $\Delta p = p_2 - p_1$ is plotted against p_2, the pressure in the warmer region, at two different temperature conditions. The solid lines appearing in the figure were calculated from the dusty-gas model on the basis of the values of T_1 and T_{2c} listed, where T_{2c} represents the temperature in the warmer region after correction for heat losses.

A more detailed description of the thermal transpiration results obtained thus far, as well as the method for the determination of the translational component of the thermal conductivity from transpiration data, is reported elsewhere.[9]

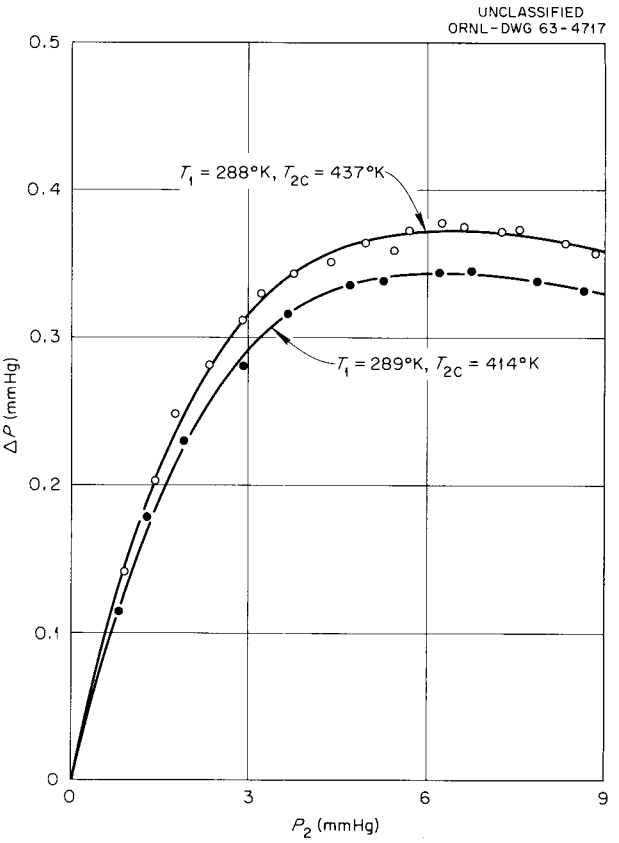

Fig. 10.2. Thermal Transpiration Effect for Argon with 0.100-mm-ID Pyrex Glass Capillaries.

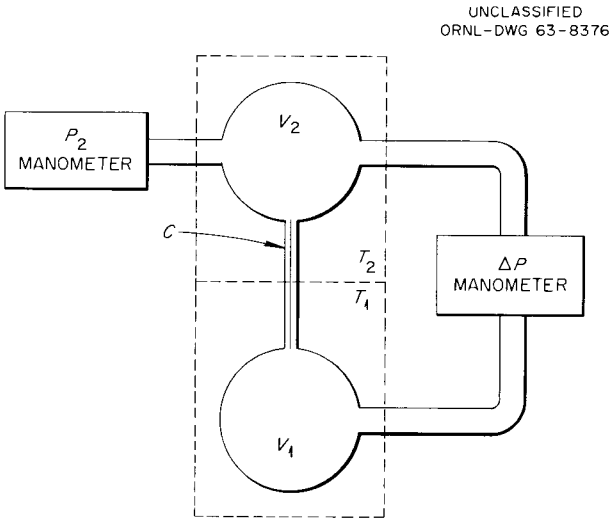

Fig. 10.1. Principal Components of a Thermal Transpiration Apparatus.

Accommodation Effect on Thermal Transpiration[7]

Recent thermal transpiration experiments with capillaries[10,11] indicate that the low-pressure limit of the ratio p_1/p_2 is always larger than the value

$$p_1/p_2 = R_0 = \sqrt{T_1/T_2}\,, \quad T_2 > T_1\,, \qquad (1)$$

predicted by theory. If the gas molecules can exchange energy with the walls during collisions

[9] A. P. Malinauskas, *Results of Preliminary Experiments on Thermal Transpiration*, ORNL-TM-801 (1964).

[10] H. H. Podgurski and F. N. Davis, *J. Phys. Chem.* **65**, 1343 (1961).

[11] J. P. Hobson, T. Edmonds, and R. Verreault, *Can. J. Phys.* **41**, 983 (1963).

in the temperature transition region, however, the dusty-gas model requires that Eq. (1) be replaced by the expression

$$p_1/p_2 = R_0^{(1 + \pi a/8)^{-1}}, \qquad (2)$$

where a is the fraction of gas molecules which undergo inelastic collisions. Thus the low-pressure limit is predicted to lie between the value determined from Eq. (1) ($a = 0$) and the value obtained from the relation ($a = 1$)

$$p_1/p_2 = R_0^{0.718}. \qquad (3)$$

The agreement with experiment is quite satisfactory. Furthermore, both experiment and theory indicate that the transpiration effect is not independent of the capillary length, as is commonly assumed.

Gaseous Diffusion

Gaseous diffusion can be most simply described as the phenomenon in which a nonuniform gaseous mixture, at constant temperature and pressure and in the absence of external forces, tends toward uniformity. The rate at which uniformity is attained, however, is much slower than that which would be expected on the basis of the molecular velocities, primarily because of collisions among *unlike* molecules. The phenomenon therefore provides a tool for the investigation of such intermolecular interactions. For this reason, and because of the dearth of diffusion data in the literature, a systematic study of gaseous diffusion has been initiated.

A prototype stainless steel diffusion cell, operationally similar to an apparatus employed earlier by Ney and Armistead,[12] has been constructed and is pictured in Fig. 10.3. The two 600-cm^3 cylinders are interconnected by a $\frac{1}{8}$-in.-ID tube and are capable of vacuum-tight isolation from each other by a specially designed gating mechanism which is centrally located along the diffusion tube.

[12] E. P. Ney and F. C. Armistead, *Phys. Rev.* **71**, 14 (1947).

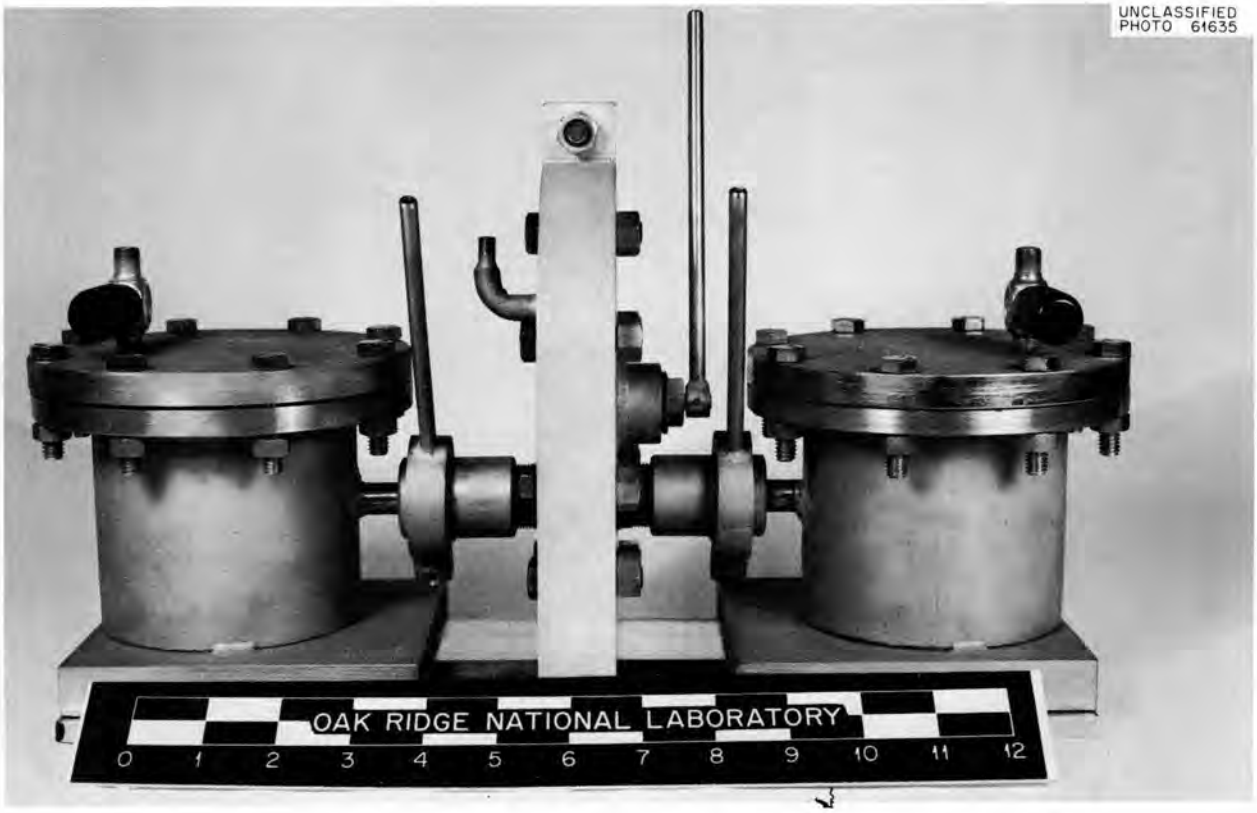

Fig. 10.3. The Prototype Gaseous Diffusion Cell.

In the normal mode of operation, the isolated chambers are filled with gas in such a way that, for a study of the gas pair 1-2, one chamber contains the pure gas 1 and the other, pure gas 2. The pressures in the two half-cells are made equal by momentarily connecting the vessels through a long external capillary, and after isolating both chambers from the peripheral gas-handling lines, the diffusion process is begun by connecting the cell halves through the diffusion tube. The experiment is terminated after a given period of time has elapsed by once again isolating the half-cells and sampling their contents for mass spectrometric (or gas chromatographic) analysis.

The diffusion coefficient for the pair 1-2, D_{12}, is related to the experimentally determined quantities through the expression

$$\log_{10}(x_a^t - x_b^t) = -(\alpha/2.303)(D_{12}p)(t/p) + \log_{10}(x_a^0 - x_b^0), \quad (4)$$

where x_a^t, x_b^t are the mole fractions of one of the two components in chambers a and b, respectively, at time t; x_a^0 and x_b^0 are the corresponding mole fractions at time $t = 0$; $(D_{12}p)$ is a pressure-independent product of the experimental pressure and the diffusion coefficient; and α is a constant characteristic of the apparatus geometry. Because of variations in the cross section of the present diffusion tube, the constant α is more accurately evaluated experimentally, by employing a gas pair whose diffusion coefficient is well known. Thus the system currently under investigation is the pair helium-argon. Experiments have been completed at five temperatures in the range 0 to 80°C and indicate that D_{12} can be determined with a precision of at least ±3%.

Typical diffusion data which have been obtained with the prototype apparatus are presented in Table 10.1. As seen in Eq. (4), the quantity $(\alpha/2.303)(D_{12}p)$, for a given set of experiments, can be averaged in two different ways, that is, either arithmetically or, by plotting $\log_{10}(x_a^t - x_b^t)$ vs t/p, from the slope of the straight line. For example, the arithmetic average of the 60.0°C data of Table 10.1 is 5.865 (±0.086) × 10^{-6} atm/sec, whereas from the slope, by the method of least squares, the average value is given by 5.952 (±0.130) × 10^{-6} atm/sec.

Completion of the calibration program will make it possible to study the diffusion phenomenon for any gas pair over the temperature range 0 to 120°C, provided the gases are compatible with the construction materials and are capable of accurate analysis by either mass spectrometry or gas chromatography.

Table 10.1. Diffusion Data for the System Helium-Argon at 60.0°C

Run	$x_a^{t\,a}$	x_b^t	t (sec)	p (atm)	$(\alpha/2.303)(D_{12}p)$ (atm/sec)
			× 10^4		× 10^{-6}
I-105	0.8184	0.1914	2.1616	0.6351	5.956
I-107	0.8425	0.1607	1.8015	0.6337	5.851
I-108	0.9253	0.0700	0.7213	0.6384	6.007
I-109	0.8557	0.1449	1.6211	0.6355	5.811
I-110	0.8705	0.1357	1.4411	0.6343	5.890
I-111	0.9017	0.1005	1.0801	0.6369	5.676

[a]The mole fractions refer to argon. For all of these experiments, $x_a^0 = 1.0000$ and $x_b^0 = 0.0000$.

DIFFUSION OF REACTOR FUELS IN GRAPHITE SYSTEMS

J. Truitt R. B. Evans III

This report summarizes progress attained in experimental studies of the diffusion of fissile and fertile materials in graphites and pyrolytic carbons. Project applications which have motivated these efforts have been reviewed earlier.[13] This work is being carried out to provide information relative to the development of coated-particle fuels. For a given fuel-graphite system, the experimental determination of two parameters is involved: a driving potential for diffusion, C_0 (g/cm^3), and a diffusion coefficient, D (cm^2/sec). Major attention was focused on the determination of diffusion coefficients, during the last year, with a limited effort devoted to the driving potential.

[13]R. B. Evans III, *Reactor Chem. Div. Ann. Progr. Rept. Jan. 31, 1963*, ORNL-3417, pp. 146–49.

The trace-layer or instantaneous-source experiment employed in the present work is the classical method used for the determination of diffusion coefficients in many solid-state systems. An amount, Q_0 (g/cm^2), of solute (thorium or uranium) is placed on a plane surface of a graphite specimen in a manner such that the solute constitutes a very thin layer. In this study, solutes are imbedded in the specimen surface by an ion-bombardment technique[14] which allows placement of isotopically pure materials. After a diffusion anneal time, t (sec), the solute concentration, C (g/cm^3), at any normal distance, x (cm), away from the original plane is given by the product $C_0 \exp(-u^2)$, where C_0 is $Q_0[\pi(\alpha_0 + Dt)]^{-1/2}$, u is $x(4\alpha_0 + 4Dt)^{-1/2}$, and α_0 (cm^2) is a correction discussed below. After the diffusion has occurred the specimens are exposed to a neutron flux to provide gamma-emitting tracers by which the location of the diffused species can be determined. Total neutron-induced gamma activities are measured as portions of the specimen are ground away. The resulting data are compared with tabulated values of erfc (u) to allow a computation of the coefficients.

Several "blank" experiments (without diffusion) indicated the presence of an initial profile that probably results from experimental difficulties associated with surface preparation and specimen orientation during grinding but not with the bombardment procedure. The α_0 in the equations above accounts for the initial profile.

Typical diffusion results are shown in Fig. 10.4. The data have been generalized, using the α_0 and coefficients, to indicate the degree of agreement with the applicable function. The extreme anisotropy of the pyrolytic carbon required determination of two sets of coefficients, namely $D_{||}$ and $D_\perp$, where the subscript refers to orientation with respect to the basal planes of the material. Three solutes (uranium, protactinium, and thorium) have been employed in the pyrolytic carbon experiments. Results have also been obtained for the diffusion of thorium in both a highly oriented graphite structure with a low defect density and an isotropic porous graphite. The low-defect material was prepared by subjecting pyrolytic carbon to temperatures well above its original deposition temperature.[15]

A majority of the experiments performed to obtain $D_{||}$ for pyrolytic carbon gave results indicative of nonuniform actinide migration, but this effect was expected since all specimens possessed microcracks in the "parallel" direction prior to the

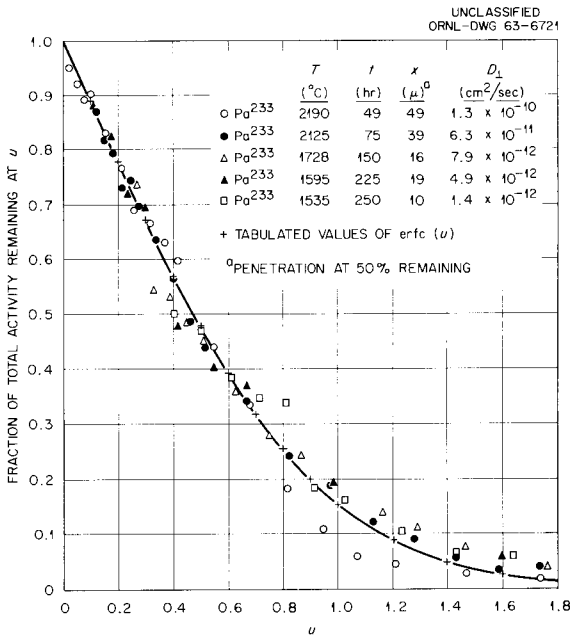

Fig. 10.4. An Example of the Penetration Data on Which Diffusion Coefficients Are Based. The u values incorporate the measured penetrations, time, reported coefficients, and an α_0 of 1.75×10^{-7} cm^2.

experiments. No evidence of actinide diffusion was observed in experiments with low-defect-density graphite. All pyrolytic carbon results that could be correlated with the uniform-diffusion equations mentioned earlier are presented in Fig. 10.5. One may summarize these and other results in the following form. For pyrolytic carbon

$$D_{||} = 1.2 \times 10^{-2} \exp(-60.8/RT) ,$$

$$D_\perp = 3.2 \times 10^{-5} \exp(-60.8/RT) ,$$

and for porous graphite

$$D = 1.5 \times 10^{-3} \exp(-65.4/RT) .$$

Dimensions of D and RT are cm^2/sec and kcal/mole respectively. Coefficients for uranium, protactinium, and thorium are equivalent for a given matrix.

---

[14] J. Truitt, G. D. Alton, and C. M. Blood, *Appl. Phys. Letters* 3(9), 150 (1963).

[15] Excellent reviews of the effects of very high temperatures on the structure and properties of pyrolytic carbons have been given by O. J. Guentert and C. A. Klein, *Appl. Phys. Letters* 2(7), 125 (1963) and by D. B. Fischbach, *Appl. Phys. Letters* 3(9), 125 (1963).

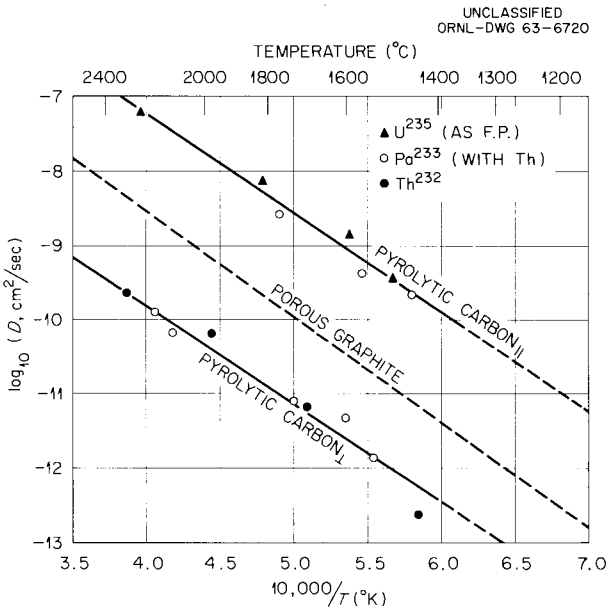

Fig. 10.5. Arrhenius Plot Summarizing the Diffusion Results Obtained Locally for Actinide–Pyrolytic-Carbon Systems.

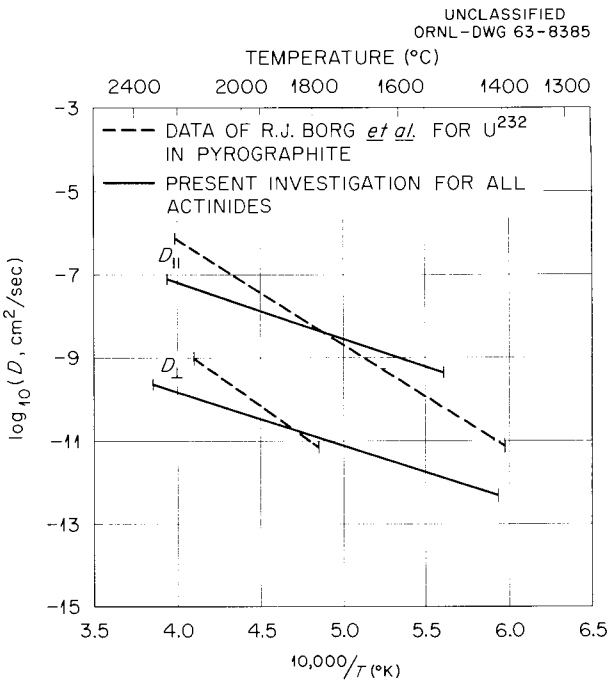

Fig. 10.6. Comparison of All Currently Available Diffusion Coefficients Applicable to Actinide–Pyrolytic-Carbon Systems. The curves are drawn to indicate the range of temperatures covered by the associated experiments.

The value of $D_{\perp}$ with thorium (and $D_{||}$ for nickel)[16] approaches zero in low-defect-density graphite.

Additional results which have been reported by Borg[17] for uranium in a different pyrolytic carbon material[18] are summarized in Fig. 10.6. It should be pointed out that the actinide concentrations employed in Borg's experiments were several orders of magnitude lower than the concentrations employed in the present work. Aside from the differences in actinide concentrations and materials, however, the two sets of experiments (and many of the results) are quite similar. Good agreement is indicated by the $D_{||}/D_{\perp}$ ratios at all temperatures and by the magnitudes of the coefficients around 1800°C. However, Borg's findings[17] and the present work show quite different activation energies (61 vs 120 kcal/mole) for the diffusion process.

Based on observations of the structural differences[19] between as-received pyrolytic carbon and the low-defect-density graphite, as well as dramatic differences in diffusion results, one is forced to conclude (in agreement with Borg) that actinide diffusion in pyrolytic carbons is primarily controlled by defect mechanisms. This conclusion appears to be consistent with the results of earlier investigations of self-diffusion mechanisms in graphite crystals.[20]

[16] J. R. Wolfe and R. J. Borg, *The Self Diffusion of Nickel and Silver in Pyrographite*, UCRL-6828-T (summary only) (1962); these results were presented orally at the Sixth Conference on Carbon, Pittsburgh, June 17–31, 1963 (abstract No. 163).

[17] R. J. Borg, D. R. McKenzie, and J. R. Wolfe, *The Self Diffusion of Uranium in Pyrographite*, UCRL-6827-T (1962); presented orally at the Sixth Conference on Carbon, Pittsburgh, June 17–31, 1963 (abstract No. 159); also summarized in *Trans. Am. Nucl. Soc.* **6**(2), 354 (1963). Although the activation energies reported in refs. 14 and 17 differ considerably the values reported in refs. 14 and 16 are comparable.

[18] The pyrographite used in the Livermore investigations was obtained from the General Electric Corp. The pyrolytic carbon used in the present work was obtained from High Temperature Materials Co., Boston, Mass.

[19] Electron-microscopic studies of the pyrolytic carbons used in the present investigations are being carried out under the supervision of J. O. Stiegler of the Metals and Ceramics Division at ORNL. Companion x-ray determinations have been performed by R. M. Steele and F. L. Carlsen of the same division.

[20] The self-diffusion of C^{14} in graphites has been studied both from the theoretical and experimental standpoints. Results are reported by G. J. Dienes, *J. Appl. Phys.* **23**, 1194 (1952); M. H. Feldman *et al.*, *J. Appl. Phys.* **23**, 1200 (1952); M. A. Kanter, *Phys. Rev.* **107**, 655 (1957).

Additional work is being carried out with renewed emphasis on constant-potential experiments using the same matrices studied in the trace-layer experiments. A uranium C_0 value of 9.2×10^{-3} g/cm^3 has been obtained for the porous graphite at temperatures ranging from 1250 to 1700°C. Similar experiments with the pyrolytic carbon have been initiated.

DIFFUSION IN BERYLLIUM OXIDE MATRICES[21,22]

H. J. de Bruin[23] C. M. Blood

By use of techniques[21,22,24] previously described, self-diffusion coefficients for beryllium in dense (97% of theoretical) polycrystalline BeO have been determined. The empirical equation

$$D = 2.49 \times 10^{-3} \exp\left(-\frac{62.5 \times 10^3}{RT}\right) \text{cm}^2/\text{sec} \quad (1)$$

yields the self-diffusion coefficients over the temperature interval 1100 to 1800°C. A physical model for the movement of beryllium species through the lattice was proposed[21,22] which predicts equal activation energies for the self-diffusion process in all crystallographic directions, but slightly higher frequency factors in the direction perpendicular to the c axis than that parallel to the c axis.

Radiation damage to BeO remains as the most serious obstacle to its use in power reactors. It is an established fact, however, that some of the radiation damage by fast neutrons to the crystal lattice of BeO is subject to recovery by annealing at high temperatures. The annealing process is probably due to self-diffusion of beryllium and of oxygen ions in the lattice to fill the vacancies created by particle collision during irradiation. Accordingly, the self-diffusion studies have been continued in three parts: (1) in-pile measurements to detect the extent to which radiation enhances self-diffusion, (2) out-of-pile measurements performed on preirradiated specimens, and (3) measurement of the effect of lower densities on diffusion rates. The latter investigation was motivated by the fact that radiation lowers the density of the BeO compacts.[25]

Enhancement of Self-Diffusion by Radiation

Figure 10.7 shows a qualitative picture of the effect which neutron irradiation should have on the self-diffusion behavior in beryllium oxide. Radiation causes an increase in defect concentration. Self-diffusion should proceed more rapidly under irradiation in the low-temperature region, and should, at low temperatures, increase with

[21] H. J. de Bruin and G. M. Watson, *Self-Diffusion of Beryllium in Unirradiated Cold-Pressed and Sintered Beryllium Oxide*, ORNL-3526 (December 1963).

[22] H. J. de Bruin and G. M. Watson, *Self-Diffusion of Beryllium in Unirradiated, Cold-Pressed and Sintered BeO*, paper presented at International Conference on Beryllium Oxide, Newport, Sydney, Australia, Oct. 21–25, 1963.

[23] Visiting scientist from the Australian Atomic Energy Commission.

[24] H. J. de Bruin, *Reactor Chem. Div. Ann. Progr. Rept. Jan. 31, 1963*, ORNL-3417, p. 153.

[25] G. W. Keilholtz, *et al.*, *Behavior of BeO Under Neutron Irradiation*, ORNL-TM-742 (December 1963).

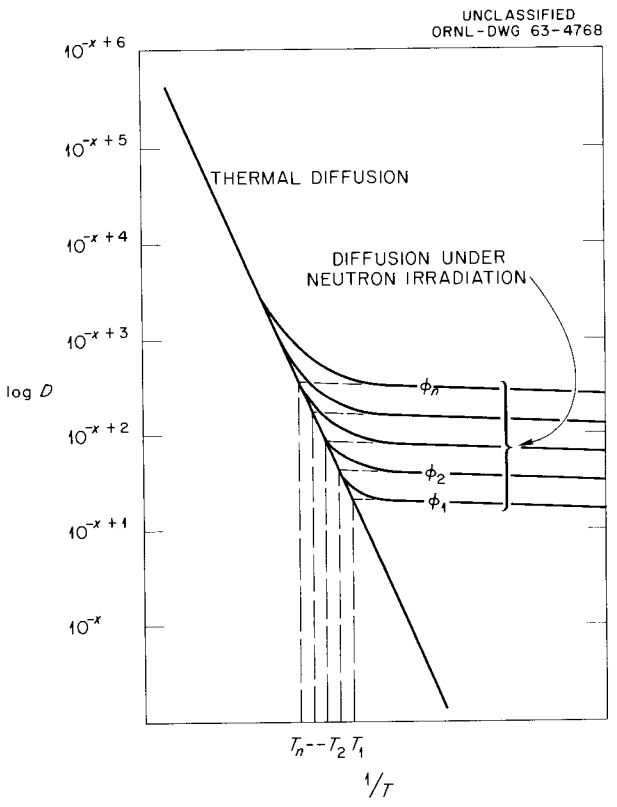

Fig. 10.7. Cation Self-Diffusion in BeO Under Neutron Irradiation.

increase in neutron flux. Self-diffusion behavior in BeO under irradiation should probably exhibit two types of diffusion regimes. At low temperatures, a regime should exist that is essentially independent of temperature and dependent only on the concentration of defects. At high temperatures, the defects anneal so fast that they contribute only to a negligible extent to the diffusion process.

An attempt was made to establish the effect of irradiation at low temperatures by use of a capsule of simple design in the ORNL Low-Intensity Test Reactor. Specimens were irradiated at 700°C and were then analyzed by the methods used previously for unirradiated compacts. A preliminary experiment in which specimens were exposed to a flux of 10^{13} *nv* at 700°C indicated a diffusion coefficient 2 to 3 orders of magnitude above that extrapolated from the data for unirradiated specimens. However, the uncertainties in diffusion measurements at such slow rates are too large to warrant further direct measurements on specimens exposed for short periods. Indirect methods based on measurement of electrical conductivity are now in progress on in-pile specimens. It is hoped that the results will provide calculated values of the self-diffusion coefficients of better accuracy in this region of low diffusivity. Some difficulties have been experienced due to the high resistance of BeO and the extraneous impedance and capacitance effects inherent in the use of high-frequency alternating currents in the circuitry between the control panels and the specimen in the reactor.

Self-Diffusion in Irradiated BeO

Diffusion experiments were carried out on BeO compacts that had been irradiated to different integrated doses of not more than 5.7×10^{19} *nvt* (>1 Mev). The method of analysis is almost identical to that for the unirradiated material except that the depth of penetration of Be^7 was determined by counting the gamma activity in the recovered grindings rather than that remaining in the sample after each lapping. The diffusion coefficient was obtained from the experimental data by plotting the natural logarithm of the ratio of the specific activities at penetration x and at zero penetration vs x^2, the square of the penetration. The slope of the line is equal to $-(\frac{1}{4} Dt_0)$, as shown in Fig. 10.8, which shows the results for pellets irradiated to 5.7×10^{19} *nvt*. These results indicate a significant decrease in activation energy (from 62.5

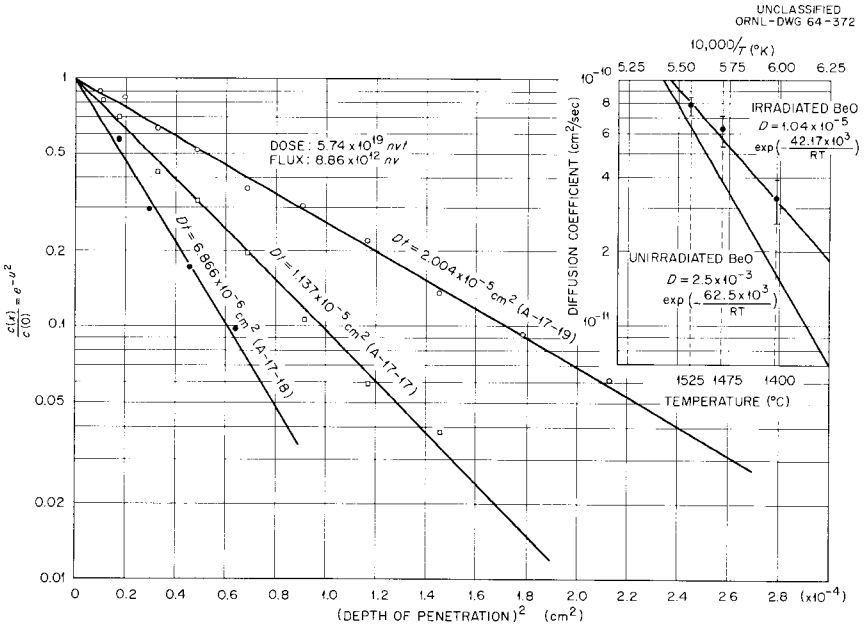

Fig. 10.8. Self-Diffusion in Irradiated BeO.

to 42 kcal/mole) and an increase in diffusion rates. Samples irradiated to only 2×10^{19} *nvt* showed no significant deviation from the diffusion relation for unirradiated material.

Self-Diffusion in Low-Density Compacts. – Since neutron irradiation causes a decrease in density in sintered beryllium compacts, it was deemed necessary to investigate the influence of density on the diffusion behavior, in order to distinguish this effect from those due to radiation-induced changes in microstructure. Compacts were lapped optically flat and contacted with similarly prepared high-density samples, with an activated surface on the optical flat. The samples were annealed under a weight of approximately 200 g. Analysis of the data was the same as for unirradiated high-density specimens.[21,22,24]

The results, shown in Fig. 10.9, indicate that diffusion rates are greatly increased in low-density compacts. The diffusing beryllium species obviously moves much faster along the surfaces of the grains than through the grains as in high-density compacts. An analysis of these data is in progress based on the suggestion that both grain boundary and volume diffusion occur simultaneously to a significant degree. It is possible to calculate a diffusion coefficient D' for the rapid diffusion along the surface of the grains using a method by Levine and McCallum.[26] In this analysis the simple differential diffusion equation is replaced by a two-dimensional equation incorporating two diffusion coefficients, D and D', and the average grain separation δ:

$$\frac{\partial C}{\partial t} - \frac{2D}{\delta}\frac{\partial C}{\partial y} - D'\frac{\partial^2 C}{\partial x^2} = 0 \, . \qquad (2)$$

A solution of Eq. (2) is obtained in terms of dimensionless variables related to x, y, and t. The solution indicates that D', the diffusion coefficient for surface diffusion, is three orders of magnitude larger than D, the volume diffusion coefficient. The activation energy is being measured at present.

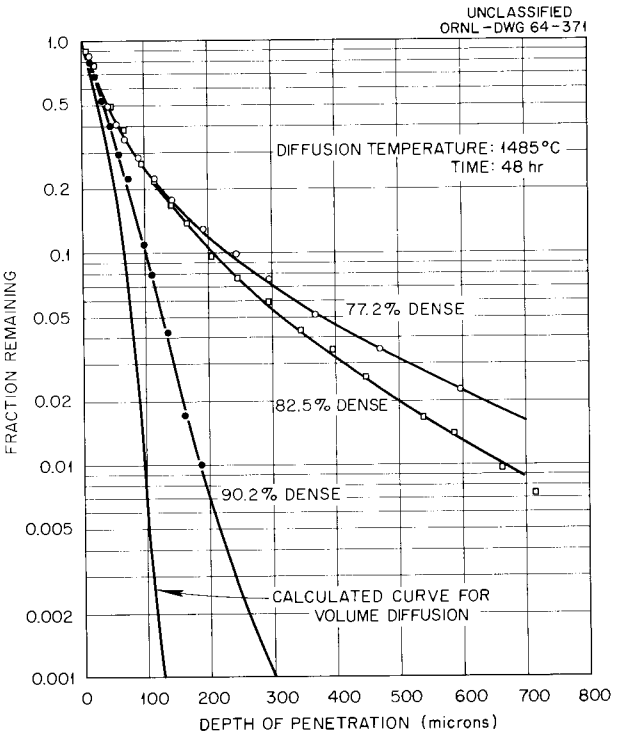

Fig. 10.9. Self-Diffusion in Low-Density Polycrystalline BeO; Effect of Density.

[26] H. S. Levine and C. J. McCallum, *J. Appl. Phys.* 31, 595 (1960).

11. Reactivity of Graphite and of Fueled Graphite Spheres with Oxidizing Gases

L. G. Overholser

Graphite-moderated gas-cooled reactors employing fueled graphite bodies and helium as coolant are being considered in order to obtain higher helium outlet temperatures than are available with metal-clad fuel bodies. One type of fuel element under consideration consists of pyrolytic-carbon-coated fuel particles dispersed in a graphite matrix in the form of a spherical fuel body. The fuel bodies, as well as any other carbonaceous material present in the core, would be slowly attacked by oxidizing impurities (O_2, H_2O, CO_2) present in the helium during prolonged periods of reactor operation. Such attack might lead to serious losses of mechanical strength of the graphite components and might result in an increase of the permeability of the carbon coating designed to contain fission products. High partial pressures of steam resulting from a ruptured tube in a steam generator could cause mechanical failure of the fuel body and failure of the coatings on the fuel particles. Coating failures would produce a rapid release of fission products. The hydrogen resulting from the steam-carbon reaction might be hazardous; a serious explosion could occur if air also were present as would be the case if both the main coolant circuit and the steam generator failed. Experimental studies have been performed to establish reaction rates of graphite with low concentrations of CO_2 and H_2O. The reaction rates of fueled and unfueled graphite spheres with steam at elevated temperatures have also been determined. A brief presentation of the studies is given in the following sections. The work has been described in detail elsewhere.[1]

[1]J. P. Blakely, J. L. Rutherford, and L. G. Overholser, *The Reactivity of Graphite and Fueled Graphite Spheres with Oxidizing Gases*, ORNL-TM-751 (February 1964).

OXIDATION OF GRAPHITE BY LOW CONCENTRATIONS OF WATER VAPOR AND CARBON DIOXIDE IN HELIUM

J. P. Blakely

Experimental studies of the reactivity of a 1-in.-diam sphere of Speer Mod-2 graphite with helium-CO_2 mixtures were continued using the equipment and methods described previously.[2-4] The apparent order of the reaction with respect to the partial pressure of CO_2 was found to be 0.7 at 975°C in the concentration range of 300 to 1650 vpm (parts per million by volume) of CO_2. Reaction rates measured at 60 and 110 vpm of CO_2 indicate an apparent order approaching unity, but the lack of precision at these low concentrations precludes an unequivocal establishment of the apparent order.

The 1-in.-diam sphere of Speer Mod-2 graphite also was used in the studies of the H_2O-graphite reaction employing helium-H_2O mixtures at temperatures from 825 to 1025°C. Reaction rates were obtained from weight changes observed with the same continuously recording balance used for the CO_2-graphite studies, and the effluent gases were analyzed with the Burrell K-7 gas chromatograph. The incoming gases also were analyzed with this instrument for all constituents of interest except H_2O, which was determined by means of a CEC

[2]L. G. Overholser and J. P. Blakely, *Reactor Chem. Div. Ann. Progr. Rept. Jan. 31, 1962*, ORNL-3262, pp. 144–45.

[3]L. G. Overholser, J. P. Blakely, and N. V. Smith, *GCRP Semiann. Progr. Rept. Sept. 30, 1962*, ORNL-3372, pp. 279–81.

[4]J. P. Blakely and N. V. Smith, *Reactor Chem. Div. Ann. Progr. Rept. Jan. 31, 1963*, ORNL-3417, pp. 157–58.

moisture monitor. Flow rates of 125 to 200 cm^3/min at a total pressure of 1 atm were used in a single-pass system.

As is seen in Fig. 11.1, the apparent order of the reaction at 975°C is 0.72 in the H_2O concentration range of 100 to 760 vpm. The apparent order changed below 100 vpm and appeared to be close to unity at 20 vpm, the lowest concentration used. The apparent order of the H_2O-graphite reaction is about the same as that of the CO_2-graphite reaction over most of the range of concentrations studied. Water, however, is about eight times more reactive than CO_2 at 975°C over the concentration ranges where the apparent order of 0.7 prevails. The same graphite specimen was used for both the CO_2 and H_2O studies, thereby providing a reliable comparison of the reactivities at 975°C. Reaction rates determined at other temperatures between 825 and 1025°C using 110 and 460 vpm of H_2O indicate (Fig. 11.1) that the apparent order is not significantly affected by temperature at these H_2O concentrations.

The activation energies determined at H_2O concentrations of 110 and 460 vpm decreased from ~60 to ~40 kcal/mole as the temperature was increased from 825 to 1025°C. The most pronounced changes in slope occurred near 900°C for both concentrations of H_2O used. These decreases of the activation energy indicate that the reaction rates were primarily determined by the chemical reaction at the lower temperatures, but that diffusional effects came into play at the higher temperatures.

Proposed mechanisms[5,6] for the steam-carbon reaction predict apparent orders varying from unity at very low partial pressures of water vapor to zero at high steam pressures. They also predict that the reaction is retarded by hydrogen in such a fashion that a plot of the reciprocal of the reaction rates, obtained at constant temperature and partial pressure of H_2O, vs the hydrogen concentration should be linear. Experiments were run at ~675°C using influent helium containing H_2O concentrations of 110 or 460 vpm and varying concentrations of hydrogen. Figure 11.2 shows that a linear plot resulted at 460 vpm of H_2O at

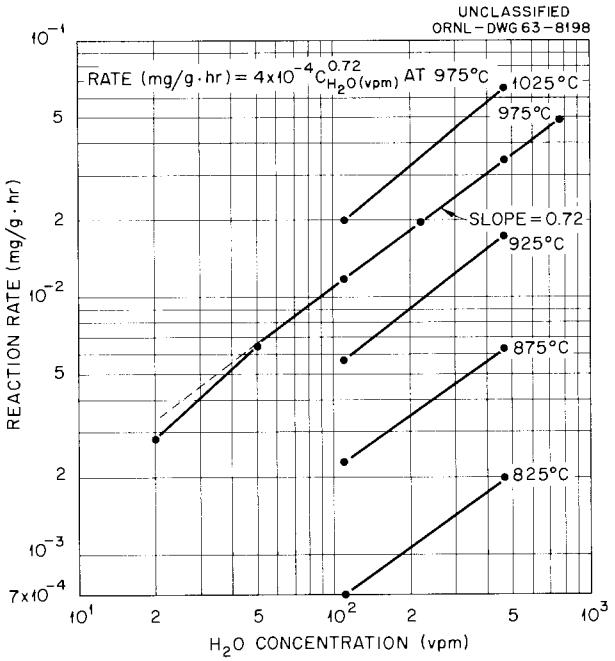

Fig. 11.1. Apparent Order of H_2O-Graphite Reaction (825 to 1025°C).

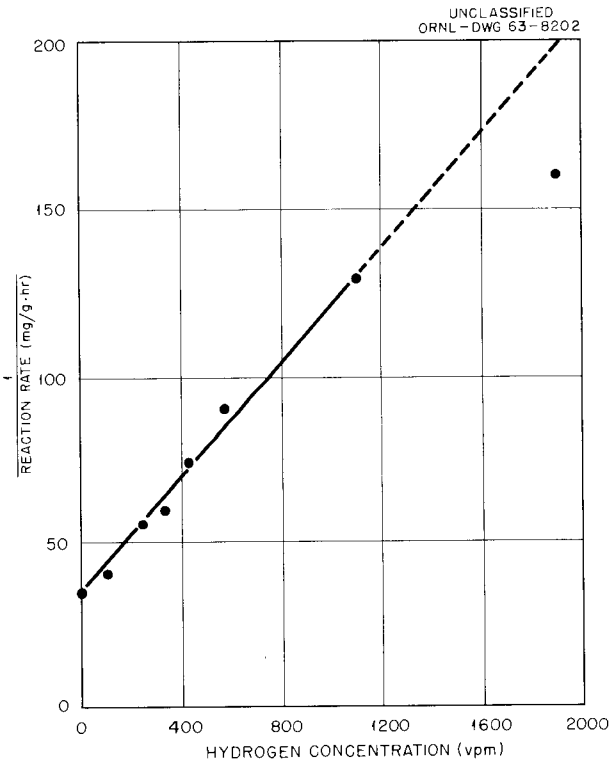

Fig. 11.2. Effect of Hydrogen on the Reciprocal of the Reaction Rate for the H_2O-Graphite Reaction at 970°C (460 vpm of H_2O).

[5] J. Gadsby, C. N. Hinshelwood, and K. W. Sykes, *Proc. Roy. Soc. (London), Ser. A* 187, 129 (1946).

[6] H. F. Johnstone, C. Y. Chen, and D. S. Scott, *Ind. Eng. Chem.* 44, 1564 (1952).

hydrogen concentrations up to 1100 vpm; the results at 110 vpm were indeterminate. Antill and Peakall[7] found that at 1000°C, hydrogen retarded the reaction of PGA graphite with argon containing 300 vpm of H_2O to a larger degree than predicted.

COMPATIBILITY OF FUELED GRAPHITE SPHERES WITH WATER VAPOR

J. P. Blakely J. L. Rutherford

Various lots of 1.5-in.-diam fueled graphite spheres prepared by General Atomic Division of General Dynamics Corporation, Minnesota Mining and Manufacturing Company, Speer Carbon Company, and National Carbon Company were exposed to a partial pressure of steam of ~730 mm Hg at 800, 900, and 1000°C. These fueled graphite spheres contained pyrolytic-carbon-coated (U, Th)C_2 particles dispersed in graphite matrices. Some of the lots of fueled graphite spheres had unfueled shells of varying thickness, others carried no unfueled shell. One lot had been impregnated during manufacture. The average rate of reaction of the fuel body with steam was determined from weighings made before and after exposure to steam for a period of 4 to 5 hr, in most cases. The effluent gases were analyzed, and the data were used to establish the rate of hydrogen formation and to provide an alternative method for determining the reaction rates of the graphite body. Similar studies were made using unfueled 1.5-in.-diam spheres of Speer Mod-2 and ATJ grades of graphite, mainly, to provide some basis for comparison of well-graphitized material with the forms of carbon present in the fueled spheres.

The reaction rates increased with increasing burnoff over the entire range (up to ~10%) of burnoff experienced. This change in rate with burnoff makes it more difficult to compare the reactivities of the various spheres, and to establish the effect of temperature on the reaction rate. Activation energies of ~60 kcal/mole were found from 800 to 1000°C for both the fueled and unfueled graphite spheres. Data given in Fig. 11.3 show that the reaction rates ranged from 1 to 5 mg g^{-1} hr^{-1} at 900°C for the various fueled spheres, excluding a value of ~0.2 found for the impregnated lot (GA-S5-11). The presence or absence of an unfueled shell had no significant effect on the reactivity. The ATJ graphite spheres were about twice as reactive as the Speer Mod-2 graphite spheres. The reaction rate of the latter was ~1 mg g^{-1} hr^{-1} at 900°C.

All lots of the Speer Carbon Company (SCC) fueled graphite spheres were more reactive than any of the other lots examined, and those that were exposed to steam at 1000°C for 1 hr failed. Some of them failed at burnoffs as low as 4%. The cause of these failures at 1000°C is due only in part to the higher reaction rates. Fueled spheres supplied by other manufacturers remained intact

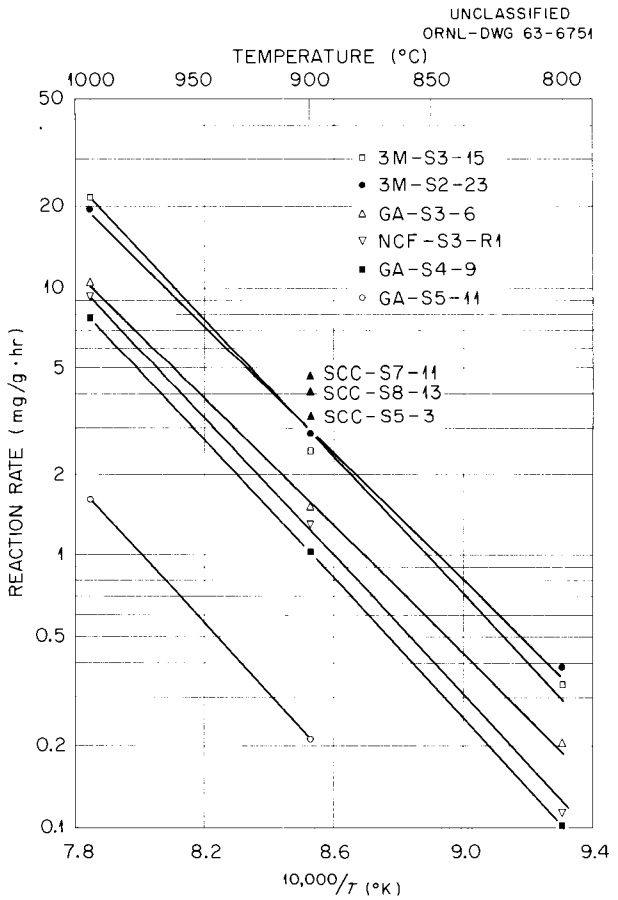

Fig. 11.3. Arrhenius Plots of the Steam Reaction with Various Fueled Graphite Spheres.

[7] J. E. Antill and K. A. Peakall, *J. Nucl. Mater.* 2, 31 (1960).

at comparable or higher burnoffs. This suggests that the attack of the SCC spheres was concentrated more heavily on the residual binder material. Microscopic examination and a nitric acid leach of the coated particles after failure of the spheres showed that no serious attack of the pyrolytic carbon coatings on the fuel particles occurred.

The CO/CO_2 ratios found in the effluent gases varied from 0.1 to 6.1 at 900°C. This ratio increased with increasing degree of burnoff at constant temperature and decreased at comparable burnoffs upon going from 900 to 1000°C. The cause of the variations in the ratios found for the various materials at a constant temperature is not known. If the primary reaction products are assumed to be H_2 and CO, then the production of CO_2 by the reaction $H_2O + CO \rightleftharpoons CO_2 + H_2$ must be catalyzed to varying degrees by the different carbons. The CO/CO_2 ratio found for a single carbon sample changed with degree of burnoff at constant temperature, however, suggesting that some change in its catalytic activity may have occurred during oxidation. The variable CO/CO_2 ratio also could be accounted for by the appearance of CO_2 along with CO as a primary reaction product. Again, no satisfactory explanation is possible for the appearance of various amounts of CO and CO_2 as primary products. The CO/CO_2 ratio is of interest if the amount of hydrogen produced per unit of carbon is being considered. Irrespective of the mechanism, the volume of hydrogen found per unit of carbon reacted will increase as the CO/CO_2 ratio decreases.

12. Irradiation Behavior of High-Temperature Fuel Materials

O. Sisman J. G. Morgan

INTRODUCTION

A rather large effort in the Gas-Cooled Reactor (GCR) Project is devoted to the development of fuel elements for the various types of gas-cooled reactors. The evaluation of the behavior of fuel material and fuel elements under irradiation is a cooperative effort of three divisions of the Laboratory. The characterization studies and preirradiation testing are performed by the Metals and Ceramics Division. Fuel-element design studies and the irradiation experiments are conducted by the Reactor Division. The postirradiation examination and radiation damage evaluation, reported here, are the responsibility of the Reactor Chemistry Division. These studies are reported in detail in the semiannual progress reports of the GCR Project, and in topical reports which are cited as references.

RADIATION EFFECTS IN PYROLYTIC-CARBON-COATED CARBIDE FUEL PARTICLES[1]

P. E. Reagan R. M. Carroll
T. W. Fulton M. T. Morgan
M. F. Osborne E. L. Long, Jr.[2]

Fission Gas Release During Irradiation

The study of fission gas release from pyrolytic-carbon-coated uranium carbide particles during irradiation[3] has been extended to higher temperatures and new materials. Of the three types of pyrolytic carbon coatings originally studied, the duplex-type coatings retained fission gas better than the laminar or columnar type coatings. Because the duplex-type coatings showed better fission gas retention at temperatures up to 1750°F and up to 26 at. % uranium burnup,[4] fission gas release rates from these particles were studied at temperatures up to 2500°F. Also, fission gas release rates from triplex-type pyrolytic-carbon-coated uranium carbide and uranium-thorium carbide particles were measured at 2500°F. The triplex-type pyrolytic carbon coatings are similar to the duplex type in that each consists of a porous graphite inner layer, a laminar intermediate layer, and a columnar outer layer. In the triplex-type coatings, the inner graphite layer is much thicker than the duplex-type inner layer. The triplex-type coated particles have a polyhedral shape and a smooth surface, while the duplex-type are more nearly round and have a more irregular surface. Sectioned views of both types of particles are shown in Fig. 12.1. Physical data for particles contained in each test capsule are given in Table 12.1.

Experiment B9-10, which contained 1590 pyrolytic-carbon-coated uranium carbide particles of the duplex type, was irradiated at 2100°F to 2.6 at. % uranium burnup. This burnup was reached in a short time at a high neutron flux (1×10^{14} *nv*), and

[1]P. E. Reagan *et al.*, "Fission Gas Release from Pyrolytic Carbon Coated Fuel Particles During Irradiation," *Nucl. Sci. Eng.* (February 1964); "Fission Gas Release from Coated Particles at High Temperatures," in preparation.

[2]Metals and Ceramics Division.

[3]P. E. Reagan, R. M. Carroll, and T. W. Fulton, *Reactor Chem. Div. Ann. Progr. Rept. Jan. 31, 1963*, ORNL-3417, pp. 210–13.

[4]P. E. Reagan, R. M. Carroll, and T. W. Fulton, *GCRP Semiann. Progr. Rept. Mar. 31, 1963*, ORNL-3445, pp. 142–51.

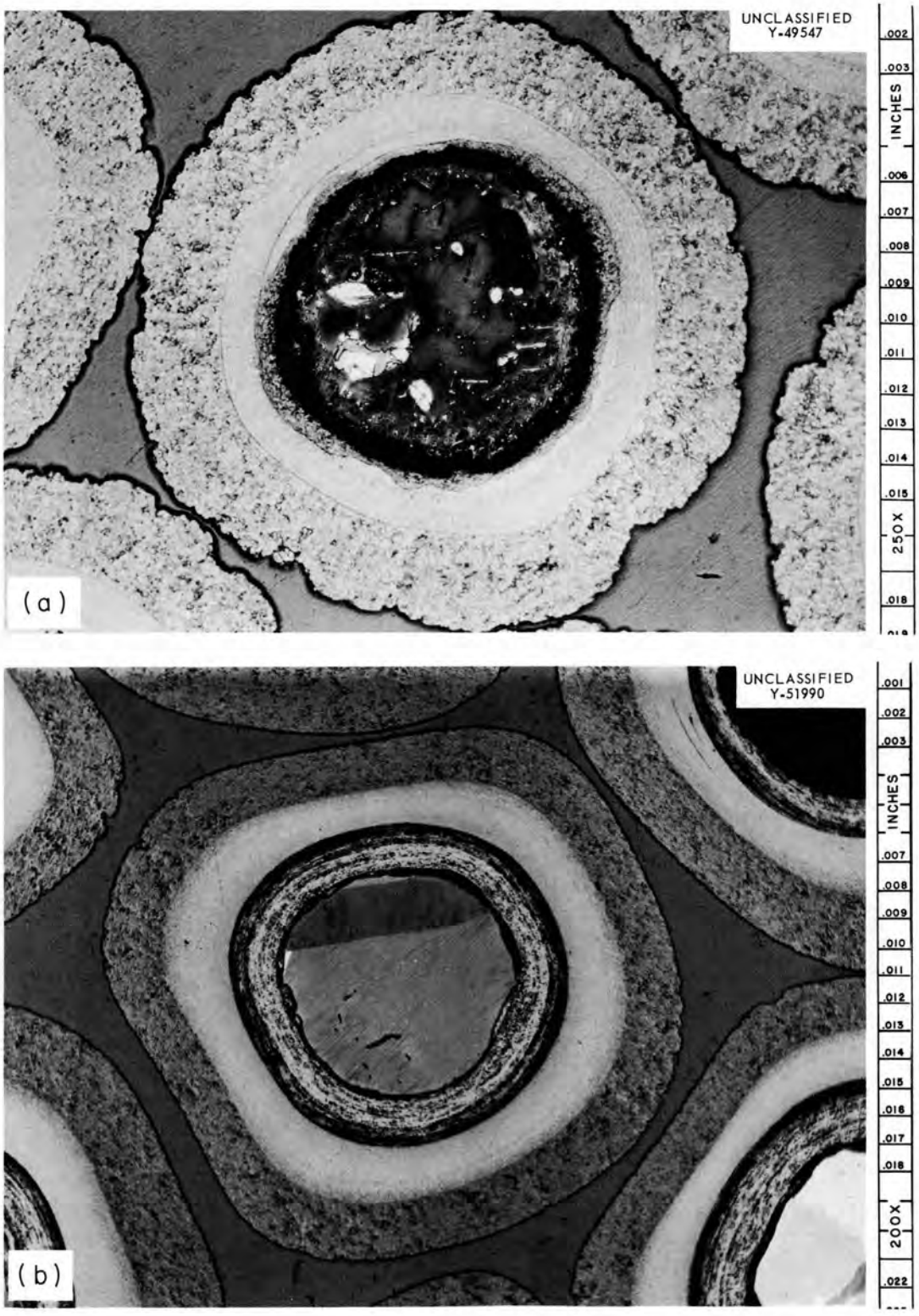

Fig. 12.1. Unirradiated Pyrolytic-Carbon-Coated Uranium Carbide Particles, Sectioned View. (*a*) Duplex type; (*b*) triplex type. Reduced 14%.

the Xe^{133} isotope did not reach production-decay equilibrium. The duration of this test was limited by thermocouple failures. The fission gas release data for this and the following high-temperature experiments are given in Table 12.2.

Experiment B9-11, which contained 1750 duplex-type pyrolytic-carbon-coated particles, was irradiated at 2050°F to 10 at. % heavy metal burnup. The cores of these particles were uranium-thorium carbide. These particles showed excellent fission gas retention properties.

Experiment B9-12, which contained 4700 duplex-type particles with uranium-thorium carbide cores, was irradiated at 2150 to 2300°F. After four days of irradiation at 2150°F, the temperature was increased to 2300°F and the fission gas release rate increased by a factor of 100. The temperature was decreased to 2150°F, but the fission gas release rates continued to increase and the experiment was terminated because of the high fission gas release.

Experiment C1-11, which contained 1200 triplex-type pyrolytic-carbon-coated uranium-thorium carbide particles, was irradiated at 2050°F to 10 at. % heavy metal burnup, after which the particles were subjected to a number of temperature cycles from 1700 to 2050°F. The fission gas release was found to be temperature-dependent, but no bursts of radioactive gas were released. The temperature

Table 12.1. Description of Pyrolytic-Carbon-Coated Uranium Carbide Particles

Experiment Number	Coating Type	Core Material	Thorium to Uranium Ratio	Average Particle Size (μ)	Coating Thickness (μ)
B9-10	Duplex	Uranium carbide		460	80
B9-11	Duplex	Thorium-uranium carbide	0.68: 1.00	460	106
B9-12	Duplex	Thorium-uranium carbide	0.68: 1.00	460	106
B9-13	Triplex	Uranium carbide		540	155
C1-11	Triplex	Thorium-uranium carbide	0.61: 1.00	470	148
B9-14	Triplex	Uranium carbide		377	97

Table 12.2. Fission Gas Release Rate Data

Experiment Number	Temperature (°F)	Heavy-Metal Burnup (at. %)	Fractional Fission Gas Release Rates, R/B				
			Kr^{85m}	Kr^{87}	Kr^{88}	Xe^{133}	Xe^{135}
B9-10	2100	2.6	5.6×10^{-6}	1.86×10^{-6}	2.42×10^{-6}	1.01×10^{-6}	3.42×10^{-6}
B9-11	2050	10.0	1.7×10^{-6}	1.01×10^{-6}	1.3×10^{-6}	2.6×10^{-6}	0.6×10^{-6}
B9-12	2150[a]	<1.0	1.8×10^{-5}	1.0×10^{-5}	1.6×10^{-5}	1.3×10^{-5}	0.9×10^{-5}
	2150[b]	1.7	4.3×10^{-3}	1.7×10^{-3}	1.9×10^{-3}	4.0×10^{-3}	5.4×10^{-3}
C1-11	2050	14.7	4.5×10^{-6}	2.8×10^{-6}	3.6×10^{-6}	2.3×10^{-6}	1.2×10^{-6}
	2400	15.0	1.5×10^{-5}	0.8×10^{-5}	1.1×10^{-5}		
B9-13	2400[a]	8.0	2.8×10^{-5}	2.2×10^{-5}	2.5×10^{-5}	2.4×10^{-5}	1.5×10^{-5}
B9-14	2500	20.6	1.9×10^{-5}	1.5×10^{-5}	1.6×10^{-5}	0.9×10^{-5}	0.4×10^{-5}

[a]Before activity bursts.

[b]Immediately after activity bursts.

was then cycled between 2050 and 2400°F (through the phase transformation) with the same results. A total of 15 at. % heavy metal burnup was reached before the experiment was terminated. The fission gas release rates remained low throughout the test.

Experiment B9-13, which contained 1000 triplex-type coated particles with uranium carbide cores, was irradiated at 2400°F to 8 at. % uranium burnup. During this test, the reactor flux drifted downward and caused the temperature to decrease to 2300°F. When the temperature was again increased to 2400°F, a burst of fission gas was released. The temperature was reduced to 2300°F for 65 hr and the fission gas release rates returned to the previous level. Again the temperature was increased to 2400°F and within 2 hr the activity began increasing in bursts that continued until the activity of the sweep gas reached the safety limit and the experiment was terminated.

Experiment B9-14, which contained 3100 triplex-type coated uranium carbide particles, was irradiated at 2500°F to 20.6 at. % uranium burnup. The final fission gas release rates were about five times as high as from triplex-type particles irradiated at 2050°F. There was a 10% increase in release rates over the irradiation period, but no activity bursts appeared.

The isotopic proportions of the fission gases from the high-temperature irradiations (above 2000°F) are different from those of lower-temperature tests. In previous irradiations, the average fractional release rates, when plotted against half-life, gave a continuous straight line,[5] which had the same slope regardless of the release rate. In those experiments, which were operated at lower temperatures (below 2000°F), the release of fission gas was through breaks in the coatings rather than diffusion through intact coatings. The release rates at high temperature, when plotted against half-life, show the escape of krypton to be about four times as fast as the longer-lived xenon. This indicates that the escape is by diffusion through the coatings rather than through cracked coatings, and that the diffusion of krypton is favored over xenon. This gas, however, is probably not from the UC_2 but from uranium contamination in the coating.

[5]W. O. Harms, F. L. Carlsen, and G. M. Watson, p. 95 in *Proceedings of a Symposium on Ceramic Matrix Fuels Containing Coated Particles, Nov. 5 and 6, 1962*, TID-7654 (June 1963).

Postirradiation Examination

After irradiation, the duplex-type particles were viewed at 30× and examined metallographically. The B9-11 particles (irradiated at 2050°F to 10% burnup) showed no broken or cracked coatings. Wedge-shaped fractures, shown in Fig. 12.2*a*, had begun to develop at the interface, but in no case had the fractures penetrated more than half the laminar inner coating. The B9-10 particles (irradiated to 2.6% burnup at 2100°F) had about 1% broken coatings. A reaction at the core-coating interface resulted in porosity in the laminar coating (Fig. 12.2*b*), and there was evidence of bulk migration of fuel into the laminar coating. Some of the particles from experiment B9-12, which failed and released gas rapidly on brief irradiation at 2300°F, were stuck together by a silver-colored material, and smaller amounts of this silver-colored material could be seen on other particles. A few wedge-shaped fractures were found at the core-coating interface, but there was no evidence of a reaction product in the fuel core.

The triplex coated particles from experiment B9-13 (irradiated to 8% burnup at 2300 to 2400°F) were examined metallographically, and no damaged coatings were evident even though the fission gas release rate at the end of the experiment was so high that it was estimated that as many as 50% of the coatings might be ruptured. There were several cracked uranium carbide cores (Fig. 12.3), but these cracks did not continue into the coatings, and there were no reaction zones at the core-coating interface. It is possible, but it does not seem likely, that the damaged particles remained stuck to the wall of the graphite holder and only the unbroken particles were examined.

It is concluded that pyrolytic-carbon-coated particles can retain fission gases at temperatures up to 2500°F with sufficient integrity to meet present gas-cooled-reactor design criteria. The reaction zones at the core-coating interface do not appear to hamper the ability of the coating to retain fission gases at least up to 20% burnup. Particles can be fabricated to withstand thermal cycles during power production in temperature ranges of 400 to 2500°F; however, it is uncertain as to what happens when the temperature is cycled between 2100 and 2500°F, particularly in the throium-uranium fuels where the material undergoes a phase transformation in this temperature range.

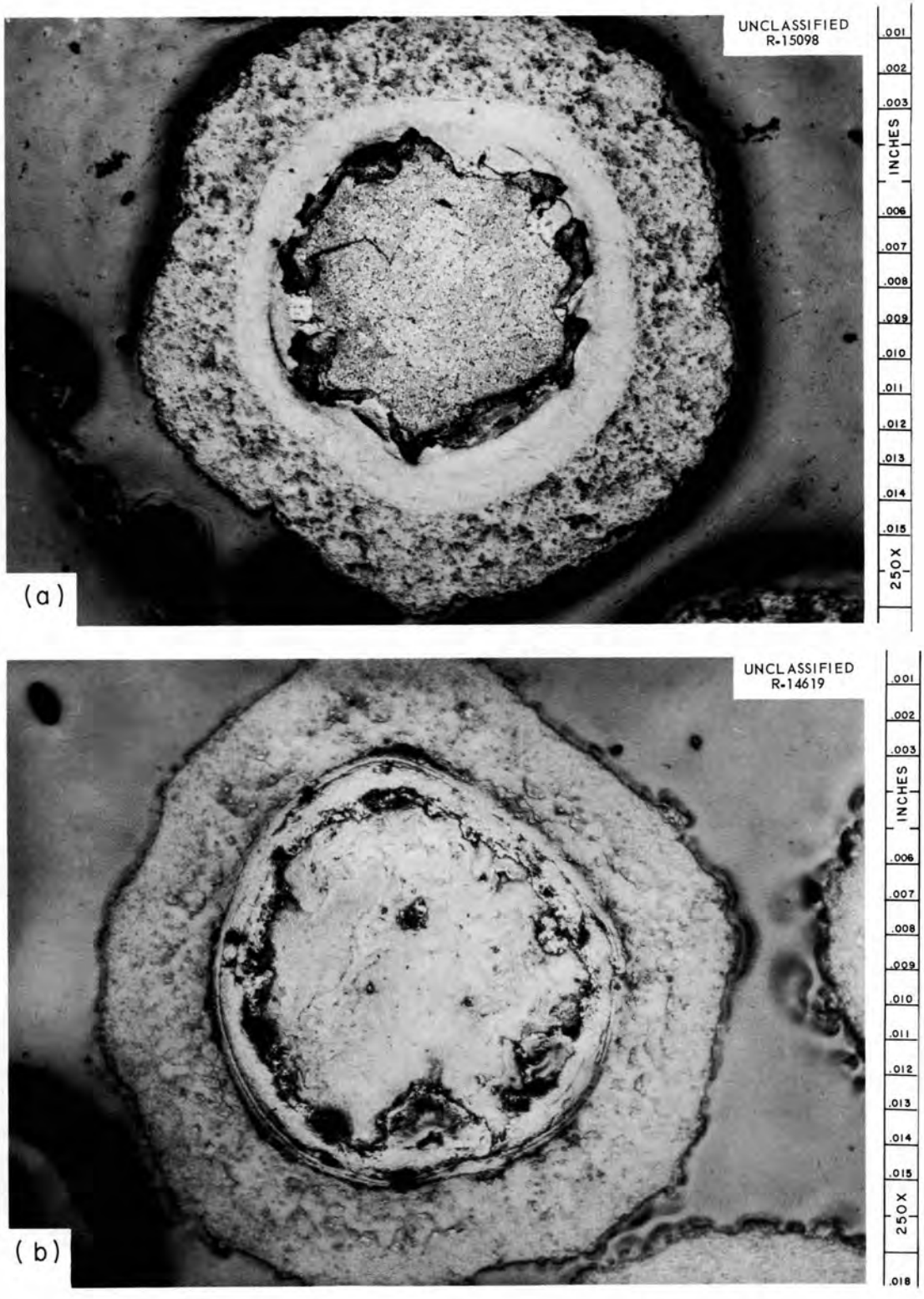

Fig. 12.2. Irradiated Duplex-Type Coated Particles, Sectioned View. (*a*) Wedge-shaped fractures at 10% burnup; (*b*) reaction zone at 2.6% burnup. Reduced 13%.

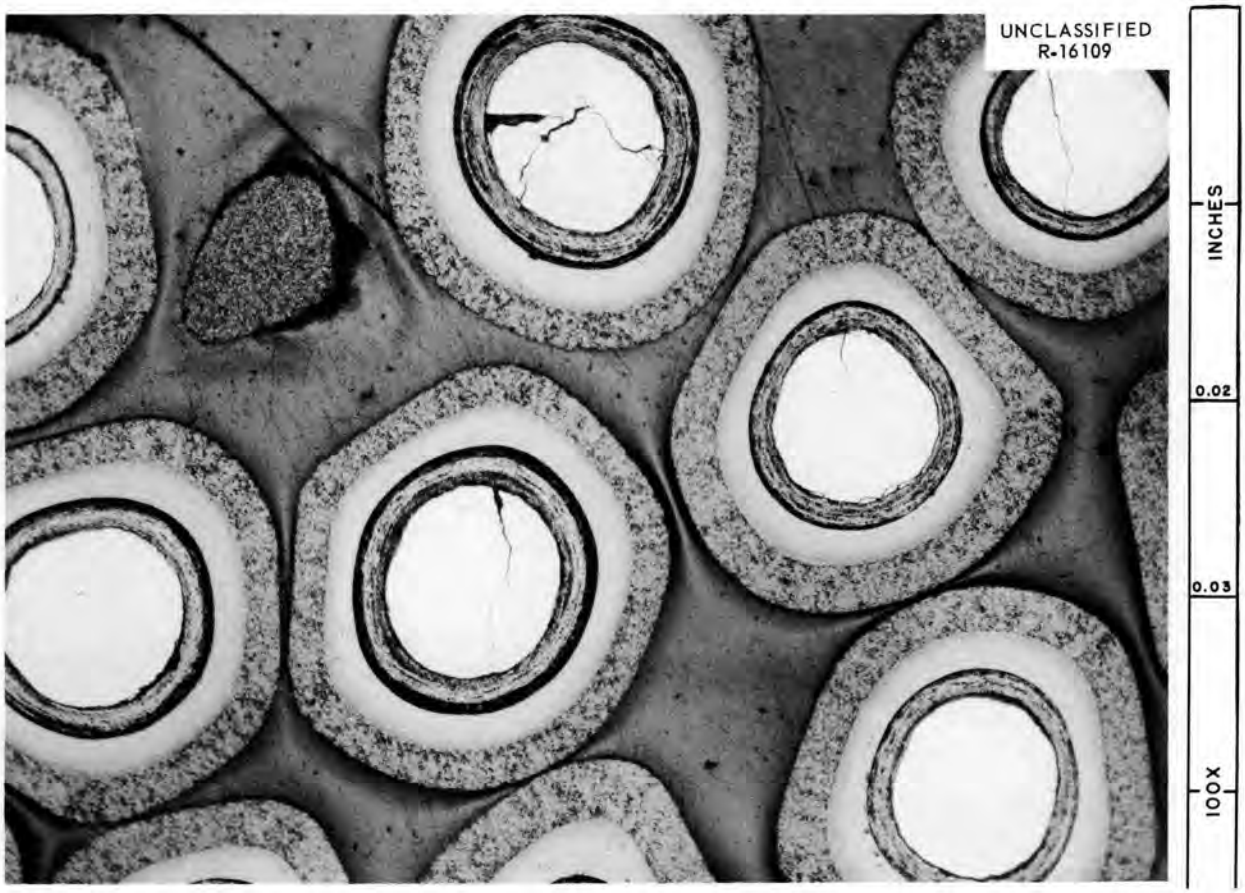

Fig. 12.3. Irradiated Triplex-Type Coated Particles, Showing Cracks in the Cores.

Postirradiation Heating. – Six particles were carefully selected from the B9-13 experiment and given a 15-hr postirradiation anneal at 3800°F. The gas release rate was 60 ppm/hr of the Kr^{85} contained in the particles.[6] Five of the six particles were then burned and found to have contained approximately the amount of Kr^{85} that would be expected in unbroken particles. One hundred particles were annealed at increasing temperatures from 2500 to 3250°F for a total of 58 hr. Most of the fission gas released was released in the initial burst, and it amounted to about 5×10^{-6} of the total Kr^{85} in the particles. The Cs^{137} released in 30 hr at temperatures up to 2750°F was about 10^{-3} of that present.

[6]M. T. Morgan *et al.*, *GCRP Semiann. Progr. Rept. Sept. 30, 1963*, ORNL-3523.

GRAPHITE SPHERES CONTAINING CARBIDE FUEL PARTICLES COATED WITH PYROLYTIC CARBON[7]

M. F. Osborne
H. E. Robertson
A. L. Johnson
J. W. Gooch
D. R. Cuneo
J. G. Morgan
E. L. Long, Jr.[8]

A program is under way to evaluate the irradiation effects on fueled graphite dispersions. The fuel elements, in the form of spheres, contain pyrolytic-carbon-coated particles of UC_2 or $(U,Th)C_2$.

The fuel spheres are irradiated under both static and dynamic gas flow conditions. In the static

[7]J. G. Morgan *et al.*, *Radiation Effects in Graphite Dispersion Fuel Spheres*, in preparation.

[8]Metals and Ceramics Division.

tests, the spheres are stacked in graphite holders with concave hemispherical surfaces that mate with the spheres. The small clearances between the spheres and the holders are filled with fluidized coke. From three to eight spheres, either $1\frac{1}{2}$ in. or 6 cm in diameter, are tested in one capsule. To determine the fission gas release during operating conditions, the upper half of a two-compartment capsule is swept with helium during irradiation, and the helium, which passes over the spheres, is analyzed for radioactive fission gas. The lower half of the capsule is sealed in helium, and is punctured for fission gas analysis after irradiation.

To achieve closer dimensional tolerances, some spheres were machined after fabrication. Since the machining operation leaves broken $(Th,U)C_2$ particles on the surface, the elements are treated with chlorine at 1000°C to remove, as volatile chlorides, any exposed heavy metal.

Another group of molded spheres was made with an unfueled graphite outer shell, whose thickness varied from $\frac{1}{16}$ to $\frac{1}{4}$ in. A third type has a fuel insert in a machined cavity in a graphite sphere; the fuel dispersion is either in the form of a right circular cylinder or a sphere, and the assembly is closed by a threaded plug, sealed with carbon cement.

The temperature was measured during irradiation by thermocouples at the surface of the spheres, and in some instances, a hole was drilled in the sphere to accommodate a central thermocouple. The central hole was treated with chlorine to remove any exposed fuel resulting from the drilling operation. Heat generation during all irradiations was about 45 w per cubic centimeter of fueled matrix.

Dimensional Stability

In a gas-cooled packed-bed reactor,[9] the elements are to be handled pneumatically; therefore, it is necessary that the spheres do not change dimensions during irradiation. Sphere diameters were measured after irradiation at the equator, temperate, and polar regions, and the weight changes were also determined. A data summary of a few typical spheres is given in Table 12.3. In general, there was little or no dimensional change in the spheres after irradiation.

Upon macroscopic examination all spheres appeared sound except the NU-SS3 spheres. The cylindrical insert in these spheres (NU-SS3) contained uncoated carbide particles manufactured by a process unlike that used for all the other dispersions. This insert increased in length (~13%). As a consequence the graphite plug holding the cylinder in its graphite shell was dislodged. Similar dimensional instability had been observed in previous investigations of fuel of this type.[10]

Fission Product Release

The elements in the sweep capsules were swept with helium during irradiation, and samples of the gas were analyzed periodically. Fission gas retention in the static capsules was determined by sampling the gas after irradiation. Except for fuel spheres with machined surfaces (no unfueled shell) and for the NU-SS spheres (which broke), the fission gas retention was quite good. Molded spheres that had no unfueled shell and that had not been machined showed no detectable fission gas release. The Kr^{85} released from some which had been machined or polished was ~0.02%.

Fluidized coke was placed around each sphere to form an expansion cushion between the sphere and its graphite holder as well as to provide a medium for transfer of heat to the holder. After irradiation, the coke powder was analyzed for fission products; in general (Table 12.4), only traces of fission products were found.

Strength

Since the fuel spheres in a PBR packed bed will have to withstand compressive forces, compression tests were made on spheres of the three types after irradiation. In these tests, the force was applied tangentially to the equator. These results are compared with similar tests on unirradiated elements in Table 12.5. Based on the necessarily limited number of measurements, it appears that the compressive strength of the elements did

[9] Staff of Oak Ridge National Laboratory, *Conceptual Design of the Pebble Bed Reactor Experiment*, ORNL-TM-201 (May 7, 1962).

[10] J. G. Morgan and M. F. Osborne, *Irradiation Effects on UC_2 Dispersed in Graphite-Final Report*, ORNL-3340 (Dec. 26, 1962).

Table 12.3. Fueled Sphere Data Summary

Sphere Type	Coated Particle	Surface Temperature (°F)	Heavy Metal Burnup (at. %)	Dimensional Change (%)
No unfueled shell	NCC-208 (duplex)	1500	4	−0.8
	GA-302 (laminar)	1500	4	+0.1
	3M-S4 (laminar)	1550	0.9	−0.15
Unfueled shell				
$\frac{1}{4}$ in. thick	NCC-208 (duplex)	1500	2.4	<0.1
$\frac{1}{4}$ in. thick	GA-302 (laminar)	1200	4	−0.1
$\frac{1}{16}$ in. thick	3M-120 (laminar)	1500	1.3	+0.3
Insert in machined graphite shell				
ZTA graphite	NCC-207 (columnar)	1100	$9(U^{235})$	−0.4
R0020 graphite	NCC-Be (duplex)	1100	$9(U^{235})$	<0.1
Impregnated graphite	NU-SS3 (not coated)	1100	$5(U^{235})$	<0.1

Table 12.4. Fission Product Analysis Results on Fluidized Coke

Sphere Type	Isotope	Percent of Total Generated
No unfueled shell	Sr^{89}	8.7×10^{-5}
	Zr^{95}	4.0×10^{-5}
	Ru^{106}	8.8×10^{-4}
	Cs^{137}	1.0×10^{-4}
	Ba^{140}	1.4×10^{-4}
$\frac{1}{4}$-in. unfueled shell	Sr^{89}	3.2×10^{-5}
	Zr^{95}	1.5×10^{-5}
	Ru^{106}	5.4×10^{-5}
	Cs^{137}	9.2×10^{-5}
	Ba^{140}	8.1×10^{-6}
Cylindrical insert in graphite shell	Sr^{89}	1.1×10^{-5}
	Zr^{95}	6.6×10^{-5}
	Ru^{106}	3.8×10^{-5}
	Cs^{137}	3.8×10^{-3}
	Ba^{140}	1.4×10^{-5}

Table 12.5. Results of Compression Tests on Fueled Spheres

Sphere Type	Compression Breaking Load (lb)	
	Unirradiated	Irradiated
No unfueled shell	1550	1400
	1540	1375
	1825	1500
$\frac{1}{4}$-in. unfueled shell	890	890
	620	625
		560
Cylindrical insert	1450	1350
	1075	1300

not change as a result of the irradiations. The typical modes of fracture for the different fuel configurations were comparable to those in preirradiation tests. The spheres containing fuel dispersed throughout the element and those with an unfueled graphite shell fractured in two or three pieces. Elements that contained fuel as a cylindrical insert and that were sealed with a threaded plug fractured in such a manner as to leave the insert intact.

In a fuel-handling system for a gas-cooled reactor using spherical elements, the spheres would be subjected to impact forces during charging. Some of the irradiated elements were therefore subjected to impact tests in which a 1325-g weight was dropped on the sphere from a height of 2 ft. The choice of weights for testing was based on an approximation of the kinetic energy at impact when charging the spheres into the reactor. After each impact, the spheres were randomly moved to provide a new point of impact. In some cases, failure was found to be gradual until a significant portion of the sphere had been chipped away. In other cases, failure was by fracture into two or three pieces. There was no evidence of a decrease in impact strength as a result of the irradiations.

POSTIRRADIATION EXAMINATION OF EGCR PROTOTYPE FUEL CAPSULES[11]

M. F. Osborne

J. G. Morgan
E. L. Long, Jr.[12]
J. W. Gooch
D. R. Cuneo
H. E. Robertson
A. L. Johnson

The program for proof-testing EGCR prototype fuel is nearing completion. Thirty-six irradiated fuel capsules have been examined (many of these have been described previously),[13–15] and four capsules are still being irradiated.

Each of these capsules simulates the EGCR fuel rods except for length – a 6-in.-long column of sintered UO_2 pellets is contained in a 0.75-in.-OD by 0.020-in.-wall type 304 stainless steel tube (Fig. 12.4). The fuel in all recent ORR capsules was supplied by Westinghouse, and is presumed to be representative of that used in the EGCR fuel elements. Some of the capsules were equipped with interior thermocouples and pressure transducers for direct monitoring of internal temperature and gas pressure during irradiation. In several instances these additional components were directly associated with leakage or failure of the capsule. Fabrication and irradiation data for the capsules discussed here are shown in Table 12.6.

Although most of the EGCR prototype capsules have performed satisfactorily, eight capsules failed during irradiation. These failures have been of three types: (1) a severe cladding fracture, (2) a small cladding leak, which was located by leak testing, and (3) a fracture in a connected component, such as a pressure transducer.

The cladding fracture in capsule E-8 (Fig. 12.5) occurred at the peak of a circumferential ridge in the cladding. This ridge (about 0.025 in. high) was caused by differential expansion and contraction of the fuel and cladding during the many thermal cycles of the 3-yr irradiation period. Although the nature of the fracture was somewhat different from the longitudinal fractures sometimes observed,[14] the causes of the fracture appeared to be

[11]M. F. Osborne *et al.*, "Performance of Prototype EGCR Fuel at Extreme Operating Conditions," submitted for publication to *Nuclear Science and Engineering*.

[12]Metals and Ceramics Division.

[13]J. G. Morgan *et al.*, *GCRP Quart. Progr. Rept. Mar. 31, 1963*, ORNL-3445, pp. 68–74, 87–95.

[14]D. F. Toner *et al.*, *Reactor Chem. Div. Ann. Progr. Rept. Jan. 31, 1963*, ORNL-3417, pp. 189–90, 193–95.

[15]J. G. Morgan, M. F. Osborne, and O. Sisman, "Irradiation Effects in the EGCR Fuel," *Nucl. Sci. Eng.* **14**, 83–100 (1962).

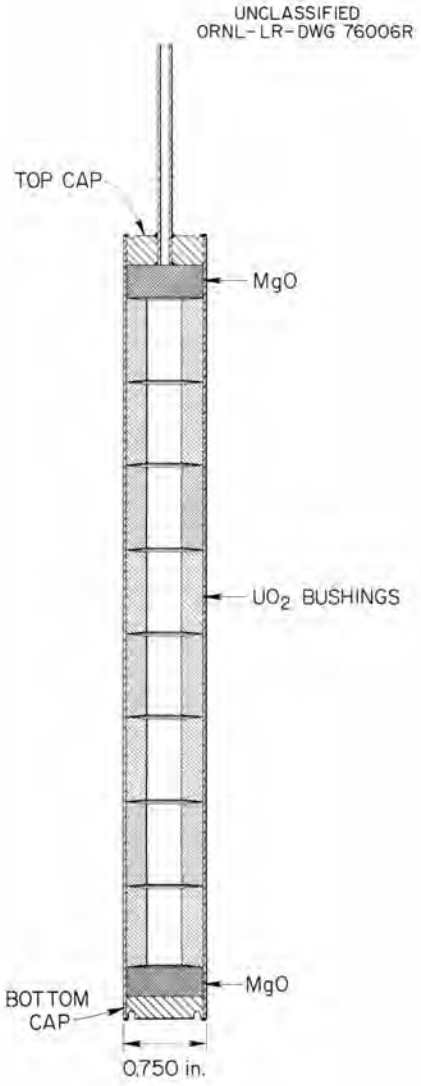

Fig. 12.4. Schematic View of a Typical EGCR Prototype Capsule.

similar. The cladding had suffered nitride embrittlement as a result of the nitride impurity in the fuel, and large stresses caused by exposure of the capsule to power levels well above design conditions were sufficient to cause failure. Metallographic examination of the fracture (Fig. 12.6) revealed an abundance of nitride precipitate and a "case" throughout the inside surface of the cladding and even along the surfaces of the fracture. Similar nitride precipitation and "case" formation have been observed in other capsules, some of which (probably because of lower cladding temperature and lower power generation rate) did not fail but for which the central region was somewhat swollen and oval in cross section.

One capsule suffered a severe cladding fracture; it is still being examined, and the exact cause of the fracture has not been determined. It is apparent that the fuel in this capsule experienced much higher temperatures than had been intended. Large columnar grains had grown from the inside surfaces of the pellets to within about 0.060 in. of the outside surfaces (Fig. 12.7). Such grain growth occurs only in steep thermal gradients at temperatures greater than about 2900°F. An examination of the cladding showed moderate grain growth and considerable void formation, presumably due to the combination of high temperature (~1600°F) and stress.

Three capsules showed leaks in areas where the cladding was depressed through lack of interior support by the UO_2. At operating temperature, the 300-psi external pressure had collapsed the cladding, and the severe stresses at the periphery of these depressions had caused intergranular void formation and grain separation. An example of failure of this type is illustrated by Fig. 12.8. The lack of internal support for the cladding in the three capsules showing this failure mechanism was caused by (1) a chip missing from the corner of a fuel pellet, (2) a groove in the fuel pellets to accommodate a thermocouple, and (3) extensive fracturing and collapse of one Westinghouse fuel

Fig. 12.5. Top End of Capsule E-8, Showing Fracture in Peak of Circumferential Ridge in Cladding. 2.3×.

Table 12.6. Fabrication and Irradiation Data for EGCR Prototype Capsules

Capsule No.	Fuel Manufacturer	Average Cladding Temperature (°F)	Burnup (Mwd per metric ton of UO_2)	Fission Gas Release (% Kr^{85})
E-1A	ORNL	1290	4450	Cladding failure
E-4	ORNL	1320	7300	Cladding failure
E-6	ORNL	1300	9100	14
E-8	ORNL	1500	9100	Cladding failure
01C-4	ORNL	1480	1380	Cladding failure
08B-4	ORNL	1460	1450	Cladding failure
02-5	Westinghouse	1400	1480	Pressure transducer failure
07-5	Westinghouse	1400	1420	Cladding failure
01A-6	Westinghouse	1425	1180	
03-6	Westinghouse	1480	630	0.1
05A-6	Westinghouse	1420	500	0.1
05B-6	Westinghouse	1450	1530	0.1
06A-6	Westinghouse	1415	490	0.1
02A-6	Westinghouse	1550	~5000	Cladding failure

Fig. 12.6. Micrograph of Fracture Region in Cladding of Capsule E-8. Note dark nitride precipitate and "case" in inside surfaces and fracture surfaces of cladding. As polished; 100×.

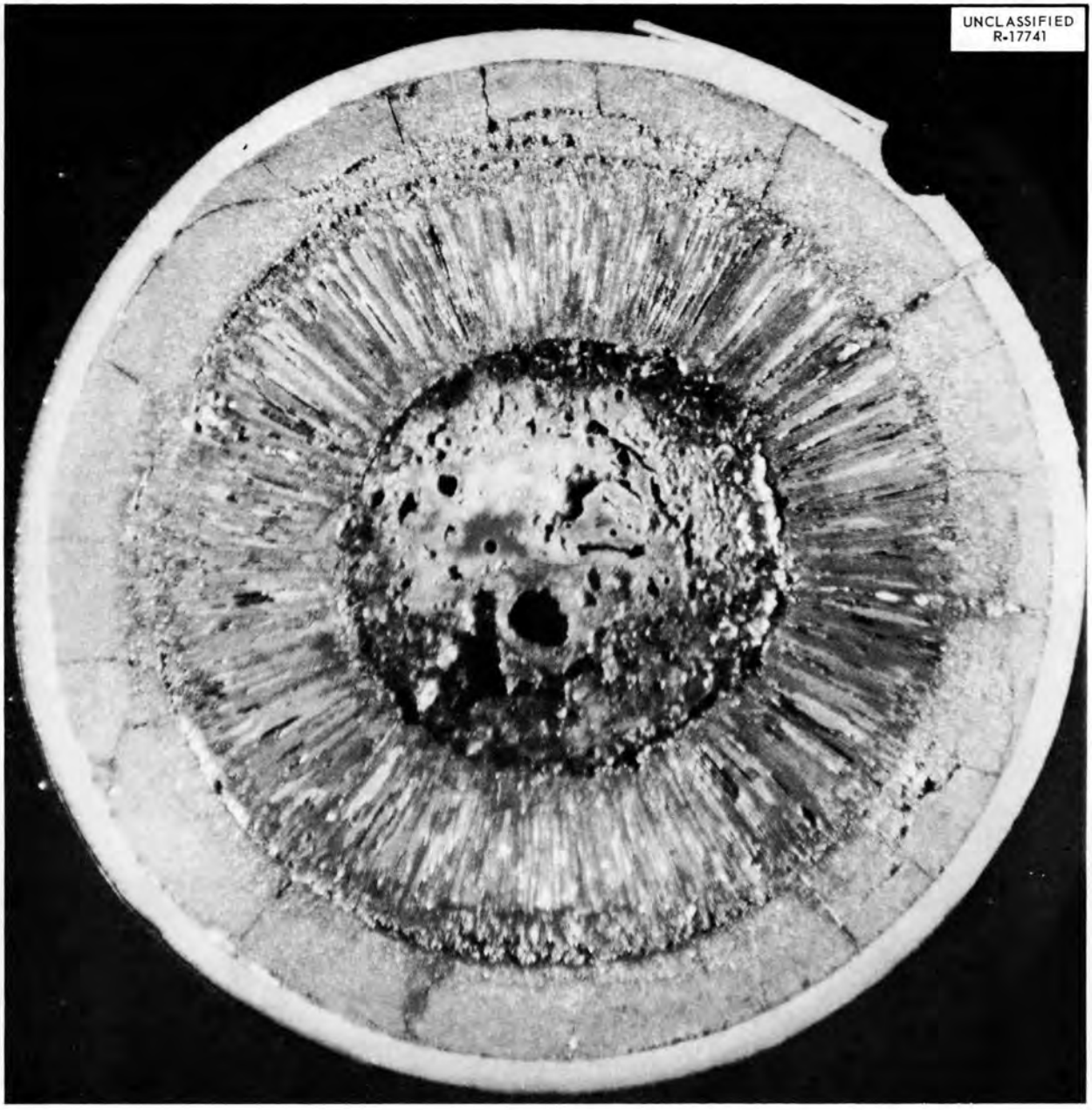

Fig. 12.7. Transverse Section Through Fracture Region of Capsule 02A-6. Note extensive columnar grain growth in fuel.

pellet. Seven other capsules containing Westinghouse "production-run" fuel pellets have been irradiated and examined, and no similar fracturing and collapse have been seen. However, some adverse cladding effects, including several cases of grain growth and intergranular void formation, have been observed in these capsules. The incidence of these adverse effects appeared to diminish after the rate of temperature change of the capsules was confined to no more than 150°F/min.

As shown in Table 12.6, except for capsule E-6 which had excessive nitride in the fuel, the Kr^{85} release for the capsules that did not fail was about 0.1% of that formed. The dimensional changes for unfailed capsules were nominal, the capsules had bowed 0.005 in. to 0.015 in., and the cladding had collapsed against the fuel in most cases.

Each of the failed capsules experienced conditions different from, and much more severe than, those of the EGCR design. With one exception, the unusual condition was directly associated with the capsule failures. Capsule 07-5, which was equipped with a pressure transducer, suffered a cladding failure that apparently was independent of the transducer and connecting capillary tubing. However, the cladding failure in capsule 07-5 was probably influenced by the unrealistically severe thermal cycles, an operating condition which was eliminated in subsequent experiments. The results of this testing program indicate that the EGCR fuel elements should perform satisfactorily under strict adherence to design conditions. However, any departure from these conditions will be potentially dangerous to the integrity of the fuel elements.

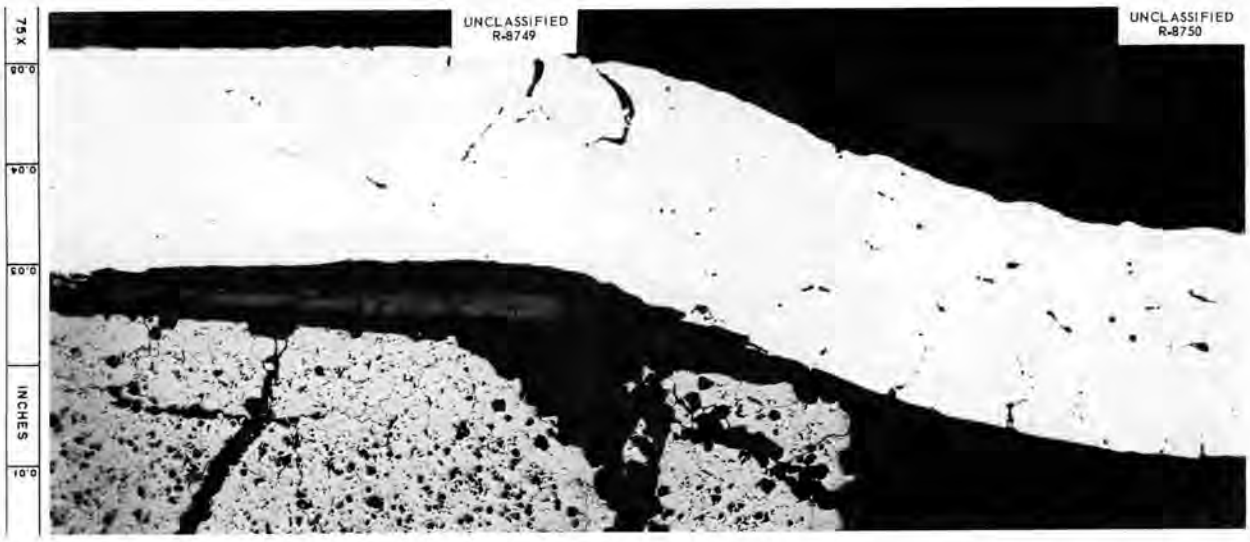

Fig. 12.8. Longitudinal Section Through Depression in Cladding of Capsule 01C-4 Caused by Chip Missing from Fuel Pellet. Note voids and grain separation in cladding. As polished; 75×. Reduced 31.5%.

13. Fission-Gas Release from Single-Crystal UO_2[1]

R. M. Carroll J. G. Morgan O. Sisman
T. W. Fulton R. B. Perez[2]

EXPERIMENTAL OBSERVATION OF FISSION-GAS RELEASE

The release of the inert fission gases, xenon and krypton, has a major influence upon the design of UO_2 fuel elements. Initially it was believed that the gas release rate could be calculated if the diffusion coefficient of the gas in UO_2 was known.[3] However, the results obtained by various investigations had a scatter that was more than three orders of magnitude, well beyond the limits of experimental error. This scatter suggested that some important variables were not being recognized.

An in-pile experiment was installed in the C-1 lattice position of the ORR.[4] The C-1 experiment was intended to eliminate many of the variables of other testing methods by measuring the steady-state fission-gas release while a UO_2 specimen was producing nuclear power. The UO_2 specimen is heated by its own fission power, which is adjusted by moving the specimen into or out of the neutron flux. The UO_2 temperature is controlled by air-cooling the specimen capsule. Fission gas is entrained in a stream of sweep gas, and the amount of each fission-gas isotope in the sweep gas is determined by gamma-ray spectrometry. The neutron flux is determined by adding argon to the sweep gas and measuring the subsequent activation of the argon.[5]

The initial results from the C-1 experiment had many unexplained phenomena, and it soon became apparent that simple diffusion theory could not explain the observed gas release.[6] Recent high-burnup studies have indicated that imperfections in the UO_2 crystal structure (such as internal voids or grain boundaries) would retard the migration of fission products.[7] In order to eliminate the complication of imperfections, very high-purity specimens of single-crystal UO_2 were irradiated in the C-1 facility to compare the gas release from single-crystal and sintered UO_2. Two sets of single-crystal specimens (experiments C1-9 and C1-10) of the same composition but from different batches of UO_2 were irradiated.

Isotopic Composition of the Fission Gas

The single-crystal UO_2 specimens were first irradiated at conditions of constant fission rate but at various temperatures. The release of fission gas was temperature dependent only for temperatures above about 600°C (Fig. 13.1). The temperature-independent gas release was considered to be caused by recoil [when fission occurred within recoil distance (about 8 μ) of the specimen surface]. At temperatures above 600°C

[1]This work is covered in detail in the following publications: R. M. Carroll and O. Sisman, *The Effect of Burnup and Fission Rate upon the In-Pile Fission Gas Release from Single Crystal UO_2*, in preparation; R. M. Carroll, R. B. Perez, and O. Sisman, *A Mathematical Model for the High Temperature In-Pile Release of Fission Gases*, ORNL-TM-743 (Dec. 20, 1963).

[2]Consultant from the University of Florida.

[3]R. M. Carroll, *Nucl. Safety* 4(1), 35–42 (1962).

[4]R. M. Carroll and C. D. Baumann, *Experiment on Continuous Release of Fission Gas During Irradiation*, ORNL-3050 (February 1961).

[5]R. M. Carroll, *Nucleonics* 20(2), 42–43 (1962).

[6]R. M. Carroll, *Reactor Chem. Div. Ann. Progr. Rept. Jan. 31, 1963*, ORNL-3417, pp. 207–10.

[7]R. M. Carroll, "Fission Product Release from UO_2," submitted for publication to *Nuclear Safety*.

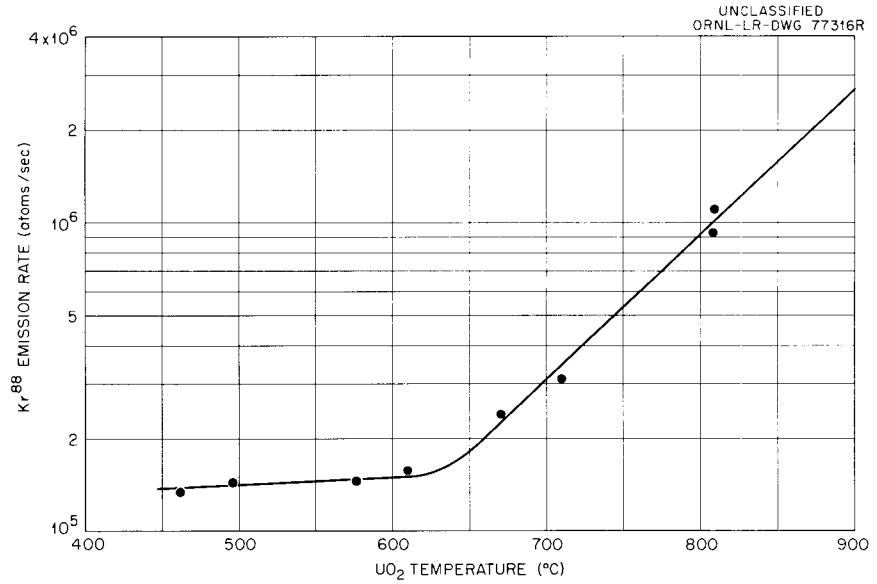

Fig. 13.1. Steady-State Release Rate of Kr^{88} from Single-Crystal UO_2 During Irradiation ($\phi = 2.0 \times 10^{13}$).

the gas release was thought to be by a diffusion mechanism (superimposed on the background of recoil release).

This theory was not found to be consistent with the results of the analysis, which consistently showed that the proportions of the isotopes in the released gas remained constant at all temperatures (400 to 1300°C). The recoil process and a diffusion process should release gases with appreciably different isotopic ratios.[8] The fact that the ratios of the isotopes did not change with temperature indicated that diffusion was not the mechanism for the temperature-dependent release. Furthermore, the composition of the fission gas at low temperatures indicated that direct recoil was not the primary release mechanism, even at temperatures below 600°C.

Release Rate as Function of Burnup

The release rate of the fission gas decreased with irradiation time. The percentage decrease was the same for all isotopes and for all temperatures. This was an unexpected result by classical theory, which predicts no effect of burnup (except for very high burnups, for which the gas release rate is predicted to increase). Recently, decreases in diffusion coefficient of as much as three orders of magnitude with low burnups have also been reported elsewhere as a result of post-irradiation annealing experiments.[7] The C-1 experiment is unique in that the decrease in fission-gas release rate can be observed during irradiation for an individual specimen. This is illustrated in Fig. 13.2 for the C1-9 specimen. Specimen C1-10 showed a similar decrease except that after one month of irradiation the gas release rate reached an apparent steady-state condition.

Based upon the observations that irradiation can smooth a surface,[7] it was suggested that the total surface area of the single-crystal UO_2 specimen was decreasing with irradiation.[9] The change in surface area could be caused by the smoothing of microscopic surface ripples by the knockout and redeposition of UO_2 molecules when fission fragments penetrate the specimen surface. This explanation may not be complete, but it can explain the observations that the proportions of the isotopes in the fission gas do not change with time and that the decrease of release

[8] R. M. Carroll, *ASTM Spec. Tech. Pub. No. 306*, pp. 110–20.

[9] R. M. Carroll, *Trans. Am. Nucl. Soc.* 6(1), 121 (1963).

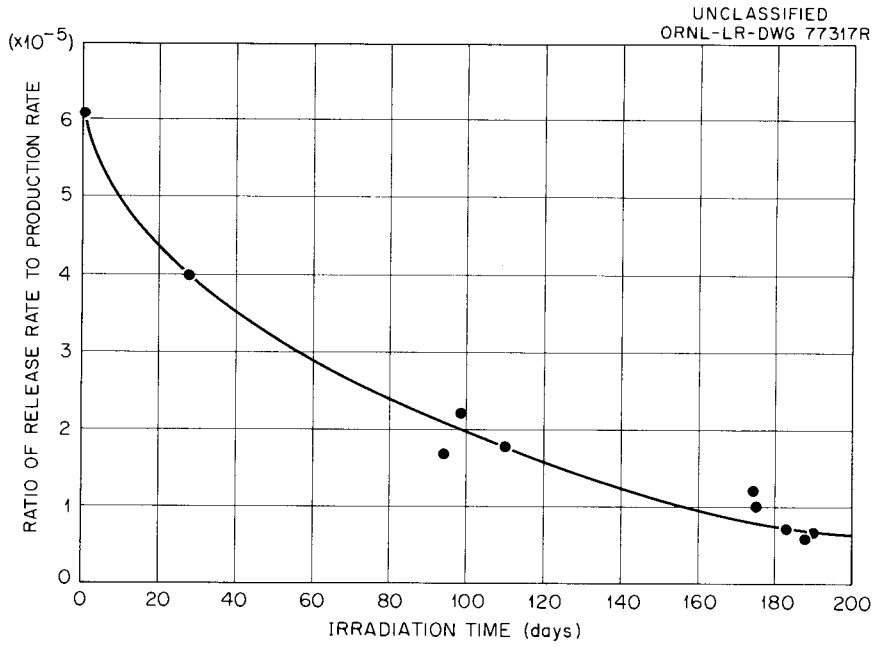

Fig. 13.2. Fractional Steady-State Release Rate of Kr^{88} from Single-Crystal UO_2 at Temperatures Below 600°C.

rate with time is the same for both the temperature-dependent and temperature-independent gas emission. The postulation of decreasing surface area is also supported by postirradiation electron microscopy studies of specimen C1-9 which showed the irradiated specimen to be definitely smoother than the control specimen.

Independence of Release Rate from Fission Rate

To find the effect of fission rate on steady-state fission-gas release, the specimens were irradiated at different neutron flux levels and the temperature dependence of the gas release was measured at each flux level. The Kr^{88} release rates from the C1-9 specimens are given in Fig. 13.3. The significant feature of Fig. 13.3 is that the curves converge to the same release rates at high temperatures. This convergence is not predicted by diffusion theory.

The fission-gas release rates below 600°C were directly proportional to the fission rate and therefore proportional to neutron flux, as illustrated in Fig. 13.4. The temperature-dependent component of the fission gas is found by subtracting the temperature-independent release (that which occurs below 600°C). An Arrhenius plot of the temperature-dependent fission-gas data (Fig. 13.5) gives a straight line, as would be expected for diffusion release; but, contrary to diffusion theory, the release rate is independent of fission rate, and conversely, the fractional release (release rate/birth rate) decreases with fission rate. The results from both experiments show that for the temperature range of 700 to 1300°C the amount of Kr^{88} in the UO_2 can change by a factor of 4 without producing a noticeable change in the amount released.

Heating Bursts

When the temperature of a UO_2 specimen is increased, an initial rapid release of fission gas (called a heating burst) occurs. A study was made of the causes of the bursts, the time required for the bursts to subside, and the proportions of different isotopes in the bursts. A typical heating burst, which occurred when the temperature of the C1-9 specimen was suddenly increased, is shown in Fig. 13.6. More gas was released during the burst than could be accounted for by diffusion theory.

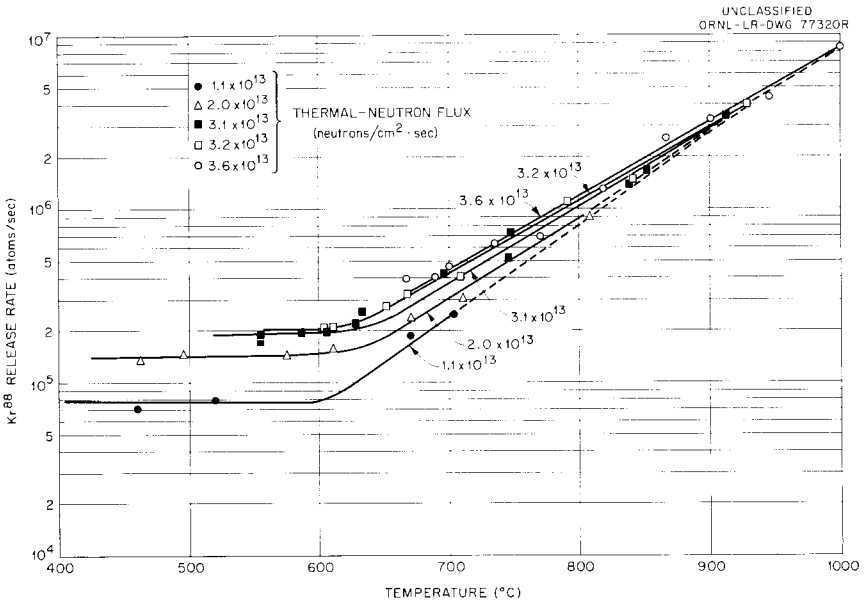

Fig. 13.3. Steady-State Release Rate of Kr^{88} from Single-Crystal UO_2.

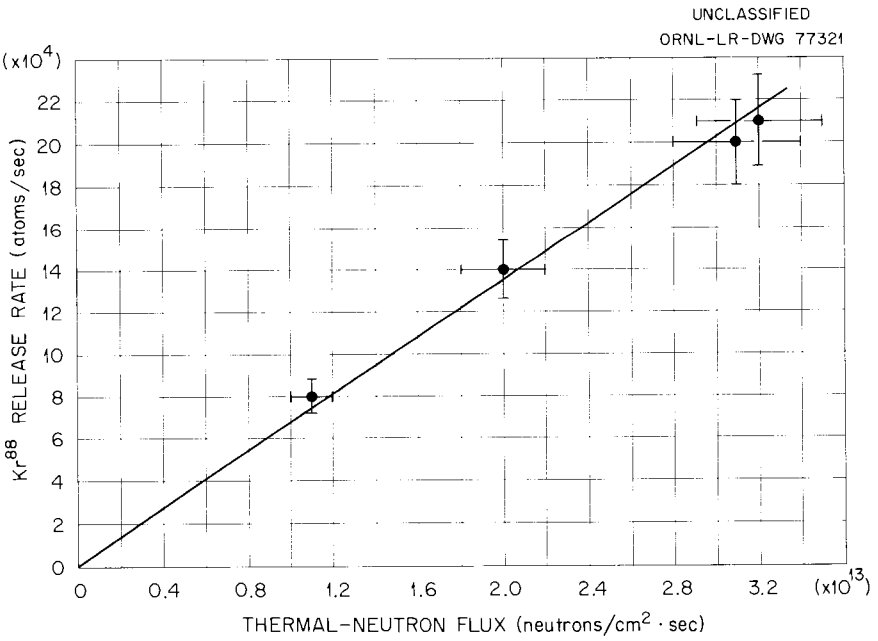

Fig. 13.4. Non-Temperature-Dependent Steady-State Kr^{88} Release Rate from Single-Crystal UO_2 vs Thermal Flux Measured by Ar^{41} Analysis.

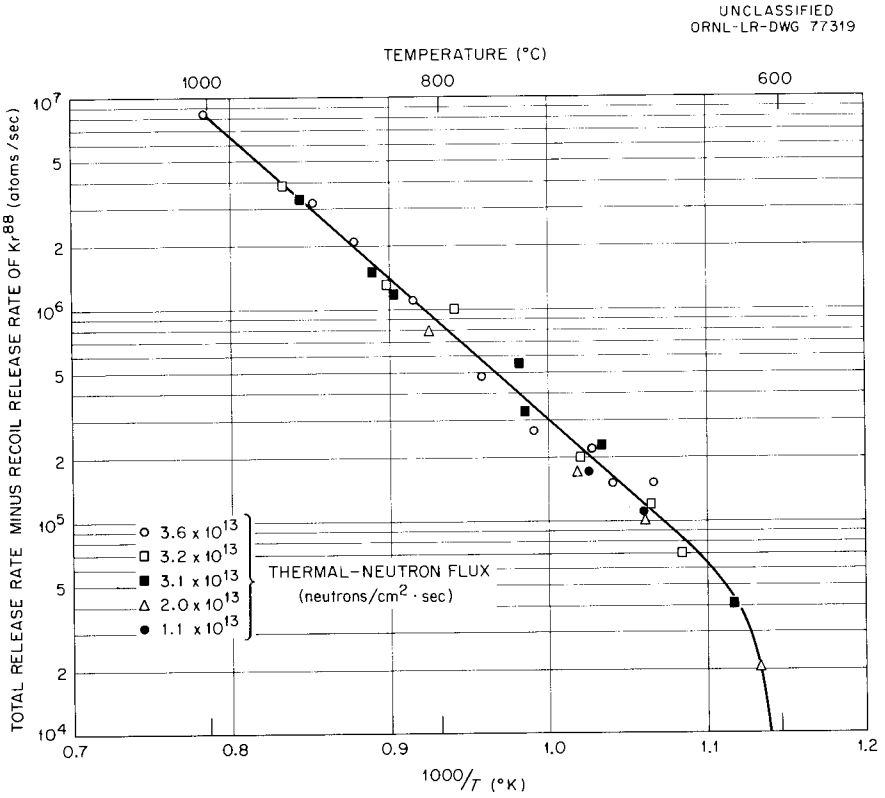

Fig. 13.5. Steady-State, Temperature-Dependent, Release of Kr^{88} from Single-Crystal UO_2 During Irradiation (Non-Temperature-Dependent Contribution Subtracted).

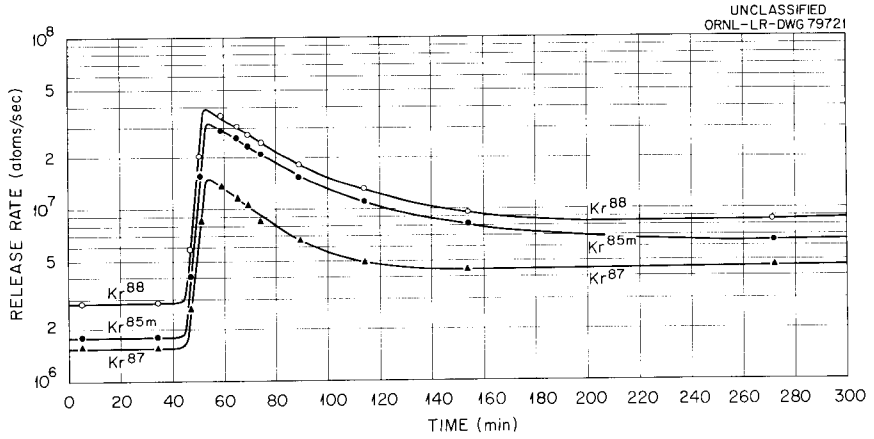

Fig. 13.6. Krypton Release when Temperature of Single-Crystal UO_2 Specimen C1-9 Was Increased from 865 to 1040°C at Constant Flux of 3.3×10^{13} neutrons cm^{-2} sec^{-1}.

MODEL FOR THE TEMPERATURE-DEPENDENT FISSION-GAS RELEASE

The above observations are the basis for a new model for the mechanism of fission-gas release during irradiation. The fundamental premise of the model is that the rate-controlling process of fission-gas release from UO_2 during irradiation is a defect-trapping mechanism. Three categories of defect traps are postulated.

1. Intrinsic traps, consisting of closed pores, grain boundaries, and impurities, do not change location during irradiation at the temperatures considered here.
2. Point defects, created by fission, can anneal and vanish, combine with another defect, or trap a fission product. The point defect can also migrate.
3. Clusters of point defects, semipermanent traps, are formed by combination of point defects.

It is assumed that the total trapping probability increases with fission rate because the point defects are created by fission. It is also assumed that the probability of escaping traps 2 and 3 increases as an exponential function of temperature. The probability of escaping the type 1 traps is very small.

A mathematical model has been derived for the steady-state high-temperature release which contains the main features of the experimental observations:[10]

1. Only a very small fraction of the total fission gas is released from the specimens.
2. The release rate is temperature dependent.
3. The fractional (release rate/birth rate) release decreases as fission rate increases.
4. The ratio of release rate for two different isotopes is neither that predicted by diffusion theory nor by birth/decay equilibrium without diffusion.
5. Bursts of gas are released when the temperature is increased.

The results of future experiments are expected to cause some modifications in the mathematical model. However, preliminary computations have shown that the equations exhibit the correct general behavior.

---

[10] R. B. Perez, R. M. Carroll, and O. Sisman, *A Mathematical Model for the High Temperature In-Pile Release of Fission Gases*, ORNL-TM-743 (Dec. 20, 1963).

14. Effect of Radiation on Ceramic Materials

EFFECT OF FAST NEUTRONS ON BERYLLIUM OXIDE

G. W. Keilholtz J. E. Lee, Jr.
R. E. Moore

Radiation Behavior of Sintered Compacts

The irradiation assembly, experimental techniques, and status of the findings of this continuing program of study have been described in several previous publications.[1-8] Progress in the past 12-month period and the present status of this program are summarized briefly in the following.

The irradiation of three assemblies, containing a total of 520 specimens of BeO, was completed during the past year. The BeO compacts were prepared (without additives) from commercial (UOX grade, Brush Beryllium Co.) BeO powder and were sintered at 1750°C. The compacts were cylinders of $\frac{1}{2}$-in. diameter by $\frac{1}{2}$-in. length or $\frac{1}{4} \times \frac{1}{4}$ in. Four types of compacts, as shown below, were prepared and used, in essentially equal numbers, in these tests.

Type	BeO Grain Size (μ)	Compact Density (g/cm^3)
I	~20	~2.7
II	35–60	~2.7
III	~24	~2.9
IV	~72	~2.9

These materials were exposed in the ETR at Arco, Idaho, to dosages as high as 4×10^{21} neutrons (of energy above 1 Mev) per cm^2. The assembly design was such that specimen temperature could be maintained at ~100°C, ~650°C, or ~1100°C; specimen temperature was nearly independent of the dose rate over the roughly fourfold range available in the ETR position.

Gross Damage to Specimens. – Figure 14.1 summarizes the gross damage to specimens at 650 and 1100°C in the assembly that was irradiated at a maximum flux of 5.7×10^{14} fast neutrons cm^{-2} sec^{-1} to total dosages shown in the figure.

The gross damage was much greater at 650°C than at 1100°C for all four types of material. Powdering did not occur at 1100°C, even at neutron doses exceeding 4×10^{21} *nvt* (>1 Mev). It is clear that BeO of type I (low density and fine grain size) withstood irradiation better than did any of the other types at both temperatures.[9-12]

When specimens of these materials were irradiated at ~100°C in approximately the same neutron

[1] G. W. Keilholtz *et al.*, *Reactor Chem. Div. Ann. Progr. Rept. Jan. 31, 1962*, ORNL-3262, pp. 157–60.

[2] R. P. Shields, J. E. Lee, Jr., and W. E. Browning, Jr., *Effects of Fast Neutron Irradiation and High Temperatures on BeO*, ORNL-3164 (Mar. 16, 1962).

[3] R. P. Shields, J. E. Lee, Jr., and W. E. Browning, Jr., *Trans. Am. Nucl. Soc.* 4(2), 338 (November 1961).

[4] G. W. Keilholtz *et al.*, "Radiation Damage in BeO," *Symposium on Radiation Damage in Solids and Reactor Materials*, STI/PUB/56, vol. II, *Intern. At. Energy Agency*, Vienna, 1962.

[5] G. W. Keilholtz, J. E. Lee, Jr., and R. E. Moore, *Behavior of BeO Under Irradiation, GCR Program Semiann. Progr. Rept. Sept. 30, 1962*, ORNL-3372.

[6] G. W. Keilholtz, J. E. Lee, Jr., and R. E. Moore, *Reactor Chem. Div. Ann. Progr. Rept. Jan. 31, 1963*, ORNL-3417, pp. 176–85.

[7] G. W. Keilholtz, J. E. Lee, Jr., and R. E. Moore, "The Effect of Fast-Neutron Irradiation on BeO Compacts at High Temperatures," *J. Nucl. Mater.* (in press).

[8] G. W. Keilholtz, J. E. Lee, Jr., and R. E. Moore, *The Effect of Fast-Neutron Irradiation on BeO Compacts at High Temperatures*, ORNL-TM-741 (Dec. 12, 1963).

[9] G. W. Keilholtz, J. E. Lee, Jr., and R. E. Moore, *GCR Program Semiann. Progr. Rept. Mar. 31, 1963*, ORNL-3445, p. 242.

[10] G. W. Keilholtz, J. E. Lee, Jr., and R. E. Moore, *GCR Program Semiann. Progr. Rept. Sept. 30, 1963*, ORNL-3523, pp. 264–75.

[11] G. W. Keilholtz *et al.*, *Behavior of BeO Under Neutron Irradiation*, ORNL-TM-742 (Dec. 12, 1963).

[12] G. W. Keilholtz *et al.*, "Behavior of BeO Under Irradiation," presented at International Conference on Beryllium Oxide, Newport, Sydney, Australia, October 1963 (to be published in *J. Nucl. Mater.*).

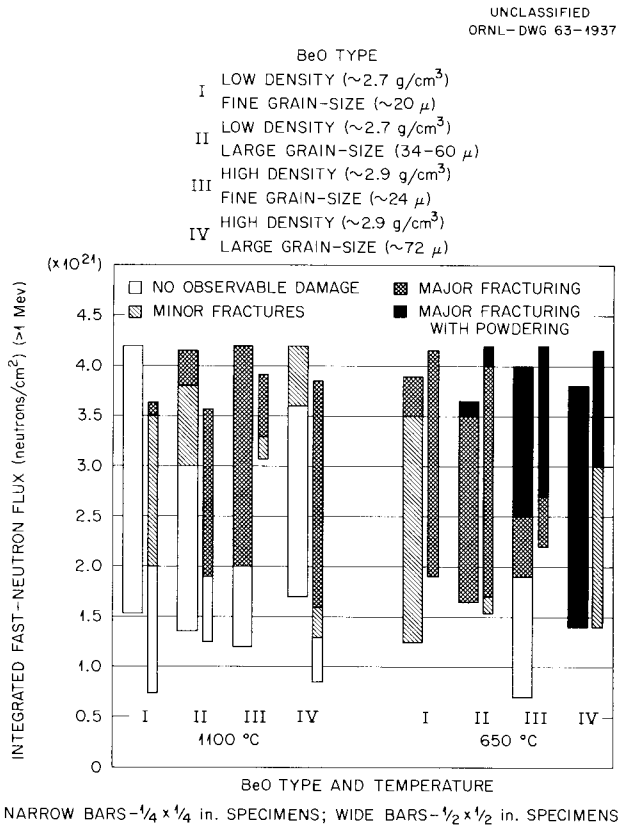

Fig. 14.1. Gross Damage to BeO Specimens in Experiment 41-9 as a Function of Integrated Fast-Neutron Flux and Temperature.

flux, severe damage occurred at a lower fast-neutron dose. There was very little difference in gross damage among the four types of material. In general, little observable damage occurred below a fast-neutron dose of 1×10^{21} *nvt*, major fracturing occurred between 1 and 2×10^{21} *nvt*, and major fracturing with powdering occurred in the specimens irradiated to doses above 2×10^{21} *nvt*.

Volume Increases of Irradiated BeO Compacts. – The volume expansion of BeO samples irradiated in these assemblies was, as expected, found to increase with increasing neutron dose and to decrease with increasing temperature. In irradiations to 4.2×10^{21} *nvt* at 1100°C the type I BeO clearly expanded the least (~1.5%), while the type of high density and large grain size expanded the most (~3.5%). No definitive differences in volume expansion among the four types of BeO were noted in the irradiations at 650 and 100°C. The volume expansion at 650°C increased approximately linearly from ~2% at 0.8×10^{21} *nvt* to ~6% at 2.2×10^{21} *nvt*; the expansion at 100°C increased from 1.5% to 6.0% over the dose range 0.4 to 1.8×10^{21} *nvt*.

Metallographic Examinations. – The primary manifestation of fast-neutron damage at high neutron dose or at low temperatures is grain-boundary separation (intergranular fracture).[6-8] In the high-temperature assembly described above, however, large-grained specimens (~70 μ) exhibited a considerable amount of transgranular fracture in addition to extensive grain-boundary separation. This is illustrated in Fig. 14.2, which shows type IV BeO that had been irradiated at 1100°C to a fast-neutron dose of 3.4×10^{21} *nvt* (>1 Mev). There is an apparent grain size reduction of about 25% as a result of the transgranular fracture. Type III BeO which had been irradiated at the same temperature but to a slightly higher neutron dose (3.92×10^{21} *nvt*), shows (Fig. 14.3) extensive though less marked grain-boundary separation. Examination of type III BeO at higher magnifications shows less transgranular fracture than in type IV BeO, and there is no significant change in the apparent grain size.

Helium Retention by Irradiated Specimens. – The reactions

$$Be^9 + n \longrightarrow 2n + 2\alpha,$$

$$Be^9 + n \longrightarrow Li^6 + \alpha, \text{ and}$$

$$Li^6 + n \longrightarrow T^3 + \alpha$$

all produce helium within the BeO; the rate of generation has been estimated[2] to be about 205 μl (STP) per gram of BeO per 10^{21} *nvt*. Analyses of specimens for retained helium continue to give results with considerable scatter, and it remains impossible to say whether the specimens behave erratically or whether the analytical procedure is faulty. In general, an appreciable fraction of the helium is retained by all specimens; those irradiated at 1100°C retain less than those irradiated at 650°C, and, for irradiations at comparable temperatures, the fine-grained material (types I and III) retain a smaller fraction than do the coarse-grained material. No real correlation of retained helium with gross damage appears to exist.

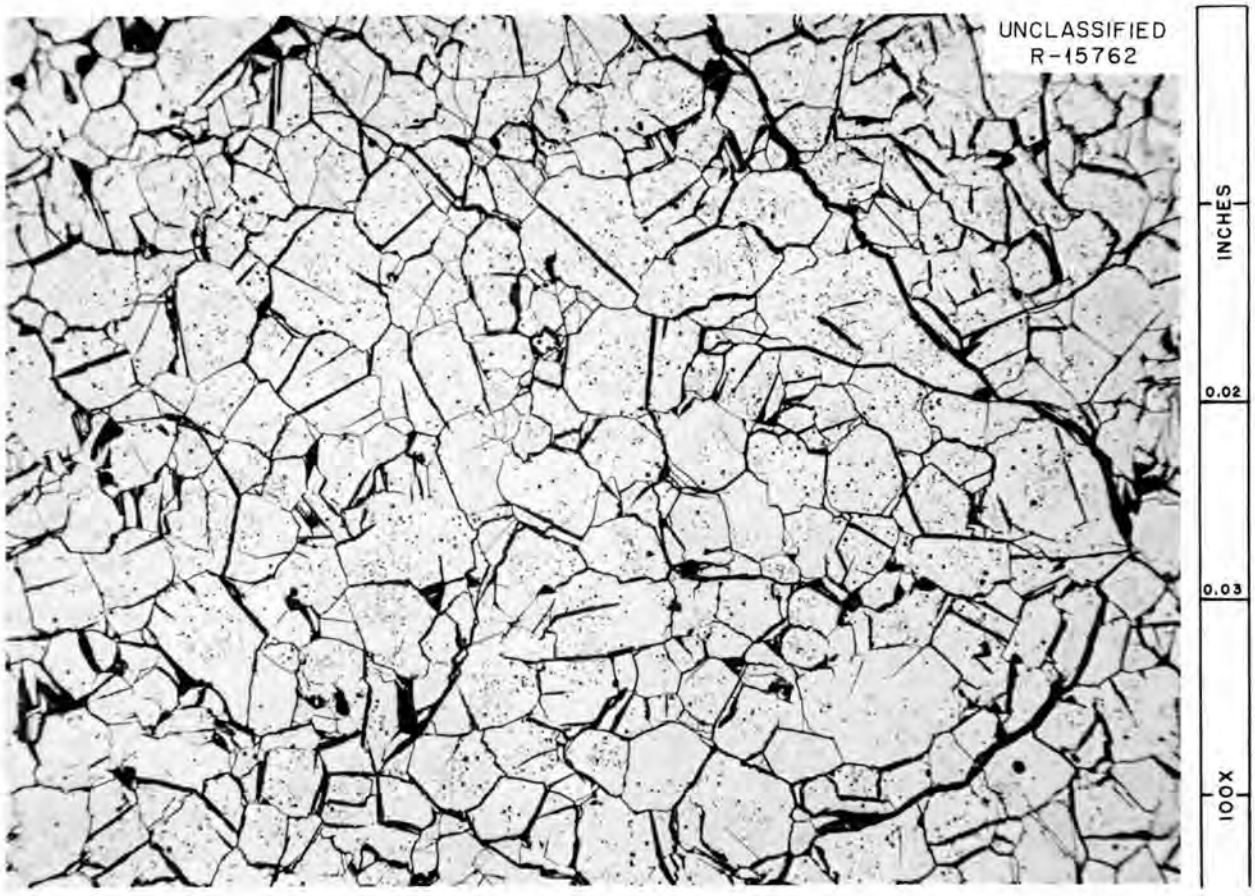

Fig. 14.2. Photomicrograph of Irradiated BeO Specimen A15-31. Density, 2.9 g/cm^3; grain size, 70 μ; exposed to 3.4×10^{21} *nvt* (>1 Mev) at 1100°C in experiment 41-9; as polished; 100X.

Radiation Behavior of BeO Single Crystals[13]

A number of small (about 1 mm on an edge) single crystals of BeO have been included in recent radiation assemblies. These single crystals are neither powdered nor cracked on irradiation to large dosages at 100°C, 650°C, or 1100°C; the crystals do, however, become fragile and require careful handling to avoid damage after irradiation. Crystals irradiated at 650°C (see Fig. 14.4) show dark bands which increase in number and intensity as dosage increases from 1 to 4 $\times$ 10^{21} *nvt*. These dark bands are isotropic material parallel to the basal planes and must be agglomerates of radiation-produced defects. Crystals irradiated at 100°C and 1100°C do not show the dark bands. Presumably, at 100°C, where solid-state diffusion is essentially negligible, agglomeration of the defects proceeds slowly and is slight, if any, and the small agglomerates remain coherently in the lattice. At 1100°C, annealing of defects is sufficiently rapid to prevent the gross agglomeration produced at intermediate temperatures.

The change in volume of the single-crystal material (see Table 14.1) generally increases with increasing dose and decreases with irradiation temperature. Volume increases of the single crystals are markedly less than those of sintered compacts; this is probably largely because grain-boundary separation is not operative in the single crystals.

[13]We gratefully acknowledge the assistance of G. W. Clark and H. L. Yakel, Metals and Ceramics Division, who furnished the single crystals and much of the data presented in this section.

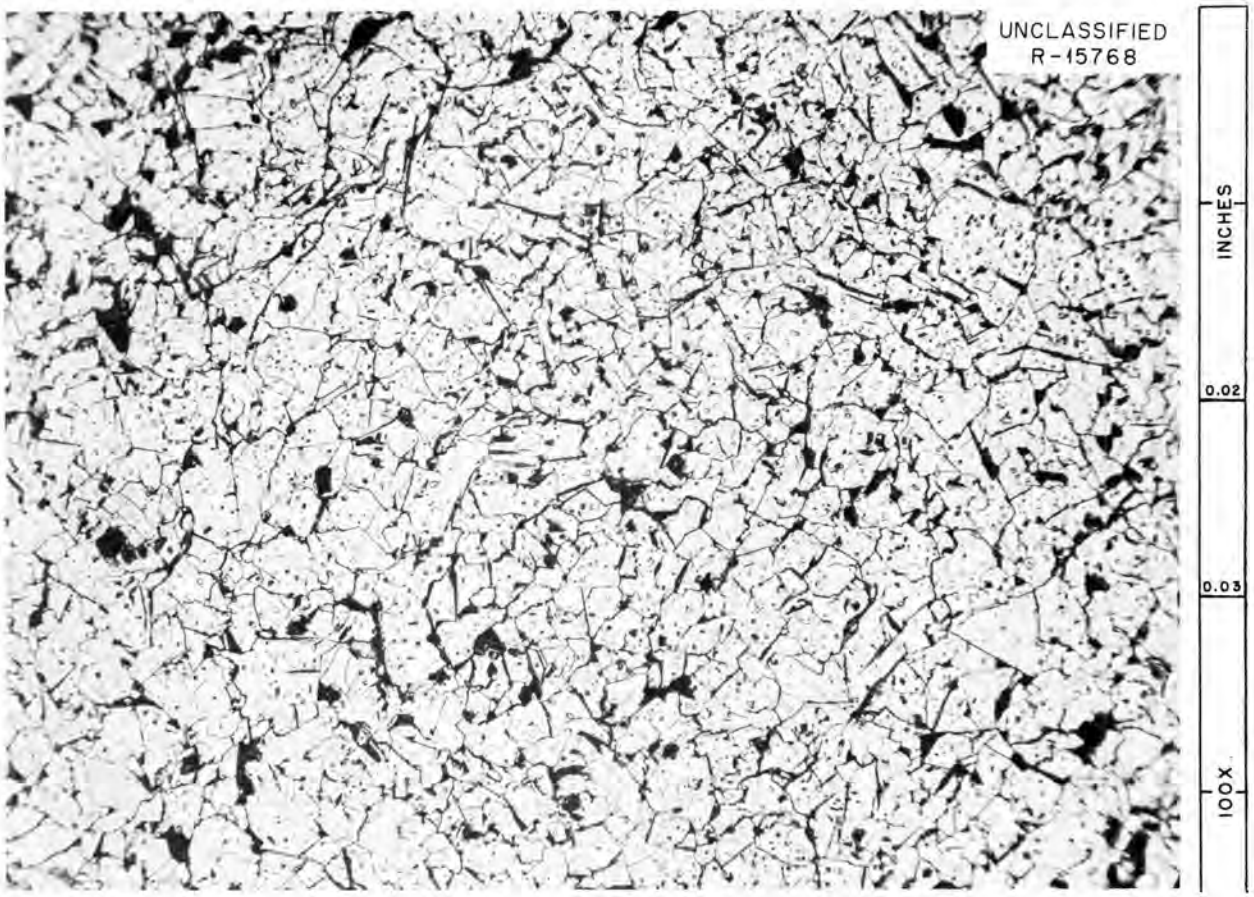

Fig. 14.3. Photomicrograph of Irradiated BeO Specimen A10-63. Density, 2.9 g/cm^3; grain size, 23 μ; exposed to 3.92×10^{21} *nvt* (> 1 Mev) at 1100°C in experiment 41-9; as polished; 100X.

Conclusions

Volume increase, ΔV_T, on irradiation may be assumed to be given by:

$$\frac{\Delta V_T}{V_o} = \frac{\Delta V_l}{V_o} + \frac{\Delta V_d}{V_o} + \frac{\Delta V_g}{V_o}$$

where V_o is original volume, ΔV_l is due to lattice parametric increases, ΔV_d is due to lattice defect agglomeration, and ΔV_g is due to grain-boundary separation.

The contribution due to grain-boundary separation cannot be a factor in volume expansion of single-crystal BeO, and a combination of lattice expansion and lattice defect agglomeration must be responsible. To assume that the difference between volume increase in single crystals and in sintered compacts is due entirely to grain-boundary separation is almost certainly an oversimplification. If that assumption is made, for want of a better, then it appears that for BeO compacts ΔV_g contributes at least 50% of ΔV_T under all irradiation conditions and a much higher percentage on irradiation at low temperatures.

Whether the helium production and retention causes, or contributes importantly to, volume increase by any of these processes remains difficult to establish. A line of reasoning that seems plausible is the following: The single crystals are very large in comparison with crystallite size in the compacts; they should (though no experimental proof is available) retain a larger fraction of their helium within the lattice than do any of the compacts. Any contribution of this gas to lattice parameter and to defect agglomeration expansion should, accordingly, be maximized in the single crystals; such effects

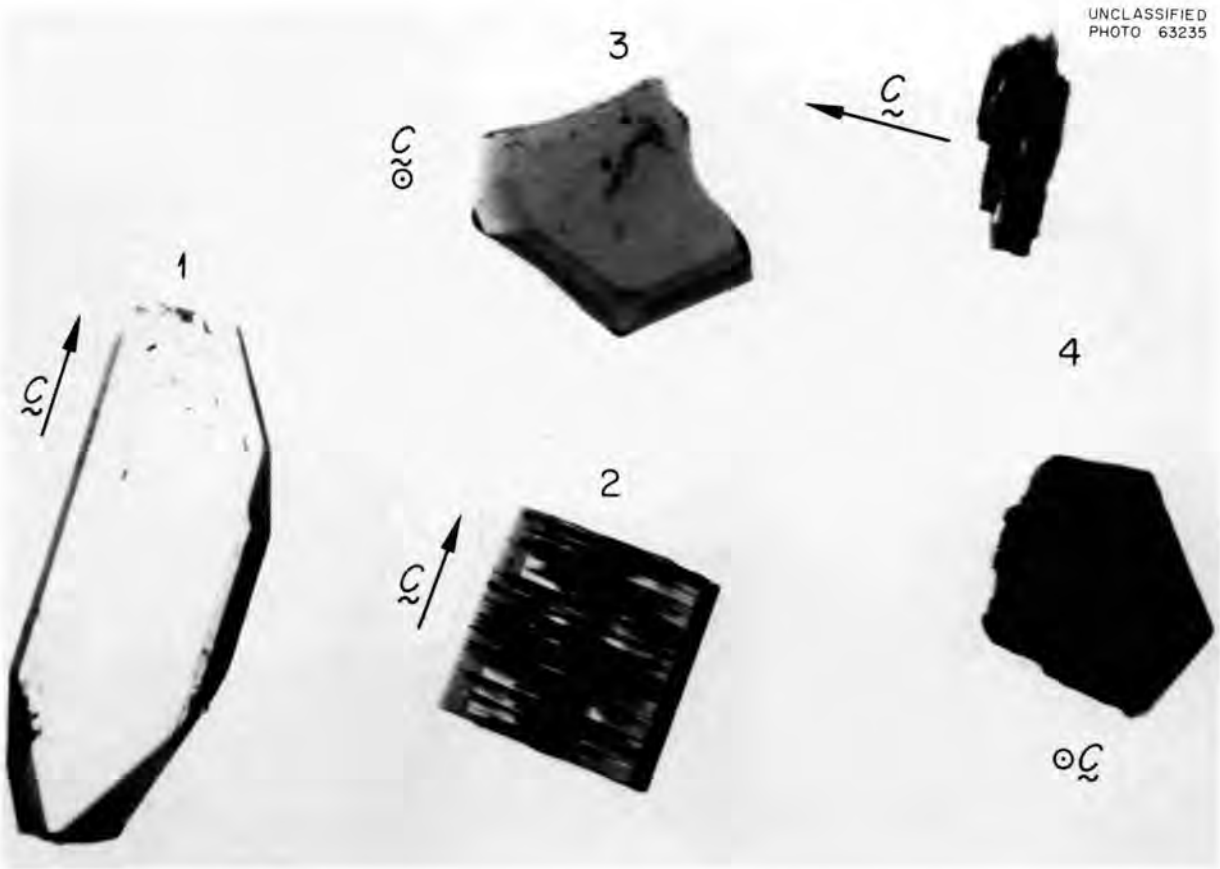

Fig. 14.4. Irradiated BeO Single Crystals. No. 1, unirradiated; No. 2, irradiated to 1.1×10^{21} *nvt* (> 1 Mev) at 650°C, showing dark banding; No. 3, irradiated to 3.6×10^{21} *nvt* (> 1 Mev) at 50°C; No. 4, irradiated to 4.1×10^{21} *nvt* (> 1 Mev) at 650°C, with the dark banding appearing to fill the crystal almost completely.

seem incapable of fracturing the single crystal under any conditions yet achieved. The gas can hardly contribute importantly to intergranular fracture (grain-boundary separation) until it arrives, by diffusion, at the grain boundaries. If this is true, its contribution should depend importantly on the amount which arrives there; accordingly, the contribution should become increasingly important as temperature increases and as crystallite size is diminished. The experimental observations show exactly the opposite effect.

It seems apparent, and is generally agreed, that anisotropic expansion of the crystal lattice is responsible for grain-boundary separation at low temperatures since, here, extensive intergranular fracture occurs at low neutron dosages (and low

Table 14.1. Volume Increases on Irradiation of BeO Single Crystals

Irradiation Conditions		Volume Increase (%)
Temperature (°C)	Fast-Neutron Dose, *nvt*	
	$\times 10^{21}$	
100	0.85	1.5
	1.8	1.7
	2.2	2.1
650	1.1	0.9
	4.1	3.8
1100	1.5	0.6
	5.7	0.9

helium accumulations).[14,15] The data from single-crystal irradiations, and the qualitative considerations above, suggest that the dose-dependent anisotropic expansion (augmented by defect agglomeration) and not gas pressure is also primarily responsible at high temperatures. It seems more likely that helium gas contributes to transgranular fracture processes at high temperature.

In an immediately practical sense, the irradiation stability of BeO for use as a moderator material may be optimized by the proper choice of grain size, density, operating temperature, and additives such as MgO to strengthen the grain boundaries – the operating temperature should be 1000 to 1100°C. Quantitative information on the effect of neutron flux on irradiation damage as separate from the neutron dose effect should result from the completion of the experiments in progress. Such information should be valuable both from the standpoint of reactor design and for the understanding of the relative importance of various proposed damage mechanisms.

ANNEALING BEHAVIOR OF CERAMIC MATERIALS

O. Sisman

Thermal Analysis of Irradiated Ceramics[16]

C. D. Bopp R. L. Towns

The thermal analysis apparatus, described previously for the study of annealing of irradiated zircon,[17] has been used to measure the temperature and energy of recrystallization of irradiated steatite, forsterite, cordierite, and lava A. Data obtained for these materials are shown in Table 14.2. The sensitivity of this apparatus, when used to heat a 0.2-g sample at 3°C/min, was about 1 cal/g at 700°C for reactions which occurred within a 30°C interval; this sensitivity is approximately proportional to the inverse cube of the absolute temperature.

A more sensitive twin-crucible assembly, in which the specific heat of the sample is compared directly with a reference substance, has been constructed and tested. The crucibles, of ½-in.-diam, ½-in.-high cylinders of 10-mil tantalum sheet, are supported by a ⅛-in.-thick alumina plate and are suspended in a vacuum furnace by an alumina thermocouple insulator. Temperature gradients within the sample are minimized by measuring the temperature at the crucible wall.[18] The actual temperature of a reaction is determined by using different rates of heating, and extrapolating the threshold temperature of the peak to zero heating rate. Preliminary testing with the twin-crucible apparatus indicates that sensitivity increases in proportion to the rate of heating over the range studied. At temperatures below 600°C, a tenfold increase in rate of heating is possible over that used with the single-crucible apparatus, but the speed of the available furnace limits the rate of heating to relative values less than this figure.

Thermal conductivity of ceramic materials is extremely sensitive to the presence of radiation defects, and measurement of this property as a function of annealing conditions is preferred especially for materials which show only small thermal effects. A previously described[19] apparatus, in which irradiated samples are heated for 1 hr to successively higher temperatures and are cooled to room temperature between heatings for measurement of thermal conductivity and density, has been readied and tested for this purpose.

Crystallization of Steatite on Irradiation and Annealing

T. N. McVay[20]

The steatite specimens shown in Table 14.2 were examined by x-ray and petrographic methods

[14] J. Elston, "Radiation Damage in Solids," *Symposium on Radiation Damage in Solids and Reactor Materials*, STI/PUB/56, vol. II, *Intern. At. Energy Agency*, Vienna, 1962.

[15] *High-Temperature Materials Program Progress Report No. 12, Part A, Nuclear Materials and Propulsion Operation*, Flight Propulsion Laboratory Department, General Electric Co., Cincinnati, GEMP-21A (June 15, 1962).

[16] C. D. Bopp, "Annealing Properties of Irradiated Ceramics," in preparation.

[17] C. D. Bopp, O. Sisman, and R. L. Towns, *Reactor Chem. Div. Ann. Progr. Rept. Jan. 31, 1963*, ORNL-3417, p. 217.

[18] H. E. Schwiete and G. Ziegler, *Ber. Deut. Keram. Ges.* **35**, 193–204 (1958); *Ceram. Abstr.* 20e (1960).

[19] O. Sisman, C. D. Bopp, and R. L. Towns, *Solid State Div. Semiann. Progr. Rept. Feb. 28, 1955*, ORNL-1852, p. 33.

[20] Consultant, University of Alabama.

Table 14.2. Thermal Analysis of Silicates

Exposure (epithermal neutrons)	Density (g/cm^3)		Threshold Temperature of Reaction ($^\circ C$)	Width of Reaction Peak ($^\circ C$)	Energy Released by Reaction (cal/g)
	Before Heating	After Heating			
$\times 10^{19}$					
		Steatite 228 (98% $MgO \cdot SiO_2$)			
0	2.79	2.79			
18[a]	2.76	2.79	840 ± 20	50	4 ± 2
7[b]	2.75	2.78	830 ± 10	50	6 ± 3
30[b]	2.55	2.64	860 ± 5	100	60 ± 10
		Cordierite 202 (98% $2MgO \cdot 2Al_2O_3 \cdot 5SiO_2$)			
0	About 2.39 to 2.59[c]				
10[a]			825 ± 5	50	5 ± 3
18[a]			825 ± 5	50	9 ± 3
5[b]			825 ± 5	50	10 ± 3
30[b]			900 ± 5	150	55 ± 10
		Forsterite 243 (98% $2MgO \cdot SiO_2$)			
0	3.06	3.06			
18[a]	3.02	3.03			0 ± 3
6[b]	3.04	3.04			0 ± 3
30[b]	2.95	3.03	835 ± 10	100	30 ± 15
		Lava A (a natural aluminum silicate of indefinite composition)			
0	2.60	2.61			
10[a]	2.57	2.59	980 ± 10	50	14 ± 3
18[a]	2.54	2.60	970 ± 5	70	40 ± 15
6[b]	2.53	2.58	975 ± 5	70	9 ± 3
30[b]	2.12	2.60	990 ± 5	70	30 ± 15

[a] Irradiated in a graphite-moderated reactor for which the flux > 1 Mev is about 0.06 of the epithermal flux and the thermal flux is about 1.2 times the epithermal flux. [M. T. Robinson, O. S. Oen, and D. K. Holmes, *Nucl. Sci. Eng.* 10, 61–69 (1960).] During irradiation the samples were contained in helium-filled aluminum cans.

[b] Irradiated adjacent to the lattice of a light-water-moderated reactor where the flux > 1 Mev is about 0.35 of the epithermal flux [G. Rowlands, *J. Nucl. Energy Pt. A (Reactor Sci.)* 11, 150–56 (1960)] and the thermal flux is about 3 times the epithermal flux. During irradiation the samples were contained in perforated cans in order that they would be cooled by the reactor cooling water.

[c] The density was not sufficiently uniform for consistent measurements.

before irradiation and before and after annealing treatments. According to L. Atlas,[21] protoenstatite is the stable form of $MgSiO_3$ above 990°C, and this crystalline form is stable at lower temperature in the presence of a material which yields a glass. Before irradiation the steatite specimens were shown by x-ray diffraction to be principally protoenstatite with, perhaps, a small amount of enstatite.[22] Petrographic examination showed a matrix of 2- to 10-μ-diam crystals surrounded by glass films about 1 μ thick; refractive index of the crystals was near 1.65, but the crystals were too small for a thorough petrographic study. After an exposure of the steatite specimens to 7×10^{19} *nvt* of epithermal neutrons in the MTR, protoenstatite was still present, and after 3×10^{20} *nvt*, the material was amorphous. After doses to 3×10^{20} *nvt*, however, the material was isotropic; a considerable expansion of the protoenstatite crystals was evident since the refractive index of the areas where crystals were originally present had dropped to 1.58. After heating the 3×10^{20} *nvt* material, small peaks, characteristic of enstatites, appeared in x-ray patterns, and minute crystals were observed petrographically.

A Vibration Method for the Elastic Constants of Small Plates[23]

C. D. Bopp

Some years ago, determination was made of the effect of radiation on the elastic constants of ceramic specimens.[24,25] The specimens irradiated and tested were in the form of small, thin, flat plates; elastic constants were obtained from experimentally determined flexural and torsional resonant frequencies of these specimens when vibrated as supported cantilever plates. The equations used[24,25] were derived from theories of vibration of beams. We have recently examined this work and have derived the equations with the help of recently presented theories[26,27] of vibration of cantilever plates; this derivation has not changed the previously accepted values but serves to place the experimental study on a less heuristic foundation.

The supported cantilever plate is treated as a compound system composed of subsystems with simple boundary conditions. Following Martin,[26] the deflection along one axis is approximated by a beam function, and the deflection along the other axis is obtained by a variational procedure. Martin showed that this approximation gives the same result as beam theory for the first flexural mode of a simple cantilever plate if the parameter W_F/b is substituted for k where

$$W_F^4 = b^4\lambda \,, \tag{1}$$

$$\lambda = k^4(1 - \sigma^2) = 48\pi^2 f^2 \rho(1 - \sigma^2)/(Eh^2) \,, \tag{2}$$

and where l is the length, b is the width, h is the thickness, ρ is the density, f is the resonant frequency (cps), E is Young's modulus, and σ is Poisson's ratio. The frequency equation is obtained for the flexural mode of a compound beam with the corresponding boundary conditions by the method of Bishop and Johnson.[27] This equation may be solved for arbitrary location of the support to give $W_F l/b$.

For the first torsional mode, the supported cantilever plate is considered as a compound system formed from two subsystems joined at the supported edges to form the compound plate. Martin's equation for a plate which is supported (hinged) at one edge and is free on the other edges is modified to apply to the subsystems described above by replacing the free beam function by a cantilever beam function. The frequency equation for the compound plate is obtained by a method similar to that outlined by Martin.[26] This equation may be solved for arbitrary location of the support to give values of the parameter

$$W_T^4 = l^4\lambda \,. \tag{3}$$

---

[21] L. Atlas, *J. Geol.* **60**, 125–48 (1952).

[22] R. E. Thoma obtained and interpreted the x-ray diffraction patterns.

[23] C. D. Bopp, "Vibration Method for the Elastic Constants of Small Plates," submitted for publication to the *Review of Scientific Instruments*.

[24] C. D. Bopp *et al.*, *Ind. Eng. Chem.* **49**, 718 (1957).

[25] C. D. Bopp, *Solid State Div. Ann. Progr. Rept. Aug. 31, 1958*, ORNL-2614, p. 210.

[26] A. I. Martin, *Quart. J. Mech. Appl. Math.* **9**, 95 (1956).

[27] R. E. D. Bishop and D. C. Johnson, *Mechanics of Vibration*, Cambridge Univ. Press, New York, 1960.

Experimental values of the resonant frequencies of the first flexural and the first torsional modes may be substituted into Eqs. (2) and (3) to give E and σ. The ratio of the flexural and torsional resonant frequencies for a square plate must be determined with about twice the accuracy required for a thin bar[28] to obtain Poisson's ratio with equal accuracy. However, Martin[26] showed that for a simple cantilever plate with known E and σ, calculated and measured frequencies agreed within a few percent.

[28] G. Pickett, *Am. Soc. Testing Mater. Proc.* **45,** 846 (1945).

15. Special Studies for Gas-Cooled Reactor Program

NEUTRON FLUX SPECTRA[1]

C. D. Baumann O. Sisman

Radiation damage to the coatings of carbon-coated fuel particles may be caused by fission-fragment recoils from the fuel kernel, or by fast neutrons of energy >0.18 Mev. The fission-fragment recoil range is such that only a fraction of the thickness of the pyrolytic carbon coating will be penetrated by the fragment from the inner side. Damage to the outer portion of the coating must, unless it comes via pressure or crack propagation from the inside of the particles, be caused by fast neutrons. Because of the obvious importance of the data to interpretation of irradiation behavior of GCR materials, the neutron flux spectra in the B-9 and C-1 core positions and the P-06 poolside irradiation facility of the ORR were measured.

All wires or foils which formed the active portions of the monitors were sealed in capsules consisting of short lengths of 3-mm quartz tubing. The "bare" (thermal) monitor capsules were enclosed in 0.25-in. aluminum tubing of 0.167-in. wall thickness. Each of the other capsules was completely enclosed in a 40-mil thickness of cadmium and was placed inside 0.25-in. stainless steel tubing of 6-mil wall thickness. These monitor elements were then assembled into irradiation assemblies appropriate to the facility to be monitored; at least a 2-cm distance was maintained between adjacent "bare" and cadmium-clad monitor elements to minimize the effect of the thermal-flux depression due to the cadmium.

The B-9 and C-1 monitor assemblies were irradiated at a nominal 5-Mw reactor power for 2 hr and 1 hr, respectively, prior to a normal reactor cycle. The P-06 assembly was irradiated during the reactor cycle at full power (30 Mw) for 2 hr.

The results of the measurements in the B-9 and P-06 facilities (normalized to 30-Mw reactor operation) are shown in Figs. 15.1 and 15.2. The resonance flux, ϕ_r, is the flux per unit lethargy range and is obtained directly from

$$R_c = \phi_r I , \qquad (1)$$

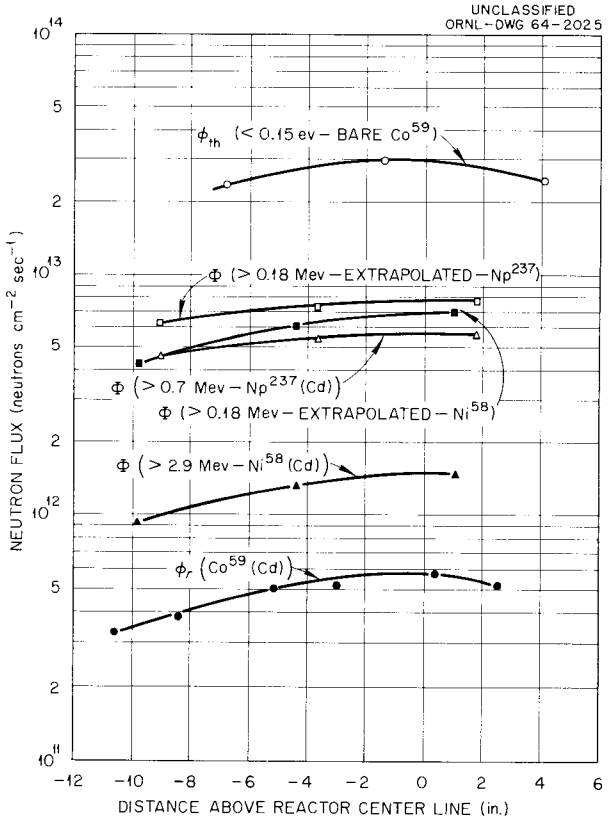

Fig. 15.1. Neutron Flux in the Poolside P-06 Position in the ORR at 30 Mw.

[1] C. D. Baumann, *Neutron Flux Spectra in the Experimental Facilities of the ORR*, in preparation.

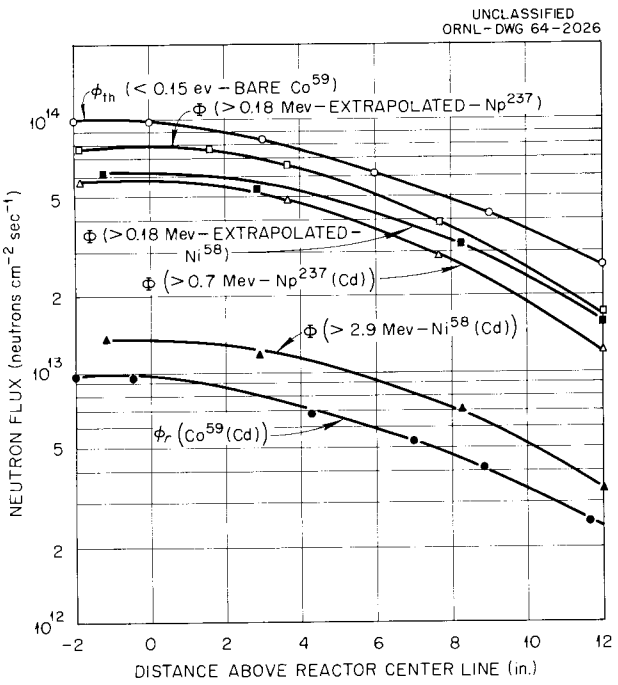

Fig. 15.2. Neutron Flux in the B-9 Position in the ORR at 30 Mw.

where R_c is the measured reaction rate per atom of Co^{59} (cadmium-covered) and I is the Co^{59} resonance integral (= 75 barns).

The thermal flux less than 0.15 ev – ϕ_{th} – is obtained from

$$R_b = \sigma_0 \phi_{th} + 2\sigma_0 \phi_r E_0^{1/2} \left(\frac{1}{\sqrt{0.15}} - \frac{1}{\sqrt{E_c}} \right) + \phi_r I , \quad (2)$$

where

R_b = measured bare Co^{59} reaction rate per atom,

σ_0 = 2200-m cross section of Co^{59} (= 37 barns),

E_0 = 0.0253 ev,

E_c = the cadmium cutoff energy (0.55 ev for 40-mil cadmium cylinders),

ϕ_r = the resonance flux for the position where the thermal-flux measurement is made.

The first term on the right in Eq. (2) represents the Maxwellian rate of reaction with neutrons of energy up to $5kT$ (i.e., 0.15 ev). The second term represents the rates of reactions with neutrons of energy between $5kT$ and E_c with the assumptions that the cross section varies as $E^{-1/2}$ and the flux varies as E^{-1} in this region; magnitude of the second term is about 5% that of the first term. The third term represents the rate of resonance reaction. The reaction rates themselves are obtained from the activity of the irradiated samples at the end of irradiation.

The fast fluxes are obtained on the assumption that the plot of cross section for reaction of the monitor vs energy of the neutron can be represented by a step function; that is, no reactions take place (or $\sigma = 0$) below an effective threshold energy (E_{ef}), and at the effective threshold energy the cross section rises abruptly to a value which is independent of energy. If this is true, then

$$R(E_{ef}) = \int_{E_{ef}}^{\infty} \sigma(E)\, \phi(E)\, dE = \bar{\sigma} \int_{E_{ef}}^{\infty} \phi(E)\, dE = \bar{\sigma}\, \Phi(E_{ef}) . \quad (3)$$

Accordingly,

$$\Phi(E_{ef}) = \frac{R(E_{ef})}{\bar{\sigma}} , \quad (4)$$

where $R(E_{ef})$ is the reaction rate per atom of the monitor, and $\Phi(E_{ef})$ is the integrated flux above E_{ef}. For the $Np^{237}(n,f)$ reaction, $\bar{\sigma}_f$ = 1.5 barns and E_{ef} = 0.7 Mev. For the reactions $Ni^{58}(n,p)Co^{58m}$ and $Ni^{58}(n,p)Co^{58}$, $\bar{\sigma}$ = 133 mb and 261 mb, respectively, with E_{ef} = 2.9 Mev.[2]

The flux above 0.18 Mev was then calculated from the neptunium and nickel activities by using the relationships

$$\Phi(0.18) = 1.37\ \Phi(0.70)$$

and

$$\Phi(0.18) = 4.60\ \Phi(2.90) ,$$

respectively, derived from the calculations of the collision density per unit lethargy range for fission neutrons slowed down by hydrogen (only) in an infinite homogeneous medium as made by G. Rowlands.[3]

---

[2] C. H. Hogg, L. D. Weber, and E. C. Yates, *Thermal Neutron Cross Sections of the Co^{58} Isomers and the Effect on Fast Flux Measurements Using Nickel*, IDO-16744 (1962).

[3] G. Rowlands, *The Slowing Down of Fission Neutrons in an Infinite Homogeneous Medium*, AERE-R/R-2695 (1958).

Data obtained in monitoring the C-1 facility showed an unexpected variation of flux with distance from reactor center line. This variation is almost certainly not real, and is probably due to an inadvertent additional irradiation of the flux monitor assembly while withdrawn 18 in. above the original irradiation position. The measurements will be repeated in that facility.

MEASUREMENT OF HIGH TEMPERATURES IN REACTOR ENVIRONMENTS

R. L. Bennett G. W. Keilholtz

Previous reports in this series[4,5] have described testing methods and experimental data obtained from various thermocouple materials in simulated reactor environments. This effort has been effectively terminated during the past year. A study of several thermocouples under simulated Pebble Bed Reactor conditions was concluded, and this work, which has been described elsewhere,[6-8] is summarized very briefly in the following.

Thermocouples in pebble bed reactors would be required to measure temperatures of about 1400°F (760°C) in the gas phase and about 1800°F (982°C) in the graphite pebbles. The coolant gas for PBRE would be helium, at about 300 psi, and this gas would probably contain about 10 to 15 ppm of H_2 and CO.

In these tests, the thermocouple wires were exposed at 760°C and at 980°C to flowing helium (15 psig) containing 500 ppm each of H_2 and CO. The wires were exposed while separated from each other in small holes in 12-in. blocks of AGOT graphite. Samples of each set were removed after 36 and 141 days and were checked at the melting point of zinc (420°C) against platinum standards.

Metals which exhibited 1% or less error in their output against platinum after exposure at 760°C were Chromel-P, Special Chromel-P, Ni-18Mo, Geminol-N, Special Alumel, Inconel, Geminol-P, 50Mo-50Re, tungsten, W-5Re, Pt-10Rh, Pt-30Rh, and Pt-5Mo. No wire remained within 1% accuracy at the higher temperature, but the first five named were within 2% of their original output under all test conditions.

STABILITY OF ALTERNATIVE GASEOUS COOLANTS

R. L. Bennett G. W. Keilholtz

The small, previously described,[9] study of alternative gaseous coolants for nuclear reactors has been continued with reduced emphasis. Major attention during the past year has been given to a literature survey of SO_2 (ref. 10) as a possible coolant and to examination of the radiation stability of CF_4.

Calculation of the products to be expected at high temperatures and pressures shows SO_2 to be quite stable. Newton[11] has calculated that at 1200°F (922°K) and 1300 psi (90 atm) equilibrium would be achieved at 4.2×10^{-5} atm of S_2. Addition of O_2 to bring the SO_3 pressure to 0.01 atm would drop the S_2 pressure to about 3×10^{-12} atm; SO_2 with this quantity of SO_3 should oxidize UO_2 but should prove tolerable if $UO_{2.12}$ were the fuel material.

It seems likely that SO_2 can be managed in structural metals. Cast iron and carbon steel are used to handle hot, dry SO_2. Nickel and Monel are resistant to dry SO_2 at temperatures up to about 300°C. Above this temperature, intergranular attack occurs which results in embrittlement. Inconel is resistant up to about 800°C. However, it has been reported[12] that hot gases containing sulfur oxides destroy the protective film on stainless steels.

---

[4]W. T. Rainey and R. L. Bennett, *Reactor Chem. Div. Ann. Progr. Rept. Jan. 31, 1962*, ORNL-3262, p. 152.

[5]W. T. Rainey, R. L. Bennett, and H. L. Hemphill, *Reactor Chem. Div. Ann. Progr. Rept. Jan. 31, 1963*, ORNL-3417, p. 163.

[6]R. L. Bennett *et al.*, *Stability of Thermoelectric Materials Under PBRE Conditions*, ORNL-TM-746 (January 1964).

[7]*GCRP Semiann. Progr. Rept. Mar. 31, 1963*, ORNL-3445, p. 336.

[8]W. T. Rainey and R. L. Bennett, *ISA (Instr. Soc. Am.) Trans.* **2**(1), 34–38 (1963).

[9]W. T. Rainey, R. L. Bennett, and G. W. Keilholtz, *Reactor Chem. Div. Ann. Progr. Rept. Jan. 31, 1963*, ORNL-3417, p. 170.

[10]R. L. Bennett and G. W. Keilholtz, *Thermal, Radiation and Chemical Stability of Sulfur Dioxide*, ORNL-TM-747 (December 1963).

[11]R. F. Newton, ORNL, personal communication.

[12]*Chem. Eng.* **57**, 157 (1950).

Sulfur dioxide is quite unstable[13] toward carbon at elevated temperatures. A typical gas at equilibrium at 1000°K, for example, would contain about 0.5 atm of CO, 0.3 atm of COS, 0.1 atm of CO_2, 0.1 atm of CS_2, and 4×10^{-8} atm of SO_2. Extensive measurement of the kinetics of the C-SO_2 reaction is sensitive to catalytic impurities and may take place at 500°C.

Although the cracking pattern for SO_2 is known for incident 50-ev electrons,[14] information on the extent of radiolytic damage appears unavailable; the material seems unlikely to be sufficiently stable for use in nuclear reactors.

Samples of gaseous CF_4 have been irradiated, in prefluorinated tubes of nickel, for one to six weeks in Co^{60} gamma radiation. A methane dosimeter indicated an absorbed dose rate of 3.0×10^6 rads/hr. Analysis (by mass spectroscopy) of the resulting gas mixture has revealed that (1) trace contamination with oxygen gas decreases with irradiation time, (2) rate of generation of COF_2 decreases as O_2 is consumed, (3) rate of generation of C_2F_6 increases with irradiation time, and (4) increase in CF_4 pressure decreases yields of all products. The fluorine yields obtained to date are less than those shown by Davidge,[15] who exposed CF_4 to pile irradiation in quartz bulbs.

---

[13] A. Own, K. Sykes, and D. Thomas, *Trans. Faraday Soc.* **47**, 419 (1951).

[14] American Petroleum Institute, *Mass Spectral Tables*, Serial No. 97, Carnegie Inst. of Tech., Pittsburgh.

[15] P. C. Davidge, *The Decomposition of Ammonia and Carbon Tetrafluoride by Pile Irradiation*, AERE-C/R-1569 (December 1955).

16. Equilibrium Studies in the System ThO_2-UO_2-UO_3

L. O. Gilpatrick H. H. Stone C. H. Secoy

An investigation of the identity of phases and equilibrium compositions in the system ThO_2-UO_2-UO_3 in equilibrium with air at 1 atm has been continued. Results reported previously[1,2] indicated that techniques employed had not been adequate, in some cases, in establishing a true equilibrium. Consequently several changes in technique were incorporated into the current work. Foremost among these was the introduction of quench-grind halts during the equilibration period. Samples heated for prolonged periods tend to sinter into more or less compact pellets. Such sintering might well prevent interior molecules from feeling the full effect of the atmospheric oxygen. Therefore, after an initial heating period at the equilibration temperature, samples were cooled rapidly to room temperature and ground in a small tungsten carbide ball mill, an aliquot removed for chemical analysis, and the remainder returned to the furnace for another period at the equilibration temperature. This process was repeated until the sample was exhausted or until it showed no further change in composition.

Samples were prepared by ball-milling appropriate mixtures of ThO_2, $UO_{2.14}$, and UO_3 or U_3O_8. The oxygen content was varied all the way from essentially stoichiometric ThO_2-UO_2, solid solutions or mixtures, to the maximum attainable by using UO_3 to supply the uranium content of the sample. In no case did the equilibrium data show any correlation with the oxygen content of the starting material, nor did the results show any significant difference depending on the use of UO_2, U_3O_8, or UO_3 to supply the uranium content.

Although the quench-grind technique served to eliminate problems of reaching an equilibrium state, it also eliminated the usefulness of metallographic and microscopic techniques in identifying phases because of the reduction of crystals to very small sizes and fragmentary shapes. X-ray powder patterns were frequently employed to confirm the number and identity of phases. No effort was made to determine lattice parameters. However, the major burden of the evidence used in establishing the deductions concerning the phase equilibria falls on the chemical analysis of the equilibrated samples.

The current study was confined to a temperature range from 700°C (above the U_3O_8-to-UO_3 transition temperature, <600°C) to 1600°C (above the U_3O_8-to-UO_{2+x} transition at ~1525°C). In this range nine isotherms have been obtained, at 700, 900, 980, 1200, 1400, 1450, 1475, 1500, and 1600°C. The ThO_2 content was limited to values of its mole fraction from 0 to 0.6. Thus this study was confined to the temperature region and compositions encompassing that portion of the phase diagram involving equilibria between the cubic solid-solution phase and the orthorhombic U_3O_{8-y} phase at an oxygen pressure of 0.2 atm.

The data obtained at 900, 1200, and 1475°C are displayed graphically in Figs. 16.1, 16.2, and 16.3 respectively. These figures will serve to illustrate the discussion, although the data at any of the other temperatures would do equally well.

Composition points representing samples containing the two phases, the cubic solid solution

[1] H. A. Friedman and R. E. Thoma, *Reactor Chem. Div. Ann. Progr. Rept. Jan. 31, 1963*, ORNL-3417, pp. 130–34.

[2] L. O. Gilpatrick, H. H. Stone, and C. H. Secoy, *Reactor Chem. Div. Ann. Progr. Rept. Jan. 31, 1963*, ORNL-3417, pp. 134–39.

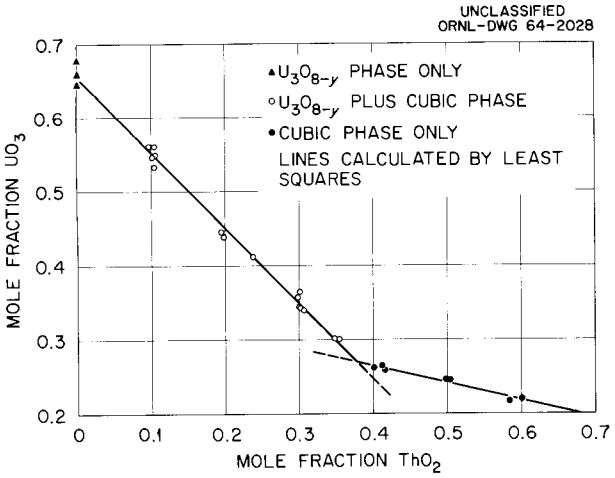

Fig. 16.1. 900°C Isotherm for the System ThO_2-UO_2-UO_3 at P_{O_2} = 0.2 atm.

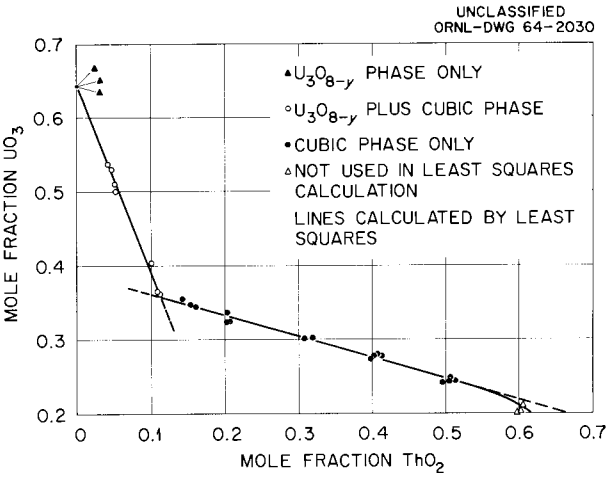

Fig. 16.3. 1475°C Isotherm for the System ThO_2-UO_2-UO_3 at P_{O_2} = 0.2 atm.

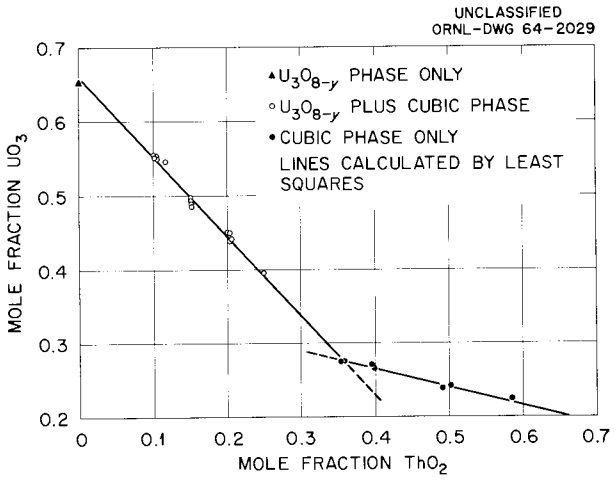

Fig. 16.2. 1200°C Isotherm for the System ThO_2-UO_2-UO_3 at P_{O_2} = 0.2 atm.

and U_3O_{8-y}, should lie on a straight line connecting the respective phase compositions. These points are, therefore, amenable to analytical expression in a linear equation of the form

$$X_{UO_3} = a_0 - a_1 X_{ThO_2} . \quad (1)$$

The constants of this equation have been evaluated from the data by the least-squares method. Values for these constants, along with the number of data points used and the standard error of estimate at each temperature, are given in Table 16.1. It should be noted that the a_0 values represent X_{UO_3} at X_{ThO_2} = 0 and therefore represent the composition of the U_3O_{8-y} phase. These values are listed again in Table 16.3 for comparison with the mean values obtained from individual experiments with samples containing no ThO_2. They are also shown graphically as a function of temperature in the top curve of Fig. 16.6.

The parameter a_1, representing the negative slopes of the tie lines, increases only slightly from 700 to 1200°C but increases more rapidly at higher temperatures, approaching infinity at the temperature of the U_3O_{8-y}-to-UO_{2+x} transition (about 1525°C).

Points obtained at each temperature from samples in which only the cubic solid-solution phase was present should lie along one of a family of curves, each representing an isothermal isobar. In a three-dimensional temperature-composition model these curves are the lines of intersection of an isobaric surface (P_{O_2} = 0.2 atm) with constant-temperature planes.

Detailed examination of these one-phase data points indicated two major conclusions. First, the experimental scatter of points in the vicinity of a fixed value of X_{ThO_2} is too great for any pattern of temperature dependence to be apparent. Second, if only points representing samples containing less than about 0.6 mole fraction of ThO_2

Table 16.1. Least-Squares Parameters for the Two-Phase Tie Lines

$$X_{UO_3} = a_0 - a_1 X_{ThO_2}$$

Temperature (°C)	Number of Data Points	a_0	a_1	Standard Error of Estimate
700	18	0.6601	1.0149	0.0041
900	18	0.6565	1.0228	0.0102
980	10	0.6570	1.0272	0.0074
1200	17	0.6610	1.0785	0.0072
1400	13	0.6512	1.3667	0.0075
1450	16	0.6452	1.7664	0.0074
1475	10	0.6434	2.5076	0.0069
1500	2	0.6422	4.0958	

are considered (at the high temperatures, less than about 0.5 mole fraction ThO_2), no curvature is apparent. This linearity is illustrated by the data points and lower straight line segments in Figs. 16.1, 16.2, and 16.3. Figure 16.3, in particular, shows the linearity up to $X_{ThO_2} = 0.5$ and the start of curvature at 0.6. The overall pattern of the phase diagram is illustrated in Fig. 16.4, in which several isotherms are shown. This diagram should not be construed as accurate insofar as the temperature dependence of the one-phase isobars is concerned. This family of curves does seem to fall entirely within the indicated band. They may actually cross each other within the band.

The coincidental linearity of the one-phase data permits its expression over the appropriate region in analytical form. Values of the parameters obtained by least-squares calculation at each temperature are given in Table 16.2. Although the variation with temperature of the constants, b_0 and b_1, may not be significant, it is considerably larger than the standard error of estimate. Therefore, on a statistical basis, these equations may give an indication of the effect of temperature on the oxygen content of the solid solutions at a fixed mole fraction of thoria. To illustrate, Fig. 16.5 displays the calculated values at $X_{ThO_2} = 0.5$. The

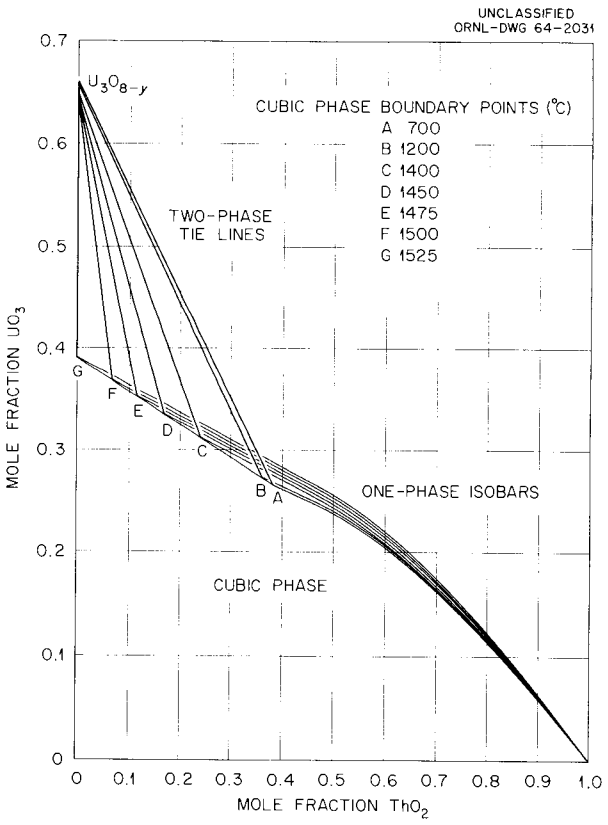

Fig. 16.4. Projection of Isotherms on the Composition Plane for the System ThO_2-UO_2-UO_3.

Table 16.2. Least-Squares Parameters for the One-Phase Isobars

$$X_{UO_3} = b_0 - b_1 X_{ThO_2} \quad (X_{ThO_2} < 0.6)$$

Temperature (°C)	Number of Data Points	b_0	b_1	Standard Error of Estimate
700	7	0.3699	0.2566	0.0012
900	7	0.3578	0.2321	0.0034
980	6	0.3578	0.2417	0.0026
1200	7	0.3576	0.2324	0.0034
1400	4	0.3623	0.2224	0.0057
1450	11	0.3804	0.2538	0.0041
1475	16	0.3905	0.2877	0.0052
1500	17	0.3829	0.2728	0.0069
1600	8	0.3797	0.2485	0.0089

Table 16.3. Phase Boundary Compositions

Temperature (°C)	Cubic Phase			U_3O_{8-y} Phase	
	X_{ThO_2}	X_{UO_3}	X_{UO_2}	X_{UO_3} [a]	$X_{UO_3} = a_0$ [b]
700	0.3827	0.2716	0.3457	0.6618 (3)	0.6601
900	0.3778	0.2701	0.3521	0.6615 (3)	0.6565
980	0.3809	0.2657	0.3534	0.6567 (2)	0.6570
1200	0.3586	0.2743	0.3671	0.6548 (1)	0.6610
1400	0.2525	0.3061	0.4414	0.6470 (5)	0.6512
1450	0.1750	0.3344	0.4906	0.6454 (7)	0.6452
1475	0.1139	0.3578	0.5283	0.6447 (3)	0.6434
1500	0.0678	0.3645	0.5677		0.6422
1525[c]	0[c]	0.4[c]	0.6[c]		0.642[c]

[a] Mean experimental; numbers in parentheses are the number of values averaged.

[b] Calculated.

[c] Extrapolated values.

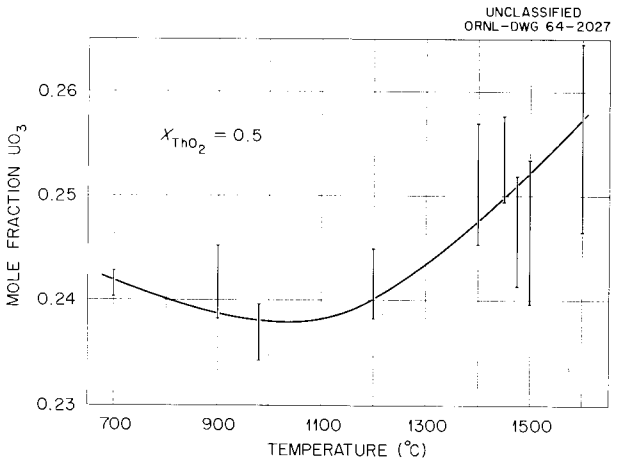

Fig. 16.5. Temperature Dependence of the Oxygen Content of the Cubic Phase at $X_{ThO_2} = 0.5$.

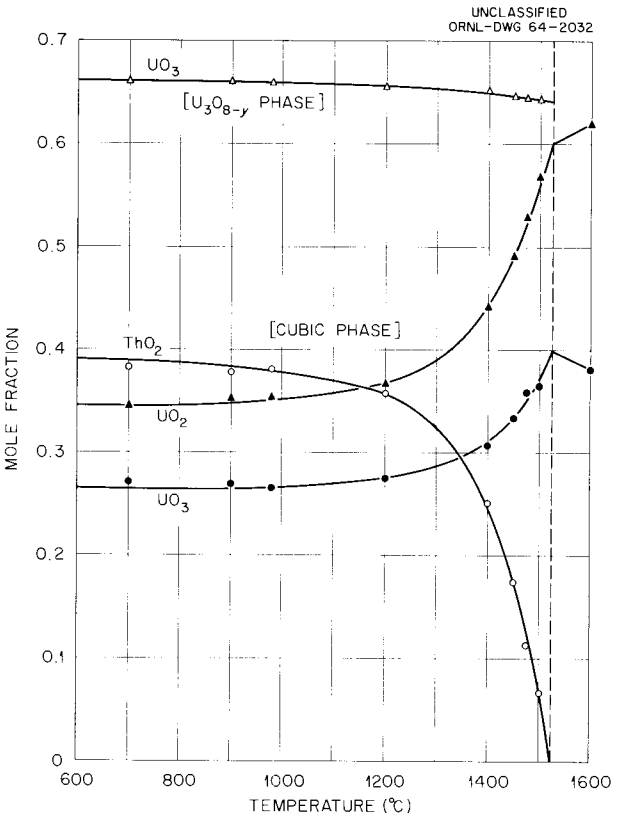

Fig. 16.6. Boundary Compositions for the Cubic and U_3O_{8-y} Phases.

length of the bars is equal to twice the standard error. It is possible to draw a smooth curve intersecting all bars. The curve indicates a slight decrease in oxygen content with increasing temperature from 700 to about 1050°C, followed by an increase at higher temperatures. If this portrayal is correct the isotherms of Fig. 16.4 do indeed cross each other.

Simultaneous solution of the corresponding equations of Tables 16.1 and 16.2 evaluates the points of intersection of these lines. These points are points on the limiting phase boundary surface for the solid-solution phase. At each temperature they represent the composition of the cubic phase in equilibrium with the corresponding U_3O_{8-y} composition. Calculated values of the boundary points are given in Table 16.3 and displayed graphically in Fig. 16.6. The composition of the cubic phase remains nearly constant to temperatures above 1200°C and changes rapidly as the U_3O_{8-y}-to-UO_{2+x} transition temperature (1525°C) is approached. The maximum oxygen content is apparently reached at this transition with $X_{UO_3} \simeq 0.4$. This result is somewhat surprising, in that most studies of the U-O system have indicated this maximum to be nearer 0.3 ($UO_{2.3}$). We have obtained one value at 1600°C of $UO_{2.381}$ which is in agreement with the maximum of about $UO_{2.4}$. This may be a reflection of the fact that we have used finely powdered material while other studies have usually involved pellets. The resolution of this question will require further experimentation. However, the power of studying an $(n + 1)$-component system to elucidate a fact about an n-component subsidiary system is illustrated.

It is of interest to note that the composition of the cubic phase at the low-temperature end, as one approaches the U_3O_8-to-UO_3 transition (<600°C), is very near $X_{ThO_2} = 0.4$ and $X_{UO_3} = 0.267$. This is a stoichiometry represented by $6ThO_2 \cdot 5UO_2 \cdot 4UO_3$. One wonders whether or not this unit has any structural significance.

The chemical analyses involved in this work were performed by the Analytical Chemistry Division group under W. R. Laing. Their help is gratefully acknowledged.

Part IV
Nuclear Safety

17. Fission Products Released by Nonnuclear Heating of Fuel Materials

G. W. Parker W. J. Martin G. E. Creek
R. A. Lorenz C. J. Barton

For a number of years, a substantial part of the ORNL Nuclear Safety Program has been devoted to parametric studies[1] of the release of fission products by nonnuclear heating of reactor fuels. Due in part to these studies, certain useful generalizations[2] can be made concerning the fractional release of the various fission products from aluminum-uranium alloys and from clad uranium dioxide as a function of the experimental conditions.

Evaluation of mechanisms that lessen the severity of reactor accidents represents a logical extension of these fission product release studies. These mechanisms include agglomeration in, and deposition of particles from, aerosols produced by overheated reactor fuels and chemical reactions of the fission products with structural materials. Filtration and sorption characteristics of various fractions of the aerosols also form an important part of the studies. Accordingly, irradiated reactor fuels continue to be melted both to study fractional release and to serve as a source of fission products; major emphasis is placed on the study of the behavior of fission product aerosols.

LABORATORY-SCALE RELEASE FROM ALUMINUM-URANIUM ALLOYS

Effect of Burnup Level

The effect of several parameters on fission product release from aluminum-uranium alloy specimens irradiated either to contain traces of fission products or to nearly 24% burnup was given in a previous report.[3] This document presents data on the burnup effect to intermediate levels of irradiation, 3.2 and 9.0% burnup.

Figure 17.1 shows the effect of burnup as measured in laboratory-scale equipment with small specimens melted in a flowing air stream. The data at the lower temperatures generally show that fuels irradiated to high burnup release a larger (by three- or fourfold) fraction of the iodine and rare gases than do lightly irradiated material. The fraction of cesium released from the 23.6%-burnup material is about twofold above the release value at tracer level. The data on ruthenium suggest a positive effect of burnup, but the fraction released is quite small in any case. In general, it appears that this effect of fuel burnup on fractional release is relatively small.

TRANSPORT BEHAVIOR IN THE HOT-CELL CONFINEMENT MOCKUP FACILITY

The Hot-Cell Confinement Mockup Facility,[4] shown schematically in Fig. 17.2, is a versatile tool for the study of fission product release and transport behavior under realistic reactor accident

[1] G. W. Parker *et al.*, *Nuclear Safety Program Semiann. Progr. Rept. June 30, 1962*, ORNL-3319, pp. 11–29; *Nuclear Safety Program Semiann. Progr. Rept. Dec. 31, 1962*, ORNL-3401, pp. 5–27; *Nuclear Safety Program Semiann. Progr. Rept. June 30, 1963*, ORNL-3483, pp. 9–20.

[2] F. R. Bruce, "Status of Nuclear Safety Research and Development at the Oak Ridge National Laboratory," paper presented at the Atomic Industrial Forum Annual Conference, New York, Nov. 18–21, 1963.

[3] G. W. Parker *et al.*, *Nuclear Safety Program Semiann. Progr. Rept. June 30, 1963*, ORNL-3483, pp. 9–12.

[4] G. W. Parker, G. E. Creek, and W. J. Martin, *Nuclear Safety Program Semiann. Progr. Rept. June 30, 1963*, ORNL-3483, p. 33.

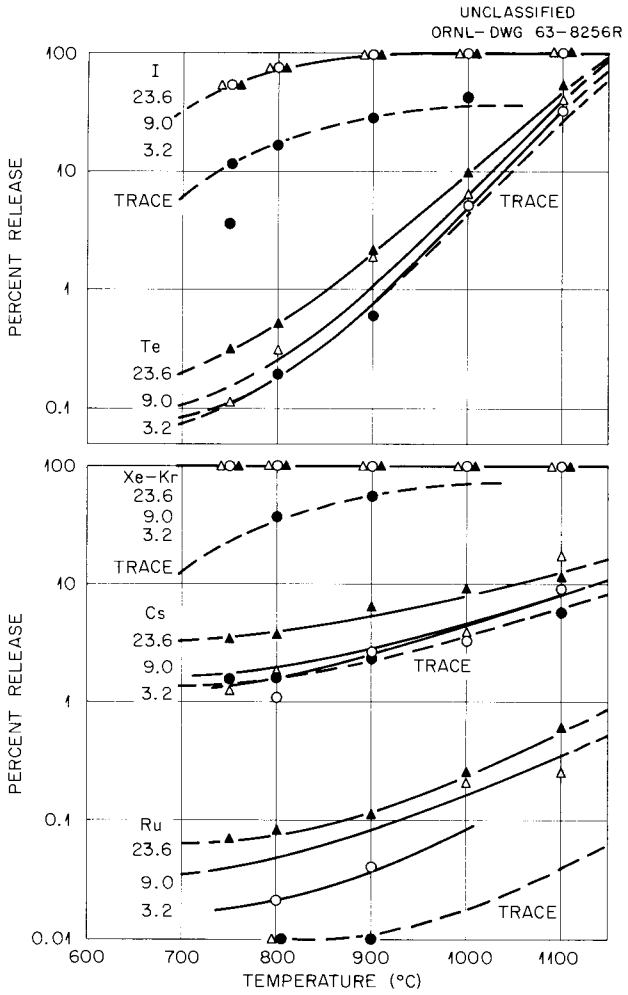

Fig. 17.1. Effect of Burnup and Temperature on Fission Product Release from Aluminum-Uranium Alloy Melted in Air.

conditions. Fission products released from irradiated fuels melted in air, steam, or air-steam mixtures pass into a 180-liter stainless steel tank that simulates the confinement shell of a reactor. Samples of the aerosol in the tank can be removed at intervals for determinations of rates of deposition of fission products as a function of time, atmosphere, and other parameters. After aging in the tank, the aerosol is pulled through a series of filters and charcoal traps, as described below, to permit a more thorough study of the aerosol and for tests of the efficiency of confinement system components. Location of this facility in a hot cell will permit use of fairly large quantities of high-burnup fuel materials.

Fission Products from Stainless-Steel-Clad UO_2 Melted in Air

Trace-level-irradiated (10^{17} *nvt*), stainless-steel-clad UO_2 specimens containing about 30 g of UO_2 were held in zirconia crucibles, and a copper conduction coil surrounding the furnace tube was connected to a 25-kw high-frequency (5-kc) power source. This heating method was employed with UO_2 fuels in place of the resistance furnace shown in Fig. 17.2, which was used with lower melting aluminum-uranium fuels, as described below.

Agglomeration, sedimentation, and deposition of the released fission products occurred in various sections of the equipment, as shown by the distribution of activity given in Table 17.1. The high stability of the aerosol is apparent from the high values (19 to 50%) of the released activity, which remained airborne approximately 1.5 hr. The relatively low deposition of iodine (55%) and tellurium (30%) on the walls of the confinement vessel may possibly be due to the very low (tracer-level) concentrations of fission products in the aerosol product in this experiment.

Cesium and Iodine from Aluminum-Uranium Alloy

Data on the distribution of cesium and iodine released from high-burnup aluminum-uranium alloy specimens heated in cell air or in air mixed with steam are given in Table 17.2. It was found that iodine deposited more extensively on dry stainless steel surfaces than on the same surfaces saturated with steam, but the reverse was found true for cesium, indicating that cesium iodide was not an important component of the aerosol formed in these experiments. For the period of aging used in the tests (45 min), deposition was found to be relatively ineffective in reducing the concentration of the total radioactivity in the confinement tank. A reduction factor of 2 to 5 for iodine was observed, but of less than 2 for cesium, tellurium, and ruthenium.

An adaptation of the May pack[5] incorporating diffusion-channel ports between stages of the filter unit is shown in Fig. 17.3. Equipment of

[5]W. J. Megaw and F. G. May, *Reactor Sci. Technol.* 16, 427–36 (1962).

this type was used to study the distribution of aerosol activity released from molten fuels as a function of particle size.

Typical data obtained by use of the modified May pack with fission products released by melting aluminum-uranium alloy fuel are displayed in Fig. 17.4. A portion of the unfiltered air from the aerosol tank was drawn through a 10-ft length of $\frac{3}{8}$-in.-diam, silver-plated copper tubing. The effluent air from the tube passed through a membrane filter and a $\frac{3}{4}$-in. bed of charcoal. After the experiment

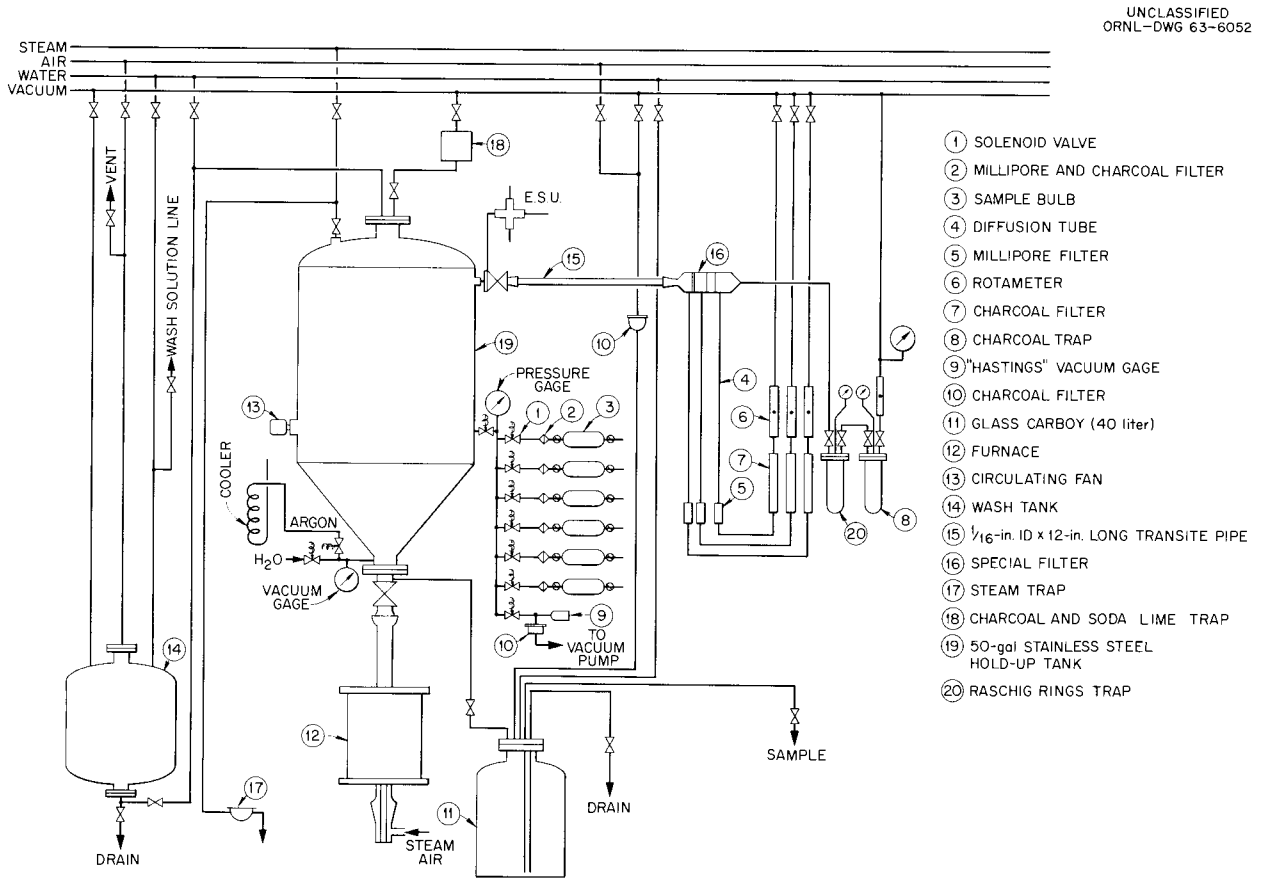

Fig. 17.2. Schematic Diagram of Hot-Cell Confinement Mockup Equipment.

Table 17.1. Distribution of Activity Released by Melting Trace-Level-Irradiated UO_2

Location of Activity	Released Material Retained (%)				
	Iodine	Tellurium	Cesium	Ruthenium	Uranium
Furnace tube	7.8	20.1	11	46.9	
Aerosol tank	56.5	30.5	70	32.4	84.4
Filter pack	35.5	49.4[a]	19.0[a]	20.7[a]	15.6[a]
Backup traps	0.2				

[a]All the activity was found in the filters, and a large fraction of it was in the roughing filters.

Table 17.2. Distribution of Iodine and Cesium Released from Molten Aluminum-Uranium Alloy

Location of Activity	Percent of Released Material Retained in Each Location			
	Iodine		Cesium	
	Dry Air	Moist Air	Dry Air	Moist Air
Furnace tube	1.8	3.9	45.8	32.5
Aerosol tank	82.0	48.1	17.3	29.4
Steam condensate (30 ml)		6.7		5.9
Transite pipe (12 in. long)	1.2	3.1	0.06	0.2
Filters	6.9	8.9	36.9	32.1
Charcoal beds	8.0	29.2	0	0

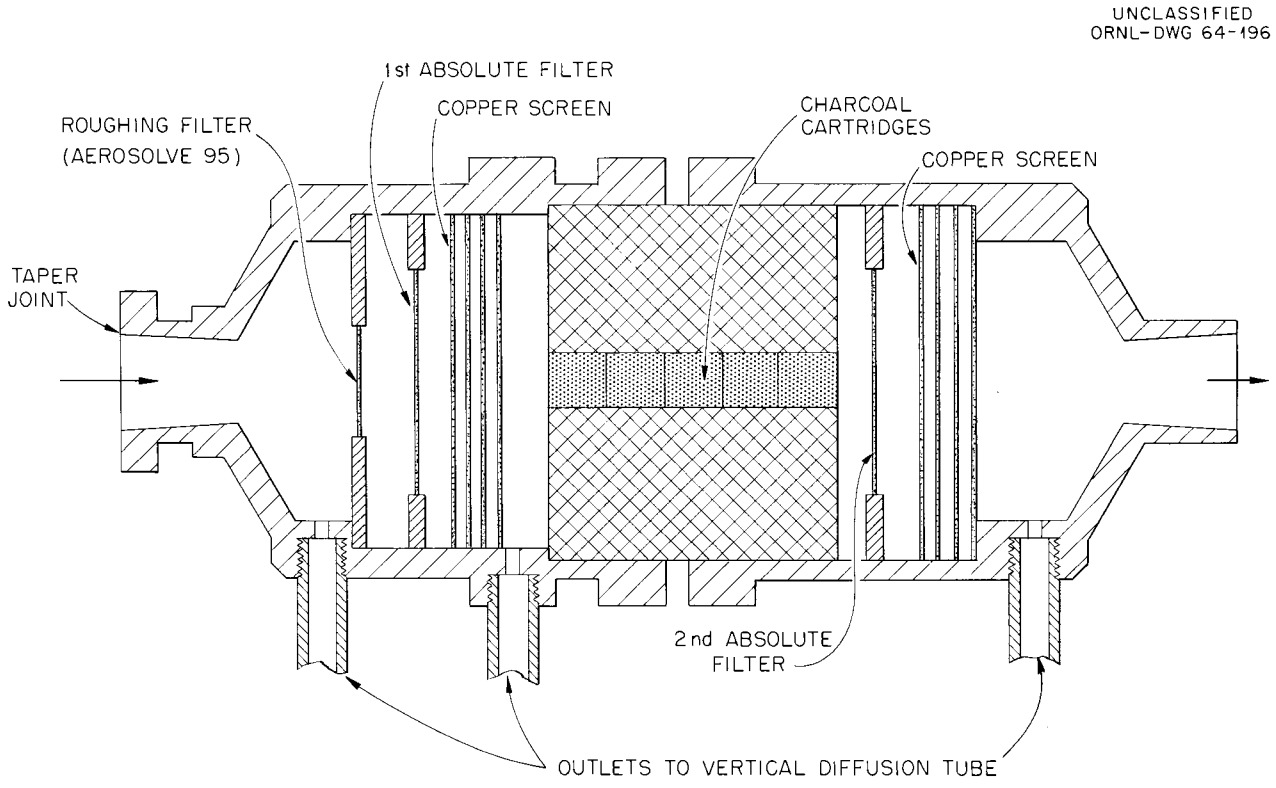

Fig. 17.3. ORNL Modification of the May Pack.

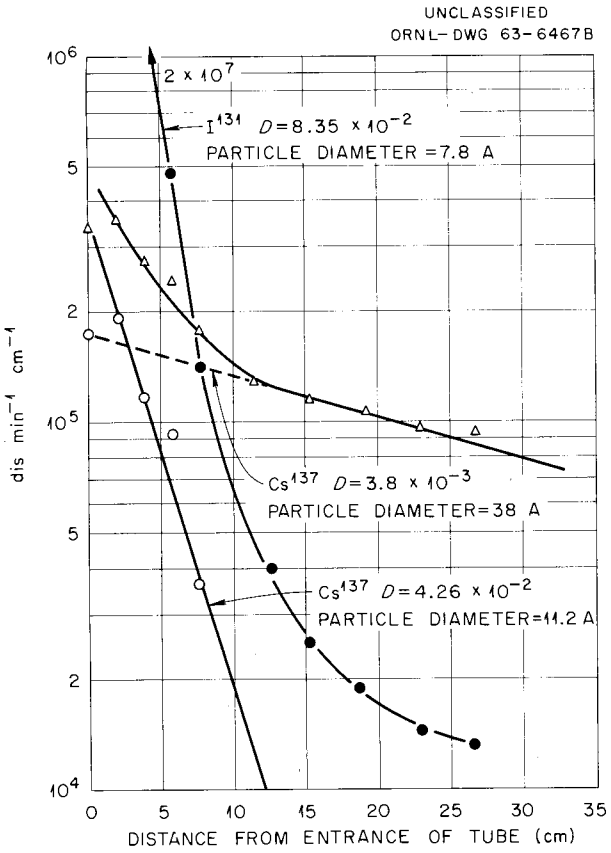

Fig. 17.4. Diffusion-Tube Data Obtained with Unfiltered Gas from Aluminum-Uranium Alloy Melted in Moist Air.

was concluded, the tube was cut into short sections. Deposition gradients, from which particle sizes were calculated by use of the Browning and Ackley adaptation[6] of the Gormley and Kennedy equation,[7] were obtained by radiochemical determinations of material deposited at known distances from the entrance end of the tube. It was thus possible to correlate sizes of particles that deposited in the diffusion tubes with type of activity. A similar test of air sampled after passing it through filters showed that the filters had little effect on particle distribution.

[6]W. E. Browning, Jr., and R. D. Ackley, *Nuclear Safety Program Semiann. Progr. Rept. Dec. 31, 1962*, ORNL-3401, p. 44.

[7]P. G. Gormley and M. Kennedy, *Proc. Roy. Irish Acad., Sect. A* 52, 163 (1949).

Diffusion-tube data shown in Fig. 17.4 indicate that cesium activity in unfiltered air was associated with particles of two sizes, 11 and 38 A, while a large fraction of the iodine exhibited a particle diameter of 7.8 A, indicating that it was molecular iodine. The iodine data also show minor indications of larger particles. A summary of the different particle sizes observed and their percentage of the total iodine activity is given in Table 17.3, along with similar data obtained in the UO_2 melting experiment discussed below.

Comparison of the ratio of iodine and cesium activity deposited from unfiltered moist air on the wall of the first diffusion tube with the theoretical ratio for cesium iodide showed that very little of this compound could have been deposited from the air sample passing through the tube. An upper limit of 7% of the iodine in the aerosol that could have been present as the compound was set by the amount of iodine found in the exit filter.

Radioiodine Released from Stainless-Steel-Clad UO_2

Iodine was the only type of activity found in the diffusion tubes under the conditions employed in the UO_2 melting experiment. Diffusion-tube data on unfiltered air removed from the aerosol tank after the aging period are presented in Fig. 17.5 and Table 17.3. One difference between the conditions employed in the UO_2 melting experiment and those used in the aluminum-uranium alloy melting experiment should be noted, namely, the use of bronze screens in the former case to remove molecular iodine. In both instances the aerosol passed through roughing and absolute filters before being sampled by the side stream passing through the second diffusion tube. This treatment presumably would remove most of the particles 0.1 μ and larger, but very little of the molecular iodine. A distinct surprise was noted in the UO_2 experiment, where a large part of the iodine activity stopped on the roughing filter. This anomaly is possibly an effect of trace concentration. The roughing filter, which includes two organic-bonded glass screens and a thick bed of mineral fiber, may have sufficient surface reactivity to pick up a large fraction of iodine activity when present at trace concentration. The air sampled by the second diffusion tube in the

Table 17.3. Distribution of Released Radioiodine Between Molecular and Particulate Forms

Distribution of Radioiodine	Diffusion Tube Number	Calculated Diameter of Particle (A)	Distribution of Radioiodine in the Aerosol, Each Size[a] (%)	Percent of Iodine Inventory in Fuel Represented by Each Size
Aluminum-Uranium Alloy (23.6% Burnup), Melted in Steam-Air Atmosphere				
Before filtration	1	7.8 (molecular)	94.6	17.3
		26	5.4	1.0
After filtration	2	11 (molecular)	98.1	14.5
		200[b] (and greater)	1.9	0.3
Trace-Irradiated Stainless-Steel-Clad UO_2, Melted in Air				
Before filtration	1	12 (molecular)	80.2	19.5
		24	14.4	3.5
		108[c] (and greater)	5.4	1.3
After filtration	2[d]	11 (molecular)	75.2	8.7
		18	21.9	2.5
		64[e] (and greater)	2.9	0.5

[a]Calculated from area under deposition rate lines for each particle size.

[b]Theoretical retention in diffusion tube of 300 cm length is 24%.

[c]Theoretical retention in diffusion tube of 300 cm length is 55%.

[d]Preceded by bronze screens to remove molecular iodine.

[e]Theoretical retention in diffusion tube of 300 cm length is 79%.

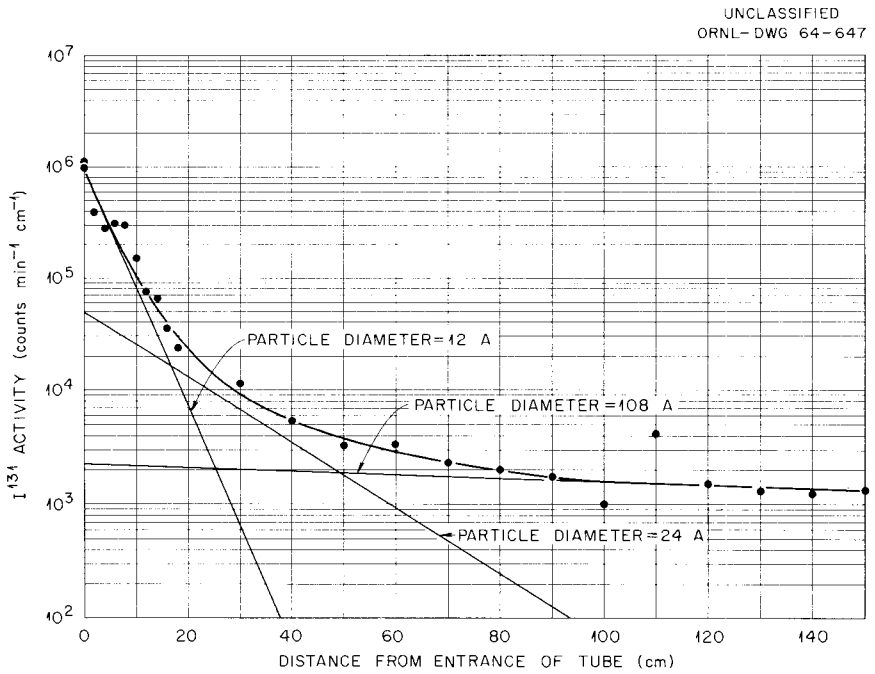

Fig. 17.5. Diffusion-Tube Data Obtained with Unfiltered Gas from Stainless-Steel-Clad UO_2 Melted in Air.

UO_2 melting experiment, as mentioned above, had passed through four thicknesses of bronze filter media in addition to the two filters, but this material removed only a fraction of the molecular iodine from the aerosol stream. Comparison of the diffusion-tube data from the UO_2 melting test, Fig. 17.5, with those obtained in the aluminum-uranium experiment shows a more complex particle spectrum in the UO_2 experiment.

PARTICLES PRODUCED BY MELTING IRRADIATED FUEL MATERIALS

Particles remaining airborne after a 45-min or longer aging period in the aerosol tank were collected on absolute filters, on an electron microscope grid of an electrostatic precipitator, and on walls of diffusion tubes. The same collection methods were employed in the aluminum-uranium and UO_2 melting experiments.

Particles from Melted Aluminum-Uranium Alloy

Particles resulting from the melting of the aluminum-uranium alloy material in a steam-air atmosphere and collected by an electrostatic precipitator from a side stream immediately after leaving the aerosol tank were measured by means of an electron microscope photograph. The smallest particles were approximately 150 A in diameter, while the larger ones had an average diameter of about 1500 A. Particles remaining in a portion of the effluent stream from the aerosol tank after passing through a 10-ft-long diffusion tube were collected on a membrane filter, and they ranged in diameter from about 0.05 to 3.0 μ. The large particles undoubtedly were agglomerates of smaller particles. Cesium was the only radioisotope found on the filters.

Particles from Melted Stainless-Steel-Clad UO_2

A sample of the aerosol was withdrawn from the stainless steel tank about 1 hr after melting of a trace-level-irradiated, stainless-steel-clad UO_2 specimen. Particles collected by passing the aerosol through a membrane included the usual wafer-like agglomerates, which were identified by their diffraction pattern as FeO. Sizes ranged from 0.1 to 1.0 μ. After 2 hr of aging, the aerosol, when sampled electrostatically, showed a large abundance of particles in the 100- to 200-A size range and a few 1- to 2-μ-diam particles.

MELTING OF UO_2 FUEL PINS BY CENTERED TUNGSTEN RESISTORS

Realistic simulation of reactor loss-of-coolant accidents has been approached on a small scale in out-of-pile experiments by melting irradiated UO_2 pellets with centered tungsten resistors. This experimental technique has progressed from the initial arrangement for melting a single fuel pin of three UO_2 pellets[8] to an apparatus for melting a cluster of seven fuel pins consisting of four UO_2 pellets each.[9] With a cluster of pins, the center pin is heated to a higher temperature than the outer pins, thus simulating a reactor loss-of-coolant accident with melted fuel in the center area and with heated, but unmelted, fuel toward the outer portions of the reactor core.

Two experiments were performed with unclad UO_2 fuel pins weighing 52 g each and arranged in a seven-pin cluster with the center pin irradiated at the tracer level and then melted in purified helium to obtain fission product release data. In one experiment, 28% of the center pin melted, and in the other 90% of the center pin melted, based on 28 and 90% release of Xe^{133} from the fuel. Release of fission products from these arrangements was approximately one-half that from similar melting tests previously reported, where single unclad UO_2 fuel pins were melted. The deposit of fission products on the outer, unirradiated fuel pins did not account completely for the difference in release from the seven- and one-pin experiments. The release data shown in Table 17.4 were corrected to 100% melting by direct proportion. These data show that 6 to 10% of the I, Te, and Cs was carried to the filter in the sample system and that less than 0.03% of the Ru, Sr, Ba, Ce, and UO_2 was on the filter. Comparable data from single-pin experiments are included for comparison.

---

[8] G. W. Parker and R. A. Lorenz, *Reactor Chem. Div. Ann. Progr. Rept. Jan. 31, 1963*, ORNL-3417, p. 226.

[9] G. W. Parker and R. A. Lorenz, *Nuclear Safety Program Semiann. Progr. Rept. June 30, 1963*, ORNL-3483, p. 14.

A third experiment with the seven-pin cluster arrangement employed pins composed of three UO_2 pellets and was constructed so that the helium sweep gas traversed a path providing longer and closer contact with the shields and base plate before leaving the furnace. The amount of I, Te, and Cs transported to the filter in this experiment was a factor of 10 less than with the other two cluster experiments, in which a direct gas path was available.

Equipment is being designed to utilize larger fuel clusters and high-burnup fuel.

Table 17.4. Release from Bare UO_2 Fuel Pins Corrected to 100% Melting

Release Zone	Experiment Type	Release (%)							
		UO_2[a]	I	Te	Cs	Ru	Sr	Ba	Ce
Total release from fuel cluster	1-pin[b]	0.81	70	90	82[c]	1.1	2.5	9.0	<1.0
	7-pin[d]	3.1	60	45	37	6.3	1.1	1.9	0.12
Deposit on outer fuel pins	7-pin[d]		4.6	1.5		12		2.1	0.7
Transported release (gas tube, filter, charcoal)	1-pin[c]	0.003	52	40	31	<0.05	0.01	0.03	<0.1
	7-pin[d]	0.0002	28	13	19	<0.07	<0.0014	<0.0033	<0.002
	7-pin, restricted gas channel[e]	0.0003	1.5	0.67	<3.1				
Transported release to filter and charcoal	1-pin[b]	0.0008	25	17	21	<0.05	<0.003	<0.01	<0.004
	7-pin[d]	0.0001	9.4	6.3	9.8	<0.03	0.0007	<0.0003	<0.001
	7-pin, restricted gas channel[e]	0.00003	0.53	<0.21	<1.2				

[a]Based on UO_2 in center irradiated pin; all irradiations were trace level (10^{14} fissions per gram of UO_2).

[b]Average of three experiments, three-pellet pin (39 g of UO_2), 360 cc(STP)/min purified helium, 0.67 fpm (2.9 volume changes per min) in furnace at 25°C.

[c]Data from one experiment in note (*b*).

[d]Average of two experiments, four-pellet pins (52 g of UO_2), 450 cc(STP)/min purified helium, 0.43 fpm (1.5 volume changes per min) in furnace at 25°C.

[e]One experiment, three-pellet pins (39 g of UO_2), 450 cc(STP)/min purified helium, 0.43 fpm (1.9 volume changes per min) in furnace at 25°C.

18. Fission Products Released During In-Pile Destruction of Reactor Fuels

W. E. Browning, Jr. C. E. Miller, Jr. B. F. Roberts
R. P. Shields W. H. Montgomery

In-pile experiments of the type previously described[1] are being continued to study the amounts and the behavior of fission products released during simulated loss-of-coolant reactor accidents. In most of these experiments, miniature stainless-steel-clad UO_2 fuel elements have been melted or vaporized in a helium atmosphere in the ORR. In addition, in a few experiments, uranium carbide–graphite fuel specimens have been burned in flowing air. Studies have been made of the effects of gas velocity on fission product release and behavior, of the fine-particle and vapor forms of released fission products, of the particulate material collected by filters, of the distribution of released fission products, and of the fractionation of fission products. These studies are described in separate sections below.

A monitor to survey the neutron and gamma fluxes throughout the reactor cycle has been installed in the fuel melting facility. This device was made by replacing the fuel in a fuel-melting experimental unit with a chamber through which argon gas can be passed; activation of the argon is measured to determine the neutron flux. The temperatures of the ceramic parts of the unit indicate the intensity of gamma heating. These measurements will assist in the control of the intensity of heating in the in-pile experiments, a factor which has been found to have a strong effect on fission product release. The off-gas system of the in-pile facility has been modified to accommodate the flux monitor and to permit transfer of the released gaseous fission products from the liquid-nitrogen-cooled charcoal trap to a reservoir where samples can be taken without removing the charcoal trap from the shielded enclosure.

IN-PILE BURNING OF URANIUM CARBIDE–GRAPHITE FUEL

Three experiments were conducted in the ORR in which fuel specimens composed of pyrolytic-carbon-coated uranium carbide particles and graphite matrix were burned at temperatures up to approximately 1400°C. In these experiments, fission and gamma heat produced a sufficiently high temperature for a large portion of the fuel to burn during the 15-min period in which air was supplied as the sweep gas. The specimens were preheated and cooled in helium. The method of performing the experiments and the results of the first experiment were described previously.[2] Specifications for the specimens and the experimental conditions are listed in Table 18.1.

As the graphite matrix burned, some of the fuel particles fell away from the unburned fuel. Metallographic examination of these particles and those in the unburned fuel showed that the damage to

[1] W. E. Browning, Jr., *et al.*, *Reactor Chem. Div. Ann. Progr. Rept. Jan. 31, 1961*, ORNL-3127, pp. 149–52; *Reactor Chem. Div. Ann. Progr. Rept. Jan. 31, 1962*, ORNL-3262, pp. 172–76; *Reactor Chem. Div. Ann. Progr. Rept. Jan. 31, 1963*, ORNL-3417, pp. 236–43.

[2] W. E. Browning, Jr., *et al.*, *Reactor Chem. Div. Ann. Progr. Rept. Jan. 31, 1963*, ORNL-3417, pp. 240–41.

Table 18.1. Fuel Specifications and Experimental Conditions for Graphite Fuel Burning Experiments

Fuel Specifications	
Particles	Uranium carbide spheres 175 to 250 μ in diameter Laminar pyrolytic-carbon coating 75 to 100 μ thick
Matrix	Graphite
Manufacturer	Minnesota Mining and Manufacturing Company
Dimensions	0.6-in. bushing, 0.5 in. long with 0.25-in. axial hole
Uranium content	8 to 10 wt % natural uranium
Experimental Conditions	
Initial temperature	890°C
Combustion temperature	Up to 1400°C
Air flow rate	400 cm^3/min
Burning duration	15 min

particles ranged from none to complete destruction of the coating and oxidation of the uranium carbide; however, it was not possible to determine the percentage of particles which belong in these categories. Some of the particles which remained in the unburned fuel also showed cracks. In experiment G-1 a count of the damaged and undamaged particles by scanning all the exposed surface of the fuel showed that about 45% of the particles had at least one crack in the coating.

The results of experiment G-3, for the most part, confirmed the conclusions from experiment G-1. In the first experiment,[2,3] 58% of the specimen burned, as compared with 41% in the third. Low uranium content of the fuel specimen in the second experiment resulted in low fuel temperature and oxidation of a small fraction of the specimen. Only a few analyses were performed in this experiment. In the third experiment, most of the uranium carbide in the specimen was concentrated on one side, and this side burned very little; 93% of the uranium was in the unburned fuel.

Fission product release data are shown in Table 18.2. The results of experiment G-1, previously reported,[2] are included for comparison. A large fraction of the less-volatile fission products was probably retained inside those particles having undamaged pyrolytic-carbon coatings, especially those in the unburned fuel. The release of Sr, Zr, Ba, Ce, and U from the high-temperature zone of the furnace was very low, but large fractions of I, Te, and Cs were released. Forty percent of the ruthenium was released from the furnace in experiment G-1 and 5.7% in experiment G-3. The high release of ruthenium in the first experiment was probably due to the formation of volatile oxides resulting from the oxidation of a larger fraction of the specimen. Analysis of krypton and xenon was omitted to avoid use of refrigerated adsorbers. The following conclusions, based on the two experiments for which complete results are available, can be made:

1. Strontium, zirconium, barium, and cerium are retained in the high-temperature zone.
2. The unburned fuel retained 88 to 97% of the iodine associated with the uranium of the unburned fuel.
3. Fifteen to twenty-five percent of the iodine, 15 to 25% of the tellurium, and 35 to 40% of the cesium were released from the high-temperature zone of the furnace.
4. The release of ruthenium from the high-temperature zone varied between 5 and 40%.
5. An appreciable amount of cesium (10% of total), ruthenium (1%), and iodine (1.5%) penetrated the filter, but tellurium was retained by the filter.

[3] W. E. Browning, Jr., *et al.*, *GCR Program Semiann. Progr. Rept. Sept. 30, 1962*, ORNL-3372, pp. 256–59.

Table 18.2. Fission Products Released by In-Pile Burning of Uranium Carbide–Graphite Fuel

	Material Found (Percentage of Total in Assembly)								
	I^{131}	Te^{132}	Cs^{137}	Ru^{106}	Sr^{89}	Ba^{140}	Zr^{95}	Ce^{144}	U
Unburned fuel[a]									
Experiment G-1	59.7	47.6	38.1	27.0	50.6	51.7	58.2	54.8	61.9
Experiment G-3[b]	82.4	76.1	39.1	87.0	75.4	84.9	83.9	85.3	93.9
Outside of fuel residue[c]									
Experiment G-1	28.9	42.7	51.3	48.2	13.8	14.5	3.7	9.05	2.12
Experiment G-3	16.5	23.2	54.5	8.81	13.1	6.96	5.04	6.98	0.877
Retained in furnace									
Experiment G-1	73.2	64.9	63.0	59.3	98.8	99.5	99.5	93.8	99.6
Experiment G-3	85.6	85.6	58.4	94.3	98.7	99.3	98.7	97.1	99.8

[a]58.6% of the sample was burned in experiment G-1 and 41% in experiment G-3.

[b]Experiment G-2 was not analyzed because of low uranium content in the specimen.

[c]Fuel residues include the unburned portion of the specimen, fuel particles and powder, and the floor of the combustion furnace.

6. The fragments which fell away from the specimen during burning contained the same percentage of carbon as did the unburned fuel.

7. The side of the fuel specimen with the least amount of uranium carbide burned preferentially.

EFFECT OF GAS VELOCITY ON RELEASE AND BEHAVIOR OF FISSION PRODUCTS

Two experiments (10 and 11) were performed to study the effect of helium flow rate on fission product release from stainless-steel-clad UO_2 specimens heated in the ORR. The gas velocity evaluated at fuel melting temperatures was increased from 60 fpm [used in previous experiments (3 to 9)] to 125 fpm in experiment 10 and to 350 fpm in experiment 11.

Radiochemical analyses of the fission product distributions in these experiments have been reported in detail.[4] The conclusions regarding the effects of flow rate are as follows:

1. An increased helium flow rate lowered the maximum temperature of the fuel; from the extent of melting and appearance of the fuel, the maximum temperature of the fuel specimen in experiment 11 appeared to be between those of experiments 7 and 8, in which the specimen did not melt completely.

2. Release of fission products from the fuel itself did not appear to be affected by flow rate (except as flow affects temperature), since the release values for experiment 11 fell between those of experiments 7 and 8.

3. Release of the more volatile isotopes I, Te, and Cs from the high-temperature zone of the furnace did not appear to be affected by an increased flow rate, but the release of the less volatile isotopes increased fourfold with a sixfold increase in rate.

4. These effects are apparently insignificant for moderate increases in flow rate; they could hardly be detected in experiment 10.

FORM OF THE FISSION PRODUCTS

Vapors and particulate matter carried in a gas that flows laminarly through a tube reach the tube wall by diffusion. If the vapors or particles are radioactive, their distribution along the tube wall

[4]W. E. Browning, Jr., *et al.*, *Nuclear Safety Program Semiann. Progr. Rept. Dec. 31, 1963*, ORNL-3547, pp. 42–59.

is easily established. Analysis of the distribution of radioactivity on such a tube wall can lead to values for diffusion coefficients of the species and decisions as to whether the radioactive material was a vapor or was carried on particles of a given size. By use of the tube leading from the reactor furnace to the filter system or the diffusion tube and the analytical technique of Browning and Ackley,[5] the behavior of fission products from the in-pile melting and burning tests has been evaluated. Preliminary results previously shown[6] in reports in this series have been refined, and data from all experiments to date have been reported in detail.[4]

In all experiments, whether melting of UO_2 or burning of uranium carbide, except that (experiment 11) with the highest gas flow rate, many particles of average diameter near 25 A were observed. Considerable amounts of I^{131}, Te^{132}, and Cs^{137} were always carried by these fine particles. When UO_2 was melted, such particles always carried smaller amounts of Sr^{89} and Ba^{140}, frequently carried uranium, and seldom carried Ru^{106}; particles formed when uranium carbide was burned did not carry these species. On the other hand, such particles usually carried Zr^{95} and Ce^{144} if they derived from uranium carbide but seldom did so if they derived from melting UO_2. Size of particles associated with given fission product species appeared to show consistent deviations from the average, but the evidence is insufficient to show a definite correspondence of particular species with different particle size in the 10- to 100-A-diam range. Uranium and fission products are probably also carried on the larger particles that pass the diffusion tube and are retained by the filter.

The calculated diffusion coefficients for fission products in experiment 11, which had the higher flow rate, are considerably greater than those for other experiments. Experiment 10 did not show these higher diffusion coefficients, even through an intermediate gas velocity was employed. The data from experiment 11 indicate that the deposited fission products were carried in the vapor state and not on small particles. Estimates of the diffusion coefficients of the various elemental fission products and their oxides are consistent with the observed values within a factor of 2; however, it is not possible to distinguish between the elemental and oxide forms of the fission product vapors by this means. Considerable amounts of released I^{131}, Sr^{89}, and Ba^{140}; appreciable amounts of Te^{132} and Cs^{137}; but only small amounts of Ze^{95}, Ce^{144}, Ru^{106}, and U were carried as vapors. The appearance of vapor forms of these materials at higher gas velocities could be caused by their rapid transport from the release site and their greater dilution, both of which would reduce the tendency for particle formation.

Diffusion-coefficient measurements have given information about the amounts and forms of fission products released in trace-level experiments. The association of significant fractions of the released fission products and uranium with fine particles approximately 25 A in diameter and their appearance in the vapor form at high gas velocity could have important effects on the behavior of these materials in reactor accidents.

PARTICULATE MATERIAL COLLECTED BY FILTERS

The sweep gas from the in-pile fuel melting and burning experiments is passed through a series of three filters to obtain information about the particulate material formed. Both the first filter (generally a roughing filter) and the second filter (generally a Gelman HV-70 high-efficiency filter) usually show a visible deposit. The deposit on the third filter (generally a membrane filter) is usually not visible to the naked eye, but can be detected by its radioactivity and by electron microscopy. The sizes of particles, their states of aggregation, and certain other information about them can be determined by electron microscopy. Most of the filters have been too radioactive for electron microscopy, but data on particles retained on a few filters have been obtained.

Electron photomicrographs of particle collections from the UO_2 melting experiments indicated that a wide range of particle sizes is present and that the particulates are highly agglomerated. Agglomerates of like-size particles and particles

---

[5]W. E. Browning, Jr., and R. D. Ackley, *Reactor Chem. Div. Ann. Progr. Rept. Jan. 31, 1962*, ORNL-3262, pp. 179–83.

[6]W. E. Browning, Jr., *et al.*, *Reactor Chem. Div. Ann. Progr. Rept. Jan. 31, 1961*, ORNL-3127, pp. 149–52; *Reactor Chem. Div. Ann. Progr. Rept. Jan. 31, 1962*, ORNL-3262, pp. 172–76; *Reactor Chem. Div. Ann. Progr. Rept. Jan. 31, 1963*, ORNL-3417, pp. 236–43.

of various densities have been observed. In some cases particles are spheres and in others they appear to be platelets.

Particle-size measurements by electron microscopy have been reported in detail elsewhere.[4] There is some evidence that the particles found on the filters from the uranium carbide–graphite burning experiments are considerably larger than those found on the filters of the UO_2 melting experiments. The data also show that particles ranging in size from 0.015 to over 1 μ occur downstream from the initial filter in the UO_2 melting experiments.

DISTRIBUTION OF RELEASED FISSION PRODUCTS THROUGH OFF-GAS SYSTEMS

The distribution of the released fission products and uranium between the various parts of the in-pile fuel destruction assemblies is determined by radiochemical and chemical analysis. The results for a typical experiment have been reported.[4] Sixty to ninety percent of the more volatile fission products, I, Te, and Cs, escaped from the high-temperature zone of the furnace and were distributed more or less evenly between the cold stainless steel enclosure of the furnace, the diffusion tube, and the roughing filter. The HV-70 filter collected about 3% of the inventory of iodine and cesium. Approximately 3% of the iodine, 4% of the cesium, and less than 0.5% of the tellurium were found downstream of the HV-70 filter. Four percent of the ruthenium escaped from the hot zone, and half of that was stopped by the HV-70 filter. Most of the remainder was found on the membrane filter or its support. The other fission products (Sr, Ba, Zr, and Ce) and uranium were released from the hot zone in amounts of 1% or less. Not more than 0.25% of the inventory of these materials was found downstream from the HV-70 filter. The filters exhibited rather low effectiveness in retaining materials which arrived at their faces, but the materials which penetrated were very small fractions of the total inventory.

FISSION PRODUCT FRACTIONATION

In fission product release experiments, fission products appear in varying proportions in various locations, and sample compositions in general differ from those predicted for normal fission yields. This fractionation occurs because differences in the physical and chemical characteristics of individual fission products result in differences in their behavior in release, transport, or deposition processes. Fractionation of fission products is expected to occur similarly in reactor accidents.

A quantitative theoretical analysis of the observed variation in fission product proportions can be used to test the validity of various proposed mechanisms of fractionation. Knowledge of these mechanisms will make available a new tool for the prediction of the hazards of fission product release associated with reactor accidents and aid in recognition of conditions that have important effects on fission product behavior and which should be explored as variables in laboratory experiments.

A study has been made in which the fractionation predicted by several different models was compared with experimental results. The vapor transpiration model, in which fractionation is brought about by evaporation of the fission products from the fuel and by their removal by a carrier-gas stream, gives the most satisfactory agreement with the data from the in-pile fission product release experiments.

Vapor Transpiration Model

The vapor transpiration model deals with the fractional vaporization of fission products from the heated fuel at various temperatures. The carrier gas removes the vaporized materials to regions of lower temperature, where they are rapidly cooled without further change in composition. These materials are then deposited at locations which depend upon their forms and indirectly upon the temperatures at which they were vaporized. These three details of the model are assumed arbitrarily; their justification depends upon the success of the model in predicting the fractionation of fission products.

The following additional assumptions are made in the development of this model:

1. The concentrations of the vapors of fission products and other materials in the gas passing over the fuel are proportional to the concentrations corresponding to solubility equilibrium between gaseous and condensed phases.

2. The modified Henry's law constants for this equilibrium are independent of temperature.

3. The fuel residue changes negligibly in composition.

The first assumption is based on the expectations that equilibrium would be achieved rapidly at very high temperatures and that the extent of dilution by unequilibrated carrier gas would be the same for various temperatures. The second assumption has been found to be reasonably accurate in other systems. The third assumption is valid in the present experiments for the fission products considered thus far; however, under some conditions it could become a limitation which requires modifications of the model.

A complete mathematical derivation of this model has been reported.[7] The form of the equation describing proportions of fission products in samples according to the model is given by

$$\ln \frac{f_{2s}}{f_{1s}} = \left(\frac{\Delta H_1 - \Delta H_2}{\Delta H_1 - \Delta H_3}\right) \ln \frac{f_{3s}}{f_{1s}} - \left(\frac{\Delta H_1 - \Delta H_2}{\Delta H_1 - \Delta H_3}\right)$$

$$\times \left(\frac{\Delta S_3}{R} - \frac{\Delta S_1}{R} + \ln \frac{\int P_1^0\, dT}{\int P_3^0\, dT}\right) + \frac{\Delta S_2}{R} - \frac{\Delta S_1}{R}$$

$$+ \ln \frac{\int P_1^0\, dT}{\int P_2^0\, dT} - \left(\frac{\Delta H_1 - \Delta H_2}{\Delta H_1 - \Delta H_3}\right) \ln \frac{f_{3g}}{f_{1g}} + \ln \frac{f_{2g}}{f_{1g}}, \quad (1)$$

where

f_s = fraction of total inventory of fission product in sample,

ΔH = heat of vaporization of fission product, cal/mole,

ΔS = entropy of vaporization of fission product at boiling point, cal mole^{-1} deg^{-1},

P^0 = vapor pressure of pure fission product, atm,

f_g = fraction of total inventory released from fuel into gas phase during temperature excursion,

and subscripts 1, 2, etc., indicate various fission products. Equation (1) predicts that plotting ln (f_{2s}/f_{1s}) vs ln (f_{3s}/f_{1s}) will produce a straight line having a slope given by

$$a = \frac{\Delta H_1 - \Delta H_2}{\Delta H_1 - \Delta H_3}, \quad (2)$$

and an intercept given by

$$b = -\left(\frac{\Delta H_1 - \Delta H_2}{\Delta H_1 - \Delta H_3}\right)\left(\frac{\Delta S_3}{R} - \frac{\Delta S_1}{R} + \ln \frac{\int P_1^0\, dT}{\int P_3^0\, dT}\right)$$

$$+ \frac{\Delta S_2}{R} - \frac{\Delta S_1}{R} + \ln \frac{\int P_1^0\, dT}{\int P_2^0\, dT} - \left(\frac{\Delta H_1 - \Delta H_2}{\Delta H_1 - \Delta H_3}\right)$$

$$\times \ln \frac{f_{3g}}{f_{1g}} + \ln \frac{f_{2g}}{f_{1g}}. \quad (3)$$

The slope a depends only upon the heats of vaporization determined by the chemical species of the fission products evaporating from the fuel. The intercept b depends upon this and also upon the ratio of the fractions in the gas phase of the total amounts of fission products during the experiment.

Comparison of Theoretical with Experimental Fractionation

The validity of the vapor transpiration model can be tested by comparing the fission product compositions of experimental samples with those predicted by theory. Figures 18.1 and 18.2 are examples of fractionation plots for strontium, barium, and zirconium in experiments in which UO_2 was melted in the ORR. The points are actual experimental data, while the lines are predicted by Eq. (1). In Fig. 18.1 the line represents the release of these fission products (experiment 5) as oxides from the fuel, while that in Fig. 18.2 represents their release (in experiment 10) as metals. The theoretical lines were drawn without adjustment of empirical parameters. The choice of whether to use the line for oxides or for metals was dictated by the slope of the data. That this decision is unambiguous can be seen

[7] W. E. Browning, Jr., *et al.*, *Nuclear Safety Program Semiann. Progr. Rept. Dec. 31, 1963*, ORNL-3547, pp. 42–59.

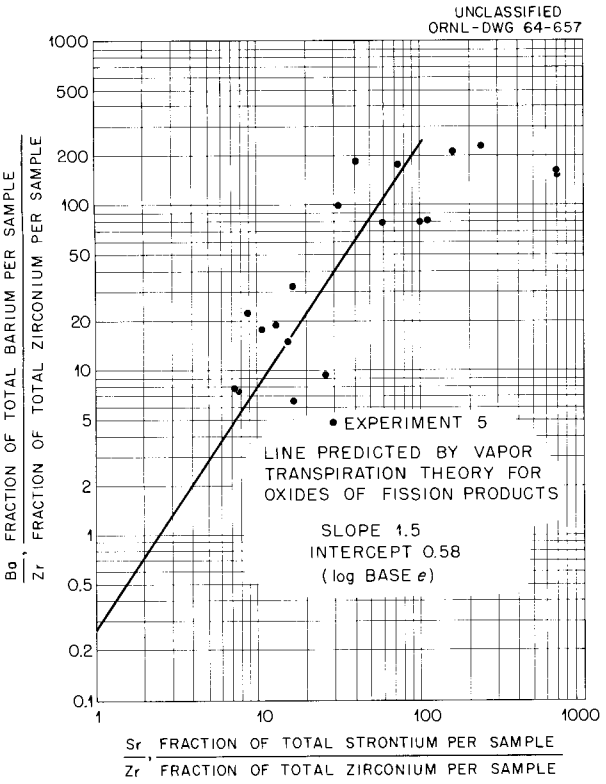

Fig. 18.1. Fractionation of Fission Products as Oxides During In-Pile Melting of UO_2.

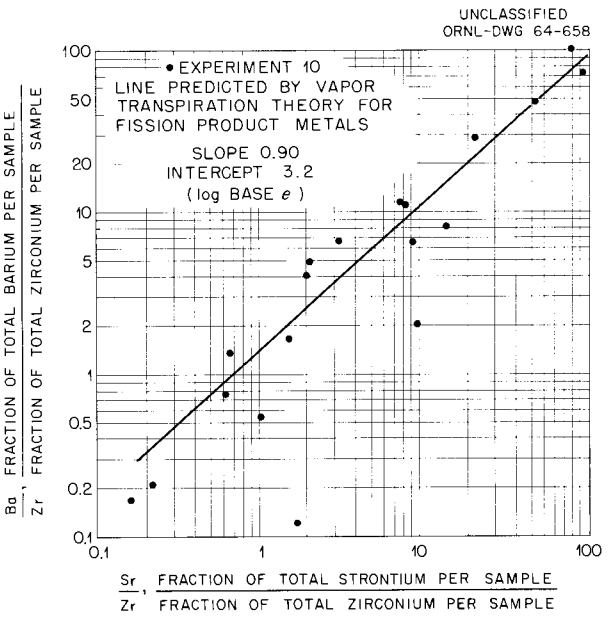

Fig. 18.2. Fractionation of Fission Products as Metals During In-Pile Melting of UO_2.

by noting the difference between the slopes in the two figures. Once this choice is made, the slope of the theoretical line is fixed. Its intercept is determined by the chemical forms of the fission products as well as by the ratio of the number of moles of fission products released to the gas phase. The latter is obtained by summing all the values of samples downstream from the fuel. The agreement between the experimental data and the theoretical lines indicates that Eq. (1) describes adequately the fractionation of strontium, barium, and zirconium in the experiments in which UO_2 is melted in-pile.

Results of Fractionation Analysis

The success of the vapor transpiration model in predicting the fractionation of fission products during in-pile melting of UO_2 validates the assumptions of the model and identifies the mechanism of fractionation. The chemical forms of the fission products during vaporization are also identified in the same operation. In most of the experiments with stainless-steel-clad UO_2, the strontium, barium, and zirconium were vaporized in the metallic form; however, in experiment 5 they were in the oxide form.

Attempts are under way to apply this model to other fission products for which data are available: I, Te, Cs, Ru, and Ce. Further fractionation studies will be made on data on fission product release from fuels melted with various gas velocities, atmospheric compositions, fission product concentrations, and fuel types to determine if there are correlations with chemical species of released fission products.

19. Release of Fission Products During Melting of Fuels Under Transient Reactor Conditions

G. W. Parker R. A. Lorenz C. E. Miller, Jr.

Release of fission products from fuel that melts rapidly under reactor transients is under study with apparatus adapted for use in the pulsed TREAT reactor operated by the Argonne National Laboratory at the National Reactor Testing Station. This program will attempt to determine and to interpret the release as a function of fuel type, cladding, extent of fuel burnup, covering atmosphere, and nature of the reactor transient. The major interest in this study is comparison of release from simulated reactor-transient accidents with that observed in simulated "loss-of-coolant" accidents.

The experimental assembly,[1,2] for which a schematic diagram is shown in Fig. 19.1, consists of a fuel autoclave, a diffusion system with a flow regulator, a filter system, and an (initially) evacuated gas-collection vessel. The fuel autoclave contains an electric heater to preheat the fuel specimens, under an argon atmosphere, to 800°C. The diffusion system consists of a tube (6 ft long by 0.195 in. in inside diameter), a flow restrictor, and a flow controller to regulate gas flow to 47 cc(STP)/min. The filter system consists of two 3.0-μ (pore size) membranes, two 0.45-μ membranes, and a glass-fiber filter that should be 98% efficient for particles as small as 0.05 μ. A more detailed description of the assembly, procedures, and results obtained to date has been presented elsewhere.[2]

Two experimental meltings under an argon atmosphere of previously unirradiated uranium dioxide specimens clad in stainless steel have been performed. A preliminary low-power transient of 60 Mwsec was performed with the first assembly to compare the actual heating rate with that calculated. The experimentally determined heat input was 0.75 cal per g of UO_2 per Mwsec; this value was only slightly lower than the calculated 0.91 cal per g of UO_2 per Mwsec. A summary of the reactor transient data, radiochemically determined fissions, and calculated specimen fission energy input is given in Table 19.1 for the two experimental meltings.

Results of the first two experiments demonstrated that meaningful fission product release data can be obtained by use of the assembly as designed and operated. Fission products deposited from the gas stream at high and at low temperature during passage from the fuel autoclave to the collection autoclave were separated and identified. Particle-size determinations were made with particles removed from the aerosol by filters and the diffusion tube. The gross appearance of the fuel specimens resembled that observed when UO_2 pellets were heated by means of centered tungsten resistors. In experiment 1 the stainless steel cladding melted away, but the UO_2 fuel did not melt, although surface cracking was quite evident. The UO_2 fuel in experiment 2 reached a higher temperature as evidenced by extensive swelling of the fuel and the fact that approximately 10% of the UO_2 flowed out of the original pellet shell. Metallographic examination of the fuel from experiment 2 also showed that

[1] G. W. Parker and R. A. Lorenz, *Reactor Chem. Div. Ann. Progr. Rept. Jan. 31, 1963*, ORNL-3417, p. 233.

[2] G. W. Parker, R. A. Lorenz, and C. E. Miller, Jr., *Nuclear Safety Program Semiann. Progr. Rept. Dec. 31, 1963*, ORNL-3547, p. 25.

65% of the UO_2 "melted" or "foamed." Fragmentation of the fuel, which has occurred in steam-fuel reactions conducted by Argonne National Laboratory experimenters in this reactor, was not observed in the experiments described here; the difference may be due to preheating of the fuel in these studies.

Release of fission products from the fuel and release from the high-temperature zone, which included the fuel, cladding, heater, and reflectors, were determined in each experiment. Table 19.2 shows the values obtained. The high release values observed for Sr^{89} and Cs^{137} resulted from their volatile precursors; their noble-gas precursors were probably responsible for occurrence of cesium and strontium isotopes throughout the experimental assembly. Most of the released I^{131} and Te^{129} was found in the stainless steel cladding; this is probably a result of alloying between their metallic precursors and the stainless

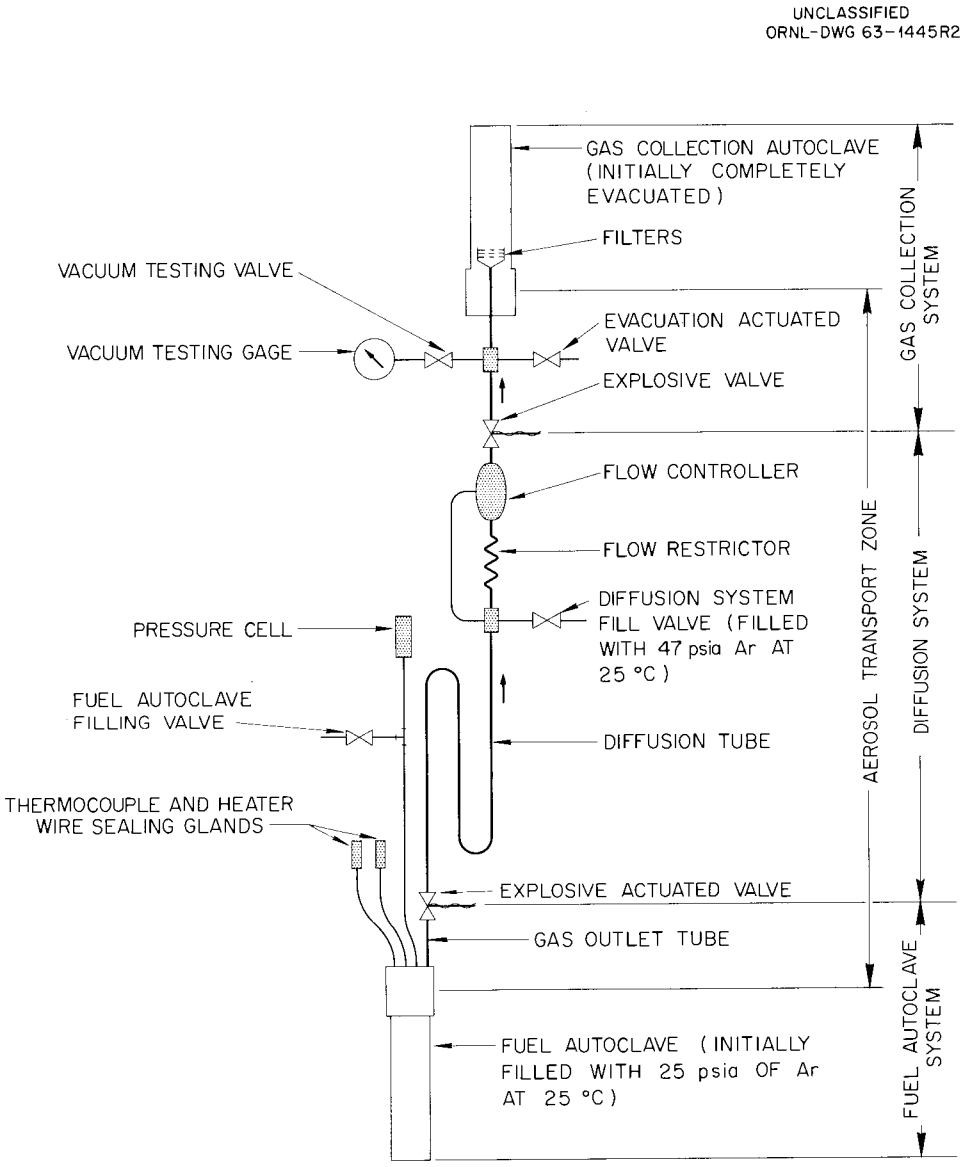

Fig. 19.1. Schematic Diagram of Assembly for Melting Fuels Under Transient Reactor Conditions.

steel. The greater release from the fuel in experiment 2 was apparently due to the more rapid rate of heating that resulted in less heat loss and a higher maximum temperature of the fuel. The release of most isotopes from the high-temperature zone, except those with volatile precursors, was quite low in these experiments, and the values were approximately proportional to the releases from the fuel. Release of isotopes in the volatile and alloying groups was surprisingly high in experiment 1, in which the fuel did not melt. This ease of release is interpreted to show very rapid diffusion rates of the precursor isotopes at temperatures near the melting point of UO_2.

Table 19.1. Summary of Reactor Transient Data

	Experiment 1[a]	Experiment 2
Reactor integrated power, Mwsec	320	328
Reactor period, msec	108	87
Estimated UO_2 temperature range, °C	800 to >2600	800 to mp
Stainless steel cladding temperature, °C	800 to mp	800 to mp
Alumina heater temperature, °C	800 to 1050	800 to 1070
Autoclave wall temperature, °C	180 to 240	140 to 200
Argon pressure, psia	39 to 42	40 to 51
Number of fissions (radiochemical analysis)	1.17×10^{15}	1.23×10^{15}
Fissions per μg of U^{235} per wsec	1.40	1.44
Fission energy input, cal per g of UO_2[b]	250	263
Fission energy input, cal per g of UO_2 per Mwsec[b]	0.78	0.80

[a]A low-power transient of 60 Mwsec was run with experiment 1 the day before the main transient. The number of fissions and the heat input value from this preliminary transient are not included in this tabulation.

[b]These values were obtained by using the radiochemically determined number of fissions and assuming 170 Mev per fission absorbed by the fuel specimen.

Table 19.2. Material Released from Transient-Heated UO_2[a]

Zone	Volatile Precursors			Alloying Precursors		Nonvolatile Precursors			Fuel
	Sr^{89} (Br + Kr)	Cs^{137} (I + Xe)	Ba^{140} (Xe + Cs)	I^{131} (Sn + Sb)	Te^{129} (Sn + Sb)	Ce^{144} (Ba + La)	Zr^{95} (Rb + Sr)	Ru^{103} (Tc)	UO_2
Total release from UO_2 fuel									
Experiment 1	23	26	8.2	46	21	7.0	0.21	0.095	0.0050
Experiment 2	58	53	42	31	21	8.8	1.53	0.60	0.75
Release from high-temperature zone									
Experiment 1	18.6	16.4	2.4	2.2	0.27	0.046	0.0088	0.038	0.00018
Experiment 2	46	38	14.8	1.10	1.26	0.32	0.130	0.064	0.059

[a]For fission products the radiochemically analyzed isotope is listed. The principal precursors present at the time of the transient are shown in parentheses. The high-temperature zone included the fuel, cladding, heater, and reflectors.

20. Behavior of Radioiodine

OCCURRENCE AND BEHAVIOR OF DIFFERENT FORMS OF RADIOIODINE

W. E. Browning, Jr. R. D. Ackley
R. E. Adams

Application of the previously described[1,2] technique of analysis of distribution profiles obtained by use of diffusion tubes to the behavior of radioiodine introduced into an air stream showed that part of the iodine was neither elemental nor on particles, but was in the form of volatile compounds. British workers had previously reported that their data, obtained under conditions not directly comparable to those employed in these experiments, indicated formation of iodine compounds when elemental iodine is released into atmospheric air.[3,4] Since such compounds could greatly affect the operating efficiency of iodine removal systems, considerable emphasis has been placed on the determination of their origin, identity, and behavior.

This work on the diffusional behavior of elemental iodine and the iodine compounds is described in detail elsewhere.[5,6] Iodine, presumed to be in the elemental form, was introduced into an air (or helium) stream, and the gas was passed through a composite diffusion tube, with successive surfaces of silver, rubber, and activated carbon; the activated carbon was applied as a dust after the inside of the tube was coated with an adhesive. The different surfaces were intended to distinguish chemically between different species of iodine.

Iodine compound formation was investigated by using elemental iodine prepared by two methods. In one method, iodine is precipitated from solution as palladium iodide, which is filtered, dried, and decomposed by heating under vacuum; the iodine is collected in a cold trap. In the other method, radioiodine in the form of sodium iodide solution is introduced into the apparatus, carrier iodine is added when desired, the solution is evaporated to dryness, potassium dichromate crystals are added, and the mixture is heated at 425°C to evolve elemental iodine. The second method is similar to that described by the British workers.[3,4]

Typical data are shown in Fig. 20.1 for an experiment in which the iodine was prepared by the dichromate method and the resulting iodine concentration in air (relative humidity, 3% or less) was in the 10- to 100-mg/m^3 range. The material deposited on silver was essentially I_2, as shown by the diffusion coefficient of 0.084 cm^2/sec. About 99% of the iodine appeared to be in the elemental form. The deposition patterns on rubber and on activated carbon indicate the presence of compounds having higher and lower molecular weights; deposition on rubber gave diffusion coefficients ranging up to 0.06 cm^2/sec, while that on carbon gave a value of 0.10 cm^2/sec.

Iodine prepared by the palladium iodide method was found to consist of two components corresponding to a more volatile fraction and a less volatile fraction. The latter exhibited behavior similar to that shown in Fig. 20.1. The more volatile fraction deposited to only a slight extent on silver and rubber and deposited primarily on the

---

[1] W. E. Browning, Jr., R. D. Ackley, and R. E. Adams, *Reactor Chem. Div. Ann. Progr. Rept. Jan. 31, 1962*, ORNL-3262, pp. 179–83.

[2] W. E. Browning, Jr., and R. D. Ackley, *Reactor Chem. Div. Ann. Progr. Rept. Jan. 31, 1963*, ORNL-3417, pp. 244–48.

[3] A. C. Chamberlain *et al.*, *Discussions Faraday Soc.* **30**, 162–69 (1960).

[4] W. J. Megaw and F. G. May, *Reactor Sci. Technol.* **16**, 427–36 (1962).

[5] W. E. Browning, Jr., and R. D. Ackley, *Nuclear Safety Program Semiann. Progr. Rept. June 30, 1963*, ORNL-3483, pp. 26–28.

[6] W. E. Browning, Jr., R. D. Ackley, and R. E. Adams, *Nuclear Safety Program Semiann. Progr. Rept. Dec. 31, 1963*, ORNL-3547, p. 60.

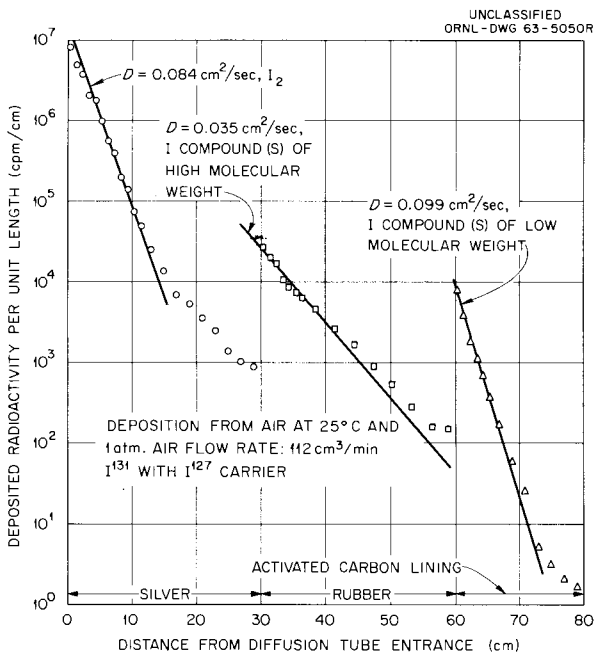

Fig. 20.1. Deposition of Iodine Prepared by the Dichromate Method.

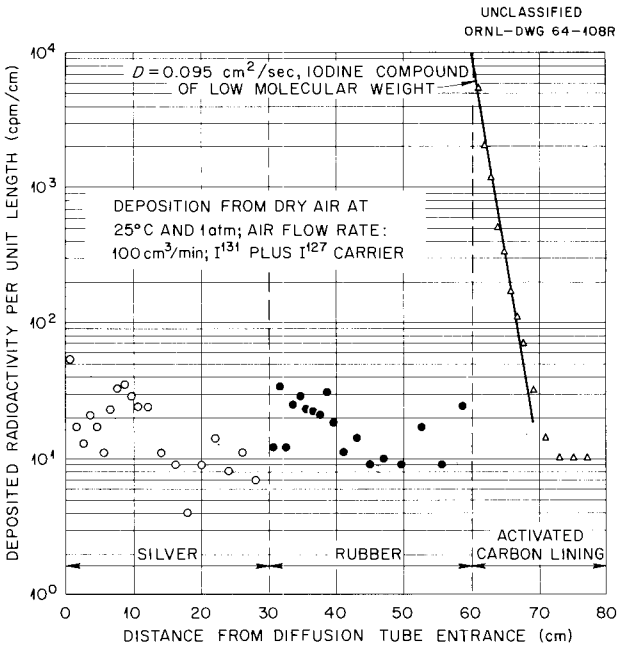

Fig. 20.2. Deposition of Volatile Fraction of Iodine Prepared by the Palladium Iodide Method.

activated carbon with a diffusion coefficient of 0.10 cm^2/sec, as shown in Fig. 20.2. Some confirmation of these observations was afforded by mass spectrometry, but the identity of the compounds responsible for the distribution profiles on rubber and on activated carbon has not been positively established. The effectiveness of charcoal adsorbers for retention of the two iodine fractions has been investigated under various conditions and is presented in Chap. 21 under the heading "Radioiodine Adsorber System for the NS 'Savannah.'"

Some of the diffusion-tube experiments were performed with iodine prepared by the dichromate method in a manner such that the resulting iodine concentrations in air or in helium were considerably less than 10^{-3} mg/m^3. At these lower concentrations the proportion of the iodine present as compounds, as measured by radioactivity and diffusion-tube deposition, increased to 30%, in contrast to the approximately 1% observed at the higher iodine concentrations. Diffusion coefficients suggested that the compounds were the same as observed earlier.

IODINE ADSORPTION BY STAINLESS STEELS

W. E. Browning, Jr. M. E. Davis

Information enabling prediction of contaminated zones in the primary coolant system of gas-cooled reactors would be of great design value. The adsorption characteristics of fission products are of significance in predicting their deposition behavior in such flowing gas systems. Experimental work at ORNL[7] and elsewhere,[8,9] and efforts toward the development of an analytical model[10–12] for fission product transport and deposition have

[7] J. L. Scott, *GCR Program Semiann. Progr. Rept. Mar. 31, 1963*, ORNL-3445, pp. 122–26.

[8] A. Abriss, R. A. Ewing, and D. N. Sunderman, *Trans. Am. Nucl. Soc.* 6(2) 263–64 (1963).

[9] T. D. Roberts, *Trans. Am. Nucl. Soc.* 6(2) 264–65 (1963).

[10] M. N. Ozisik, *An Analytical Model for Fission Products Transport and Deposition from Gas Streams*, ORNL-3379 (July 26, 1963).

[11] M. N. Ozisik, *Temperature Effects on Fission-Product Deposition*, ORNL-3542 (to be issued).

[12] G. E. Raines, *Trans. Am. Nucl. Soc.* 6(2), 265 (1963).

indicated that a strongly temperature-dependent factor exists in the deposition behavior of gas-borne fission products. Such behavior is indicative of adsorption involving relatively high interaction energies. An investigation of the adsorption behavior of several fission product elements has been undertaken with single-element sources rather than with irradiated fuel specimens.

In this work, iodine vapor at controlled densities was brought into contact with the stainless steel surface, in most experiments by molecular diffusion in vacuum. The amount of iodine adsorbed was usually measured continuously by *in situ* gamma-ray detection of I^{131} tracer. In one series of experiments, however, stable iodine was used, and the adsorbed iodine was leached and was determined by chemical analysis. From information available on the expected I^{131} content of a pebble-bed reactor coolant system, the I^{131} concentration in the gas phase was estimated to be 0.1 mg/m^3. Iodine vapor densities in this work were varied from 0.0004 to 2200 mg of I_2 per m^3, and the temperature of the metal surface under study ranged from 24 to 700°C. Experimental conditions and results have been reported in detail.[13] The results of these experiments and information in the literature indicate that a major fraction of the iodine vapor–stainless steel surface interaction is a chemical reaction. Analysis of the reaction product of iodine with types 302 and 304 stainless steel indicates that Fe, Cr, Ni, and Mn react with iodine roughly in proportion to the amount of these metals present in the steel. There is no evidence from this work that the different types of stainless steel used, 302, 304, and 321, demonstrate any differences in behavior toward iodine. The standard heats of formation of anhydrous iron, chromium, and nickel iodide are −30.0, −54.2, and −20.5 kcal/mole respectively. Such literature values for heats of reaction may be of use in the mathematical deposition model under development. Also of interest is the loading at which the surface becomes saturated with respect to iodine adsorption. Coverages of up to 60 monolayers have been observed in the present work; however, there is large variation in the saturation coverage, and a complete passivity of stainless steel toward iodine adsorption is sometimes observed. It has been observed in a recent experiment that there is a maximum in the quantity of iodine adsorbed by type 321 stainless steel at around 150°C. This is not in agreement with the observations of Scott,[7] made under somewhat different conditions. The reasons for the differences in results are not readily explainable simply in terms of the different conditions prevailing in the two experiments. The adsorption of iodine is believed to be influenced by changes occurring in the surface structure. Prediction of the adsorption behavior will require a more complete understanding of these changes.

Kinetics of the Surface Interaction

From the available literature on chemisorption, it is found that the kinetics of many gas-surface reactions fit an expression of the form $dq/dt = ae^{\alpha q}$, where q is the amount of material adsorbed, t is time, and a and α are empirically determined constants. This is termed the Elovich equation, and analyses of experimental data are usually made with an integrated form of the equation by plotting the amount adsorbed vs log time. A wide variety of data when plotted in this way yield straight lines with one or more abrupt changes in slope; the constants a and α are determined from the slopes and intercepts of the lines.[14] Elovich plots of data taken during a series of exposures of stainless steel at 500°C to iodine vapor at 220 mg/m^3 are shown in Fig. 20.3. The numbers over the lines refer to the sequence of the series of exposures. This surface had initially adsorbed only a few monolayers at an iodine vapor pressure of 0.0004 mg/m^3 and had exhibited no further sorptive capacity in an iodine atmosphere of approximately 5 mg/m^3. The values for a and α at any given length of exposure to iodine vapor appear to increase with successive exposures, corresponding to increasing extent and rate of reaction. After several exposures, adsorption took place very rapidly for reasons that are being investigated further and then decreased during subsequent exposures. It appears that during the exposure of a metal to a vapor, surface changes have a pronounced effect on the adsorption process, and more detailed analysis of surface reaction

[13] W. E. Browning, Jr., and M. E. Davis, *GCR Program Semiann. Progr. Rept. Sept. 30, 1963*, ORNL-3523, p. 168.

[14] M. J. D. Low, *Chem. Rev.* **60**, 267–312 (1960).

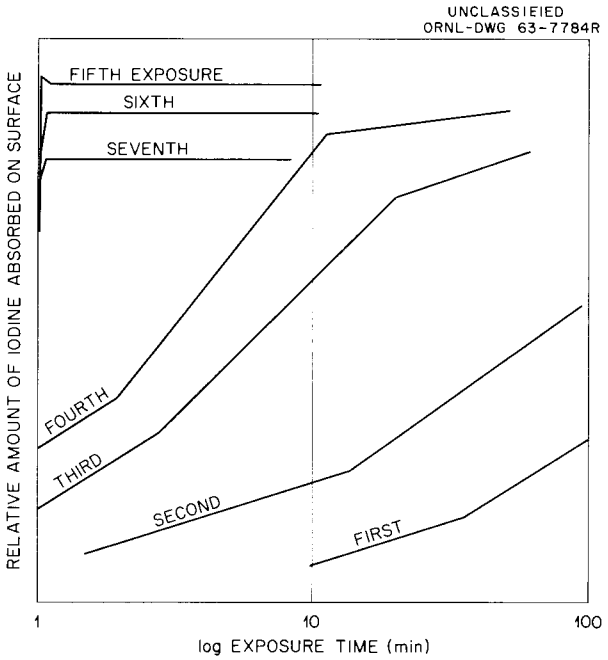

Fig. 20.3. Iodine Adsorption on a Stainless Steel Surface at 500°C During Successive Exposures to Iodine Vapor (220 mg/m^3).

kinetics will require more complete characterization of surface conditions.

Chemical Form of the Iodine Sources Used

The reactions of gas-borne fission products with metal surfaces will be affected by the chemical forms of the fission products. It is thus important that their forms be known both in laboratory experiments and under reactor conditions. The presence of nonelemental forms of iodine, for example, methyl iodide, in fission product material has been reported.[15] Accordingly, the composition of the sources used in the current series of experiments has been investigated. The radioiodine sources (I_2) as received from the Isotopes Division have been fractionated into components of differing volatility. Mass spectrometric examination of these fractions indicates that methyl iodide is the major component in the volatile fractions, and this amounted to about 0.09% of the total iodine obtained in one particular source. Hydrogen iodide and possibly ethyl iodide were present in much smaller amounts. No measurable quantity of these materials was found in the iodine fraction taken for use in an adsorption experiment after the fractionation procedure was put into use.

[15]A. E. J. Eggleton and D. H. F. Atkins, *Trans. Am. Nucl. Soc.* 6(1), 129 (1963).

IODINE REMOVAL FROM OXIDIZING GASES AT HIGH TEMPERATURES

C. J. Barton M. E. Davis
G. E. Creek G. W. Parker

The efficiency of charcoal for trapping molecular iodine has been well demonstrated, but concern has been expressed about the possibility of ignition of charcoal beds by exposure to high-temperature oxidizing gases during a reactor accident. It would be desirable, therefore, to have alternate extraction materials available that would be less susceptible to destruction under such conditions. Preliminary experiments were performed to test two different approaches to the problem: the use of activated alumina containing about 0.5% platinum (a hydroforming catalyst),[16] and iodide salts as a chemical exchange medium for gaseous radioiodine. Details of most of these experiments have been reported elsewhere.[17]

About 0.1 mc of I^{131} mixed with 1 mg of I^{127} was collected on a 3-in. bed of −10 +16 mesh potassium iodide from a helium stream at 500°C, and the distribution was determined by use of a slit collimator and a gamma-ray detector. In Fig. 20.4 this is compared with the I^{131} distribution on the same bed after it had been subjected to the following sequence of treatments: flowing helium at 500°C for 6.5 hr and at 600°C for 3.5 hr;

[16]The authors are indebted to P. H. Emmett for suggesting the testing of platinized alumina as a possible iodine extractant.

[17]C. J. Barton, G. W. Parker, and M. E. Davis, *Nuclear Safety Program Semiann. Progr. Rept. June 30, 1963*, ORNL-3483, p. 36.

flowing air at 500°C for 7.6 hr and at 600°C for 4.0 hr. The gas velocity was 250 cm/min at all times. The activity in a charcoal trap following the potassium iodide bed increased only 15% over background during the exposure to air at 600°C, which resulted in some decomposition of the bed. Summation of the iodine activity under the distribution curves indicated that about 53% of the original iodine activity remained in the bed after rather drastic treatment. It appears, therefore, that the chemical-exchange method holds some promise for the removal of gas-free fission products from hot oxidizing gases, and further studies of this type are planned.

Fission product I^{131} was deposited on a bed of 30-mesh platinized alumina (Girdler G-43) at 525°C, and its distribution on the bed was determined after exposure to flowing air (200 cm/min) at 325, 425, 525, and 625°C consecutively. The data shown in Fig. 20.5 indicate that some movement of iodine on the bed occurred at the higher temperatures and that almost 100% elution occurred at 625°C.

A comparison of the iodine-retention ability of platinized and unplatinized alumina (−12 +16 mesh) is shown in Fig. 20.6. In these tests the distribution of I^{131} on the bed was determined after loading the iodine, obtained by melting irradiated uranium-aluminum alloy, on the bed at 100°C and then after successive 0.5-hr treatments with flowing air (200 cm/min) at increasing temperatures. The fraction retained was determined from the area under the distribution curves. While the platinized alumina was found to have significantly higher iodine retention ability under the test conditions than unplatinized alumina, the data show that either material would serve only to delay passage of iodine.

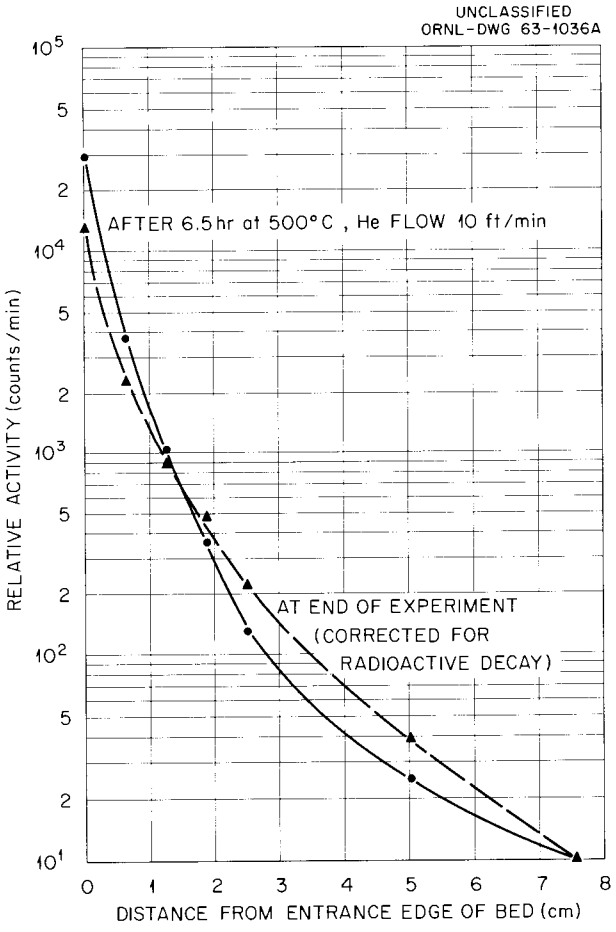

Fig. 20.4. Distribution of Radioiodine on a Potassium Iodide Bed.

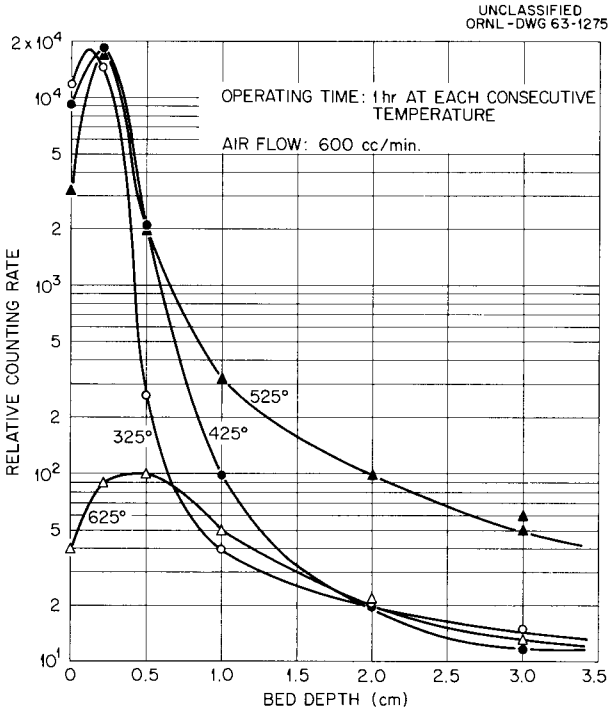

Fig. 20.5. Distribution of Radioiodine on a Platinized Alumina Bed.

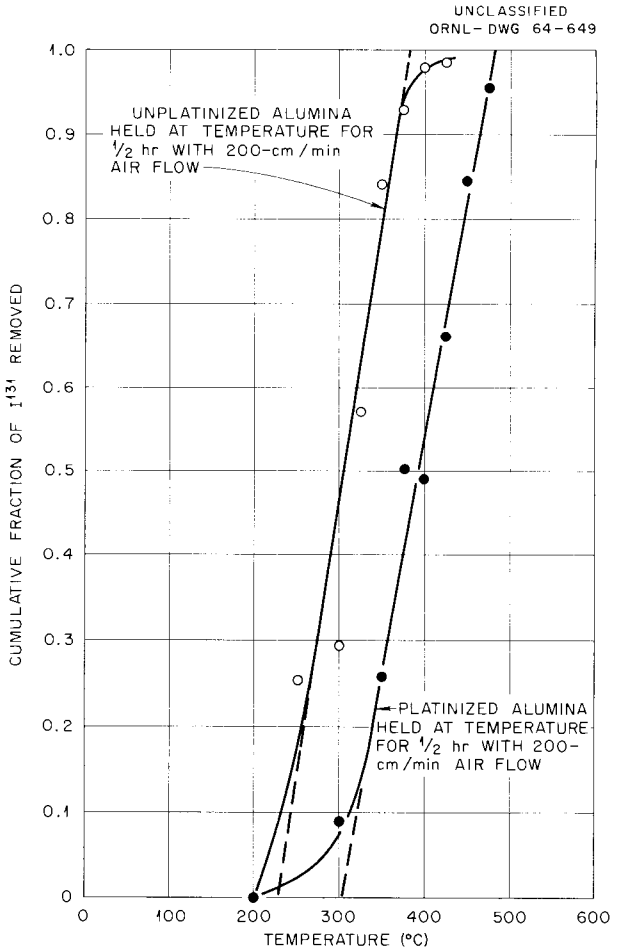

Fig. 20.6. Comparison of Retention of Iodine on Platinized and Unplatinized Alumina.

21. Fission Product Retention in Reactor Confinement Systems

EFFICIENCY OF THE ORR CONFINEMENT SYSTEM

G. W. Parker W. J. Martin
G. E. Creek C. J. Barton

Results of two laboratory tests of the filter and charcoal adsorption traps proposed for use in the containment system of the ORR are presented in Table 21.1. The radioiodine used in these tests was produced by melting irradiated uranium-aluminum alloy specimens, the type of fuel that is employed in the ORR. Two additional tests were performed in the Hot-Cell Confinement Mockup Facility described elsewhere in this report. The filter and charcoal holder employed in laboratory-

Table 21.1. Filter Tests with Radioiodine and Particulates Released by Melting High-Burnup Uranium-Aluminum Alloy in Air

	Percent of Activity Reaching Filters Retained in Each Location			
	Charcoal No. 6249[a]		Charcoal No. 45[b]	
	Iodine	Gross Gamma	Iodine	Gross Gamma
Location of activity				
Roughing filter (Aerosolve No. 3A-95)	1.98	44.6	1.21	17.6
1st absolute[c] filter		1.3	0.887	1.7
1st charcoal ($\frac{3}{4}$-in. bed)	97.89	53.8	97.88	80.7
2d charcoal ($\frac{3}{4}$-in. bed)	0.113	0.1	0.015	0.02
2d absolute[c] filter		0.2	0.004	0
Hot charcoal (backup)	0.009	0.009[d]	0.0013	0.002[d]
Iodine activity ratio, $\frac{\text{1st charcoal}}{\text{2d charcoal}}$	867	538	6520	4035
Efficiency of 1st charcoal bed	99.885	99.42	99.98	99.97
Overall efficiency of ORR filter-charcoal system	99.991	99.991	99.9987	99.998

[a] 4–20 mesh.

[b] 4–20 mesh, slightly finer than No. 6249.

[c] High-efficiency, 99.97% retention in 0.3-μ DOP (dioctylphthalate) test.

[d] Represents loss through the confinement system.

scale tests was modified to permit the addition of two more $\frac{3}{4}$-in.-long charcoal cartridges and one more absolute filter following the charcoal traps.

The results of these tests demonstrated that the iodine-retention capacity of the proposed ORR confinement system is high (99.97%) and that the aging of the released aerosol from molten uranium-aluminum alloy for more than an hour or mixing steam with air had little, if any, effect on the retention efficiency. The data are summarized in Table 21.2. These experiments are described elsewhere[1] in more detail.

RADIOIODINE ADSORBER SYSTEM FOR THE NS ''SAVANNAH''

W. E. Browning, Jr. R. E. Adams
W. M. Johnson

The ventilation gases from the reactor compartment of the NS "Savannah" are processed through particulate filters and iodine sorption units to provide for control of any radioactive iodine vapor and particulate material present in the compartment atmosphere through accident. Although this fission-product confinement system was designed for specific application to this case, the results of the extensive testing program applied to this system may be of interest to confinement system designers and others concerned with the safety of nuclear reactors.

Two parallel systems for ventilating the compartment were installed in March–April 1963; one unit operates continuously at a flow rate of 1000 to 1100 cfm and the other is in standby condition. Five stages of gas cleaning are provided. The gases are passed through a package consisting of (1) a prefilter, (2) a high-efficiency filter, (3) a silvered-copper mesh unit, (4) an activated charcoal unit, and (5) a second silvered-copper mesh unit.

An experimental program, involving both laboratory studies and shipboard testing, is being conducted to determine the iodine efficiency that can be expected of the activated charcoal units installed aboard the NS ''Savannah.'' The experimental results will be reported in a condensed version, since they have been reported in full elsewhere.[2]

[1] G. W. Parker *et al.*, *Nuclear Safety Program Semi-ann. Progr. Rept. Dec. 31, 1963*, ORNL-3547, p. 7.

[2] *Maritime Reactor Program Ann. Progr. Rept. Nov. 30, 1963*, to be issued.

Table 21.2. Retention of Iodine and Cesium by ORR Confinement System Components

Component of Filter Pack	Percent of Activity Reaching Filters Retained by Each Component			
	Iodine		Cesium	
	Dry Air	Moist Air	Dry Air	Moist Air
Roughing filter[a]	43.50	11.18	98.56	98.85
1st absolute filter[a]	2.88	12.23	1.44	1.15
1st charcoal trap[a]	53.0	76.2		
2d charcoal trap[a]	0.40	0.39		
3d charcoal trap	0.03	0.026		
4th charcoal trap	0.003	0.008		
2d absolute filter[a]			8×10^{-6}	9×10^{-5}
3d absolute filter			3×10^{-8}	3×10^{-6}
Backup traps	0.007	0.0003	0.0005	$<10^{-5}$
Percent net ORR system efficiency	99.97	99.97	99.99+	99.99+

[a] Units included in the proposed ORR confinement system and included in the calculation of ORR system efficiency.

Laboratory Studies of Removal of Radioiodine Vapor from Gases

Small-scale tests have been and are being conducted on samples of various charcoal materials to obtain information on the iodine behavior at design and off-design conditions. Forty-three tests were completed on three types of charcoal under various combinations of temperature and humidity. A summary of the results is presented in Table 21.3. For the most part, these charcoal units exhibited what may be termed normal penetration of iodine considering the conditions specified for the tests. However, abnormal penetration of iodine was observed in too many instances to be ignored.

A series of exploratory experiments was performed yielding information which indicated that the iodine sources used in the experiments was probably the primary cause of the observed abnormal iodine behavior. Later experiments designed to study the behavior of the iodine sources (prepared by the palladium iodide method described in Chap. 20) revealed the presence of iodine in forms which penetrated the charcoal beds more readily than did elemental iodine vapor.

Mass spectrometry was applied to identify the components of iodine sources, and masses corresponding to those of HI, ICl, CH_3I, I_2, and two higher-molecular-weight compounds were observed. Diffusion channel analysis was also used to investigate these iodine compounds. These analyses, reported in Chap. 20, showed that the more volatile fraction deposited on a charcoal-lined diffusion tube with a diffusion coefficient of approximately 0.10 cm^2/sec, but not on silver or rubber surfaces; it may be HI or CH_3I. The less volatile fraction (at −70°C) deposited primarily on silver with a diffusion coefficient of 0.08 cm^2/sec; it is probably molecular iodine.

Initial results of the study of the behavior of different forms of iodine in charcoal beds are presented in Table 21.4. The behavior of iodine in tests 1 and 2 is representative of that in a charcoal system when no effort is made to separate the two fractions of the iodine source. Test 3 illustrates the efficiencies that are obtained when the iodine source is divided into two fractions, the first being that part which is vaporized in less than 10 min at −70°C, and the second being that which is vaporized after 10 min. Tests 4 to 7 give some indication of the variation of efficiency with the parameters of humidity, temperature, and type of charcoal. Elevated temperature and the presence of metallic impregnants in the Whetlerite charcoal together seem to enhance the adsorption or retention of the volatile iodine fraction by charcoal.

Efforts to identify the various forms of iodine and to characterize fully their behavior in activated charcoal adsorbers are continuing. It is necessary to know their identity and the circumstances of their occurrence so that an evaluation can be made of the possibility of their appearing in a reactor accident. Their behavior in adsorbers under Savannah conditions must be investigated so that appropriate adsorber efficiencies may be determined. These nonelemental compounds (volatile

Table 21.3. Results of Charcoal Media Tests[a]

Charcoal	Number of Tests	Temperature (°C)	Steam	Efficiency (%)	
				Range	Average
BPL	16	97–100	Yes	19.9–99.7	80.0
PCB	8	97–100	Yes	50.7–99.9	86.8
Whetlerite[b]	3	98–99	Yes	82.9–97.6	92.2
BPL	4	97–100	No	96.3–99.7	98.4
BPL	12	24–25	No	90.4–99.9+	98.5

[a] I_2 vapor concentration $\sim 10^{-4}$ mg/m^3, superficial linear velocity 21–33 fpm, bed depth 1.2 in.

[b] BPL charcoal containing salts of silver, copper, and chromium.

Table 21.4. Efficiency of Charcoal in Removing Iodine and Volatile Iodine Compounds from Air

Test	Iodine Fraction[a]	Charcoal	Temperature (°C)	Humidity[b] (%)	Efficiency (%)
1	*A* + *B*	BPL	23	~60	90–95
2	*A* + *B*	BPL	23	1–3	>99.9
3	*A*	BPL	23	1–3	>98.0
	B	BPL	23	1–3	>99.9
A-1	*A*	BPL	23	~60	50.3
	B	BPL	23	~60	97.9
4	*A*	BPL	100	1–3	98.5
	B	BPL	100	1–3	>99.9
5	*A*	BPL	100	~60	99.1
	B	BPL	100	~60	>99.9
6	*A*	Whetlerite[c]	24	~60	90.5
	B	Whetlerite	24	~60	>99.8
7	*A*	Whetlerite	100	~60	>99.9
	B	Whetlerite	100	~60	>99.9

[a]When the iodine source is at −70°C, *A* is the volatile fraction (low-molecular-weight iodine compounds) and *B* is the less volatile fraction (primarily elemental iodine).

[b]Relative humidity of air sweep evaluated at room temperature.

[c]BPL charcoal impregnated with salts of silver, copper, and chromium.

fraction) are by no means the major fraction of the iodine vapor source; thus, it is probable that only moderate efficiencies for removal of these forms of iodine may be required to yield adequate overall iodine efficiencies.

Shipboard Tests

Concurrently with the laboratory work a program is being conducted to develop and apply test procedures and equipment for accomplishing in-place tests on the shipboard reactor compartment ventilation system. The purpose of these tests is to demonstrate that the installation of the iodine sorption units is such that the iodine efficiency of charcoal can be realized. Tests on the original ventilation system were reported previously,[3] and only the tests on the new ventilation system will be covered here.

Basically, the in-place iodine tests are conducted by injecting iodine vapor into the ventilation duct while sampling up- and downstream of the charcoal unit. When I^{131} is used the amount of iodine in the samplers is determined by analyzing the charcoal with the gamma spectrometer aboard the ship. When normal iodine is used, the iodine content of the samplers is determined by neutron activation at Oak Ridge. A total of 16 normal iodine tests (I^{127}) of the two charcoal units has been conducted. Also eight radioactive iodine tests (I^{131}) have been conducted. Of the 24 tests, 22 have indicated efficiencies greater than 99.9%. Two I^{127} tests on the F-1 system (on stream since April 1963) produced an efficiency of ~90%. A review of the test procedure and analytical determinations failed to produce sufficient information that would permit the low efficiency of the F-1 system to be explained by either faulty test procedures or analytical techniques. Sixteen additional I^{127} and I^{131} tests on the two systems have not substantiated the observation of low system efficiency. It is con-

[3]W. E. Browning, Jr., *et al.*, *Reactor Chemistry Div. Ann. Progr. Rept. Jan. 31, 1963*, ORNL-3417, pp. 260–66.

cluded, based upon data at hand, that the reactor compartment ventilation systems, as installed, are capable of achieving at least the iodine removal efficiency observed in the series of 14 laboratory tests of 11 × 11 in. Savannah-type charcoal units under accident conditions. These tests, conducted with continuous iodine injection at 96 to 100°C and with 80 to 90% saturated steam in air, have shown[3] the efficiency of the charcoal unit alone to be (99.86 ± 0.07)% at the 95% confidence level.

ATTENUATION OF FISSION PRODUCT ESCAPE BY INTRINSIC PROCESSES

W. E. Browning, Jr.

Certain processes which tend to limit the escape of fission products have been given more attention than others in assessing the potential hazard of reactor accidents. Credit is claimed for the partial retention of fission products by the fuel material during an accident. In various reactor designs, different amounts of credit are claimed for containment vessel performance and for engineered safeguards such as filtered ventilation systems. It is generally conceded that there may be significant attenuation of fission product release by other processes which occur naturally. Advantages of these processes have not been fully utilized in reducing the assumed consequences of reactor accidents for various reasons including complexity of the theoretical treatment of some of the processes, inability to describe satisfactorily the conditions under which these attenuation processes might take place, and uncertainty as to the possible magnitude of attenuation effects. Theoretical analyses of some of these attenuation processes will make it possible to judge whether the effects are of sufficient magnitude to warrant investigation in further detail and may suggest ways in which design changes can result in significant reduction of the potential hazard of reactor accidents. Two mechanisms which are of possible importance are diffusional deposition within a leak in a containment vessel and agglomeration of particles during aging prior to filtration. Therefore, theoretical treatments were carried out to determine the reduction of fission product release which would occur under various conditions as a result of these mechanisms.

Decontamination Factors for Particle Deposition in Leaks as Applied to Leak Testing of Containment Vessels

R. D. Ackley

In the event of a major nuclear reactor accident, a significant fraction of the radioactivity released from the reactor core would probably be in the form of airborne radioactive particulates. When such an aerosol escapes through viscous leaks in the containment vessel wall, particles would tend to be removed from the leaking air by diffusional deposition on the inner surfaces of the leaks. Diffusional deposition results from the transport by Brownian diffusion of particles to surfaces, where they are held by van der Waals forces. It would be of considerable value when establishing criteria for the leak testing of containment vessels to have some idea of the expected extent of removal of fine particles by this mechanism, since, if the effect is important, a potentially large cleanup factor might be built into the containment system, provided the leak-testing procedures are sufficiently stringent. Accordingly, a theoretical study has been made of this process, particularly with regard to applying the results to containment vessel leak testing. Since this study is reported in detail elsewhere,[4,5] the work will be only outlined here in order to indicate its scope.

Since the leaks might be in the form of pinholes or cracks, leak models that were right circular cylinders or the space between parallel planes appeared suitable. Viscous flow equations for these two cases are that of Poiseuille and its analogy for parallel planes, and may be found, for example, in Kennard.[6] By making certain approximations, deemed satisfactory from a practical standpoint, these equations were respectively combined with equations for the fraction of particles penetrating cylindrical and thin rectangular channels to yield expressions for calculating decontamination factors; in connection with

---

[4]W. E. Browning, Jr., and R. D. Ackley, *Nuclear Safety Program Semiann. Progr. Rept. June 30, 1963*, ORNL-3483, pp. 39–42.

[5]W. E. Browning, Jr., and R. D. Ackley, *Nuclear Safety Program Semiann. Progr. Rept. Dec. 31, 1963*, ORNL-3547, p. 66.

[6]E. H. Kennard, *Kinetic Theory of Gases*, p. 294, McGraw-Hill, New York, 1938.

this purpose, the equation of Gormley and Kennedy[7] and that of DeMarcus[8] were respectively employed. The resulting expressions follow:

$$\text{cylindrical, } \log \text{DF} = 0.0867 + 203.2 \frac{\eta D L^2}{\Delta P\, d^4}\,, \quad (1)$$

$$\text{thin rectangular, } \log \text{DF} = 0.0386 + 39.35 \frac{\eta D L^2}{\Delta P\, b^4}\,, \quad (2)$$

where DF is the decontamination factor (ratio of number of particles entering the channel to the number penetrating); η is the coefficient of viscosity, poises; D is diffusion coefficient of particle in air, cm^2/sec; L is length of leak, cm; ΔP is pressure drop through leak, $dynes/cm^2$; d is leak diameter, cm; and b is smallest cross-sectional leak dimension, cm. To utilize these equations, particle diffusion coefficients were calculated, by what is now a classical method, for particle radii ranging from 10^{-3} to 1 μ. The range of applicability of these equations with regard to the extent of the viscous flow regime was investigated by calculating Reynolds numbers and slip corrections. For the particular situation of air leaking under a pressure drop of 7 psig and through a wall thickness of 1 in., Eq. (1) should apply over the approximate d range of 5 to 200 μ; the corresponding b range of Eq. (2) is 5 to 100 μ. Equations (1) and (2) predict that the decontamination factor is a very strong function of leak dimension (d or b), and, through D, of particle size, with DF increasing as d or b or particle size decreases. An example of the calculated DF values follows. For the aforementioned situation (7 psig, 1 in.), with a particle diameter of 0.1 μ and d or b equal to 10 μ, Eq. (1) yields a DF of 4000 or Eq. (2), a DF of only 5. Diffusional deposition of atomic and molecular species of fission products was also treated in this study, but only briefly.

The rather idealized results which were obtained as indicated above suggest their possible application in determining specifications for containment vessel testing using conventional leak detectors. To provide some idea of the potential value, as measured by the calculated decontamination factor, of eliminating all leaks corresponding to a given leak detector sensitivity (LDS), Fig. 21.1 is presented. In this figure, the LDS flow rates reflect the values which would be obtained if they were metered at the average pressure in the leak during leak testing. Cylindrical geometry was assumed in calculating these results since, for a given flow rate, it gives more pessimistic decontamination factors than the thin rectangular geometry (notwithstanding the impression perhaps given by the example of calculated DF values for fixed leak dimensions). Figure 21.1 was obtained from

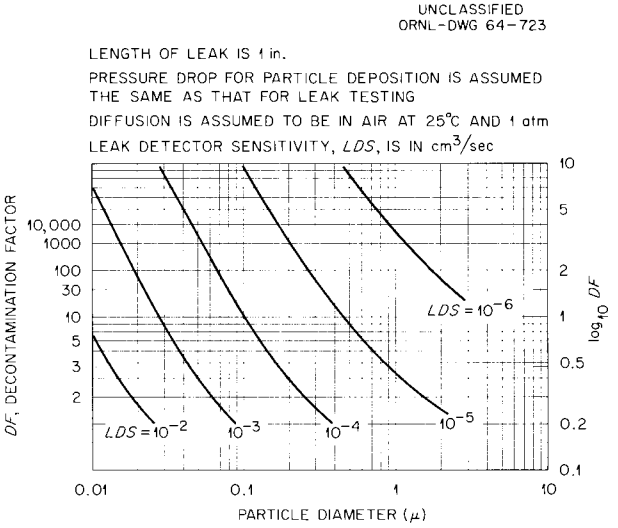

Fig. 21.1. Calculated Decontamination Factors for Cylindrical Leaks Corresponding to Various Leak Detector Sensitivities.

$$\log \text{DF} = 0.0867 + 4.989 \frac{DL}{\phi}\,, \quad (3)$$

where ϕ is the average volumetric flow rate in the leak and the other quantities are as already defined. Equation (3) was obtained by writing an abbreviated form of the Gormley and Kennedy equation[7] in terms of the decontamination factor.

Referring to Fig. 21.1, it appears that the elimination of all leaks equal to or greater than those represented by a sensitivity of 10^{-6} cm^3/sec would be a highly worthwhile objective. Achieving such an objective appears possible but very costly. However, the hazard reduction which would

[7]P. G. Gormley and M. Kennedy, *Proc. Roy. Irish Acad., Sect. A* **52**, 163–69 (1949).

[8]W. DeMarcus and J. W. Thomas, *Theory of a Diffusion Battery*, ORNL-1413 (Oct. 16, 1952).

be obtained might possibly more than offset the extra cost.

The interpretation and utilization of containment-vessel leak-testing data were discussed with regard to estimating the extent of particle deposition under accident conditions. Factors such as flow rates so high as to be in the turbulent regime, unknown leak geometry, nonuniform cross sections of individual leaks, multiple leaks, and leaks beyond the limit of detection did not appear to preclude the calculation of decontamination factors, which, in some cases, would be pessimistic. However, this is the proper direction from a nuclear safety viewpoint for any bias that might be introduced.

Prior to applying these results in practice, additional experimental investigation may be required of the assumption, not previously mentioned, that the leak wall is a perfect sink for the particles. Such an investigation would need to include determination of the resistance to movement, during subsequent air flow, of a deposit of particles.

This theoretical analysis of the decontamination of aerosols by passage through containment-vessel leaks indicates that it may be possible to prove the safety of such vessels by quantitative measurement of leak rates at all points on the surface of the vessel. From the standpoint of particle decontamination, a containment vessel could have a relatively large overall leak rate and still be acceptable, provided no leak or small group of leaks exhibited a flow rate in excess of a certain computed value. However, to utilize this aspect, it would be necessary to prove that the overall leak rate was adequately explained by the combined total of the smaller leaks.

Effect of Particle Agglomeration on the Penetration of Filters in Double Containment Systems

M. H. Fontana[9]

A theoretical study was made of particle agglomeration and its effect on the penetration of filter systems in dual containment systems by fission products carried by particulate matter. This study has been reported in detail[10] and is described here only briefly.

A simplified model was analyzed, in which the particulate matter was pessimistically assumed to be pure iodine, and all particles with diameters less than 0.3 μ were assumed to penetrate the filters. It was shown that agglomeration would occur rapidly enough so that the particles, even though initially much smaller, would reach a 0.3-μ size in a short time (<20 min for typical water reactor systems). This time is directly proportional to the containment volume and inversely proportional to the power level. Assuming that the filter efficiency of the secondary-containment sweep-gas filtration system is zero for particles less than 0.3 μ in diameter, the fraction of the core activity released to the atmosphere during that time was calculated for some conditions of interest. For one reactor system treated, less than 10^{-5} of the iodine available would be released. It was shown that conditions existing during a reactor accident could not be as pessimistic as those of this model.

MEASUREMENT OF THE CHARACTERISTICS OF RADIOACTIVE AEROSOLS USING FIBROUS FILTERS

W. E. Browning, Jr. M. D. Silverman

Prediction of the probable extent of escape of fission products from reactor confinement systems in a reactor accident, or the effectiveness with which they can be removed from gas streams, requires a knowledge of the amounts of various fission products associated with the different sizes of particles which may be released. Presently available techniques do not appear to be adequate for this purpose. A method for characterizing radioactive aerosols has been developed which interprets the distribution of radioactive particles in a series of uniform fiber filters in terms of the three main mechanisms of filtration, that is, diffusion, interception, and inertial impaction. The data for this analysis are obtained by previously reported[11] experimental techniques. The radioactive aerosol is transported through a series of

---

[9]Formerly with Reactor Division.

[10]M. H. Fontana and W. E. Browning, Jr., *Effect of Particle Agglomeration on the Penetration of Filters Utilized with Double Containment Systems*, ORNL-NSIC-1 (Sept. 25, 1963).

[11]W. E. Browning, Jr., and M. D. Silverman, *Reactor Chem. Div. Ann. Progr. Rept. Jan. 31, 1963*, ORNL-3417, pp. 248–50.

uniform Dacron filters, and the particle distribution vs depth in the filter bed, composed of discrete layers of fibers, is determined by radioassay.

Data from the initial series of experiments, using a radioactive test aerosol containing Zn^{65} particles in the diameter range 20 to 300 A and conducted at linear velocities from 0.4 to 88 fpm, have been analyzed in terms of the three mechanisms of filtration. Analysis of the data in the diffusion region has been reported.[12-14]

The data obtained in the initial series of experiments, at the higher flow rates of 10 to 88 fpm (interception and impaction regions), have been analyzed in terms of theories of fiber filtration as evolved by Davies,[15] Chen,[16] and Torgeson.[17] All these theories are derived on the basis of the collection efficiency of a single isolated fiber. However, all filters are composed of many fibers; most have a variable porosity. The effect of neighboring fiber interference on the collection efficiency of individual fibers has been investigated to some extent,[16,18,19] but there is disagreement on how to correct for varying porosity. Chen[16] found that fiber efficiencies in mats were always greater than those calculated for isolated fibers, and he developed a linear expression to correct for α, the volume fraction of fibers in filter mats. Wong and co-workers[18] tried to correct for this term by interpreting pressure drop measurements. The initial series of experiments in the present work was conducted with filter mats having an α of 0.28, well above the region treated theoretically by the above investigators. Extrapolation of the theories by correcting for the high α values according to Davies[15] has yielded fiber efficiencies not in agreement with those obtained experimentally, making it difficult to estimate particle sizes accurately in the higher flow range. A second series of experiments, in which the volume fraction α has been lowered to less than 0.1, has been completed, and analysis of the data is in progress. It is believed that these data can be treated according to a theory of filtration to characterize particle sizes more accurately in this flow region.

---

[12]W. E. Browning, Jr., and M. D. Silverman, *Nuclear Safety Program Semiann. Progr. Rept. June 30, 1963*, ORNL-3483, pp. 29–31.

[13]W. E. Browning, Jr., R. D. Ackley, and M. D. Silverman, "Characterization of Gas-Borne Fission Products," paper presented at the Eighth AEC Air Cleaning Conference, held at Oak Ridge National Laboratory, October 22, 1963.

[14]M. D. Silverman and W. E. Browning, Jr., *Science* **143**, 572–73 (1964).

[15]C. N. Davies, *Proc. Inst. Mech. Engrs. (London)* **B1**, 185 (1952).

[16]C. Y. Chen, *Chem. Rev.* **55**, 595 (1955).

[17]W. L. Torgeson, "A Study of Filtration Mechanisms," Appendix B (June 1, 1961) of *Upper Atmosphere Monitoring Program*, TID-16988 (August 1, 1962).

[18]J. B. Wong, W. E. Ranz, and H. F. Johnstone, *J. Appl. Phys.* **27**, 161 (1956).

[19]H. L. Sadoff and J. W. Almlof, *Ind. Eng. Chem.* **48**, 2199 (1956).

Part V
Other ORNL Programs

22. Corrosion Studies for Chemical Reprocessing Plants

J. C. Griess

J. L. English L. L. Fairchild P. D. Neumann

CORROSION STUDIES FOR THE TRANSURANIUM PROCESSING FACILITY

Corrosion tests have been continued to evaluate the behavior of candidate materials for fabrication of process equipment for the transuranium processing facility. A résumé of the more important studies conducted during the past year is presented below.

Corrosion of Hastelloy C by Mixed Acids

Hydrochloric and nitric acid, individually, are used at various stages in the separation of the transuranium elements. Since it is possible that the two acids may become mixed either in process or waste solutions, it was of interest to determine how Hastelloy C, a possibly useful material for waste tanks, corroded in solutions of the mixed acids. Therefore tests were conducted in 3 and 6 *M* HCl to which various concentrations of nitric acid had been added. The tests were conducted at 43°C as estimated for process conditions, and the test solutions were replaced at 100-hr intervals.

Table 22.1 summarizes the corrosion data for both solution- and vapor-exposed specimens. The rates represent average values for duplicate specimens which usually agreed within 5 to 10%.

The presence of HNO_3 at concentration levels of 0.01, 0.05, or 0.10 *M* does not improve the corrosion resistance of Hastelloy C to 3 *M* HCl solution. Solutions 3 *M* in HCl and 1 *M* in HNO_3 are, however, less corrosive to this alloy. Of additional significance was the fact that no preferential attack took place in heat-affected

Table 22.1. Effect of Nitric Acid on the Corrosion of Welded Hastelloy C by Oxygenated Hydrochloric Acid Solutions at 43°C

HCl Concentration (*M*)	HNO_3 Concentration (*M*)	Exposure Time (hr)	Corrosion Rate (mils/yr)	
			In Solution	In Vapor
3.0	0	1000	87.6	8.4
	0.01	500	143	9.6
	0.05	600	54.0	3.6
	0.10	400	84.0	2.4
	1.0	336	8.4	2.4
6.0	0	1000	66.0	63.6
	0.01	300	185	289
	0.05	100	702	810
	0.10	100	1170	460

zones adjacent to welds on specimens exposed to the 3 *M* HCl–1 *M* HNO_3 environment. In all other tests, such attack was quite severe, and penetrations up to a depth of approximately 35 mils were not uncommon during the tests listed in Table 22.1.

Vapor-phase corrosion in the 3 *M* HCl tests was little influenced by the absence or the presence of nitric acid in any concentration. With the exception of the vapor specimen in the 3 *M* HCl–1 *M* HNO_3 test, all other vapor-exposed specimens exhibited a mild susceptibility to heat-affected-zone attack adjacent to welds.

Solutions which are 6 *M* in HCl become more corrosive to Hastelloy C, whether exposed to the liquid or to its vapor, as HNO_3 is added. Corrosion by the liquid increases markedly and regularly as HNO_3 concentration is raised to 0.1 *M*. Moreover, unusually severe attack of heat-affected zones was experienced by all specimens exposed to solutions of 6 *M* HCl with added HNO_3. In a number of cases, the attack was sufficient to cause complete separation of the 125-mil-thick specimens at the weld–base-metal interface.

Behavior of Hastelloy C in Organic Processing Solutions

Tests of 1000-hr duration were made with welded specimens of Hastelloy C exposed in the solution and vapor phases of two transuranium processing solutions at 43°C. The solutions consisted of 1 *M* mono-2-ethylhexylphenylphosphonic acid in diethylbenzene and 30% Alamine 336 chloride in diethylbenzene. The solutions were changed every 100 hr.

The corrosion behavior of the specimens was excellent. In all cases, observed corrosion rates were less than 1 mil/yr and there was no evidence of heat-affected-zone attack in areas immediately adjacent to welds.

Hydrogen Pickup in Zircaloy-2

Welded Zircaloy-2 specimens were exposed to a number of transuranium processing solutions to determine the sensitivity of the alloy to hydride formation through pickup of H_2 formed during corrosion of the specimen. Test solutions were oxygenated and were replaced with new solutions at 100-hr intervals. All specimens were cut from 125-mil sheets from the same heat of Zircaloy-2; this material as tested contained between 38 and 53 ppm of hydrogen. Table 22.2 summarizes the observed corrosion rates and the hydrogen contents of the solution-exposed specimens after exposure periods of 1000 hr.

Neither corrosion nor hydrogen pickup was a problem in tests at 43°C. The maximum corrosion rate, 3.6 mils/yr, was encountered in a 6 *M* HCl–0.1 *M* HNO_3 environment; observed corrosion rates in other media were generally less than 1 mil/yr. There was no evidence of any hydrogen pickup.

At the boiling temperature, corrosion rates were quite acceptable with two exceptions. Rates of 19.2 and 22.8 mils/yr, respectively, were obtained in the 6 *M* HCl–0.1 *M* HNO_3 and the 6 *M* HCl–0.0023 *M* $LaCl_3$–H_2O_2 environments. In addition, specimens from these two solutions exhibited hydrogen contents of 440 and 360 ppm. Hydrogen pickup to a lesser extent (89 ppm) was experienced also by a specimen exposed in an oxygenated 6 *M* HCl solution.

Tests with a different heat of Zircaloy-2, obtained as vacuum-annealed strip of 10 mils thickness, suggest that although the hydride content of the sample may be low, relatively high concentrations of hydride are formed in thin layers on specimen surfaces. Unwelded specimens of this foil were exposed for 1000-hr periods in oxygenated and boiling 6 *M* HCl and 6 *M* HCl–0.1 *M* HNO_3 solutions. The hydrogen content of the specimen removed from the 6 *M* HCl solution was found to be 5300 ppm while that of the specimen removed from the 6 *M* HCl–0.1 *M* HNO_3 test was 2600 ppm.

Corrosion of Zircaloy-4 by Acid Solutions

Specimens of 125-mil-diam Zircaloy-4 rod were exposed in several oxygenated and boiling acid solutions to determine if the corrosion behavior and resistance to hydrogen pickup were superior to that of Zircaloy-2. The Zircaloy-4 heat contained less than 20 ppm of nickel compared to a nominal value of 500 ppm present in Zircaloy-2. The hydrogen content of the heat was 19 ppm.

After 1000 hr in boiling and oxygenated 6 *M* HCl solutions, which were replaced with fresh solution at 100-hr intervals, a solution-exposed specimen of Zircaloy-4 corroded at a rate nearly ten times faster than Zircaloy-2 in a similar test.

Table 22.2. Corrosion of Welded Zircaloy-2 by Oxygenated Acids

Exposure time: 1000 hr

Medium	Test Temperature (°C)	Corrosion Rate (mils/yr)	Final H_2 Content in Specimen (ppm)[a]
6 *M* HNO_3	43	<1.0	42
6 *M* HNO_3–0.1 *M* HCl	43	<1.0	41
6 *M* HNO_3–0.5 *M* HCl	43	<1.0	36
6 *M* HCl	43	<1.0	40
6 *M* HCl–0.1 *M* HNO_3	43	3.6	48
6 *M* HCl–0.5 *M* HNO_3	43	2.4	43
6 *M* HNO_3	110	<1.0	39
6 *M* HNO_3–0.1 *M* HCl	110	<0.1	45
6 *M* HNO_3–0.5 *M* HCl	110	<1.0	48
6 *M* HCl	110	2.4	89
6 *M* HCl–0.1 *M* HNO_3	110	19.2	440
6 *M* HCl–0.5 *M* HNO_3	110	1.8	50
6 *M* HCl–0.0023 *M* $LaCl_3$–H_2O_2	110	22.8	360

[a]Initial hydrogen content varied between 38 and 53 ppm.

The hydrogen content in the Zircaloy-4 specimen after test was 1000 ppm.

The corrosion resistance of Zircaloy-4 in boiling and oxygenated 6 *M* HCl–0.1 *M* HNO_3 was slightly better (12 mils/yr in 1000-hr tests) than that of Zircaloy-2; the final hydrogen content of the 125-mil-diam Zircaloy-4 specimen was 130 ppm.

Behavior of Tantalum-Plated Specimens in 6 *M* HCl

Two tantalum-plated specimens (plating performed by Union Carbide Corporation, Parma, Ohio) have received a total exposure of 1600 hr in boiling and oxygenated 6 *M* HCl solution. One specimen consisted of 3 to 5 mils of tantalum plated directly onto type 316 stainless steel base metal. The second specimen was plated with the same thickness of tantalum onto Hastelloy C base metal which was first given a 0.3-mil-thick flash coat of copper before the application of the tantalum.

During the first 800 hr of exposure, the behavior of both plated specimens was excellent. However, in the interval between 800 and 900 hr, a blister developed in the tantalum plate deposited on the stainless steel base metal. Examination disclosed the blister to be approximately 125 mils in diameter. During an additional 200 hr of test, the blister increased in size to nearly 200 mils in diameter. After a total of 1600 hr, no further increase in size was observed. No appreciable damage to the tantalum-plated Hastelloy C has been observed.

CORROSION TESTING PROGRAM IN SUPPORT OF POWER-REACTOR FUEL-ELEMENT REPROCESSING

This corrosion testing program assists the Chemical Technology Division in the development of power-reactor fuel reprocessing and the storage and disposal of the associated waste products. Each new dissolution and separation process

proposed must be evaluated in terms of the corrosion problems resulting from the process. Candidate materials for construction of containers, piping, reaction vessels, and other process equipment are screened under simulated process conditions. Those with potentially useful corrosion resistance are subjected to longer-term tests, depending on their required service life. Because of the wide scope of the chemical processing development, a large variety of materials are tested under many different conditions.

In the chemical processing area, tests have been mainly concerned with the selection of materials for various phases of the Chloride Volatility Process and for reprocessing of graphite-bearing fuels, both by high-temperature oxidation and subsequent acid dissolution and by direct acid treatment of the fuels. The latter process involves the use of hydrofluoric acid in combination with nitric acid, both with and without additional oxidizing agents.

Waste storage tests have been carried out to choose suitable materials for temporary storage of liquid waste and for concentration of wastes by evaporation. Tests were also made to determine the corrosive effects of calcining the residues, either alone or with the addition of glass-producing substances, on the container materials. A few tests are also in progress related to the storage of these wastes in salt mines.

The results of this testing program are an integral part of the process development program and as such are included in reports issued by the Chemical Technology Division.[1]

ACCEPTANCE TESTS

Approximately 150 boiling 65% HNO_3 tests and electrolytic oxalic acid etching tests (ASTM: A262-55T) were completed on austenitic stainless steels for use in various ORNL and Y-12 programs. In addition, a small number of acceptance tests with Hastelloy C in acidified ferric sulfate solution were performed. Approximately 80% of the nitric and oxalic acid tests were concerned with Y-12 programs; the remaining tests dealt with materials for the High Flux Isotope Reactor.

---

[1] R. E. Blanco and F. L. Parker, *Waste Treatment and Disposal Quart. Progr. Rept. February–April 1963*, ORNL-TM-603; *Waste Treatment and Disposal Quart. Progr. Rept. May–October 1963*, ORNL-TM-757; *Chem. Tech. Div. Ann. Progr. Rept. May 31, 1963*, ORNL-3542.

23. Chemical Support for Saline Water Program[1]

SOLUBILITY AND THERMODYNAMIC RELATIONSHIPS FOR $CaSO_4$ IN NaCl-H_2O SOLUTIONS

W. L. Marshall Ruth Slusher
E. V. Jones

Calcium sulfate is a major constituent of scales that form on heat exchanger surfaces when seawater or other saline waters are distilled. The purpose of this present investigation was to obtain solubilities of $CaSO_4$ in NaCl-H_2O solutions at high temperature for application to desalination programs and to obtain additional data for testing solubility theory at temperatures above 25°C.

This study presents solubilities of metastable $CaSO_4 \cdot 2H_2O$ at 40 and 60°C, of metastable $CaSO_4 \cdot \frac{1}{2}H_2O$ at 125°C, and of anhydrous $CaSO_4$ at 125 to 200°C in NaCl-H_2O solutions and interprets the results in terms of the Debye-Hückel theory. Values of the thermodynamic solubility products and of ΔF^0, ΔH^0, and ΔS^0 are given for several temperatures from 25 to 200°C. Experimental procedures, which are similar to those used for solubility of $CaSO_4$ in water,[2] are given in detail in a paper to be published elsewhere.[3]

The solubility of $CaSO_4 \cdot XH_2O$ in H_2O solution can be described by the equilibrium

$$CaSO_4 \cdot XH_2O(\text{solid}) \rightleftharpoons Ca^{2+} + SO_4^{2-} + XH_2O , \quad (1)$$

which can be expressed by the thermodynamic solubility product,

$$K^0_{sp} = [m_{Ca^{2+}}][m_{SO_4^{2-}}][\gamma_{Ca^{2+}}][\gamma_{SO_4^{2-}}][a_{H_2O}]^X , \quad (2)$$

where X = number of moles of H_2O in the hydrate, $m_{Ca^{2+}}$ and $m_{SO_4^{2-}}$ are molal concentrations, $\gamma_{Ca^{2+}}$ and $\gamma_{SO_4^{2-}}$ are their respective activity coefficients, and a_{H_2O} is the activity of H_2O in the solution phase. Upon taking the logarithm of K^0_{sp}, substituting $[-4\delta I^{1/2}/(1 + AI^{1/2})]$ from the Debye-Hückel theory both for log $\gamma_{Ca^{2+}}$ and log $\gamma_{SO_4^{2-}}$, and rearranging, the expression

$$\log K_{sp} = \log K^0_{sp} + 8\delta \frac{I^{1/2}}{1 + AI^{1/2}} - X \log a_{H_2O} \quad (3)$$

is obtained where K_{sp} = the solubility quotient as a function of I, δ = the limiting Debye-Hückel slope, A is a constant, and I = the ionic strength = $4m_{CaSO_4} + m_{NaCl}$. If $m_{Ca^{2+}}$ equals $m_{SO_4^{2-}}$, then log K_{sp} = 2 log S and log K^0_{sp} = 2 log S^0; thus,

$$\log S = \log S^0 + 4\delta \frac{I^{1/2}}{1 + AI^{1/2}} - \frac{X}{2} \log a_{H_2O} , \quad (4)$$

where S = the molal solubility of $CaSO_4$ at ionic strength I, and S^0 = the hypothetical molal solubility at I = 0.

Figures 23.1 and 23.2 present the experimental data for the solubilities in NaCl-H_2O solutions of $CaSO_4 \cdot 2H_2O$ (metastable) at 40 and 60°C, of $CaSO_4 \cdot \frac{1}{2}H_2O$ (metastable) at 125°C, and of $CaSO_4$ at 125, 150, 175, and 200°C, plotted as log S +

---

[1]Work performed at ORNL for the Office of Saline Water, U.S. Department of the Interior.

[2]W. L. Marshall and E. V. Jones, *Reactor Chem. Div. Ann. Progr. Rept. Jan. 31, 1963*, ORNL-3417, p. 277.

[3]A detailed paper by W. L. Marshall, Ruth Slusher, and E. V. Jones is in press [*Journal of Chemical and Engineering Data* (1963)]. An abstract of this paper is presented here.

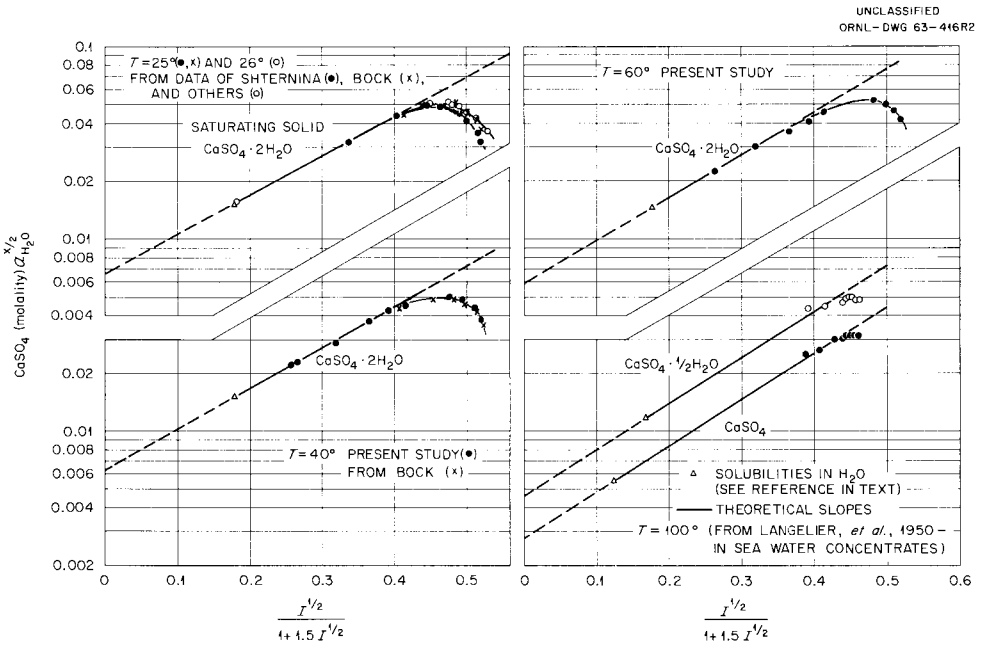

Fig. 23.1. The Solubilities of $CaSO_4$ and Its Hydrates in NaCl-H_2O Solutions vs $I^{1/2}/(1 + 1.5I^{1/2})$, at 25–100°C. a_{H_2O} = activity of H_2O, X = number of moles of H_2O in solid phase.

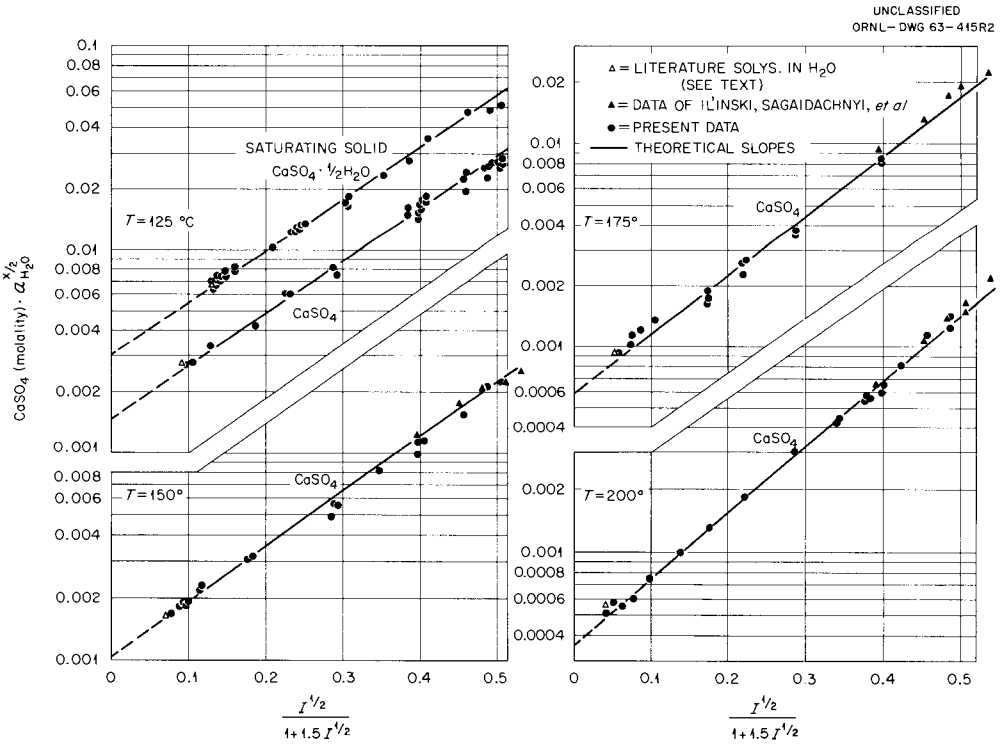

Fig. 23.2. The Solubilities of $CaSO_4 \cdot \frac{1}{2}H_2O$ (at 125°C) and $CaSO_4$ in NaCl-H_2O Solutions vs $I^{1/2}/(1 + 1.5I^{1/2})$, at 125–200°C. a_{H_2O} = activity of H_2O, X = number of moles of H_2O in solid phase (= 0 for $CaSO_4$).

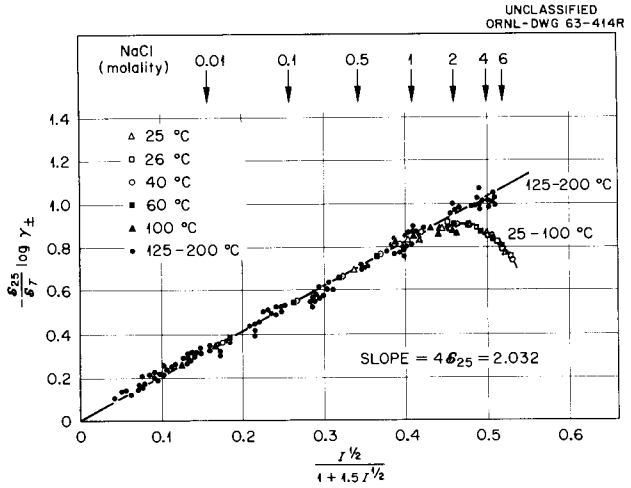

Fig. 23.3. Variation of $-\log\gamma_\pm$ with $I^{1/2}/(1 + 1.5I^{1/2})$ for Solubility of $CaSO_4$ and Its Hydrates in NaCl-H_2O, at 25–200°C. Debye-Hückel slopes, δ_T, normalized to volue at 25°C.

$(X/2)\log a_{H_2O}$ against the Debye-Hückel function,

$$\frac{I^{1/2}}{1 + AI^{1/2}}, \qquad (5)$$

where $A = 1.5$. This frequently used value of A gave approximately the best fit to the data at 200°C and provided a good fit at most of the other temperatures. Solubility data of other workers[4–8] are included in these figures. The straight lines drawn through the data at each temperature correspond to the theoretical Debye-Hückel limiting slope at the particular temperature times a valency factor, $z^+ \cdot z^-$, which for $CaSO_4$ equals 4.[9]

Figure 23.3 shows all data plotted as

$$\frac{1}{2}(\delta_{25}/\delta_T)\log\frac{K_{sp}\,a^X_{H_2O}}{K^0_{sp}} = -(\delta_{25}/\delta_T)\log\gamma_\pm \text{ vs } I^{1/2}/(1 + 1.5I^{1/2}).$$

All theoretical slopes thus are normalized to the limiting Debye-Hückel slope at 25°C shown by the straight line. Deviations at the low temperatures and high ionic strengths are observed. Nevertheless, the agreement with Debye-Hückel theory at all other ionic strengths and temperatures indicates that $CaSO_4$ in NaCl-H_2O solution behaves as a strong electrolyte and does not associate or form complexes to any appreciable extent.

Smoothed values for the solubility of $CaSO_4$ and its hydrates in NaCl-H_2O solutions (presented in detail elsewhere,[3] but not included in this document) were obtained by use of Eq. (4) and the experimental data shown in Figs. 23.1 and 23.2. The more recent results at 25°C in concentrated NaCl-H_2O (ref. 4) appeared to be more self-consistent with temperature than the earlier data[7] and were used to obtain the smoothed values.

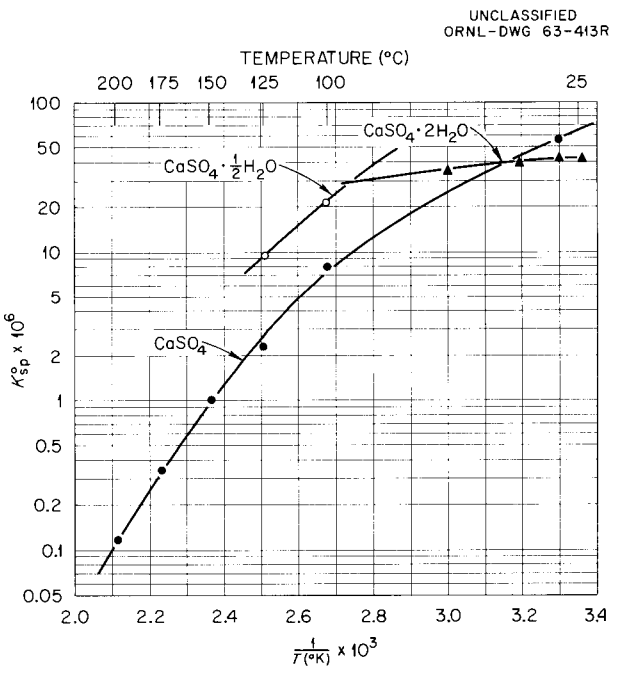

Fig. 23.4. The Thermodynamic Solubility Products of $CaSO_4$ and Its Hydrates, at 25–200°C, K^0_{sp}, on Logarithmic Scale vs $1/T\,(°K)^{-1}$.

---

[4] E. Bock, *Can. J. Chem.* **39**, 1746 (1961).

[5] F. K. Cameron, *J. Phys. Chem.* **5**, 556 (1901); Orloff, *J. Russ. Phys. Chem. Soc.* **37**, 949 (1902); C. Cloez, *Bull. soc. chim.* [3] **29**, 167 (1903); d'Anselme, *Bull. soc. chim.* [3] **29**, 372 (1903).

[6] W. F. Langelier *et al.*, *Ind. Eng. Chem.* **42**, 126 (1950).

[7] E. B. Shternina and E. V. Frolova, *Izv. Sektora Fiz.-Khim. Analiza, Inst. Obshch. Neorgan Khim., Akad. Nauk SSSR* **21**, 271 (1952); E. B. Shternina, *Izv. Sektora Fiz.-Khim. Analiza, Inst. Obshch. Neorgan. Khim., Akad. Nauk. SSSR* **17**, 351 (1949); E. B. Shternina, *Compt. rend. acad. sci. SSSR*, **40**, 247 (1948).

[8] A. B. Zdanovskii, *Tr. Vses. Nauchn. Issled. Inst. Galurgii* **21**, 345 (1949).

[9] H. S. Harned and B. B. Owne, *The Physical Chemistry of Electrolytic Solutions*, 3d ed., Reinhold, New York, 1958.

Table 23.1. Thermodynamic Values for the Equilibrium $CaSO_4 \cdot XH_2O(solid) \rightleftharpoons Ca^{2+} + SO_4^{2-} + XH_2O$

T (°C)	K^0_{sp}	ΔF^0 (kcal/mole)	ΔH^0 (kcal/mole)	ΔS^0 (cal mole^{-1} deg^{-1})
		Solid Phase, $CaSO_4$		
	($\times 10^{-6}$)			
25	63.0	+5.75	−1.9	−25.7
30	54.5	+5.88	−2.6	−28.1
40	47.8	+6.19	−4.0	−32.6
60	28.7	+6.92	−6.5	−40.3
100	7.73	+8.78	−10.7	−52.2
125	2.25	+10.2	−12.9	−58.0
150	1.00	+11.7	−14.8	−62.7
175	0.336	+13.3	−16.6	−66.6
200	0.114	+15.0	−18.1	−70.0
		Solid Phase, $CaSO_4 \cdot \frac{1}{2}H_2O$		
	($\times 10^{-6}$)			
100	21.2	+8.00	−9	−45.7
125	9.49	+9.15	−10	−49.2
		Solid Phase, $CaSO_4 \cdot 2H_2O$		
	($\times 10^{-6}$)			
25	42.2	+5.96	∿+1.6	−14.6
30	43.6	+6.05	∿+0.6	−17.9
40	42.5	+6.26	∿−1.3	−24.1
60	35.7	+6.77	−2.0	−26.3

The thermodynamic solubility products, K^0_{sp}, for the reaction $CaSO_4 \cdot XH_2O_{(solid)} \rightleftharpoons Ca^{2+} + SO_4^{2-} + XH_2O$ were calculated at each temperature and are given in Table 23.1 together with calculated values of ΔF^0, ΔH^0, and ΔS^0. The quantity ΔH^0 was obtained from the slopes of the curves of Fig. 23.4 at each temperature.

CORROSION OF ALUMINUM ALLOYS IN SALT SOLUTIONS

E. G. Bohlmann

Replacement of conventional copper or stainless steel alloys with aluminum in seawater applications would result in substantial capital savings.[10] This possibility is given encouragement by the successful use of aluminum in marine equipment.[11,12] Unfortunately, little is known about the effects of particular seawater variables on aluminum corrosion, particularly at higher tem-

[10]Ralph Horst, Jr., and R. T. Marchese, *Aluminum Surface Condenser Tubes for Steam Power Plants*, ASME Paper No. 62WA-330, presented at Winter Annual Meeting, New York, Nov. 25–30, 1962.

[11]E. T. Wanderer, *Mater. Protect.* 2, 54–60 (1963).

[12]R. J. Gainey, *Use of Aluminum for Sea Water Distillation Equipment*, U.S. Army Engineers Research and Development Laboratories, Fort Belvoir, Va., Report 1705-TR (Jan. 9, 1962).

peratures in dynamic systems. This program is directed towards attaining such information.

The studies are being carried out in two 100-gpm dynamic loops constructed of titanium alloys. The loops can be operated at temperatures to 300°C, at pressures to 200 psi, and with flow rates in the range 0 to ~100 fps over corrosion specimens. They are equipped for sampling, atmosphere control, and continuous replenishment as required.

During the past year the studies have emphasized significant variables suggested by high-purity water investigations in 1 *M* NaCl at 150°C.

Replacement or Area Effect

The so-called "replacement or area effect" has plagued investigations of aluminum corrosion in flowing high-purity water for many years. This is the designation given to the observation that the initial and continuing corrosion of aluminum in dynamic systems is substantially affected by the area, location, and corroded state of the exposed aluminum, as well as the loop volume, refreshment rate, and other variables. The effect has been attributed to leaching of an underlying protective oxide,[13] the behavior of short-lived colloidal aluminum species,[14] and rate and degree of saturation of the water with water-soluble oxide.[15]

The work of Biefer and Krenz[15] indicated that the effect was saturated by the presence of greater than 170 cm^2 of aluminum area per liter of water, so ~200 cm^2/liter was added to the loop circulating system at the start of each run in the early studies, with the hope of eliminating the effect. However, subsequent studies showed this remedy was only partially effective, as shown by the data given in Table 23.2. The conditions used in the studies were: deaerated 1 *M* NaCl, pH 8.5–9, 150°C, and 10.5 and 19.2 fps flow rate over pin specimens of alloys 3003 and 5052. New solution was charged and ~200 cm^2/liter of "excess" new aluminum surface (in addition to that associated with the specimens) was introduced whenever the loop was shut down to remove and replace specimens.

The data are divided into two groups in the table to separate the replacement specimens and the specimens introduced at the start of the run series. The data show the specimens introduced at the start of the run series corroded only ~0.1 mil in the first 100 hr and at a continuing rate of about 1 mil/yr over the next 1100 hr. The replacement specimens, however, showed both high initial (100 hr) and continuing corrosion. Subsequent studies under the same conditions but without added excess aluminum showed high initial (6 to 10 mg/cm^2) and continuing (20 to 30 mils/yr) corrosion for both the initial and replacement specimens. Thus the added excess aluminum substantially affected the specimen behavior, but did not entirely overcome the effect of varying specimen area.

It was noted, however, that the rapid continuing corrosion in the absence of the excess aluminum was quite uniform; this suggested (see pH discussion below) that the pH range 8.5–9 was too high for the reduced area condition; exploratory studies of this possibility were undertaken. Preliminary results from short-term experiments indicate a close interrelation between the effects of pH and the amount of new surface exposed on aluminum corrosion, the lower areas demanding lower pH's for minimum attack. Continuing studies are directed at defining this interrelationship.

pH

Results of a series of runs investigating the effect of pH on the corrosion of aluminum alloys in 1 *M* NaCl are summarized in Table 23.3. Conditions were: pH – 6–8, 8–8.5, 9–9.5, and 10–10.5; 150°C; flow velocity – 9.6 and 37.5 fps; 300 hr duration. Alloys exposed were EC, 1100, 3003, 5052, 5154, and 6061. In addition to the specimens, ~200 cm^2 of new aluminum surface per liter

---

[13] R. L. Dillon, *Dissolution of Aluminum Oxide as a Regulating Factor in Aqueous Aluminum Corrosion*, HW-61089 (Aug. 31, 1959).

[14] J. E. Draley and W. E. Ruther, "The Corrosion of Aluminum Alloys in High Temperature Water," pp. 477–98 in *Corrosion of Reactor Materials*, vol. 1, International Atomic Energy Agency, Vienna, 1962.

[15] G. J. Biefer and F. H. Krenz, "Corrosion of Aluminum-Nickel-Iron Alloys in High Temperature Water," pp. 1–16 in *High Purity Water Corrosion of Metals*, National Association of Corrosion Engineers Publication 60-13 (Aug. 2, 1960).

Table 23.2. Corrosion of Aluminum Alloys[a] in Saline Water

Conditions: 1 *M* NaCl, deaerated (200–500 ppm He), pH 8.5–9.0, 150°C
New solution charged for each run

Specimen Exposure History						Corrosion Data					
Runs in Which Exposed					Total Time Exposed (hr)	Flow Rate = 10.5 fps			Flow Rate = 19.2 fps		
12	13	14	15	16		Number of Specimens	Weight Loss (mg/cm^2)[b] Range	Av	Number of Specimens	Weight Loss (mg/cm^2) Range	Av
Original Specimens											
X					98	9	0.57–0.81	0.64	4	0.85–1.25	1.06
X	X				195	2	0.66–0.79	0.73			
X	X	X			289	4	0.90–1.07	1.01			
X	X	X	X		578	4	1.07–1.47	1.27	4	1.18–1.40	1.31
X	X	X	X	X	1178	4	0.94–1.97	1.41	2	1.79–2.49	2.14
Replacement Specimens											
	X				97	4	3.41–3.83	3.67			
		X			94	6	2.49–3.00	2.61			
	X	X			192				2	7.51–7.90	7.71
			X		288	4	2.63–2.91	2.75	2	4.29–5.71	5.00
	X	X	X		480	3	4.00–4.95	4.45	2	6.56–7.22	6.89
				X	600	4	5.23–5.86	5.51	2	12.69–13.65	13.17

[a] 3003 (1.2% Mn) and 5052 (2.5% Mg, 0.25% Cr); data for the two alloys are combined in the table since no difference in behavior was observed.

[b] 6.9 mg/cm^2 = 1 mil.

of solution was inserted in the loop at the beginning of each run.

All the alloys showed substantial corrosion variation with pH. In general, the corrosion was characterized by pitting attack at the lower pH's and generalized rapid attack at the higher pH's with minimum attack indicated in the range 8.5 to 9. Thus, the behavior of the alloys in salt water was similar to that in high-purity water except that the optimum pH was two units higher. As indicated above, however, this apparently was related to the area effect.

Alloys

The compositions of the various alloys which have been tested are given in Table 23.4. The alloys are divided into three groups according to relative performance.

Good. – The superiority of the 5052 and 3003 alloys was indicated in pH studies described above and was confirmed in comparison studies with recently acquired alloys. Under comparable conditions, the 5052 alloy often shows slightly greater generalized attack but more resistance to pitting than the 3003 alloy. The 5454 alloy became available only recently but has shown comparable generalized corrosion and better resistance to pitting than the 3003 and 5052 alloys.

Intermediate. – In general, these alloys showed an appreciably greater susceptibility to pitting attack and were downgraded for that reason.

Poor. – The relatively poor performance of the 6061 alloy was surprising in view of the many successful applications of this alloy in marine

Table 23.3. Effect of pH on Corrosion of Aluminum Alloys in Saline Water

Conditions: 1 *M* NaCl, 150°C, ~300 hr, >200 cm^2 Al surface per liter of loop volume

Alloy	fps	Weight Loss (mg/cm^2)[a]			
		pH = 6–8	pH = 8–8.5	pH = 9–9.5	pH = 10–10.5
EC	9.6	2.3–9.6[b]	0.7–0.9	15–30	>300
	37.5	2–17[b]	1.6–2.6	>250	>300
1100	9.6	1.9–8.4[b]	0.7–1.8	2.9–6.2	8.7–12
	37.5	4.5–9.5[b]	1.9–2.1	7–10	28–48
3003	9.6	0.9–1.6	0.9–1.9	3.1–4.3	11–15
	37.5	1.4–2.6	3.4–4[b]	9.5–26	33–36
5052	9.6	1.8–17	0.8–0.9	3.4–4.2	11–14
	37.5	2.5–32	1.7–2.0	0.9–2.1	23–35
5154[c]	9.6	5.7–81	0.7–2.1	3.6–4.5	13–15
	37.5	15–76	2.1–5.7	9.6–16	33–35
6061	9.6	2.6–4.9	1.6–7.9[b]	3.4–4.6	12–15
	37.5	2.9–13[b]	2.1–4.5[b]	7.6–10	28–35

[a] 6.9 mg/cm^2 = 1 mil.

[b] Frequent gross pitting.

[c] Intergranular attack and exfoliation at pH 6–8 and 8–8.5; weight loss data are misleading.

Table 23.4. Commercially Available Alloys Tested

Alloy	Percent Composition[a]									Relative Performance
	Mg	Mn	Si	Fe	Cu	Cr	Ni	Zn	Ti	
5052	2.2–2.8	0.10	0.45[b]		0.10	0.15–0.35		0.10		Good
5454	2.4–3.0	0.50–1.0	0.40[b]		0.10	0.05–0.20		0.25	0.20	Good
3003		1.0–1.5	0.6	0.7	0.20			0.10		Good
EC[c]										Intermediate
1100		0.05	0.1[b]		0.20			0.10		Intermediate
3004	0.8–1.3	1.0–1.5	0.30	0.7	0.25			0.25		Intermediate
5050	1.0–1.8	0.10	0.40	0.7	0.20	0.10		0.25		Intermediate
6061	0.8–1.2	0.15	0.40–0.8	0.7	0.15–0.40	0.15–0.35		0.25	0.15	Poor
5154	3.1–3.9	0.10	0.45[b]		0.10	0.15–0.35		0.20	0.20	Poor
4032	0.8–1.3		11.0–13.5	1.0	0.50–1.3	0.10	0.50–1.3	0.25		Poor
X8001			0.17	0.6	0.15		1.1			Poor

[a] Percent maximum unless shown as a range.

[b] Fe plus Si.

[c] 99.6% Al minimum.

environments.[16] Excessive generalized and gross pitting attack were often encountered. In addition, the copper released by the corrosion of the 6061 alloy specimens usually deposited on specimens of other alloys with resultant localized attack.

The 5154 alloy showed intergranular attack and exfoliation characteristic of alloys containing magnesium in excess of the equilibrium solid solution amount.[17]

The 4032 high-silicon alloy showed high generalized attack.

The X8001 alloy developed for high-temperature high-purity water service[18,19] was subject to gross pitting attack.

---

[16]F. R. LaQue and H. R. Capson, *Corrosion Resistance of Metals and Alloys*, 2d ed., p. 198, Reinhold, New York, 1963.

[17]E. H. Dix, Jr., W. A. Anderson, and M. B. Shumaker, *Corrosion* **15**, 55t–62t (1959).

[18]J. E. Draley and W. E. Ruther, *Corrosion* **12**, 480t–90t (1956).

[19]M. H. Brown, R. H. Brown, and W. W. Binger, "Aluminum Alloys for Handling High Temperature Water," pp. 82–96 in *High Purity Water Corrosion of Metals*, National Association of Corrosion Engineers Publication 60–13 (Aug. 2, 1960).

24. Solvents for Fluoride Volatility Process

B. J. Sturm R. E. Thoma E. H. Guinn
H. Insley[1] T. N. McVay[2]

The Fluoride Volatility Process recovers uranium as volatile UF_6 from molten fluoride mixtures in which solid fuel elements from nuclear reactors have been dissolved by hydrofluorination. In the ORNL version of this process the UF_6 is freed from fission products that are volatile or have volatile fluorides by selective adsorption and desorption on beds of solid sodium fluoride; in the final step, UF_6 is removed and several fission product materials remain on the bed. The process has been notably successful[3,4] in reprocessing of elements of zirconium-uranium alloy clad with zirconium; it seems capable of easy extension to reprocessing elements of aluminum-uranium alloys clad with aluminum and, with more difficulty, to reprocessing of uranium oxide fuels clad with stainless steels. Successful application of the process to fuels of each type requires a solvent which will, at temperatures below 600°C, (1) permit rapid reaction of the cladding and the fuel with anhydrous HF and (2) dissolve large quantities of fluorides of the cladding and the fuel as they form during the hydrofluorination step. A search for such solvents is the objective of this study; primary emphasis has remained during the past year on solvents for reprocessing of aluminum-uranium fuels.

The equilibrium solubility of AlF_3 in $LiF\text{-}BeF_2$ mixtures seemed[5,6] to make the $LiF\text{-}BeF_2\text{-}AlF_3$ system a promising candidate. However, in pilot-scale tests,[7] the rate of hydrofluorination and dissolution of aluminum in such media proved to be disappointingly low.

A brief study of the $LiF\text{-}KF\text{-}AlF_3$ system (see Table 24.1 and Fig. 24.1) showed that the several merits of LiF-KF mixtures as solvents were completely offset by the high liquidus temperatures in the ternary system. A brief search for additional components that would substantially depress the liquidus temperatures, particularly those near the minimum in the $3KF\cdot AlF_3\text{-}LiF$ quasi-binary system, was unsuccessful. Addition of alkaline-earth fluorides, Na_3AlF_6, and Cs_3AlF_6 lowered the liquidus temperatures to some extent but not enough to give practical importance to the solubility of AlF_3 in the melt at 600°C. It should be noted that Fig. 24.1 shows the formation of immiscible liquid phases over a considerable composition interval. Such behavior may ultimately prove of practical value, as in separations processes, but no such possible use has yet been studied.

The partially completed investigation of the $KF\text{-}ZrF_4\text{-}AlF_3$ system and some preliminary testing[8] suggest that the $KF\text{-}ZrF_4$ system has great potential for processing of uranium-aluminum alloys. The liquidus surface of this ternary system has been determined (Fig. 24.2 and Table 24.1) by the

[1]Consultant, National Bureau of Standards (retired).

[2]Consultant, University of Alabama (retired).

[3]*Chem. Tech. Div. Ann. Progr. Rept. May 31, 1963*, ORNL-3452, p. 26; *Chem. Tech. Div. Ann. Progr. Rept. June 30, 1962*, ORNL-3314, p. 39.

[4]F. L. Culler, Jr., internal memorandum, Aug. 30, 1963.

[5]R. L. Boles and R. E. Thoma, *Volatility Process Phase Studies — A Survey of Molten Fluoride Solvent Mixtures Suitable for Dissolution of AlF_3*, ORNL-TM-400 (Oct. 22, 1962).

[6]R. E. Thoma *et al.*, *Reactor Chem. Div. Ann. Progr. Rept. Jan. 31, 1963*, ORNL-3417, pp. 257–59.

[7]These tests were conducted in ORNL Chemical Technology Division.

[8]*ORNL Status and Progr. Rept. July 1963*, ORNL-3491, pp. 8–9.

Table 24.1. Invariant Points in Certain Molten Fluoride Systems Containing AlF_3

System	Composition (mole %)	Type of Invariant	Temperature (°C)
$LiF-BeF_2-AlF_3$	46-52-2	Eutectic	325 ± 12
	35-60-15	Eutectic	335 ± 12
$LiF-KF-AlF_3$	33-42-25	Peritectic	780 ± 3
	45.5-53-1.5	Eutectic	490 ± 3
	59-20-21	Eutectic	640 ± 3
	6-48-46	Eutectic	500 ± 3
$LiF-K_3AlF_6-CaF_2$	78-13-9	Eutectic	700 ± 5
$LiF-K_3AlF_6-SrF_2$	79-11-10	Eutectic	695 ± 5
$LiF-K_3AlF_6-ZnF_2$	61-8-31	Eutectic	668 ± 10
$LiF-NaF-AlF_3$	37-25-37	Eutectic	605 ± 10
$KF-AlF_3-ZrF_4$	63-15-22	Eutectic	490 ± 3
	53-6-41	Eutectic	400 ± 12

use of recently developed visual methods for obtaining crystallization data.[5] Compositions near the limiting ZrF_4-AlF_3 binary system have not been examined because of the volatility of these components in mixtures with little alkali fluoride. Mixtures containing ~65–35 mole % ZrF_4 and ~35–65 mole % KF display liquidus temperatures below 600°C and may be used as AlF_3 solvents. The greatest solubility of AlF_3 occurs in mixtures rich in KF. A three-step process was devised to make maximum use of $KF-ZrF_4$ solvents: in the first step, $KF-ZrF_4$ mixtures containing 35–37 mole % ZrF_4 are used to dissolve ~15–17 mole % AlF_3; in the second step, additional KF is added to the mixture to substantially increase the solubility of AlF_3 at 600°C; in the final step, additional aluminum is dissolved to ~26 mole % AlF_3 at temperatures below 600°C. Such a process path, indicated by the results of these phase studies, has recently been tested on a larger scale by the Chemical Technology Division with good results.[8] During hydrofluorination, the aluminum dissolves smoothly and rapidly; aluminum is corroded (dissolved) at about 30 mils/hr. Such a melt, when saturated with AlF_3 as described above, can dissolve ~20 mole % NaF before the liquidus temperature rises above 600°C. It is possible, therefore, after volatilization of uranium from a dissolved batch of fuel elements and recovery of the UF_6 from the NaF bed, to dissolve the contaminated NaF in the dissolver solution and discard these radioactive materials in a single operation.

Studies of this kind, in which the location of the liquidus surface is all-important, are best conducted by visual observation of crystallization and melting phenomena. A glove box, fitted with a furnace and in which an inert atmosphere can be maintained, is used for this purpose.[5] Manual addition of known increments of material to a melt contained in a large open crucible within the furnace permits observation of many closely related compositions in a short time. The apparatus has also proved valuable in study of the solubility of oxides in molten fluorides, the changes in electrical conductivity of melts as they undergo phase transitions, and boiling points of salt mixtures.

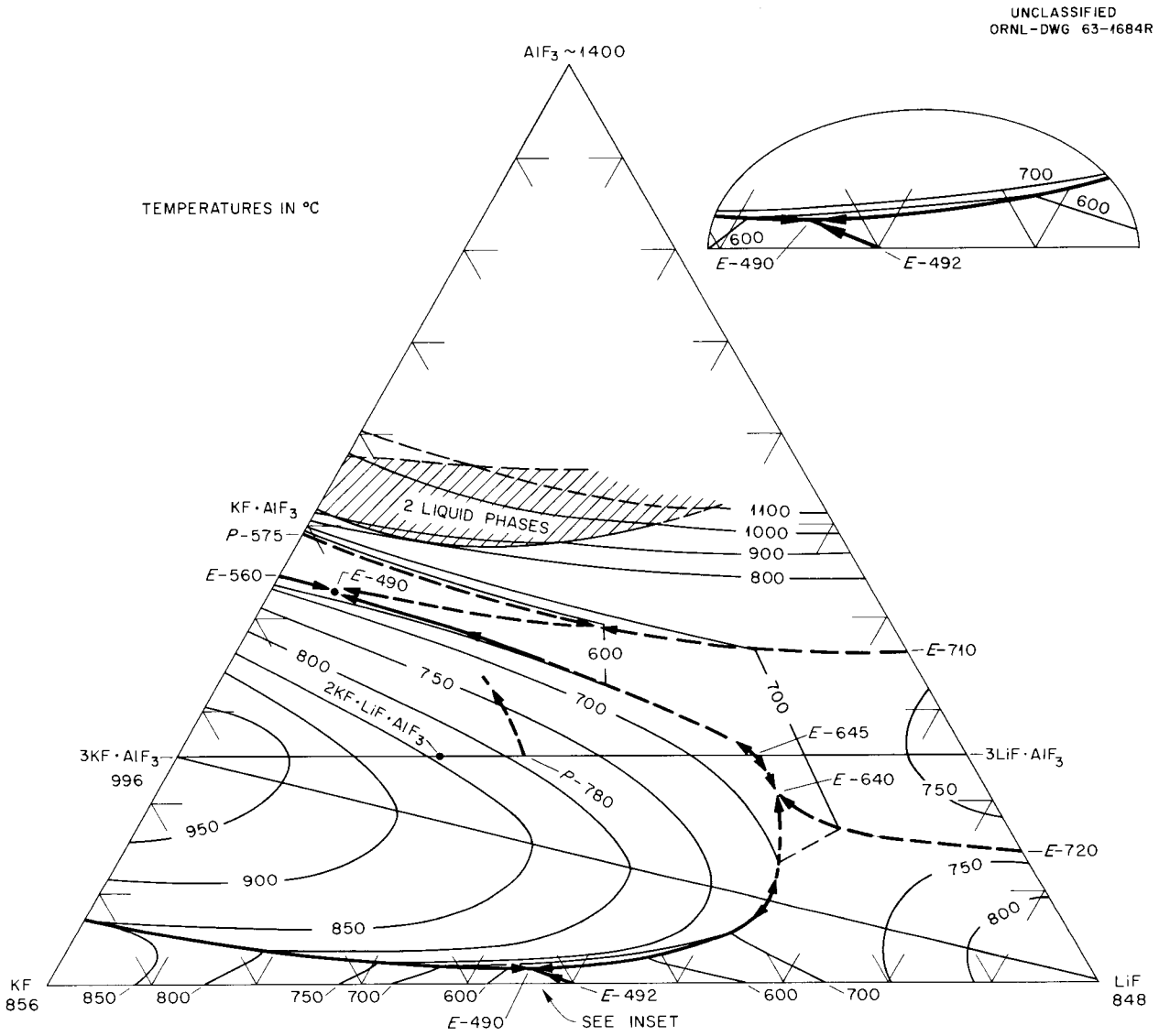

Fig. 24.1. The System LiF-KF-AlF_3.

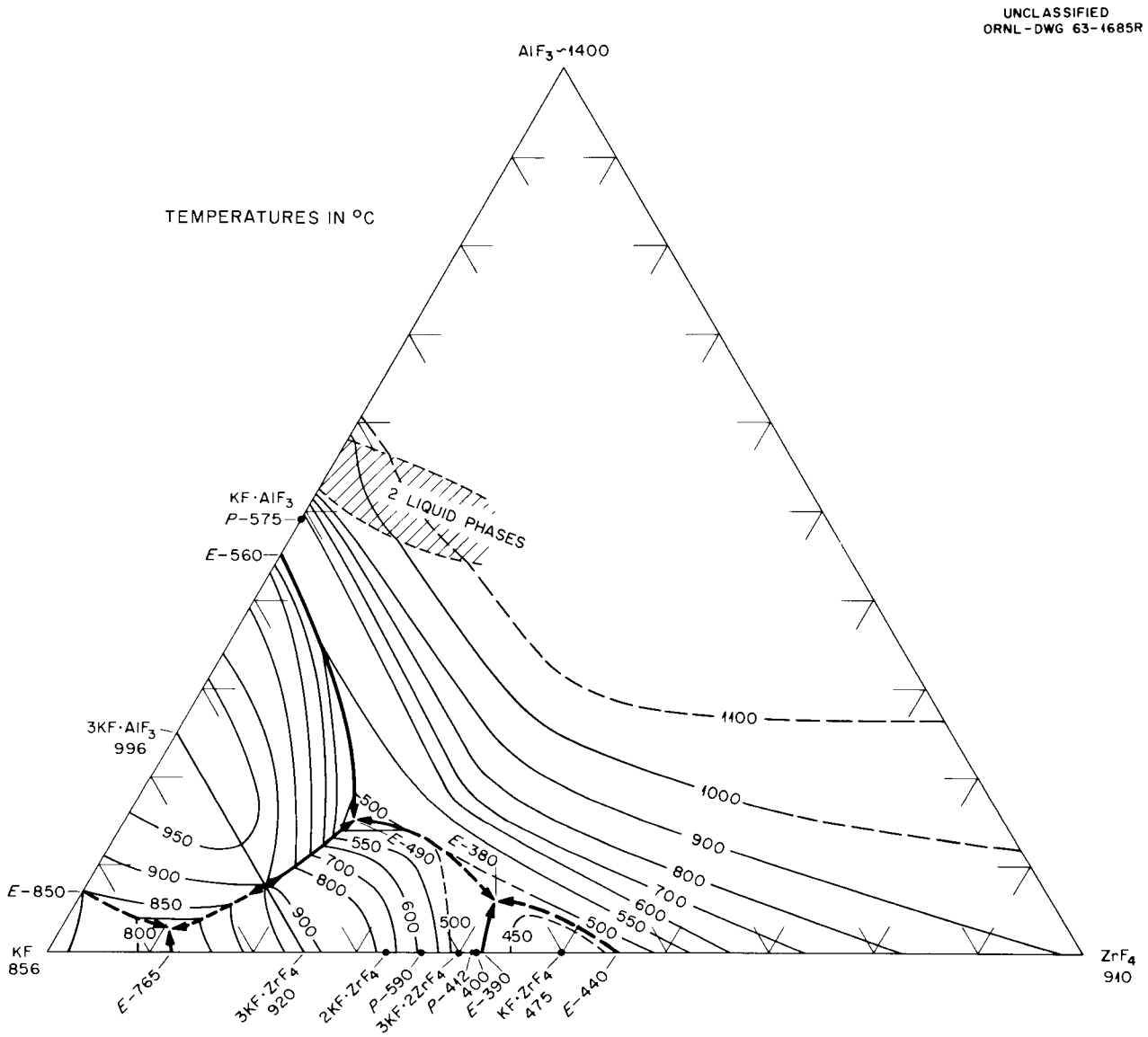

Fig. 24.2. The System $KF\text{-}ZrF_4\text{-}AlF_3$.

25. SNAP-8 Chemistry Studies: The Chemistry of Hydrogen-NaK Systems

E. L. Compere
J. E. Savolainen
H. C. Savage
T. H. Mauney

The SNAP-8 reactor will use a compact core of uranium-zirconium hydride fuel rods cooled by circulating sodium-potassium alloy and a secondary mercury boiler-turbogenerator system, with a radiator heat sink. The reactor is designed to provide substantial quantities of electric power for operation of equipment in space. Optimum system parameters require fuel-rod temperatures high enough to release hydrogen, which can diffuse through the fuel cladding into the primary coolant. Various potential problems arising from this must be considered.

The fate of the hydrogen entering the circulating NaK of the primary coolant circuit from the zirconium-uranium hydride fuel elements depends on the hydrogen diffusion rates into and out of the primary system and on factors governing hydrogen solubility in NaK.[1]

Part of the hydrogen will diffuse through system walls from the primary system into space and most of the rest will diffuse into the secondary mercury boiler system. Some of the hydrogen will dissolve in the NaK primary coolant and may cause precipitation of alkali-metal hydride. Diffusion of hydrogen from the primary circuit should leave a comparatively low partial pressure of hydrogen in that system; hydrogen pressure will probably be less than 10^{-3} atm at the steady state. These estimates are based on the characteristics of diffusion of hydrogen, initially in the gaseous state, through clean metal walls (diaphragms) into vacuum. No information was found in the literature on the effect of dissolution of the hydrogen in NaK on subsequent diffusion rates.

Two kinds of studies are in progress to establish the boundary of tolerable hydrogen concentration in the coolant system. The first is to determine whether the rate of hydrogen diffusion through a metal wall exposed to the gas phase is the same when the wall is in contact with NaK in equilibrium with the gas phase. The second is to determine the solubility of hydrogen in NaK at various pressures and temperatures. From suitable solubility data, two important relations may be determined. The relation between dissolved hydrogen concentration and hydrogen pressure is important in the higher temperature regions of the system. The relation between dissolved hydrogen concentration and the precipitation of solid alkali-metal hydride is important at lower temperatures, where such solids could be formed at system cold spots.

HYDROGEN DIFFUSION STUDIES

The diffusion of hydrogen through clean metal at elevated temperatures should follow the expression:[2]

$$\frac{d(H_2)}{dt} = \frac{kA}{d}\left(\sqrt{P_1} - \sqrt{P_2}\right),$$

where $d(H_2)/dt$ is hydrogen permeation rate (std cc/hr), A is area (cm^2), d is thickness (mm)

[1] H. W. Savage, E. L. Compere, W. R. Huntley, and A. Taboada, *SNAP-8 Corrosion Program Quart. Progr. Rept. Aug. 31, 1963*, pp. 28–40.

[2] R. M. Barrer, *Diffusion In and Through Solids*, Cambridge University Press, 1951.

of metal through which diffusion occurs, P_1 and P_2 are upstream and downstream hydrogen pressures (atm), and k is the hydrogen permeability coefficient for the metal, at the given temperature, expressed in std cc mm hr^{-1} cm^{-2} $atm^{-1/2}$.

According to Barrer[2] the diffusion of hydrogen through metal oxides usually varies as the first power of the pressure. Thus at low partial pressures such films may control the rate of diffusion. Such films should not persist in the SNAP-8 primary system; on the inside they would be reduced by the sodium-potassium alloy, and on the outside by the diffusion of hydrogen.[3] However, precautions must be taken in experimental work to prevent such films from affecting the results.

[3]Saul Dushman, *Scientific Foundations of Vacuum Technique* (ed. by J. M. Lafferty), 2d Ed., pp. 752–58, Wiley, New York, 1962.

Equipment has been constructed to measure the diffusion rate of hydrogen at elevated temperatures through metals of interest to the SNAP-8 program. The metals include Hastelloy N (INOR-8), type 316 stainless steel, and Croloy 9M.

The apparatus for measuring hydrogen diffusion rates through metal diaphragms closely resembles the equipment used by others.[4,5] However, provisions are included permitting the system to contain liquid NaK which may be recovered after the experiment.

The diffusion cell shown in Fig. 25.1 consists of three parts: a central cylindrical section, with the diaphragm, and two end caps. The diaphragm,

[4]D. W. Rudd and J. B. Vetrano, *Permeability of Metals and Enameled Metals to Hydrogen*, NAA-SR-6107 (Oct. 30, 1961).

[5]E. A. Steigerwald, *The Permeation of Hydrogen Through Constructional Materials*, Tech. Memo ER-4776, Thompson Ramo Woolridge, Inc. (Nov. 30, 1961).

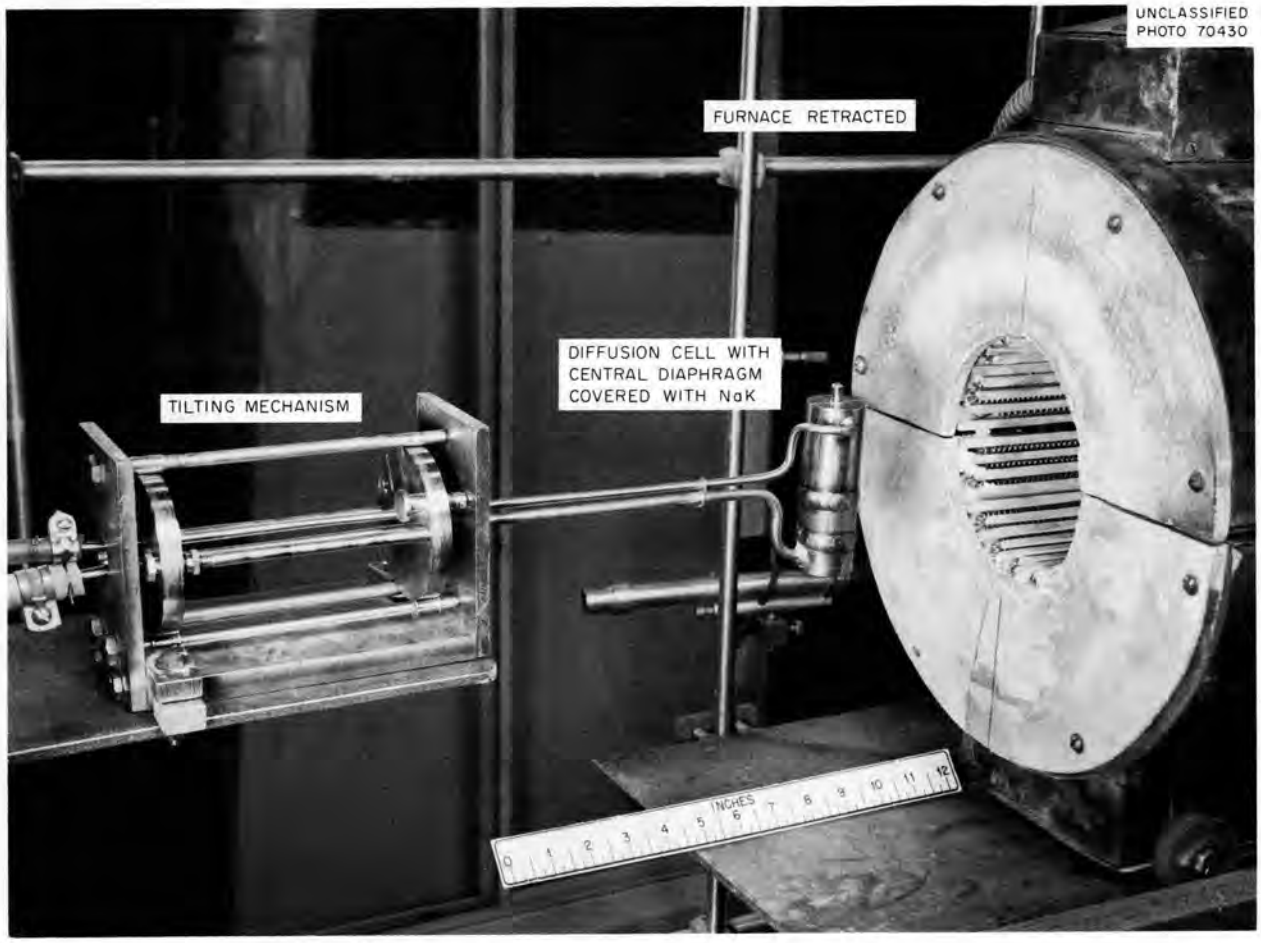

Fig. 25.1. Hydrogen Diffusion Cell and Furnace.

perpendicular to the cylinder axis, is 0.75 in. in diameter and 0.125 in. thick. The end caps, each with an attached tube, are welded to the central section. During operation, the cell, supported by the attached tubes, can be rotated 120° from the vertical position, with the NaK completely covering the diaphragm, to a downward-tilted position in which the diaphragm is exposed only to the gas phase. Beyond this, the measurements are carried out in the conventional manner.

The initial measurements of hydrogen diffusion through a Hastelloy N diaphragm were made at increasing temperature steps from 350 to 550°C, with an upstream pressure of 1 atm and a vacuum (below 100 μ) downstream. Results of five experimental runs are listed in Table 25.1.

Analyses of the diffused gases from runs 1, 2, and 3 indicated the gas recovery system had an air leak. Such an air leak may account for the low diffusion rates shown in tests 2 and 3 by causing surface oxides. After correcting the various causes of air leaks, subsequent experiments yielded a diffused gas which was comparatively pure hydrogen. The permeability coefficients for runs 1, 4, and 5 are consistent with extrapolations of such coefficients for Inconel (a similar alloy), as reported by Flint.[6]

A measured amount of NaK was subsequently introduced into the high-pressure side of the cell under vacuum. A gamma radiograph of the loaded cell showed the NaK level was ~2 cm above the diaphragm.

The hydrogen permeability was measured at 550°C with the NaK tilted away from the diaphragm and also with the cell rotated to the vertical position so that the NaK covered the diaphragm. Results of these determinations are shown in Table 25.2. The values of the permeability are in general approximately 40% of the values which had been obtained at 550°C before the introduction of the NaK. However, no particular difference is shown for diffusion rates with or without NaK covering the diaphragm. The results are highly tentative, and no conclusions are drawn at the present time. The

[6]P. S. Flint, *Diffusion of Hydrogen Through Materials of Construction*, KAPL-659 (1951).

Table 25.1. Diffusion of Hydrogen Through Hastelloy N Diaphragm

Area, 2.84 cm^2; thickness, 2.9 mm

Sample No.	Temperature (°C)	Time (hr)	Diffused Gas Volume (scc)[a]	Analysis[b] (mole %)								Permeability,[d] K [scc (H_2) mm hr^{-1} cm^{-2}]
				H_2	CH_4	H-C[d]	H_2O	CO_2	O_2	N_2 + CO	Ar	
Feed Gas												
1				99.82	0.003	0.008	0.098	0.006	0.006	0.056		
2				99.82	0.003	0.008	0.098	0.006	0.006	0.056		
3				97.26	0.06	0.05	0.21	1.37	<0.005	1.05		
4				99.95	0.004	0.008	0.025	0.001	<0.001	0.010		
5				99.95	0.004	0.010	0.020	0.002	<0.001	0.014		
Diffused Gas												
1	~350	4.25	0.028	79.9	0.5	0.6	9.3	2.0	0.08	7.9		0.0054
2	~400	4.20	0.039	62.9	0.5	0.6	14.7	13.3	0.08	8.3		0.0055
3	430	4.75	0.020	66.89	0.04	0.03	1.55	0.49	6.59	24.9	0.35	0.0030
4	493	4.17	0.294	97.26	0.06	0.05	0.21	1.37	<0.005	1.05		0.072
5	550	2.67	0.456	99.12	0.03	0.08	0.06	0.19	<0.005	0.051		0.215

[a]scc = standard (1 atm, 0°C) cubic centimeters.

[b]By mass spectrometry.

[c]Higher hydrocarbons.

[d]At 1 atm upstream pressure, vacuum downstream.

Table 25.2. Diffusion of Hydrogen Through Hastelloy N Diaphragm at 550°C With and Without Diaphragm Covered by NaK

Area, 2.84 cm^2; thickness, 2.9 mm

Run No.	Time (hr)	Diaphragm Surface[a]	Diffused Gas Volume (scc)[b]	Gas Analysis[c] (mole %)								Permeability,[e] K [scc (H_2) mm hr^{-1} cm^{-2}]
				H_2	CH_4	H-C[d]	H_2O	CO_2	O_2	N_2 + CO	Ar	
Feed Gas												
6				99.905	0.004	0.009	0.043	0.005	<0.0005	0.032	[f]	
7				99.905	0.004	0.009	0.043	0.005	<0.0005	0.032	[f]	
8				99.905	0.004	0.009	0.043	0.005	<0.0005	0.032	[f]	
9				99.905	0.004	0.009	0.043	0.005	<0.0005	0.032	[f]	
Diffused Gas												
6	1.17	Exposed	0.114	97.55	0.04	[f]	0.61	0.30	0.02	1.53	[f]	0.099
7	1.17	Covered with NaK	0.089	97.50	0.04	[f]	0.28	0.46	0.02	1.65	[f]	0.080
8	2.08	Covered with NaK	0.22	95.81	0.04	[f]	2.40	0.21	0.007	1.54	[f]	0.106
9	2.00	Exposed	0.135	99.71	<0.005	[f]	0.02	0.03	<0.005	0.24	<0.005	0.075

[a]The diaphragm was exposed to hydrogen gas with capsule tilted or the diaphragm was covered with NaK with capsule in vertical position.
[b]scc = standard (1 atm, 0°C) cubic centimeters.
[c]By mass spectrometry.
[d]Higher hydrocarbons.
[e]At 1 atm upstream pressure, vacuum downstream.
[f]Not detected.

somewhat erratic behavior of the hydrogen permeability is consistent with reported effects[7] of impurities absorbed on the metal surface. Results after a more effective outgassing treatment of the metal should give a more consistent Arrhenius plot of logarithm of the permeability coefficient vs inverse absolute temperature.

PHASE EQUILIBRIA IN THE H-Na-K SYSTEM

Very little information is available from the literature on phase equilibria in the three-component H-Na-K system, although some estimates[8] and indirect measurements[9] in connection with the Dounreay reactor have been reported.

For the SNAP-8 reactor, temperatures up to 775°C, and as low as 300°C, must be considered. Fairly low pressures of hydrogen – certainly below 1 atm – are indicated by the diffusion considerations[10] noted earlier.

It has been found[11] that the solubility of hydrogen in pure liquid sodium is of the order of 10 to 30 at. % at 600°C, at a hydrogen pressure of about 55 atm. The decomposition pressures of sodium and potassium hydrides are similar.[12] Consequently, it would appear likely that in the SNAP-8 high-temperature regions, the item of concern will be the relation between hydrogen partial pressure and the concentration of hydrogen which dissolves in the NaK, forming unsaturated solutions.

[7]C. L. Huffine and J. M. Williams, *Corrosion* **16**, 430 (1960).

[8]V. M. Sinclair, R. A. H. Pool, and A. E. Ross, "Impurities in a Liquid Metal Coolant and Their Effect on the Fuel Element Canning Materials Niobium and Vanadium," TID-7622, *Nuclear Reactor Chemistry, Second Conference, Gatlinburg, Tennessee, Oct. 10–12, 1961*, pp. 35–56.

[9]A. Thorley and C. Tyzack (UKAEA), "The Embrittlement of Niobium in Hydrogen-Contaminated NaK," *Thermodynamics of Nuclear Materials, IAEA Symposium Vienna, Austria, May 21–25, 1962*, pp. 365–97.

[10]H. W. Savage, E. L. Compere, W. R. Huntley, and A. Taboada, *SNAP-8 Corrosion Program Quart. Progr. Rept. Aug. 31, 1963*, ORNL-3538, pp. 28–40.

[11]M. D. Banus, J. J. McSharry, and E. A. Sullivan, *J. Am. Chem. Soc.* **77**, 2007–10 (1955).

[12]Albert Herold, *Ann. Chim.* (Paris) **6**, 536–81 (1951).

It is likely[13] that Sievert's law ($C = KP^{1/2}$) will serve as the functional relation in this region.

In cool regions of the SNAP-8 system, however, the possibility of precipitation of alkali-metal hydride must be considered.[14] For example, the solubility of sodium hydride in liquid sodium has been reported by Williams[15] to be 0.005 wt % at 250°C and 4.3 wt % at 445°C.

The solubility of solid alkali-metal hydride in the liquid metal can be determined from a series of pressure-composition measurements, since the phase rule requires that in a two-component system at a given temperature the pressure should remain constant as long as three phases are in equilibrium. Such plateaus were observed by Banus.[11] In the three-component H-Na-K system, a similar break in the pressure-composition diagram should indicate the saturation solubility and the decomposition pressure of the equilibrium solid hydride.

The saltlike character of the solid alkali-metal hydrides indicates the likelihood of strong similarities in the solubility behavior to the metal-halide–liquid-metal systems studied by Bredig.[16]

An apparatus for determining the solubility of hydrogen in NaK as a function of pressure and temperature has been constructed. The apparatus is shown in Fig. 25.2. At temperatures as high

[13]T. R. P. Gibb, Jr., pp. 315–509 in *Progress in Inorganic Chemistry* (ed. by I. A. Cotton), vol. III, Interscience, New York, 1962.

[14]M. A. Perlow, *SNAP-2 Primary Coolant Development*, NAA-SR-6439 (July 15, 1961).

[15]D. D. Williams, J. A. Grand, and R. R. Miller, *J. Phys. Chem.* **61**, 379–80 (1957).

[16]M. A. Bredig, *Mixtures of Metals with Molten Salts*, ORNL-3391 (Aug. 16, 1963).

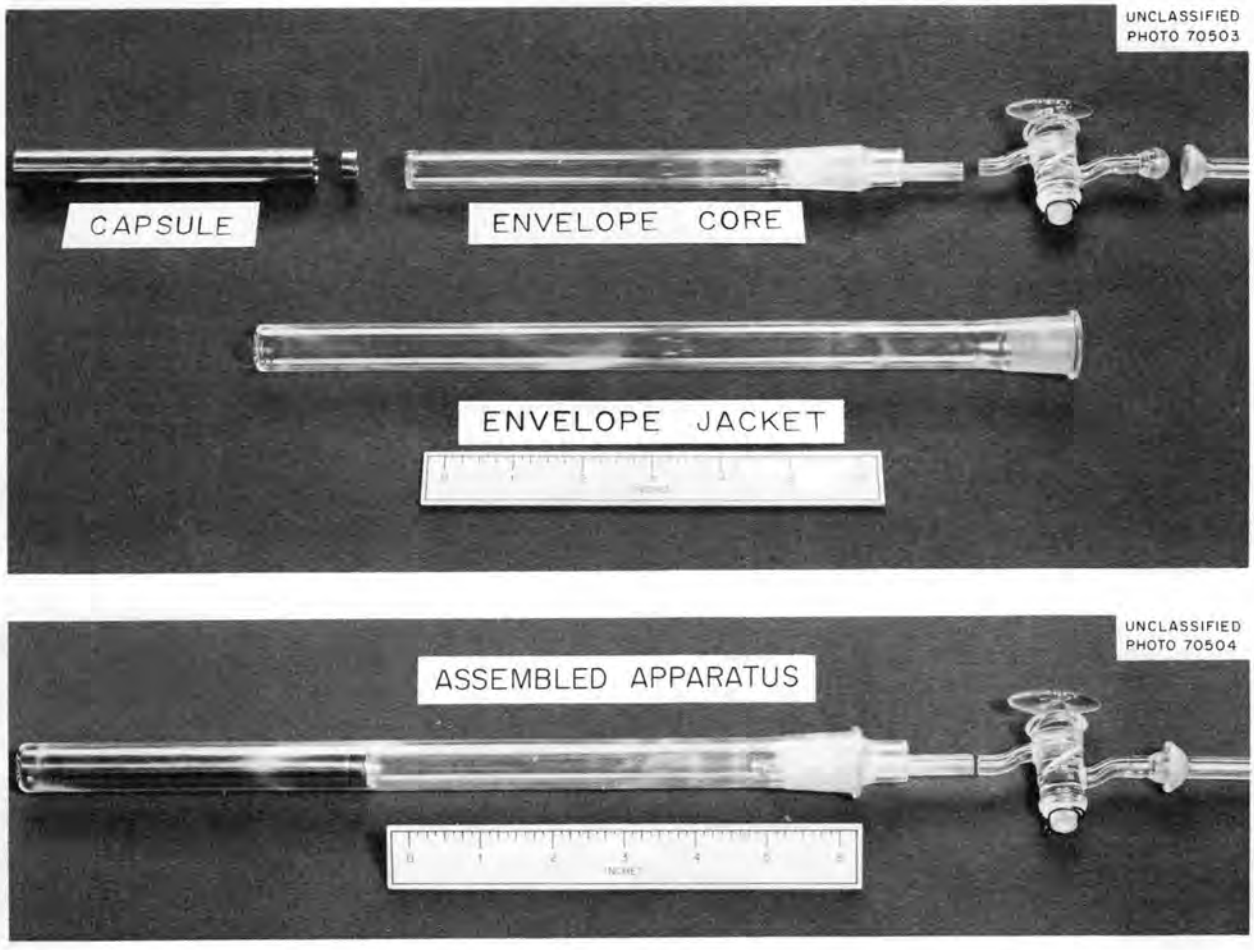

Fig. 25.2. Hydrogen Solubility Capsule and Envelope.

as 1400°F, the vapor pressure of NaK becomes appreciable and may well be higher than the partial pressure of the hydrogen to be added to the system. Consequently, the NaK must be enclosed in a container which will not permit its escape but which is permeable to hydrogen. Other investigators have used pure iron and pure nickel for this purpose.

An iron or nickel capsule containing a measured quantity of NaK under an inert gas will be welded shut. These operations will be conducted in a dry inert-atmosphere glove box, using electric arc welding. The capsule and its cover can be hydrogen fired at elevated temperatures in the quartz envelope prior to filling with NaK in the glove box.

As shown in Fig. 25.2, the capsule containing the NaK will rest in the end of a quartz envelope, which is to be inserted into a furnace. An inner core tube will serve to close the envelope, to fill up most of the dead space, and to permit entry and exit of hydrogen gas from the system. The envelope and core will be connected to the gas feed system by means of a capillary tube and can be isolated by a stopcock. The gas-feed system consists of two burettes and a manometer. With two burettes the envelope may be either evacuated or pressurized with hydrogen and its evolution or consumption measured.

The various dead spaces in the envelope, capsule, etc., will be calibrated. Then the equilibrium hydrogen uptake of the system will be observed at selected pressures and temperatures. Following a series of equilibrations of hydrogen with the encapsulated NaK, the envelope will be closed off and all hydrogen within the envelope, capsule, and NaK determined. These determinations will provide direct confirmation of the uptake measurements.

To prevent contamination of the NaK it must be loaded and recovered under an inert-gas atmosphere in the hydrogen diffusion and solubility experiments. For this purpose a four-hand inert-gas stainless steel glove box with a 655-liter volume has been reconditioned and equipped for the necessary operations.

26. Effects of Radiation and Heat on Organic Materials

GAMMA DOSIMETER FOR REACTOR USE[1]

W. W. Parkinson
C. D. Bopp
O. Sisman
W. K. Kirkland

Hydrogen has a high relative efficiency for absorption of energy from fast neutrons. If a dosimeter having maximum hydrogen content and one with little or no hydrogen are exposed to the mixed neutron-gamma radiation field of a nuclear reactor, a comparison of the energy imparted to each may be used to determine the fractions of the total dose from neutrons and from gamma radiation. The development of a low-hydrogen-content dosimeter, based on a solution of 0.3 wt % $C_{10}H_{22}$ and 0.3 wt % $C_2H_2Cl_4$ in C_8F_{16}, has been described. Radiation dose is determined from the concentration of acid (H^+) resulting from irradiation.

It was found earlier[2] that the addition of water in excess of saturation (~0.2 wt %) was necessary for consistent acid yields. The infrared spectrum of the cyclic fluorocarbon solvent revealed that it was not free of hydrogen but was approximately C_8HF_{15}. Dosimeters made of this solvent with ~0.2% water were irradiated in the Oak Ridge Graphite Reactor for comparison with acid yields from the same dosimeter by gamma irradiation. The results from this series are presented in Fig. 26.1, which shows the acid yields along with data from earlier reactor irradiations of similar solutions in C_8HF_{15} and in C_7F_{16} that was known to be completely fluorinated. The line in Fig. 26.1 represents the acid yield for dosimeters of this type

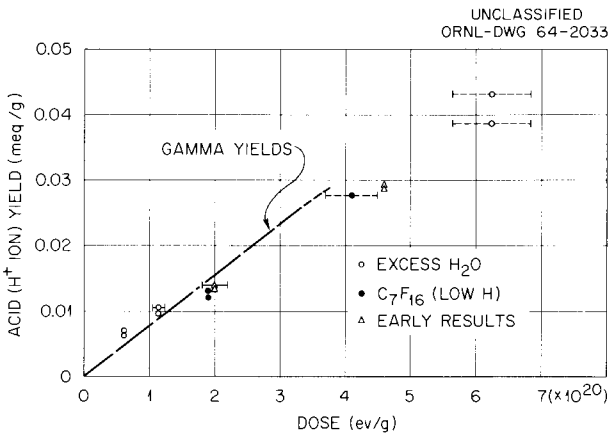

Fig. 26.1. Acid Production in Reactor Irradiations of Fluorocarbon Dosimeters.

in pure gamma fields. The technique for freezing, evacuating, and encapsulating solutions used in the "earlier" tests probably resulted in condensation of some moisture, but not of enough to exceed saturation.

It is believed that the acid produced is HCl; if it is, some departure from linearity above yields of 0.025 meq/g might be expected since the $C_2H_2Cl_4$ becomes appreciably depleted above this range. Figure 26.1 shows evidence of slightly decreased yields at high dosages. Acid yields in pure gamma fields have not been established at such high dosages. It is certain that at dosages to 3.5×10^{20} ev/g the acid yields from reactor irradiation agree among themselves and with those from gamma irradiation alone to well within the absolute accuracy (±15%) of the reactor dose determinations; it is likely that this agreement extends to higher dosages. It appears that a relatively simple dosimeter for the gamma contribution of reactor radiation is available.

[1] W. W. Parkinson and C. D. Bopp, "A Fluorocarbon Dosimeter Insensitive to Neutrons," in preparation.

[2] C. D. Bopp *et al.*, *Reactor Chem. Div. Ann. Progr. Rept. Jan. 31, 1963*, ORNL-3417, p. 267.

EFFECTS OF RADIATION ON POLYMERS

W. W. Parkinson O. Sisman

Effect of Radiation on Polystyrene[3]

R. M. Keyser W. K. Kirkland

The irradiation of polystyrene causes decreased solubility in organic solvents and increased softening temperature and elastic modulus of the polymer. The basic radiation-induced process responsible for these changes is the generation of cross links between molecules. Earlier work demonstrated that the mixed neutron-gamma radiation field of the Oak Ridge Graphite Reactor was 2.4 times as efficient in producing cross links in polystyrene as gamma radiation alone.[4] The various methods (viscosity, solubility, and solvent-swelling ratio) for determining extent of cross-linking gave rates of cross-link formation that differed considerably in absolute value. To resolve this discrepancy the extent of cross-linking has been established by measurement of the solubility of gel fraction coupled with an absolute measurement of the weight-average molecular weight.

The absolute determination of the molecular weight has been carried out by measurement of the light scattered by dilute solutions of the polystyrene in benzene. The dissymmetry of scattering and the depolarization of light of 436 mμ wavelength were measured to give corrections for molecular shape and depolarization. Scattering measurements at 436 and 546 mμ, with these corrections, gave values of 2.72×10^5 and 2.85×10^5, respectively, for the average molecular weight. With this molecular weight the solubility data indicate that one cross link requires 1420 ev imparted by mixed reactor radiation (ORNL Graphite Reactor) or 3280 ev absorbed from a gamma source.

The gamma-radiation dose required per cross link is somewhat above values reported in the literature, 1800 to 2200 ev per cross link. It is possible that a small amount of oxidation reduced the cross-link yield in the present specimens. It is also possible that a higher content of unsaturated styrene monomer accelerated cross-linking in the polystyrene described in the literature.

The irradiation of polystyrene also produces free radicals and compounds of low molecular weight. The yields of these materials on irradiation of polystyrene in a gamma source and in the Graphite Reactor have been determined.[5] The major volatile products are hydrogen, methane, and benzene; in addition unidentified materials are produced in very small yields. Benzene and methane have been identified and their yields have been quantitatively determined by means of gas chromatography; yields of hydrogen were measured with a Toepler pump.[6]

Hydrogen, methane, and benzene yields have been plotted in Figs. 26.2–26.4 as a function of

[3]J. E. White, W. W. Parkinson, C. D. Bopp, and D. Binder, "A Comparison of Fast Neutron and Gamma Irradiation of Polystyrene. Part I. Cross-Linking Rates," in preparation.

[4]W. W. Parkinson *et al.*, *Reactor Chem. Div. Ann. Progr. Rept. Jan. 31, 1963*, ORNL-3417, p. 269.

[5]R. M. Keyser, W. W. Parkinson, and R. A. Weeks, "A Comparison of Fast Neutron and Gamma Irradiation of Polystyrene. Part II. Decomposition Products and Long-Lived Free Radicals," in preparation.

[6]W. W. Parkinson *et al.*, *Reactor Chem. Div. Ann. Progr. Rept. Jan. 31, 1963*, ORNL-3417, p. 270.

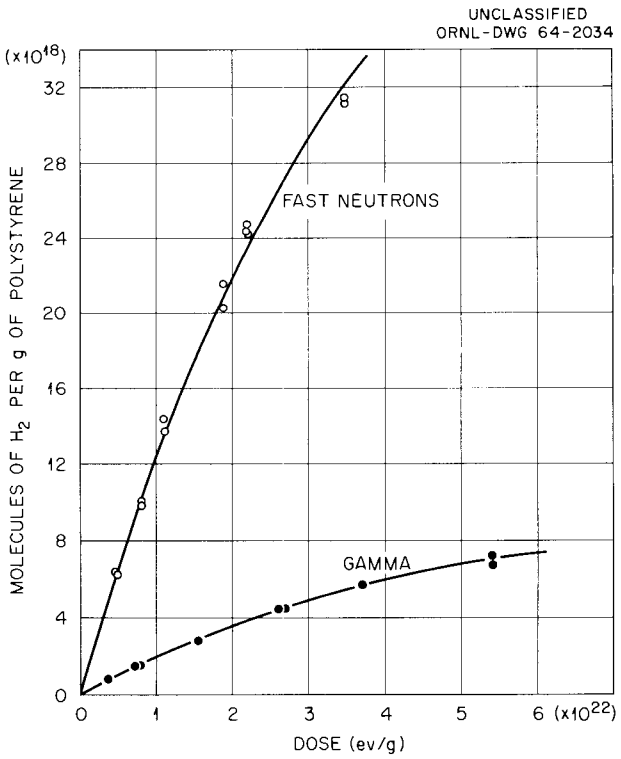

Fig. 26.2. Hydrogen Yields from Irradiated Polystyrene.

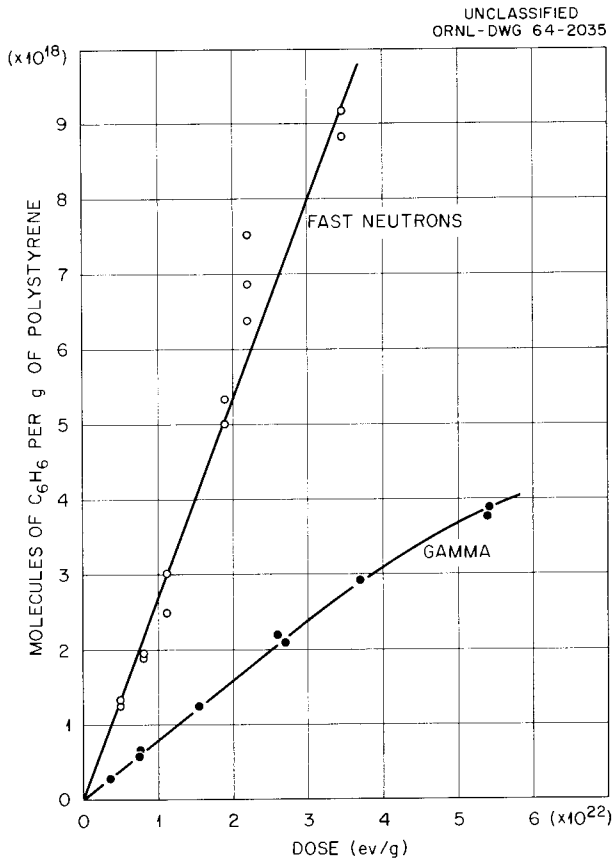

Fig. 26.3. Benzene Yields from Irradiated Polystyrene.

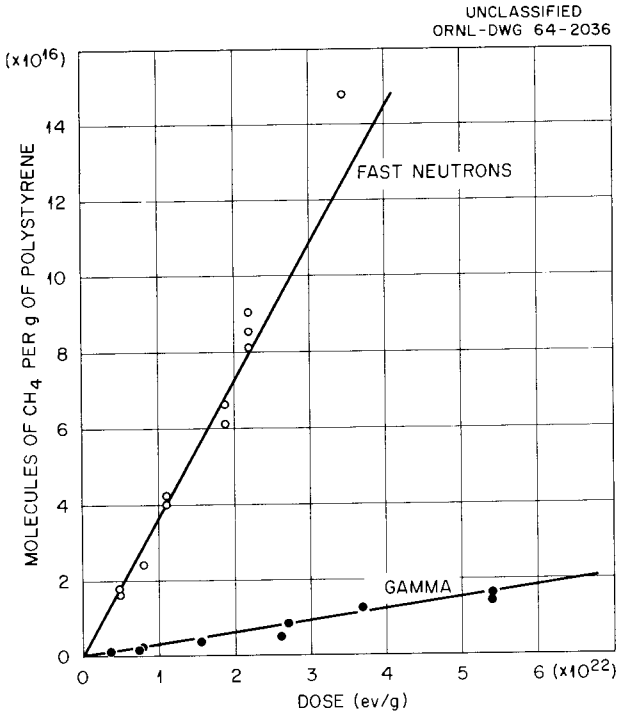

Fig. 26.4. Methane Yields from Irradiated Polystyrene.

energy deposition in polystyrene for gamma radiation and for fast neutrons. The fast-neutron yields were determined from yields observed for reactor radiation by subtracting the contribution from the gamma component of the reactor radiation field. It is apparent that for equal energy deposition, fast-neutron irradiation produces more product than does gamma radiation. The G values (yield per 100 ev absorbed) of benzene and methane for the linear portions of the curves in Figs. 26.3 and 26.4 are listed in Table 26.1; this table also shows the limiting yield of hydrogen at zero dosage.

The nonlinearity of the H_2 yields (Fig. 26.2) can be accounted for in terms of a kinetic analysis involving a zero-order growth of H_2 followed by a first-order decay. On this basis, the rate of hydrogen production with dose is given by

$$\frac{d(H_2)}{dD} = \frac{[G(H_2)]_0}{100} - k_1(H_2) , \qquad (1)$$

where $[G(H_2)]_0$ is the limiting value of $G(H_2)$ at zero dose, (H_2) is the hydrogen yield in molecules/g, D is the radiation dose in ev/g, and k_1 is the first-order decay constant in g/ev. According to Eq. (1), a plot of $d(H_2)/dD$ against (H_2) should be linear, with a slope of $-k_1$ and with $[G(H_2)]_0$ given by the intercept at (H_2) equal to zero. The experimental data gave linear plots, confirming the validity of the treatment. The value of k_1 was $(0.22 \pm 0.02) \times 10^{-22}$ g/ev and $(0.25 \pm 0.05) \times 10^{-22}$ g/ev for gamma and fast-neutron irradiation respectively. Thus it can be concluded that k_1 is the same in both cases, within experimental error. For gamma irradiation, the experimental value of $[G(H_2)]_0 = 0.022 \pm 0.002$ is in very good agreement with the value of 0.0223 found by Wall and Brown.[7]

The reason for the decrease in rate of hydrogen production with increasing dose is not clear; a similar effect has been noted in irradiated polyethylene.[8] One possible mechanism for loss of

[7] L. A. Wall and D. W. Brown, *J. Phys. Chem.* **61**, 129 (1957).

[8] D. Dole *et al.*, *J. Chem. Phys.* **37**, 2449 (1962).

Table 26.1. G Values for Production of Volatile Products from Polystyrene Irradiated with Fast Neutrons and Gamma Rays

	$G(H_2)^a$	$G(C_6H_6)^b$	$G(CH_4)^b$
Gamma rays	0.022 ± 0.002	0.008 ± 0.001	$\sim 10^{-5}$
Fast neutrons	0.14 ± 0.01	0.027 ± 0.002	$(3.5 \pm 0.5) \times 10^{-4}$

[a]Limiting G values as radiation dose approaches zero.

[b]Applicable in the dose range $(0.4 \text{ to } 4.0) \times 10^{22}$ ev/g.

hydrogen is the radiolytic disruption of molecular hydrogen to form hydrogen atoms, which can then add to the phenyl groups in polystyrene. Another possibility is a back reaction of hydrogen initiated by the postirradiation thermal treatment of the sample. Experiments designed to test the latter theory are not yet conclusive.

Yields of free radicals, stable at room temperature and observed at liquid-nitrogen temperature, were determined using electron spin resonance techniques.[9] Samples were irradiated in vacuum at 20°C. Free-radical spectra were recorded as the first derivative of the absorption line and were found to consist of a complex pattern of unresolved lines. The general shape of the spectra was the same for gamma and reactor irradiation with indications of perhaps a small difference in intensity of some of the lines. Double numerical integration of the derivative curves revealed that the radical yields were the same for both types of radiation, in contrast to the yields of cross links and volatile products.

The results of this study demonstrate that quite significant differences in product yields from irradiated polystyrene can occur depending on the type of radiation used. It is believed that these differences can be understood in terms of the higher linear energy transfer rate (LET) of neutron radiation compared to gamma radiation. An increase in LET can be expected to favor bimolecular reactions of reactive species (free radicals, excited molecules, ions, etc.) leading to formation of the observed products at the expense of competing reactions such as decomposition of excited molecules or ions (which are first-order in reactive species). The equal yields of free radicals by gamma and reactor radiation are not surprising since these are yields of radicals which are stable at room temperature. Such radicals are probably formed in reactions with species which have migrated long distances from a spur along the ionization track. In such a case, any LET effect would be insignificant.

[9]We are indebted to R. A. Weeks of the Solid State Division for carrying out the ESR measurements.

Radiation-Induced Reactions in Polybutadiene[10]

W. K. Kirkland

Polybutadiene is interesting as a model rubber polymer because of the similarity of its main chain to that of natural rubber and of the more complex synthetic rubbers. Furthermore, polybutadiene can be obtained in forms which have a large fraction of the unsaturated groups in one or the other of the three possible isomeric configurations. Since these groups participate in cross-linking as well as in other radiation-induced reactions, it is significant to measure the changes in these groups resulting from irradiation. A previous report[11] described an infrared spectral method of measurement of the concentration of each isomeric form of the unsaturated groups.

[10]W. W. Parkinson and W. C. Sears, "An Infrared Study of Radiation-Induced Reactions in Polybutadiene," in preparation.

[11]W. W. Parkinson *et al.*, *Reactor Chem. Div. Ann. Progr. Rept. Jan. 31, 1963*, ORNL-3417, p. 271.

Known concentrations of various hydrocarbon standards have been measured to establish spectral calibration curves. For the infrared peak characteristic of the "cis" isomeric form, it was found that different hydrocarbon standards gave absorption coefficients varying by almost a factor of 2 when band height was used as an indication of optical absorption. To eliminate this variation of absorption coefficient with compound, the areas under the characteristic band were calculated by use of a computer integration technique.[12] This method gave satisfactory agreement for concentration of "cis" groups in the standard compounds.

Polybutadiene specimens of high "cis," high "trans," high side-chain, and of mixed type have been irradiated and are now being measured. To observe the influence of temperature, irradiations have been carried out at 112°C, as well as at room temperature. To study the influence of irradiation dose rate, irradiations have been performed in gamma sources of different intensities. Finally, since substances having aromatic unsaturation show effects which depend on the LET of the radiation, specimens have also been exposed to the mixed neutron-gamma radiation of a reactor.

THERMAL DECOMPOSITION OF BIPHENYL

L. B. Yeatts D. N. Hess W. T. Rainey, Jr.

Biphenyl is the simplest compound representative of the mixtures of polyphenyls which have been under serious consideration as coolants for nuclear reactors.[13–15] It has, accordingly, been studied here in an attempt to establish a detailed mechanism for its thermal decomposition. Such a study required the use of material of the highest purity, careful control of the conditions of pyrolysis, including the nature of the confining surfaces, and complete analyses of all the products of the pyrolysis. It had been hoped that when sufficient knowledge of the thermal decomposition of biphenyl was available a study of the combined effects of thermal and radiation decomposition could be undertaken.

Experimental studies of the pyrolysis of biphenyl in the vapor phase were discussed in a previous report in this series.[16] During the past year, experimental studies of the pyrolysis of biphenyl in the liquid phase were performed at temperatures of 422, 438, and 446°C. The analytical procedures and full details of the experimental work have been described elsewhere.[17,18]

If cracking of the phenyl rings to smaller fragments is not an important reaction, material balance requires that the sum (on a mole basis) of the quaterphenyls plus half the terphenyls be equal to the hydrogen plus half the benzene. Table 26.2 summarizes the results of liquid-phase experiments in which the vapor phase occupied less than 5% of the volume of the silica ampoules during pyrolysis. Inspection of Table 26.2 shows that excellent material balances were obtained; recovery and analysis of the products seem quite adequate. Alphatic hydrocarbons appeared only in traces; methane was the most important of these, but its yield was only one-tenth that of hydrogen.

The yields of hydrogen, benzene, and polyphenyls were all apparently linear with time during the limited decomposition which was permitted; this behavior did not permit an assignment of order to the reaction. Other workers[19,20] have reported that the reaction is first-order up to at least 20% decomposition, and the data for biphenyl decomposition from the present studies are plotted in a first-order form in Fig. 26.5. A specific rate constant for biphenyl decomposition between 422 and 446°C, based on the assumption of first order, is $1.2 \times 10^{-12} \exp(-62{,}000/RT)\ \mathrm{hr}^{-1}$. Activation

[12] The computer integration was carried out by the group in the Mathematics Division under H. P. Carter and M. T. Harkrider.

[13] K. L. Hall *et al.*, *Relative Effects of Fast Neutrons and Gamma Rays on the Radiolysis of Polyphenyls*, Calresearch-AEC Report No. 23 (June 1963).

[14] R. H. J. Gercke, "Status of Organic Coolant Technology," *Proceedings of the Organic Cooled Reactor Forum, Oct. 6–7, 1960*, NAA-SR-5688, p. 5.

[15] W. G. Burns, *Radiation and Thermal Stability of Some Potential Organic Moderator Coolants*, AERE-R-3989 (August 1962).

[16] W. T. Rainey, Jr., and L. B. Yeatts, Jr., *Reactor Chem. Div. Ann. Progr. Rept. Jan. 31, 1963*, ORNL-3417, pp. 272–76.

[17] L. B. Yeatts, Jr., D. N. Hess, H. F. McDuffie, and W. T. Rainey, Jr., "Kinetics of the Thermal Decomposition of Biphenyl," ORNL-3602 (in press).

[18] L. B. Yeatts, Jr., J. E. Attrill, and W. T. Rainey, Jr., *Gas Chromatographic Analysis of Biphenyl Pyrolytic Products*, ORNL-TM-523 (Mar. 13, 1963).

[19] V. T. Gaumann and J. M. Rayroux, *Helv. Chim. Acta* **45**(5), 1563 (1962).

[20] D. G. Kuper, *Organic Coolant Degradation Studies*, IDO-16851 (Mar. 25, 1963).

Table 26.2. Material Balance of Biphenyl Pyrolytic Products

2.86×10^{-2} mole of biphenyl

Temperature (°C)	Time (hr)	Yield (moles)				Material Balance (moles)		Biphenyl Pyrolyzed (%)
		Hydrogen	Benzene	Terphenyls	Quaterphenyls	$\frac{1}{2}\phi_3 + \phi_4$	$H_2 + \frac{1}{2}\phi H$	
		$\times 10^{-5}$	$\times 10^{-5}$	$\times 10^{-5}$	$\times 10^{-5}$	$\times 10^{-5}$	$\times 10^{-5}$	
422	12	0.24	4.0	2.85	0.89	2.3	2.1	0.23
	24	0.38	7.2	4.99	1.25	3.8	4.0	0.48
	48	0.76	15.4	9.15	3.51	8.1	8.5	1.0
438	8	0.47	6.7	4.78	1.59	4.0	3.8	0.49
	12	0.70	11.0	7.09	2.96	6.5	6.2	0.77
	16	0.77	14.3	9.03	3.23	7.8	7.9	0.95
446	8	0.61	10.4	6.11	2.60	5.7	5.8	0.69
	12	0.95	16.8	9.73	4.72	9.6	9.4	1.1
422[a]	12	0.21	3.1	3.12	0.71	2.2	1.8	0.27
422[b]	12	0.51	7.2	5.25	4.73	7.4	4.1	0.73

[a] 5×10^{-4} mole of H_2O added.

[b] 2×10^{-5} mole of O_2 added.

energies for the following processes were calculated from the data:

Product	$E_{act.}$ (kcal/mole)
Benzene formation	61
Terphenyl formation	56
Quaterphenyl formation	67
Hydrogen formation	65

The effects of added oxygen and added water are shown in the last two lines of Table 26.2. Water was essentially without effect, but the addition of oxygen was followed by a marked increase in the rate of formation of all products. The yield of carbon monoxide was also great. Inability to achieve a material balance for the products was probably due to the formation of water and organic oxygen compounds, neither of which could be detected by the analytical procedures in use.

The effect of deuterium gas, added in an amount equal to that of the hydrogen normally produced, was studied in a 12-hr pyrolysis at 422°C. Mass spectrometric analysis of the benzene product failed to reveal the presence of any benzene enriched in deuterium.

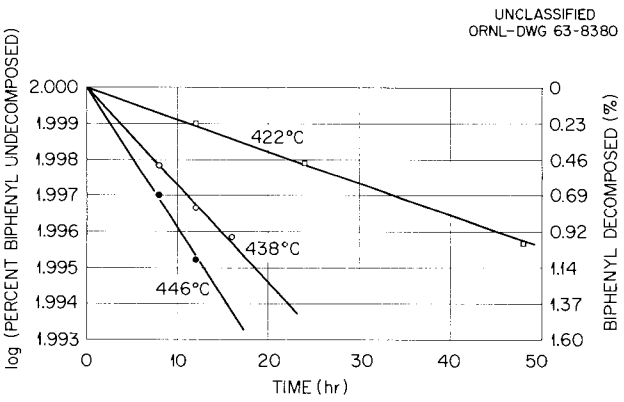

Fig. 26.5. Variation in Decomposition of Biphenyl with Time.

The effects of increased surface area and of the nature of the surface upon the rate of product formation are shown in Table 26.3. Reference data, without added surface, were obtained using

Table 26.3. Material Balance for Biphenyl Pyrolysis in the Presence of Added Surfaces

Conditions: 500 cm^2 surface area, 12 hr, 422°C, 1.95×10^{-2} mole of biphenyl

Surface	Yield (moles)				Material Balance (moles)		Biphenyl Pyrolyzed (%)
	Hydrogen	Benzene	Terphenyls	Quaterphenyls	$\frac{1}{2}\phi_3 + \phi_4$	$H_2 + \frac{1}{2}\phi H$	
	$\times 10^{-5}$	$\times 10^{-5}$	$\times 10^{-5}$	$\times 10^{-5}$	$\times 10^{-5}$	$\times 10^{-5}$	
Reference (25 cm^2)	0.14	2.6	1.67	0.59	1.4	1.4	0.26
Pyrex	0.30	1.6	1.31	0.34	1.0	1.1	0.18
Quartz	0.14	2.0	1.31	0.34	1.0	1.1	0.19
Iron	1.2	2.3	2.06	0.52	1.6	2.4	0.28
Stainless steel	1.38	1.3	1.04	0.16	0.7	2.0	0.14
Quartz + SS (1:1)	1.60	1.8	1.35	0.39	1.0	2.5	0.20
Pyrex (2850 cm^2)	0.22	0.72					
Quartz (7000 cm^2)	0.21	0.71					

Pyrex ampoules, with a surface area of 25 cm^2, and were calculated from data in Table 26.2. The surface-to-volume ratio was varied from 3.6 (the reference case) to as high as 1000 by adding materials in the form of "wool." The presence of Pyrex and quartz surfaces decreased the benzene yield to about 25% of its reference value; insufficient data prevent conclusive statements as to yields of other products. Yields of hydrogen and methane were increased by factors of about 10 above the reference yields by iron surfaces while the amounts of benzene, terphenyls, and quaterphenyls remained unchanged. (Results for metal surfaces were obtained from the pyrolysis of a single sample in each instance; therefore, differences less than an order of magnitude are probably best assigned to experimental error at this time.) The cases in which the yield of hydrogen gas was high exhibited poor material balances, indicating that reactions other than those involved in the simple material balance considerations had become important; the ability of iron surfaces to crack aromatic compounds is well known.

All data from these studies are consistent with a mechanism that involves radical chain reactions with steps that have relatively low activation energies, similar to those proposed[21] for the thermal decomposition of other organic substances. The simplest initiating reaction is probably decomposition of a biphenyl molecule into two phenyl radicals, which then abstract hydrogen from adjacent biphenyl molecules to form benzene and biphenylyl radicals. Results from the experiment with deuterium suggest that the benzene is *not* formed by the capture of hydrogen atoms from hydrogen molecules, and hydrogen atoms are not generally important thermal decomposition products of organic hydrocarbons.[22] The energies of the C-H bond in aromatic compounds and the C-C bond in biphenyl are higher than the 62 kcal/mole observed as the activation energy for biphenyl decomposition; this lends support to the idea that radical reactions of low activation energy are involved in the decomposition. The effect of oxygen is probably to obscure the pure thermal decomposition reaction; oxidation of hydrocarbons is known to proceed via radical chain mechanisms. The effect of metal surfaces is best attributed to reactions initiated at the catalytically active surfaces. Pyrex and quartz surfaces, on the other hand, are known to act as sites for chain breaking through radical recombination, and their effect upon biphenyl decomposition is quite in accord with this behavior.

[21] F. O. Rice and K. F. Herzfeld, *J. Am. Chem. Soc.* **56**, 284 (1934).

[22] P. Sykes, *A Guidebook to Mechanism in Organic Chemistry*, p. 233, Wiley, New York, 1961.

The experimental techniques have been demonstrated to be of precision sufficient to permit determination of the nature of reactions occurring at the interface between biphenyl and various fuel-element cladding materials; in addition, the effects of chlorine-containing impurities, reported to be deleterious,[23] could be examined in detail. Interesting information as to the mechanism of the "pure" thermal decomposition of biphenyl might well be obtained by the deliberate generation of hydrogen and deuterium atoms and labeled phenyl and biphenylyl radicals (from nonpyrolytic sources) in biphenyl at temperatures just below those at which significant thermal decomposition occurs; analysis of the products should reveal whether some of the postulated reactions do occur and whether hydrogen is transferred freely among biphenyl molecules.

---

[23]D. H. Charlesworth, *Fouling in Organic Cooled Systems*, CRCE-1096 (April 1963).

27. Preparation of Pure Materials

PREPARATION OF SINGLE-CRYSTAL LITHIUM FLUORIDE

C. F. Weaver[1] R. E. Thoma
R. G. Ross H. L. Hemphill

Techniques for preparing lithium fluoride single crystals (by a modified Stockbarger method in which molten LiF is slowly lowered through a temperature gradient) were developed until products containing less than 1 ppm cationic impurity were obtained by a standardized procedure. Details of the preparation procedures are discussed in an ORNL topical report.[2] Design and construction details of the apparatus and equipment are available in a set of ORNL blueprints.[3] During the past year, the most efficacious innovation for improving the purity of the product was the use of a "clean" box supplied with filtered air to prevent exposure of reagents to particulate contaminants from the laboratory atmosphere at any step of the low-temperature portion of the procedure.

Three single crystals of lithium fluoride, each weighing slightly more than 300 g, were grown in the Stockbarger apparatus. These crystals, designated ORNL-4, -5, and -6, contained 99.99, 96.50, and 79.28 at. % Li^7 respectively. Refinements in the methods of preparation and purification are reflected in the analytical data shown in Table 27.1.

The ORNL-produced crystals were all made available for use at the Materials Science Center of Cornell University as part of an AEC Pure Materials Program. At Cornell the crystals are first cleaved to obtain fresh specimens of the desired dimensions. Then the low-temperature thermal conductivity is measured for each specimen. The effect of isotopic composition upon

[1] On leave at the University of California, Berkeley.

[2] C. F. Weaver *et al.*, *The Production of LiF Single Crystals with Selected Isotopic Ratios of Lithium*, ORNL-3341 (in press).

[3] ORNL engineering drawings D-56550, -56551, -56552, -56553, -56554, -56555, -56556, -56557 (1963).

Table 27.1. Results of Spectroscopic and Activation Analyses of Lithium Fluoride Single Crystals

Crystal Product Number	Li^7 Concentration (at. %)	Contaminant Concentration (ppm)[a]							
		Sodium		Potassium		Magnesium[b]		Manganese	
		Spectroscopic	Activation	Spectroscopic	Activation	Spectroscopic	Activation	Spectroscopic	Activation
ORNL-1	99.99	30–100		20		20–100		70	
ORNL-2	99.99	30–100		20		20–100		70	
ORNL-3	98.06	5		<1		<10		2	1.4
ORNL-4	99.99	0	0.01	0	$\leq$0.2			0.5–1.0	0.13–0.35
ORNL-5	96.50	0	0.01	0	$\leq$0.2	2.0		0	0.03
ORNL-6	79.28[c]								

[a] These elements are the principal contaminants. Small amounts of the additional contaminants Al, Ca, Fe, Si, and Ti were found in ORNL-1 and -3.

[b] Not detectable by activation analysis.

[c] Not yet returned from Cornell for analysis.

phonon scattering is inferred from the results of these measurements. (Crystals ORNL-4 and -5 were found to be sufficiently pure that the proportional constants of the Rayleigh scattering term could be shown to be dependent on the isotopic composition.) After the measurements have been completed, the various portions of the original crystal are returned to ORNL for careful analysis and for storage or use in other solid-state research programs.

The results of the Cornell measurements supported a decision to make additional crystals with differing isotopic composition by methods identical to those used for ORNL-4, -5, and -6.

PURIFICATION OF LITHIUM FLUORIDE BY ZONE REFINING

A. J. Singh[4] R. G. Ross
E. H. Guinn R. E. Thoma

The Stockbarger method of growing crystals of lithium fluoride was found to concentrate cationic impurities such as manganese, magnesium, and sodium in the upper parts of the crystals.[5] A study of the segregation behavior of these cations in lithium fluoride was initiated in an attempt to develop more effective methods for obtaining even purer lithium fluoride than is currently available.[6]

A test charge of lithium fluoride doped with 1000 ppm each of MnF_2, CaF_2, and MgF_2 was used to load a cylindrical nickel capsule so that the final ingot dimensions were 40 × 1.5 cm. The nickel capsule encased in a quartz tube was lowered at 1 cm/hr through a 4-in.-long hot zone to provide a molten zone from 945 to 848°C.

Chemical analyses of the frozen ingots produced in one-pass experiments indicated that separation coefficients greater than unity were obtained for Mn, Mg, and Ca, and less than unity for Na, with the separation coefficient for Mn much greater than for the other cations. Exact reasons for the large separation factor for manganese are not known. In search for an explanation of this behavior, a brief investigation was made of the system LiF-MnF_2, using the visual-observation furnace. Phase diagrams for each of the other three binary systems were available in the literature.[7–9] The phase diagram of the system, tentatively described from relatively few data, does not indicate that crystallization behavior of MnF_2 in the presence of LiF is markedly different from that exhibited by CaF_2, MgF_2, or NaF. Intermediate compounds are not formed in any of the systems. Neither the melting points of the components [decreasing in the sequence CaF_2 (1418°C), MgF_2 (1270°C), NaF (995°C), and MnF_2 (918°C)], the temperatures of the binary eutectics with LiF (773, 750, 652, and 700°C), nor the compositions of the eutectics (each ~60 to 80 mole % LiF) suggest reasons for the behavior of MnF_2.

An automatic apparatus which produces two molten zones simultaneously has been constructed and is now undergoing tests. The apparatus is to be used for a more accurate determination of the separation coefficients for various cations in LiF.

PURIFICATION OF FLUORIDES AND GROWTH OF CRYSTALS BY VOLATILIZATION

B. J. Sturm R. G. Ross
R. E. Thoma E. H. Guinn
A. J. Singh[4]

Lithium fluoride single-crystal needles as long as 1.25 mm have been reported as deposits from the vapor in a helium atmosphere at pressures of 1000 to 1300 mm Hg.[10] During the past year, vacuum volatilization has proved to be a useful procedure for purifying and growing single crystals of LiF, KF, AlF_3, and ZrF_4. When these salts were maintained at 900 to 1000°C and at pressures of approximately 10 mm Hg, crystals as large as

[4]International Atomic Energy Agency Fellow from Atomic Energy Establishment, Trombay, Bombay, India.

[5]*Reactor Chem. Div. Ann. Progr. Rept. Jan. 31, 1963*, ORNL-3417, p. 290.

[6]C. F. Weaver *et al.*, *The Production of LiF Single Crystals with Selected Isotopic Ratios of Lithium*, ORNL-3341 (in press).

[7]C. J. Barton *et al.*, p. 29 in *Phase Diagrams of Nuclear Reactor Materials* (ed. by R. E. Thoma), ORNL-2548 (Nov. 2, 1959).

[8]W. E. Counts, R. Roy, and E. F. Osborn, *J. Am. Ceram. Soc.* **36**, 15 (1953).

[9]A. G. Bergman and E. P. Dergunov, *Compt. rend. acad. sci. U.R.S.S.* **31**, 753 (1941).

[10]C. F. Weaver, B. J. Sturm, and R. E. Thoma, *Reactor Chem. Div. Ann. Progr. Rept. Jan. 31, 1962*, ORNL-3262, pp. 187–90.

several millimeters on an edge were formed in the cooler regions of the containing vessel.

The fluorides so prepared were sufficiently pure for use in phase equilibrium studies by a visual procedure (see Chap. 24), in which the determination of a liquidus temperature depended on the first observation of the appearance of a precipitate in a cooling melt. Consequently, any impurity which clouded the melt interfered with the study. Because they yielded very sparingly soluble phases, oxides and precursors thereof, for example, hydroxides and moisture, proved to be especially objectionable and in some cases initially very difficult to remove or avoid in the preparation of these fluorides. Hydroxides and moisture were additionally objectionable because they attacked the metal container, thus contaminating the melt with highly colored nickel ion. Often such melts displayed irreproducible liquidus temperatures, presumably due to a progressive increase in concentration of contaminant oxides.

The vacuum volatilization technique was easily applied to AlF_3 and ZrF_4, each of which has a very much higher vapor pressure than the corresponding oxide; ZrF_4 was obtained with an analytically determined oxygen content as low as 250 ppm. The volatility of KOH, which is comparable to that of KF, interfered with the application of the technique to the KF starting material (which contained KOH equivalent to 1200 ppm of oxygen); for this material a pretreatment of the melt with an appropriate metal fluoride, for example, FeF_2, FeF_3, or UF_4, caused the precipitation of oxide by the reaction

$$2MF_x + xKOH \rightarrow 2MO_{x/2}\downarrow + xHF\uparrow + xKF \ .$$

After the oxide had been removed with the use of UF_4, volatilization of the KF gave a product which contained only 500 ppm of oxygen. When molten, this product did not noticeably corrode the nickel container, in contrast with the behavior of previous melts.

The clear melts and reproducible liquidus temperatures obtained from the purified fluorides were taken as additional indication of their low oxygen content.

PURIFICATION OF BERYLLIUM BY ACETYLACETONE-EDTA SOLVENT EXTRACTION AND PRODUCTION OF PURE $Be(OH)_2$

C. E. L. Bamberger[11] H. F. McDuffie
C. F. Baes, Jr.

The research on the chemistry of the solvent extraction process for beryllium purification[12–15] and on the production of kilogram quantities of purified $Be(OH)_2$ was brought to a close at the end of the IAEA fellowship through which this work was supported. As previously reported, the starting material, $Be(OH)_2$, is dissolved in a CCl_4 solution of acetylacetone, HX, to form the chelate BeX_2. Metallic impurities are removed by extraction with an aqueous solution of an ammonium salt of EDTA, ethylenediaminetetraacetic acid, $(NH_4)_2H_2Y$; the beryllium is back extracted with aqueous nitric acid; and beryllium hydroxide is precipitated upon the addition of ammonia.

The original procedure was modified to include removal of HX from the HNO_3-$Be(NO_3)_2$ strip solution by chloroform scrubbing and precipitation of beryllium in the presence of EDTA with gaseous ammonia at 75°C. The product was a granular, easily dried, free-flowing powder having approximately the composition $Be(OH)_2 \cdot 0.3H_2O$. Ignition of the product, 4 kg of which was prepared in 85% yield in 1-kg batches in all-plastic bench-scale equipment, gave BeO in which the total of measurable metallic impurities was <5 ppm. Analysis of the $Be(OH)_2$ starting material by the Brush Beryllium Company showed (in parts per million parts of BeO) Fe, 116; Cu, 40; Si, 32; Al, 17; Na, 12; B, 6; Li, 6; Ni, 4; and Pb, 4. Table 27.2 presents the analytical information obtained on the final product.

---

[11] International Atomic Energy Agency Fellow from CNEA, Argentina, 1961–63.

[12] R. E. Moore, *Purification of Beryllium Compounds: A Literature Survey*, ORNL-2938 (June 1, 1960).

[13] R. E. Moore, J. H. Shaffer, and H. F. McDuffie, *The Preparation of High Purity Beryllium Oxide Through the Acetylacetone-EDTA Solvent Extraction Process*, ORNL-3323 (Sept. 13, 1962).

[14] R. E. Moore *et al.*, *Nucl. Sci. Eng.* **17**, 268–73 (1963).

[15] C. E. L. Bamberger, C. F. Baes, Jr., and H. F. McDuffie, "The Preparation of High Purity Beryllium Oxide by Solvent Extraction; Procedure and Chemistry," to be submitted for publication.

Table 27.2. Analysis of $Be(OH)_2$ Product

Elements	Parts per Million Parts of BeO
Found	
Si[a]	16
Na[b]	2
Al[c]	1.5
Cl[c]	1
Ga[c]	1
Cu[c]	0.1
Mn[c]	0.02
Below detectable limits	
Au[c], Dy[c], Eu[c], In[c], Ir[c], Lu[c], Re[c], V[c]	<0.02
Pb[c], Sb[c], W[c]	<0.1
Br[c], Er[c], Hg[c], Ho[c], Sc[c], Tb[c], U[c]	<0.2
Ag[d], Au[c], Cd[c], Cs[c], Gd[c], Li[e], Mg[d], Mo[c] Os[c], Ru[c], Sr[c], Th[c], P[f]	<1
Ce[c], Co[c], Cr[c], La[c], Rh[c], Se[c], Tm[c]	<2
B[e], Ba[e], Fe[e], Ge[e], Hf[e], K[e], Nd[c], Ni[e], Sn[e], Ti[e]	<4
Ca[d], Pr[c], Pt[c], Te[c], Tl[e], Zr[e]	<10
Zr[c,d]	<20
Rb[e]	<40

[a]Spectrographic analysis; O. Brisco and others, Analytical Laboratory, Y-12. Since Si is an element very common in any laboratory atmosphere, the determinations usually lack precision at very low concentrations due to contamination. Spectrographic analysis on the separate batches before blending show the following.

Batch	Parts of Si per Million Parts of BeO	
1st	14	18
2d, 3d	16	4
4th	10	18
Average	14	11

[b]Neutron activation; W. Ross, Analytical Chemistry Division, ORNL. Sodium content high, partially due to contamination during analysis.

[c]Neutron activation; W. Ross, Analytical Chemistry Division.

[d]Spectrographic analysis; J. Norris, Z. Combs, and others, Analytical Chemistry Division, ORNL.

[e]Spectrographic analysis; O. Brisco and others, Analytical Laboratory, Y-12.

[f]Analytical Chemistry Division, ORNL.

X-ray diffraction of the $Be(OH)_2 \cdot 0.3H_2O$ product, as prepared or after vacuum drying for 18 hr at 90 to 95°C, indicated the alpha form of $Be(OH)_2$, with no BeO detected. Electron microscopic examination of the product revealed it to be in the form of rosettes (Fig. 27.1*a*) made up of polycrystalline sheets (Fig. 27.1*b*) which extended 1 μ or more in two dimensions, but were only about 0.015 μ thick (150 A). Upon holding a sample in the electron beam for a prolonged period, it was converted by the resultant heating to BeO. This material (Fig. 27.1*c*) revealed the same platelet structure, but the sheets were stacked together.

With respect to the chemistry of the purification process, systematic study of the effect of changes in solution composition upon important extraction parameters provided a basis for the information summarized in Table 27.3.

Studies of the kinetics of the extraction process suggested that the various steps were essentially instantaneous (limited only by mass transfer), except those involving the formation and hydrolysis of BeX_2 in the aqueous phase. The reaction

$$BeX^+ + H^+ \rightarrow Be^{2+} + HX$$

was found to be the rate-controlling step in the hydrolysis of BeX_2, the rate expression being

$$-d[BeX^+]/dt = k[BeX^+][H^+] .$$

Figure 27.2 shows the effect of ionic strength upon the rate of the reaction; the effect is consistent with the Brønsted[16] prediction for the reaction of two univalent, like-charged species to form an activated complex.

The decontamination of beryllium from a large number of metallic species is, of course, facilitated by the existence of the stable charged complexes which EDTA forms in the aqueous phase with many cations:

$$M^{z+}(aq) + Y^{4-}(aq) \rightleftharpoons MY^{(4-z)-}(aq) . \quad (1)$$

In the presence of both HX and EDTA, the extraction coefficient (D_M) of M^{z+} may be written in the form

$$D_M = \frac{[MX_z]_o}{([MH^{(4-z)-}] + [M^{z+}] + [MX^{(z-1)+}] \ldots [MX_z])_a} . \quad (2)$$

The numerator is the concentration of the neutral metal acetylacetonate in the organic phase; it is assumed to be the only extractable species. The denominator, equal to the total aqueous concentration of the cation contains a term for each species assumed to be present in the aqueous phase.[17]

A function, useful for estimating the extractability of a given cation into the organic phase, was defined as

$$f = \frac{[MX_z]_a}{([MY^{(4-z)-}] + [M^{z+}] + [MX^{(z-1)+}] \ldots [MX_z])_a} , \quad (3)$$

that is, the fraction of the total aqueous concentration of M^{z+} in the extractable form. Calculations of f were made for all cases in which sufficient formation-constant data are available. The results are plotted in Fig. 27.3 as log f vs pH for HX = 0.1 *M* and EDTA = 0.02 *M*, typical conditions in the present procedure. The unique position of beryllium is fully consistent with the success of the purification method.

The remarkably effective decontamination attainable by the purification procedure was demonstrated by processing a batch of $Be(OH)_2$ (equivalent to 23 g of BeO), to which soluble salts containing Na^+, Mg^{2+}, B(III), Cu^{2+}, Al^{3+}, Fe^{3+}, and Cr^{3+} were added (to 1000 ppm in each case) during the initial dissolution step. Analyses were performed at various stages in the procedure, giving the results shown in Table 27.4. It is noteworthy that while Al^{3+} was not completely removed during the EDTA scrub steps, presumably because of low extraction rates, the remainder was retained in solution by EDTA during the precipitation step. To a lesser extent, Cu^{2+} and Fe^{3+} exhibited similar behavior; Na^+ and K^+ were found at all stages of the procedure, except in the product, the sum for Na^+ being many times the amount added initially. This may be attributed

[16] S. Glasstone, *Textbook of Physical Chemistry*, p. 1092, Van Nostrand, New York, 1943.

[17] Hydrolysis products are neglected in Eq. (2), since it is expected that these concentrations will, in most instances, be low compared with those of $MY^{(4-z)-}$ or M-X species.

Fig. 27.1*a*. Electron Micrograph of $Be(OH)_2$ Product. 8000X. Reduced 16%.

Fig. 27.1*b*. Electron Micrograph of $Be(OH)_2$ Product. 68,000X. Reduced 15%.

Fig. 27.1c. Electron Micrograph of BeO Resulting from Decomposition of Sample in Electron Beam. 20,000X. Reduced 15.5%.

to the use of glass equipment in the test. Silica was the only element consistently found in the product, two analyses giving 14 and 40 ppm.

The purified beryllium hydroxide prepared in this program is available to other research workers whose needs for such pure material are consistent with its value. It is obvious that much larger amounts could be made by the relatively simple process demonstrated if a need for material of high purity is shown.

Table 27.3. Variation of System Parameters with Solution Composition at 25°C

Parameter	Relation	Solution Composition	Source
	Aqueous Phase		
BeX^+ formation quotient, Q_1	$\log Q_1 = -0.94 - \frac{1.018\sqrt{I}}{1 + 1.3\sqrt{I}}$	0.1 – 2 *M* NaCl	*a*
BeX_2 formation quotient, Q_2	$\log Q_2 = -3.07 - \frac{1.018\sqrt{I}}{1 + 0.4\sqrt{I}}$	0.1 – 2 *M* NaCl	*a*
BeX_2 distribution quotient, Q_{DB}	$\log Q_{DB} = 1.81 + 0.35I$	0 – 4 *M* NaCl	*a*
	$\log Q_{DB} = 1.81 + 0.1I$	0 – 4 *M* NH_4NO_3	*b*
HX distribution quotient, Q_{DX}	$\log Q_{DX} = 0.53 + 0.16I$	0 – 1 *M* NaCl	c
	$\log Q_{DX} = 0.53 - 0.13I$	0 – 1 *M* HNO_3	*b*
BeX_2 solubility	$\log [BeX_2]_a = -1.527 - 0.35I$	0 – 4 *M* NaCl	*a*
HX solubility	$\log [HX]_a = 0.238 - 0.16I$	0 – 1 *M* NaCl	c
	Carbon Tetrachloride Phase		
BeX_2 distribution quotient, Q_{DB}	$\log Q_{DB} = 1.81 + 0.04M$	$M = [HX]_o + [BeX_2]_o = 0$ to $2.8\,M\,[BeX_2]/[HX] = 5$	*b*
HX distribution quotient, Q_{DX}	$\log Q_{DX} = 0.53 + 0.10M$	$M = [HX]_o + [BeX_2]_o = 0$ to $2.8\,M\,[BeX_2]/[HX] = 5$	*b*
	$\log Q_{DX} = 0.53 + 0.12[HX]_o$	0 – 1 *M* HX	*b*

[a] R. E. Moore *et al.*, *Nucl. Sci. Eng.* 17, 268–73 (1963).

[b] Present measurements.

[c] The variation of HX solubility with I is based on data of J. F. Steinbach, *Acetylacetone as an Analytical Extraction Agent*, thesis, NYO-6347 (1953). Variation of Q_{DX} with I is assumed from that for the HX solubility.

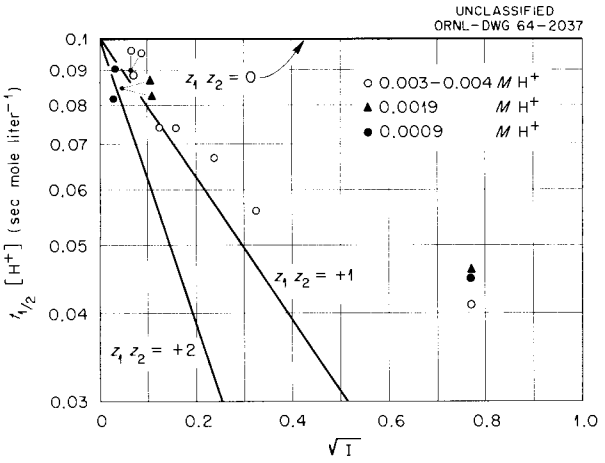

Fig. 27.2. Dependence of BeX_2 Hydrolysis Rate on Ionic Strength.

Table 27.4. Purification of Contaminated $Be(OH)_2$

(1000 parts per million parts of BeO of listed impurities were initially present)

Step	Total Impurities Found (parts per million parts of BeO)[a]					
	B	Mg	Cu	Al	Fe	Cr
Initial aqueous phase after beryllium extraction	990	986	260	363	66	1000
1st H_2O scrub	10	5	117	30	13	
2d H_2O scrub			144	15	17	
1st EDTA scrub		4	442	326	860	
2d EDTA scrub		3	5	145	8	
3d EDTA scrub		2	5	51	6	
3d H_2O scrub			7	13	5	
4th H_2O scrub			4	10	7	
Filtrate after precipitation			16	47	18	
Product	<4	<1	<4	<4	<4	<4

[a]These figures have been normalized to 1000 ppm, the amount of impurity added initially, in order to correct for apparent systematic errors in spectrochemical analyses. The total ppm reported in each case was as follows: Mg, 775; Cu, 465; Al, 902; Fe, 989; Cr, 655.

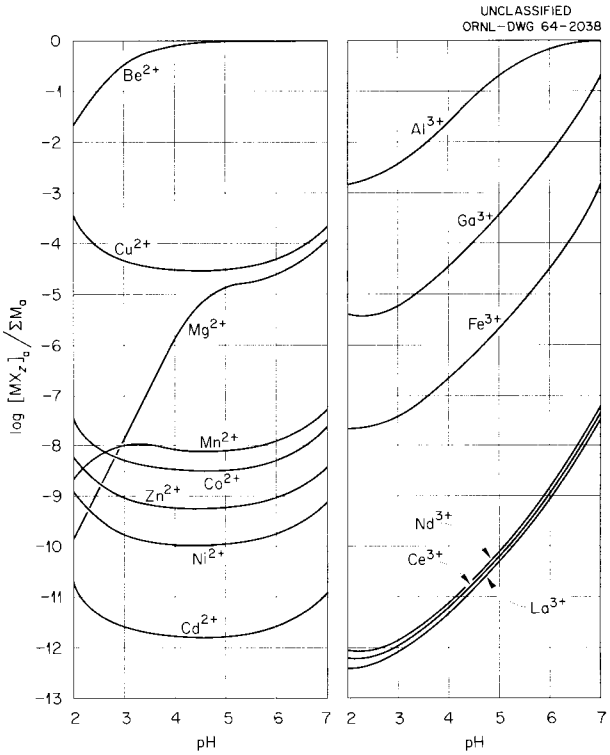

Fig. 27.3. Calculated Fraction of Aqueous Cation Concentration Present as the Extractable Acetylacetonate [f in Eq. (3)], for Various Cations as a Function of pH. 0.1 *M* aqueous HX, 0.02 *M* aqueous EDTA.

28. Chemical Support for the Controlled Thermonuclear Program

J. D. Redman D. M. Richardson
R. A. Strehlow

Achievement of better vacuum conditions in large thermonuclear experimental devices is the principal goal of the chemical support program for the Sherwood Project. The regular attainment of base pressures of less than 10^{-9} torr in DCX-1, one of the plasma research devices, has given added impetus to studies of the materials used for vacuum system construction and of instrumentation for the ultrahigh-vacuum region.

IMPROVEMENTS IN VACUUM TECHNOLOGY

Detection and Significance of Organic Fragments

During the past year, a Bendix time-of-flight mass spectrometer (model 12 with a 170-cm flight tube and a model 14 ion source) was obtained and put into operation for the purpose of analyzing the constituents of vacuum systems under many different conditions.

The first study with this instrument was devoted to the analysis of organic fragments. The sources of organic compounds which yield these fragments on analysis of the residual gases of vacuum systems are principally:

1. neoprene O-ring degassing,
2. mechanical-pump oils introduced into the vacuum chamber during initial evacuation,
3. lubricating greases and oils introduced either intentionally or inadvertently when the vacuum is being assembled,
4. diffusion-pump oils, which customarily consist of mixed hydrocarbons.

A series of tests was made with the spectrometer connected to a vacuum chamber over an operating mechanical vacuum pump; several commercially available oils were sequentially compared. The total peak intensities were compared, as well as the resolved spectra. At the same time, tests were made of the ultimate pressure obtainable as measured by a conventional thermocouple gage. As a result of these tests, it was recommended that a mixed hydrocarbon *diffusion-pump* fluid be used in the mechanical roughing and forepumps for the project experiments, instead of the conventional oils used in mechanical pumps.

In another series of experiments with the time-of-flight mass spectrometer, the fragmentation spectra for decane, heptane, and other organic compounds were obtained. This information is expected to be useful in the diagnosis of organic compounds in vacuum systems in subsequent studies. A typical result (for heptane) is shown in Table 28.1, in which the spectra at two ionizing voltages are compared with one from the literature for a momentum-sensitive spectrometer. The enhancement at the lower energy of the principal peaks (masses 100, 71, 57, and 43), relative to the ion peaks which are indicative of more extensive fragmentation (masses 41, 39, and 29), appears to be more marked than for a similar determination[1] with a conventional spectrometer. The effect of source temperature, however, has not yet been studied.

As a result of these preliminary studies, which showed reasonable correlation between the results

[1]W. A. Chupka and M. Kamiski, *J. Chem. Phys.* 35, 1991 (1961).

Table 28.1. Heptane Mass Spectrum

Formula	Mass	Approximate Peak Heights Relative to Mass 100		
		Electron Energy (v)[a]		
		30	70	API Standard Table
CH_2^+	14	0	1.30	
$C_2H_2^+$	26	0	0.04	
$C_2H_3^+$	27	0	0.77	
$C_2H_4^+$, N_2^+, CO^+	28	See text		
$C_2H_5^+$	29	0.34	0.89	
C_2H_6[b]	30	0.07	0.02	
C_3H_3	39		0.46	0.5
$C_3H_5^+$	41	0.66	1.61	2.5
$C_3H_6^+$	42	0.72	0.77	1.4
$C_3H_7^+$	43	3.07	3.07	5.0
$C_4H_7^+$	55	0.17	0.42	0.73
$C_4H_8^+$	56	1.45	1.23	0.85
$C_4H_9^+$	57	1.93	1.81	2.8
$C_5H_{10}^+$	70	1.07	0.92	1.0
$C_5H_{11}^+$	71	2.14	1.81	2.5
$C_6H_{13}^+$	85	0.03	0.04	
$C_7H_{16}^+$	100	1.00	1.00	1.0

[a]Source pressure, 1×10^{-5} torr.

[b]Probable impurity.

of theoretical and conventional mass spectrometry, an apparatus was designed which will permit studies of the effect of a retarding potential difference, and samples of 12 commercially available vacuum-pump oils were submitted for fractionation by molecular distillation. Analysis of the behavior of the various fractions is expected to furnish information which may permit further improvements in oils for ultrahigh-vacuum systems.

Diffusion Pumps in Series – Measurements of Compression Ratio

A recent publication by Hengevoss and Huber[2] reported that the use of two high-performance diffusion pumps in series gave a very low ultimate pressure. Analysis of their data suggested that the effective compression ratio of diffusion pumps might be a stronger function of molecular weight than indicated by the earlier derivations of Matricon[3] and Dayton;[4] the Hengevoss and Huber data yielded compression ratios ranging from 300 for hydrogen to 10^8 for krypton. An attempt to confirm the result for hydrogen was made with the use of the ultrahigh-vacuum test facility (see the following section) with dual or tandem arrangements of the pumps; compression ratios at least as large as 5×10^4 (the maximum limit of detection) were obtained. The discrepancy between these data and the report of Hengevoss and Huber has not been resolved, but may be due to design

[2]J. Hengevoss and W. K. Huber, *Vacuum* 13, 1 (1963).

[3]M. Matricon, *J. Phys. Radium* 3(7), 127 (1932).

[4]B. B. Dayton, *Rev. Sci. Instr.* 11, 793 (1948).

differences in the diffusion pumps. Apparatus has been constructed for more precise study of the behavior of diffusion pumps in series.

Surface Adsorption and Desorption

Heats of adsorption have been measured[5,6] for a variety of gases on a practical metal vacuum liner surface under conditions of low surface coverage ($< 10^{11}$ molecules/cm^2). These are summarized in Table 28.2.

Table 28.2. Heats of Desorption of Selected Gases (kcal/mole)

Gas	Mo[a]	Ag[b]	Pt[b]	Fe[b]
CH_4	4.3			
Ar	3.5	3.5	3.3	3.2
CO	3.0	3.2	3.6	3.4
N_2		3.6	3.4	3.1
H_2	2.2			

[a]This work.

[b]M. H. Armbruster and J. B. Austin, *J. Am. Chem. Soc.* **66**, 159 (1944).

Work on this problem has proceeded with the redesign and modification of the ultrahigh-vacuum apparatus as shown in Figs. 28.1–28.3. Figure 28.1 shows the vacuum tank with the bottom of the liner (shroud) in position, ready to be lowered into the tank. Figures 28.2 and 28.3 show the shroud with some of the gage and tubulation details. The bottom view (Fig. 28.2) shows a variable-conductance plate which allows pumping speeds to be controlled from 3.8 liters/sec to about 100 liters/sec for air at room temperature. The volume of the shroud is about 280 liters. Additional liquid-nitrogen-cooled trapping apparatus is present in the tank. Mean outgassing rates have been measured after baking of the shroud to 200°C for some hours. These rates at the elevated temperature are about 4×10^{-9} torr-liters sec^{-1} cm^{-2}. The outgassing rate, with an estimated ΔH for outgassing of water equal to about 14 to 18 kcal/mole, decreases with temperature, of course, and yields base pressures of $< 10^{-9}$ torr. A controlled-leak apparatus which allows gas to be introduced at a rate less than 0.1 monolayer/hr on the 3×10^4 cm^2 shroud surface was also constructed during this period.

Desorptions from liquid-nitrogen-cooled surfaces, upon being warmed, have yielded seven or more distinct desorption peaks, depending upon the condition and history of the surface and the vacuum system. Evolution of even 10^{-5} monolayer in an experimental plasma device can result (for DCX-1) in neutral density increases of 10^{-9} torr; hence, vacuum procedures and materials selection should be optimized carefully in order to eliminate this potential source of difficulty. (Ion and electron bombardment and tiny temperature fluctuations appear to cause desorption of species bonded with low energies.)

Acceptance Tests for High-Vacuum Valves

In cooperation with the plant purchasing department, a program has been pursued to develop appropriate acceptance tests for certain classes of vacuum valves in order to take economic advantage of the increased level of competition in the vacuum-equipment industry. Tests on Knudsen conductance, leak and permeation rates, closing torque, and gasket materials have led to the development of tentative acceptance standards which are to be reviewed by other Laboratory personnel.

Development of High-Temperature, High-Vacuum Flange-Gasket Combinations

For thermonuclear studies involving large metal equipment, the flange-gasket combinations will have to be alternately taken to high temperatures (during "bakeout") and then used at low temperatures, all under high vacuum. It is, of course, desirable that a flange assembly be usable through many such cycles without leaking and without requiring constant attendance. In cooperation with the Engineering Section of the Thermonuclear Division, a program of test and evaluation was performed which led to tentative correlations of the

[5]*Thermonuclear Div. Semiann. Progr. Rept. Apr. 30, 1963*, ORNL-3472, p. 114–18.

[6]*Transactions*, American Vacuum Society Symposium, October 1963, in press.

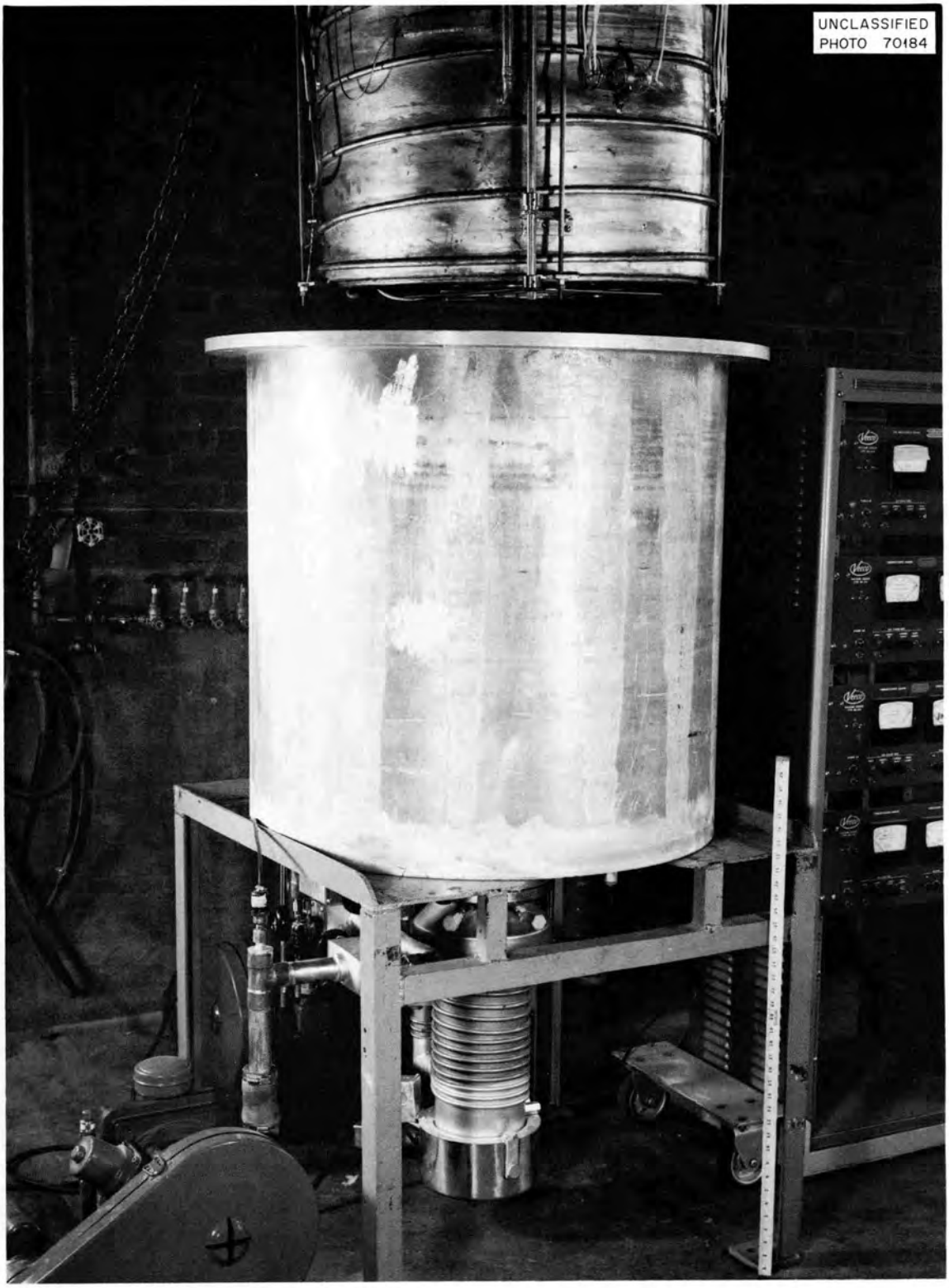

Fig. 28.1. Ultrahigh-Vacuum Test Facility Vacuum Vessel.

Fig. 28.2. Bottom View of Shroud, Showing Variable-Conductance Valve to Outer Vacuum Region.

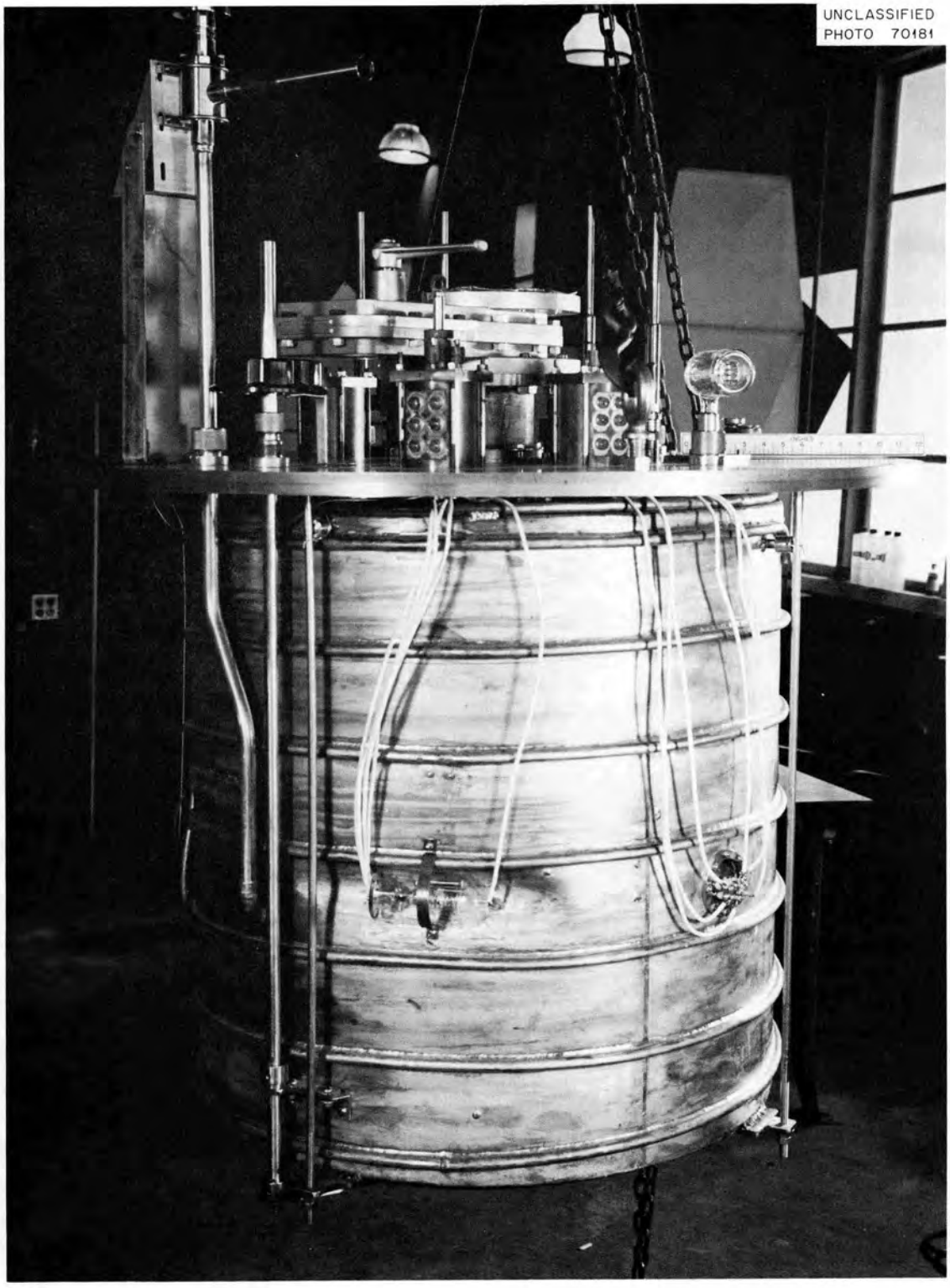

Fig. 28.3. View of Shroud (Liner), Showing Gages and Valves.

behavior of flange-gasket assemblies with the metallurgical properties of the deformable gaskets. Part of this work is treated in a separate publication.[7] More recent studies on commercially available gaskets have been carried out, using the 10-in. test assembly, with results that corroborate the basic conclusions of the earlier work. It appears that although many varieties of gasket-flange combinations yield bakeable ultrahigh vacuum closure, most are quite costly in terms of machining time. The selection of a closure design for large flanges (>6-in. gasket diameter) for expected closure frequencies is less related to gasket cost than to the intricacy of the flange design.

STUDIES OF IONIZATION GAGES

Applications and Diagnosis

The application of findings reported earlier[8] regarding ionization gage readings in oil-contaminated vacuum systems has been developed to yield an apparently satisfactory diagnostic technique for the simple determination of the presence of gage pumping or gage outgassing, and a consequent improvement in the measurement of pressure in these complex systems. This is reported elsewhere[9] and involves the varying of electron emission currents to yield ion currents which, for contaminated systems, are proportional to the first power of the emission at low emissions only. The emission current at which significant departure begins is related to the amount of gage contribution to the reading. The direction of departure from linearity indicates qualitatively the presence of irreversible gage pumping or gage outgassing.

Ion emission from the molybdenum grid in hot-cathode ion gages due to outgassing and to electron bombardment has been observed to be one of the principal limitations of the Bayard-Alpert gage geometry. Part of the current interest of the present chemical support effort in thermal emission of ions (see below) is due to these observations.

Chemical Reactions Catalyzed by Hot Filaments

Mass spectra obtained with a magnetic deflection spectrometer during routine residual gas analysis of the oil-contaminated region of the test facility have suggested that the use of a thoriated iridium filament in an ionization gage is accompanied by reactions of the filament with organic gases; the resulting carbon dioxide and carbon monoxide are introduced into the vacuum system at rates of the order of 10^{13} molecules/sec for total organic compound partial pressures of less than 10^{-7} torr. This gas generation appears to be sensitive to temperature rather than to electron emission current, and does not occur on molybdenum surfaces (at 1000°C) that are nearly as hot as the thoria filament. Whether water vapor is involved in the reactions has not yet been established. All the monitored organic compound peaks show a reduction which is about equivalent to the increase of CO plus CO_2.

This series of observations may account for the conflicting reports in the literature about the presence of CO_2 as a residual gas in ultrahigh-vacuum facilities, since it appears that both organic compounds and an oxidizing surface seem to be minimum requirements. The possibility of developing scavenging procedures for organic compounds in vacuum systems is under consideration.

ION EMISSION FROM HEATED SURFACES

Since Richardson's work of 1913,[10] it has been generally known that alkali-metal ions are emitted from heated metals. The presence of potassium in various mass spectrometer sources is often detected and has been the subject of investigation relative to surface ionization studies at this Laboratory.[11]

As part of the controlled thermonuclear research chemical support program, a procedure was developed for preparation of synthetic samples of the mineral β-eucryptite ($LiAlSiO_4$). These samples have been prepared by the Metals and Ceramics Division on several occasions, for use by Thermonuclear Division members and others, as a source

---

[7] J. D. Redman, *High-Vacuum Flange Test of a Bakeable Aluminum Wire Seal*, ORNL-3509, in press.

[8] *Reactor Chem. Div. Ann. Progr. Rept. Jan. 31, 1963*, ORNL-3417, p. 283; *Reactor Chem. Div. Ann. Progr. Rept. Jan. 31, 1962*, ORNL-3262, p. 199.

[9] *Thermonuclear Div. Semiann. Progr. Rept. Oct. 31, 1963*, ORNL-3564, pp. 126–29.

[10] O. W. Richardson, *Proc. Roy. Soc. (London)* **89**, 507 (1913).

[11] R. E. Mintum, S. Datz, and E. H. Taylor, *J. Appl. Phys.* **31**, 876–83 (1960).

of lithium ions, inasmuch as the glassy material emits lithium ions when heated. A source-sample introduction system for the time-of-flight spectrometer was modified so that ion purity from this source might be assessed. Significant peaks at masses 7, 14, 23, 30, 39, and 41 have been observed for the eucryptite-loaded tantalum filament. Only the order of appearance and the constancy of the peaks have been observed; a temperature measurement method has not yet been developed. The principal peaks were at masses 7, 23, and 39, presumably due to the alkali metals; the 39:41 ratio was found to be that expected for potassium. The presence of a peak at mass 30 indicates the possible presence of Li_2O^+ from this source, which would imply that at least a part of the mass-23 signal may be LiO^+. A sample is to be prepared with Li^6 so that the lithium-containing species may be readily distinguished.

MISCELLANEOUS STUDIES

Cooperation with personnel of all the groups working on controlled thermonuclear research, concerning both materials and a variety of chemical problems, has involved assistance in several forms. Aid in prevention of probe failure due to deposition of lithium from lithium arcs, attempts to minimize corrosion in magnet cooling water, studies of beam–secondary plasma interactions,[12] development work on some additional test procedures for vacuum hardware and materials, and development of procedures to apply, at the earliest possible date, the results of the studies of the chemical support program have been and will continue to be an integral part of this work.

---

[12]E. D. Shipley, private communication.

Publications

AUTHOR(s)	TITLE	PUBLICATION
Adams, R. E., C. J. Barton, W. E. Browning, Jr., and G. W. Parker	Particle and Fission Product Behavior in Nuclear Accidents	*Nucl. Safety* **4**(3), 62 (1963)
Baes, C. F., Jr.	Activity Buildup in PWR Systems	*Nucl. Safety* **5**(1), 45 (1963)
Baes, C. F., Jr.	The Synergistic Effect in Organophosphate Extraction Systems	*Nucl. Sci. Eng.* **16**, 405 (1963)
Baes, C. F., Jr., and T. H. Handley	PWR Chemistry: Studies of the ORR In-Pile Loop	TID-7641 (June 1963)
Baes, C. F., Jr., J. H. Shaffer, and H. F. McDuffie	UO_2 and ZrO_2 Behavior in Molten Fluorides	*Trans. Am. Nucl. Soc.* **6**, 393 (1963)
Baker, H. T., and C. F. Baes, Jr.	An Infrared and Isopiestic Investigation of the Interaction Between Di(2-ethylhexyl)phosphoric Acid and Tri-*n*-octylphosphine Oxide in Octane	*J. Inorg. Nucl. Chem.* **24**, 1277 (1962)
Barton, C. J.	Hazards of Hydrogen Handling	*Nucl. Safety* **5**(1), 84 (1963)
Barton, C. J.	Glove Box Techniques	*Technique of Inorganic Chemistry*, vol. III, Interscience, New York, 1963
Bennett, R. L., and G. W. Keilholtz	Thermal, Radiation and Chemical Stability of Sulfur Dioxide	ORNL-TM-747, (Dec. 31, 1963)
Bennett, R. L., W. T. Rainey, G. W. Keilholtz, and H. L. Hemphill	Stability of Thermoelectric Materials Under PBRE Conditions	ORNL-TM-746 (Jan. 10, 1964)
Blakely, J. P., J. L. Rutherford, and L. G. Overholser	Reactivity of Graphite and Fueled Graphite Spheres with Oxidizing Gases	ORNL-TM-751 (Jan. 9, 1964)
Blander, M., J. Braunstein, and M. D. Silverman	Heats of Solution of Solids in Molten Reciprocal Salt Systems	*J. Am. Chem. Soc.* **85**, 895 (1963)
Blood, C. M., and R. B. Evans III	Diffusion of Uranium in Pyrolytic Carbon, p. 36 in "Coated Particle Fuel Development at ORNL"	ORNL-TM-431 (Feb. 14, 1963)
Bohlmann, E. G.	Metal-Water Reactions	*Nucl. Safety* **5**(1), 51 (1963)
Browning, W. E., Jr., and R. D. Ackley	Particle Size Distribution of Radioactive Aerosols by Diffusion Coefficient Measurement	TID-7641 (June 1963)

AUTHOR(s)	TITLE	PUBLICATION
Browning, W. E., Jr., C. E. Miller, Jr., R. P. Shields, and B. F. Roberts	Release of Fission Products During In-Pile Melting of UO_2	*Trans. Am. Nucl. Soc.* **6,** 125 (1963)
Burns, J. H., R. D. Ellison, and H. A. Levy	The Crystal Structure of the Molecular Addition Compound Xenon Difluoride Xenon Tetrafluoride	*J. Phys. Chem.* **67,** 1569 (1963)
Burns, J. H., P. A. Agron, and H. A. Levy	The Crystal and Molecular Structure of Xenon Tetrafluoride by Neutron Diffraction	*Noble Gas Compounds,* ed. by H. H. Hyman, University of Chicago Press, 1963
Burns, J. H., R. D. Ellison, and H. A. Levy	The Crystal Structure of $XeF_2 \cdot XeF_4$ by X-Ray Diffraction	*Noble Gas Compounds,* ed. by H. H. Hyman, University of Chicago Press, 1963
Burns, J. H., P. A. Agron, and H. A. Levy	Xenon Tetrafluoride Molecule and Its Thermal Motion: A Neutron Diffraction Study	*Science* **139,** 1208 (1963)
Burns, J. H.	A Second Crystalline Phase of Xenon Tetrafluoride	*J. Phys. Chem.* **67,** 536 (1963)
Cantor, S.	Fission Product Vaporization and Deposition from Uranium Carbide	*Nucl. Safety* **4**(3), 58 (1963)
Cantor, S., and W. T. Ward	Freezing Point Depressions in Sodium Fluoride. III. Effects of 3*d* Transition Metal Difluorides and Cadmium Fluoride	*J. Phys. Chem.* **67,** 1868 (1963)
Carroll, R. M.	Fission-Gas-Release from Single Crystal UO_2 During Irradiation	*Trans. Am. Nucl. Soc.* **6,** 121 (1963)
Compere, E. L., H. C. Savage, A. J. Shor, and E. G. Bohlmann	In-Pile Testing of Circulating Thoria Suspensions	*Proceedings of the Thorium Fuel Cycle Symposium,* TID-7650 (1963)
Compere, E. L., S. A. Reed, D. M. Richardson, and L. F. Woo	Compatibility Studies with Liquid Coolants	*Proceedings of a Symposium on Ceramic Matrix Fuels Containing Coated Particles,* TID-7654 (June 1963)
de Bruin, H. J., and G. M. Watson	Self-Diffusion of Beryllium in Unirradiated, Cold-Pressed and Sintered Beryllium Oxide	ORNL-3526 (Jan. 14, 1964)
English, J. L., and J. C. Griess	Stress-Corrosion Cracking Behavior of Austenitic Stainless Steel and Other Materials	*Mater. Protect.* **2**(11), 18 (1963).
Evans, R. B., G. M. Watson, and J. Truitt	Interdiffusion of Gases in a Low Permeability Graphite. II. As Influenced by Pressure Gradients	*J. Appl. Phys.* **34,** 2020 (1963)
Fletcher, W. H., and C. S. Shoup, Jr.	The Infrared Spectrum of Methyl-d_3 Cyanide	*J. Mol. Spectr.* **10,** 300 (1963)
Fontana, M. H., and W. E. Browning, Jr.	Effect of Particle Agglomeration on the Penetration of Filters Utilized with Double Containment Systems	ORNL-NSIC-1 (Sept. 25, 1963)
Friedman, H. A.	Analytical Techniques Used in Evaluating High-Temperature Phase Equilibria: Application to the UO_2-ThO_2-O_2 System	TID-7655 (1963)

AUTHOR(s)	TITLE	PUBLICATION
Gill, J. S., and W. L. Marshall	Glass to Metal Tube Connector for Visual Observation of the Effect of Pressure on Phase Equilibria	*Rev. Sci. Instr.* **34**, 442 (1963)
Griess, J. C.	Stress Corrosion Cracking of Stainless Steel	*Nucl. Safety* **4**(3), 32 (1963)
Griess, J. C., H. C. Savage, J. G. Rainwater, J. L. English, and T. H. Mauney	The Corrosion of Aluminum Alloys Under Simulated ATR and HFIR Conditions	TID-7642 (June 1963)
Grimes, W. R.	Radiation Chemistry of MSR System	ORNL-TM-500 (Mar. 13, 1963)
Hess, D. N., L. Rice, B. Willis, W. E. Clark, and E. S. Snavely	Corrosion of Stainless Steel in Acidic Nitrate Waste Solutions from Processing Stainless Steel Reactor Fuels	ORNL-3474 (Sept. 30, 1963)
Jenks, G. H., and J. E. Baker	In-Pile Radiation Corrosion Experiments with Zirconium, Titanium, and Steel Alloys in 0.17 *m* UO_2SO_4 Solutions at 280°C	ORNL-3099 (June 24, 1963)
Jenks, G. H.	Zircaloy-2 Corrosion in Aqueous Homogeneous Reactor Solutions	*Trans. Am. Nucl. Soc.* **6**(2), 367 (1963)
Jenks, G. H., and J. E. Baker	In-Pile Loop Corrosion Experiments with Uranyl Sulfate Solutions at 235 and 250°C	ORNL-3131 (Aug. 1, 1963)
Jenks, G. H., and R. J. Davis	Effect of Reactor Radiations on Zircaloy-2 Corrosion in High Temperature Aqueous Environments	TID-7641 (June 1963)
Keilholtz, G. W., J. E. Lee, Jr., and R. E. Moore	The Effect of Fast-Neutron Irradiation on BeO Compacts at High Temperature	ORNL-TM-741 (Dec. 11, 1963)
Keilholtz, G. W., J. E. Lee, Jr., R. E. Moore, and R. L. Hamner	Behavior of BeO Under Neutron Irradiation	ORNL-TM-742 (Dec. 11, 1963)
Kirslis, S. S.	Corrosion and CF_4 Generation in the MSRE Environment	TID-7641 (June 1963)
Levy, H. A., P. A. Agron, and J. H. Burns	Crystal and Molecular Structures of Xenon Fluorides	*Acta Cryst.* **16**, A25 (1963).
Manning, D. L., M. Blander, and J. Braunstein	Association Constants of Lead and Bromide Ions in Molten Sodium Nitrate–Potassium Nitrate Mixtures and Their Comparison with the Quasi-Lattice Theory	*Inorg. Chem.* **2**, 345 (1963)
Marshall, W. L., J. S. Gill, and Ruth Slusher	Aqueous Systems at High Temperature. VI. Investigations on the System $NiO-SO_3-H_2O$ and Its D_2O Analog from 10^{-4} to 2 *m* SO_3, 150–400°C	*J. Inorg. Nucl. Chem.* **24**, 889 (1962)
Marshall, W. L., and Ruth Slusher	Aqueous Systems at High Temperature. VIII. The Solubility of UO_3 Hydrates in HNO_3-H_2O Solutions, 25–350°C, 10^{-4} to 6 molal Nitrate	*J. Inorg. Nucl. Chem.* **25**, 283 (1963)

AUTHOR(s)	TITLE	PUBLICATION
Marshall, W. L., Ruth Slusher, and F. J. Smith	Aqueous Systems at High Temperature. IX. Investigations on the System Li_2SO_4-H_2SO_4-H_2O and Its D_2O Analogue, 200–470°C. Solubilities and Critical Phenomena	*J. Inorg. Nucl. Chem.* **25,** 559 (1963)
Marshall, W. L., and E. V. Jones	Aqueous Systems at High Temperatures. X. Investigations on the Systems UO_3-CuO-D_2O, UO_3-NiO-SO_3-D_2O, and UO_3-CuO-NiO-SO_3-D_2O, 260–410°C; Liquid-Liquid Immiscibility and Critical Phenomena	*J. Inorg. Nucl. Chem.* **25,** 1021 (1963)
Marshall, W. L., and J. S. Gill	Aqueous Systems at High Temperature. XI. Effect of Pressure on Liquid-Liquid Immiscibility in the System UO_2SO_4-H_2O and Liquid–Supercritical Fluid Equilibria in the System UO_2SO_4-H_2SO_4-H_2O; 290–430°C, 75–300 Bars	*J. Inorg. Nucl. Chem.* **25,** 1033 (1963)
Mason, E. A., and A. P. Malinauskas	The Effect of Accommodation on Thermal Transpiration	ORNL-TM-754 (Jan. 6, 1964)
Mason, E. A., R. B. Evans III, and G. M. Watson	Gaseous Diffusion in Porous Media. III. Thermal Transpiration	*J. Chem. Phys.* **38,** 1808 (1963)
Moore, R. E., J. H. Shaffer, C. F. Baes, Jr., H. F. McDuffie, and C. E. L. Bamberger	Purification of Beryllium by Acetylacetone-EDTA Solvent Extraction	*Nucl. Sci. Eng.* **17,** 268 (1963)
Neumann, P. D., and J. C. Griess	Stress-Corrosion Cracking of Type 347 Stainless Steel and Other Alloys in High-Temperature Water	*Corrosion* **19**(10), 345t (1963)
Osborne, M. F., J. G. Morgan, F. L. Carlsen, and J. A. Conlin	The Radiation Stability of UC_2, Graphite Matrix Fuels	*Trans. Am. Nucl. Soc.* **6,** 134 (1963)
Overholser, L. G., N. V. Smith, and J. P. Blakely	Compatibility of Pyrolytic-Carbon-Coated Uranium Carbide Particles with Water Vapor	TID-7654 (June 1963)
Overholser, L. G., and J. P. Blakely	Outgassing Characteristics of Various Graphites	ORNL-3396 (Feb. 14, 1963)
Parker, G. W., and R. A. Lorenz	Fission-Product Release from Meltdown of a Cluster of Center-Heated UO_2 Fuel Pins	*Trans. Am. Nucl. Soc.* **6**(1), 124 (1963)
Parker, G. W.	A Review of Fission-Product-Release Research	*Trans. Am. Nucl. Soc.* **6**(1), 120 (1963)
Parker, G. W., G. E. Creek, and W. J. Martin	Parametric Studies of Fission Product Release from UO_2 Fuels	TID-7641 (June 1963)
Perez, R. B., R. M. Carroll, and O. Sisman	A Mathematical Model for the High Temperature In-Pile Release of Fission Gases. Part I. Steady State	ORNL-TM-743 (Dec. 20, 1963)
Quist, A. S., E. U. Franck, H. R. Jolley, and W. L. Marshall	Electrical Conductances of Aqueous Solutions at High Temperature and Pressure. I. The Conductances of K_2SO_4-H_2O Solutions from 25 to 800°C and at Pressures Up to 4000 Bars	*J. Phys. Chem.* **67,** 2453 (1963)

AUTHOR(s)	TITLE	PUBLICATION
Rainey, W. T., Jr., and L. B. Yeatts, Jr.	Studies of Pyrolysis Products of Pure Biphenyl	TID-7641 (June 1963)
Reagan, P. E., F. L. Carlsen, and R. M. Carroll	Fission-Gas Release from Pyrolytic Carbon Coated Uranium Carbide During Irradiation	*Trans. Am. Nucl. Soc.* **6,** 133 (1963)
Rainey, W. T., Jr., and R. L. Bennett	Stability of Base Metal Thermocouples in Helium Atmospheres	*ISA Trans.* **2,** 34 (1963)
Rainey, W. T., Jr., and R. L. Bennett	Thermal and Radiation Stability of Suggested Alternative Gas Coolants	ORNL-TM-475 (Feb. 5, 1963)
Reed, S. A., W. J. Leonard, and E. L. Compere	Hydriding of Zirconium Alloys in Circulating High Temperature Aqueous ThO_2 and Thorium-Uranium Oxide Slurries	TID-7641 (June 1963)
Richardson, D. M., and R. A. Strehlow	Gaseous Desorption at Low Pressures and Liquid Nitrogen Temperatures	*Transactions of the 10th National Vaccum Symposium,* p. 97, American Vacuum Society (1963)
Roberts, B. F., C. E. Miller, Jr., R. P. Shields, and W. E. Browning, Jr.	Release of Fission Products on the In-Pile Melting of UO_2	TID-7641 (June 1963)
Robinson, R. A., and H. F. McDuffie	Radioisotope Source Testing and Handling	*Nucl. Safety* 4(4), 16 (1963)
Savage, H. C.	Pump Loops Used for Materials Testing in High Temperature Aqueous Solutions and Slurries	ORNL-3449 (June 10, 1963)
Shaffer, J. H., and H. F. McDuffie	Moisture Removal from Graphites by Purging with Dry Helium Below 700°C	*Trans. Am. Nucl. Soc.* **6**(2), 355 (1963)
Shaffer, J. H., J. E. Strain, D. R. Cuneo, and M. J. Kelly	Separation of Pa from Molten Salt Reactor Fuel Compositions	U. S. Patent 3,110,555 (Nov. 12, 1963)
Shields, R. P., W. E. Browning, Jr., C. E. Miller, Jr., and B. F. Roberts	Release of Fission Products During In-Pile Burning of UC_2-Graphite Fuel	*Trans. Am. Nucl. Soc.* **6**(1), 135 (1963)
Silverman, M. D., and W. E. Browning, Jr.	Fibrous Filters as Particle Analyzers	*Trans. Am. Nucl. Soc.* **6,** 401 (1963)
Silverman, M. D., B. O. Heston, and P. S. Rudolph	Radiation Damage to Freon-11, CCl_3F	*Nucl. Sci. Eng.* **15,** 217 (1963)
Soldano, B. A., and M. Meek	Osmotic Behavior of Aqueous Salt Solutions at Elevated Temperatures. Part III	*J. Chem. Soc.* **1963,** 4424
Steinfink, H., and J. H. Burns	The Crystal Structure of Cr_2F_5	*Acta Cryst.* **16,** A29 (1963)
Stuckey, J. E., and C. H. Secoy	Critical Temperatures and Densities of the SO_3-H_2O System	*J. Chem. Eng. Data* **8,** 386 (1963)
Sturm, B. J., and C. W. Sheridan	Vanadium(III) Fluoride	*Inorganic Syntheses,* ed. by J. Kleinberg, vol. 7, pp. 87–92, McGraw-Hill, New York, 1963

AUTHOR(s)	TITLE	PUBLICATION
Sturm, B. J.	Method for Preparation of Sinterable Beryllium	U. S. Patent 3,100,686 (Aug. 13, 1963)
Thoma, R. E., C. F. Weaver, H. Insley, and G. M. Hebert	Phase Studies of the MSRE Fuel System	TID-7641 (June 1963)
Thoma, R. E., H. Insley, G. M. Hebert, H. A. Friedman, and C. F. Weaver	Phase Equilibria in the System NaF-ThF_4-UF_4	ORNL-3304 (Feb. 7, 1963)
Thoma, R. E., H. Insley, G. M. Hebert, H. A. Friedman, and C. F. Weaver	Phase Equilibria in the System NaF-ThF_4-UF_4	*J. Am. Ceram. Soc.* **46**, 37 (1963)
Thoma, R. E., G. M. Hebert, H. Insley, and C. F. Weaver	Phase Equilibria in the System NaF-YF_3	*Inorg. Chem.* **2**(5), 1005 (1963)
Truitt, J., G. D. Alton, and C. M. Blood	Thorium Diffusion in a Pyrolytic Carbon and Porous Graphite	*Appl. Phys. Letters* **3**, 150 (1963)
Watson, G. M., C. M. Blood, and R. B. Evans III	Solid State Diffusion of Uranium Through Graphites	TID-7654 (June 1963)
Weaver, C. F., R. G. Ross, and R. E. Thoma	LiF Crystals with Selected Isotopic Ratios of Lithium	ORNL-RMIC-1 (June 1963)
Weaver, C. F., R. G. Ross, and R. E. Thoma	Production of High Purity Li^7F Crystals	*J. Appl. Phys.* **34**, 1827 (1963)
Weaver, C. F., H. L. Hemphill, R. G. Ross, and R. E. Thoma	Welding of Pure Copper for Containers for High Purity Molten Fluorides with H_2 and HF	*J. Sci. Instr.* **40**, 543 (1963)
Yeatts, L. B., Jr., and W. T. Rainey, Jr.	Retention Data for Benzene and Its Derivatives	*J. Gas Chromatog.* **1**(10), 31 (1963)
Yeatts, L. B., Jr., and W. T. Rainey, Jr.	Retention Data for Benzene and Related Compounds	*J. Gas Chromatog.* **1**(10), 31 (1963)
Yeatts, L. G., Jr., and W. T. Rainey, Jr.	Preparation and Storage of Volatile Standard Solutions for Gas Chromatographic Analysis	*J. Gas Chromatog.* **1**(11), 30 (1963)
Yeatts, L. B., Jr., J. E. Attrill, and W. T. Rainey, Jr.	Gas Chromatographic Analysis of Biphenyl Pyrolytic Products	ORNL-TM-523 (Mar. 13, 1963)

Papers Presented at Scientific and Technical Meetings

AUTHOR(s)	TITLE	PLACE PRESENTED
Bacarella, A. L., and A. L. Sutton	Electrochemical Measures on Zircaloy-2	Electrochemical Society, New York, Sept. 29—Oct. 3, 1963
Baes, C. F., Jr., J. H. Shaffer, and H. F. McDuffie	UO_2 and ZrO_2 Behavior in Molten Fluorides	American Nuclear Society, Winter Meeting, New York, Nov. 18—21, 1963
Baes, C. F., Jr.	Potentiometric Measurements of Cation Hydrolysis at Elevated Temperatures	American Chemical Society, Regional Meeting, Houston, Dec. 5—7, 1963
Barton, C. J., D. R. Cuneo, M. J. Kelly, and J. E. Strain	Protactinium Stability in Thorium Nitrate—Nitric Acid Solutions	Protactinium Chemistry Symposium, Gatlinburg, Tenn., Apr. 25—26, 1963
Blankenship, F. F., S. S. Kirslis, and W. R. Grimes	Generation of Fluorine by Radiolysis of Fluoride Mixtures	Symposium on Inorganic Fluorine Chemistry, Argonne National Laboratory, Sept. 4—6, 1963
Browning, W. E., Jr., C. E. Miller, Jr., R. P. Shields, and B. F. Roberts	Release of Fission Products During In-Pile Melting of UO_2	American Nuclear Society, 9th Annual Meeting, Salt Lake City, Utah, June 17—19, 1963
Browning, W. E., Jr., R. D. Ackley, and M. D. Silverman	Characterization of Gas-Borne Fission Products	8th AEC Air Cleaning Conference, Oak Ridge, Tenn., Oct. 22, 1963
Burns, J. H., P. A. Agron, and H. A. Levy	A Neutron Diffraction Study of Xenon Tetrafluoride	American Crystallographic Association, Cambridge, Mass., Mar. 28—30, 1963
Burns, J. H., P. A. Argon, and H. A. Levy	The Crystal and Molecular Structure of Xenon Tetrafluoride by Neutron Diffraction	Conference on Inert Gas Compounds, Argonne National Laboratory, Apr. 23, 1963
Carlsen, F. L., Jr., W. O. Harms, J. A. Conlin, J. G. Morgan, V. A. DeCarlo, and D. F. Toner	Oak Ridge National Laboratory Irradiation Experiments on Graphite Matrix Fuel Elements Containing Pyrolytic-Carbon Coated Fuel Particles	American Nuclear Society, Salt Lake City, Utah, June 17—19, 1963
Carroll, R. M.	Fission-Gas Release from Single Crystal UO_2 During Irradiation	American Nuclear Society, Salt Lake City, Utah, June 17—19, 1963

AUTHOR(s)	TITLE	PLACE PRESENTED
Carroll, R. M.	Fission Gas Release from Various Types of UO_2 During Irradiation	U. S.–Japan Meeting on Oxide and Carbide Fuels, Tokai, Japan, May 13–17, 1963
Carroll, R. M.	Fission Gas Release from UO_2 Single Crystals During Irradiation	U. S.–Japan Meeting on Oxide and Carbide Fuels, Tokai, Japan, May 13–17, 1963
Carroll, R. M.	Burst Release of Fission Gas from UO_2	U. S.–Japan Meeting on Oxide and Carbide Fuels, Tokai, Japan, May 13–17, 1963
Carroll, R. M.	Deposition of Fission Products Released by In-Reactor Burning or Melting of UO_2 and UC_2	U. S.–Japan Meeting on Oxide and Carbide Fuels, Tokai, Japan, May 13–17, 1963
Carroll, R. M.	Fission Gas Release from Pyrolytic Graphite Enclosed UC Particles During Irradiation	U. S.–Japan Meeting on Oxide and Carbide Fuels, Tokai, Japan, May 13–17, 1963
Carroll, R. M.	Fission Recoil Release Effects from UO_2	U. S.–Japan Meeting on Oxide and Carbide Fuels, Tokai, Japan, May 13–17, 1963
Compere, E. L.	Fission and Chemical Problems in Irradiated Suspension Experiments at Elevated Temperatures	Traveling Lecture Program, Ouachita Baptist College, Arkadelphia, Ark., Mar. 14, 1963
de Bruin, H. J., and G. M. Watson	Self-Diffusion of Beryllium in Unirradiated, Cold-Pressed, and Sintered Beryllium Oxide	International Conference on Beryllium Oxide, Newport, Sydney, Australia, Oct. 21–25, 1963
de Bruin, H. J., and G. M. Watson	Self-Diffusion of Beryllium in Polycrystalline Unirradiated and Irradiated Beryllium Oxide	International Conference on Beryllium Oxide, Newport, Sydney, Australia, Oct. 21–25, 1963
Gill, J. S., and W. L. Marshall	Effect of Pressure on Liquid-Liquid Immiscibility in the System UO_2SO_4-H_2O and Liquid–Supercritical Fluid Equilibria in the System UO_2SO_4-H_2SO_4-H_2O; 290–430°C, 75–1800 Bars	Tennessee Academy of Science, Annual Meeting, Chattanooga, Tenn., Nov. 29–30, 1963
Hebert, G. M., and T. N. McVay	New Fluoride Compounds Predicted from Cation Size Considerations -- Synthesis and Properties	Tennessee Academy of Science, Annual Meeting, Chattanooga, Tenn., Nov. 29–30, 1963
Jenks, G. H.	Zircaloy-2 Corrosion In-Pile in Aqueous Homogeneous Reactor Solutions	American Nuclear Society, New York, Nov. 18–21, 1963
Johnson, G. L., D. R. Cuneo, H. F. McDuffie, and M. J. Kelly	Removal of Protactinium and Uranium from Thorium Nitrate–Nitric Acid Solutions	Protactinium Chemistry Symposium, Gatlinburg, Tenn., Apr. 25–26, 1963

AUTHOR(s)	TITLE	PLACE PRESENTED
Jones, E. V., and W. L. Marshall	Investigations on the System UO_3-Li_2O-SO_3-D_2O; Liquid-Liquid Immiscibility and Critical Phenomena, 300–410°C	Tennessee Academy of Science, Annual Meeting, Chattanooga, Tenn., Nov. 29–30, 1963
Keilholtz, G. W., J. E. Lee, Jr., R. E. Moore, and R. L. Hamner	Behavior of BeO Under Neutron Irradiation	International Conference on Beryllium Oxide, Newport, Sydney, Australia, Oct. 21–25, 1963
Keilholtz, G. W., J. E. Lee, Jr., and R. E. Moore	Effect of Radiation on Beryllium Oxide	United Kingdom Meeting under Libby/Cockcroft Information Exchange Agreement, Harwell, England, April 1–2, 1963
Keilholtz, G. W., J. E. Lee, Jr., and R. E. Moore	Effect of Radiation on Beryllium Oxide	U. S.–French BeO Information Exchange Meeting, Centre d'Etudes Nucleaires de Grenoble, France, April 8, 1963
Kirslis, S. S., F. F. Blankenship, and W. R. Grimes	Behavior of Noble Gases in Molten Fluoride Reactor Fuels	Conference on Inert Gas Compounds, Argonne National Laboratory, Apr. 22–23, 1963.
Kirslis, S. S., and F. F. Blankenship	Fluorine Generation in Solid Fluorides by Radiolysis	American Chemical Society, New York, Sept. 8–13, 1963
Kreyger, P. J., and S. S. Kirslis	Sessile Drops of Molten Halides on Graphite and Metals	American Chemical Society, Winter Meeting, Denver, Colo., Jan. 19–24, 1964
Levy, H. A., P. A. Agron, and J. H. Burns	Crystal and Molecular Structures of Xenon Fluorides	Sixth General Assembly of the International Union of Crystallography, Rome, Italy, Sept. 9–18, 1963
McDuffie, H. F., M. J. Kelly, G. L. Johnson, and D. R. Cuneo	Removal of Protactinium and Uranium from Thorium Nitrate–Nitric Acid Solutions	Protactinium Chemistry Symposium, Gatlinburg, Tenn., Apr. 25–26, 1963
Mamantov, Gleb	Electrochemical Studies in Molten Fluorides	7th Conference on Analytical Chemistry in Nuclear Technology, Gatlinburg, Tenn., Oct. 8–10, 1963
Mamantov, Gleb, and D. L. Manning	Voltammetry and Chronopotentiometry of Iron in Molten Fluorides	American Chemical Society, Southeastern Regional Meeting, Charlotte, N. C., Nov. 14–16, 1963
Marshall, W. L.	Effects of Pressure on Second Liquid Phase Formation from UO_2SO_4 Solutions, 0 to 1500 Atmospheres, 300C to 400C	International Congress of Pure and Applied Chemistry, 19th, London, July 10–17, 1963

AUTHOR(s)	TITLE	PLACE PRESENTED
Marshall, W. L.	Multicomponent Aqueous Systems, 300C to 450C	International Congress of Pure and Applied Chemistry, 19th, London, July 10–17, 1963
Osborne, M. F., J. G. Morgan, F. L. Carlsen, and J. A. Conlin	The Radiation Stability of UC_2, Graphite Matrix Fuels	American Nuclear Society, Annual Meeting, Salt Lake City, Utah, June 17–19, 1963
Parker, G. W., G. E. Creek, W. J. Martin, and C. J. Barton	Test of the Provisional Filtration-Adsorption Containment for an Aluminum Alloy Fueled Research Reactor	International Conference on the Radioactive Pollution of Gaseous Media, Saclay, France, Oct. 21–26, 1963
Parker, G. W.	A Review of Fission-Product-Release Research	American Nuclear Society, 9th Annual Meeting, Salt Lake City, Utah, June 19–21, 1963
Parker, G. W., and R. A. Lorenz	Fission Product Release from Meltdown of a Cluster of Center-Heated UO_2 Fuel Pins	American Nuclear Society, 9th Annual Meeting, Salt Lake City, Utah, June 19–21, 1963
Quist, A. S., H. R. Jolley, and W. L. Marshall	The First and Second Dissociation Constants of Sulfuric Acid to 600°C and 4000 Bars as Derived from Conductance Measurements	American Chemical Society, Winter Meeting, Denver, Colo., Jan. 19–24, 1964
Quist, A. S., and W. L. Marshall	The Electrical Conductance of Aqueous Electrolyte Solutions to 800°C and 4000 Bars	American Chemical Society, New York, Sept. 8–13, 1963
Rainey, W. T., Jr., L. B. Yeatts, Jr., D. N. Hess, and H. F. McDuffie	Kinetics of the Pyrolytic Decomposition of Polyphenyl Hydrocarbons	American Chemical Society, Southestern Regional Meeting, Charlotte, N. C., Nov. 14–16, 1963
Reagan, P. E., F. L. Carlsen, and R. M. Carroll	Fission-Gas-Release from Pyrolytic Carbon-Coated Uranium Carbide During Irradiation	American Nuclear Society, Annual Meeting, Salt Lake City, Utah, June 17–19, 1963
Richardson, D. M., and R. A. Strehlow	Gaseous Desorption at Low Pressures and Liquid Nitrogen Temperatures	10th National Vacuum Symposium, Boston, Oct. 16–18, 1963
Roberts, B. F.	A Procedure for Estimating Pore Volume and Area Distributions from Sorption Isotherms	American Chemical Society, New York, Sept. 8–13, 1963
Silverman, M. D., and W. E. Browning, Jr.	Fibrous Filters as Particle Analyzers	American Nuclear Society, New York, Nov. 17–19, 1963
Shaffer, J. H., and H. F. McDuffie	Moisture Removal from Graphites by Purging with Dry Helium Below 700°C	American Nuclear Society, New York, Nov. 18–21, 1963

AUTHOR(s)	TITLE	PLACE PRESENTED
Shaffer, J. H., G. M. Watson, D. R. Cuneo, J. E. Strain, and M. J. Kelly	Recovery of Uranium and Protactinium from Molten Fluoride Systems by Precipitation as Oxides	Protactinium Chemistry Symposium, Gatlinburg, Tenn., Apr. 25–26, 1963
Shields, R. P., W. E. Browning, Jr., C. E. Miller, Jr., and B. F. Roberts	Release of Fission Products During In-Pile Burning of UC_2-Graphite Fuel	American Nuclear Society, Salt Lake City, Utah, June 17–19, 1963
Shields, R. P., W. E. Browning, Jr., C. E. Miller, Jr., and B. F. Roberts	Release of Fission Products on the In-Pile Melting or Burning of Reactor Fuels	8th AEC Air Cleaning Conference, ORNL, Oak Ridge, Tenn., Oct. 22–25, 1963
Steinfink, H., and J. H. Burns	The Crystal Structure of Cr_2F_5	Sixth General Assembly of the International Union of Crystallography, Rome, Italy, Sept. 9–18, 1963
Sturm, B. J., and R. E. Thoma	Application of Visual Observation Furnace for Studies of Phase Equilibria at High Temperature	American Chemical Society, Southeastern Regional Meeting, Charlotte, N. C., Nov. 14–16, 1963
Thoma, R. E., G. M. Hebert, H. Insley, and C. F. Weaver	Liquid-Solid Equilibria Among NaF-YF_3 Phases	XIXth Congress of Pure and Applied Chemistry, London, England, July 10–17, 1963
Thoma, R. E., G. M. Hebert, H. Insley, and C. F. Weaver	Order-Disorder Effects and Solid Solutions in the System NaF-YF_3	Third Rare-Earth Conference, Clearwater, Fla., Apr. 21–24, 1963

ORNL-3591
UC-4 – Chemistry
TID-4500 (28th ed.)

INTERNAL DISTRIBUTION

1. Biology Library
2-4. Central Research Library
5. Reactor Division Library
6. Laboratory Shift Supervisor
7-8. ORNL – Y-12 Technical Library
Document Reference Section
9-58. Laboratory Records Department
59. Laboratory Records, ORNL R.C.
60. C. E. Larson
61. A. M. Weinberg
62. J. A. Swartout
63-77. G. E. Boyd
78. F. R. Bruce
79. W. H. Jordan
80. H. G. MacPherson
81. A. H. Snell
82. G. Young
83. A. L. Boch
84. R. B. Briggs
85. K. A. Kraus
86. J. A. Lane
87. H. C. McCurdy
88. G. D. Whitman
89. M. Bender
90. D. S. Billington
91. F. L. Culler
92. J. H Frye, Jr.
93. M. T. Kelley
94. E. H. Taylor
95. S. E. Beall
96. M. A. Bredig
97. L. T. Corbin
98. J. E. Cunningham
99. J. H. Crawford
100. A. P. Fraas
101. E. M. King
102. R. N. Lyon
103. A. J. Miller
104. J. C. White
105. M. J. Skinner
106. W. R. Grimes
107. E. G. Bohlmann
108. H. F. McDuffie
109. G. M. Watson
110. F. F. Blankenship
111. C. H. Secoy
112. C. F. Baes
113. C. J. Barton
114. W. E. Browning
115. J. H. Burns
116. S. Cantor
117. R. M. Carroll
118. E. L. Compere
119. R. B. Evans III
120. J. C. Griess
121. G. H. Jenks
122. G. W. Keilholtz
123. M. J. Kelly
124. G. Long
125. W. L. Marshall
126. C. E. Miller
127. J. G. Morgan
128. L. G. Overholser
129. G. W. Parker
130-131. R. B. Parker
132. W. W. Parkinson
133. W. T. Rainey
134. H. C. Savage
135. J. H. Shaffer
136. O. Sisman
137. R. A. Strehlow
138. R. E. Thoma
139. D. B. Trauger
140-151. G. C. Warlick
152. C. F. Weaver
153. G. C. Williams
154. L. Brewer (consultant)
155. F. Daniels (consultant)
156. R. W. Dayton (consultant)
157. J. W. Cobble (consultant)
158. J. F. Eastham (consultant)
159. P. H. Emmett (consultant)
160. D. G. Hill (consultant)
161. H. Insley (consultant)
162. H. R. Jolley (consultant)
163. E. V. Jones (consultant)
164. T. N. McVay (consultant)
165. G. Mamantov (consultant)
166. E. A. Mason (consultant)
167. R. F. Newton (consultant)
168. R. B. Perez (consultant)
169. J. E. Ricci (consultant)
170. G. Scatchard (consultant)
171. D. A. Shirley (consultant)
172. H. Steinfink (consultant)

EXTERNAL DISTRIBUTION

173. R. W. McNamee, Union Carbide Corporation, New York
174. Research and Development Division, AEC, Washington
175. Research and Development Division, AEC, ORO
176. Reactor Development Division, AEC, Washington
177. Reactor Development Division, AEC, ORO
178. Union Carbide and Carbon Chemicals Company, South Charleston
179-769. Given distribution as shown in TID-4500 (28th ed.) under Chemistry category (75 copies – OTS)